Turbine Engine Hot Section Technology 1984

NASA

Turbine Engine Hot Section Technology 1984

NASA

FOREWORD

Aircraft gas turbine engine designs have been pushed to ever higher levels of performance, primarily due to competition and the need for improved fuel efficiency. The resulting higher pressures and temperatures have led to a decrease in engine durability. In hot section components - the combustor and turbine - the more hostile environments have accelerated the damage and wear of parts, with subsequent dramatically increased maintenance costs. In the past, minimal efforts have been made to assure required durability, since technology advances have been directed primarily toward improving performance.

The activities of the NASA Turbine Engine Hot Section Technology (HOST) Project are directed toward durability needs, as defined by industry, and a more balanced approach to engine design. The HOST efforts will improve the understanding and prediction of aerothermal environments and material structural responses by focused experimental and analytical research activities. The overall approach is to assess existing analysis methods for strengths and deficiencies, conduct supporting analytical and experimental research to rectify the deficiencies, incorporate state-of-the-art improvements into the analysis methods, and finally verify the improvements by systematic test programs. The research is supported by the Project with contracts, grants, and Lewis in-house activities.

To provide representatives from government, industry, and academia with the latest findings and progress toward improved aircraft turbine engine durability, a two-day workshop was held in October 1984. This publication contains the papers presented at the workshop.

Daniel E. Sokolowski
Manager, HOST Project

CONTENTS

OVERVIEWS

INSTRUMENTATION

SURFACE PROTECTION

COMBUSTION

STRUCTURAL ANALYSIS

FATIGUE AND FRACTURE

TURBINE HEAT TRANSFER

TURBINE ENGINE HOT SECTION TECHNOLOGY (HOST) PROJECT

Daniel E. Sokolowski and C. Robert Ensign
National Aeronautics and Space Administration
Lewis Research Center

The Hot Section Technology (HOST) Project is a NASA-sponsored endeavor to improve the durability of advanced gas turbine engines for commercial and military aircraft. Through improvements in the analytical models and life prediction systems, designs for future hot section components - the combustor and turbine - will be analyzed more accurately and will incorporate features required for longer life in the more hostile operating environment of high performance engines.

Started in 1981, the HOST Project has activities planned through 1988 with an estimated total cost of over $50 million. While the Project's focused research activities are necessarily analytical in nature, significant experimental testing is required for benchmark quality assessments as well as model verifications. The efforts are being conducted inhouse at the NASA Lewis Research Center, under contracts with major domestic turbine engine manufacturers and under grants to qualified universities. Currently, the contract and grant funding equals about 55 percent of the total budget for FY 1985.

At the NASA Lewis Research Center, the HOST Project Office serves as the focal point for advocacy, funding, technical coordination, and information exchange. This workshop serves as the primary vehicle for this last function; that is, to disseminate information and elicit the exchange of ideas among participants.

Basic activities of the HOST Project are categorized under six disciplines as shown in figure 1. The six disciplines are (1) Instrumentation, (2) Combustion, (3) Turbine Heat Transfer, (4) Structural Analysis, (5) Fatigue and Fracture, and (6) Surface Protection. Management of the project uses the matrix approach as shown in figure 2. A Subproject Manager is responsible for each discipline and reports to the Manager of the HOST Project Office.

To further understand the organization of the Project and, more importantly, the reasons for its activities, it is useful to review the critical steps leading to life prediction. The flow diagram in figure 3 shows such critical steps and may be used for any hot section subcomponent, for example, liners, blades, or vanes. The first series of steps (see fig. 4) defines the engine subcomponent geometry, material, and operating requirements. Shown in figure 5 are the steps which lead to characterizations of the subcomponent environment along with the thermal and mechanical loads. Activities in the first three disciplines, Instrumentation, Combustion, and Turbine Heat Transfer, support these characterizations. The next steps, shown in figure 6, determine the material and structural behavior due to the above imposed loads. Activities primarily in Structural Analysis provide for these determinations. Finally, prediction of subcomponent life, shown in figure 7, is supported by activities in Fatigue and Fracture as well as Surface Protection.

Activities under each discipline represent research which is focused on improving life prediction and, in turn, subcomponent durability. To summarize the

activities supported by the HOST Project and reported herein, instrumentation is being developed to obtain high temperature, benchmark quality data to develop and verify analysis methods. These include flow sensors (LDV), heat flux sensors (thin film), strain sensors (1800° F static thin film), gas temperature sensors (frequency compensated), and hot section optical viewing systems. Combustion work includes aerothermal model assessment and development, dilution jet modeling, high pressure flame radiation/heat flux testing, and development of a thermal structural cyclic test facility. Turbine Heat Transfer is studying two- and three-dimensional flow and heat transfer on airfoil external boundaries, emphasizing boundary layer transition and viscous modeling. It also investigates coolant passage heat transfer, including midchord jet impingement cooling and rotational passage effects. Structural Analysis includes research into thermal mechanical load models, component geometry specific models, and three-dimensional inelastic analysis methods development. Fatigue and Fracture includes constitutive model development for both isotropic and anisotropic materials, including single crystal and directionally solidified forms. It also includes research in life prediction methods for creep-fatigue interactions, and elastoplastic crack propagation. The Surface Protection research includes studies of corrosion and oxidation phenomena, environmental mechanics models, and metallic and thermal barrier coating analysis method developments.

Workshop publications and most contractor final reports carry the label "For Early Domestic Dissemination" (FEDD) to protect national interests and, thus, are available only to qualified U.S. citizens. Several contractor final reports have been published. However, they often represent initial phases of multiphased work. Thus, this annual workshop report is the primary document for reporting technical results for the entire Project.

WORK BREAKDOWN STRUCTURE
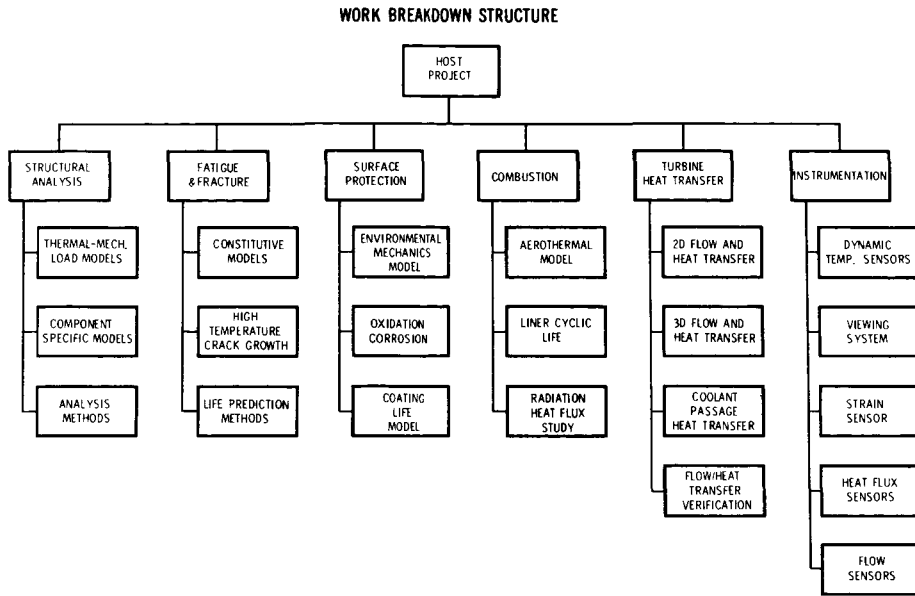
Figure 1

ORGANIZATION: HOT SECTION TECHNOLOGY (HOST) PROJECT
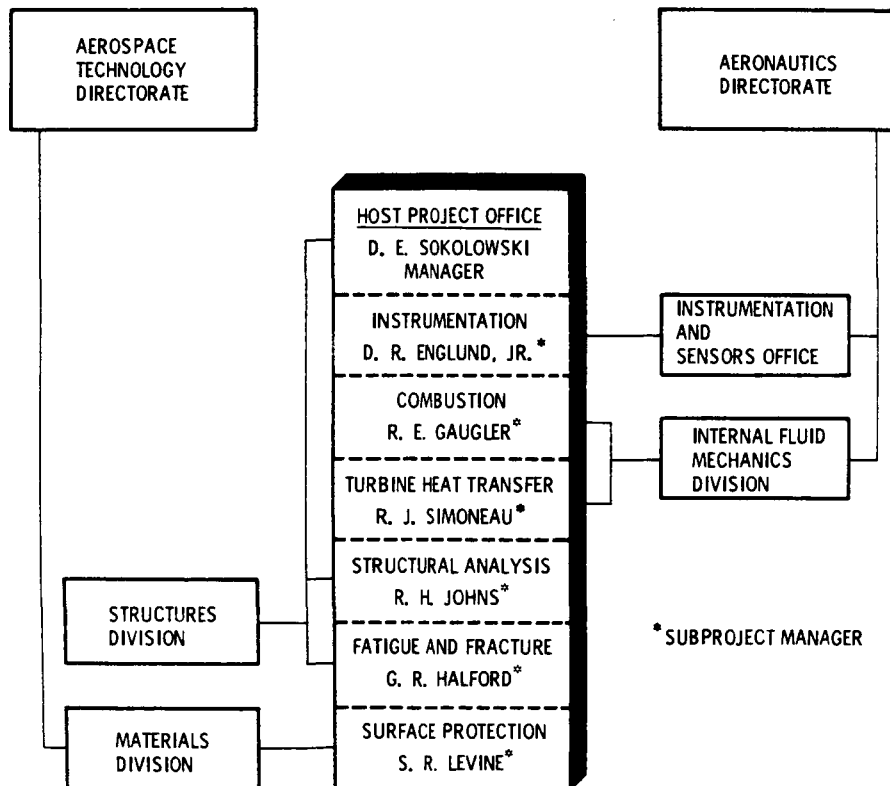
Figure 2

LIFE PREDICTION
FOR
TURBINE ENGINE HOT SECTION SUBCOMPONENTS
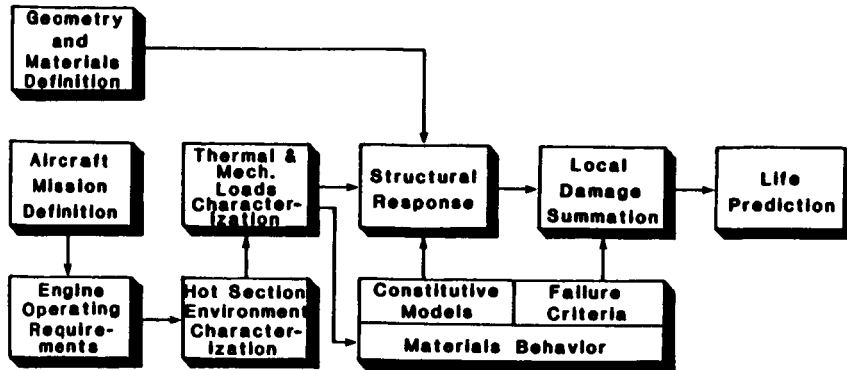
Figure 3

DEFINITION OF ENGINE PART AND OPERATION

Figure 4

CHARACTERIZATION OF HOT SECTION ENVIRONMENT & LOADS

```
┌─────────────┐
│ Thermal &   │
│   Mech.     │
│   Loads     │
│ Character-  │
│  ization    │
└─────────────┘
      ▲
      │
┌─────────────┐
│ Hot Section │
│ Environment │
│ Character-  │
│  ization    │
└─────────────┘
```
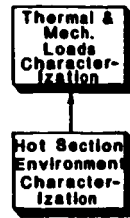
Figure 5

DETERMINATION OF MATERIAL AND STRUCTURAL BEHAVIOR

```
┌─────────────┐
│ Structural  │
│  Response   │
└─────────────┘
      ▲
      │
┌──────────────┬──────────────┐
│ Constitutive │   Failure    │
│   Models     │   Criteria   │
├──────────────┴──────────────┤
│    Materials  Behavior       │
└──────────────────────────────┘
```
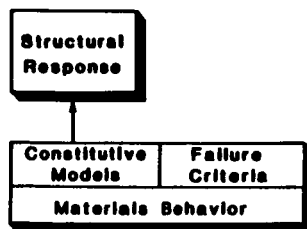
Figure 6

PREDICTION OF SUBCOMPONENT LIFE

```
┌──────────┐      ┌────────────┐
│  Local   │      │    Life    │
│  Damage  │ ───▶ │ Prediction │
│Summation │      │            │
└──────────┘      └────────────┘
```
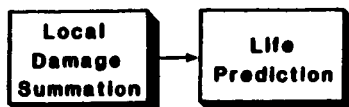
Figure 7

HOST INSTRUMENTATION R&D PROGRAM OVERVIEW

D. R. Englund
National Aeronautics and Space Administration
Lewis Research Center

The HOST Instrumentation R&D program is directed at the development of two categories of instrumentation. One is instrumentation capable of characterizing the environment imposed on turbine engine hot-section components. This category includes instruments for the measurements of gas flow, gas temperature, and heat flux. The second category is instrumentation to measure the effect of the environment on the hot-section components. This category includes strain measuring instruments and an optical system capable of providing interior views of a burner liner during operation.

The HOST Instrumentation R&D program was formulated to concentrate on critical measurements that could not be made with available instruments or with instruments under development via NASA- or DOD-funded programs, or with IR&D programs. In the past year we have added one project to the program: a university grant to study electrical resistance of high-temperature materials which have potential for use in high-temperature strain gauges. The intent is to gain a better understanding of the factors which affect the resistance, the repeatability of resistance with time and temperature cycles, and the temperature coefficient of resistance. This study was started in January 1984.

The schedule for the HOST Instrumentation R&D program is shown in the accompanying figure. This schedule shows both HOST-funded and non-HOST-funded efforts that have HOST-related goals. Each line represents a separate effort, either contract, grant, or in-house work. In two of these efforts, the dynamic gas temperature measuring system and the turbine blade/vane static strain gauge, follow-on work is indicated. In addition, two of the efforts have been completed. The combustor viewing system was described in the 1983 HOST Conference in some detail and will not be discussed this year. The test schedule for this system was stretched out in order to include tests on an operating engine. The final report on this contract will be available later this year. The second effort to be completed is the non-HOST-funded burner liner strain measurement experiment. In this experiment measurements of strain in the knuckle region of a JT12 burner can were attempted using both a laser speckle strain measuring system and FeCrAl alloy wire strain gauges. The laser speckle
strain measuring system was not successful because high-pressure turbulent gas within the viewing path caused excessive distortion of the specklegrams. This problem was anticipated, but its magnitude could not be assessed prior to the experiment. Results from the wire strain gauge work are discussed in the instrumentation session of this conference. A final report on this contract will be available this fall.

HOST INSTRUMENTATION R&D PROGRAM

SHOWING ACTIVE EFFORTS AS OF 10/83

MEASUREMENT	FISCAL YEAR						GOAL
	1980	1981	1982	1983	1984	1985	
VIEWING SYSTEM							HIGH-TEMPERATURE SYSTEM FOR VIEWING COMBUSTOR INTERIORS DURING OPERATION
GAS TEMPERATURE							DYNAMIC GAS TEMPERATURE MEASUREMENT SYSTEM WITH 1 kHz RESPONSE
STRAIN							TURBINE BLADE/VANE STATIC STRAIN GAUGE
							BURNER LINER STATIC STRAIN MEASUREMENT SYSTEM
							HIGH TEMPERATURE STRAIN GAUGE MATERIALS
HEAT FLUX							BURNER LINER TOTAL HEAT FLUX SENSOR
							TURBINE BLADE/VANE TOTAL HEAT FLUX SENSOR
GAS FLOW							LASER ANEMOMETER SYSTEM FOR HIGH-PRESSURE HIGH-TEMPERATURE FLOWS
							OPTIMIZATION OF LASER ANEMOMETER SYSTEMS

HOST STRUCTURAL ANALYSIS PROGRAM

OVERVIEW

by

R. H. Johns, Subproject Manager

Hot section components of aircraft gas turbine engines are subjected to severe thermal-structural loading conditions, especially during the start-up and take-off portions of the engine cycle. The most severe and damaging stresses and strains are those induced by the steep thermal gradients induced during the start-up transient. These transient stresses and strains are also the most difficult to predict, in part because the temperature gradients and distributions are not well known or readily predictable, and also because the cyclic elastic-viscoplastic behavior of the materials at these extremes of temperature and strain are not well known or readily predictable.

A broad spectrum of structures-related technology programs is underway to address these deficiencies. The problems are being addressed at the basic as well as the applied level, including participation by industry and universities as well as in-house at NASA Lewis. In addition to the HOST structural analysis program, some related program elements are being supported through our Base R&T program.

One element of the structures program is developing improved time-varying thermal-mechanical load models for the entire engine mission cycle from start-up to shutdown. The thermal model refinements will be consistent with those required by the structural code including considerations of mesh-point density, strain concentrations, and thermal gradients. Models will be developed for the burner liner, turbine vane and turbine blade. One aspect of this part of the program is a thermal data transfer module recently developed which automates the transfer of temperatures from available heat transfer codes or experimental data sets to the structural analysis code. Another part of the program is an automated component-specific geometric modeling capability which will produce 3-D finite element models of the components. Self-adaptive solution strategies will be developed and included to facilitate selection of appropriate elements, mesh sizes, etc.

Another major part of the program is the development of new and improved nonlinear 3-D finite elements and associated structural analysis programs, including the development of temporal elements with time-dependent properties to account for creep effects in the materials and components. Two contracts were recently signed to accomplish these developments. Improved constitutive modeling methods to facilitate improved prediction of cyclic thermomechanical viscoplastic material behavior are also under development. Experimental facilities to aid in developing and verifying theories and models are currently being established in-house at Lewis.

Further explanation and details about the various structures program elements mentioned above are given in the following write-ups.

STRUCTURAL ANALYSIS...IT'S ROLE IN HOST

GOAL:

DEVELOP AND VALIDATE INTEGRATED TIME-VARYING THERMOMECHANICAL LOAD MODELS, COMPONENT-SPECIFIC AUTOMATED GEOMETRIC MODELING AND SOLUTION STRATEGY CAPABILITIES, AND ADVANCED INELASTIC ANALYSIS METHODS INCLUDING PLASTICITY AND CREEP EFFECTS FOR NONLINEAR ANISOTROPIC FINITE ELEMENT STRUCTURAL ANALYSIS AND DESIGN COMPUTER CODES FOR TURBINE ENGINE HOT SECTION COMPONENTS

PROGRAM INTEGRATION

```
              MATERIALS
              BEHAVIOR
                  │
THERMOMECHANICAL  │   ANALYSIS METHODS
LOADS MODELING    │   FOR LIFE PREDICTION
                  │
            STRUCTURAL ANALYSIS
              AND MODELING

            LAB SPECIMEN TESTS
          AND MODEL VALIDATION
```
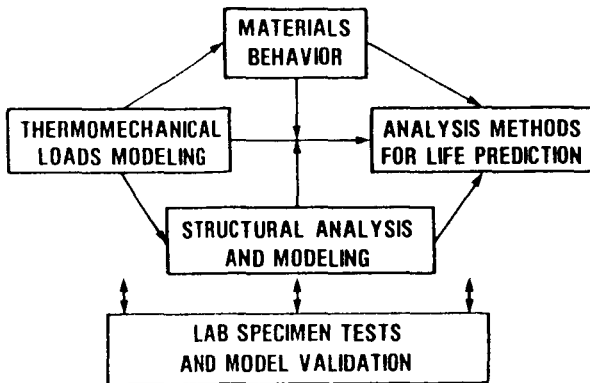
PROGRAM ELEMENTS:

- THERMAL/STRUCTURAL DATA TRANSFER MODULE

- THERMAL/MECHANICAL LOAD/MISSION AND COMPONENT-SPECIFIC STRUCTURAL MODELS

- 3-D INELASTIC ANALYSIS METHODS

- BURNER LINER CYCLIC RIG (STRUCTURAL ASPECTS)

- HIGH TEMPERATURE STRUCTURES LABORATORY   CS-83-0643

HOST

STRUCTURAL ANALYSIS PROGRAM

OBJECTIVE:

TO DEVELOP AND VALIDATE INTEGRATED TIME-VARYING THERMAL/MECHANICAL LOAD MODELS, COMPONENT-SPECIFIC AUTOMATED GEOMETRIC MODELING AND SOLUTION STRATEGY CAPABILITIES, AND ADVANCED INELASTIC ANALYSIS METHODS AND CONSTITUTIVE MODELS, INCLUDING PLASTICITY AND CREEP EFFECTS, FOR NONLINEAR, ANISOTROPIC, FINITE ELEMENT STRUCTURAL ANALYSIS AND DESIGN COMPUTER CODES.

STRUCTURAL ANALYSIS

PROGRAM ELEMENT	FISCAL YEAR							EXPECTED RESULT
	81	82	83	84	85	86	87	
THERMAL DATA TRANSFER		(C)						COMPUTER MODULE LINKING THERMAL AND STRUCTURAL ANALYSES
COMPONENT SPECIFIC MODELING			(C)			▼		COMPONENT-RELATED, TIME VARYING, THERMAL-MECHANICAL LOAD HISTORY & GEOMETRIC MODELS
3-D INELASTIC ANALYSIS			(C)	▼				ADVANCED 3-D INELASTIC STRUCTURAL/ STRESS ANALYSIS METHODS AND SOLUTION STRATEGIES
LINER CYCLIC RIG		(IH)						BURNER STRUCTURAL/LIFE EXPERIMENTS
HIGH-TEMPERATURE STRUCTURES LAB		(IH)						INTEGRATED EXPERIMENTAL /ANALYSIS RESEARCH
MATERIAL BEHAVIOR TECHNOLOGY		(IH)						CONSTITUTIVE THEORY & MODELING METHODS

HOT SECTION COMPONENTS REQUIRING 3-D INELASTIC ANALYSIS
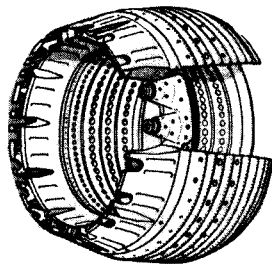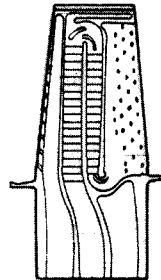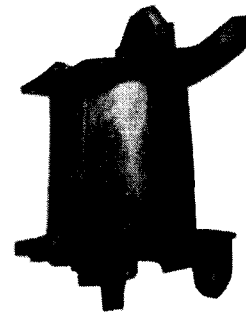
COMBUSTOR LINER   TURBINE BLADE   TURBINE VANE

CS-83-0641

11

BURNER LINER THERMAL LOAD TRANSFER MODULE (HOST)

EXPERIMENTAL COMBUSTOR LINER TEMPERATURES

STAGES OF MODEL DEVELOPMENT FOR COMBUSTOR LINER

$(T,t)_1$ $(T,t)_2$ $(T,t)_3$ ...

(T,t) $(T,t)_{n-1}$ $(T,t)_n$

A. GEOMETRIC MODEL DEFINITION

B. DISCRETE MODEL DEFINITION-COARSE MESH

C. DISCRETE MODEL DEFINITION-FINE MESH

| HEAT TRANSFER CODE | | DATA TRANSFER MODULE | | STRUCTURAL ANALYSIS CODE |

TEMPERATURE CONTOUR PLOTS

STRESS/STRAIN CONTOUR PLOTS

CS-83-0648

COMPONENT—SPECIFIC MODELING (HOST)

GEOMETRIC MODELING

THERMO-MECHANICAL LOAD MODELS

HIGH TEMPERATURES, COMPLEX GEOMETRY

HIGH GAS PRESSURES, CENTRIFUGAL FORCE, STEEP TEMP. GRADIENTS

SELF-ADAPTIVE SOLUTION STRATEGIES

MISSION MODELING

CS-83-0640

3-D INELASTIC ANALYSIS (HOST)

3-NONLINEAR CONSTITUTIVE RELATIONS
- APPROXIMATE
- STATE-OF-THE-ART
- FUNCTIONAL

4-DIFFERENT FORMULATIONS
- LINEAR SEGMENTS
- POLYNOMIAL
- SPECIAL FUNCTIONS
- GENERAL FUNCTIONS

3-DIFFERENT THEORIES
- MECHANICS OF MATERIALS
- SPECIAL F. E.
- ADVANCED

VALIDATION/VERIFICATION
- TURBINE BLADE
- TURBINE VANE
- BURNER LINER

CS-83-0639

AUTOMATED HIGH TEMPERATURE STRUCTURES RESEARCH LABORATORY

UNIAXIAL

BIAXIAL

MULTIAXIAL

MINI

MINI

MINI

CONST. REL. EXP. DATA GENERATION

COMPUTED STATE

CONST. REL. UPDATES

HOST SUPERMINI

SUPERMINI MODEL (RE) GENERATOR

SOLVER (MAINFRAME) CLASS VI

CS-83-0649

13
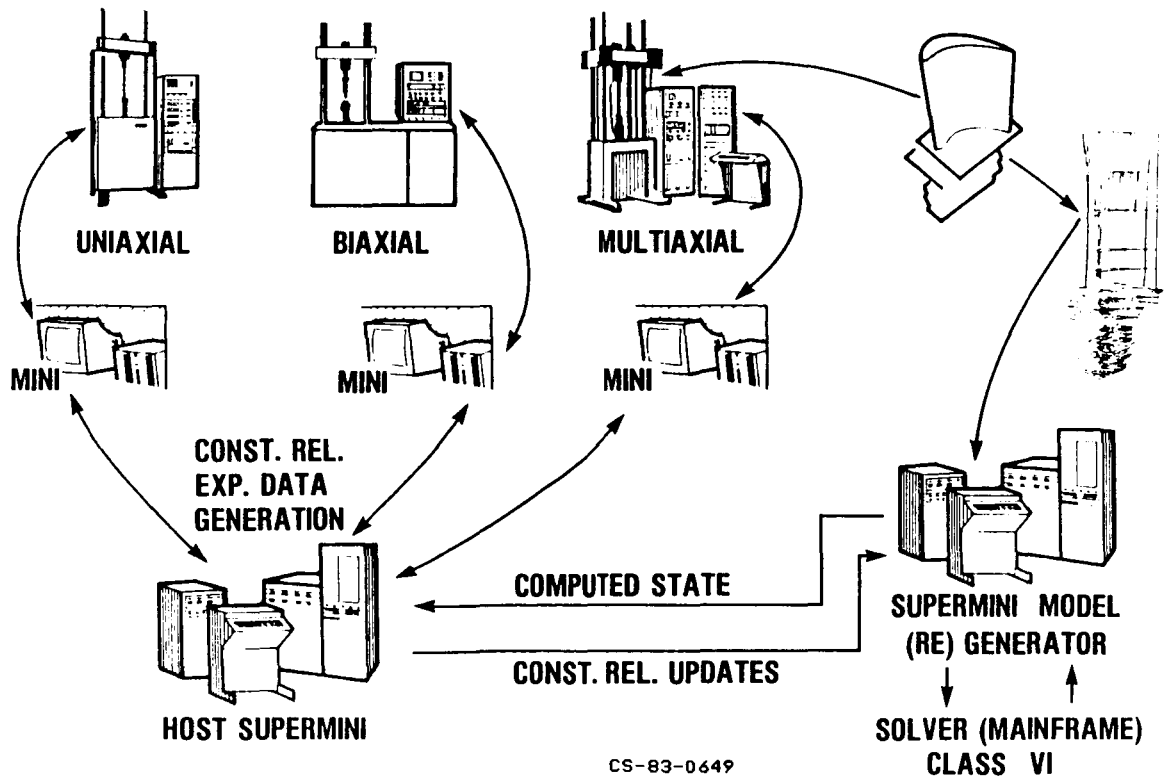
COMBUSTION OVERVIEW

Donald F. Schultz
National Aeronautics and Space Administration
Lewis Research Center

The objective of this effort is to develop improved analytical models of the internal combustor flow field and liner heat transfer as a means to shorten combustor development time and increase turbine engine hot section life.

A four-element approach has been selected to meet this objective. First, existing models were utilized to determine their deficiencies. Supporting research was then commenced to improve the existing models. While the research effort is in progress, the models are being refined to improve numerics and numerical diffusion. And lastly, the research results and improved numerics will be integrated into existing models.

This work has been divided into seven tasks illustrated in the schedule in figure 1. One task has been completed, The Aerothermal Modeling Assessment, and one task has been suspended because of test facility closing, The Flame Radiation/Heat Flux Experiment. A new task has been added in the past year, Diffuser Studies, a jointly funded project with the Air Force. This task will be an advanced diffuser combustor analytical code.

CONTRACTOR EFFORTS

AEROTHERMAL MODELING ASSESSMENT
Aerothermal Modeling - Phase I

This work was performed under three contracts, by the following contractors and principal investigators:

Contractor	Principal investigator
Garrett Turbine Engines	R. Srinivasan
General Electric Company	M. K. Kenworthy
Pratt & Whitney Aircraft	G. J. Sturgess

A consensus of major results indicated four shortcomings in the existing models. First, faster convergence techniques via improved numerical schemes are required, as is an improved three-dimensional code coordinate system. These two are vitally necessary to reduce the size of computers required to perform the convergences. The other two shortcomings are a more accurate hot gas heat transfer input and improved turbulence and turbulence/chemistry treatment.

Status: This task has been completed. All results were published in early 1984.

COMBUSTION MODELING DEVELOPMENT
Aerothermal Modeling - Phase II

The objective of this element is to address the modeling shortcomings determined in the Aerothermal Modeling Assessment. Both analytical and experimental research will be conducted. The approaches include: incorporation of a new finite difference scheme or error reduction formula into a currently existing numerical model and experimental work to generate benchmark quality test data in the area of three-dimensional aerodynamics and combustor dynamics.

It is the intent to award five contracts under this task. These would be awarded under the following proposed titles:

Improved Numerical Methods I
Improved Numerical Methods II
Flow Interaction Experiment
Fuel Swirl Characterization I
Fuel Swirl Characterization II

Status: Contracts awarded in September 1984.

DILUTION JET ANALYSIS AND MULTIPLE JET DILUTION MIXING

The objective here is to develop correlating expressions for jet mixing in gas turbine combustors that will aid in the design of combustors and directly aid in the reduction of combustor exhaust temperature pattern factor.
A contracted study will be used to investigate the penetration and mixing of various combinations of combustor dilution jets. Effects of hole size, spacing, momentum ratio, and hole geometry are being studied, as are combustor geometric design parameters such as flow acceleration, and pressure drop is being experimentally investigated. The effects of opposed and staggered-opposed jets are being studied.

This work is being performed both under contract and as an in-house effort. The principal investigators are R. Srinivasan of Garrett Turbine Engines and J. Holdeman of NASA Lewis Research Center.

Status: Work in progress; contract effort to be completed in FY 1985.

DIFFUSER STUDIES

The objective of the Diffuser Studies is to perform analysis and diagnostic experiments necessary to develop and improve analytic models that will accurately predict the combustor-diffuser flow field for advanced aircraft turbine engines. The approach is to apply existing codes to a baseline diffuser and select the most promising. This code will be updated to handle a variety of geometric changes. The updated code will then be used to design a full annular diffuser which will be used to demonstrate and assess improved modeling capabilities.

It is a jointly funded NASA - Air Force project.

Status: Contract to be awarded in early FY 1985.

FLAME RADIATION AND HEAT FLUX STUDIES

Principal Investigator, J. Wear

The objective of the Flame Radiation and Heat Flux Studies is to generate fundamental data and develop correlations needed to improve design analysis for the calculation of radiant heat transfer to combustor liner walls. This task utilized a full annular combustor designed for operation at pressures in excess of 30 atmospheres. Testing was conducted to inlet pressures of 20 atmospheres. The effects of combustor inlet conditions and fuel type were determined. Unique features included the ability to vary the primary zone fuel-air ratio while maintaining constant overall pressure loss. Both ASTM Jet A and ERBS II fuels were utilized in this program. Special instrumentation used in this program included total radiation instruments and heat flux gages, which were arranged in both axial and circumferential patterns on the outer liner.

At 15 atmospheres and 0.04 fuel-air ratio overall, 90 percent of the total heat flux was by radiation as opposed to only 40 percent at a 0.0015 fuel-air ratio. Also, total heat flux was proportional to overall fuel-air ratio in a range of pressures from 5 to 15 atmospheres.

Status: Program suspended because of test facility closing.

LINER CYCLIC TEST RIGS

The objective of the Liner Cyclic Test Rigs is to design a combustor liner low cycle thermal fatigue test facility that duplicates the actual engine creep low cycle fatigue interaction phenomena and to thermally cycle combustor liners to failure to provide data to evaluate and improve structural analysis models.

This project utilizes two test rigs, both of which operate at atmospheric pressure. One is a 5- by 8-inch flat plate cyclic rig, a totally in-house effort that serves as a test bed for special instrumentation, facility operation, and data reduction. It is shown in operation in figure 2. The principal investigators are D. Schultz from Combustion and R. Thompson from Structures. The second apparatus is a 21-inch-diameter outer liner cyclic rig shown in figure 3. This rig is being operated under a cooperative agreement with Pratt & Whitney Aircraft. Thus, in addition to Messrs. Schultz and Thompson of NASA, G. Pfeifer of Pratt & Whitney Aircraft is also a coinvestigator on this project.

Under terms of the cooperative agreement, Pratt & Whitney Aircraft supplies the test rig and NASA supplies the test facility and services. The data are shared by both.

Three flat plate cyclic rigs have been tested to date. The first rig, a three 6-kVA lamp installation, was operated under adverse conditions to determine feasibility of using quartz lamps for cyclic testing. This work, performed in December 1981, looked promising.

The second flat plate rig, again using three 6-kVA lamps, was operated to obtain instrumentation durability information and initial data input into a finite element model. This limited test program was conducted in August 1983. Five test

plates were run. Instrumentation consisted of strain gages, thermocouples, and thermal paint. The strain gages failed at 1200° F, as expected, though plates were heated to 1700° F.

The third box rig, containing four 6-kVA lamps, is presently operational. In addition to 33 percent greater power input, this rig has provision for 400° F back-side liner cooling air and a viewing port suitable for infrared television viewing. The casing is also water cooled for extended durability.

The 21-inch-diameter outer liner simulator uses one hundred twelve 6-kVA lamps to heat the test liner cyclicly. Power levels will be adjusted to simulate typical liner heat loadings. Air will be supplied to provide typical liner film and back-side cooling. In addition to the test liners being supplied by P&W, which are pro-duction configurations, several liners will be tested to obtain confidence in the finite element model. These will consist of simple shapes, such as cylinders, and cylinders with rows of holes.

This apparatus, in addition to drawing up to 672 kVA of 480 V power, requires 7.5 lb/sec of 500° F air at 35 psia, 3.5 lb/sec of ambient temperature air at 5 psig, 1.5 lb/sec of ambient temperature air at 1 psig, and 80 gal/min of specially treated cooling water.

Special features of the latest rigs include an infrared television system for measuring backside liner temperatures without distortions caused by thermocouple lead wires, and high temperature strain gages both special 1300° F wire strain gages and laser specklegram strain systems.

Status: The bench rig is operational, while the annular rig is in startup checkout.

COMBUSTION PROGRAM SCHEDULE

PROGRAM ELEMENT	FISCAL YEAR							EXPECTED RESULT
	81	82	83	84	85	86	87	
AEROTHERMAL MODELING ASSESSMENT								KEY MODEL AND DATA DEFICIENCIES IDENTIFIED
COMBUSTION MODELING DEVELOPMENT								NEW PHYSICAL MODELS AND COMPUTING METHODS
MULTIPLE JET DILUTION MIXING								EXIT TEMPERATURE PROFILE PREDICTION TECHNOLOGY
DIFFUSER STUDIES								ADVANCED DIFFUSER COM- BUSTOR ANALYTICAL CODE
FLAME RADIATION/HEAT FLUX								HIGH PRESSURE FLAME RADIATION AND HEAT FLUX
DILUTION JET ANALYSIS								JET MIXING MODEL
LINER CYCLIC RIG								CYCLIC TEST FACILITY

Figure 1

OPERATING CYCLIC BENCH TEST RIG
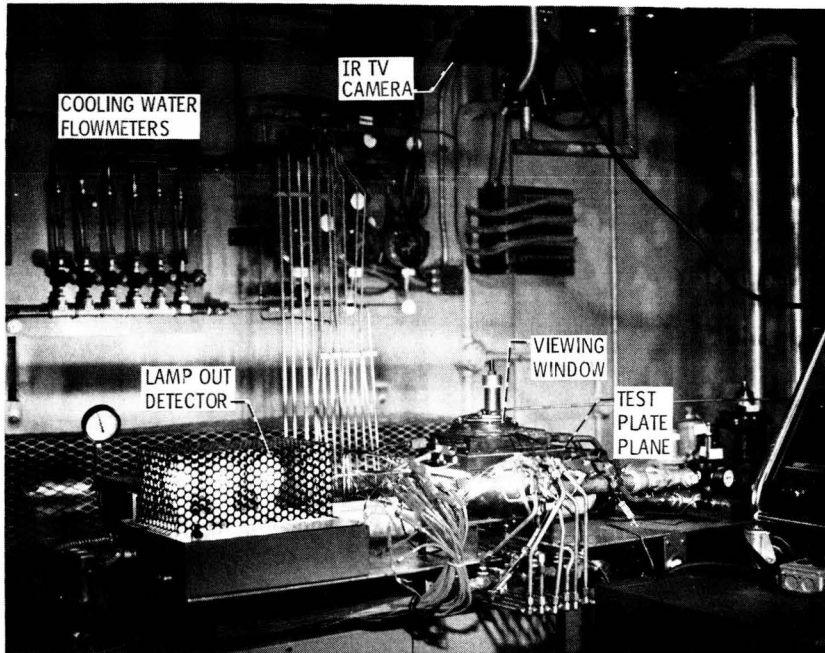
CS-84-3964

Figure 2

ANNULAR QUARTZ LAMP CYCLIC COMBUSTOR TEST RIG
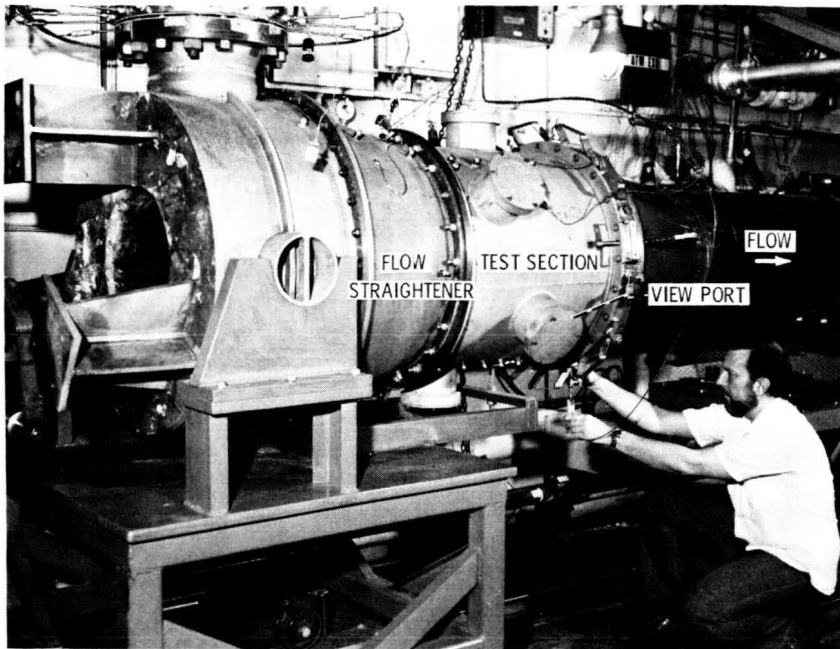
CS-84-3965
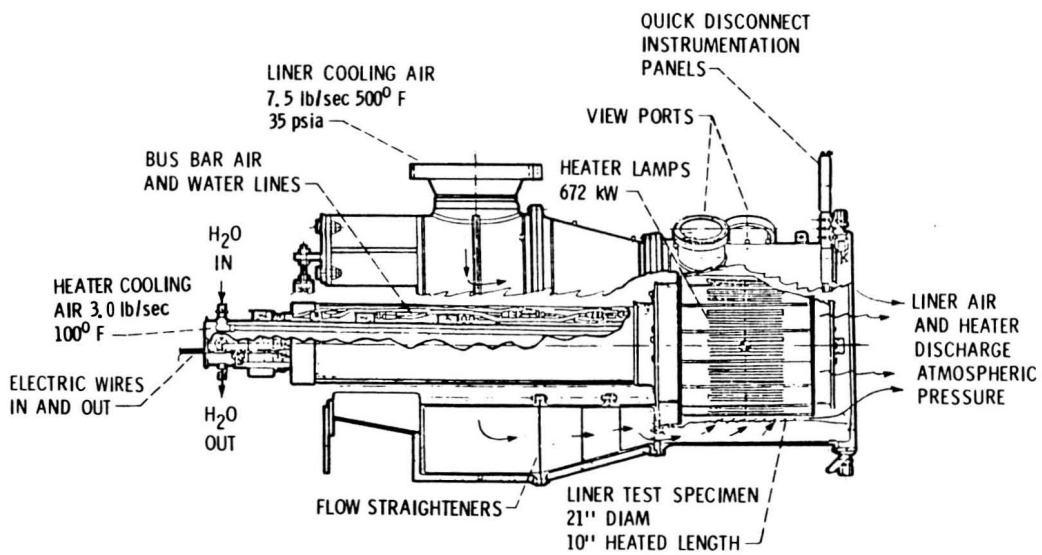
Figure 3

SURFACE PROTECTION

Stanley R. Levine
National Aeronautics and Space Administration
Lewis Research Center

INTRODUCTION

The hot section of an aircraft gas-turbine engine presents a severe chemical environment due to the presence of available oxygen and nitrogen under kinetically favorable conditions as well as due to the occasional presence of potentially more aggressive air-borne and fuel-borne impurities which can be collected as corrosive salt deposits. Thus, (as shown in fig. 1) one must consider such phenomena as high-temperature oxidation, corrosion, and erosion of base metals and their protective coatings as well as the materials' creep and fatigue responses to imposed mechanical and thermal loads. The consequences of unexpected severe environmental attack are illustrated in figure 2. However, even less dramatic environmental attack degrades system efficiency, reduces life, and ultimately costs us money.

The chemical response and the mechanical response of hot-section materials are not isolated phenomena. The influence of the chemical response on the mechanical response (and vice versa) must be understood to adequately design a component. Thus, the goal of the surface protection subproject is to develop an integrated, environmental attack, life-prediction methodology for metaland ceramic-coated hot-section components. This scheme will consider environmental attack life prediction as well as the effects of environment and coatings on mechanical response. As illustrated in figure 3, thermal and mechanical loads are inputs, and the analysis methods result from studies of material behavior in laboratory and engine tests. The surface protection subproject consists of three major thrusts:

(1) Airfoil deposition model
(2) Metallic coating life prediction
(3) Thermal barrier coating (TBC) life prediction

The time frame for each of these thrusts and the expected outputs are displayed in figure 4. The airfoil deposition model will predict the location and potential severity of hot-corrosion attack of turbine airfoils by late 1987. The metallic coating life prediction effort will produce models to predict metallic coating life as well as, in conjunction with the fatigue and fracture subproject, the effects of the environment and coatings on mechanical response. Finally, the thermal barrier coating (TBC) life-prediction thrust, which has grown to maturity during the past year, will yield life-prediction tools to permit use of TBC in the performance improvement mode. Such aggressive TBC use places the burden for component integrity on the life of the coating, and therefore progress of this technology is life-prediction-capability critical. Figure 5 gives further details of each thrust insofar as specific element schedules and whether they are being conducted in-house (I), via grant (G), or via contract (C).

AIRFOIL DEPOSITION MODEL

The direction of the airfoil deposition model effort is shown in figure 6. The goal, approach, and status for the airfoil deposition model thrust are as follows:

Goal: To develop and verify a model to predict corrodant deposition quantity and location on turbine airfoils.

Approach:
  Airfoil model development via grant with Dan Rosner of Yale
  Model verification via in-house research with support from S. Gokoglu
    - Mach 0.3 burner rig
    - High pressure burner rig
  Burner rig modernization.
    - Computer data acquisition and limit monitoring
    - Computer control

Status:
  Prodigious output of papers by Rosner and Gokoglu
  Initial turbine airfoil deposition model developed
  CFBL theory documented and verified in burner rigs by accounting for particle impaction

Air-borne and fuel-borne impurities can be collected on stationary or rotating airfoils by vapor deposition and particle impaction mechanisms. Such salt deposits can be depleted by evaporation or by molten salt flow and shedding. The purpose of the deposition model is to account for the local temporal inventory of molten salt as an input to the coating life prediction model. The airfoil deposition model is being developed, via a grant, by Professor Dan Rosner and coworkers at Yale. Model verification is being carried out in-house in Mach 0.3 burner rig and ultimately in a high-pressure burner rig. This effort is supported by the work of Dr. S. Gokoglu of Analex Corporation at Lewis. In parallel with the model development, in-house burner rig facilities are being modernized in support of this and other HOST thrusts.

To date, the work of Rosner, Gokoglu, and coworkers has been documented by numerous publications in the open literature (refer to their workshop papers for references). These papers describe the initial airfoil deposition model and its verification.

The goal, approach, and status of the rig and engine correlation is as follows:

Goal: Provide a unique and relatively inexpensive laboratory facility to aid in the development of environmental attack life-prediction tools for hot-section materials.

Approach: Verify advances made in the life prediction of hot-section materials at pressure levels encountered in gas turbine engines

Verify deposition theory and dew point shift in the deposition of Na_2SO_4 corrodant at elevated pressures

Determine the effect of high heat fluxes on the life of thermal barrier coatings

Status: Checkout nearly complete. Scheduled to be operational this fall

A key feature of the surface protection subproject is the verification of the airfoil deposition model and the thermal barrier coating failure mechanism and life-prediction models in a simulated engine environment. This will be accomplished in the high pressure burner rig facility which is currently under construction at Lewis. Key features of this facility are described in figure 7. This unique facility will be dedicated to materials research and will offer temperatures to 1650° C (3000° F) and pressures to 50 atmospheres.

METALLIC COATING LIFE PREDICTION

As shown schematically in figure 8, metallic coatings protect structural alloys from the environment by providing a reservoir of a protective oxide-scale-forming element, for example, an aluminum bearing alloy which is selectively oxidized to form aluminum oxide. Aluminum is depleted by oxidation and thermal-cycle-induced oxide-scale spallation. Aluminum is also diluted by interdiffusion with the substrate. Exposure to corrosive salts may lead to accelerated hot corrosion attack of the oxide scale and coating. Finally, the coating must withstand thermal-mechanical loads without degrading system mechanical response.

The metallic coating life-prediction thrust deals with the chemical and mechanical aspects of the problem. The goal, approach, and status for this thrust are as follows:

Goal: To develop a coating life model for oxidation, spalling, hot corrosion, and coating/substrate diffusion and to account for environmental and coating effects on mechanical response.

Approach:

Environment/mechanical property interactions
Support contract efforts managed by fatigue and fracture subproject.

Oxidation/diffusion life prediction (I)
- Integrate cyclic oxidation spalling prediction and coating/substrate interdiffusion models for coated superalloy and verify

Hot corrosion surface chemistry (GE/TRW)
- Assess effects of aging environment and time on hot corrosion life for various coating/alloy systems as a basis for proposing and verifying a life model

Oxidation/hot corrosion dual cycle attack (I)
- Determine feasibility of an empirical linear damage model for oxidation/mild hot-corrosion attack of coated superalloy

Life prediction Verification (C)
 - Integrate results into a mission simulation prediction model and verify

Status:

Determined that diffusion model required to predict spalling parameters and breakaway oxidation

Hot corrosion efforts initiated in FY 1983.

An oxidation/diffusion life model is being developed in-house by building on existing interdiffusion and cyclic oxidation/spalling models developed for model systems. This task has proven far more difficult than envisioned due to spall measurement problems. The hot corrosion efforts, one in-house and one under contract with General Electric, were initiated in fiscal year 1983. These three efforts are scheduled to culminate in a contractual life prediction integration and verification effort.

The roles of the environment and coatings on the mechanical responses of isotropic and anisotropic materials are being addressed by our support of contract efforts managed through the fatigue and fracture subproject.

THERMAL BARRIER COATING LIFE PREDICTION

Thermal barrier coatings are presently used in noncritical gas-turbine applications to extend component life. Present coatings suffer from limited coating life and inadequate design capability when considered for more critical applications such as turbine airfoils. Both life prediction and advanced coatings are vital to the future use of TBC on airfoils for large improvements in system performance. Strong HOST support in the life-prediction area is now being provided. The TBC life-prediction thrust has grown during the past year to become the major thrust of the surface protection subproject. The direction of the thrust is shown in figure 9. The goal, approach, and status are described as follows:

Goal: To develop and verify life prediction methodologies for thermal barrier coatings

Approach:

TBC life prediction model development (C)
 - Phase I: failure analysis and preliminary model (multiple contracts)
 - Phase II: design capable models of TBC's

Mechanical behavior of TBC (G-JIAPP/CSU)
 - Fracture mechanisms (C. Berndt, on-site)
 - Residual stress modeling (G. Chang, CSU)

Rig/engine correlation (I) - high-heat-flux tests in high-pressure burner rig to
 complement contract effort.
 - Failure mechanisms
 - Model verification

24

Status:

Grant in place July 1983 and contracts in place April 1984.

The mechanical behavior effort is being conducted through a grant with Professor George Chang and Dr. Chris Berndt of Cleveland State University. The core effort involves parallel, complementary contracts with Garrett Turbine Engine Company, General Electric, and Pratt & Whitney Aircraft. These contracted efforts build on our research and technology base failure mechanisms research and are supported by parallel in-house high-heat-flux tests in the high pressure burner rig facility. Some of the key complementary features of the paralleled TBC life-prediction contracts are illustrated in figure 10. All three contractors are investigating their current advanced plasma-sprayed TBC which consists of a low-pressure plasma sprayed MCrAlY bond coat and an air plasma-sprayed yttria, partially stabilized zirconia ceramic layer. In addition, Garrett is conducting a parallel effort involving a vapor deposited zirconia layer.

CONCLUDING REMARKS

The past year has been one of significant expansion and progress for the HOST surface protection subproject. Some progress highlights are enumerated here. In the airfoil deposition thrust, the chemically frozen boundary layer (CFBL) theory was documented and extended to multicomponent salts, and particle impaction theory was verified in the Mach 0.3 burner rig. In the metallic coating life prediction effort, field components were analyzed, and service life was directly related to average mission duration. The initial approach for the oxidation/diffusion life model was assessed and alternative approaches developed. Finally, the TBC life-prediction effort matured. Parallel life-prediction development contracts were awarded. Initial results relating TBC degradation to acoustic emission signature were documented, and initial finite-element calculations for stresses near the undulating interface between the ceramic coat and bond coat were completed. Further details of these and other efforts can be found in the subsequent papers covering each of the major program elements.

SCHEMATIC OF HOT SECTION COMPONENT
LIFE CONTROLLING FACTORS
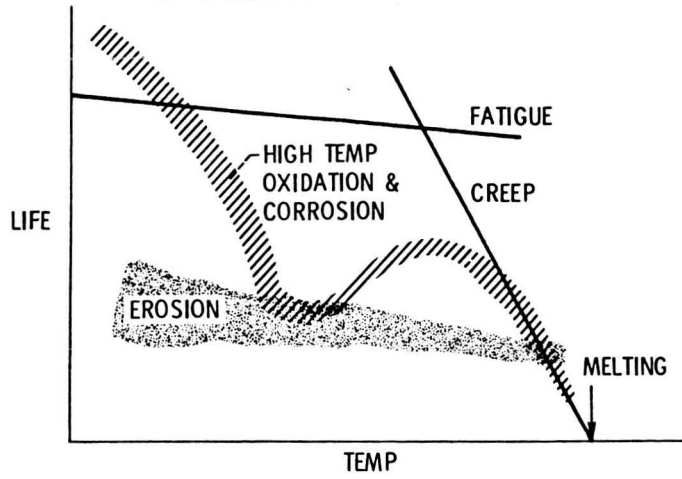
Figure 1

**HIGH TEMPERATURE
ENVIRONMENTAL ATTACK**
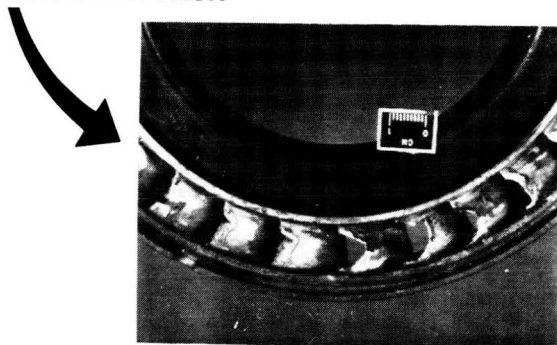
- **REDUCES EFFICIENCY**
- **LIMITS LIFE**
- **COSTS $**

Figure 2

SURFACE PROTECTION-IT'S ROLE IN HOST

GOAL

DEVELOP AN INTEGRATED ENVIRONMENTAL
ATTACK LIFE PREDICTION METHODOLOGY
FOR METAL AND CERAMIC COATED HOT
SECTION COMPONENTS

PROGRAM INTEGRATION

PROGRAM ELEMENTS

● AIRFOIL DEPOSITION MODEL
  AIRFOIL MODEL
  MODEL VERIFICATION
  RIG/ENGINE CORRELATION
  BURNER RIG MODERNIZATION
● METALLIC COATING LIFE PREDICTION
  ENVIRONMENT/MECH. PROP. INTERACTIONS
  OXIDATION/DIFFUSION
  HOT CORROSION SURFACE CHEMISTRY
  OXIDATION/CORROSION ATTACK
  LIFE PREDICTION VERIFICATION
● THERMAL BARRIER COATINGS
  THERMAL BARRIER LIFE PREDICTION
  TBC MECHANICAL BEHAVIOR
  RIG/ENGINE CORRELATION

CD-84-14781

Figure 3

SURFACE PROTECTION

PROGRAM ELEMENT	FISCAL YEAR									EXPECTED RESULTS
	1981	1982	1983	1984	1985	1986	1987	1988	1989	
AIRFOIL DEPOSITION MODEL										MODEL TO PREDICT THE LOCATION & POTENTIAL SEVERITY OF CORROSION ATTACK OF TURBINE AIRFOILS
METALLIC COATING LIFE PREDICTION										MODELS TO PREDICT METALLIC COATING LIFE ON BLADES & VANES AND ENVIRONMENT & COATING MECHANICAL EFFECTS
THERMAL BARRIER COATING LIFE PREDICTION										MODELS TO PERMIT DESIGN OF COMPONENTS WITH TBC YIELDING PERFORMANCE IMPROVEMENT

Figure 4

CD-84-14791

PROGRAM ELEMENT	FISCAL YEAR								
	1981	1982	1983	1984	1985	1986	1987	1988	1989
●AIRFOIL DEPOSITION MODEL									
AIRFOIL MODEL (G)									
MODEL VERIFICATION (I/G)									
RIG/ENGINE CORRELATION (I/G)									
BURNER RIG MODERNIZATION (I)									
●METALLIC COATING LIFE PREDICTION									
ENV./MECH. PROP. INTERACTIONS (C)									
OXIDATION/DIFFUSION (I)									
HOT CORROSION SURFACE CHEMISTRY (C)									
OXIDATION/CORROSION ATTACK (I)									
LIFE PREDICTION VERIFICATION (C)									
●THERMAL BARRIER COATINGS									
THERMAL BARRIER LIFE PRED. (C)									
MECHANICAL BEHAVIOR OF TBC (G)									
RIG/ENGINE CORRELATION (I)									

CD-84-14792

Figure 5

AIRFOIL DEPOSITION MODEL
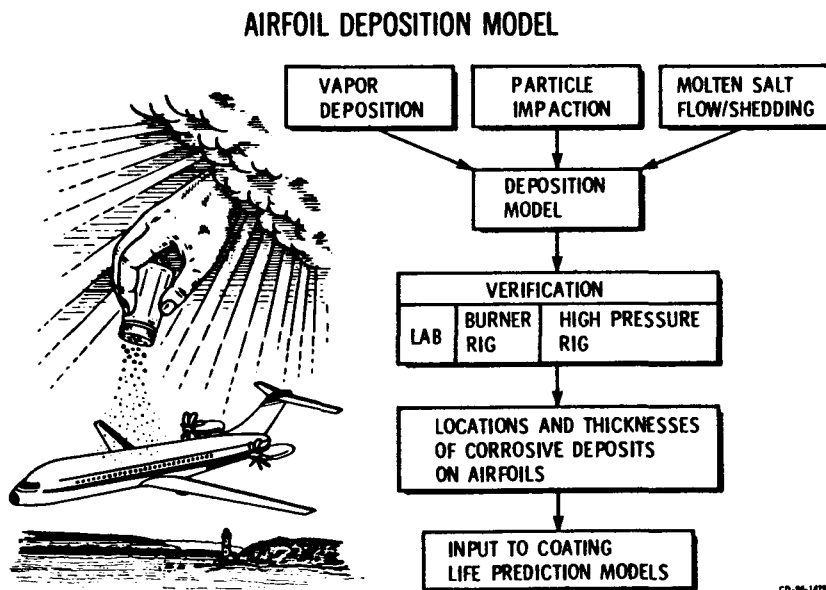
Figure 6

HIGH-PRESSURE BURNER-RIG FACILITY
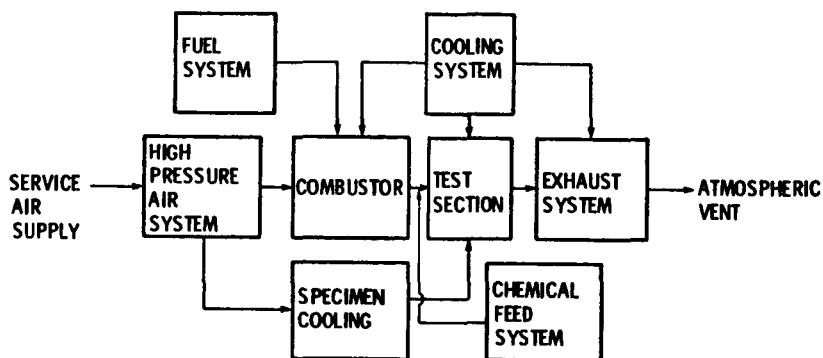
TEST SECTION SPECIFICATIONS
- 1800 TO 3000° F
- 3 TO 50 ATM
- MACH 0.3 TO 1.0
- 8-SAMPLE CAPACITY
- CYCLIC CAPABILITY
- INDEPENDENT SAMPLE TEMPERATURE CONTROL
- MASS FLOW RATE, 2 lb/sec, max.

CD-82-13326

Figure 7

METALLIC COATING LIFE PREDICTION
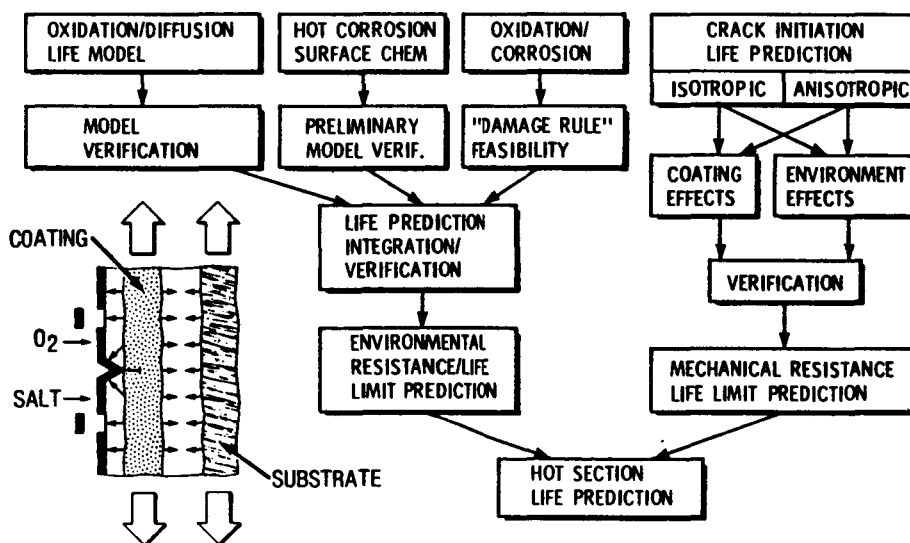
CD-84-14705

Figure 8

THERMAL BARRIER COATING LIFE PREDICTION

- EXTEND LIFE
- INCREASE TEMPERATURE
- REDUCE COOLING
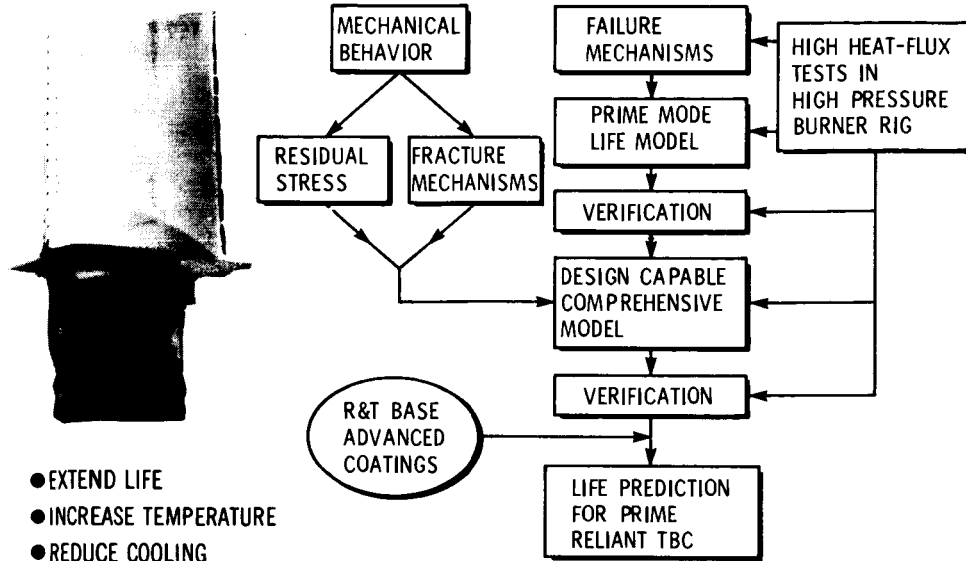
CD-84-14783

Figure 9

MULTIPLE CONTRACTS INCORPORATE BEST
FEATURES OF MULTIPLE APPROACHES
FOR TBC LIFE PREDICTION

	GARRETT	GE	P&W
MULTIPLE VENDORS	*		
ENGINE TESTS	*		
NDE	*		
QUALITY CONTROL			*
FAILURE MODE SEPARATION		*	
HOST INTEGRATION/CONTINUUM MODEL		*	
EROSION			*
FOREIGN OBJECT DAMAGE			*
STATISTICAL MODEL			*
FRACTURE MECHANICS	*		
HOT CORROSION MODEL	*		
MECHANICAL PROPERTIES		*	
MODEL INTEGRATION			*

Figure 10

30

FATIGUE AND FRACTURE - OVERVIEW

G. R. Halford
National Aeronautics and Space Administration
Lewis Research Center

We are pleased to report that all of the planned contractual and grant research programs in the fatigue and fracture discipline of the HOST Project are now in place. Many are producing important new results. These results and detailed aspects of the individual efforts will be conveyed by the responsible technical principal investigators in Session IVa scheduled for the last afternoon of this workshop. At this point I would like to give a brief overview of the status of the fatigue and fracture programs.

The programs involve the development of appropriate analytic material behavioral models for cyclic stress-strain-temperature-time/cyclic crack initiation, and cyclic crack propagation. It was convenient to divide the research efforts into two camps, depending upon the nominally isotropic or anisotropic mechanical response of the materials. Five industrial contracts with three different research organizations, three university grants, and two in-house programs round out the overall effort.

Figures 1 to 6 provide a block flow diagram of the activities within the various programs. I will address these figures one by one, but the reader is encouraged to study the individual contributions for more specific details.

I do want to emphasize the underlying thrust of these programs: the development and verification of WORKABLE engineering methods for the calculation, in advance of service, of the local cyclic stress-strain response at the critical life governing location in hot section components, and the resultant cyclic crack initiation and crack growth lifetimes.

FATIGUE & FRACTURE ... IT'S ROLE IN HOST

GOAL: DEVELOP AND VERIFY ANALYTIC ENGINEERING MODELS THAT CAN BE
USED ON A ROUTINE DESIGN BASIS FOR THE PREDICTION OF CYCLIC
STRESS-STRAIN-TEMPERATURE-TIME RESPONSE (i.e., CONSTITUTIVE RESPONSE)
AND FATIGUE CRACK INITIATION AND PROPAGATION LIFETIMES OF TURBINE
ENGINE HOT SECTION COMPONENTS MADE OF ISOTROPIC OR ANISOTROPIC ALLOYS

PROGRAM INTEGRATION

PROGRAM ELEMENTS:

- CONSTITUTIVE MODELING-ISOTROPIC — (48 mos)
- LIFE PREDICTION-ISOTROPIC — (60 mos)
- CRACK PROPAGATION-ISOTROPIC — (48 mos)
- LIFE PREDICTION & CONSTITUTIVE MODELING-ANISOTROPIC — (60 mos)
- IN-HOUSE ACTIVITIES — (60 mos)

CS-84-3929
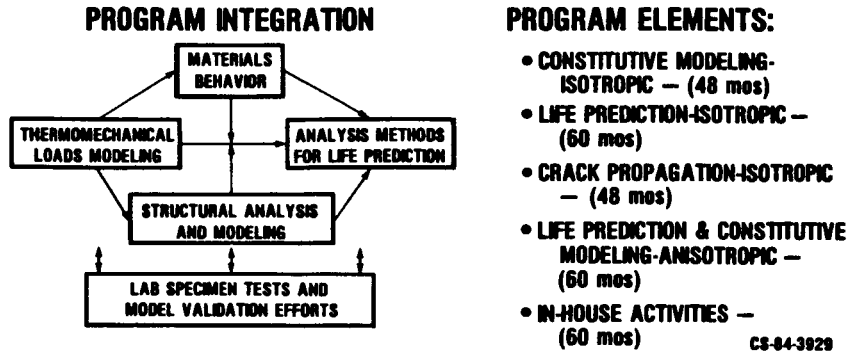
Figure 1

CONSTITUTIVE MODELING—ISOTROPIC MATERIAL
SOUTHWEST RESEARCH, LINDHOLM; AND GENERAL ELECTRIC, LAFLEN

CS-84-3928
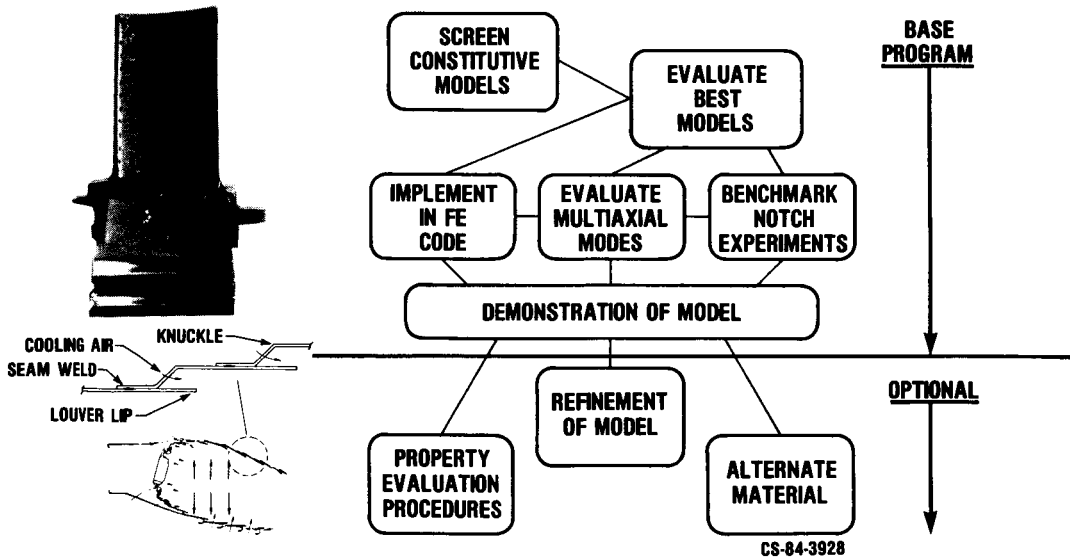
Figure 2

32

LIFE PREDICTION - ISOTROPIC MATERIAL
PRATT AND WHITNEY, MORENO

BASE
PROGRAM

SCREEN
LIFE-PREDICTION
METHODS

EVALUATE
BEST MODELS
FOR CREEP-FATIGUE

OPTIONAL

KNUCKLE
COOLING AIR
SEAM WELD

THERMAL
MECHANICAL
MODULE

MULTIAXIAL
MODULE

CUMULATIVE
DAMAGE
MODULE

MEAN
STRESS
MODULE

ENVIRONMENTAL
ATTACK MODULE

COATINGS
MODULE

LOUVER LIP

INTEGRATED LIFE-PREDICTION MODEL

VERIFICATION ON
BASE ALLOY SYSTEM

ALTERNATE ALLOY
SYSTEM EVALUATION

CS-84-3932

Figure 3

CRACK PROPAGATION—ISOTROPIC MATERIAL
GENERAL ELECTRIC, LAFLEN; AND SYRACUSE, LIU

BASE
PROGRAM

SCREEN
SPECIMEN
CONFIG.

SCREEN
CMOD/CTOD
METHODS

SCREEN
PATH-INDEPENDENT
INTEGRALS

PATH

REVERSED
LOADING
MODULE

THERMAL
GRADIENT
MODULE

TMF
PROPAGATION
MODULE

$$J = \oint W_{dy} - T_i \frac{\partial u_{i\,dx}}{\partial x_o}$$

PATH

TIME INDEPENDENT
CRACK PROPAGATION PREDICTION METHODOLOGY

TIME DEPENDENT
CRACK PROPAGATION PREDICTION METHODOLOGY

OPTIONAL

VERIFY USING
HIGH TEMPERATURE ENGINE ALLOY

CS-84-3931

Figure 4

33
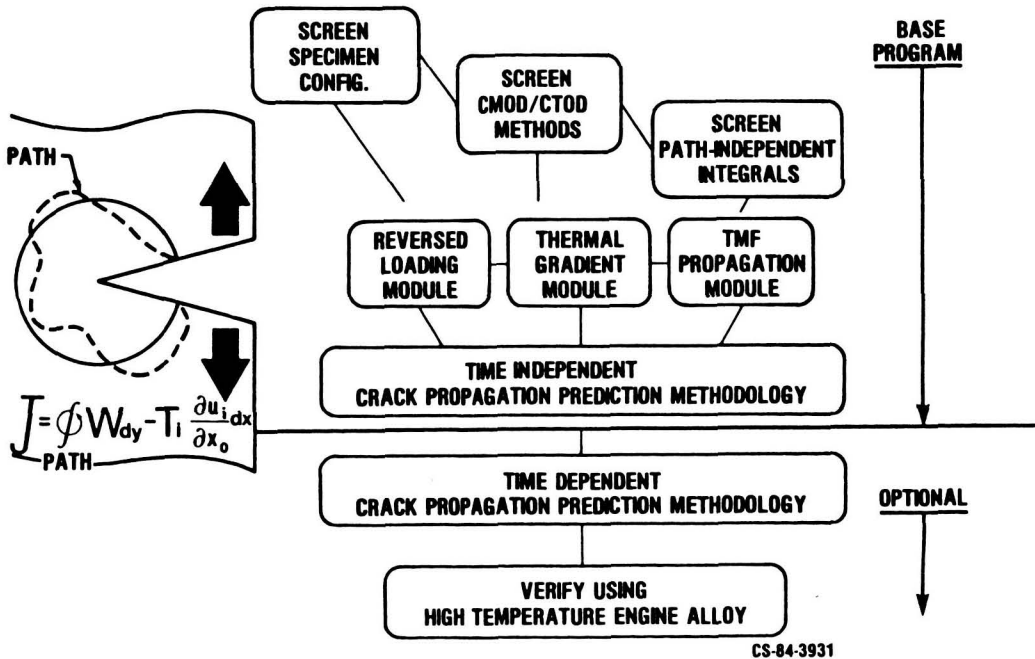
LIFE PREDICTION & CONSTITUTIVE MODELING -ANISOTROPIC MATERIAL

PRATT AND WHITNEY, SWANSON

THEORETICAL MODEL DEVELOPEMENT
U OF CIN, STOUFFER
U OF CT, JORDAN

SCREEN ALLOYS AND MODELS

PRELIMINARY EVALUATION OF MODELS

COATING, TMF, MULTIAXIAL MODULES

FULL EVALUATION ON COATED SINGLE XTAL ALLOY SYSTEM

ALTERNATE COATED SINGLE XTAL ALLOY SYSTEM EVALUATION

BASE PROGRAM

UNCOATED SINGLE XTAL ROOT ATTACHMENT — OPTION 1

DS/DR ALLOY EVALUATION AIR FOIL & ROOT ATTACH. — OPTION 2

CS-84-3933

Figure 5

IN-HOUSE ACTIVITIES

UPGRADE FATIGUE LABORATORY

- HOST/SATELLITE COMPUTER SYSTEM
- EXPANDED HYDRAULIC SYSTEM
- EXPANDED TEST CELL AREA
- CENTRALIZED CONTROL ROOM
- TENSION/TORSION BIAXIAL FATIGUE MACHINES
- HCF/LCF MACHINES FOR CUMULATIVE DAMAGE
- TMF MACHINE

SINGLE CRYSTAL/COATING THERMAL MECHANICAL FATIGUE PROGRAM

- PWA 1480 BARE AND COATED
- STAND ALONE COATING
- TROIKA EFFORT
- FUNDAMENTAL APPROACH TO UNDERSTANDING OF CYCLIC FLOW AND CRACKING BEHAVIOR OF COMPLEX ALLOY/COATING SYSTEM

CS-84-3930

Figure 6

34

HOST TURBINE HEAT TRANSFER OVERVIEW

John E. Rohde
National Aeronautics and Space Administration
Lewis Research Center

The HOST Turbine Heat Transfer program is focused on improving methods of predicting airfoil local metal temperatures. Improved methods of predicting airfoil local metal temperatures require advances in the understanding of the physics and methods of analytically predicting the following four aerothermal loads: hot gas flow over airfoils, heat transfer rates on the gas-side of airfoils, cooling air flow inside airfoils, and heat transfer rates on the coolant-side of airfoils. A systematic "building block" research approach is being pursued to investigate these four areas of concern from both the experimental and analytical sides. Experimental approaches being pursued start with fundamental experiments using simple shapes and flat plates in wind tunnels, progress to more realistic cold and hot cascade tests using airfoils, continue to progress in large low-speed rigs and turbines and warm turbines, and finally combine all the interactive effects in tests using real engines or real-engine-type turbine rigs. Analytical approaches being pursued also build from relatively simple steady two-dimensional inviscid flow and boundary-layer heat transfer codes to more advanced steady two- and three-dimensional viscous flow and heat transfer codes and unsteady two-dimensional viscous flow and heat transfer codes. These advanced codes provide more physics to model better the interactive effects and the true real-engine environment.

HOST TURBINE HEAT TRANSFER PROGRAM

OBJECTIVES:

- OBTAIN A BETTER UNDERSTANDING OF THE PHYSICS OF THE AEROTHERMODYNAMIC PHENOMENA OCCURRING IN HIGH-TEMPERATURE TURBINES

- ASSESS AND IMPROVE ANALYTICAL METHODS USED TO PREDICT THE FLOW AND HEAT TRANSFER IN HIGH TEMPERATURE TURBINE

CS-84-3935

Figure 1

TURBINE AEROTHERMAL DESIGN SYSTEM

HOT GAS BOUNDARY CONDITIONS
-LOCAL TEMP. & PRESS.

HOT GAS FLOW CODE
-2-D OR 3-D NON-VISCOUS
OR VISCOUS FLOW

COOLANT FLOW CODE
-2-D OR 3-D VISCOUS FLOW
-1D NETWORK FLOW

HOT GAS-SIDE HEAT TRANSFER CODE
-2-D OR 3-D BOUNDARY LAYER
-3-D VISCOUS FLOW

COOLANT-SIDE HEAT TRANSFER CODE
-CORRELATIONS
-2-D BOUNDARY LAYER
-3-D VISCOUS FLOW

NODE GENERATOR

CONDUCTION CODE
3-D STEADY STATE AND TRANSIENT

LOCAL AIRFOIL METAL TEMPERATURES

CS-84-3936

Figure 2

36

BUILDING BLOCK AEROTHERMAL TURBINE RESEARCH APPROACH
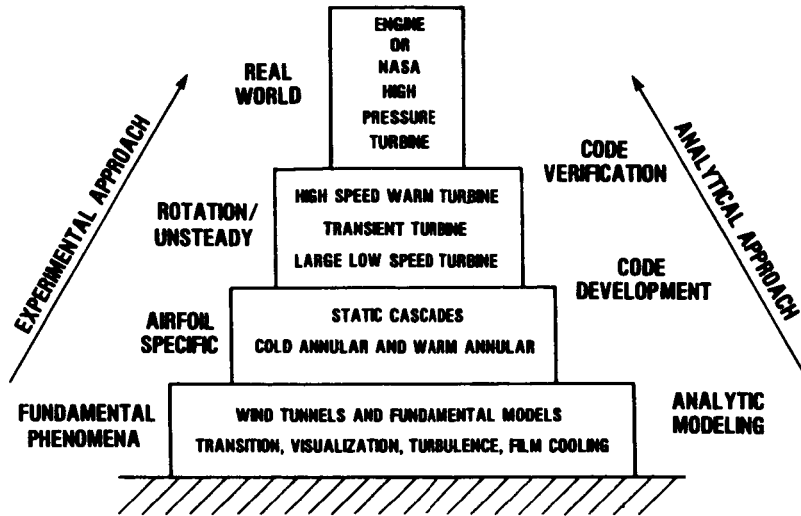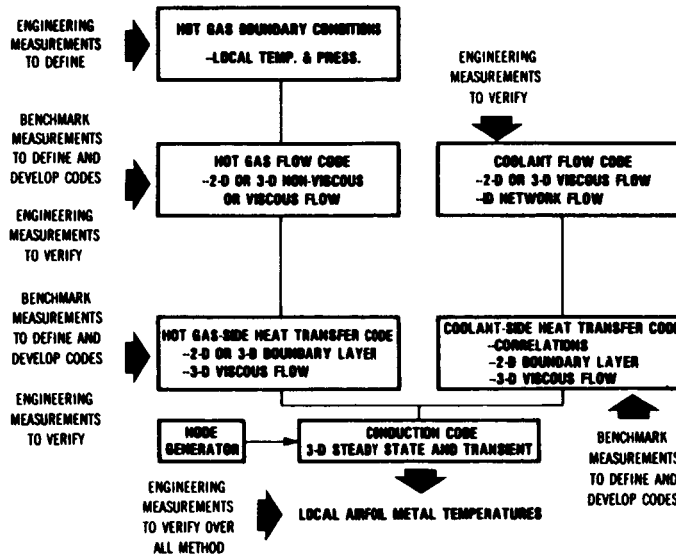

Figure 3

ASSESS TURBINE AEROTHERMAL DESIGN SYSTEM

Figure 4

RANGE OF TURBINE AEROTHERMAL DESIGN SYSTEM CODES
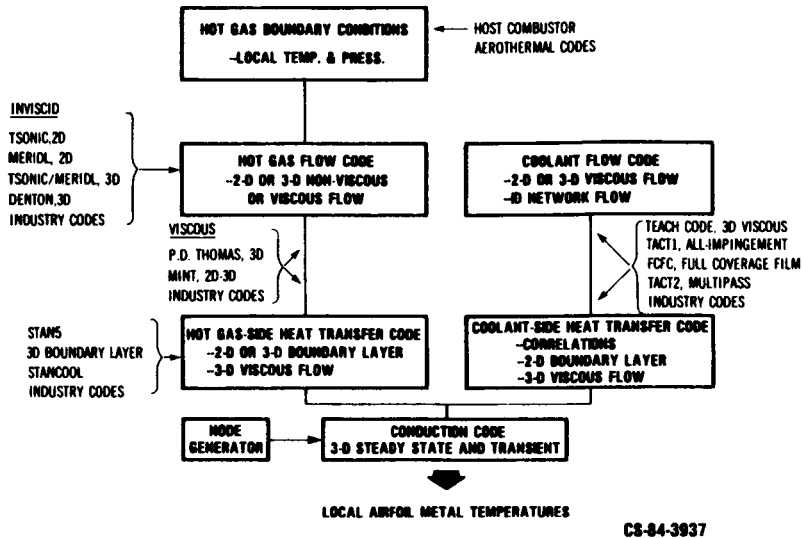
Figure 5

TURBINE HEAT TRANSFER SUBPROJECT SCHEDULE

Figure 6

TURBINE HEAT TRANSFER SESSION AGENDA

GAS-SIDE HEAT TRANSFER	E. TURNER, ALLISON
	B. WEINBERG, SRA
GAS-SIDE HEAT TRANSFER IN A TURBINE STAGE WITH ROTATION	R. DRING, UTRC
EFFECTS OF HIGH TURBULENCE AND VORTICES ON HEAT TRANSFER	R. MOFFAT, STANFORD
THREE-DIMENSIONAL VISCOUS FLOW AND HEAT TRANSFER	R. CRAWFORD, UTSI
ASSESSMENT OF THREE-DIMENSIONAL BOUNDARY LAYER CODE	O. ANDERSON,UTRC
COOLANT-SIDE HEAT TRANSFER WITH ROTATION	F. KOPPER, P&W

CS-84-3934

Figure 7

FURTHER DEVELOPMENT OF THE
DYNAMIC GAS TEMPERATURE MEASUREMENT SYSTEM

D. L. Elmore, W. W. Robinson, and W. B. Watkins
Pratt & Whitney Engineering Division

SUMMARY

Candidate concepts capable of generating dynamic temperatures have been identified and analyzed for use in verifying experimentally the frequency response of the dynamic gas temperature measurement system of reference 1. A "rotating wheel" concept and one other concept will be selected for this purpose. Modifications to the data reduction code algorithms developed in the reference 1 program have been identified and evaluated to reduce substantially the data reduction execution time. These modifications will be incorporated in a new data reduction program to be written in Fortran IV.

INTRODUCTION

The measurement system developed in reference 1 uses a compensated two element thermocouple probe. The compensation technique uses the ratio of the signal amplitudes from the two thermocouples' passive responses to gas temperature variations. Comparisons with a numerical heat transfer model allows compensation of temperature fluctuations to above 1 Khz.

The objectives (Figure 1) of the present program, "Further Development of the Dynamic Gas Temperature Measurement System", (Contract NAS3-24228) are; 1) to verify experimentally the frequency response of the dynamic gas temperature measurement system developed under a previous contract (Reference 1); 2) to optimize the computer compensation method for execution speed; and 3) to implement the reference 1 computer code in Fortran IV for use on generally available computers.

The program is organized into four basic tasks including (1) frequency response experimental verification; (2) compensation code execution streamlining; (3) implementation of the compensation code in Fortran IV; and (4) data acquisition at NASA Lewis Research Center. Efforts to data have been on Tasks 1 and 2 and the preliminary results are discussed below.

FREQUENCY RESPONSE EXPERIMENTAL VERIFICATION

Task I (Figure 2) involves designing and conducting two experiments which can be used to verify the frequency response of the dynamic gas temperature measurement system. The first experiment is defined in the contract requirements and consists of a "rotating wheel" concept. The second experiment to be designed under Task I involves the identification and evaluation of several candidate concepts and the selection of the most promising one. During the identification and evaluation of the candidate concepts consultation was provided by Dr. Robert J. Moffat of Stanford University. The experimental test conditions required for the frequency response verification are for a working fluid of air or combustion gases at a pressure of atmospheric or greater, minimum peak-to-peak temperature fluctuations of 278K

(500°F), mach number of 0.1 or greater, and temperature fluctuations of 250 Hz or greater.

Methods identified so far fall into two general categories, the first using an atmospheric pressure laboratory-scale combustor, and the second using one of a number of candidate techniques for generating periodic or step-impulse temperature signals using air as a working fluid.

An available atmospheric pressure combustor produces a dynamic temperature signal with peak-to-peak temperature variations in excess of 278K (500°F) (reference 1). The advantages of such a combustor as a temperature source are 1) the temperature spectrum qualitatively resembles the desired application (i.e. a turbine engine combustor), and 2) the assumptions of the analysis are fulfilled, namely low correlation between temperature and velocity fluctuations. Various test concepts defined for use with the laboratory burner are listed in figure 3 and discussed in the following paragraphs.

- Impulse Actuated Two Wire Probe - Two gas streams would be established having the desired high and low temperature. The probe would be moved from one to the other stream by a mechanical actuator. A small fine wire or other temperature standard would be used with the two wire probe. It is recognized that it may be difficult to attain the required 250 Hz frequency response due to the actuator speed limitations.

- Two Wire Probe and Aspirating Hot Film Probe - In this concept, the natural frequency fluctuations of the laboratory burner would be the only source of fluctuations, and a reference probe of high frequency response, such as an aspirating (TSI Model 1735) probe (figure 4) would be used as the standard measurement of the gas temperature fluctuations. The referenced TSI probe has a frequency response of up to 100K Hz and is capable of operation at 3500°C (6330°F), 152 m/s (500 f/s), and 1 atmosphere. However, the accuracy of this probe may be limited due to conduction errors.

- Two Wire Probe and Anemometer Probe - In this concept, the temperature standard would be a hot wire anemometer probe replacing the previously discussed aspirating hot film probe. The anemometer would be a high temperature probe such as a TSI Series A4 probe (figure 5) operated as a constant current temperature sensor.

- Three Wire Probe - In this concept, again the natural frequency fluctuations occurring in the combustor would be the source. An additional very small third thermocouple element would be added to the two-wire probe. This thermocouple element would provide additional verification by compensating data in three combinations: very small-small, very small-large, and small-large. Previous test experience (reference 1) suggests that very small wires (25 μm or less) will survive for many minutes in this environment.

- Oscillating Splitter Plate and Two Wire Probe - This concept is similar to the previously described test where a splitter plate is used having two different temperature gas streams in the combustor. However, instead of moving the probe from the cold to the hot stream the splitter plate would be oscillated mechanically to divert the streams over a stationary probe assembly and temperature standard. The principal difficulties in this

42

concept is in making certain that the flow stays attached to both faces of the splitter plate and in the complex mechanical system required.

The second category of verification experiments involves hardware configurations which use air as the working fluid and which suggest an obvious temperature variation. The configurations are:

- Rotating Wheel - The original rotating wheel experiment which has been tested at Pratt & Whitney is shown in Figure 6. It consists of two rotating wheels which have circles of holes which turn the air flows (hot and cold) on and off. The hole patterns are phased to alternately heat and cool the test probe which is positioned between the wheels. Phasing of the two hole patterns suggests a temperature variation, i.e, if the holes in pattern "A" are 180° out of phase with the holes in pattern "B", an approximate square-wave temperature variation will result as the wheels are rotated. The primary frequency is the number of holes in one pattern multiplied by the rotation rate, and peak-to-peak variation in temperature is the difference in stream temperatures. Figure 7 presents typical test data for the temperature and velocity profiles.

- Modified Rotating Wheel - One of the drawbacks to the previously described rotating wheel is that the streams flow in opposite directions. Based on recommendations from Dr. Robert Moffat the rotating wheel experiment was modified (Figure 8) to use one wheel with two hole patterns and collector/transition duct which blends the two gas streams through a single nozzle at the probe. Proper design of the phasing of the holes and using a screen in the transition duct should make it possible to achieve a nearly sinusoidal temperature waveform, which is preferred.

- Blow Down Tube - This concept (figure 9) would use a burst diaphragm and a capacitive heater to provide a step input. The disadvantages to this system are problems with probe damage due to particles from the burst diaphragm and inaccuracy resulting from not generating a sharp instantaneous step function.

- Pulsatile Pressure System - This system, shown in Figure 10, consists of a flow channel with two orifices. The first orifice is operated critically so the flow is constant. The second orifice would be periodically occluded by a rotating disk valve which would cause the pressure in the volume between the orifices to fluctuate. This would result in temperature fluctuations due to isentropic compression. The primary disadvantage is the large variations in flow required to produce the temperature fluctuations.

- Piston In Cylinder - This system, shown in Figure 11, again uses two orifices but uses a piston to compress the gas between the orifices and thus obtain a temperature fluctuation. This system still has a flow variation, however, it is smaller than the pulsatile system.

- Sprinkler Head - This concept, shown in figure 12, consists of a wheel made from two halves containing milled passages. The passages are curved so that the air flow will provide the momentum to rotate the assembly. The passages would also be canted slightly in the axial direction so that the flow from each stream would impinge on the test probe located near the

wheel. This configuration has the advantage of providing temperature fluctuations with a relatively uniform and constant velocity. The primary disadvantages would be associated with the large amount of air required and the complexity of designing the rotating seals and bearings.

● Fluidic Oscillator – This concept, shown in figure 13, is based on a modification of a fluidic switch to oscillate two streams (hot and cold). Switching of the two flow streams (hot and cold) would be achieved by alternately applying pressure pulses to the control ports. The pressure pulses could be supplied by a rotating valve assembly. The probe would be positioned in the area shown in figure 13.

The principal difficulty with the above methods concerns the degree of correlation between velocity fluctuations and temperature fluctuations, and consequent applicability of the compensation method.

The concepts will be evaluated for technical merit and subsequent selection of the most promising method.

COMPUTER CODE OPTIMIZATION

Task II, Compensation Code Execution Streamlining, involves developing a more efficient numerical compensation method. In the reference 1 numerical method (Figure 14) thermocouple response is calculated at each of several individual frequencies, and the compensation spectrum is derived by cumulating individual frequency results. The calculation time may be shortened through the following approach (shown in Figure 15). Unit amplitude input frequency over the bandwidth of interest is first inverse Fourier transformed to yield an impulse function, which then can be used as time-dependent boundary condition for the thermocouple response calculation. Fourier transform of thermocouple response then yields the compensation spectrum directly. Calculation time is greatly reduced with the impulse function approach. The remainder of the compensation method involving ratios of the two thermocouple outputs remain unchanged.

REFERENCE

1.   Elmore, D. L., Robinson, W. W., and W. B. Watkins, "Dynamic Gas Temperature Measurement System Final Report, Vol. I, Technical Efforts", prepared for NASA-Lewis Research Center by United Technologies, Pratt & Whitney, Contract No. NAS3-23154, Report NASA CR-168267, 10 May 1983.

FURTHER DEVELOPMENT OF THE DYNAMIC GAS TEMPERATURE MEASUREMENT SYSTEM

- Objectives

    Experimentally verify the frequency response

    Optimize the computer compensation methods

    Implement the code in FORTRAN IV

- Talk outline - progress report on

    Definition of experimental test concepts

    Preliminary results of concept analyses

    Preliminary results of computer code
    optimization

Figure 1

EXPERIMENTAL VERIFICATION CONCEPTS

Laboratory burner concepts

- Impulse actuated 2 wire probe

- 2 wire probe and TSI probe

- 2 wire probe and anemometer probe

- 3 wire probe

- Oscillating splitter and 2 wire probe
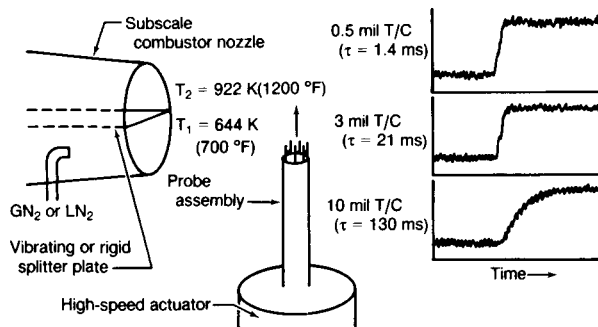
Figure 3

EXPERIMENTAL VERIFICATION

Task I

- Requirements

    Conduct surveys to define experimental test concepts

    Analyze, rank, and select 1 concept to be
    tested in addition to the rotating wheel

    Fabricate, test, and analyze results

- Test conditions

    Frequency response: 250 Hz (min)

    Temperature fluctuations: 278K (500°F) P-P (min)

    Pressure: atmospheric or greater

    Flow rate: Mach 0.1 (min)

    Gas composition: air is acceptable

Figure 2

LABORATORY BURNER TEMPERATURE STANDARD

TSI aspirating probe
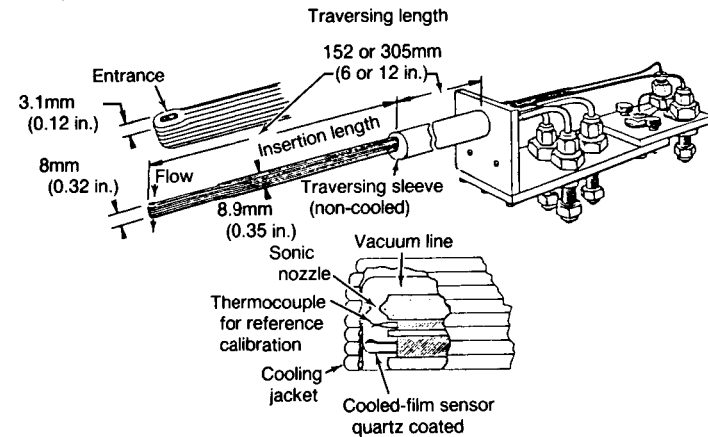
Figure 4

LABORATORY BURNER TEMPERATURE STANDARD

High temperature anemometer probe

TSI high temperature anemometer series A4

Max temp = 800°C (1471 °F)
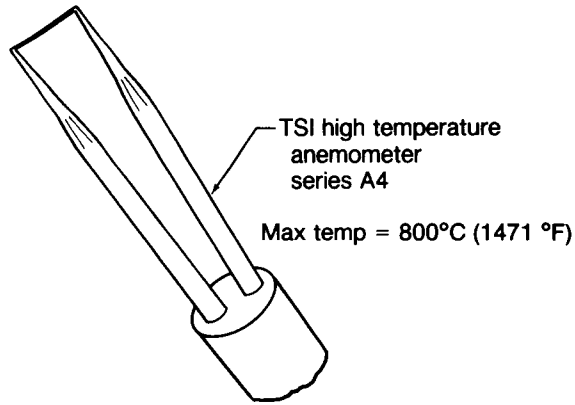
Figure 5

EXPERIMENTAL VERIFICATION CONCEPTS

Existing rotating wheel schematic

Smaller single element probe

12.7 μm bare wire TC

Two element probe

Ambient air supply

Heated air supply

Pulley

Hole pattern A

Hole pattern B

Hole pattern A

1 in.

Rotating wheels 20.3cm (8 in.) dia with eight 2.54cm (1 in.) dia holes

Electric motor
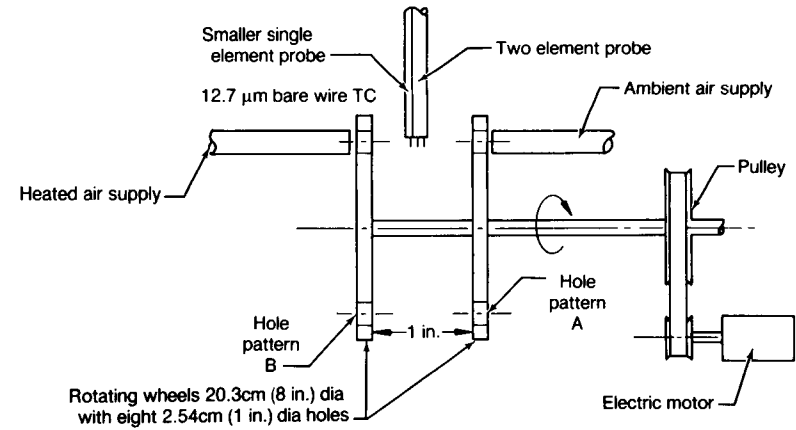
Figure 6

46

EXISTING ROTATING WHEEL CONCEPT

Typical test data

ft/sec

Supply - 107 M/S (250 ft/sec) ambient temperature

Velocity, m/s

400
300
200
100

100

50

0

Time

Temperature, K

250 Hz

°F

400
300
200
100

400

300

12.7 μm bare wire TC

17 Hz

200 Hz

107 M/S (350 ft/sec)

Time
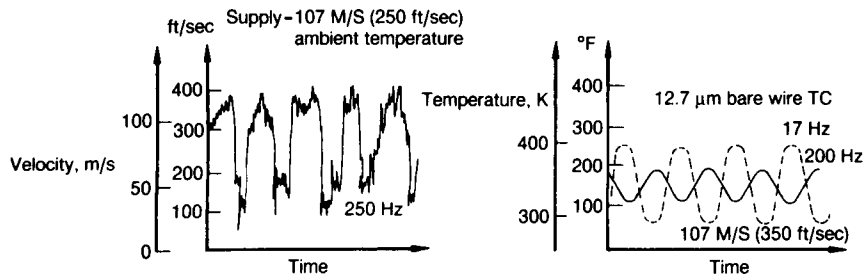
Figure 7

EXPERIMENTAL VERIFICATION CONCEPTS

Modified rotating wheel schematic

Ambient air supply

Collector transition duct

Temperature standard

Two element probe

Pulley

Heated air supply

Rotating wheel (2 sets of holes)

Electric motor
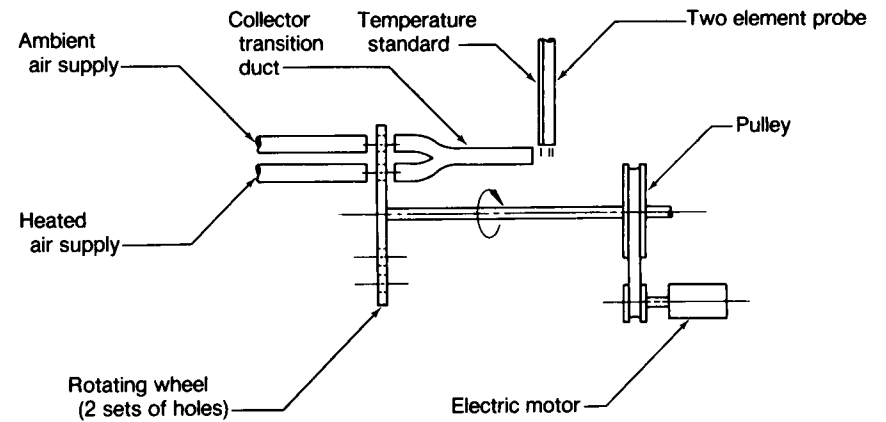
Figure 8

EXPERIMENTAL VERIFICATION CONCEPTS

Blowdown tube
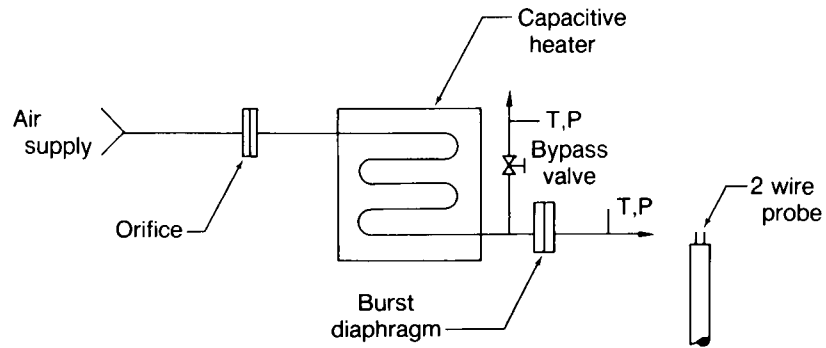
Figure 9

EXPERIMENTAL VERIFICATION CONCEPTS

Pulsatile pressure system
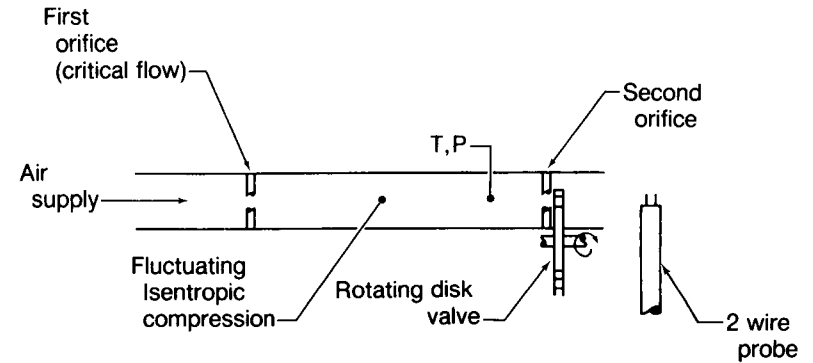
Figure 10

EXPERIMENTAL VERIFICATION CONCEPTS

Piston in cylinder
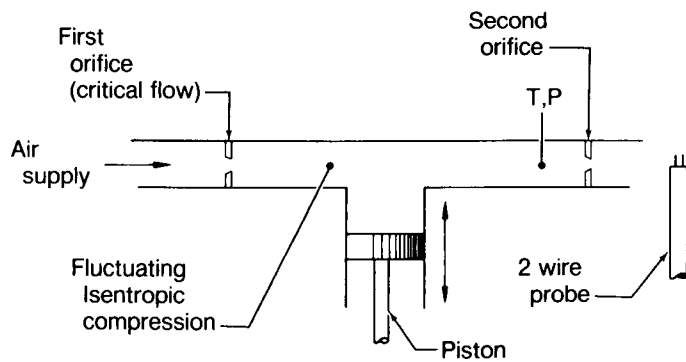
Figure 11

EXPERIMENTAL VERIFICATION CONCEPT

Sprinkler head

Figure 12

47
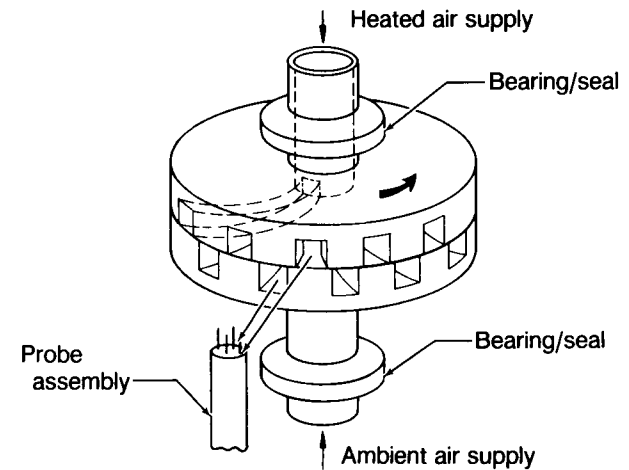
EXPERIMENTAL VERIFICATION CONCEPT

Fluidic oscillator
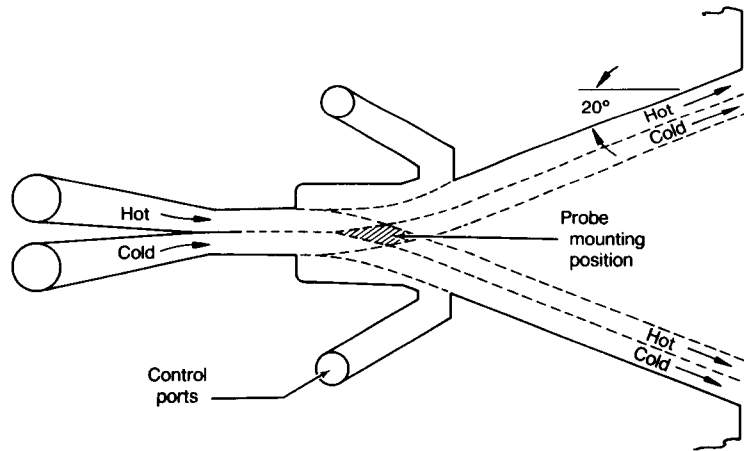
Figure 13

COMPUTER CODE OPTIMIZATION

Original numerical compensation method
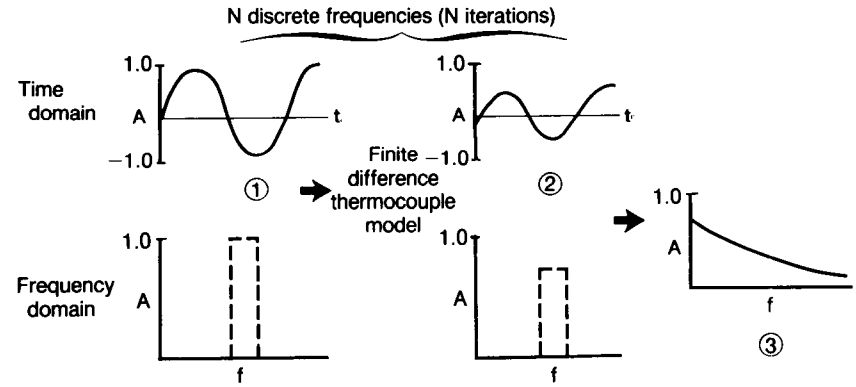
- Individual frequencies input to finite difference T/C models

- Output from model complex added to yield compensation spectrum

Figure 14

COMPUTER CODE OPTIMIZATION

Advanced numerical compensation method
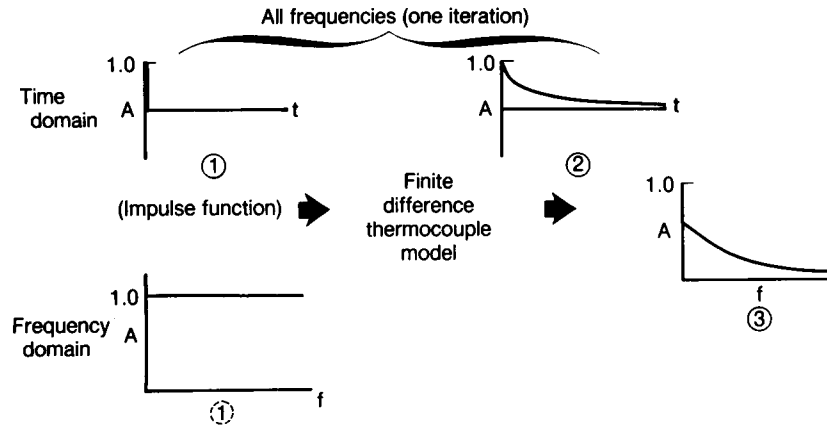
- Impulse function handles all frequency components simultaneously

Figure 15

DEVELOPMENT OF HEAT FLUX SENSORS IN TURBINE AIRFOILS

William H. Atkinson and Richard R. Strange
United Technologies Corporation
Pratt & Whitney

This paper describes the work performed under contract NAS3-23529 "Turbine Blade and Vane Heat Flux Sensor Development." The objective of this contract is to develop heat flux sensors suitable for use on turbine airfoils and to verify the operation of the heat flux measurement techniques through laboratory experiments.

The design of durable turbine airfoils that use a minimum amount of cooling air requires knowledge of the heat loads on the airfoils during engine operation. Measurement of these heat loads will permit the verification or modification of the analytical models used in the design process and will improve the ability to predict and confirm the thermal performance of turbine airfoil designs. Heat flux sensors for turbine blades and vanes must be compatible with the cast nickel-base and cobalt-base materials used in their fabrication and must be capable of operation in a hostile environment with regard to temperature, pressure and thermal cycling. In order to not perturb heat flows to be measured, it is necessary to use the smallest possible sensors.

During the first phase of this contract two sensor designs were identified that met the established criteria for turbine airfoils. These sensors were the embedded thermocouple sensor and the Gardon gage sensor. Both were fabricated into the airfoil wall.

Figure 1 is a schematic of the embedded thermocouple sensor. This type of one-dimensional steady-state sensor determines the heat flux by measuring the temperature drop across a thermal barrier. In this case, the airfoil wall acts as the thermal barrier. The Gardon gage sensor is shown schematically in figure 2. This type of steady-state sensor determines the heat flux from the temperature rise due to radial conduction from the insulated section of the hot side of the airfoil wall.

Both types of sensors were fabricated into turbine blades and vanes. The installation of the sensors required access to the inside wall of the airfoil. The blades used for the heat flux sensor installations were two-piece bonded blades. The instrumentation was installed in one blade half. The two halves were then joined using a 1255K braze material. For installation in turbine vanes, a window, through which instrumentation was installed, was cut into the opposite airfoil wall. Figure 3 shows a vane being instrumented. After completion of instrumentation the window was heliarc welded back in place. The airfoil wall was then smoothed to restore aerodynamic integrity. NASA has fabricated vanes by cutting them in half, installing the instrumentation and then brazing the vane halves back together.

A calibration fixture, shown in figure 4, was designed and fabricated for the calibration of airfoil-mounted heat flux sensors. This fixture was mounted below a quartz lamp bank heat source, shown in figure 5. The fixture allowed positioning of the airfoil so that the surface of the heat flux sensor was normal to the incident radiation. The surface of the airfoil was coated with material having a known and stable absorptance and emittance. The incident radiation was measured with a reference Hy-Cal asymptotic calorimeter. The sensors were calibrated at a number of

heat flux levels and over a range of sensor temperatures. The data was then normal-ized to a temperature of 1200K. Figure 6 shows a typical calibration result for a Gardon Gage sensor. This same apparatus was used for thermal cycle and thermal soak tests as well as the calibration tests.

The sensors developed under the first phase of the turbine blade and vane heat flux sensor program proved capable of measuring the heat loads on turbine airfoils up to 1.6 megawatts/m^2 incident with an accuracy of ±5 percent. They withstood thermal cycling and thermal soak conditions expected in a real gas turbine engine environment. Sensors must be carefully installed in airfoils with complex internal cooling schemes. In such airfoils there may be regions where strong non-one-dimensional heat flows exist. These non-one-dimensional flows make it dif-ficult to obtain meaningful sensor calibrations. The full details of the sensor de-velopment and laboratory testing are contained in references 1 and 2.

The second phase of this program demonstrated a variety of heat transfer meas-urement methods on a simple test piece in an atmospheric pressure combustor rig. A cylinder in cross-flow was chosen because this configuration has been tested exten-sively and is well documented in the literature.

The combustor rig selected is a general purpose laboratory combustor shown sche-matically in figure 7. The mixing and flow in the combustor closely approximated those of many conventional gas turbine combustors, and the critical features of the combustion chemistry were reproduced. The fuel was introduced at the front of the combustor by a pressure atomizing fuel nozzle. The combustion was stabilized in the forward section of the combustor by developing a strong, swirl-stabilized re-circulation zone. The hot combustion gases were cooled by dilution jets located at the back of the combustor. The primary and secondary jets have independent air sup-plies to permit adjustment of the velocity and temperature profiles at the exit. The ignitor, a flame monitor, and instrumentation ports were mounted in an instrumenta-tion rig located between the primary and secondary sections. The 5 cm diameter ex-haust could be operated at a temperature up to 1700K at Mach numbers up to 0.7 at this maximum temperature.

The instrumentation cylinder selected was a 1.6 cm diameter tube made of Hastelloy-X with a wall thickness of 0.15 cm. The diameter of the cylinder was a compromise between a size large enough to permit installation of the instrumentation and small enough to cause minimal flow blockage. During test the cylinder will be cooled with channel-flow coolant in the tube. To obtain the required internal heat transfer coefficient, the channel height was reduced by adding a center tube concentric with the cylinder. The cylinder was prepared for instrumentation by slicing a portion of the tube length in half. This allowed direct access to the interior of the cylinder for the necessary Elox operations as well as installation of instrumentation.

Figure 8 shows a cylinder following the Elox operation but before installation of the instrumentation. The sensor on the left will be a transient slug calorimeter; the center sensor will be a Gardon Gage; and the sensor on the right will be an embedded thermocouple sensor. Figure 9 shows the same cylinder after installation of lead wires but before the interior wall has been smoothed or the Gardon gage cavity has been filled with ceramic. Figure 10 shows the completed installation, with the center tube installed, prior to cylinder rewelding. The instrumentation is led out through the center tube. Figure 11 is an end-on view of the cylinder following rewelding of the cylinder halves.

Following construction, the heat flux sensors in the cylinder were calibrated using the quartz lamp bank calibration facility. Figure 12 shows typical calibrations for a Gardon gage sensor installed in a cylinder. All of the calibrations were well-behaved. None of the steady-state sensors appeared to be affected by non-one-dimensional flow problems.

Preparations are now underway to test the sensors in the cylinders in front of an atmospheric pressure combustor. Initial tests are being conducted to characterize the conditions at the combustor exit at a number of run conditions. Pratt & Whitney is conducting tests to characterize the thermal and pressure profiles; both the spatial and temporal variations of these quantities are being measured. In a parallel effort, NASA Lewis Research Center is conducting Laser Doppler Velocimeter (LDV) tests on a similar combustion rig. These tests are to characterize the turbulence profiles behind the combustor. Testing will be done both with and without a flow straightener. The preliminary test data looks good. The combustor has uniform thermal profile at the exit, and relatively constant temporal variation and turbulence levels.

When the combustor characterization tests are complete, testing of the cylinder behind the combustor will begin. The cylinder will be mounted 5 cm from the combustor exit. Any free-stream instrumentation will be located upstream from the cylinder, 2.5 cm from the combustor exit. Preliminary test data shows this will put the cylinder in an area of uniform thermal and Mach number profiles, minimizing both cylinder blockage effects and the effect of the cylinder on the free-stream instrumentation.
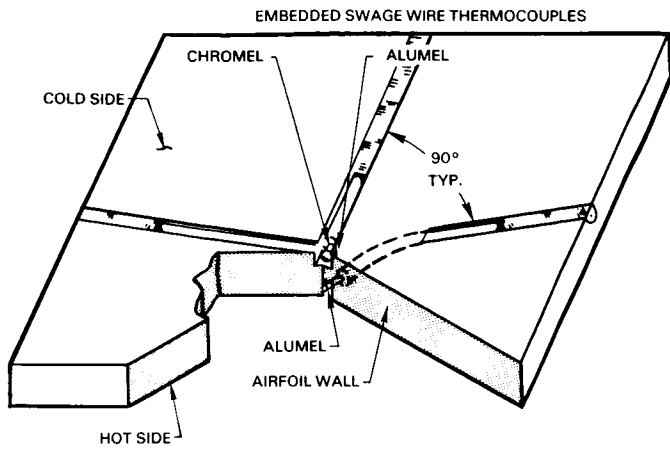
The cylinder will be mounted on a traverse can. This will allow the various sensor types to be sequentially moved into place behind the combustor, permitting multiple sensor types to be tested at the same conditions. All three sensors (the steady-state embedded thermocouple sensor, the steady-state Gardon gage, and the transient slug calorimeter) will be run over a range of test conditions. The resulting data should allow a good comparison between sensor types as well as between the sensor results and the expected value (which will be calculated from the measured free-stream conditions).

A second cylinder will be tested under a limited number of conditions. That cylinder will be a 1.6 cm diameter NiCoCrAlY tube with wall thickness of 0.48 cm. An array of sputtered thin film thermocouples will be installed on this cylinder. These will be run in front of the combustor rig in conjunction with a high response thermocouple probe (developed under NASA contract NAS3-23154, reference 3). The heat transfer coefficient is calculated from the ratio of the thermal variations of the free-stream gas and the surface thermocouples.

The work done under this contract has yielded accurate durable sensors for use on those sections of turbine airfoils where the heat flow conditions are relatively uniform. It also will yield a data base of high temperature heat flux measurements by several methods on a cylinder in cross-flow. In addition, the requirement for a program to investigate the measurement of heat flux on airfoils in areas of strong non-one-dimensional flow has been identified.

REFERENCES

1. Atkinson, W.H.; Cyr, M.A.; and Strange, R.R.: Turbine Blade and Vane Heat Flux Sensor Development. NASA Contract, NAS3-23529, August 1984.

2. Atkinson, W.H.; and Strange, R.R.: Development of Advanced High Temperature Heat Flux Sensors. NASA Report, CR-165618, September 1982.

3. Elmore, D.L.; Robinson, W.W.; and Watkins, W.B.: Dynamic Gas Temperature Measurement System. Final Report, CR-168167. NASA Contract, NAS3-23154. May 10, 1983.

EMBEDDED SWAGE WIRE THERMOCOUPLES

ELECTRICAL SCHEMATIC EMBEDDED THERMOCOUPLE SENSOR

CHROMEL

ALUMEL

COLD SIDE

90°
TYP.

ALUMEL

AIRFOIL WALL

HOT SIDE

ALUMEL 1

CHROMEL 2

COLD SIDE

AIRFOIL WALL

HOT SIDE

ALUMEL 3
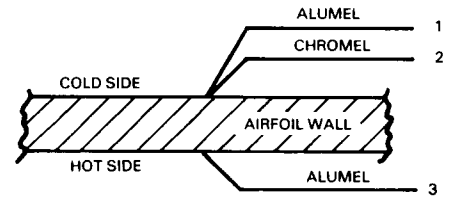
1-2 = REFERENCE TEMPERATURE

1-3 = SENSOR OUTPUT

Figure 1   Schematic of the Embedded Thermocouple Heat Flux Sensor
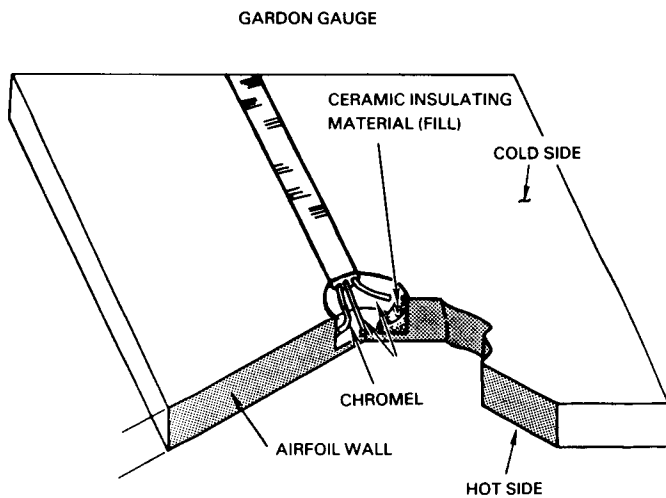
GARDON GAUGE

ELECTRICAL SCHEMATIC GARDON GAUGE SENSOR

CERAMIC INSULATING
MATERIAL (FILL)

COLD SIDE

CHROMEL

AIRFOIL WALL

HOT SIDE

ALUMEL 1

ALUMEL 2

CHROMEL 3

COLD SIDE

AIRFOIL WALL

HOT SIDE
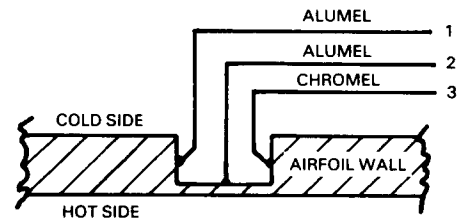
1-2 = SENSOR OUTPUT

1-3 = REFERENCE TEMPERATURE

Figure 2   Schematic of the Gardon Gage Heat Flux Sensor
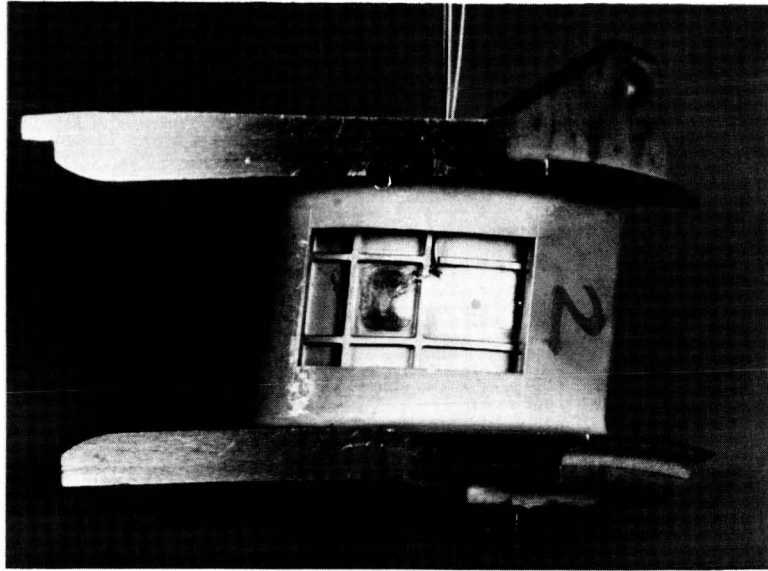
Figure 3   Vane in Process of Being Instrumented

WATER COOLED REFLECTOR

QUARTZ HALOGEN LAMP

QUARTZ WINDOW

WATER COOLED
REFLECTOR

WATER COOLED REFLECTOR

REFERENCE SENSOR
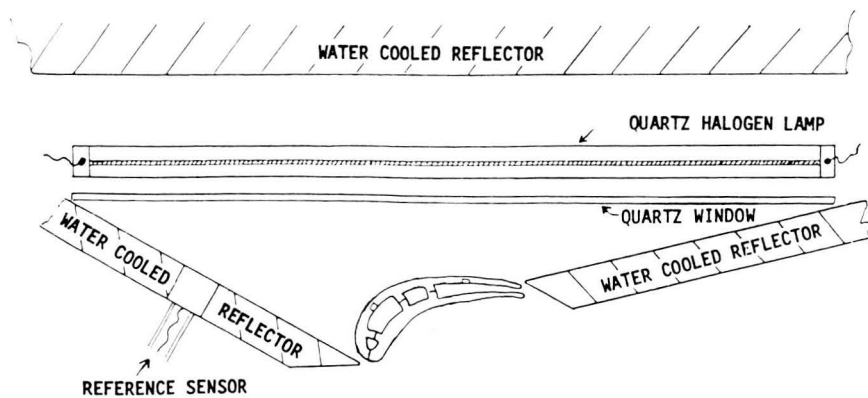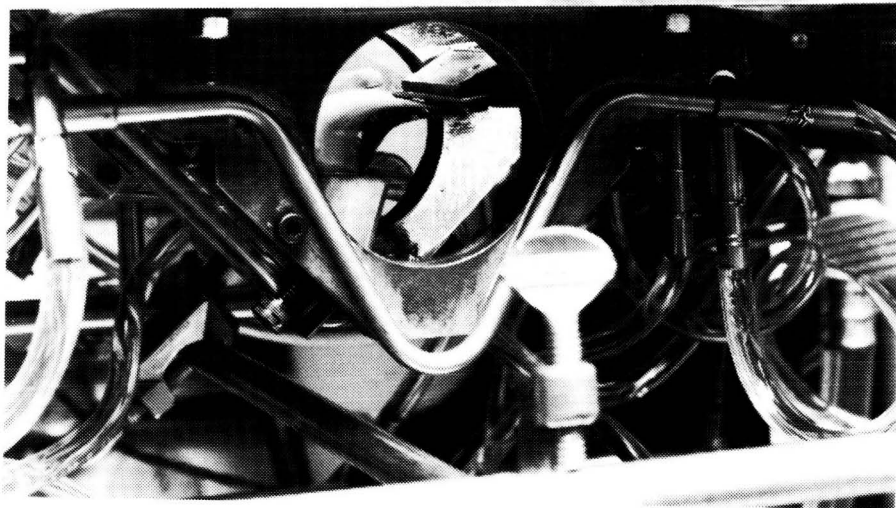
Figure 4   Calibration Fixture

54

Figure 5   Lamp Face of Quartz Lamp

Figure 6   Calibration Curve - Gardon Gage Installed in Turbine Vane
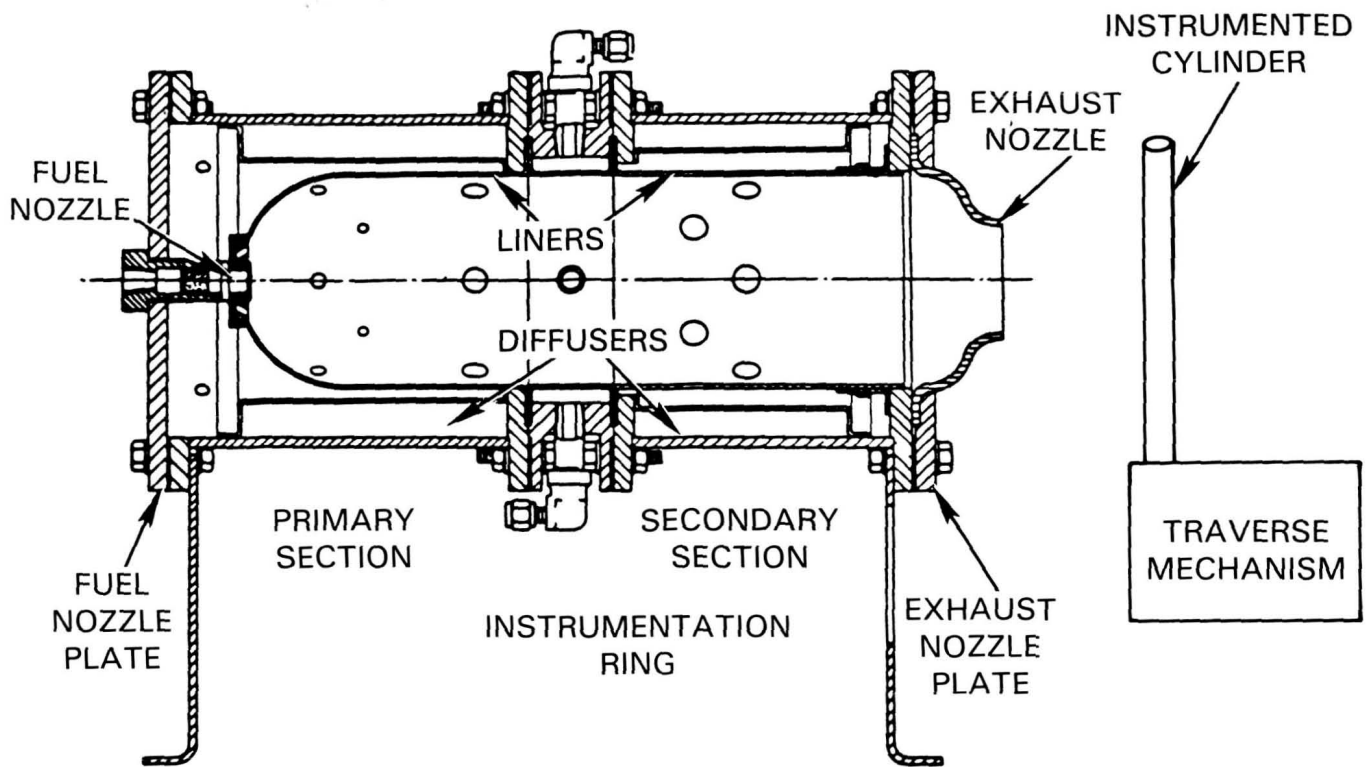
Figure 7   Schematic of Combustor Rig
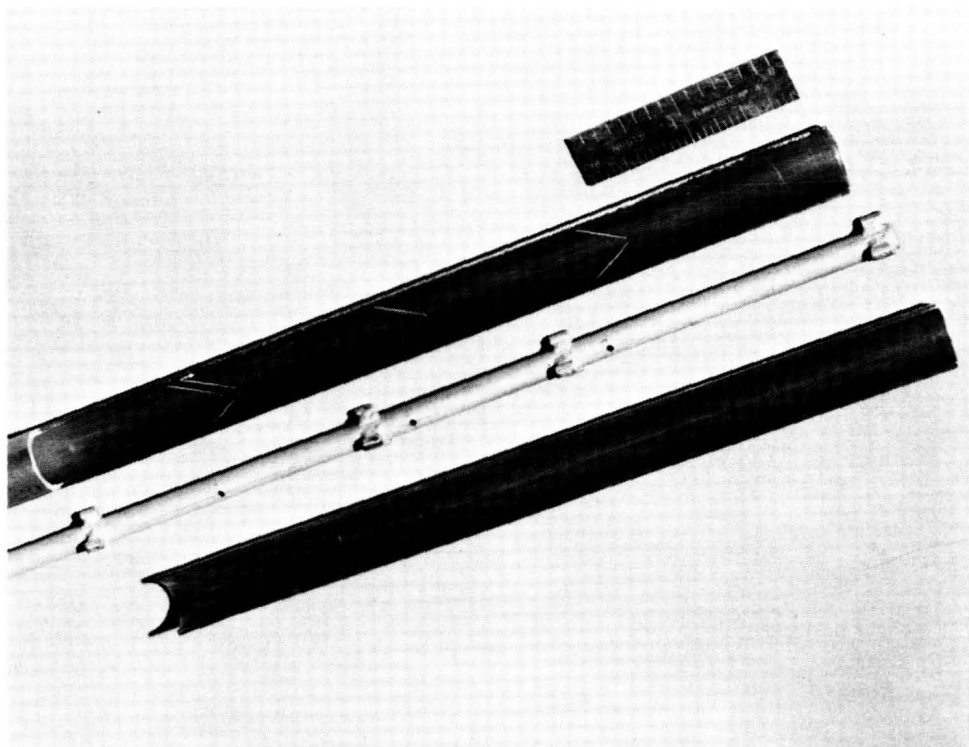
Figure 8   Open Cylinder - Elox Completed
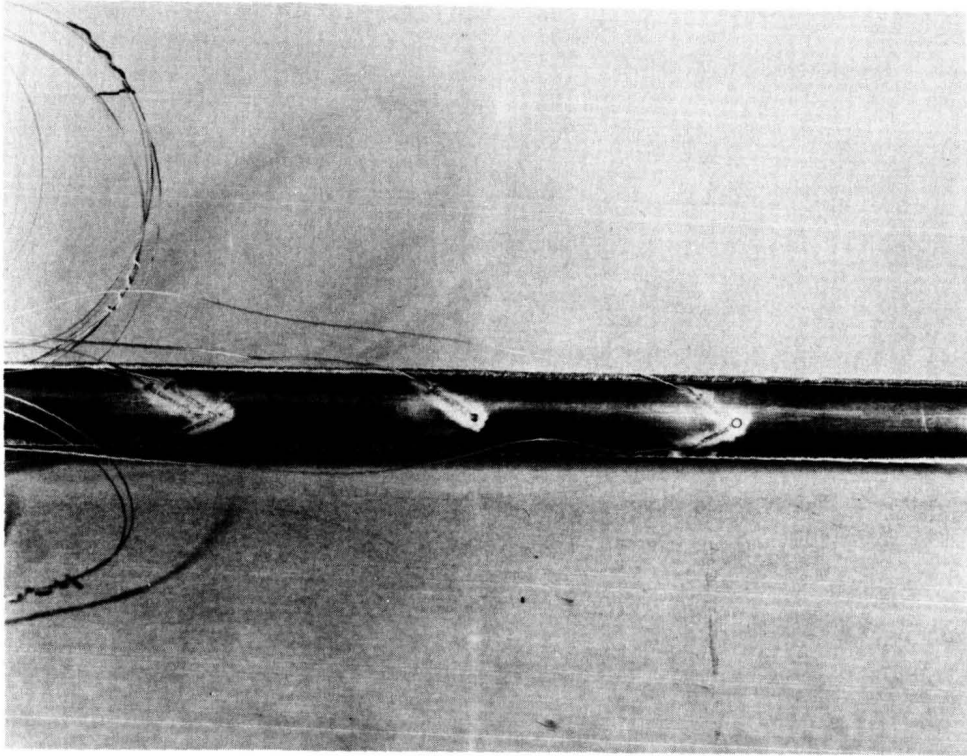
Figure 9   Open Cylinder - Lead Wires Installed
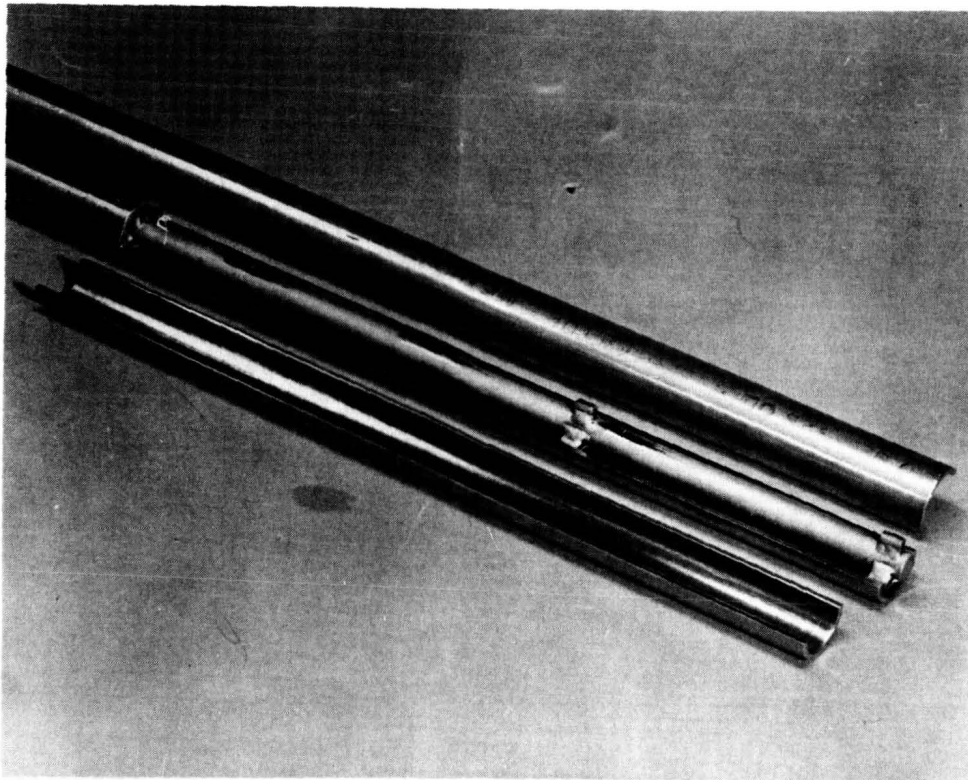
Figure 10   Open Cylinder With Center Tube

57
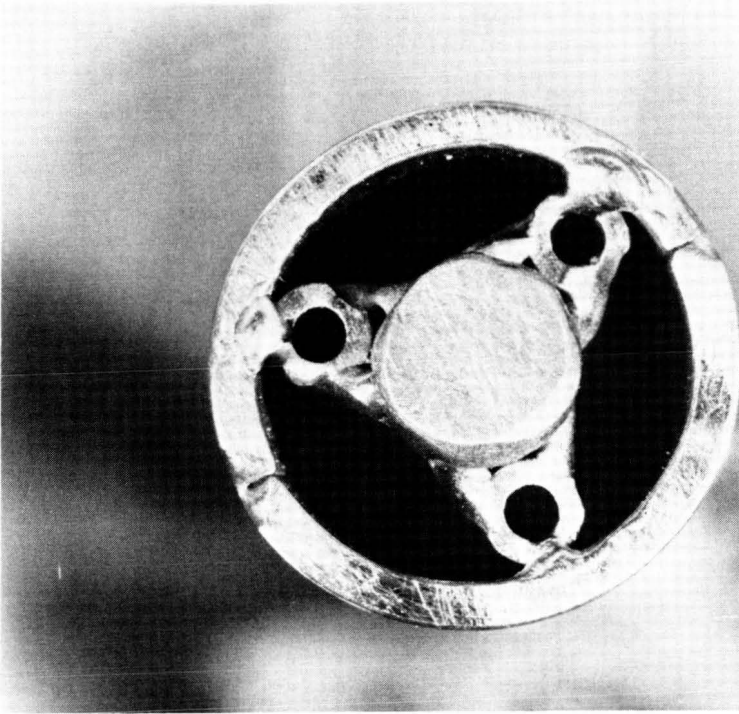
Figure 11   End View of Completed Cylinder
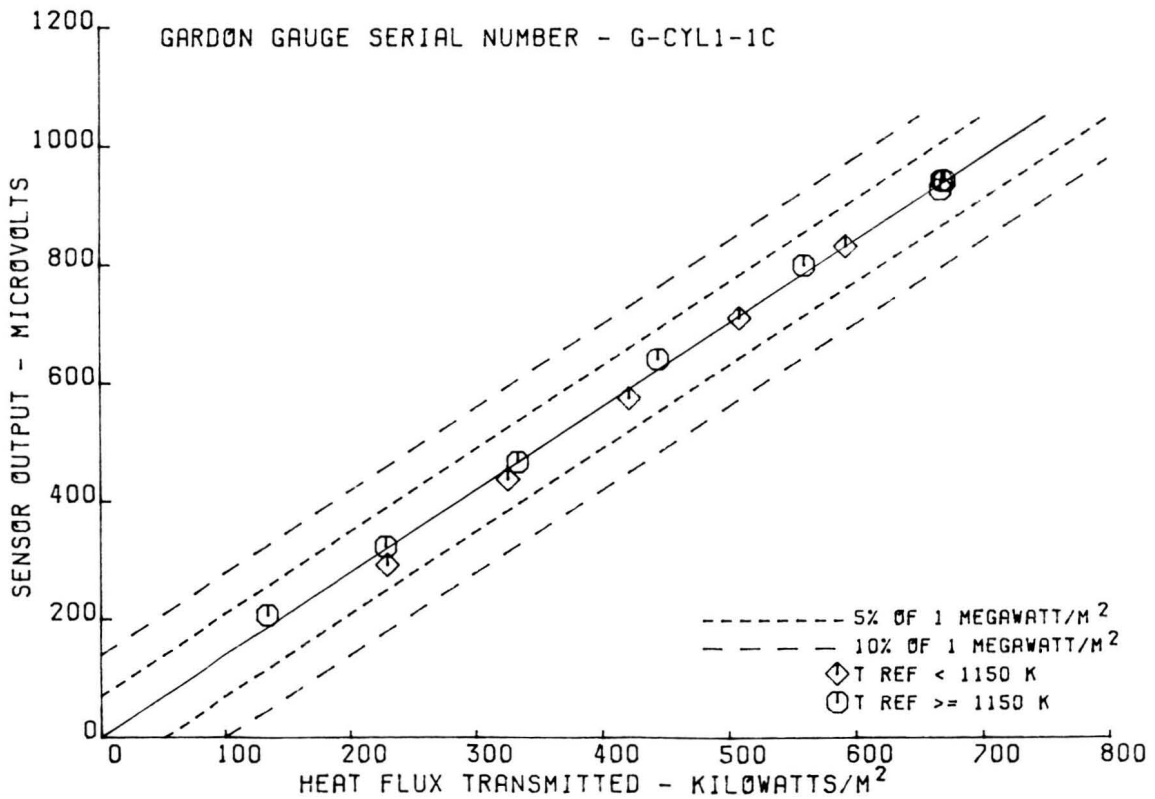
Figure 12   Calibration Curve - Gardon Gage Installed in Cylinder

LASER ANEMOMETERS OF HOT-SECTION APPLICATIONS

Richard G. Seasholtz, Lawrence G. Oberle, and Donald H. Weikle
National Aeronautics and Space Administration
Lewis Research Center

E-2267-14

INTRODUCTION

The objective of this in-house program is to develop laser anemometers (LA's) for use in the study of the hot-section components of turbomachinery. Specifically, laser anemometers are being developed for use in the turbine facilities at Lewis that are involved in the HOST program. In this paper a brief review of the status of the program is given along with some results of work accomplished since the report to the 1983 HOST Workshop (ref. 1).

SUMMARY OF ACCOMPLISHMENTS

The PDP 11/44 minicomputer acquired for the open-jet burner facility is fully operational. It is used both for the control of the three-axis traversing system and for data acquisition. In addition, it provides on-line graphics that allows the operator to monitor the data as it is acquired. Software was written for off-line data reduction. Mean velocity and turbulence intensity profiles are generated, and, for sufficiently high data rates, the autocorrelation of the velocity can be computed, which gives the turbulence scale.

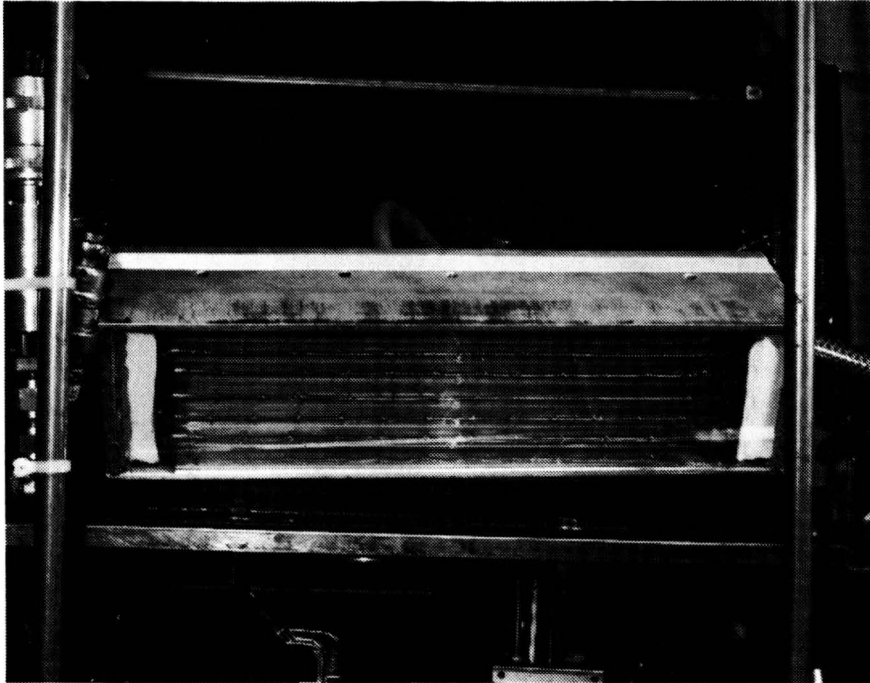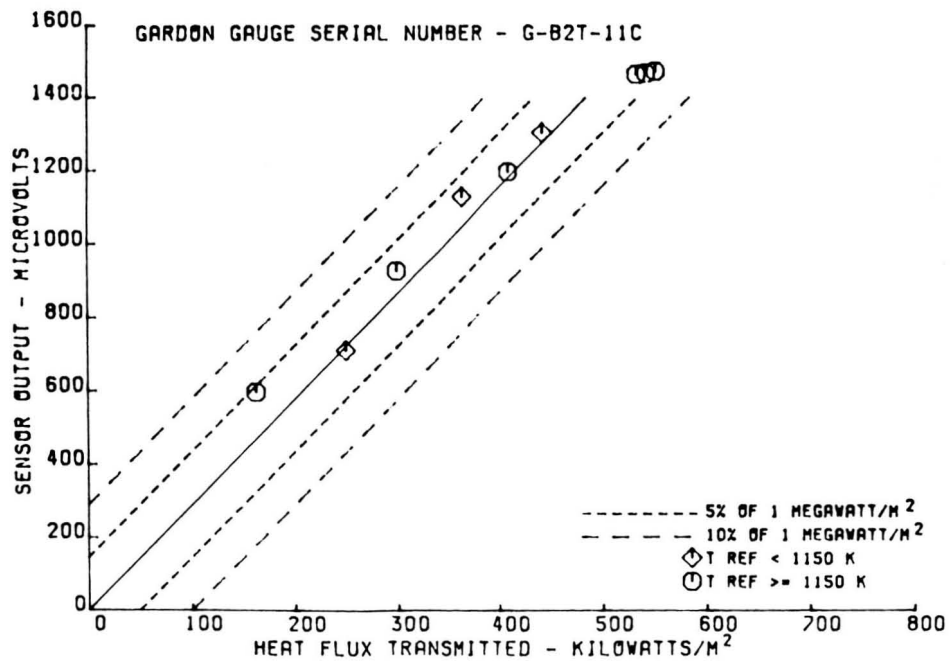A preprocessor was designed, fabricated, and tested; its function is to allow computer control of several previously manual controls of the counter processor.

The open-jet burner facility was used to test the LA system. An experiment was conducted that used the LA to measure the mean velocity and turbulence intensity near a cylinder located in the hot exhaust jet.

Analytical work done as part of the LA optimization was reported at the AIAA/SAE/ASME Joint Propulsion Conference (ref. 2). Computer programs were written to calculate Mie scattering from spheres with complex index of refraction.

The design for the housing, windows, and traversing system for the Lewis Warm Turbine Facility was completed.

The new design, four-spot, time-of-flight laser anemometer developed at Case Western Reserve University under a NASA grant is now operational.

APPROACH

The overall approach being followed in this program is outlined in figure 1. Based on an analysis of particle lag for the expected flow field, the required particle size is determined. A particle generator can then be selected (with additional size selection if required). A commercial particle sizing instrument (described in ref. 1) is used to evaluate particle generators. Mie scattering theory is used to evaluate the scattering cross sections of the particles, which are needed for the analysis of the optics design. Another important input needed for the system analysis is the reflectivity of surfaces located near the probe volume. Laser light scattered from these surfaces (flare) limits the proximity of measurement to surfaces. A model for the sig- nal processor completes the elements needed to define the system. Prediction analysis methods are then used to optimize the system design to achieve the desired accuracies of the flow parameters in the minimum run time.

MODELING OF FRINGE-TYPE LASER ANEMOMETER

The fringe-type LA (fig. 2) was analyzed using the Cramer-Rao bound for the variance of the estimate of the Doppler frequency as a figure of merit. Mie scattering theory was used to calculate the Doppler signal with both the amplitude and phase of the scattered light taken into account. The noise from wall scatter was calculated using the wall bidirectional reflectivity and the irradiance of the incident beams. A procedure was developed to determine the optimum mask for the probe volume located a given distance from a wall (fig. 3). The rapid decrease in the signal-to-noise ratio as the probe volume approaches a wall is shown in figure 4. A complete description of this work is given in reference 2.

MIE SCATTERING CALCULATIONS

Mie scattering algorithms for spheres with a complex refractive index were developed for both the IBM 370/TSS and PDP-11 computers. These are used both for the selection of seed material and to evaluate the effect of other particulates found in the flow (e.g., soot). They are also an integral part of the fringe-type LA modeling work. Figure 5 shows the differential cross section for aluminum oxide, one of the principal candidate seed materials for high-temperature flows. Note that the cross section decreases significantly as the scattering angle moves from direct backscatter. The complex behavior of the backscatter cross section as a function of particle size is shown in figure 6 for aluminum oxide and in figure 7 for silicon carbide. Note that silicon carbide, whose index of refraction is much larger than that of aluminum oxide, does not offer any advantage in scattering ability over aluminum oxide. Figure 8 shows the differential cross section of soot (an absorbing material with a complex refractive index). An important point shown by this figure is that the backscatter for soot is relatively small. Finally, it must be pointed out that these Mie calculations are only for spheres; indeed, the actual refractive seed materials usually have irregular shapes. We are assuming, for the purposes of our modeling work, that the scattering cross section for irregular shapes of a given aerodynamic size can be approximated by the results for spheres of the same aerodynamic size.

PREPROCESSOR FOR COUNTER

One limitation encountered when using counter-type burst processors in computer-based laser anemometer systems is that many of the counter controls must be set manually. Examples of these manual settings are the high- and low-pass filter cutoff frequencies and the threshold level. In many experiments it is necessary to change these settings frequently. This is a major impediment to the development of the automated data taking procedures needed to minimize experimental run time. To overcome this limitation, a separate preprocessor was developed (fig. 9). The preprocessor provides both local and computer control of the high- and low-pass filter selections (eight each), the system gain (controlled by means of an RF amplifier and programmable attenuator), and the PMT high voltage. Other functions of the counter can also be controlled, such as the resolution of the time between measurements and the number of words sent from the counter to the computer for each measurement. Finally, the preprocessor monitors the PMT average current, and, if it exceeds the maximum permitted value, sounds an alarm.

CYLINDER IN CROSS-FLOW MEASUREMENTS

One of the applications of the laser anemometer installed in the open-jet burner facility (fig. 10) was the measurement of the mean velocity and turbulence intensity distributions near a cylinder in cross flow (fig. 11). These measurements are being used for another HOST project, the development of advanced heat flux sensors. The cylinder had an diameter of 1.6 cm and was mounted 56 mm from the jet exit. An example of a survey of mean axial velocity and tubulence intensity with the cylinder removed from the flow is shown in figure 12. Figure 13 shows a survey taken about 1 mm upstream at the cylinder. Each survey consisted of measurements at 50 points and took about 2 minutes.

FOUR-SPOT TIME-OF-FLIGHT LASER ANEMOMETER

The four-spot, time-of-flight LA being developed at Case Western Reserve University under a NASA grant is now operational. A description of this new type of anemometer is given in references 3 to 5. A second version of that system, based on an argon-ion laser, has been designed for use in high-velocity gas flows. This system will be fabricated and tested in the open-jet burner facility to evaluate its suitability for use in hot-section flow experiments.

REFERENCES

1. Seasholtz, Richard G.; Oberle, Lawrence G.; and Weikle, Donald H.: Laser Anemometry for Hot Section Applications. Turbine Engine Hot Section Technology-1983, NASA CP-2289, 1983, pp. 57-68.

2. Seasholtz, R. G.; Oberle, L. G.; and Weikle, D. H.: Optimization of Fringe-Type Laser Anemometers for Turbine Engine Component Testing. AIAA Paper-84-1459, June 1984.

3. Edwards, R. V.: Laser Anemometer Optimization. Turbine Engine Hot Section Technology (HOST), NASA TM-83022, 1982, pp. 113-136.

4. Edwards, Robert V.: Time-of-Flight Anemometer for Hot Section Applications. Turbine Engine Hot Section Technology 1983, NASA CP-2289, 1983, pp. 69-72.

5. Lading, L.: Estimating Time and Time-Lag in Time-of-Flight Velocimetry. Appl. Opt., vol. 22, no. 22, Nov. 15, 1983, pp. 3637-3643.

LASER ANEMOMETER DEVELOPMENT

```
                              ┌─────────────┐
                              │  COMPUTED   │
                              │ FLOW FIELD  │
                              └─────────────┘
                                     │
                                     ▼
┌──────────────┐              ┌─────────────┐
│   PARTICLE   │              │    LAG      │
│  GENERATOR   │              │  ANALYSIS   │
└──────────────┘              └─────────────┘
       │                             │
       ▼                             ▼
┌──────────────┐              ┌─────────────┐
│    SIZE      │─────────────▶│    MIE      │
│  SELECTOR    │              │ SCATTERING  │
└──────────────┘              └─────────────┘
                                     │
                                     ▼
┌──────────────┐              ┌─────────────┐
│    FLARE     │─────────────▶│   OPTICS    │
└──────────────┘              └─────────────┘
                                     │
                                     ▼
                              ┌─────────────┐
                              │   SIGNAL    │
                              │  PROCESSOR  │
                              └─────────────┘
                               │          │
                               ▼          ▼
                    ┌──────────────┐  ┌──────────────┐
                    │  PREDICTION  │  │  PARAMETER   │
                    │   ANALYSIS   │  │ ESTIMATION   │
                    └──────────────┘  └──────────────┘
                               │          │
                               ▼          ▼
                          ┌──────────────────┐
                          │   FLOW FIELD     │
                          │   PARAMETERS     │
                          │   +  ERRORS      │
                          │   +  TIME        │
                          └──────────────────┘
```
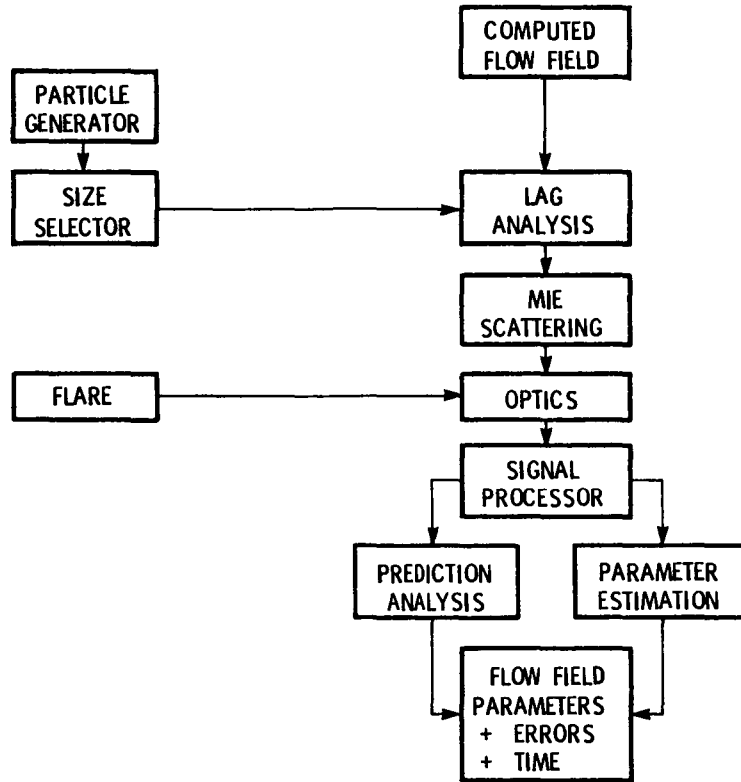
Figure 1

FRINGE-TYPE LASER ANEMOMETER

Figure 2

CS-84-2235

63
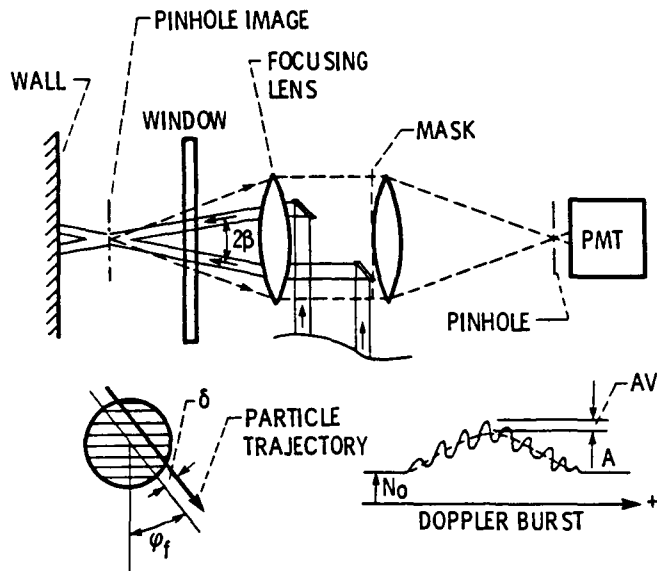
OPTIMUM APERTURE MASK FOR PROBE VOLUME 1 mm FROM WALL, f/4 SYSTEM
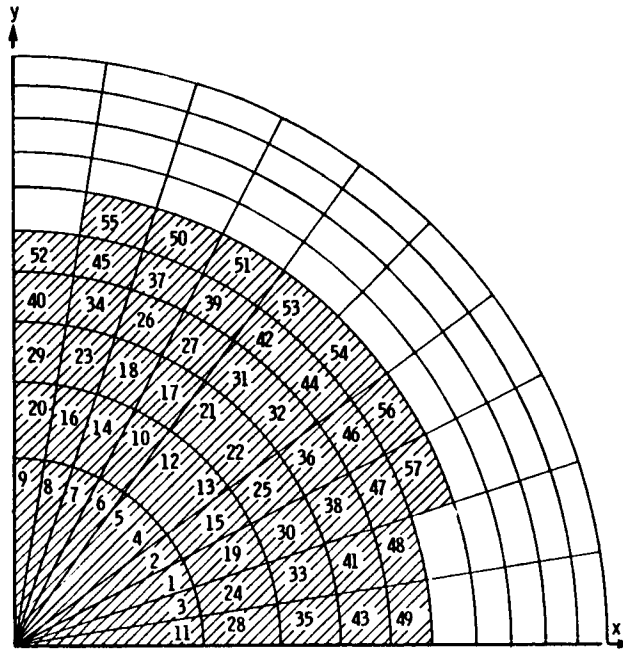
Figure 3   CS-84-2238

SNR VS. DISTANCE OF PROBE VOLUME FROM WALL, f/4 SYSTEM
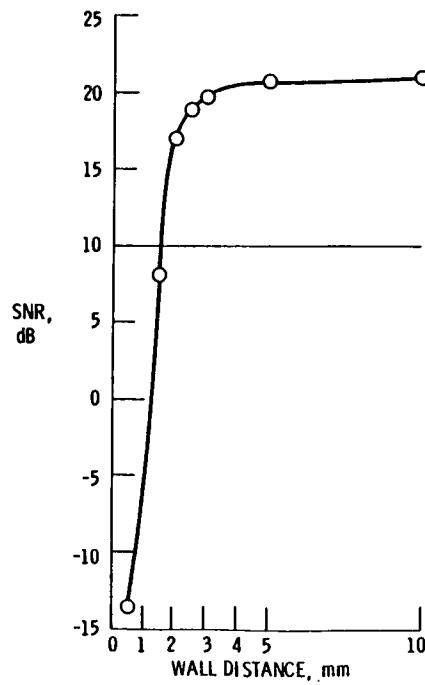
Figure 4   CS-84-2231

DIFFERENTIAL CROSS SECTION

Al_2O_3 (n = 1.77); DIAMETER = 0.9 μm; WAVELENGTH = 0.5145 μm;
BACKSCATTER CROSS SECTION, CR(180) = 4.34x10^{-13} m^2
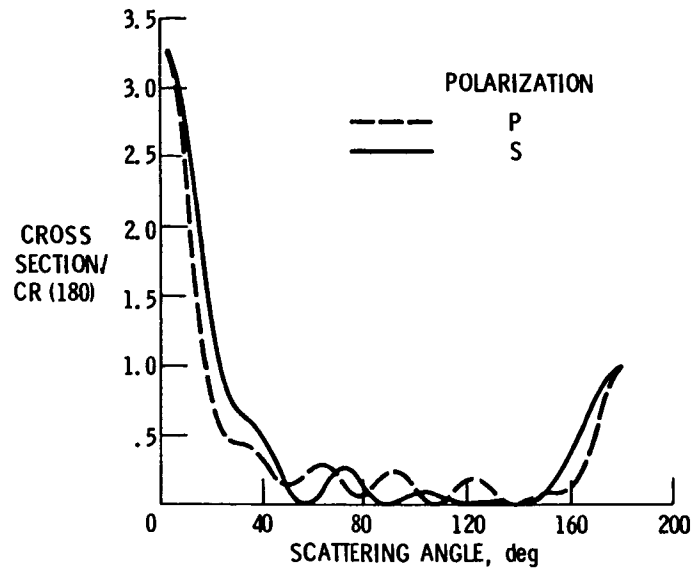
Figure 5

BACKSCATTER CROSS SECTION
Al_2O_3 (n = 1.77)
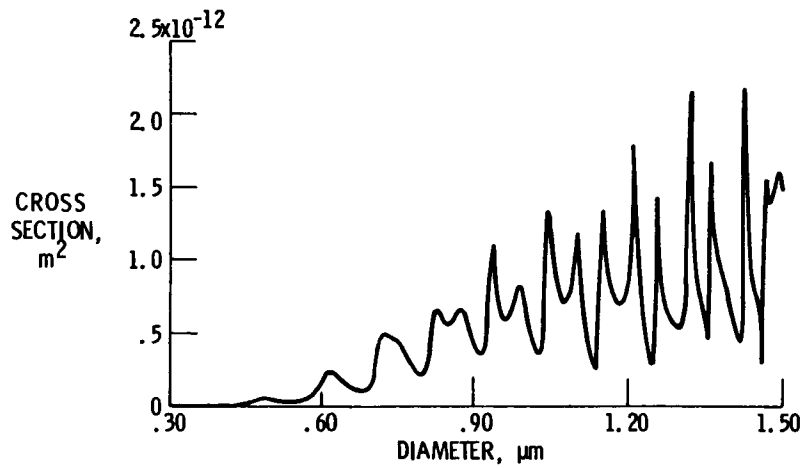
Figure 6

BACKSCATTER CROSS SECTION
SiC (n = 2.6)
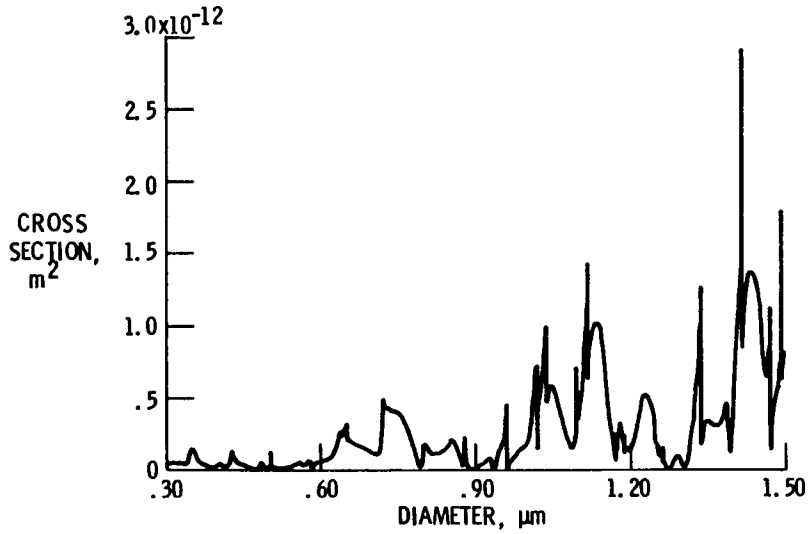
Figure 7

DIFFERENTIAL CROSS SECTION

SOOT (n = 1.9 + 0.52i); DIAMETER = 1.0 µm; WAVELENGTH = 0.5245 µm; BACKSCATTER CROSS SECTION, CR (180) = 6.79x10^{-15} m^2

Figure 8

66
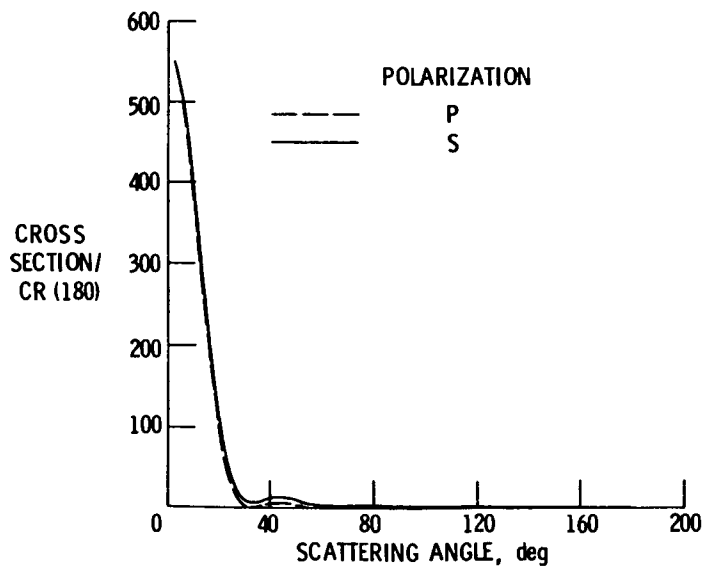
LASER ANEMOMETER PREPROCESSOR
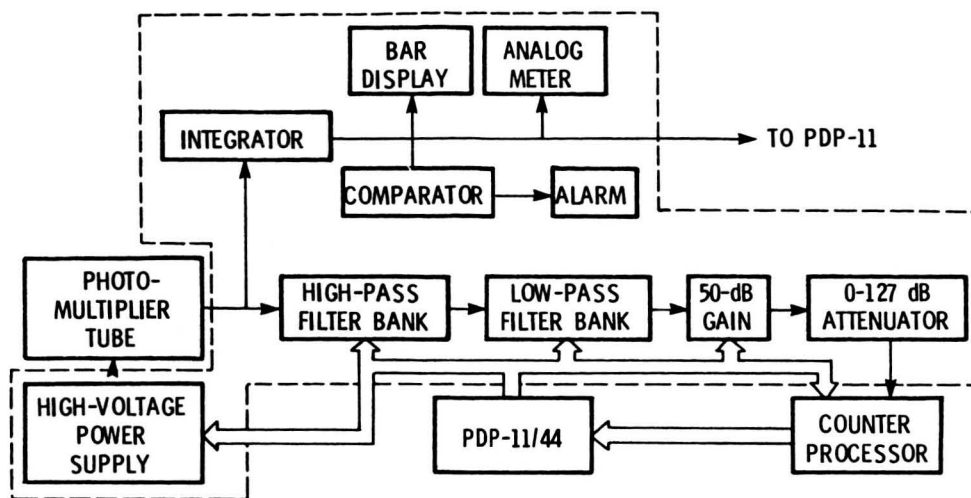
Figure 9

OPEN-JET BURNER AND LASER ANEMOMETER

CS-84-3875

Figure 10

67
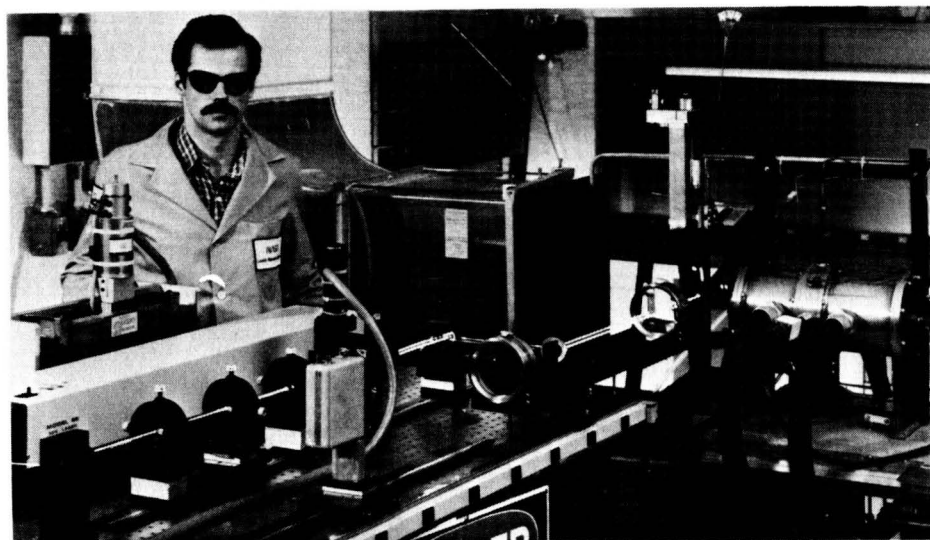
CYLINDER IN CROSS FLOW EXPERIMENT

CS-84-3874

Figure 11

AXIAL VELOCITY AND TURBULENCE INTENSITY

AXIAL POSITION, 51 cm; MACH 0.7; T = 800° C

Figure 12

68
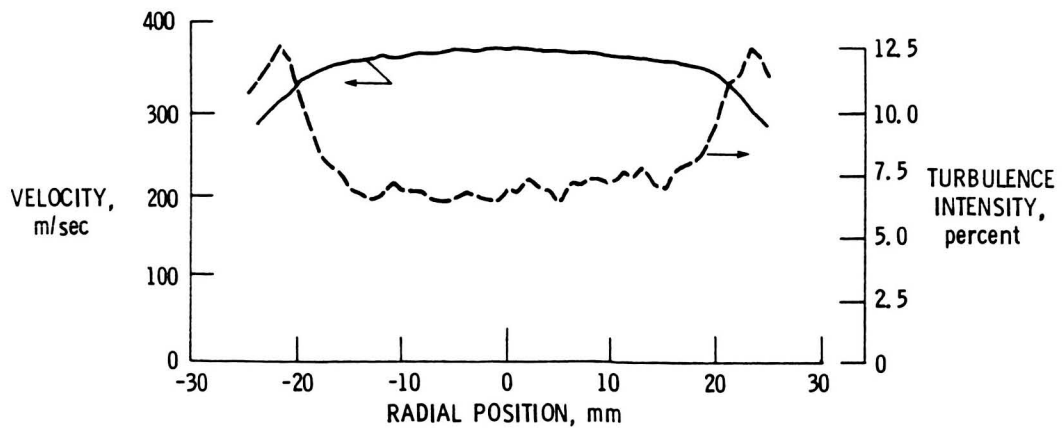
AXIAL VELOCITY AND TURBULENCE INTENSITY

CYLINDER IN CROSS FLOW
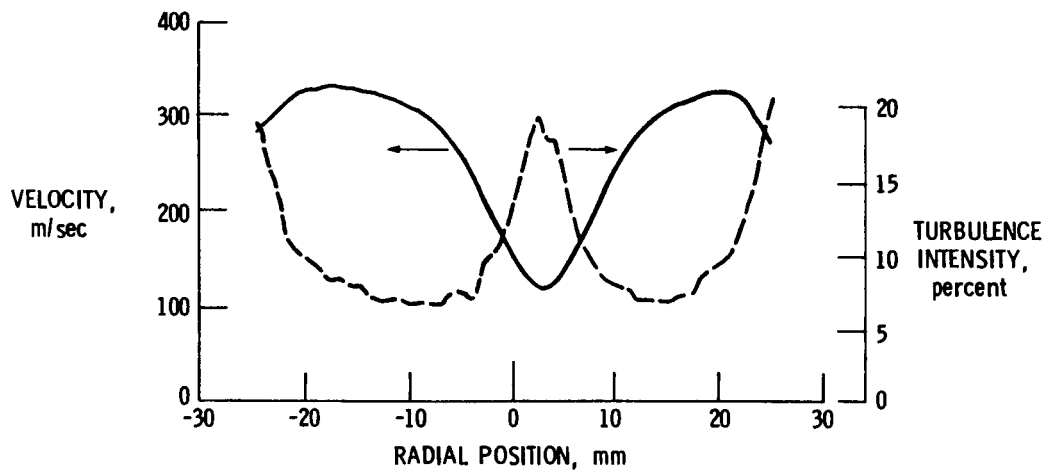
Figure 13

HIGH TEMPERATURE STATIC STRAIN
GAGE PROGRAM

Charles Hulse and Richard Bailey
United Technologies Research Center

and

Howard Grant
Pratt and Whitney Aircraft

The purpose of this program is to develop electrical resistance strain gages for static strain measurements of nickel or cobalt superalloy parts inside a gas turbine engine on a test stand. Measurements of this type are of great importance in meeting the goals of the HOST Program because, without reliable knowledge of the stresses and strains which exist in specific components, it will be difficult to fully appreciate where improvements in design and materials can be implemented. The first part of this effort consists of a strain gage alloy development program which is to be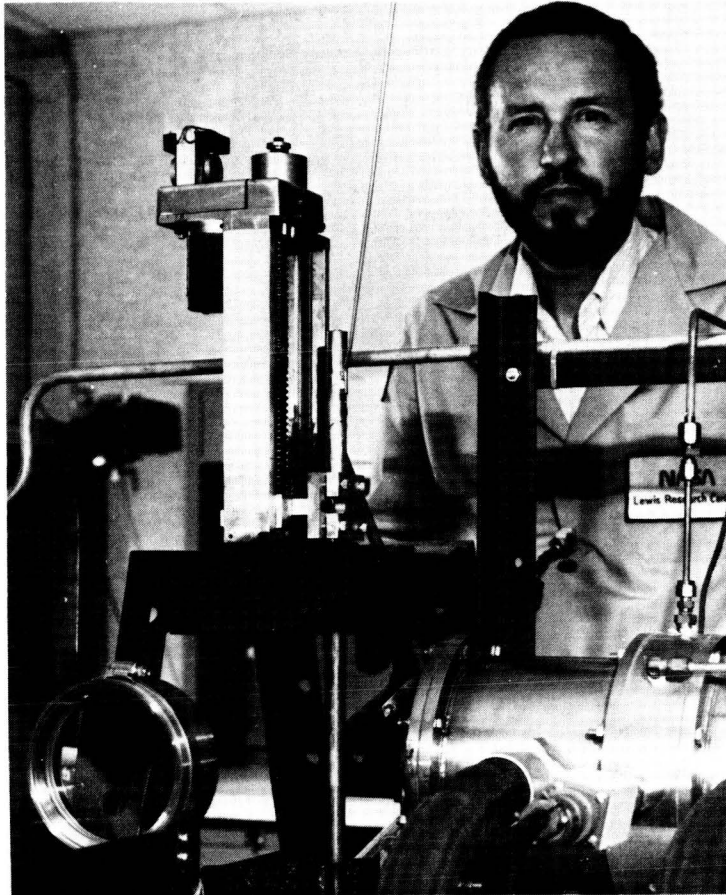 followed by an investigation of complete strain gage systems which will use the best alloys developed together with other system improvements.

The specific goal for the complete system is to be able to make measurements to $\pm$ 2,000 $\mu\varepsilon$ with an error of no more than $\pm$ 10% over a 50 hour period. In addition to simple survival and stability, attaining a low thermal coefficient of resistivity, of the order of 100 ppm/K or less, is also a major goal. This need results from the presently unavoidable uncertainty in measurements of exact temperatures in the turbine. The first year of effort resulted in the indentification of an FeCrAl alloy and the Pd-Cr systems as the best candidates. This years effort has been concentrated on additional alloy development, fabrication and alloy evaluation studies.

Although the size and thickness requirements to avoid aerodynamic effects suggest sputtering as the best strain gage fabrication technique, this approach is too slow and expensive for alloy studies. An arc-melting and drop-casting facility, shown schematically in Figure 1, was therefore developed. This has provided a relatively quick and inexpensive way to prepare rod samples which can be subsequently ground and polished to produce flat ribbon samples. A differential pressure in the titanium gettered argon above the molten sample supplies the force to quickly move the molten alloy down into the ceramic casting tube when the bottom film across the hole becomes melted enough to rupture.

As an alternative fabrication approach, palladium alloy were prepared as thin foils about 2.5 in. in diameter using the splat cooling approach. For this purpose, the ram shown in Figure 1 was used to splat a small arc-melted drop on a water-cooled hearth which did not include the casting hole shown in Figure 1.

These foils were subsequently polished down from thickness of about 0.075 to be about 0.050 mm thick and then cut into strips for testing.

The thermal cycling apparatus in Figure 2 was used to make resistivity measurements up to 1250K by the use of a split metal tube heater which could be cycled or held at a constant temperature under program control. The test samples were positioned axially in the center of this tube with platinum leads for voltage measurements and a thermocouple attached to the center of the test section by spot welding. This system was improved by the addition of an external plenum to permit cooling gases to be introduced at lower temperatures for better control. A variety of circuit and computer program program changes were also made to improve the accuracy of the data.

Our previous work had identified the FeCrAl composition Fe-11.9Al-10.6Cr, in weight percent, as an improved strain gage alloy candidate. The effects on the oxidation of this alloy of a number of alloying additions were examined by weight change measurements made over a 50 hour period in air at 1250K. A total of 12 different samples were examined with different additions of Y, Co, Zr, Hf, Sc and Ni. None of these elements appeared by this measure to provide a significant improvement. It was subsequently observed, as shown in Figure 3, that the resistivity versus temperature curves for this base alloy show a gradual change with increasing times of exposure to 1250K. Because of this effect and concern over the oxidation of this alloy, work on this system was discontinued in favor of work on PdCr alloys.

Efforts were made to examine the effects of alloying additions on the Pd-13 wt % Cr alloy previously developed. Thirty four samples with various amounts of Cr, Gd, Er, La, Nc, Re, Ta, Y, Mo and W were prepared and evaluated to determine the alloying limits. The oxidation behavior of seven alloy compositions were also examined by measurements of weight changes over a 50 hour period in static air at 1250K. Figure 4 shows with electron microprobe data how the chromium becomes concentrated at the surface of the alloy where other measurements confirm that it reacts with oxygen to form Cr_2O_3. The electrical behavior of 12 different alloy samples were examined during thermal cycling at different heating and cooling rates and during thermal soaks at 1100 and 1250 K in air and in argon. The results of this work indicated that the original Pd-13 Wt % Cr alloy was still the most desirable condidate. Table I presents data on the reproducibility of resistance and apparent strain from cycle to cycle at 50K/min assuming a gage factor of 2.0. Figure 5 shows electrical drift data for drop-cast rod material at 1100 and 1250 K in air and in argon. These repeatability and stability measurements are close to the program goals for a complete strain gage system.

72

TABLE I

Cycle to Cycle Reproducibility of Pd - 13 wt % Cr

Temp. (K)	Std. Dev. (ΔR/R)	Difference in apparent strain in microstrain from avg. (G.F. = 2.0)							
		Cycle #2		Cycle #3		Cycle #4		Cycle #5	
		Heat	Cool	Heat	Cool	Heat	Cool	Heat	Cool
300	.000035	-9	22	-9	8	-9	-20	-9	29
450	.000167	66	-86	67	-97	51	-92	108	-18
600	.000134	74	-49	54	-76	33	-80	78	-35
675	.000173	102	-76	65	-94	54	-91	95	-54
725	.000243	137	-110	103	-131	96	-106	117	-105
825	.000117	60	-58	37	-62	47	-54	71	-40
975	.000071	46	-26	30	-25	-4	-42	45	-24
1125	.000061	35	-18	20	-26	37	-48	11	-10
1225	.000063	27	-17	29	-16	19	-53	33	-21
1250	.000043	30		-16		-15		1	

Avg. Std. Dev. = .000130
Runs rezeroed between cycles

TRI-ARC MELTER SHOWING POSITION OF SPLAT COOLING RAM AND DROP CASTING TUBE

SPLAT COOLING RAM

TUNGSTEN ELECTRODE

MOLTEN ALLOY

COLD COPPER HEARTH

SiO_2 CASTING TUBE

FIGURE 1
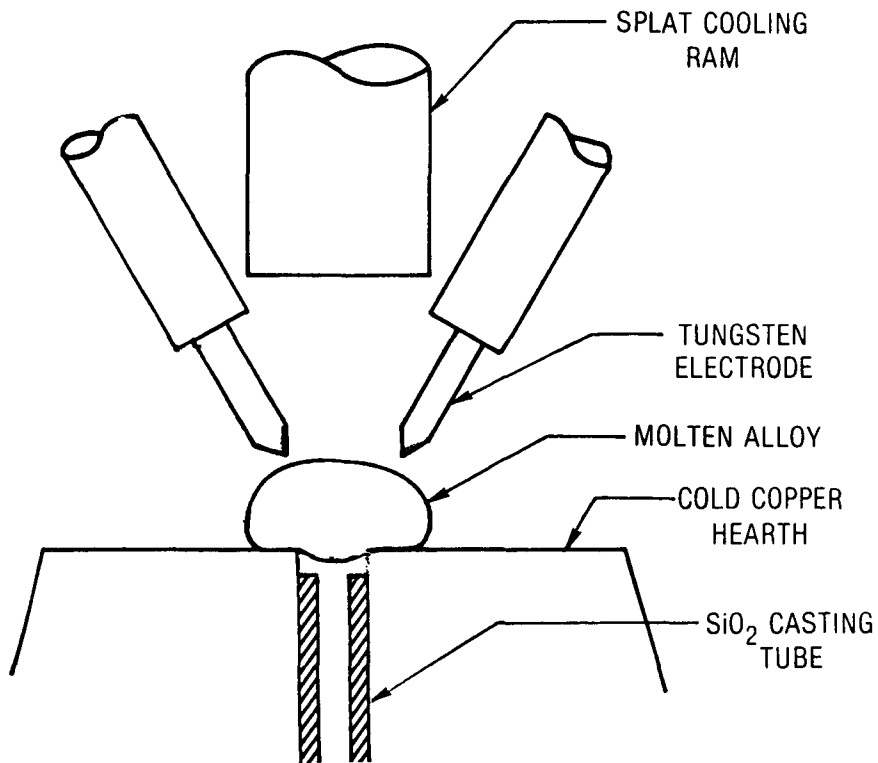
84-8-70-1

HIGH SPEED THERMAL CYCLE/RESISTIVITY MEASUREMENT APPARATUS
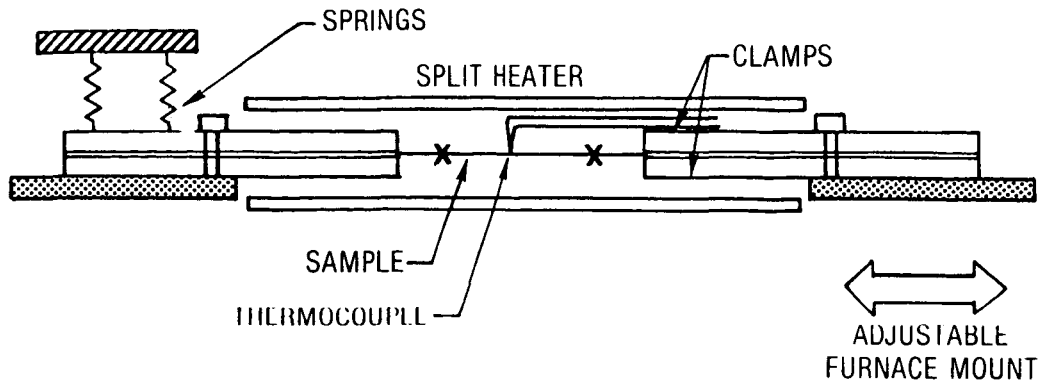

FIGURE 2

CHANGE IN FeCrAl ALLOY RESISTANCE VS TEMPERATURE AFTER DIFFERENT SOAK TIMES AT 1250K
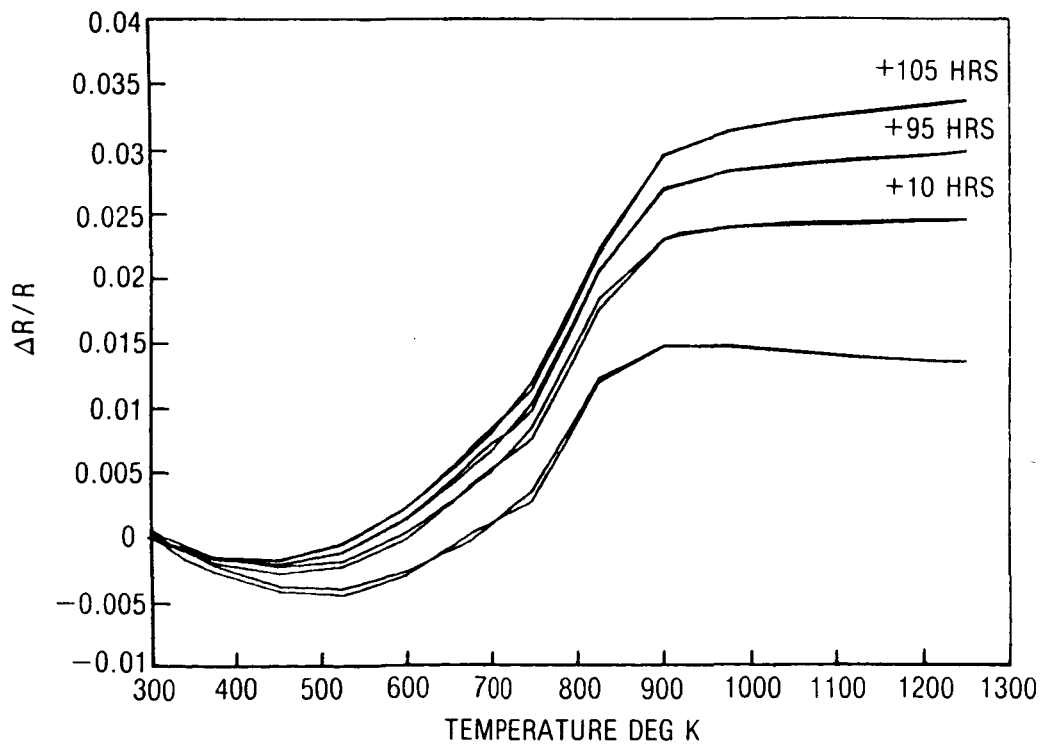

FIGURE 3

84—8—70—2

ELEMENTAL COMPOSITION PROFILES AT THE SURFACE OF Pd-13 WT% CR
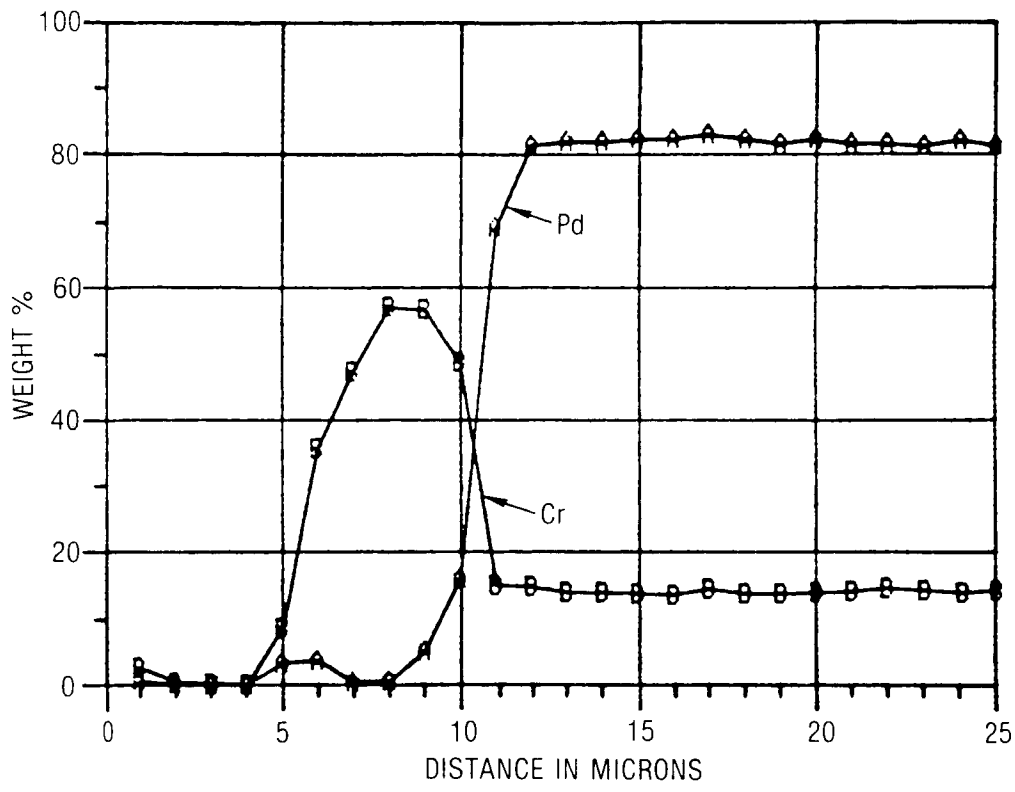SAMPLE AFTER 40 HOURS IN AIR AT 1250K

FIGURE 4

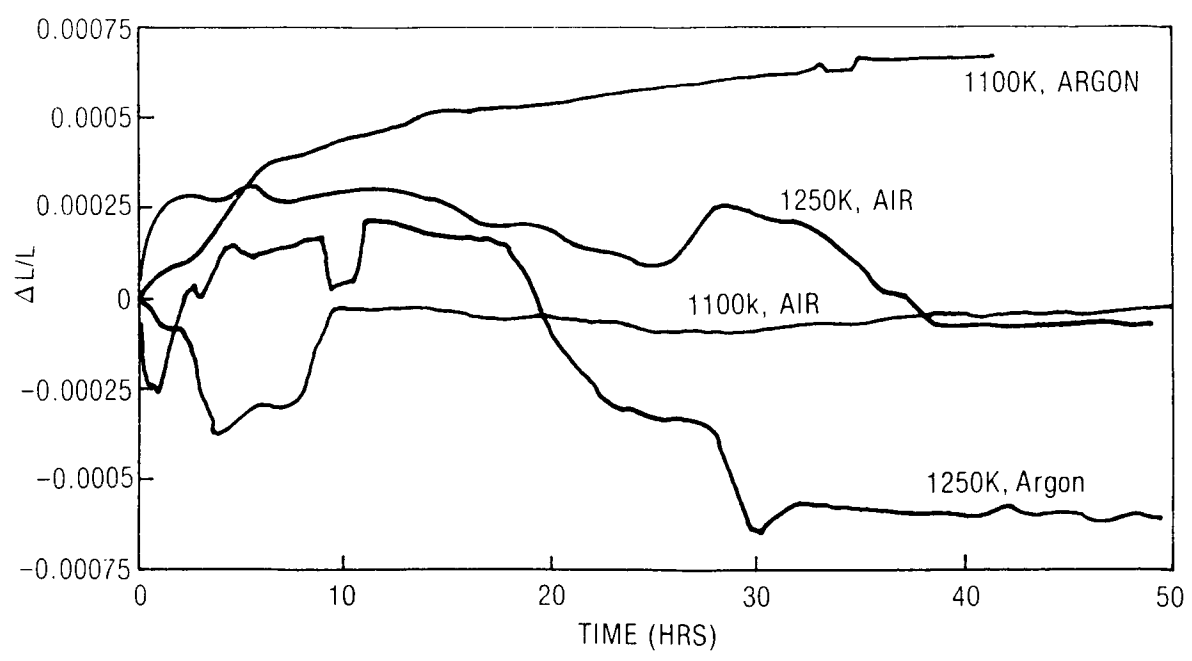DRIFT IN APPARENT STRAIN OF Pd-13 Wt% Cr ASSUMING A GAGE FACTOR OF 2.0

FIGURE 5

76

EVALUATION RESULTS OF THE 700 °C CHINESE STRAIN GAGES

Howard F. Hobart
National Aeronautics and Space Administration
Lewis Research Center

INTRODUCTION

There has been a continuing interest and need for resistance strain gauges capable of making static strain measurements on components located in the hot section of gas-turbine engines. A paper by Tsen-tai Wu, et al., (ref. 1) describes the development and evaluation of high-temperature (700 °C) gauges fabricated from specially developed Fe-Cr-Al-V-Ti-Y alloy wire. As part of the Lewis HOST program, several of these gauges and a quantity of P12-2 ceramic adhesive were purchased for evaluation from the China National Aero-Technology Import and Export Corporation of Beijing, China.

Nine members of the aircraft turbine engine community were invited to participate in an evaluation of these gauges. Each participant was sent one strain gauge, a small amount of ceramic adhesive, instructions for mounting the gauge on a test beam (not supplied), and a set of suggestions for the evaluation experiment.

The following discussion includes data on gauge factor variation with temperature, apparent strain, and drift. The reported results are from six participants.

DISCUSSION

Gauge Factor

Figure 1 is a plot of percentage change in gauge factor from its room temperature value versus temperature for five evaluators. The trend is for gauge factor to decrease with increasing temperature. The average slope is -3.5 percent per 100 K, with a maximum data spread of 18 percent. The curve labeled Wu is from reference 1 and is based on eight gauges bonded to both sides of a constant-moment beam strained to 938 microstrain. Curves from the other evaluators are averaged data in both tension and compression at several strain levels in the range 300 to 2000 microstrain.

By way of comparison, some interesting results have recently been reported on by Stetson (ref. 2) with Kanthal A-1 (Fe-Cr-Al-Co) gauges. These gauges exhibit gauge factor characteristics similar to the Chinese gauges (fig. 2). The solid line curves are the envelope of curves from figure 1 and the dashed line curves show the data spread on the eight Kanthal A-1 gauges tested.

The average values of gauge factor at room temperature and the indicated high temperatures are listed in table I. All the Chinese gauges used in the evaluation had a specified room temperature gauge factor of 2.62, which is within 4 percent of the average of the five gauges listed in table I.

Apparent Strain

The comparison of apparent strain data between evaluators is difficult because several factors influence the shape of the resistance-temperature curve. Aside from the sensor temperature coefficient of resistance, the magnitude and curve shape appear to be most strongly affected by the cooling rate of the previous temperature excursion and to a lesser degree by the difference in temperature coefficient of expansion between the gauge alloy and the substrate material. A further consideration is the construction of the Chinese gauges. These gauges have a relatively large amount of ceramic cement, which encapsulates the wire and, together with the large size of the gauge, could influence apparent strain by causing a bending moment to occur, especially if bonded to a thin substrate.

Table II lists the evaluator, the substrate material used in the test, and the number of thermal cycles reported.

Figure 3, a plot of apparent strain versus temperature, is based on an average of the number of cycles from table II. All curves are normalized to pass through zero at room temperature. A gauge factor of 2.0 was used to calculate microstrain.

In order to compare the Kanthal A-1 data with the Chinese gauges, figure 4 was drawn to show the envelope of the curves from figure 3, shown as solid lines, and the Kanthal A-1 data, plotted as dashed lines. It is obvious from figure 4 that both alloys have similar S-shaped curves, but the Kanthal A-1 has a much higher value of apparent strain at elevated temperatures. The maximum data spread for the alloys at any temperature is similar in spite of the fact that the Kanthal data were obtained from a single facility and the same substrate material for all eight gauges as opposed to how the Chinese gauge data were obtained. The implication here is that under carefully controlled tests, the Chinese alloy should exhibit much better repeatability in cycle-to-cycle apparent strain testing.

Figure 5 has been reproduced directly from the data of evaluator 5. This figure is a typical slow cycle and is presented to illustrate the inflection point, which is present in each cycle at about 700 K (425 °C). Two other evaluators also show a bump occurring near that same temperature. A possible explanation for this anomaly is the extremely high negative drift rate in the range of 700 to 870 K, as reported by evaluator 3. This behavior, which is related to some specific metallurgical process, reinforces the statements in the CONCLUSIONS pertaining to the care required in using these gauges in that unstable temperature region.

Drift

Drift test results are shown in figure 6. All evaluators reporting drift data agree on the slope of the curves, with the long-term (50 hr) Lewis data having an overall drift rate of about -9 microstrain/hr. Short-term drift rates, however, are higher, in the range -30 to -50 microstrain for the first hour.

Recent supplementary data by evaluator 3 (fig. 7) indicates that drift rate is a strong function of temperature level. There appears to be short-term instability in the 700 to 870 K range, with drift rates as high as 1700 microstrain for the first hour at 870 K.

CONCLUSIONS

Test results have been presented from five participants in the comparative evaluation of the Chinese strain gauges. Data are also included from work done by Professor Wu from his original paper describing the Chinese alloy. K. Stetson of UTRC and H. Grant of PWA, as part of a recent contract effort for NASA, have published data in a contractor report on Kanthal A-1 gauges. Kanthal A-1 is a ternary alloy similar to the Chinese alloy, but with different trace elements. These data are also included. Howard Grant will discuss the Kanthal A-1 results fully in the following session.

Gage factor. - Results of gauge factor versus temperature tests show gauge factor decreasing with increasing temperature. The average slope is -3.5 percent per 100 K, with an uncertainty band of 18 percent. Values of room temperature gauge factor for the Chinese and Kanthal A-1 gauges averaged 2.73 and 2.12, respectively. The room temperature gauge factor of the Chinese gauges was specified to be 2.62.

Apparent strain. - The apparent strain data for both the Chinese alloy and Kanthal A-1 showed large cycle to cycle nonrepeatability. This variability is influenced by heating and cooling rates of the previous cycle, dwell times at various temperatures and type of substrate to which the gauge is bonded. H. Grant of PWA in Connecticut as a result of extensive testing, has identified cooling rate as the predominant factor.

All apparent strain curves had a similar S shape, first going negative and then rising to positive value with increasing temperatures. The mean curve for the Chinese gauges between room temperature and 1000 K had a total apparent strain of 1500 microstrain. The equivalent value for Kanthal A-1 was about 9000 microstrain.

Drift. - Drift tests at 950 K for 50 hr show an average drift rate of about -9 microstrain/hr. Short-term (1 hr) rates are higher, averaging about -40 microstrain for the first hour. In the temperature range 700 to 870 K, however, short-term drift rates can be as high as 1700 microstrain for the first hour. Therefore, static strain measurements in this temperature range should be avoided, and care must be taken in making drift corrections, especially when drift rate is expressed as a small hourly rate based on some longterm test.

The results of these tests indicate that to use these gauges at high temperatures for measuring static strain to a reasonable accuracy level, certain precautions are required. Gauge temperature must be known to allow compensation for gauge factor and apparent strain; also, gauges must be calibrated at known cooling rates to establish repeatable apparent strain. A hightemperature soak for at least 1 hr appears necessary to ensure that the apparent strain reaches the same value "starting point" for each cycle. The actual strain measurement should then be made at the same cooling rate if possible.

REFERENCES

1. Wu, Tsen-tai, et al.: Development of Temperature-compensated Resistance Strain Gauges for Use to 700 °C. Exp. Mech.. vol. 21, no. 3, Mar. 1981, pp. 117-123.

2. Stetson, Karl A.: Demonstration Test of Burner Liner Strain Measuring System," UTRC Report No. R84-926376-15, United Technologies Research Center, June 1984.

TABLE I. - AVERAGE GAUGE FACTOR

Evaluator	Average gauge factor at -	
	Room temperature	High temperature[a]
1	2.60	2.21 (946)
2	2.79	2.14 (955)
3	3.06	2.19 (950)
NASA Lewis	2.66	1.96 (973)
Wu	2.56	1.90 (973)
	Avg. 2.73	
UTRC[b]	2.12	1.81 (800)

[a]The parenthetical values are the temperatures
(in kelvins) at which the data are valid.
[b]Kanthal A-1 gauges from ref. 2.

TABLE II. - SELECTED TEST PARAMETERS

Evaluator	Substrate	Substrate thickness		Number of cycles
		mm	in.	
Evaluator 1	Hastelloy X	6.35	0.25	7
Evaluator 2	Incoloy 901	-----	-----	8
Evaluator 3[a]	René 41	4.75	.187	3
Evaluator 4	IN-100	-----	-----	5
Evaluator 5	IN-600	12.70	.5	10
NASA Lewis[a]	IN-718	3.28	.129	7
Wu	GH 30	-----	-----	3

[a]Beams used by these evaluators had gauges bonded
to both sides of the test beam in a symmetrical
arrangement.

GAUGE FACTOR VARIATION VERSUS TEMPERATURE
ROOM TEMPERATURE VALUE AS REFERENCE

Figure 1

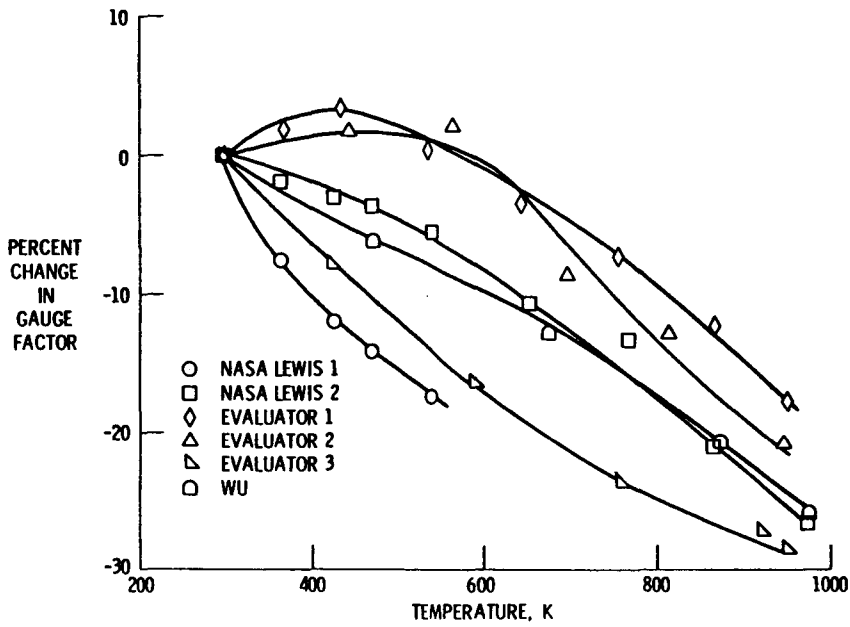## GAUGE FACTOR VARIATION VERSUS TEMPERATURE
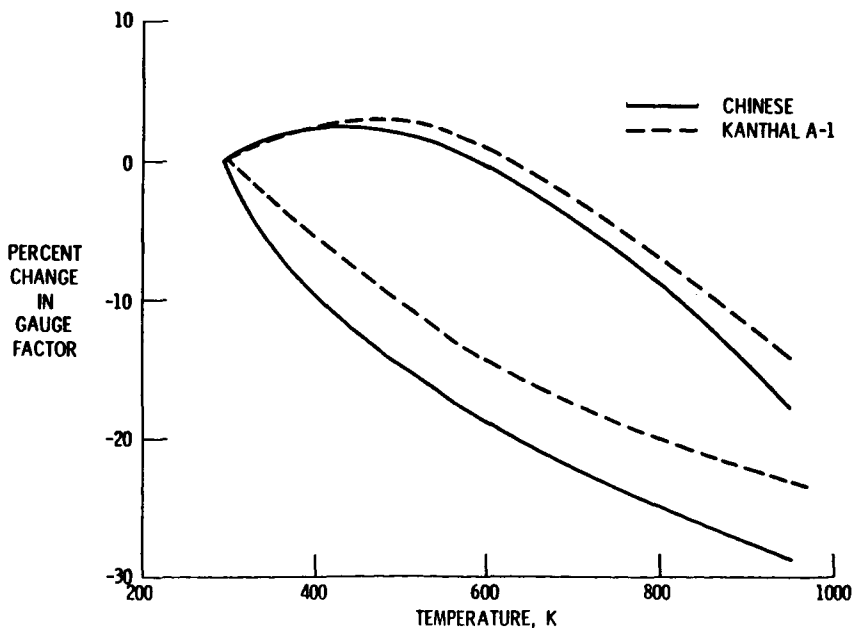### ROOM TEMPERATURE VALUE AS REFERENCE

Figure 2

81

APPARENT STRAIN VERSUS TEMPERATURE

Figure 3

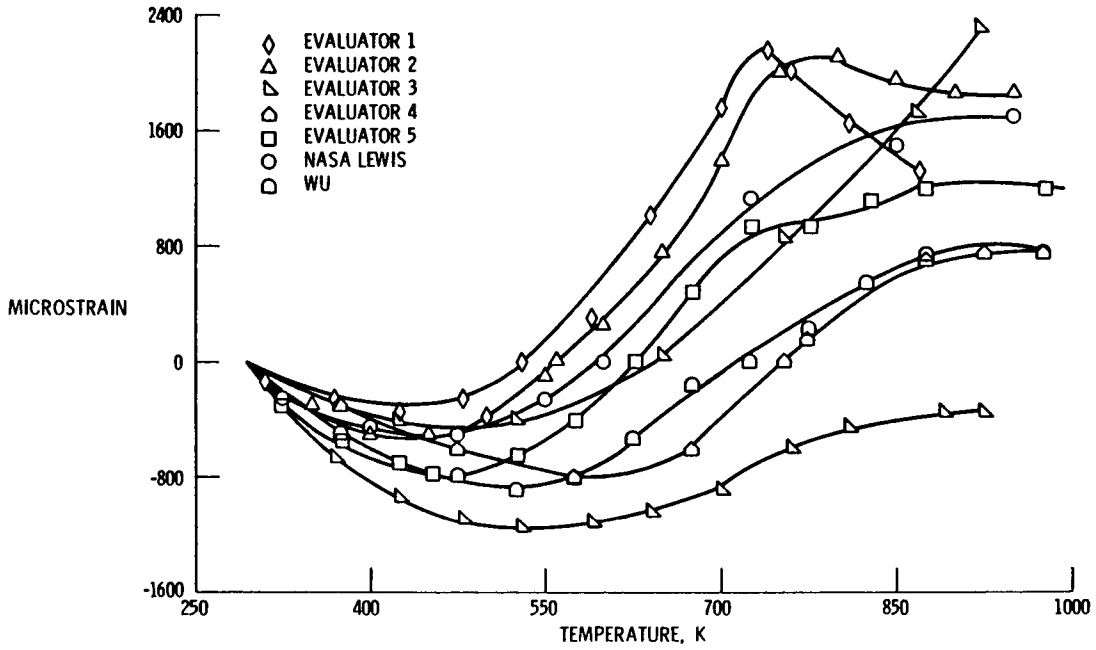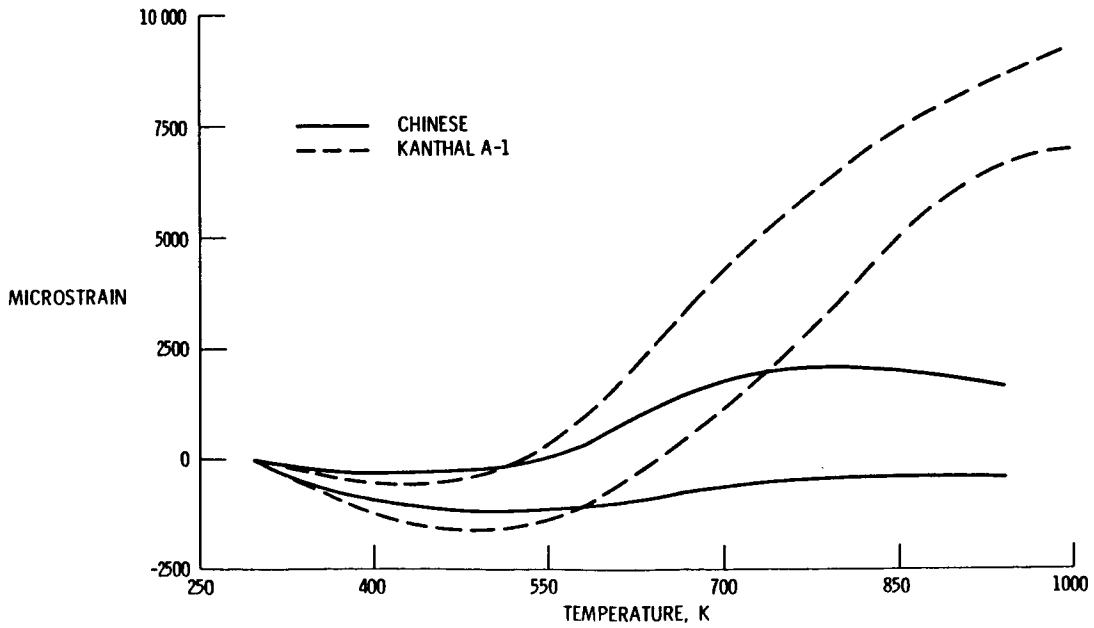## APPARENT STRAIN VERSUS TEMPERATURE

Figure 4

82

APPARENT STRAIN VERSUS TEMPERATURE

Figure 5

MICROSTRAIN VERSUS TIME
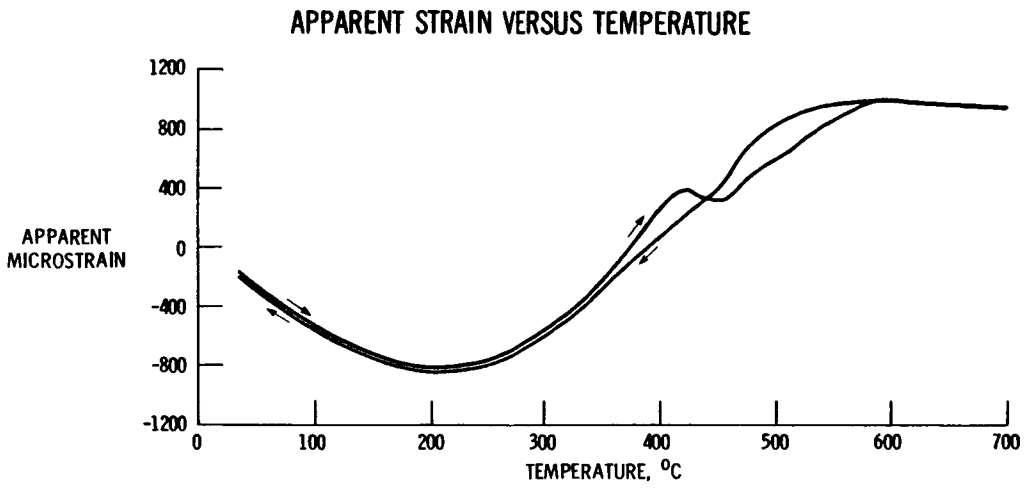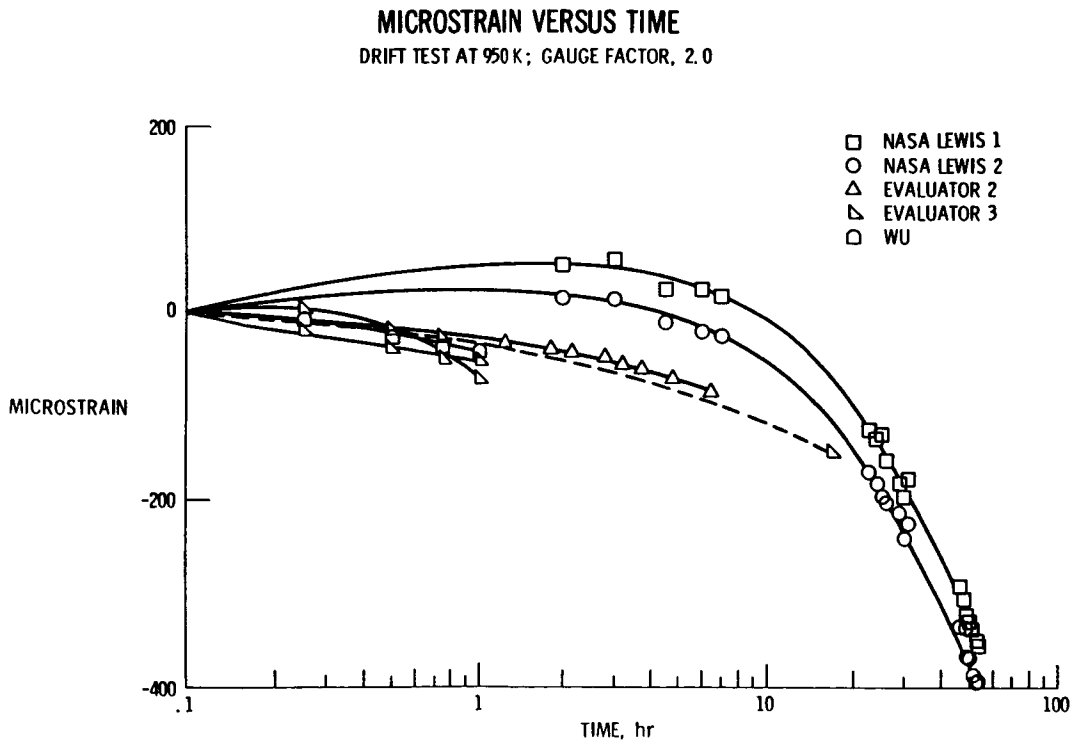### DRIFT TEST AT 950 K; GAUGE FACTOR, 2.0

Figure 6

83

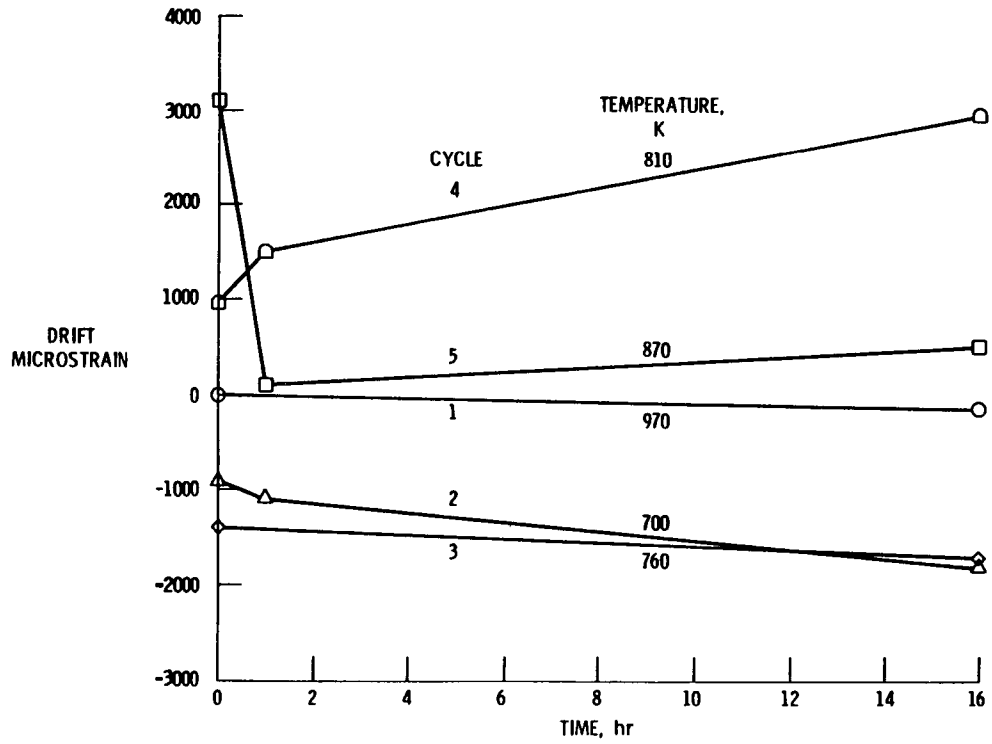## DRIFT VERSUS TIME AT FIVE TEMPERATURE LEVELS

Figure 7

DEMONSTRATION TEST OF BURNER LINER STRAIN MEASUREMENTS
USING RESISTANCE STRAIN GAGES

Howard P. Grant and Wilbur L. Anderson
United Technologies Corporation
Pratt & Whitney

SUMMARY

This program includes a demonstration test of burner liner strain measurements using resistance strain gages as well as a feasibility test of an optical speckle technique for strain measurement. The strain gage results are reported. Ten Kanthal A-1 wire strain gages were used for low cycle fatigue strain measurements to 950K and 2000 x 10-6 strain on a JT12D burner can in a high-pressure (10 atmospheres) burner test at the United Technologies Research Center under NASA Contract NAS3-23690 (ref. 1). The United Technologies Program Manager was Dr. Karl A. Stetson; the NASA Project Manager was Frank W. Pollack.

The procedure for use of the strain gages was developed under a previous contract, NAS3-22126 (ref. 2), and involved extensive pre-calibration and post-calibration to correct for cooling-rate dependence, drift, and temperature effects of about 6000 x 10-6 apparent strain. Results were repeatable within +-200 x 10-6 to +-600 x 10-6 strain, with best results during fast decels from 950K. (Scatter was worst during decels from lower temperatures and during slow decels.) The results agreed with analytical prediction based on an axisymmetric burner model, and results indicated a non-uniform circumferential distribution of axial strain, suggesting temperature streaking.

BACKGROUND

The measurement of local strain with wire resistance strain gages of less than 6 mm gage length in engine hot section testing at elevated temperatures during cycling from idle to high-power conditions has typically been limited to strain gage temperatures below 670K (750°F). At higher temperatures, stability and repeatability of strain gage electrical resistance deteriorates. The deterioration is due either to resistance drift in the gage alloy with time at temperature because of continuous or reversible formation of oxides, intermetallic compounds, or other metallurgical phases (including lattice order-disorder changes) or due to large resistance change with temperature (high temperature coefficient of resistance, tcr).

For low tcr, the metal alloy must be complex, but complex alloys tend to be unstable at high temperatures. The gage resistance then depends not only on temperature but also on cumulative time at temperature and on heating rates and cooling rates during engine accelerations and decelerations. One way to extend the use of wire strain gages above 670K is to recognize the dependence on the additional variables (especially the rate of temperature change during heat-up and cool-down) in the calibration and use of the gages. The effect of these variables on Kanthal A-1 wire was examined in detail during bench tests as part of a previous contract, NAS3-22126. Kanthal A-1 is an iron-chromium-aluminum alloy long used for high-temperature electrical heating elements because of its durability. It has been tested by several investigators (notably Bertodo, reference 3, and Lemcoe, reference 4) as a possible strain gage candidate.

C-2

Rules were developed to extend the use of these gages to about 980K (1300°F):

(1) Measure strain during fast cool-down only (less than one minute) to minimize rate-dependent apparent strains.

(2) The temperature is not to exceed 980K (1300°F) at any time.

(3) Precondition by baking at least one hour at 980K (1300°F).

(4) Monitor temperature with an adjacent thermocouple.

(5) Precalibrate apparent strain during fast temperature cycles. To do this, install the gages on a piece cut from the burner liner; measure apparent strain due to temperature during fast isothermal cycles (strain-free except for uniform thermal expansion); and then weld the instrumented piece back into the burner liner. This procedure is described in greater detail below.

BURNER TEST CONFIGURATION

A version of a burner can designed for the Pratt & Whitney JT12D engine was selected for the test (fig. 1). Methods of analysis for predicting strain had been developed under contract NAS3-21836 (ref. 5) at Pratt & Whitney for this type of burner structure (fig. 2). Some outside liner temperatures were documented in previous tests (fig. 3). Locations A, B, and C (fig. 1) in the vicinity of the third knuckle of the burner can were selected for strain measurement. The test consisted of seven cycles of burner operation using jet engine fuel, each cycle consisting of an acceleration (caused by an increase in fuel flow rate) from idle to high-power in about one minute, dwell time at the operating point for a minute or two, and a deceleration to idle in about a minute. Strain gage data was reduced for the fast deceleration portion of the cycle only.

STRAIN GAGE INSTALLATION

The Kanthal A-1 wire static-strain gages were installed using the flame-spray aluminum-oxide precoat and SermeTel (TM) P-1 ceramic cement overcoat technique (fig. 4) developed in the previous contract NAS3-22126. Application of the cement is a critical step. If the gage wire is not thoroughly cleaned, or the cement layer is too thick, the result could be a partially bonded gage with internal voids, or a completely unbonded gage floating inside a cement envelope.

Ten Kanthal A-1 gages and seven Type K (Chromel-Alumel) thermocouples were installed on the piece cut from the burner can (fig. 5). This arrangement provided axial and hoop strain measurements on the weld flange and at a location aft of the knuckle, and hoop strain only on the knuckle. The thermocouple junctions were formed of 0.13 mm diameter bare thermocouple wires welded together (but not welded to the burner can) and embedded in the ceramic cement. Figures 6, 7, and 8 are photographs of the can with piece removed, the instrumented piece, and the can with the instrumented piece reinstalled by tungsten inert gas weld.

STRAIN GAGE CALIBRATION

Before the combustor tests, apparent strain tests were run on the ten Kanthal A-1 gages on the piece cut from the burner can. The piece was installed in the can and the combustor tests were run. Then the piece was again cut from the can and many more apparent strain tests were run. Table 1 lists pertinent details of these calibration tests. Figure 9 is an example of the resistance behavior of a Kanthal A-1 strain gage on the piece cut from the burner can (gage no. 2) during fast and slow cool-downs from various temperatures. Smaller apparent strain is more typical during fast cool-down than during slow. Larger drift is more likely at temperatures in the 700K to 800K range than at 950K. The material memory is evident at temperatures near 950K (the gage always returns to a resistance value extremely close to the original) despite various drifts at the lower temperatures.

Calibration curves for each of the ten Kanthal A-1 gages on the burner can, and for eight Kanthal A-1 gages mounted on two gage-factor test bars (Figure 10) are presented in figures 11, 12, 13, 14, 15, and 16. In particular the results shown in figure 15 confirmed that the behavior of any one gage was repeatable from before to after the combustor tests. It is this repeatability that makes the use of Kanthal A-1 gages feasible. At 950K only one gage shows a difference larger than 250 parts per million in resistance change due to temperature. Table 2 lists the scaling factor showing the relative sensitivity to temperature for each gage. The factor varies from 0.93 to 1.08.

Gage factor versus temperature was measured for the eight gages on the two test bars. Gage numbers 1, 2, 3 on bar 1 were found to have low and erratic gage factors (fig. 17). Voids were found in the cement under the end loops of these three gages. The average gage factor of the remaining five gages was used to reduce the burner liner gage test data (fig. 18).

COMBUSTOR TEST RESULTS

During the first test cycles in the high-pressure combustor rig the gages at location A (fig. 1) were accidentally over-temperatured to 1040K (1400°F) and either failed or became erratic. The remaining six gages survived the entire test program and post-test calibrations. Typical results are presented in fig. 19, where all measurements obtained during the final four cycles of combustor test are summarized. The test conditions were about the same during each of these four cycles and are listed in Table 3.

At location B (fig. 1) on the knuckle the measured hoop strain was consistently in the predicted direction (tensile) with magnitude averaging about 80 percent of the predicted 1750 microstrain. During the final four cycles the two-sigma scatter was 268 microstrain.

At the aft location (C) (fig. 1) the measured hoop strain was consistently in the predicted direction (tensile) with magnitude larger than the predicted 355 microstrain by about 1000 microstrain. During the four cycles with gages 1 and 2, the two-sigma scatter of all measurements of hoop strain at this location was 314 microstrain. The two-sigma scatter for gage 1 alone was notably small: only 52 microstrain.

87

The axial strain increments measured were surprising. One gage (no. 7) consistently indicated an increment of about 700 microstrain in compression while the other gage (no. 8) consistently indicated an increment of about 1000 microstrain in tension. The predicted value was 1400 microstrain in compression. The repeatability of measurements with each gage was excellent (fig. 19). In fact, during the four cycles the two-sigma scatter for gage no. 7 was only 52 microstrain and for gage no. 8, 270 microstrain. The indicated difference in axial strain increment at the two locations is believed to be real, even though the temperatures at the two gage locations were the same. The difference may be a result of circumferential temperature gradients (streaks) at the liner lip inside the can.

CONCLUDING REMARKS

Strain gages made from Kanthal A-1 wire can be successfully employed in burner liner low-cycle fatigue strain measurements provided they are protected from temperatures higher than 980K. Careful attention to the application of ceramic cement is required to assure proper functioning of the gages. The individual gages, as installed on the test object, must be subjected to temperature calibration for apparent strain after a minimum of one hour preconditioning at 980K. The removal of a section of a burner for instrumentation and calibration makes this practical if the section can be welded back into place for subsequent testing. Strain measurements must be limited to strain change during rapid cooling of the test section in order to minimize apparent strain corrections and obtain best repeatability. More detailed comparison with computer modeling of strain fields will require more detailed mapping of temperature patterns.

REFERENCES

1. Contract NAS3-23690 final report.

2. Contract NAS3-22126 final report.

3. Bertodo, R.: Resistance Strain Gauges for the Measurement of Steady Strains at High Temperatures. Proc. Instn. Mech. Engrs., v178, pt 1, no. 34, pg. 907, 1964.

4. Lemcoe, M. M.: Development of Electrical Resistance Strain Gage System for Use to 2000°F. ISA Paper 75-572, 1975.

5. Moreno, V: Combustor Liner Durability Analysis. NASA Report CR-165250, NAS3-21836, February 1981.

TABLE 1

RESISTANCE CHANGE VERSUS TEMPERATURE, FOR GAGES ON THE BURNER LINER. TESTS 1 THROUGH 8 WERE CONDUCTED BEFORE THE HIGH PRESSURE BURNER TESTS, AND TESTS 9 THROUGH 40 AFTER.

$$10^6 (r_{T1} - r_{T2})/[R_0 (T1-T2)]$$

Test No.	Max. Temp. T3 (K)	Approx. Dwell Time at T3 (Minutes)	Cooling Time t_x T1 to T2 (Sec)	T1 (K)	T2 (K)	$\frac{T_1-T_2}{t_x}$ (K/sec)	parts per million per Kelvin						
							Gage 1	Gage 2	Gage 3	Gage 4	Gage 5	Gage 7	Gage 8
1	950	10	12.8	811	727	6.54	57.9	59.3	62.4	56.5	61.9	61.0	58.8
2	950	10	14.2	811	727	5.92	72.7	68.7	72.0	66.4	68.4	65.3	62.4
3	950	10	13.7	811	727	6.12	64.4	67.6	67.7	60.6	63.1	58.8	57.9
4	950	10	18.2	811	727	4.62	75.0	70.9	72.2	73.4	77.6	73.9	70.9
5	950	10	95.2	811	727	.88	85.8	84.0	89.1	88.1	87.1	86.0	90.9
6	950	10	26.4	811	727	3.19	75.2	70.7	76.7	72.2	78.3	70.4	71.1
7	950	10	54.4	811	727	1.54	80.3	78.1	83.3	81.4	82.2	80.3	82.9
8	950	10	11.1	811	727	7.55	63.9	62.5	67.2	64.6	70.4	69.6	66.7
9	950	10	12.0	811	727	6.98	63.2	62.2	68.4	58.4	67.8	57.4	57.6
10	950	10	13.1	811	727	6.41	59.4	61.2	61.4	53.9	61.3	55.6	59.3
11	950	10	16.6	811	727	5.05	70.1	73.2	74.0	70.1	76.9	63.1	63.3
12	950	10	22.2	811	727	3.79	74.8	77.4	75.3	78.1	83.9	70.8	74.1
13	950	10	30.5	811	727	2.76	80.9	82.1	79.4	82.4	82.6	76.3	78.7
14	950	10	57.6	811	727	1.46	81.5	74.3	83.3	77.1	94.8	80.4	78.7
15	950	10	38.9	811	727	2.16	79.5	76.9	81.1	81.0	89.2	78.9	81.6
16	950	10	12.2	811	727	6.89	59.3	59.4	62.0	60.7	70.2	64.7	65.4
17	819	10	20.0	811	727	4.21	68.7	65.5	65.8	68.8	80.8	65.6	72.1
18	819	20	18.6	811	727	4.53	66.0	65.0	66.4	70.1	83.1	66.9	74.0
19	819	10	113.6	811	727	.74	89.6	90.4	94.5	91.4	103.5	88.6	93.5
20	819	10	19.1	811	727	4.40	66.2	64.8	66.1	69.6	81.9	66.1	72.4
21	819	20	18.0	811	727	4.66	66.6	65.1	66.0	68.4	79.8	64.5	70.9
22	733	10	12.6	733	700	2.63	32.1	29.6	34.8	35.5	52.1	45.2	62.1
23	733	20	9.7	733	700	3.42	31.1	34.2	46.3	57.8	74.1	66.0	84.7
24	733	10	28.6	733	700	1.15	54.6	44.8	59.9	50.1	59.2	55.4	56.2
25	733	20	29.6	733	700	1.12	53.9	48.8	62.6	52.9	71.8	57.4	57.0
26	733	10	9.4	733	700	3.51	30.3	33.6	48.1	52.2	62.6	59.5	74.7
27	733	20	14.7	733	700	2.24	58.8	58.8	64.0	72.1	94.5	71.7	81.4
28	950	10	4.0	811	727	21.21	71.4	69.7	73.4	72.8	82.7	61.1	61.9
29	783	10	19.8	780	700	4.04	43.2	38.0	45.2	45.5	56.2	42.2	52.8
30	783	20	19.7	780	700	4.06	38.8	35.1	39.3	41.5	56.9	50.6	63.6
31	783	10	69.8	780	700	1.15	56.9	54.3	63.9	58.0	70.5	57.3	61.3
32	783	10	18.4	780	700	4.35	45.4	41.5	43.5	50.8	65.6	56.2	70.9
33	1041	10	27.3	1037	819	7.99	29.3	28.3	31.2	34.4	37.2	37.0	44.4
34	1041	10	105.4	1037	819	2.07	30.4	29.0	32.9	31.1	41.3	32.4	36.7
35	1041	10	264.3	1037	819	.89	28.0	30.3	36.0	29.3	41.0	18.7	23.4
36	1041	10	145.3	1037	819	1.50	29.3	39.7	35.8	38.2	35.9	16.1	24.4
37	1041	10	37.4	1037	819	5.83	44.9	46.8	46.7	52.8	57.2	35.3	42.2
38	1041	10	92.2	1037	819	2.36	42.7	44.0	45.1	48.8	55.2	31.4	36.8
39	1041	10	67.5	1037	819	3.23	42.2	45.0	44.8	48.5	56.3	31.4	38.1
40	1041	10	19.5	1037	819	11.17	32.8	29.3	33.6	31.3	26.7	27.6	37.9

TABLE 2

VALUES OF SCALING FACTOR C

Component	Gage No.	C
Burner Liner	1	0.95
Burner Liner	2	1.00
Burner Liner	3	1.08 ←
Burner Liner	4	1.01
Burner Liner	5	1.02
Burner Liner	6	0.99
Burner Liner	7	0.93 ←
Burner Liner	8	1.03
Burner Liner	9	1.03
Burner Liner	10	0.95
Test Bar 1	1-1	1.03
Test Bar 1	1-2	1.02
Test Bar 1	1-3	0.99
Test Bar 1	1-4	1.04
Test Bar 2	2-1	0.99
Test Bar 2	2-2	1.02
Test Bar 2	2-3	1.00
Test Bar 2	2-4	1.01

$$C = [(R_{950K} - R_{min})/R_{min}]/0.0165,$$

where R_{950K} and R_{min} are measured during rapid cooling from 950K (t_c = 12 seconds).

TABLE 3

COMBUSTOR TEST TYPICAL STRAIN GAGE DATA AND ANALYSIS
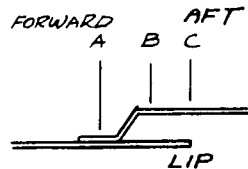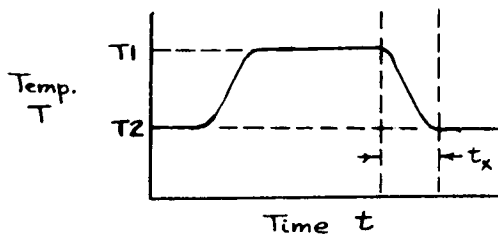
Cycle No.	6
Burner Run No:	5
Cum. Time At T1:	22 min.
Cooling time t_x:	15 sec.
$(TT4)_1$	1255K
$(TT4)_2$	955K
TT3	710K

P = 9 ATM.

Location		C				B	A		LIP
Orientation		HOOP	HOOP	AX.	AX.	HOOP	HOOP	AX.	- -
Gage No.		1	2	7	8	3	5	9	-
Thermocouple No.		51	52	51	52	53	55	55	57
T1	(K)	761	761	761	761	777	1041	1041	1072
T2	(K)	722	722	722	722	722	819	819	833
$(T_1-T_2)/t$ (K/sec.)		2.60	2/60	2.60	2.60	3.67	14.8	-	-
$10^6 (r_{T1}-r_{T2})/R$ (T1-T2)		49.8	46.4	53.4	61.6	46.1	14.1	-	-
$10^6 (r_{T1}-r_{T2})/R \cdot G_1$		956	891	1025	1182	1255	1728	-	-
$10^6 (E_1-E_2) K/G_1$		1970	2069	296	2118	2427	3476	-	-
$10^6 (G_1-G_2) e_2/G_1$		3	3	-10	-10	21	-16	-	-
$e_1 - e_2$ (Equ. 1, Microstrain)		1011	1175	-719	946	1151	1764	-	-

90

Figure 1   JT12D Burner Liner

	Ⓐ	Ⓑ	Ⓒ
TEMP K	950	839	839
HOOP STRAIN	− 0.000840	+ 0.002200	+ 0.001080
AXIAL STRAIN	+ 0.000600	− 0.000250	− 0.001750

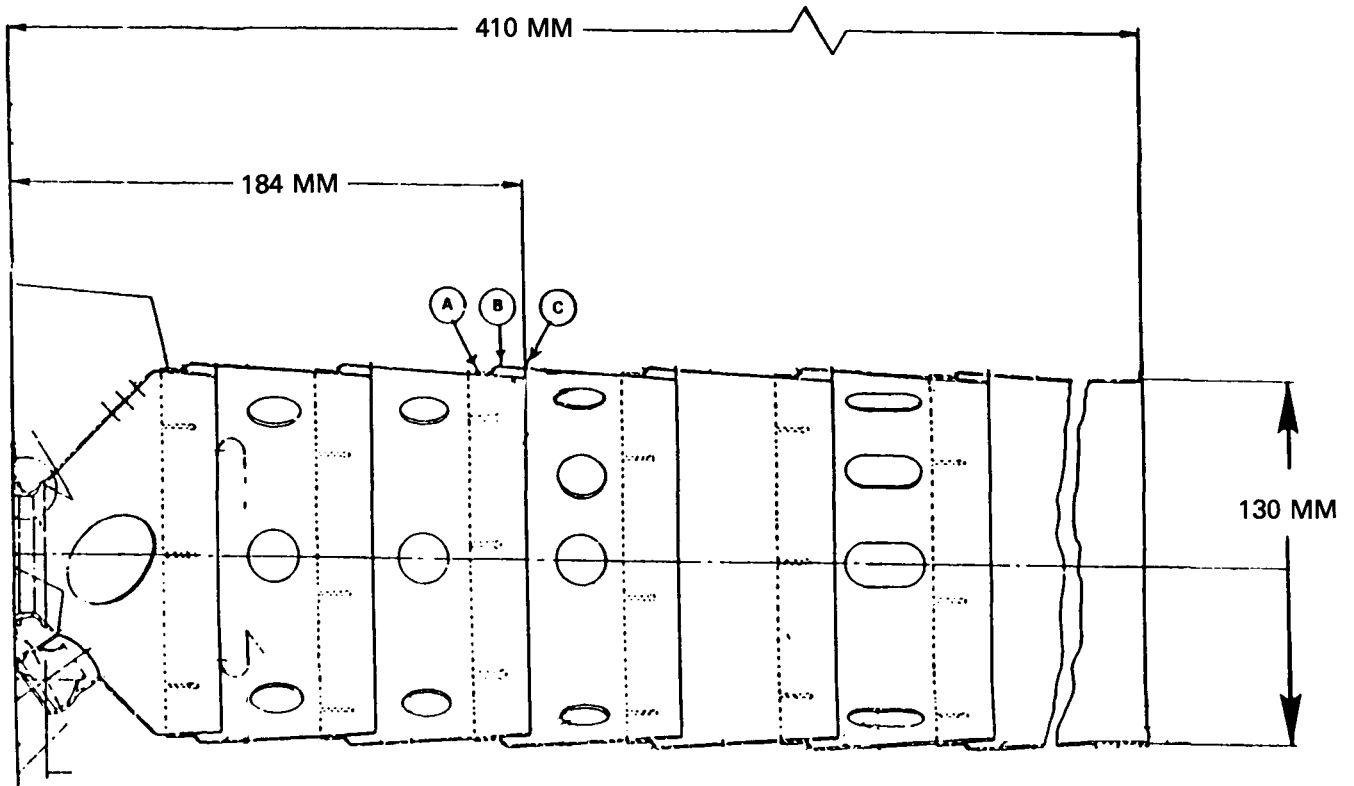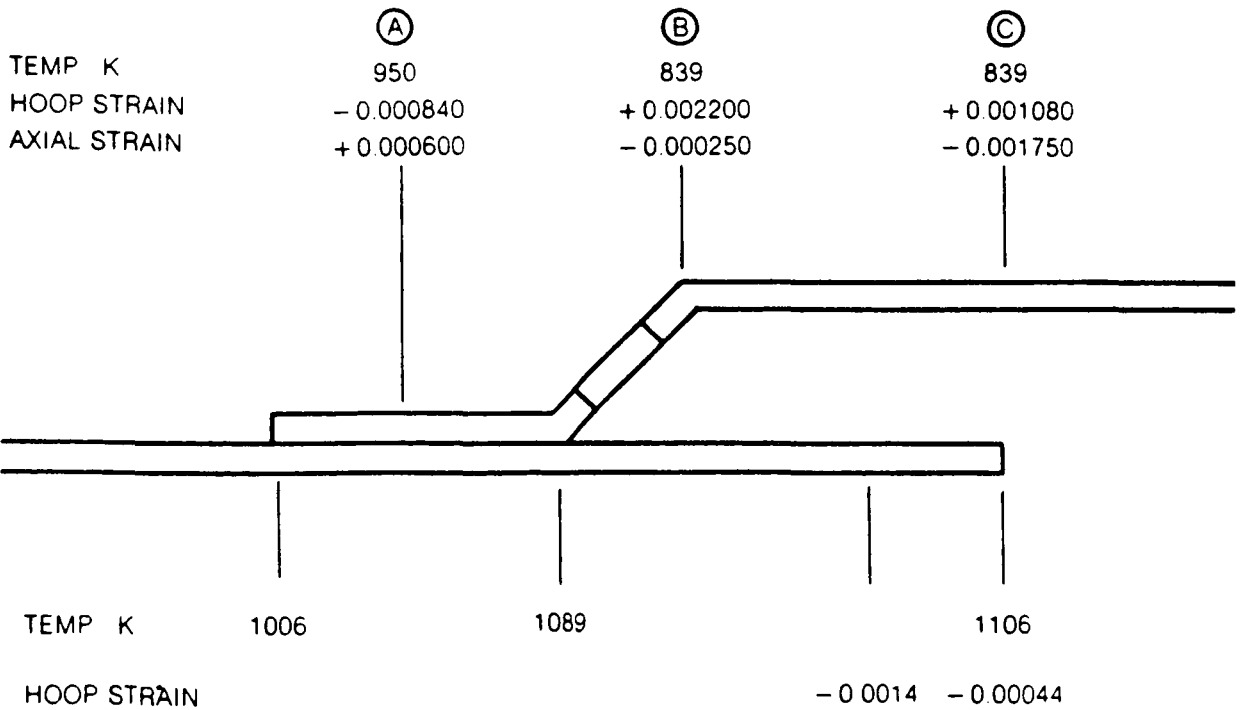| TEMP K	1006	1089		1106
HOOP STRAIN			− 0 0014 − 0.00044	

Figure 2   Strains Estimated For JT12D Burner Liner in Vicinity of Third Knuckle

91

CURVE	RUN	P13 PSIA	TT3 K	F/A OVERALL	TT4 IDEAL K
BOTTOM	69	176	587	0.0167	1207
TOP	72	187	693	0.0158	1267

TEMP (K)

1200
1150
1100
1050
1000
950
900
850
800
750
700
650

X (mm)

100   200   300   400

LOUVER NO. ← 1 → 2 → 3 → 4 → 5 → 6 →
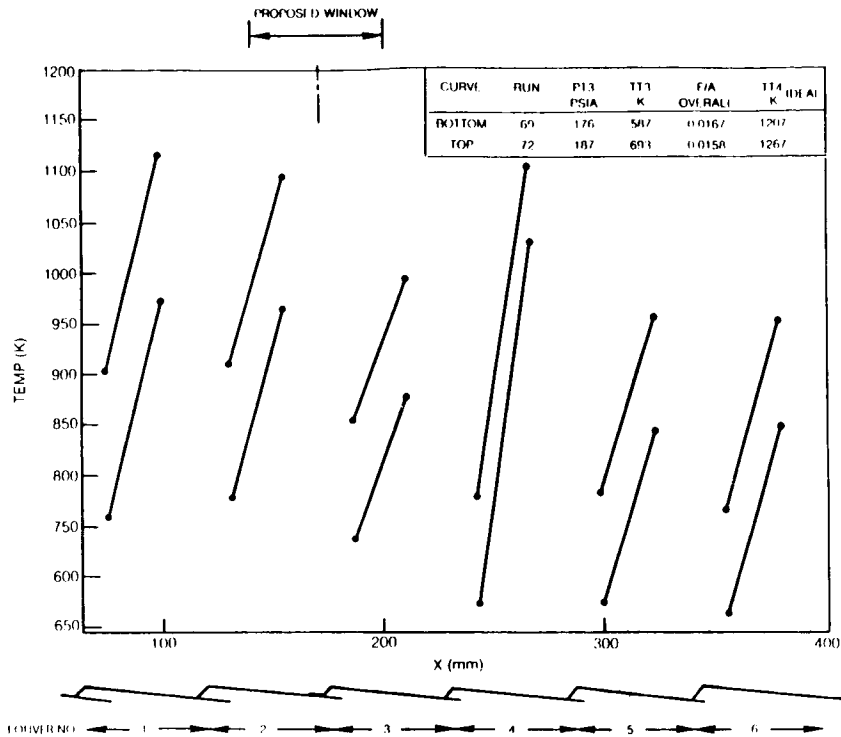
Figure 3   Surface Temperature Profiles Previously Measured on JT12D Burner Liner

2.79 mm
6 LOOPS

3.17 mm

0.25 mm

RESISTANCE WELDED

1.27 MAX

0.25 mm

0.025 mm DIAMETER
KANTHAL A-1 WIRE (Fe-22Cr-5.75Al-0.5Co w/o)
123Ω SENSOR RESISTANCE

0.25 mm DIAMETER
Ni CLAD Cu

0.076 mm DIAMETER
CHROMEL WIRE

1.57 mm DIAMETER SHEATH
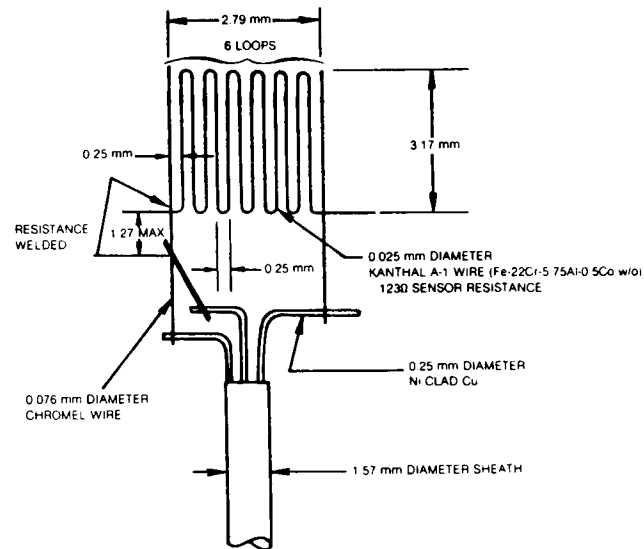
INSTALLATION

SURFACE PREPARATION NiCrAl (METCO 443) FLAME SPRAYED. ABOUT 0.127 mm THICK
PRECOAT Al₂O₃ (ROKIDE "H") FLAME SPRAYED. ABOUT 0.127 mm THICK
OVERCOAT AlP₄ (SERMETAL P-1) CERAMIC CEMENT. ABOUT 0.127 mm THICK
EXTENSION LEADS 3c Ni CLAD Cu WIRE WITH 1.57 mm DIAMETER
                 S/S SHEATH AND 0.025 mm DIAMETER CONDUCTORS
                 CABLE IS STRAP WELDED TO SUBSTRATE AND SPLICES
                 ARE BRAZED WITH NICROBRAZE 50 (AWS BNi-7)

Figure 4   Gage Installation
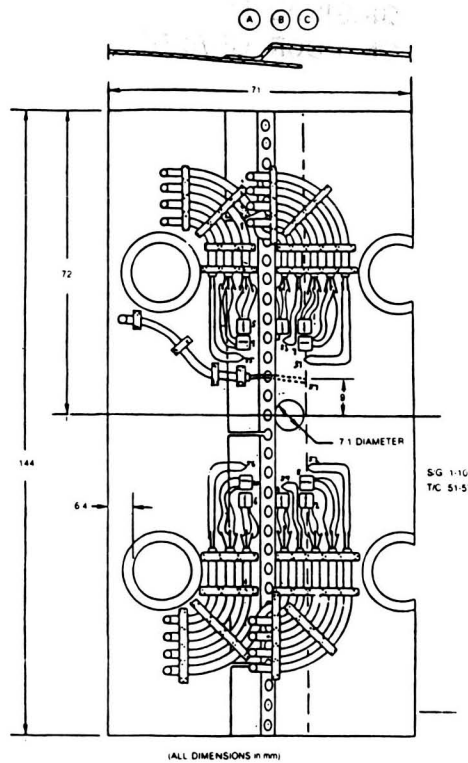
Figure 5   Strain Gage & Thermocouple Locations

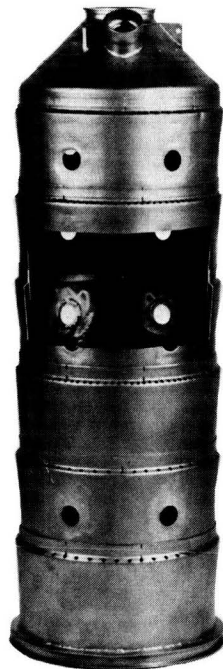
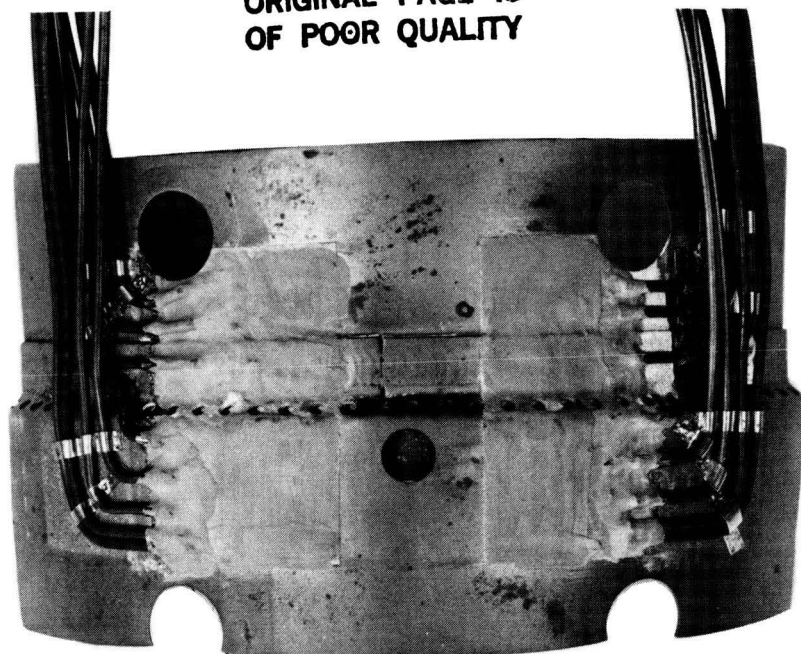Figure 6   Burner Can with Section Cut Out

93
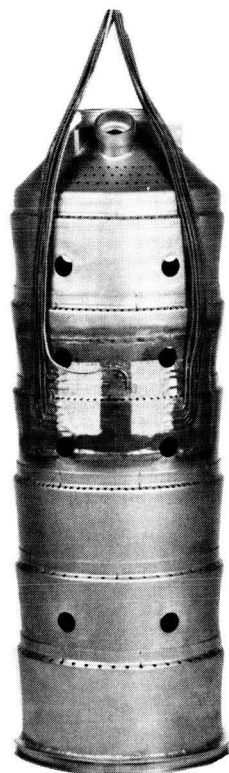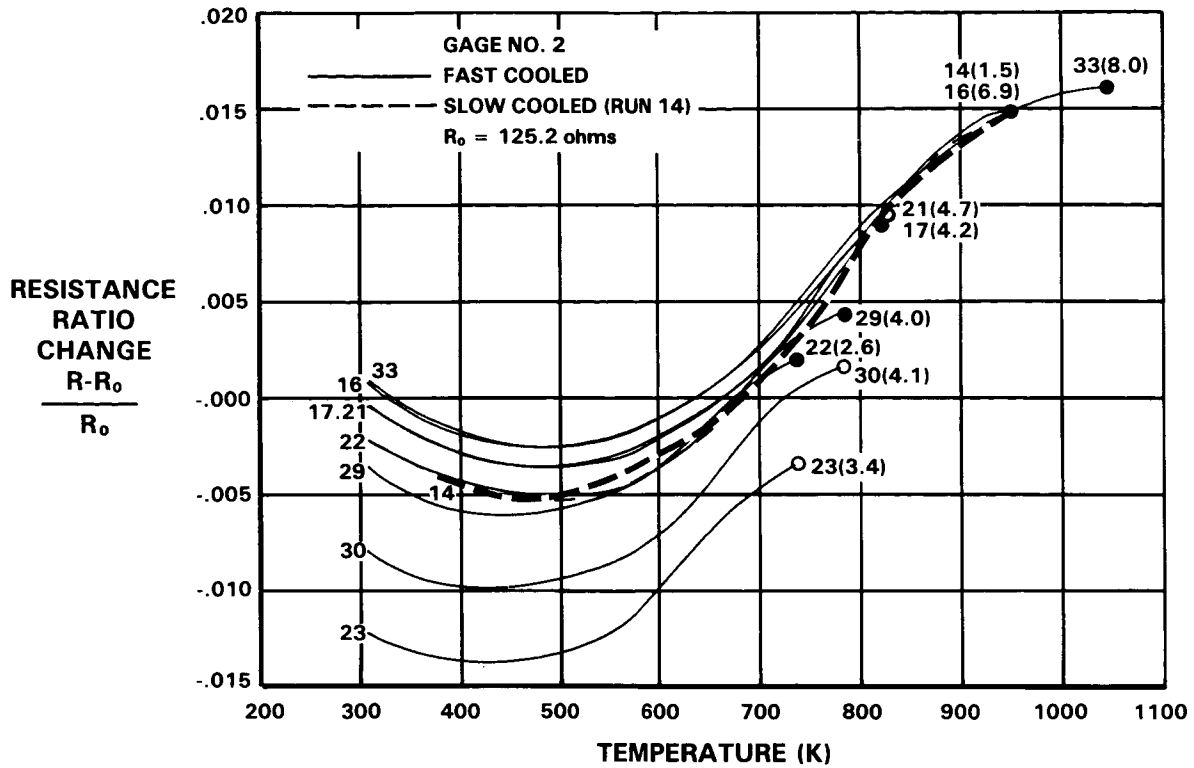
Figure 7   Instrumented Section of Burner Can

Figure 8   Burner Can with Instrumented Section Reinstalled

RESISTANCE RATIO CHANGE VERSUS TEMPERATURE OF KANTHAL A-1 STRAIN GAGE NO.2
DURING RAPID COOLING FOR VARIOUS STARTING TEMPERATURES AND VARIOUS DWELL TIMES
AT THE STARTING TEMPERATURE. A SOLID SYMBOL INDICATES DWELL TIME OF FIVE TO
TEN MINUTES; AN OPEN SYMBOL INDICATES DWELL TIME OF TWENTY TO THIRTY MINUTES.
THE NUMBER ON THE CURVE IS THE RUN NUMBER OF TABLE 1 AND THE NUMBER IN PAREN-
THESES IS THE COOLING RATE (K/sec) IN THE 800K TO 700K RANGE.

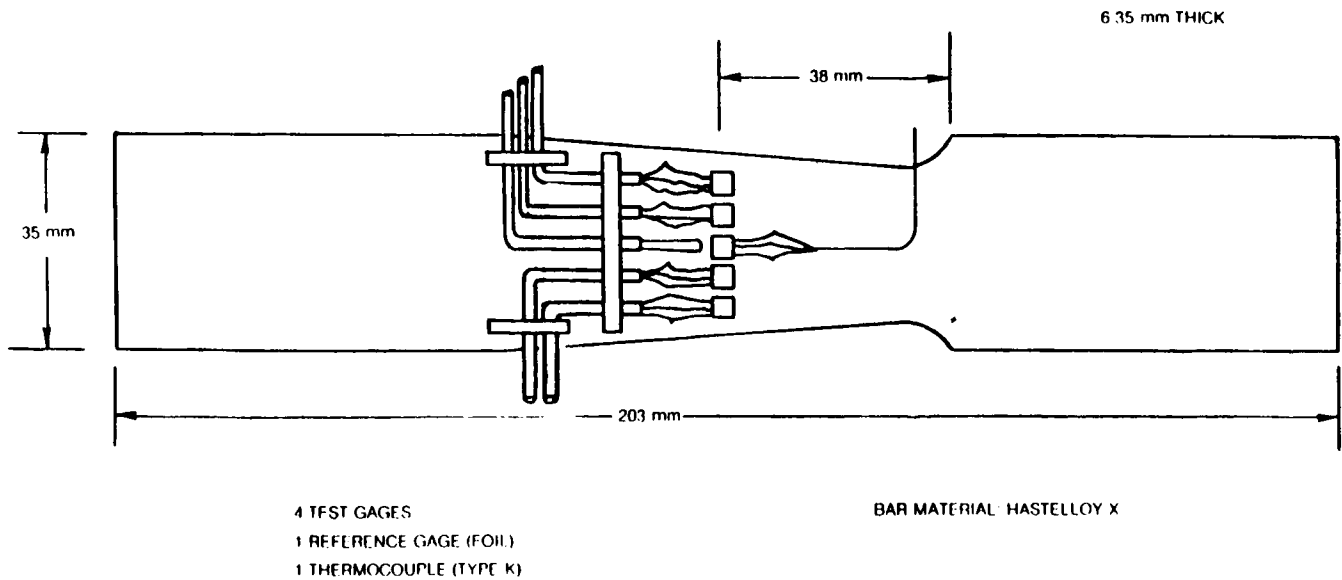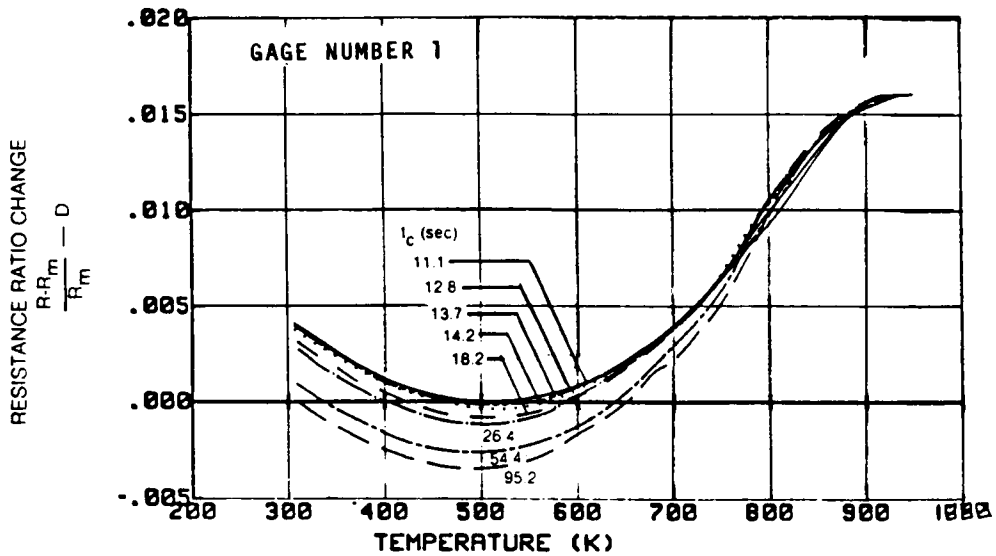Figure 9   Effect of Initial Temperature and Dwell on Change in Resistance Ratio

Figure 10   Gage Factor Test Bar

95

GAGE RESISTANCE RATIO CHANGE VERSUS TEMPERATURE FOR ONE GAGE ON THE BURNER
LINER AT EIGHT COOLING RATES BEFORE THE COMBUSTOR TESTS. THE QUANTITY D IS AN
ARBITRARY OFFSET ADJUSTMENT TO SUBTRACT THE EFFECTS OF SMALL DRIFTS AT 950K
FROM ONE TEST TO ANOTHER SO THAT ALL CURVES PASS THROUGH THE SAME POINT AT
950K.

R = GAGE RESISTANCE
R_m = MINIMUM RESISTANCE DURING FASTEST TEST (t_c = 12 seconds)
t_c = COOLING TIME FROM 811K (1000°F) TO 727K (858°F)

## Figure 11   Gage Resistance Ratio for 8 Cooling Rates
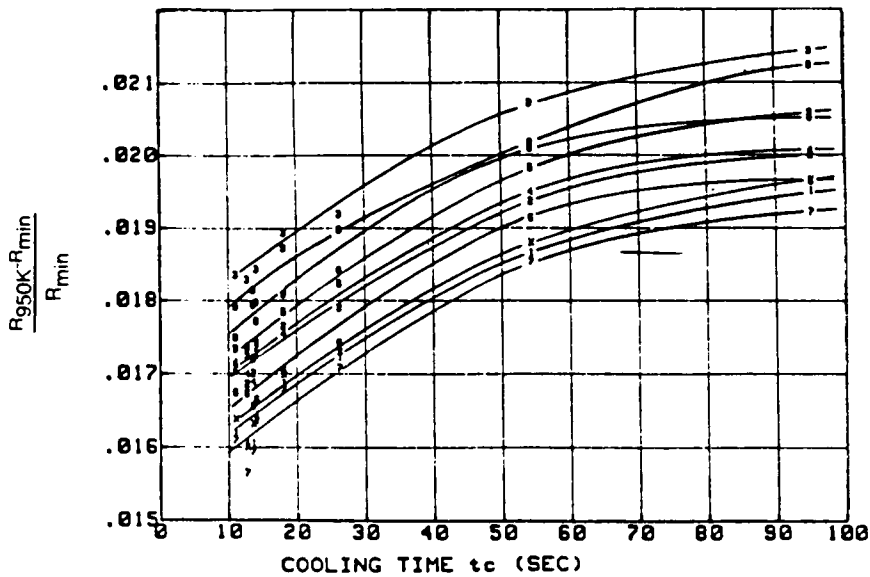
GAGE RESISTANCE CHANGE FROM 950K TO MINIMUM-RESISTANCE TEMPERATURE VERSUS t_c,
THE COOLING TIME PARAMETER, FOR EACH OF THE TEN GAGES ON THE BURNER LINER DUR-
ING COOL-DOWN TESTS BEFORE THE COMBUSTOR TESTS.

R_{950K} = GAGE RESISTANCE AT 950K
R_{min} = MINIMUM GAGE RESISTANCE OBSERVED DURING EACH COOL-DOWN TEST

THE SYMBOL USED FOR EACH DATA POINT IS THE GAGE NUMBER FOR GAGES 1 THROUGH 9.
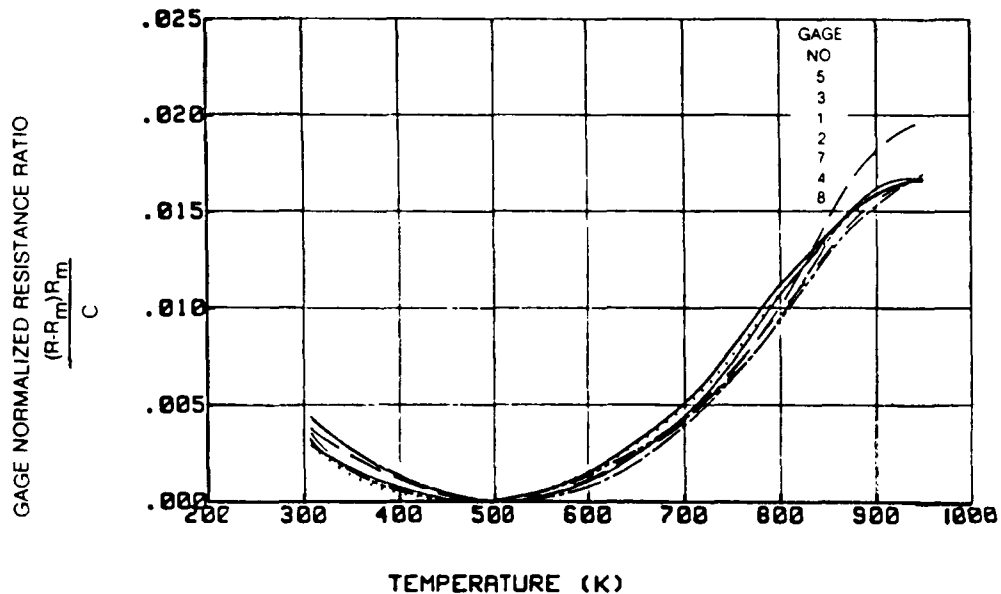SYMBOL X IS GAGE 10.

Figure 12   Gage Resistance Change Versus t_c
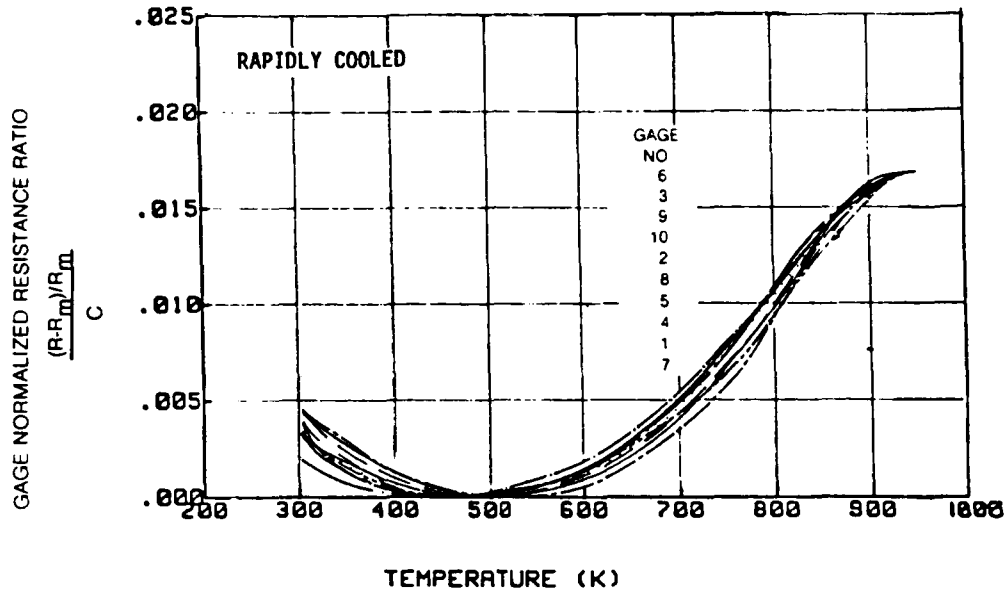
96

GAGE NORMALIZED RESISTANCE RATIO VERSUS TEMPERATURE DURING RAPID COOLING (t_c = 12 seconds) FROM 950K FOR THE TEN GAGES ON THE BURNER LINER BEFORE THE COMBUSTOR TESTS.
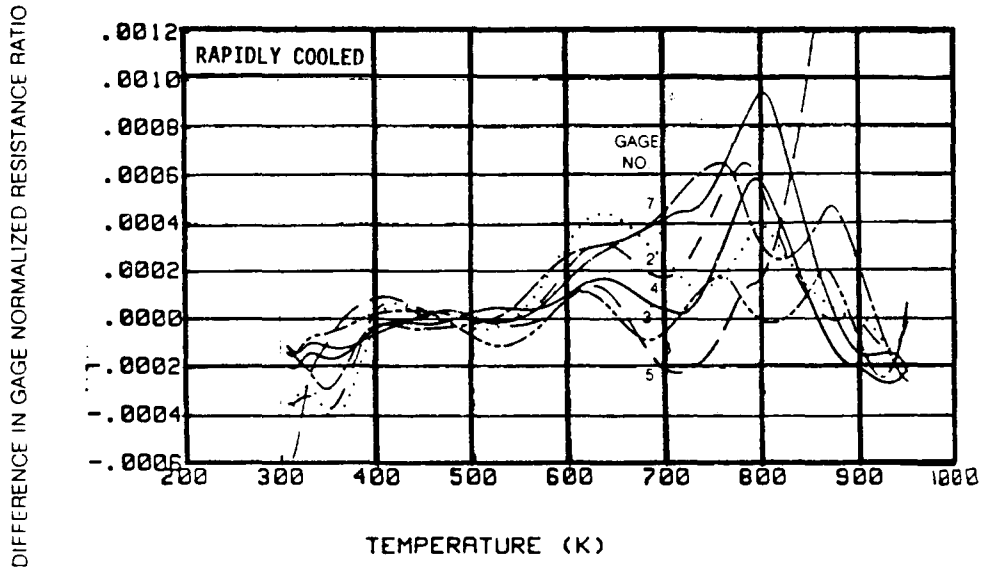
R = GAGE RESISTANCE
R_m = MINIMUM RESISTANCE IN EACH TEST
C = CALIBRATION CONSTANT FOR EACH GAGE

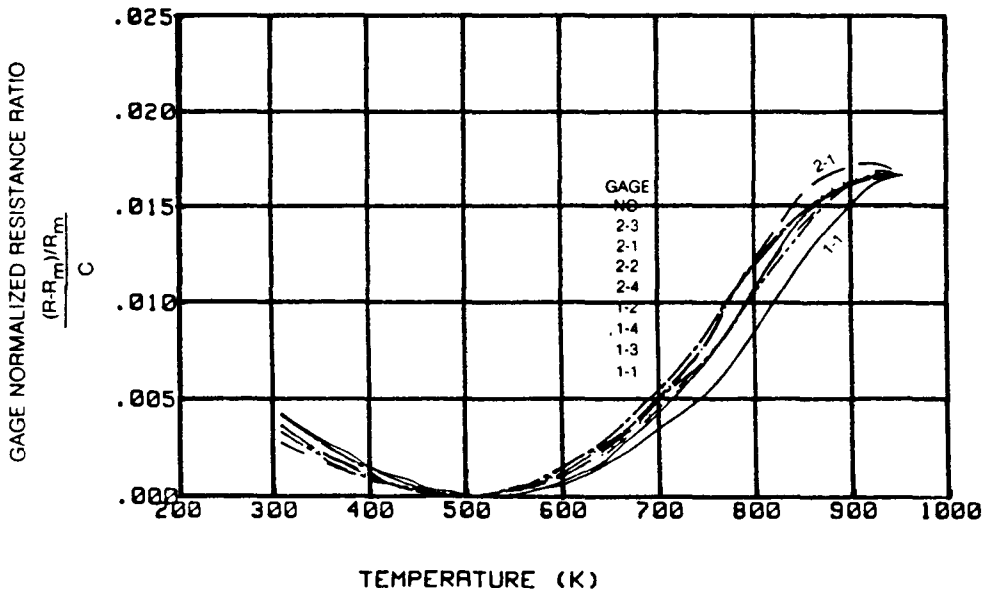Figure 13   Normalized Gage Resistance Ratio for Combustor Gages Before Tests

GAGE NORMALIZED RESISTANCE RATIO VERSUS TEMPERATURE DURING RAPID COOLING (t_c = 12 seconds) FROM 950K FOR THE SEVEN GAGES ON THE BURNER LINER. AFTER THE COMBUSTOR TESTS THE CALIBRATION CONSTANT C FOR EACH GAGE IS THE SAME AS THAT USED IN FIGURE 13. THE RESULTS ARE ALL WITHIN THE ENVELOPE OF THE ORIGINAL CALIBRATION CURVES OF FIGURE 13 EXCEPT FOR GAGE NO. 5 WHICH EXPERIENCED OVER-TEMPERATURES TO 1041K DURING THE COMBUSTOR TESTS.

Figure 14   Normalized Gage Resistance Ratio for Combustor Gages After Tests

97

DIFFERENCE IN GAGE NORMALIZED RESISTANCE RATIO VERSUS TEMPERATURE FROM BEFORE
TO AFTER THE BURNER TESTS FOR RAPID COOLING (t_c = 12 seconds) FROM 950K. THE
DIFFERENCE BETWEEN FIGURE 13 and FIGURE 14 IS PLOTTED FOR EACH GAGE.

Figure 15   Effect of Combustor Tests on Normalized Gage Resistance Ratio

GAGE NORMALIZED RESISTANCE RATIO VERSUS TEMPERATURE DURING RAPID COOLING
(t_c = 12 seconds) FROM 950K FOR THE EIGHT GAGES ON THE TWO GAGE-FACTOR TEST
BARS. ALL OF THESE CURVES FALL WITHIN THE ENVELOPE OF FIGURE 13.

Figure 16   Normalized Gage Resistance Ratios for Test Bar Gages
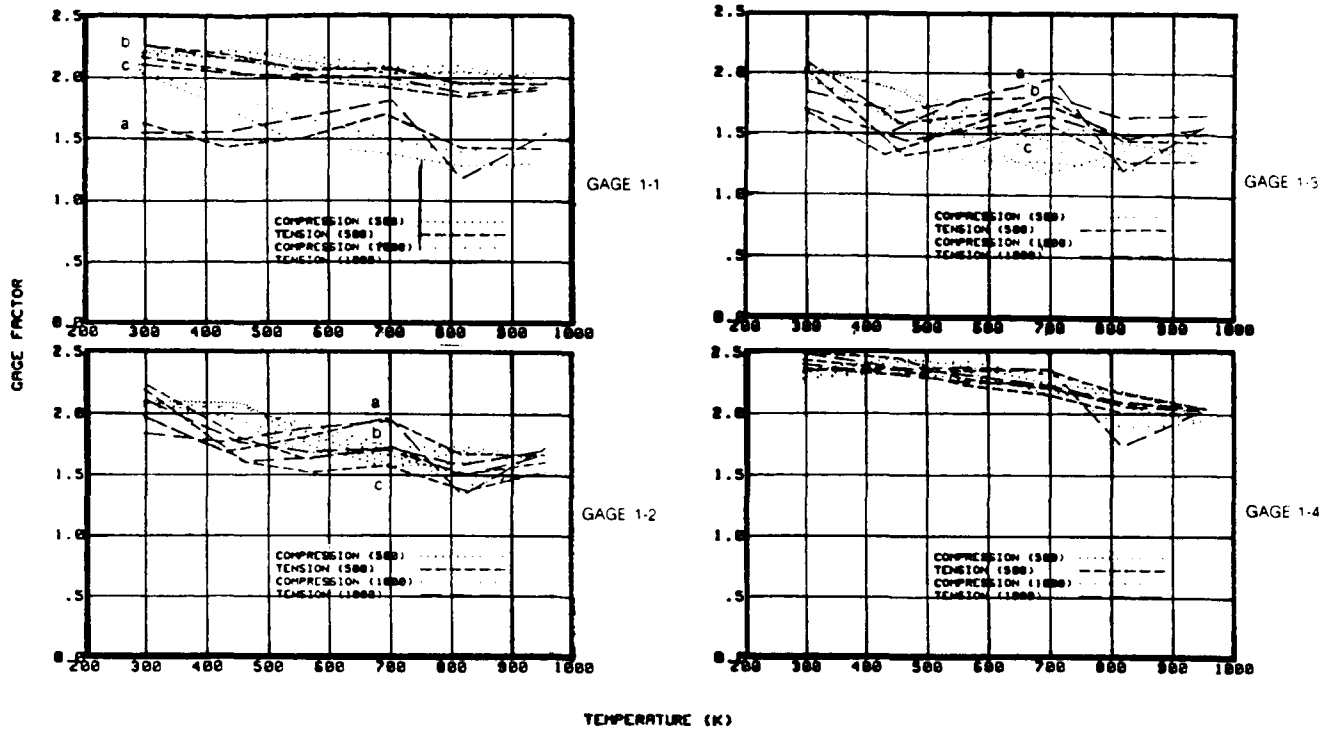
TEMPERATURE (K)

GAGE FACTOR VERSUS TEMPERATURE FOR THE FOUR GAGES ON BAR #1 (a) FIRST TEST,
(b) AFTER 200 HOURS AT 950K, (c) Repeat of b.

Figure 17   Gage Factors for Bar 1 Gages
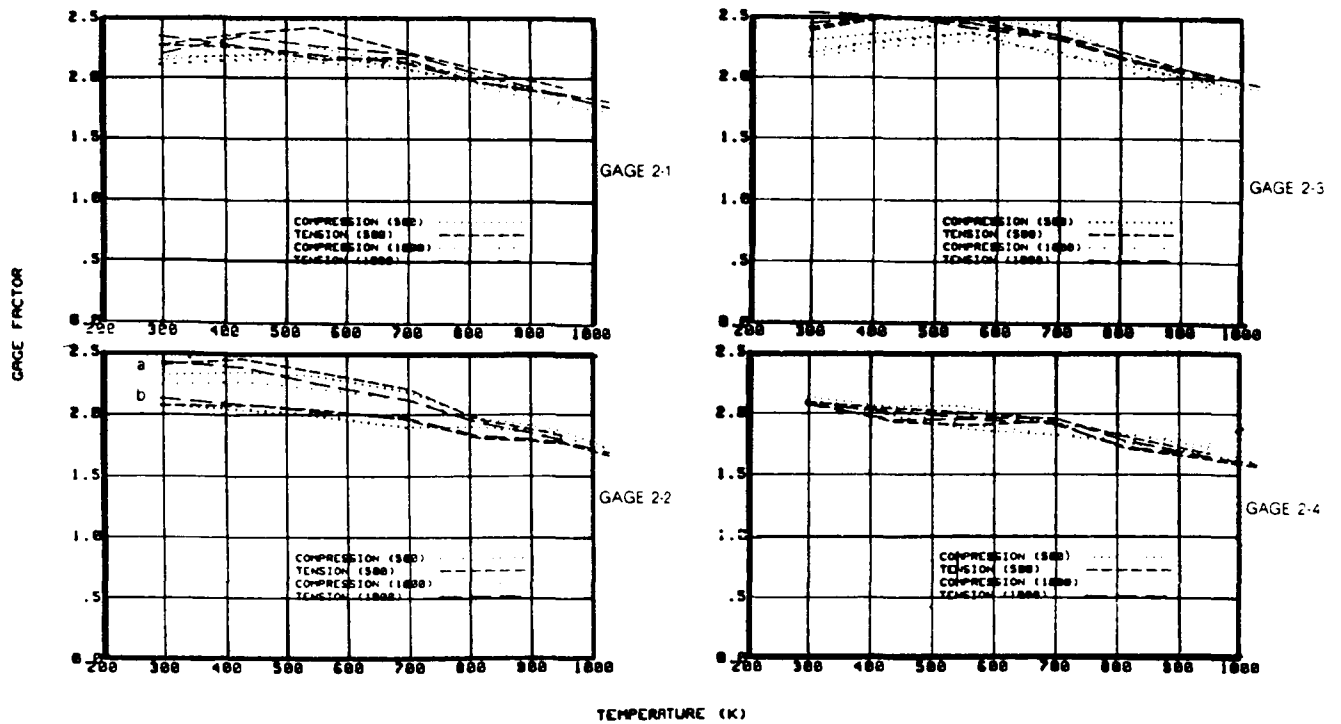
TEMPERATURE (K)

GAGE FACTOR VERSUS TEMPERATURE FOR FOUR GAGES ON BAR #2 (a) FIRST TEST, (b)
AFTER RAPID COOLING FROM 950K TO ROOM TEMPERATURE AT t_c = 12 seconds.

Figure 18   Gage Factors for Bar 2 Gages

99
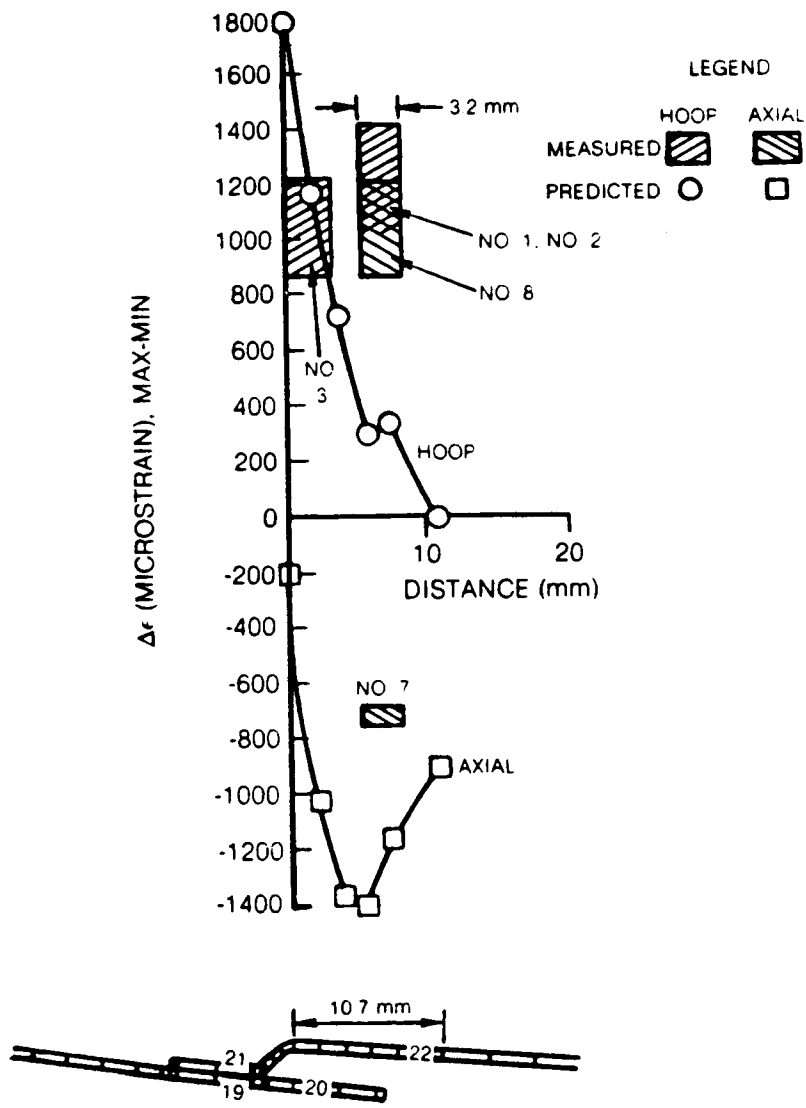
PREDICTED MECHANICAL STRAIN RANGE (USING AVERAGE TEMPERATURES) AND MEASURED
STRAIN RANGE (USING KANTHAL A-1 GAGES) DURING BURNER CYCLES 4, 5, 6, 7.

Figure 19   Predicted and Measured Strains During Final Four Burner Cycles

TURBINE AIRFOIL DEPOSITION MODELS

Daniel E. Rosner
Yale University
Department of Chemical Engineering
High Temperature Chemical Reaction Engineering Laboratory

1. INTRODUCTION, OUTLINE

Gas turbine failures associated with sea-salt ingestion and sulfur-containing fuel impurities have directed attention to alkali sulfate deposition and the associated "hot corrosion" of gas turbine (GT) blades under some GT operating conditions. These salts deposit and form thin, molten films which undermine the protective metal oxide coating normally found on GT blades. This research project deals with the prediction of molten salt deposition, flow and oxide dissolution and their effects on the lifetime of turbine blades. Our goals include rationalizing and helping to predict corrosion patterns on operational GT rotor blades and stators, and ultimately providing some of the tools required to design laboratory simulators and future corrosion-resistant high-performance engines. In the program summary below, we first review necessary background developments[*] (Sections 2, 3 and 4) and then introduce our recent results and tentative conclusions (Sections 5, 6), along with a brief account of our present research plans.

2. VAPOR DEPOSITION (VD-) RATE THEORY

The first step in a complex sequence of events leading to hot corrosion failures is the deposition of alkali salts from the combustion products onto turbine stator vanes and rotor blades. Our NASA-supported laboratory experiments,[1-3] and those carried out in collaboration with NASA-Lewis Research Laboratories,[4] have enabled advances in salt deposition rate theory, as briefly outlined here. A comprehensive but tractable method for predicting the rates of chemical vapor deposition (CVD) of, say, alkali sulfates from multicomponent salt-laden combustion products was first developed, illustrated and tested in part.[4,5,8] This theory predicts important effects of multicomponent diffusion and thermal (Soret) diffusion[6] on dew points, CVD-rates and deposit compositions.[7] For present purposes an important feature of the deposition rate is its dependence on surface temperature, which ordinarily reveals the existence of a dew point temperature (above which a macroscopic surface condensate is not stable) and a temperature-insensitive plateau deposition rate at temperatures sufficiently far below the dew point — i.e., features included in the above-mentioned CVD-rate theory.[4,5,7,8] While in its most general form, allowance is made for the transport of each chemical species (i = 1,2, ...) containing the elements of interest (Na, S ...) across the diffusion boundary layer (BL) (Fig. 1), to study the dynamics of the resulting molten salt condensate layer (Section 3 below), we use the single-component limiting form of the CVD theory to economically provide the spatial distribution of condensate "arrival." This approach also applies without fundamental modifications to the deposition rate of pre-existing fine particles,[9,10] i.e., mist droplets small enough to behave like "heavy molecules" in the prevailing carrier gas flow field. The inclusion of chemical reactions and/or phase change (e.g., "mist formation") within the BL requires further research, some of which is in progress (Section 6).

---

[*] and update bibliographic information on our recently published papers.

[†] NAG 3-201

3. CONDENSATE LAYER DYNAMICS

An important process in the molten salt attack of GT blades is evidently the dissolution ("fluxing") of the normally protective metal oxide, and this in turn, implies dynamic processes which allow dissolution/reaction to occur without saturating the molten salt solvent. For these reasons, we have carried out studies of the dynamics of thin condensate liquid layers[11], allowing for the interplay of salt arrival rate (Section 2) and runoff induced by aerodynamic shear stress τ_w and blade rotation rate, Ω (Fig. 2). These studies should ultimately prove useful in the interpretation of observed hot corrosion maps on blades removed from operational engines. They have already guided the development and interpretation of laboratory simulator experiments[3,4,8] in which molten salt deposition and runoff necessarily occur at seed levels such that $T_{dp} > T_{mp}$.

In ref. 11 the necessary liquid layer theory was developed and used to predict steady-state laminar single component condensate layers on smooth non-rotating, isothermal targets, with emphasis on the circular cylinder in high Reynolds number cross-flow (a common test configuration). In our recent studies, this approach has been extended to include the treatment of single component condensate layer flow along smooth non-isothermal _rotor_ blades (Fig. 2). Illustrative calculations have thus far been made for a test turbine (NASA TP 1018 (1977)), but most of our methods will carry over to operational engine vanes and blades (except in the immediate vicinity of cooling slots/holes). From the inviscid stream velocity data, we compute, using efficient integral methods, the corresponding distributions of gas-side momentum; heat- and mass-transfer coefficients, and the distribution of blade "recovery" temperature (used to estimate this root-cooled blade temperature distribution). The corresponding condensate arrival rate distribution and liquid viscosity distributions are then inserted into the partial differential equation (PDE) governing the liquid layer thickness $\delta_\ell(x,z)$ (Fig. 2). This nonlinear first-order PDE is numerically solved (by the method-of-characteristics) to provide the condensate layer streamline pattern (Fig. 3), as well as the corresponding liquid layer _thickness_ $\delta_\ell(x,z)$. Two important by-products of these calculations are (a) the solvent inventory on the blade, and (b) relative tip and trailing edge salt runoff rates. It is also interesting to note that _surface flow_ can lead to the presence of condensate on portions of the blade which are hotter than the prevailing dew point. One such region is shown in Fig. 4, in which the span-wise flow associated with blade rotation causes the steady-state presence of molten salt at $T_w > T_{dp}$, and hence, the possibility of appreciable local hot corrosion rates above T_{dp}.

4. METAL OXIDE "DISSOLUTION" RATE DISTRIBUTIONS

As mentioned at the outset of Section 3, non-stoichiometric molten sodium sulfate is known to be a solvent for $Al_2O_3(s)$ or $Cr_2O_3(s)$ — the oxides ordinarily relied upon for corrosion protection of the underlying blade alloys. Accordingly, we have utilized the above-mentioned formulation to predict _dissolution rate distributions_ associated with solvent flow patterns of the type shown (Fig. 3). Indeed, it will be instructive to compare such predictions with hot corrosion rate patterns observed on blades removed from operational GT engines. Toward this end, estimates have been made of the oxide diffusion coefficient in the solvent, equilibrium solubility, and maximum (kinetic) rate of dissolution. This information was then used to predict the solute diffusion-limited dissolution rate along each streamline (cf. Fig. 5) using a generalization of Leveque-Levich BL-theory. The corresponding arrival rate distribution is shown in Fig. 6 for comparison. Preliminary dissolution rate maps are being checked, generalized and discussed in terms of their parametric dependencies, and to the limited extent possible, agreement with operational experience. This research will be summarized in our final report on Grant NAG 3-201, and in a paper[12] currently in preparation. Publication seems to be timely, since even though high-quality operational data are not generally available, we believe that the _formalism_ we have developed will make possible in the U.S.-GT industry instructive and economical parametric studies for both stator and rotor

blades over a wide variety of environmental conditions (salt level, turbine inlet temperature, stagnation pressure level, blade contour and cooling, tip speed, etc.). Moreover, the stage has been set to generalize many aspects of the theory, including commonly encountered mixed alkali deposits, condensate arrival by both vapor diffusion and thermophoretic capture of BL-nucleated droplets,[13] and *transient* condensate flows. It should also be useful to examine in greater detail the effects on localized dissolution rates of secondary flows, produced in part by surface tension gradients associated with the oxide dissolution process itself.

5. PRELIMINARY INVESTIGATON OF BINARY CONDENSATE LAYER EFFECTS

All properties of thin liquid condensate films, including their aggressiveness as corrodants, are expected to be composition-dependent. Moreover, appreciable amounts of adulterants (e.g. Ca- and Mg-compounds) are often found in GT-blade deposits upon engine shut-down and blade removal. This information, combined with the remarkable effect the addition of a second salt can have on the deposition rate of the primary salt (see ref. 14, based on our experiments carried out under NASA Grant NSG 3169) suggests that attention should be directed toward the deposition, dynamics and dissolution rate properties of *multicomponent* molten salt layers, not just the behavior of pure $Na_2SO_4(\ell)$. Toward this end, we are proposing intensive studies of the expected behavior of binary sulfate salt layers.

Among the effects anticipated for *binary* molten salt cases, perhaps the most significant are the alteration of:

   (a) deposition rates and associated dew point temperature,
   (b) liquid properties, including the important oxide solubility and associated Fick diffusivity,
   (c) freezing point of the solution.

While the property effects (b) remain to be studied, it is clear that effects (a) and (c) can considerably broaden the important temperature interval: $T_{dp} - T_{mp}$ within which hot corrosion is known to take its toll on GT blade alloys.

To illustrate the consequences of the altered freezing point, we have performed a preliminary steady-state analysis of the binary $(K_2SO_4 + Na_2SO_4)$ condensate layer expected along the leading edge of a non-isothermal (root-cooled) rotor blade, with a specified root temperature (cf. $T_{mp}(Na_2SO_4)$ = 1157K and $T_{mp}(K_2SO_4)$ = 1343K) and Ω = 6786 rad/s. Figure 7 reveals that if $T_w(0,0)$ is as low as 1110K then the condensate on the leading edge would be entirely solid in the absence of potassium addition to the mainstream (with $T_{dp}(Na_2SO_4)$ = 1242K). However, with increasing potassium levels, an increasing fraction of the condensate would become molten (becoming fully molten at $([K]/[Na])_\infty$-ratios above about 0.13. More comprehensive prototypical examples, including effects (a), (b) and (c) above, are planned.

6. TENTATIVE CONCLUSIONS, IMPLICATIONS, FUTURE WORK

While much of the required input information remains to be sharpened up (based on independent experiments), we believe that the present *formalism* has reached the point where instructive parametric studies can now be economically performed for both GT stator vanes and rotor blades over a wide variety of environmental conditions (salt level, turbine inlet temperature, stagnation pressure level, blade contour and cooling, tip speed, etc.).

For the present, the following conclusions have emerged from our recent investigations:

   (a) On rotor blades, qualitatively different condensate behavior (thickness, composition) is observed depending upon whether the liquid streamlines emerge from the blade leading edge or root (see e.g. Fig. 3).

103

(b) For surfaces everywhere below T_{dp} predicted oxide dissolution rate distributions (Fig. 5) are strongly coupled to the predicted local condensate arrival rate distribution (Fig. 6).

This observation, combined with formal computations which presume highly undersaturated liquid layers, lead us to conclude that:

(c) The tendency toward local saturation of the condensate layer strongly influences the distribution of metal oxide dissolution rate.

(d) Owing to liquid layer convection across blade isotherms, liquid layers (hence corrosion) can occur on some areas of a GT blade which are above the prevailing dew point temperature.

(e) The simultaneous presence of chemical elements capable of entering into the condensate solution considerably broadens the temperature interval $T_{dp}-T_{mp}$ (within which hot corrosion is likely to take its toll on GT blade alloys) but improves the chances of reduced deposition rates via BL mist formation.[13,14]

Finally, we realize that to fully exploit and test the presently developed liquid layer theory:

(f) Additional fundamental data will be needed (e.g. temperature and stoichiometry dependence of the solubility of Al_2O_3 and Cr_2O_3 in $Na_2SO_4(\ell)$).

(g) Well-documented test data on hot-corrosion rate distributions from simulated and/or real turbine blades run under nearly constant environmental conditions will be needed.

7. REFERENCES

1. Rosner, D. E. and Atkins, R. M., in Fouling and Slagging Resulting from Impurities in Combustion Gases (R. Bryers, ed.) Engineering Foundation (New York) 1983, pp. 469-492.

2. Rosner, D. E. and Seshadri, K., in Eighteenth Int. Symposium on Combustion, The Combustion Institute (Pittsburgh, PA), 1981, pp. 1385-1394.

3. Seshadri, K. and Rosner, D. E., AIChE J. 30(2), 187 (1984).

4. Kohl, F. J., Santoro, G. J., Stearns, C. A., Fryburg, G. C. and Rosner, D. E., J. Electrochem. Soc. 126, 1054 (1979).

5. Rosner, D. E., Chen, B.-K., Fryburg, G. C. and Kohl, F. J., Comb. Sci. and Tech. 20, 87 (1979).

6. Rosner, D. E., J. Physicochem. Hydrodynamics 1, 159 (1980).

7. Rosner, D. E. and Nagarajan, R., "Transport-Induced Shifts in Condensate Dew Point and Composition in Multicomponent Systems with Chemical Reaction," Chemical Engrg. Sci. (in press, 1984).

8. Santoro, G. J., Kohl, F. J., Stearns, C. A., Rosner, D. E. and Gokoglu, S. A., _Experimental and Theoretical Deposition Rates from Salt-seeded Combustion Gases of a Mach 0.3 Burner Rig_, NASA TP 225 (1984).

9. Gokoglu, S. A. and Rosner, D. E., Int. J. Heat and Mass Trans. 27, 639 (1984).

10. Rosner, D. E., Gokoglu, S. A. and Israel, R., in _Fouling of Heat Exchange Surfaces_ (R. Bryers, ed.) Engineering Foundation (New York) 1983, pp. 235-256.

11. Rosner, D. E., Gunes, D. and Anous, N., Chem. Engrg. Commun. 24, 275 (1983).

12. Rosner, D. E. and Nagarajan, R., "Theoretical Model to Predict/Understand the Corrosion Rate Consequences of Molten Alkali Sulfate Condensation on Combustion Turbine Blades" (in preparation, 1984).

13. Castillo, J. L. and Rosner, D. E., "Mass Transfer Consequences of Droplet Thermophoresis and Local Vapor/Liquid Equilibrium in Dilute Binary Condensible Vapor Laminar Boundary Layers" (in preparation, 1984).

14. Rosner, D. E. and Liang, B., "Development and Demonstration of Flash Evaporation Technique for Binary Alkali Sulfate Salt-Seeded Flames" (in preparation, 1984).

VAPOR DEPOSITION
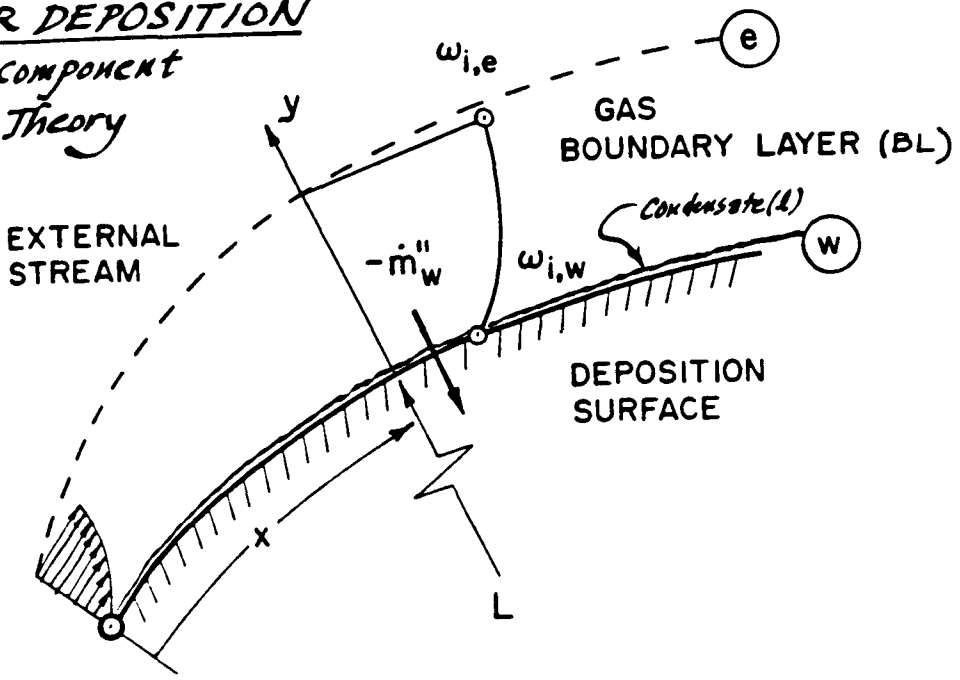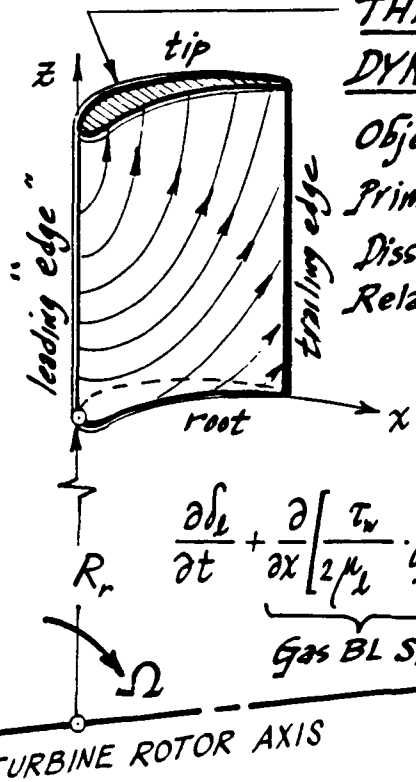### Multi-component "CFBL" Theory

Fig. 1: Vapor phase boundary layer near turbine blade surface source of momentum and mass for thin condensate layer.

THIN CONDENSATE LAYER DYNAMICS - ROTOR BLADES

Objectives:

Primary Flow, and its Metal Oxide Dissolution Rate Consequences;
Relation to observed hot corrosion patterns?

$$\frac{\partial \delta_{\ell}}{\partial t} + \frac{\partial}{\partial x}\left[\frac{\tau_w}{2\mu_{\ell}}\cdot\delta_{\ell}^2\right] + \frac{\partial}{\partial z}\left[\frac{\Omega^2(R_r+z)}{3\nu_{\ell}}\delta_{\ell}^3\right] = \frac{-\dot{m}''(x,z,t)}{\rho_{\ell}}$$

Gas BL Shear — "Centrifugal" term — "Arrival" from Vapor BL

Fig. 2: Factors influencing the evolution of liquid condensate layer dynamics on a turbine rotor blade.
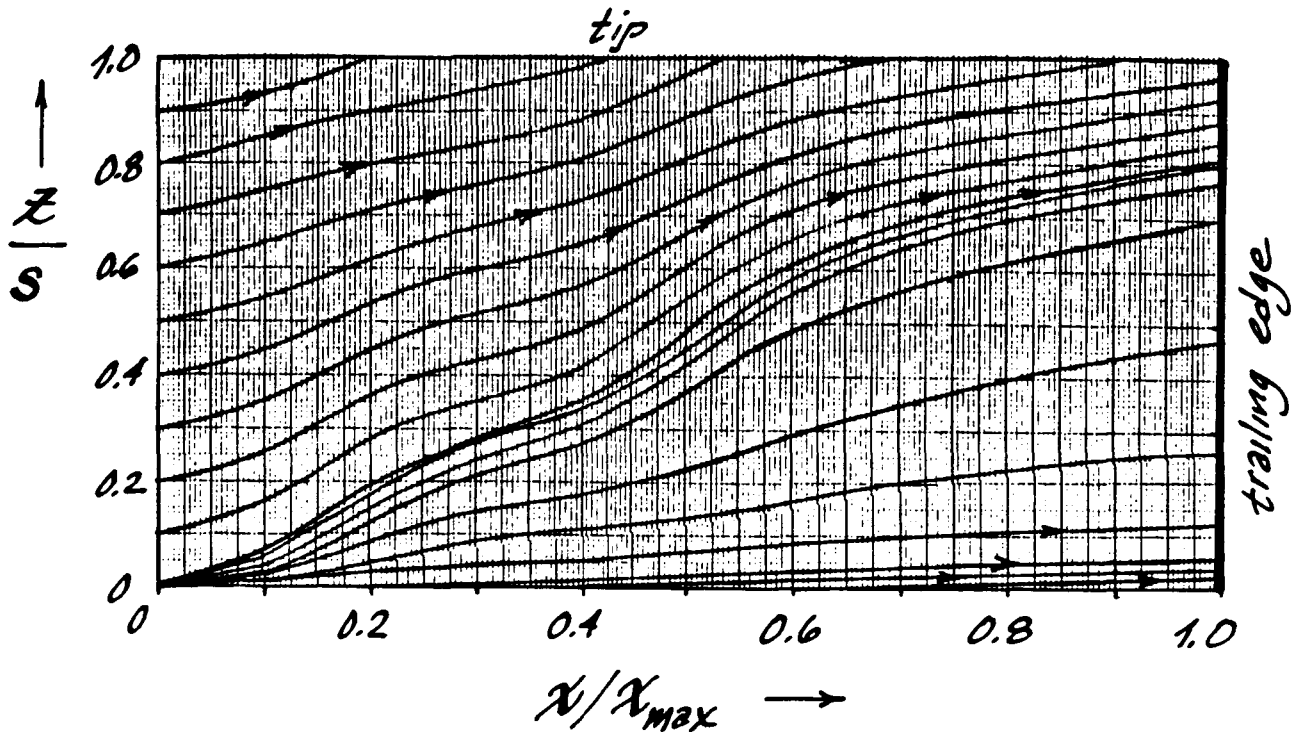
Fig. 3: Predicted streamline pattern in molten salt condensate layer along suction surface of test turbine rotor blade (Ω = 6786 rad/s).
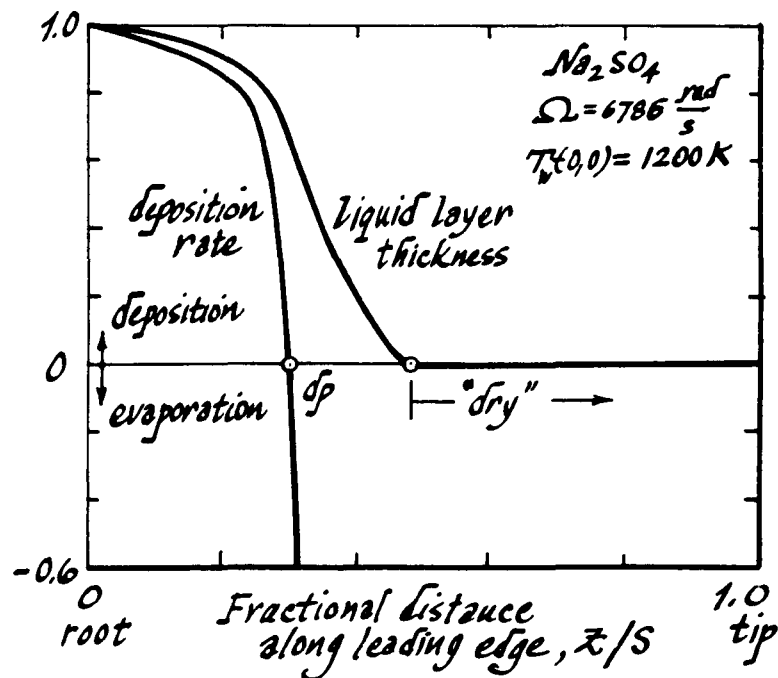

Fig. 4: Predicted molten salt layer thickness distribution along leading edge of root-cooled test turbine blade. (Note flow of liquid layer onto region of blade above prevailing dew point.)
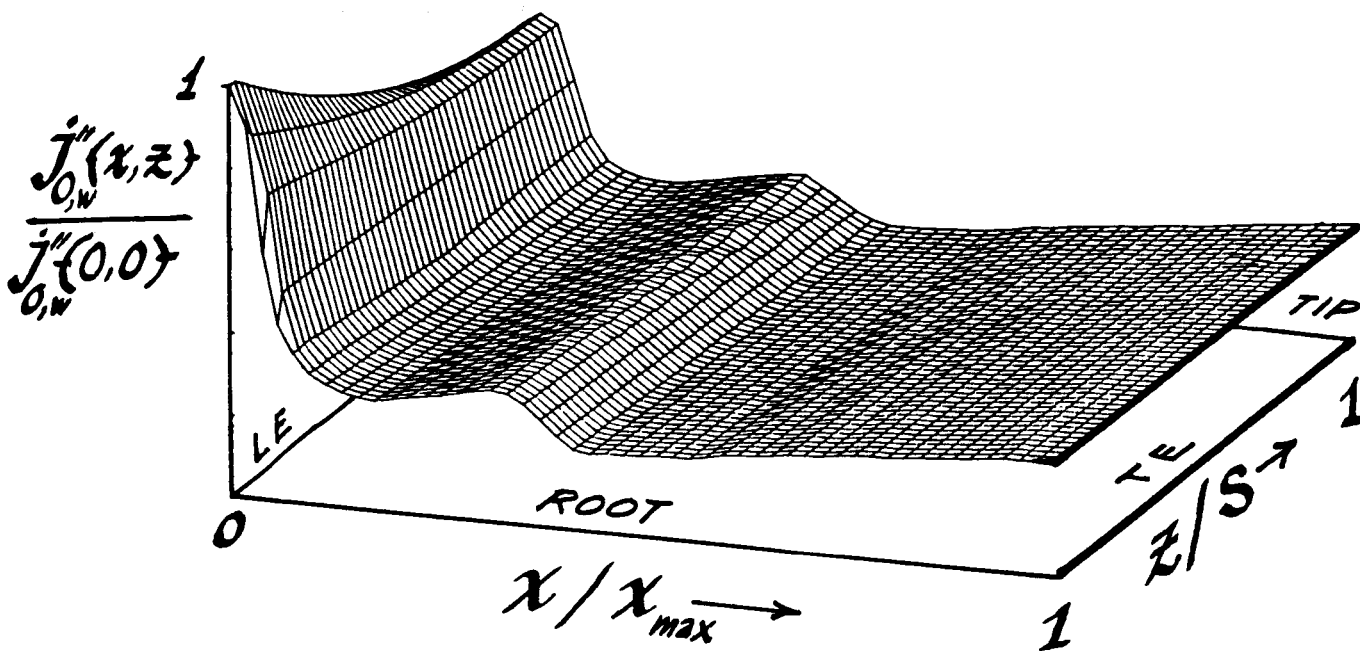
Fig. 5: Predicted distribution of metal oxide dissolution rates caused by molten salt condensate layer flow on root-cooled turbine rotor blade.
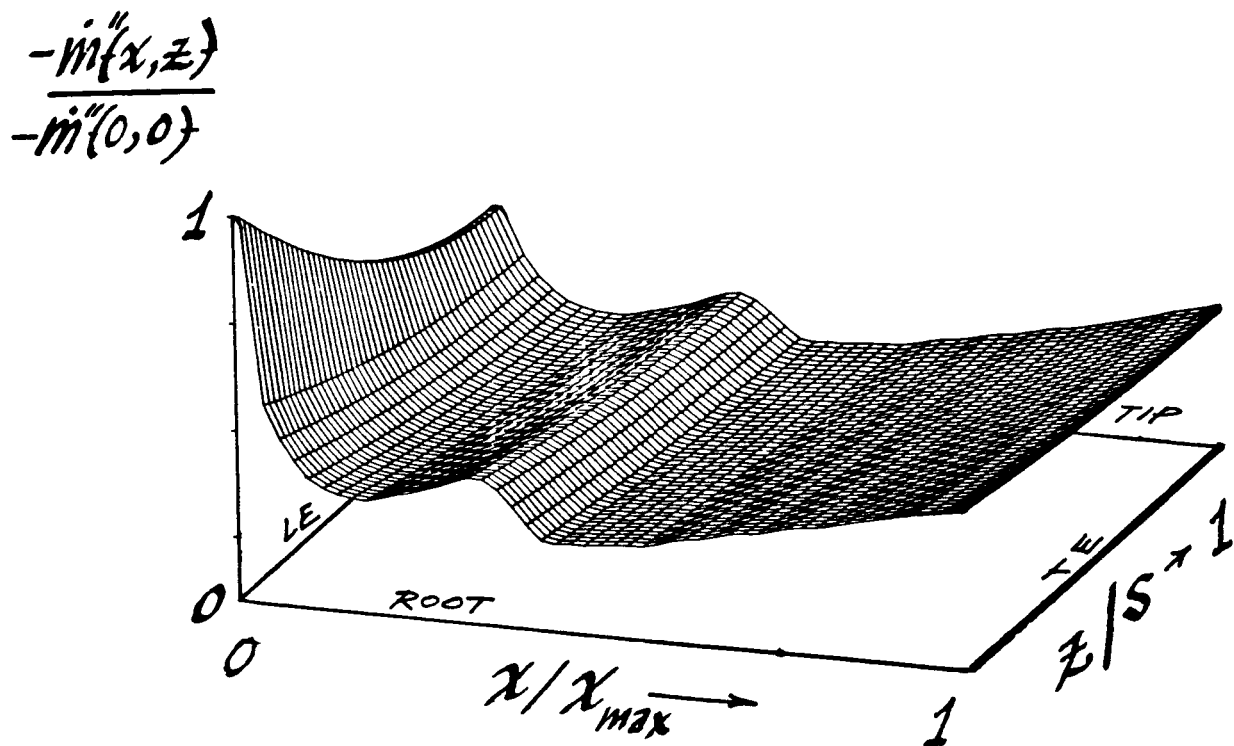

Fig. 6: Normalized Na_2SO_4 arrival rate distribution (from vapor phase boundary layer) on turbine rotor blade suction surface.
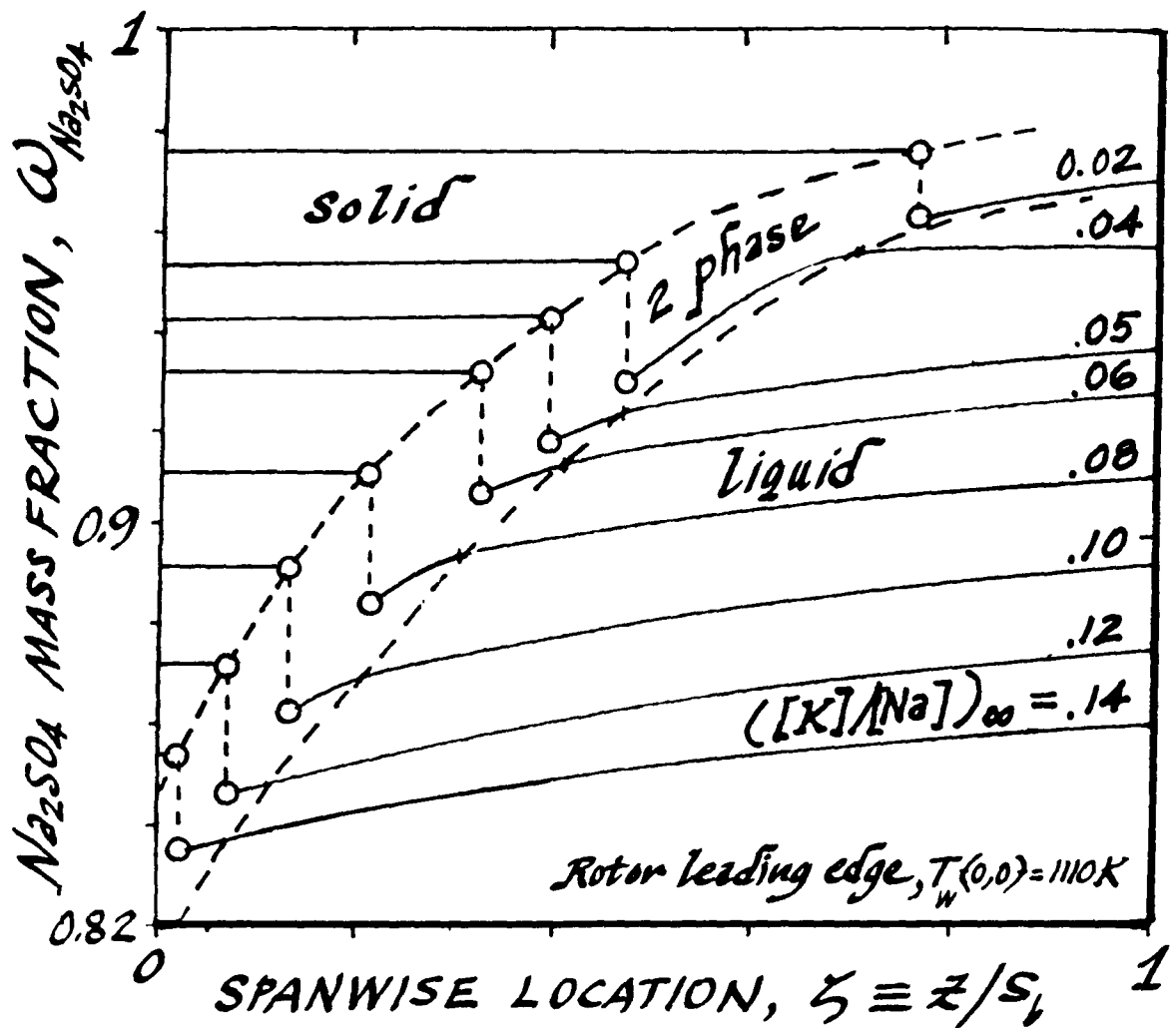
Fig. 7: Predicted distribution of condensate phase and composition along leading edge of a root-cooled turbine rotor blade ($T_w(0,0)$ = 1110K) vs. mainstream potassium: sodium ratio.

EXPERIMENTAL VERIFICATION OF VAPOR DEPOSITION MODEL IN MACH 0.3 BURNER RIGS[*]

Süleyman A. Gökoğlu
Analex Corporation

Gas turbine failures associated with accelerated "hot" corrosion motivated this research intended to obtain a better understanding of the deposition phenomenon of corrosive species on turbine blades. A comprehensive yet tractable theoretical framework of deposition from combustion gases has been developed covering the spectrum of various mass delivery mechanisms including vapor (refs. 1 and 2), thermophoretically enhanced small particle (ref. 3), and inertially impacting large particle (ref. 4) deposition. Rational yet simple correlations have been provided to facilitate engineering surface arrival rate predictions (refs. 5 to 7). The objective of the program at the NASA Lewis Research Center has been the experimental verification of the deposition theory using burner rigs. Toward this end, a Mach 0.3 burner rig apparatus has been designed to measure deposition rates from salt-seeded combustion gases on an internally cooled cylindrical collector (ref. 8).

The results of the previous experiments have been reported in detail in reference 8. Different sodium salt solutions (e.g., NaCl, sea salt, $NaNO_3$, and Na_2SO_4) were sprayed into the combustor; however, in all cases the expected deposit was Na_2SO_4. Indeed, the X-ray analysis of the deposit verified this prediction. There were two regions of disagreement between the deposition rate prediction of the chemically frozen boundary layer (CFBL) vapor deposition theory and the experimentally observed deposition rates of Na_2SO_4, depending on whether the collector temperature was above or below the melting point of Na_2SO_4. The discrepancy for collector temperatures above the melting point of the deposit is attributed to the shear-driven molten deposit layer run off from the smooth collector surface (ref. 9). However, for collector temperatures below the melting point of the deposit the results were puzzling. Although both the theory and the experiments showed plateau deposition rate behavior, the disagreement level depended on the sodium salt sprayed, ranging from good agreement for NaCl seeded experiments to almost three times the predicted deposition rate for Na_2SO_4 seeded experiments.

As a first attempt to analyze the experimental system more carefully and systematically, droplet sizes were determined from the salt solution probe using a Malvern particle/droplet size analyzer as a function of atomizing air pressure and solution composition for different probes. Based on the droplet sizes obtained, vaporization time calculations of the droplets during their residence times inside the combustor showed that droplets survived and were, in fact, large enough to impact inertially on the collector. Deposition rate predictions for Na_2SO_4 seeded experiments based on the particle inertial impaction theory agreed well with the experimental observations. A particle capture test was designed to verify experimentally the theoretical prediction of the presence of particles in the previous experiments. Indeed, SEM

---

photographs of the deposits collected on targets in a few seconds at the original collector location show the particles very clearly even for NaCl seeded flames (ref. 10). Therefore, the agreement between the CFBL vapor deposition theory and the previous NaCl seeded experiments was coincidental, the arrival rate by particle inertial impaction mechanism giving the same rate as one would expect from vapor convective-diffusion mechanism. Moreover, the chemical analysis of the deposit collected in about 5 sec in particle capture tests for a NaCl seeded flame showed about 80 percent NaCl and 20 percent Na_2SO_4 by weight. This indicates that NaCl particles of 1 to 5 μm size range are able to react chemically and convert to Na_2SO_4 on the collector in such short durations. The fact that only Na_2SO_4 was observed in X-ray analysis of the deposits for all sodium salts seeded is explained by the fast reaction times of small (1 to 5 μm) sodium salt particles to convert to Na_2SO_4 as compared with the deposition run times of 30 min. Only those particles that deposited during the last few seconds of the experiment had no time to react and, therefore, were able to preserve their identity. However, their concentration was too low to be detected by X-ray analysis.

When predicting vapor deposition rates the CFBL theory makes use of the "cylinder-in-crossflow" assumption in estimating the average mass transfer coefficient (Nusselt number). This assumption needed to be checked, because our cylindrical collector diameter (3/4 in) is not small compared with the jet stream diameter from the burner rig nozzle exit (1 in). Indeed, under typical experimental conditions there is about 250° to 300° C difference in temperature between the forward and the backward stagnation point of the stationary collector (ref. 10), which invalidates the "cylinder-in-crossflow" assumption. In order to regain a correct predictive capability of vapor deposition rates, even if there were no particles present, an experimentally determined mass transfer Nusselt number has to be supplied to the theory.

Having determined the problematic features of the previous experiments and having been able to interpret the previous results to our sufficient satisfaction, new experiments and procedures have been designed as remedies. In order to eliminate the presence of particles two possible routes are being taken: (1) Na dispersions in light oil or mineral spirits which are both soluble in Jet A-1 fuel will be used, or (2) alcohol will be used as fuel, and Na acetate (Na source) and thiourea (S source) will be dissolved in it to desired concentrations. The predictions based on (1) the experimentally determined droplet size distributions of the fuel nozzles used in our experiments, (2) Na particle size in the dispersions, and (3) the longer residence times of the droplets in the combustor show that both methods are feasible and complete vaporization (burning) should be attained.

The naphthalene sublimation technique (ref. 11) will be used at room temperature for the cylindrical collectors to determine the average mass transfer coefficient as a function of the Reynolds number in our experimental configuration. This technique is superior to the previously tried calorimetry technique in eliminating the temperature gradients that inevitably exist in our experiments. Another approach that will provide a predictive capability is to use a simpler collector geometry. For that purpose only a segment which is 20° on both sides of the forward stagnation point of our previous cylindrical targets will be used as the collection (deposition) surface. In this way, the stagnation region mass transfer will be studied simulating the nose region of blades.

REFERENCES

1. Rosner, Daniel E., et al.: Chemically Frozen Multicomponent Boundary Layer Theory of Salt and/or Ash Deposition Rates from Combustion Gases. Combust. Sci. Technol., vol. 20, no. 3/4, 1979, pp. 87-106.

2. Gökoğlu, Süleyman A.; Chen, Bor-Kuan; and Rosner, Daniel E.: Computer Program for the Calculation of Multicomponent Convective Diffusion Deposition Rates from Chemically Frozen Boundary Layer Theory. NASA CR-168329, 1984.

3. Gökoğlu, Süleyman Akif: Thermophoretically Enhanced Deposition of Particulate Matter Across Nonisothermal Boundary Layers, Ph.D. Thesis, Yale University, 1983.

4. Fernandez de la Mora, J.; and Rosner, D. E.: Inertial Deposition of Particles Revisited and Extended: Eulerian Approach to a Traditionally Lagrangian Problem. PCH, PhysicoChem. Hydrodyn., vol. 2, no. 1, 1981, pp. 1-21.

5. Gökoğlu, S. A.; and Rosner, D. E.: Correlation of Thermophoretically Modified Small Particle Diffusional Deposition Rates in Forced Convection Systems with Variable Properties, Transpiration Cooling and/or Viscous Dissipation. Int. J. Heat Mass Transfer, vol. 27, no. 5, May 1984, pp. 639-646.

6. Israel, R.; and Rosner, D. E.: Use of a Generalized Stokes Number to Determine the Aerodynamic Capture Efficiency of Non-Stokesian Particles from a Compressible Gas Flow. Aerosol Sci. and Tech., vol. 2, no. 1, 1983, pp. 45-51.

7. Rosner, D. E.; Gökoğlu, S. A.; and Israel, R.: Rational Engineering Correlations of Diffusional and Inertial Particle Deposition Behavior in Non-isothermal Forced Convection Environments. Fouling of Heat Exchanger Surfaces, Richard W. Bryers, ed., Engineering Foundation Inc., 1983, pp. 235-256.

8. Santoro, Gilbert J., et al.: Experimental and Theoretical Deposition Rates from Salt-Seeded Combustion Gases of a Mach 0.3 Burner Rig. NASA TP-2225, 1984.

9. Rosner, D. E.; Gunes, D.; and Nazih-Anous, N.: Aerodynamically Driven Condensate Layer Thickness Distributions on Isothermal Cylindrical Surfaces. Chem. Eng. Commun., vol. 24, 1983, pp. 275-287.

10. Santoro, G. J.; Gökoğlu, S. A.; Kohl, F. J.; Stearns, C. A.; and Rosner, D. E.: Deposition of Na_2SO_4 From Salt-Seeded Combustion Gases of a High Velocity Burner Rig. NASA TM-83751, 1984.

11. Sparrow, E. M.; Stahl, T. J.; and Traub, P.: Heat Transfer Adjacent to the Attached End of a Cylinder in Crossflow. Int. J. Heat Mass Transfer, vol. 27, no. 2, Feb. 1984, pp. 233-242.
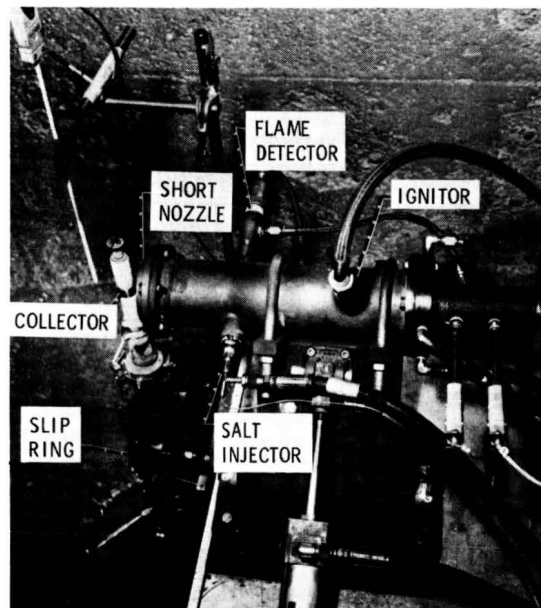
BURNER RIG
COLLECTOR ASSEMBLY
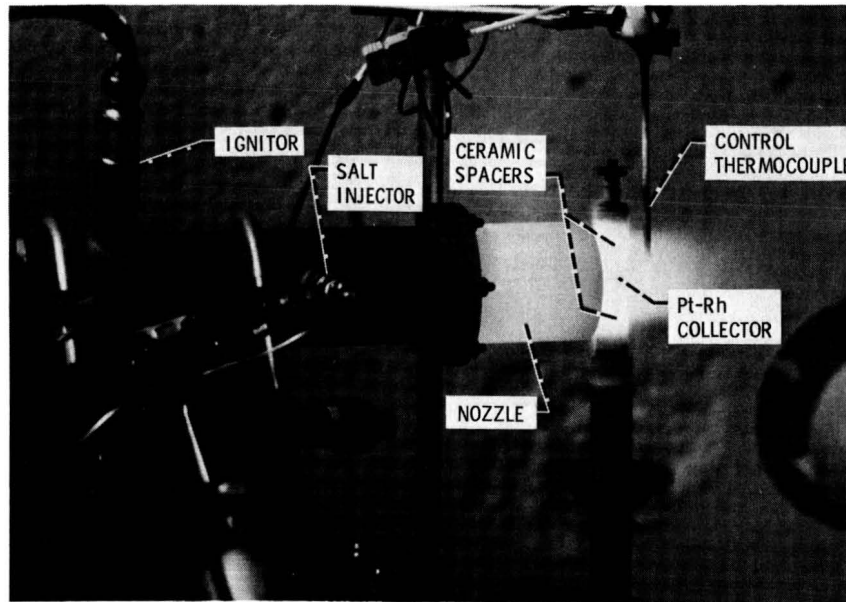
CS-83-2823

Figure 1

BURNER RIG
SHORT EXIT NOZZLE

CS-83-2822

Figure 2
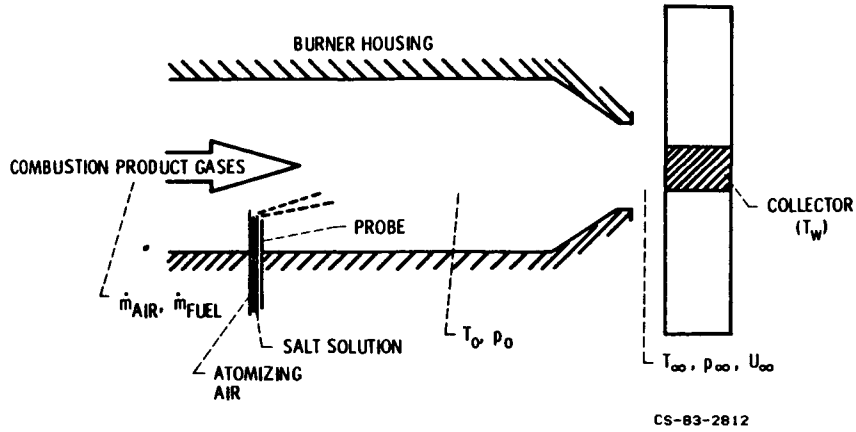
BURNER RIG AND COLLECTOR CONFIGURATION

Figure 3

NaCl SEEDED

Figure 4

114

Na$_2$SO$_4$ SEEDED

T$_{mp}$: MELTING POINT OF Na$_2$SO$_4$ (884 °C)

Figure 5

PREDICTED DEPENDENCE OF DEPOSITION RATE ON PARTICLE SIZE

Figure 6

115

Na$_2$SO$_4$ SEEDED

T$_{mp}$: MELTING POINT OF Na$_2$SO$_4$ (884 °C)
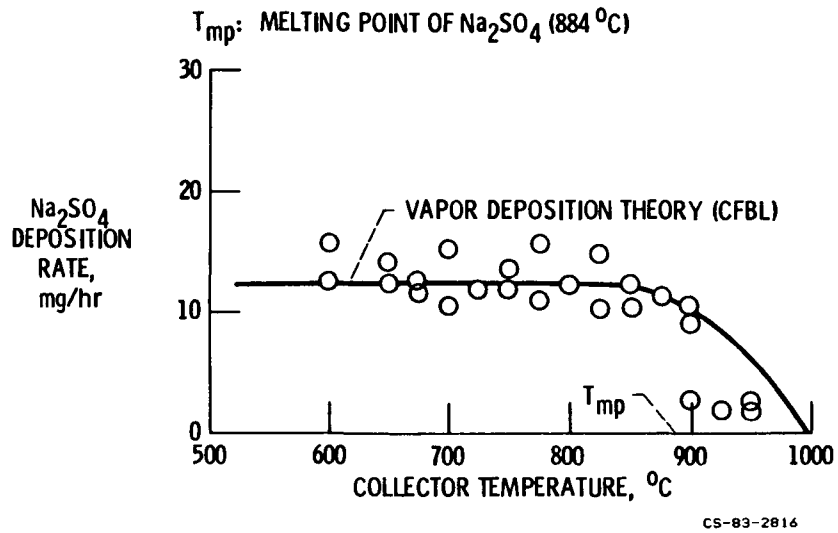
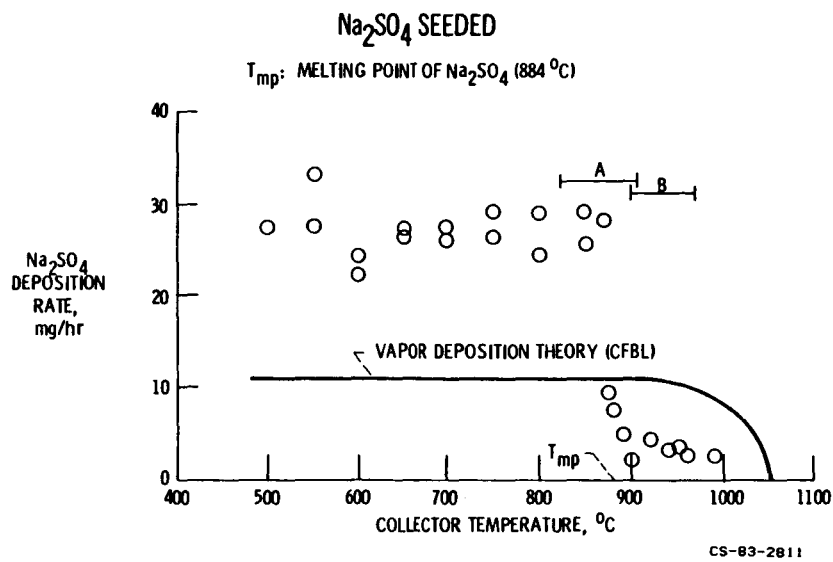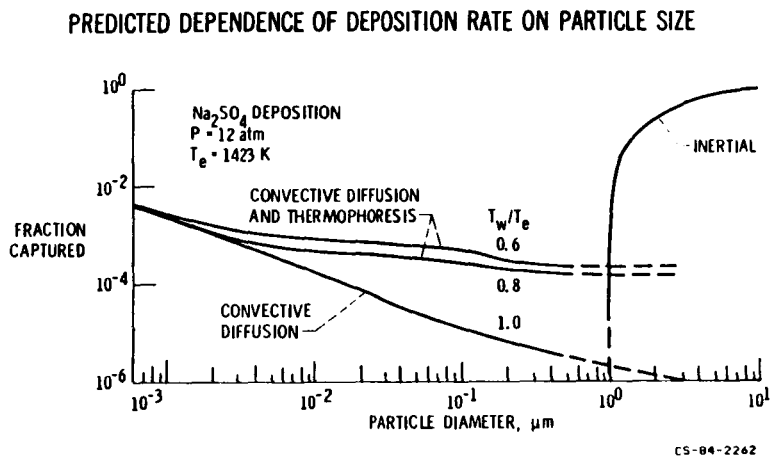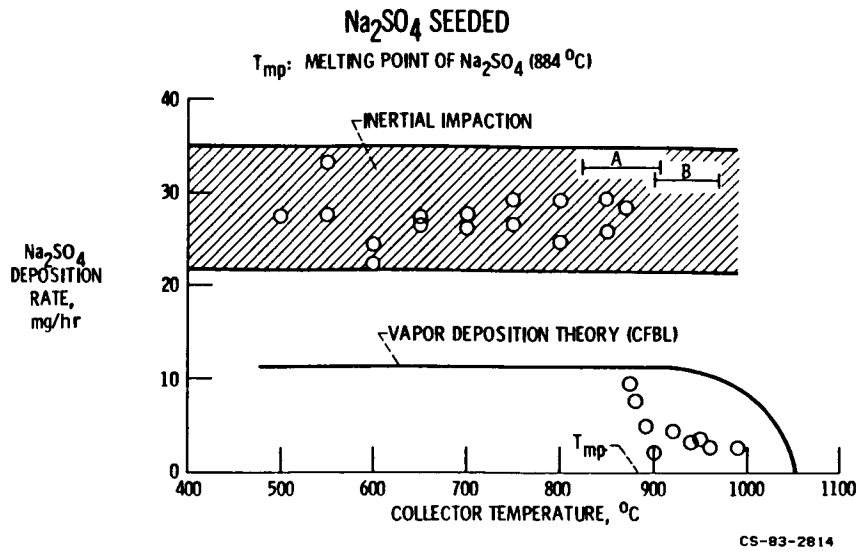Figure 7

INITIAL DROPLET SIZE INFORMATION
COMBINED SMD DATA VS ATOMIZING AIR PRESSURE
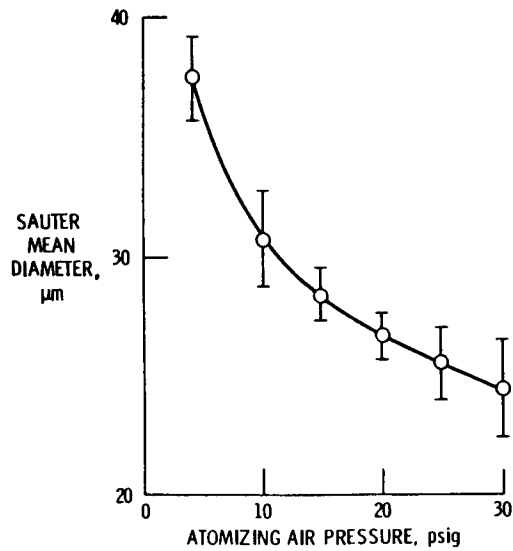
Figure 8

INITIAL DROPLET SIZE INFORMATION
TYPICAL HISTOGRAM
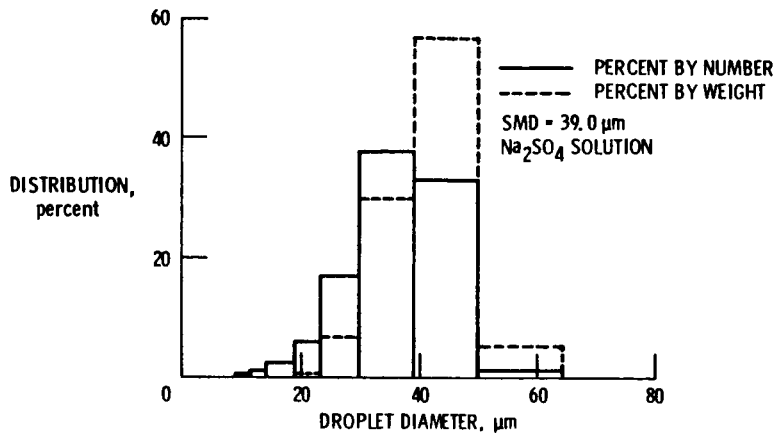
Figure 9

NaCl PARTICLES CAPTURED   ELEMENTS DETECTED BY EDS
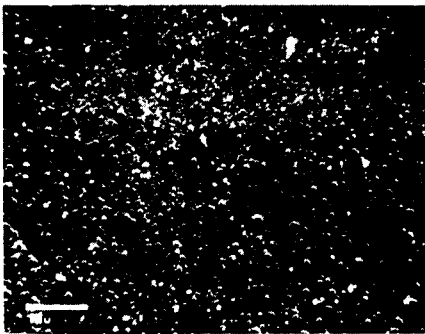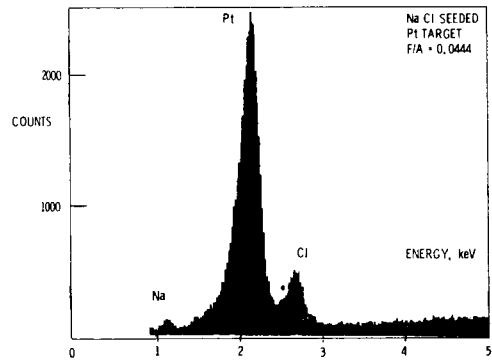
CS-84-3927

Figure 10

117

Na$_2$SO$_4$ PARTICLES CAPTURED
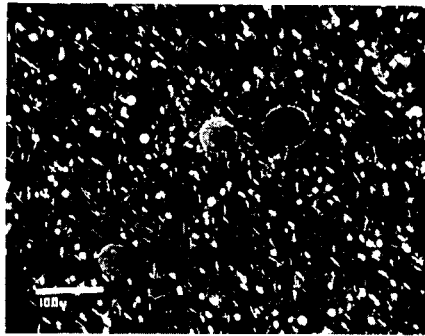
ELEMENTS DETECTED BY EDS
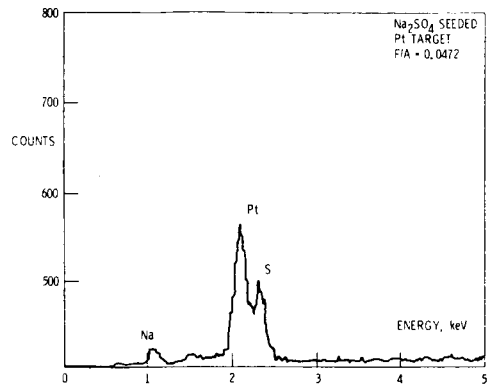
CS-84-3926

Figure 11

PARTICLE CAPTURE EXPERIMENTS
CHEMICAL ANALYSIS OF DEPOSIT

FLAME SEEDED WITH NaCl SOLUTION
PARTICLE CAPTURE DURATION, ~5 sec

83% NaCl
17% Na$_2$SO$_4$ (BY WEIGHT)

OR

93% NaCl
7% Na$_2$SO$_4$ (BY MOLE)

Figure 12

APPROACHES TO ELIMINATE PARTICLES

(A) USE Na DISPERSIONS IN LIGHT OIL (OR MINERAL SPIRIT)
    WHICH IS SOLUBLE IN JET A-1 FUEL. Na PARTICLES ARE
    IN 1 TO 10 μm SIZE RANGE

(B) USE ALCOHOL AS FUEL. DISSOLVE Na-ACETATE (Na-SOURCE)
    AND THIOUREA (S-SOURCE) IN ALCOHOL

(C) FUEL NOZZLE DROPLET SIZE MEASUREMENT RESULTS
    ENCOURAGING

Figure 13

DETERMINATION OF AVERAGE MASS TRANSFER COEFFICIENT ($\longrightarrow Nu_m$)

"CYLINDER IN CROSSFLOW" ?
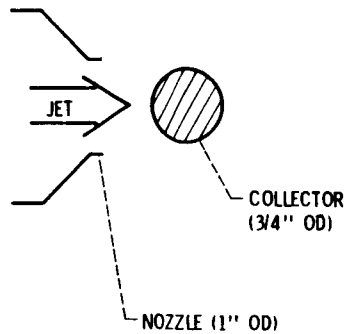
Figure 14

TEMPERATURE DISTRIBUTION ON STATIONARY Pt-Rh COLLECTOR
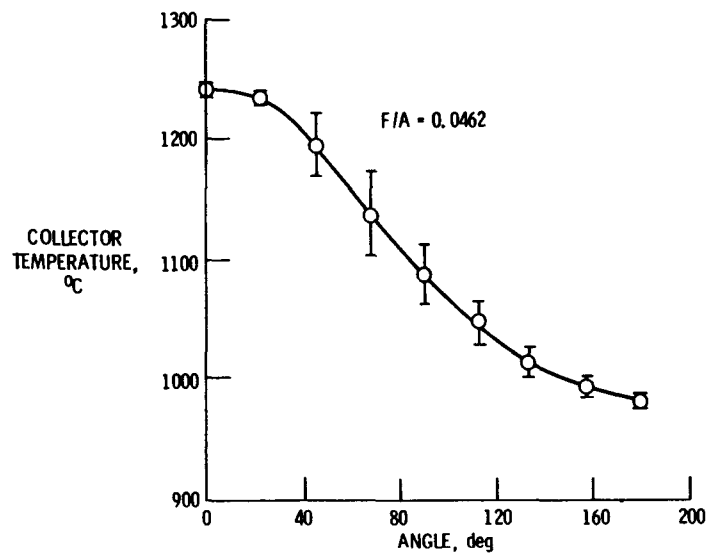
Figure 15

DETERMINATION OF AVERAGE MASS TRANSFER COEFFICIENT
$(\longrightarrow Nu_m)$

(A) NAPHTHALENE SUBLIMATION EXPERIMENTS FOR PRESENT
CYLINDRICAL COLLECTORS

(B) DESIGN SEGMENTED COLLECTORS TO STUDY STAGNATION
POINT MASS TRANSFER, SIMULATING NOSE REGION OF
BLADES
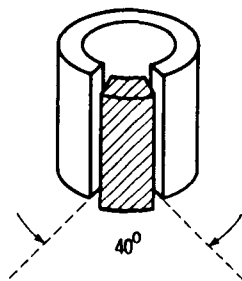
Figure 16

SUMMARY

● CAREFUL ANALYSIS AND INTERPRETATION OF PREVIOUS
  EXPERIMENTAL RESULTS

● DETERMINATION OF PROBLEMS

    (A) PRESENCE OF PARTICLES

    (B) "CYLINDER IN CROSSFLOW" ASSUMPTION NOT TRUE

● REMEDIES

    (A) CONTAMINATE FUEL

    (B) NAPHTHALENE SUBLIMATION EXPERIMENTS

    (C) SEGMENTED COLLECTORS

Figure 17

EFFECTS OF SURFACE CHEMISTRY ON HOT CORROSION LIFE*

R. E. Fryxell

General Electric Company
and
B. K. Gupta

TRW, Inc.

This program has as its primary objective the development of hot corrosion life prediction methodology based on a combination of laboratory test data and evaluation of field service turbine components which show evidence of hot corrosion. This program is divided into five tasks. Burner rig testing is being performed by TRW. The discussion will describe the overall program with a summary of results obtained in the first two tasks which have been completed.

Task I involves a comprehensive evaluation of six hot corroded turbine components, having known operating history, to establish the degradation mechanisms in the corroded areas. The six components selected are identified in Table I. Four of these are the same component from engines of the same model to afford maximum opportunity to make cause and effect correlations. The high pressure turbine (HPT) components were obtained only after examining blades from a large number of disassembled engines; hot corrosion is only infrequently substantial in the HPT of engine models available for this study. On the other hand, hot corrosion is more frequently encountered in the low pressure turbine (LPT) since at the lower temperatures involved, corrosive contaminants are more likely to accumulate in significant amounts and/or be present a greater percentage of operating time. One LPT vane is included in this study for comparison.

Evaluation of these components included optical metallography, scanning electron microscopy (SEM), and electron microprobe (EMP) examination. Several transverse sections of each airfoil were prepared using nonaqueous cutting and polishing techniques.

PRECEDING PAGE BLANK NOT FILMED

Results of the evaluation of the four CF6-50 Stage 1 blades are summarized in Table II. Locations at which maximum degradation was observed in individual sections are defined by % span (radial)/% chord (distance from leading edge (LE) to trailing edge). These observations are limited to the leading edge and concave/pressure surface; the convex surface of such blades rarely suffers significant environmental degradation. The listed temperatures refer to the blade surface at the location of maximum degradation; these must be regarded as approximate for two reasons: (1) the observed distress occurs over some distance along the surface, and (2) assigned temperatures are calculated and will, in general, change somewhat as the turbine ages.

Typical sulfidation was noted at some locations in all of these blades, including development of a depletion layer (loss of aluminum) in the coating or substrate alloy. Typical microstructures are shown in Figures 1 and 2. However, sulfides were found in the most distressed areas in only two of these blades. In the other two blades, although sulfides were found, the most severely distressed regions did not contain any detectable sulfides.

This points up a primary difficulty in interpretation, namely that contaminant ingestion occurs only when the aircraft is near ground level; during most of a mission, simple oxidation is probably to be expected. Table II exhibits one attempt to relate the observed degradation to operating history. Using flight pattern information and the criterion given in footnote (a), total times were estimated during which each engine might be considered vulnerable to contaminant ingestion: total hours near coastal airports, and total hours (in life of engine). One way of displaying this information is shown in Figure 3. There is in fact a trend showing increased hot corrosion with increased low altitude operating time; the curvature is upwards as is not unreasonable, i.e., above about 60-80 μm (nominal original coating thickness) the substrate alloy is exposed. However, with this limited sampling, it is not possible to make inferences concerning coastal versus total low altitude exposure.

Alternatively, the trends shown in Figure 3 may reflect total times at takeoff/thrust reverse (higher) temperatures, a parameter which is clearly related to total hours at low altitudes. This is shown in rate units (Figure 4). The highest rates correspond to the shortest lengths of mission for which the percentage of time at higher temperatures (or lower altitude) is greater.

These are in fact interesting and instructive exercises, but remembering that the present four blades were selected as rather extreme examples, the actual amounts of corrosive degradation (Table II and Figures 3 and 4) do not define possible curves which other examples should be expected to match. Further, since oxidation and hot corrosion rates are competitive in some instances (Table II), the cause and effect relationships with respect to environmental degradation have that additional degree of complexity.

The trend shown in Figure 4 has, however, long been recognized in a qualitative sense and hopefully continued quantitative evaluations coupled with compilations of operating histories will lead to a reliable choice between various possible correlations such as those depicted in Figures 3 and 4.

With respect to the ultimate blending of this type of information with the burner rig studies to be performed in this program and application to life prediction methodology, it should be pointed out that previous burner rig corrosion tests at General Electric with very low salt ingestion levels (at barely the threshold level for salt condensation) produced conventional Type 1 sulfidation but at rates indistinguishable from oxidation. This may relate to the results in Table II, namely that oxidation and corrosion rates may vary relative to each other, depending on the circumstances. Possibly as well there are implications with respect to the design of somewhat more complex burner rig tests; i.e., temperature cycling, intermittent salt ingestion, etc.

Evaluation of the other two components listed in Table I revealed extensive Type 1 sulfidation in the low pressure turbine vane but not in the J79 high pressure turbine blade. Since these are different components/different engine models, the observations cannot be factored into an operating history correlation together with the other four components. Yet the structural features of the degradation do contribute to baseline service related information to be compared with hot corrosion burner rig tests which comprise the remainder of this program.

Two of the three burner rig tests are to be conducted under identical conditions as described in Table III for a maximum time of 1000 hours (see Figure 5). The first of these, Task II, provides a hot corrosion baseline for the program alloys and coatings in the as-processed condition. Included in this task are duplicate specimens of U700 and Rene' 80, both uncoated and with the following coatings:

pack aluminide RT21 (Chromalloy) and Codep (General Electric)
low pressure plasma NiCoCrAlY (Ni-23Co-18Cr-12Al-0.3Y)

At approximately 20 cycle intervals, specimens are visually examined, photographed, and coil inductance measurements made in a series mode at 10MHz with a multifrequency LCR meter as shown in Figures 6 and 7. These measurements are patterned after studies at NASA-LeRC during the past several years. Specimens are removed from the test when visual evidence of hot corrosion is noted in three successive inspections. Additional specimens are also exposed for lesser time periods. Specimen evaluation is performed as in Task I.

A second identical hot corrosion burner rig test (Task IV) will be performed with specimens which have been given a variety of aging treatments at 1100C (Task III) to determine the effect on hot corrosion behavior caused by surface oxidation and/or interdiffusion between coating and substrate alloy. Triplicate specimens of the above coated alloys will be aged under the following conditions: isothermal inert atmosphere (vacuum) for 100 hours, isothermal air furnace oxidation for 100, 300, 600 hours, one hour air furnace cycles for 100 hours and cyclic burner rig oxidation for 100, 300 and 600 hours. One specimen of each material representing each of these conditions will be metallographically evaluated and the remaining duplicates used in the Task IV hot corrosion burner rig test.

The Task II burner rig test has been completed. Coil inductance measurements are shown in Figure 8 for six uncoated specimens. The four long term specimens were removed at the third inspection interval at which hot corrosion was visually observed. Although Rene' 80 and U700 survived about the same

lengths of time, based on this criterion, the coil inductances were widely different, and metallographic measurements indicated a factor of two greater corrosion rate for U700, in accordance with previous experience. Typical microstructures with subsurface sulfides are shown in Figure 9 for one specimen of each alloy.

Coil inductance measurements for coated specimens are shown in Figure 10 with an expanded scale below 200 hours to show clearly the negative changes which appeared at the first inspection, particularly for the aluminide coated specimens. The overall changes are in all cases much smaller than for the uncoated alloys (Figure 8) reflecting the corrosion protection offered by all of the coatings. The four Codep coated specimens are shown in Figure 10 to their time of removal and the greater coil inductance changes suggest a greater corrosion rate; for all of these, coating penetration was confirmed metallographically. The three RT21 coated specimens shown in Figure 10 ran the full term 1000 hours with only minor visual evidence of hot corrosion. However, metallographic evaluation showed essential coating penetration in all three, although clearly less extensive than for the Codep coated specimens. One specimen of RT21 coated Rene' 80 (not shown in Figure 10) was removed at 697 hours and did exhibit coating penetration with additional corrosion of the substrate to about 100 µm depth. All of the NiCoCrAlY coated specimens showed extensive alloy depletion within the coating, occasional pits, but no complete penetration was observed. Typical microstructures are shown in Figure 11.

Subsequent to the completion of Task II, all the aging treatments in Task III have been performed and Task IV is underway. At the conclusion of the Task IV test, all the data generated in Tasks I through IV will be evaluated and an empirical hot corrosion life prediction model based on these data will be proposed. Also, recommendations will be made for other test parameters to be evaluated, and evaluation methodology necessary to permit prediction of hot corrosion life.

Task V will be a hot corrosion high velocity cyclic burner rig test designed to check the validity of the proposed life prediction model. Duplicate specimens of a maximum of four alloys and five coatings will be tested up to

a maximum of 1000 hours and evaluated as in Tasks II and IV. The alloys and coatings will be those from this program plus additional alloy-coating systems selected by the NASA Project Manager.

The Task V experiment will be designed to test two aspects of the life prediction model developed in Task IV. The ability of the model to predict hot corrosion life under different rig test conditions than those previously used in Task II and IV will be tested in one portion of the experiment. The second portion of the experiment will test the ability of the model to predict hot corrosion life of new alloys and coatings.

The ability of the model to predict hot corrosion life under different rig test conditions will be evaluated using alloys and coatings previously tested in Task II and Task IV. The hot corrosion tests for this portion of the program will use one or more variations of the test parameters used in Task II, III and IV. Test parameter variations that will be considered include the following:

- A different salt level
- A different test temperature
- Intermittent salt injection
- A different sulfur level in the fuel
- Additional or modified aging cycles

The specific testing parameters will be derived from the results of Task II and Task IV, previous experience in evaluating field service hardware and previous experience in conducting hot corrosion testing under a variety of test conditions.

The ability of the model to predict hot corrosion resistance of new coatings and alloys will be evaluated using alloys and coatings that have not been evaluated previously in Task II and Task IV. The aging cycle will be chosen from the results of Task IV.

Life prediction for both portions of the Task V experiment will be based on the model developed in Task IV as well as extensive experience gained from evaluating field service components and conducting hot corrosion tests. Knowledge of the effect of variations in both engine operating conditions and rig testing conditions will be used in predicting hot corrosion life under different rig test conditions in the first portion of the experiment with the same alloys and coatings tested in Task II and Task IV. With respect to testing of additional alloys and coatings, use will be made of extensive empirical correlations of composition and hot corrosion performance in predicting hot corrosion life.

Table I. Components Selected for Evaluation.

Carrier Base	Aircraft	Component	Total Hours	Number of Cycles	% Takeoffs at Coastal Airports
Southern Asia	A300B	(1)	2,694	1560	67
Northern Africa	A300B	(1)	4,641	2169	77
Southern Africa	A300B	(1)	1,830	1471	50
Western Europe	DC10-30	(1)	2,625	610	46
South America	DC10-30	(2)	15,155	2987	72
U.S. Military	F4	(3)	2,700		

(1) CF6-50 Stage 1 high pressure turbine blade, Codep coated Rene' 80.
(2) CF6-50 Stage 1 low pressure turbine vane, uncoated Rene' 77.
(3) J79 Stage 1 high pressure turbine blade, Codep coated Rene' 80.

Table II. Summary of Metallographic Evaluations and Operating History for Four Stage 1 High Pressure Turbine Blades from CF6-50 Engines.

Carrier Base	Total Hours	No. of Cycles	Hours/ Cycle	Hours <2000' El.[a] Near Coastal AP	Hours <2000' El.[a] Total	Location[b]	Temp. °C (Est.) Max.	Temp. °C (Est.) Avg.	Maximum Depth of Attack, μm[c] Total	Maximum Depth of Attack, μm[c] per 1000 Hours	Type 1 Sulfides
Southern Asia	2694	1560	1.72	350	520	40/70-90	1090	820	100	37	Yes
						60/LE	980	740	50	20	Yes
						60/80	1090	820	200	75	No
Northern Africa	4641	2169	2.14	560	720	50/60-90	1090	820	230	50	Yes
						80/50-80	1090	820	230	50	Yes
Southern Africa	1830	1471	1.24	240	490	10/LE	910	680	50	27	Yes
						10/60-80	1020	760	75	40	Yes
						60/90	1090	820	180	100	No
Western Europe	2625	610	4.30	95	200	10/60-80	1020	760	45	17	No
						20/60-80	1020	760	50	20	Yes

[a]Estimated, using 20 minutes as approximate total time per cycle; gate to takeoff, climb to 2000 ft.

[b]% Span/% Chord.

[c]Including depletion zone.

Table III Burner Rig Operating Conditions.

Specimen Temperature - 900° C ± 9° C

Test Cycle - 1 hour at temperature followed by 6 minutes of forced air cooling

Sodium Concentration - 0.5 ppm sodium (±10%) in the combustion gases introduced as aqueous NaCl

Combustion Air Preheat Temperature - 232° C ± 10° C

Specimens - Eight positioned equally on a 4.2 cm (1.64 inch) diameter circle of a holder rotating at 600 rpm

Burner Nozzle Throat Diameter - 2.54 cm (1.0 inch)

Burner Pressure - 1.0 psig

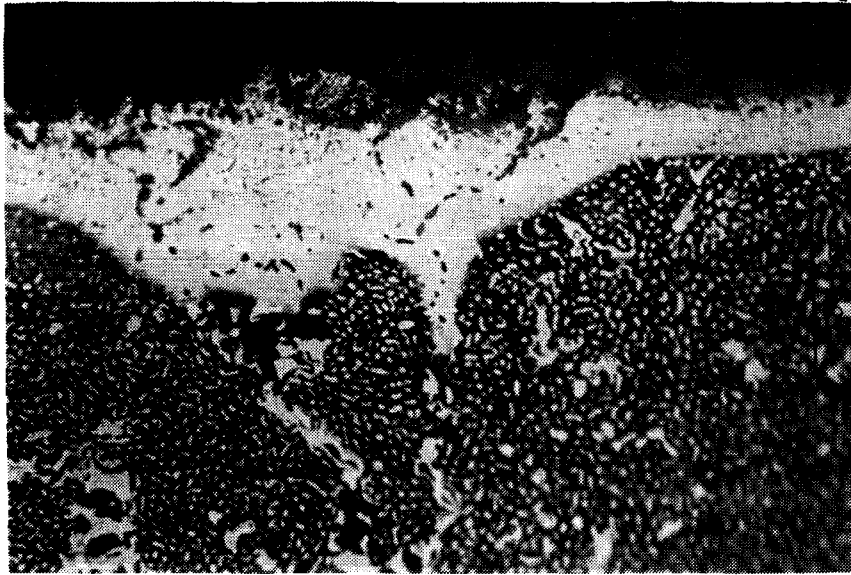Nozzle Throat to Nearest Specimen - 4.45 cm (1.75 inch)

130

Figure 1. Photomicrograph on the concave airfoil of a
Stage 1 high pressure turbine blade from a Northern Africa
CF6-50 engine. Sulfides are present in the Rene' 80 de-
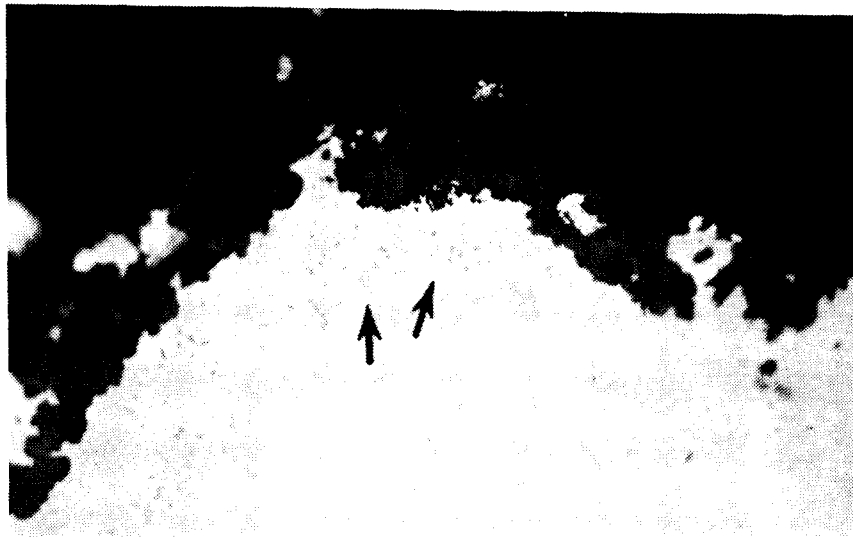pletion zone. Etched, 500X.

Figure 2. Photomicrograph at the leading edge on an airfoil of a
Stage 1 high pressure turbine blade from a Southern Africa CF6-50
engine. Sulfides are present within residual coating (arrows).
As-polished, 500X.

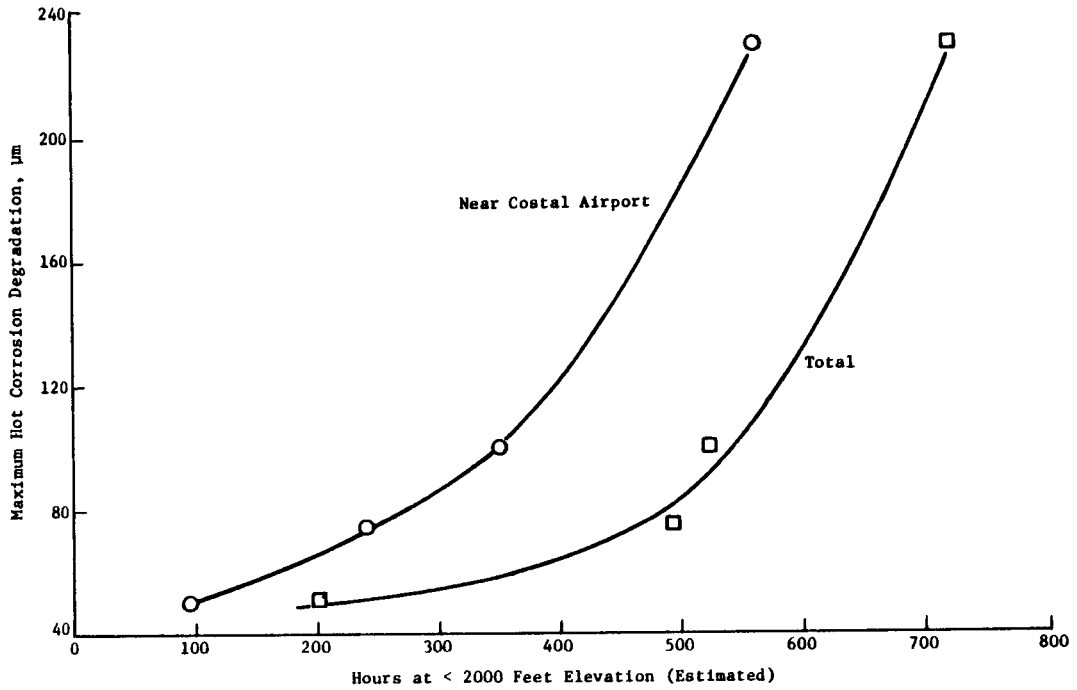Figure 3. Hot Corrosion Degradation for CF6-50 Stage 1 High Pressure Turbine Blades as Function of Time at Less Than 2000 Feet Elevation.
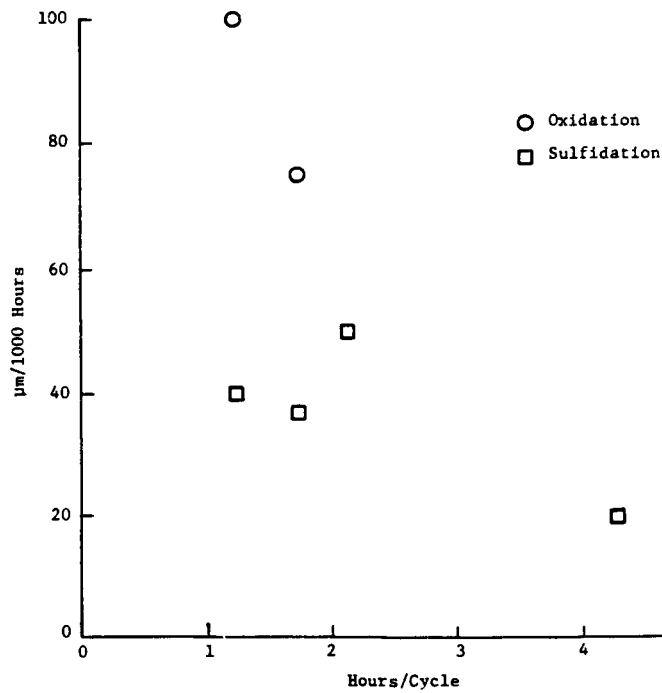
Figure 4. Maximum Degradation Rates for CF6-50 Stage 1 High Pressure Turbine Blades as Function of Average Mission Duration.
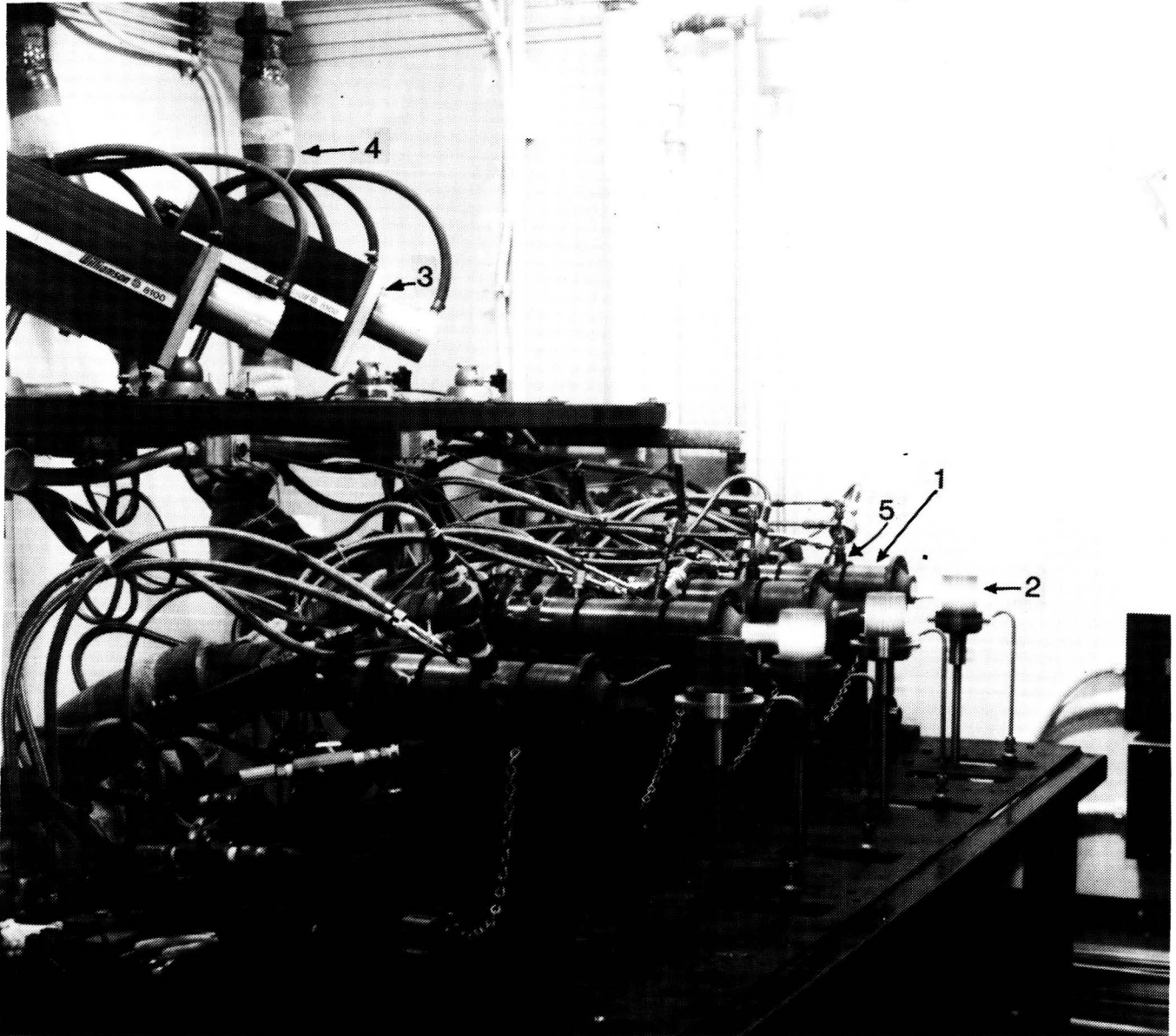
Figure 5. Burner Rigs.

1. Burner
2. Specimens on holder rotating at 600 rpm.
3. Optical pyrometer
4. Preheated combustion air
5. Salt solution spray nozzle
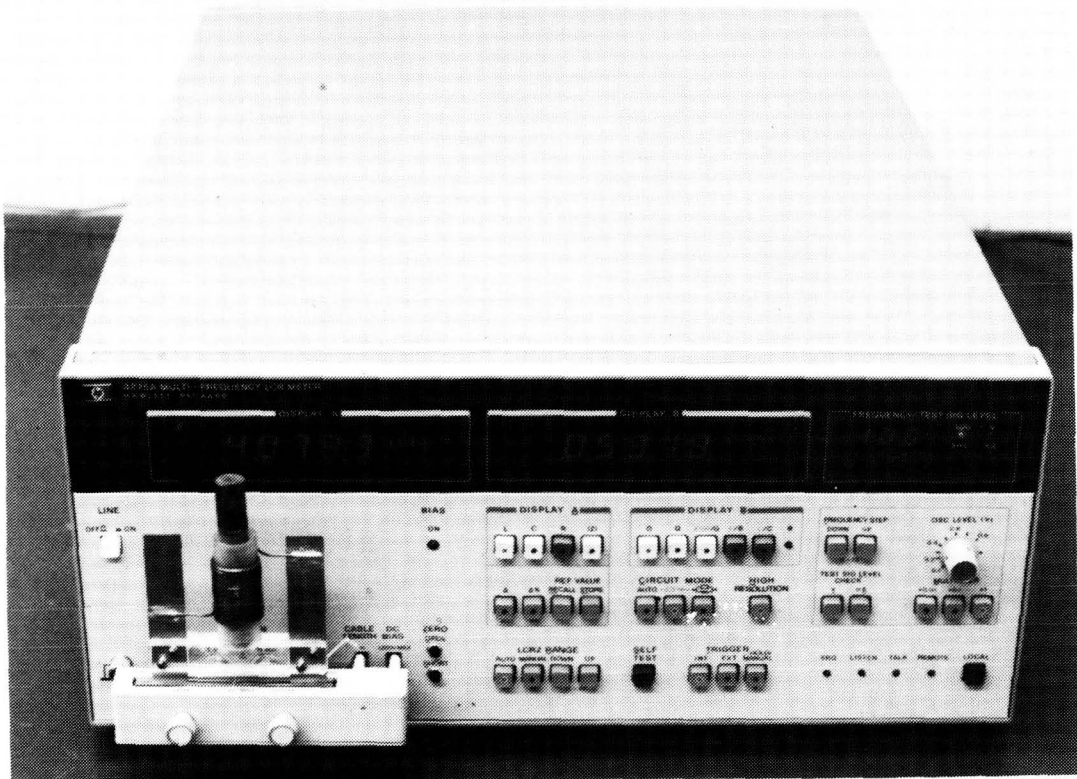
Figure 6.   Inductance rig/coil with specimen core.
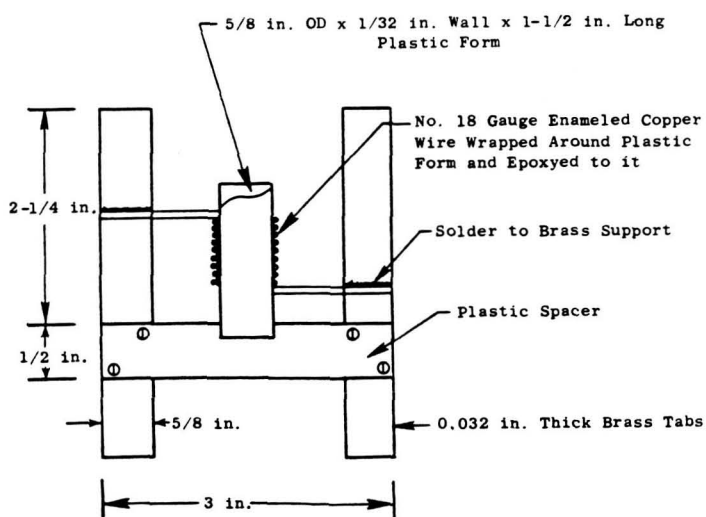
Figure 7.   Inductance Coil and Support.
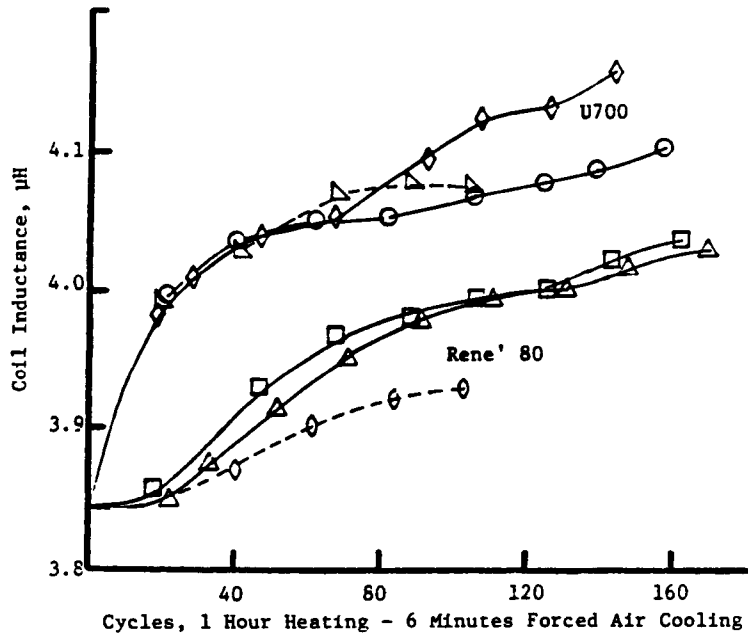
Figure 8. Uncoated Alloy Coil Inductance Changes with Hot Corrosion at 900° C, Cyclic Exposure.

U700, 142.65 hours.

Rene' 80, 167.7 hours
Figure 9. Photomicrographs of specimens from burner rig hot corrosion test. Type 1 sulfides are present. Etched, 200X.
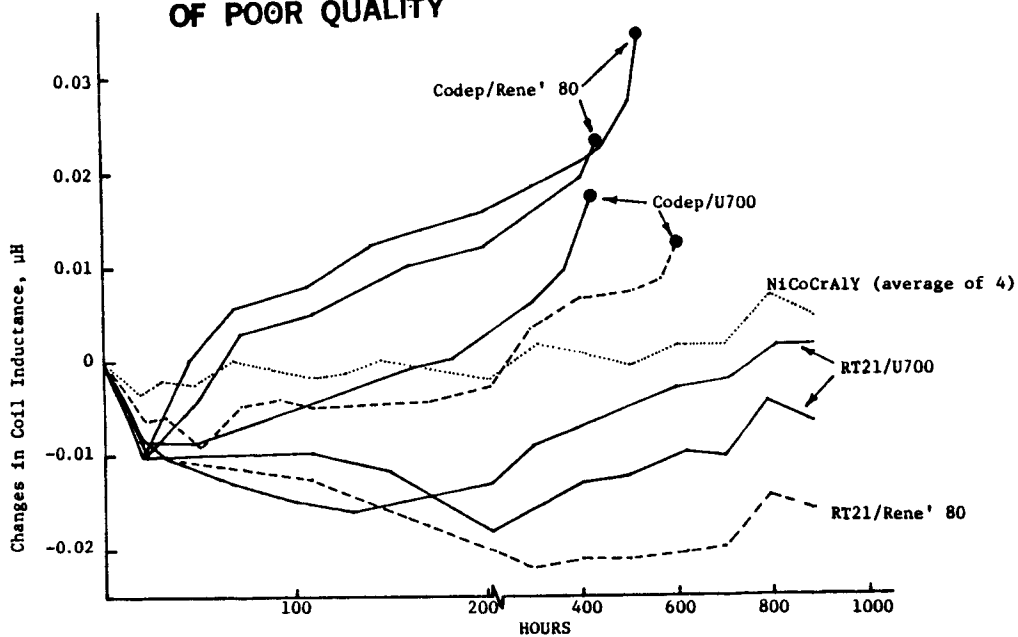
Figure 10. Changes in Coil Inductance with Hot Corrosion at 900C, Cyclic Exposure.
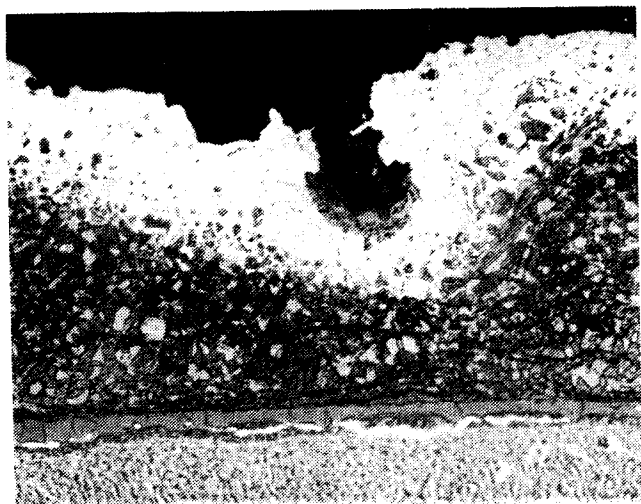
(a)
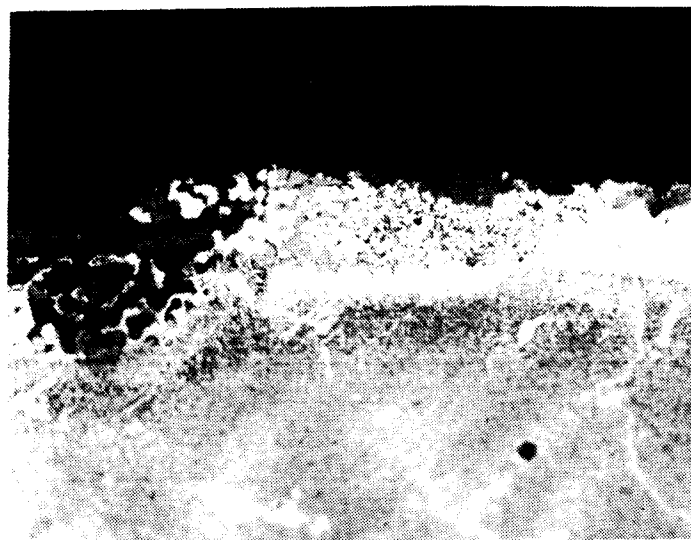
(b)

Figure 11. Photomicrographs of specimens from burner rig
hot corrosion test. Type 1 sulfides are present. Etched.

(a) NiCoCrAlY coated U700, 1004.6 hours (500X)
(b) RT21 coated Rene' 80, 697.1 hours (200X)

136

COATING LIFE PREDICTION

James A. Nesbitt and Michael A. Gedwill
National Aeronautics and Space Administration
Lewis Research Center

INTRODUCTION

Hot-section gas-turbine components typically require some form of coating for oxidation and corrosion protection. These coatings are generally either aluminide coatings or MCrAlY overlay coatings where M represents nickel, cobalt, or a combination of these two elements. Both types of coating are protective as a result of the selective oxidation of aluminum to form an external, continuous Al_2O_3 scale. The coatings act as a reservoir of aluminum since the aluminum content of the coating is always greater than that of the substrate. In service environments, coatings degrade by several mechanisms including oxidation and hot corrosion, interdiffusion of the coating and substrate, foreign object damage, and erosion (ref. 1). Coating/substrate interdiffusion involves not only the loss of the aluminum from the coating into the substrate but also the diffusion of less-desirable elements to the coating surface where they may oxidize and hinder or prohibit formation of the Al_2O_3 scale. In addition, cycling of a coated component results in cracking and spalling of the Al_2O_3 oxide scale, which further accelerates coating degradation.

Efficient use of coatings requires reliable and accurate predictions of the protective life of the coating. Currently, engine inspections and component replacements are often made on a conservative basis. As a result, there is a constant need to improve and develop the life-prediction capability of metallic coatings for use in various service environments. The purpose of the present work is aimed at development of an improved methodology for predicting metallic coating lives in an oxidizing environment and in a corrosive environment.

APPROACH

The present study combines both experimental studies and numerical modeling to predict coating life in an oxidizing environment. The experimental work provides both input to the numerical models and verification of the model predictions. The coatings being examined are an aluminide coating on Udimet 700 (U-700), a low-pressure plasma spray (LPPS) NiCoCrAlY overlay coating also on U-700, and bulk deposits of the LPPS NiCoCrAlY coating. The approach taken in this study is shown schematically in figure 1.

Experimental Testing

The experimental testing involves isothermal and cyclic furnace oxidation at 1050, 1100, and 1150 °C. In addition, Mach 0.3, cyclic burner rig testing of the aluminide and LPPS NiCoCrAlY coatings (125 and 625 μm thicknesses) on

U-700 is also being undertaken at 1100 °C. Isothermal oxidation of the coated U-700 and bulk coating yields the growth rate of the $Al_2O_3/NiAl_2O_4$ scales which form on these coatings. At the conclusion of the test it is often possible to measure the weight of oxide which spalls on cooling. The fraction of oxide that spalls is used as in input to the cyclic oxidation/spalling model discussed below. Cyclic furnace and burner rig oxidation yield the weight changes of the coated specimens reflecting the oxide growth and spallation which occurs during thermal cycling. Analysis of the coating after an oxidation exposure includes x-ray diffraction and polarized light metallography of the retained surface oxides, observation of microstructural changes, scanning electron microscopy, and electron microprobe analysis to measure concentration/distance profiles across the coating and substrate.

Numerical Modeling

Two computer models are being used to predict the oxidation-limited life of the metallic coatings. A cyclic oxidation/spalling model (ref. 2) predicts the oxide growth and amount of oxide spallation that occurs during cyclic oxidation. The isothermal oxide growth rate and spall fraction (the ratio of the oxide which spalls on cooling to the total oxide present before cooling) are input to the spalling model. The spalling model predicts the weight change of a coated specimen undergoing cyclic oxidation, the rate of metal consumption, and the total weight of metal consumption during cyclic oxidation. A diffusion model (ref. 3) simulates the diffusional transport associated with both coating oxidation and coating/substrate interdiffusion. Diffusion coefficients and the rate of metal consumption predicted by the spalling model are input to the diffusion model. The diffusion model predicts aluminum and chromium concentration/distance profiles in the coating and substrate and the time for which the coating is able to supply sufficient aluminum to continue forming an Al_2O_3 scale. The diffusion model therefore predicts coating failure when there is insufficient transport of aluminum to the oxide scale.

CURRENT STATUS AND RESULTS

Isothermal and cyclic furnace oxidation testing is nearly complete. Cyclic furnace testing of the coated U-700 specimens are being carried out to failure of the coatings for the three test temperatures of 1050, 1100, and 1150 °C. For the purpose of this study, coating failure has been defined as the occurrence of one or more of the following: accelerated weight loss during cyclic oxidation; the presence of less-protective oxides (as NiO, Cr_2O_3, or $NiCr_2O_4$) on the coating surface; the massive spallation of the coating; or the internal oxidation of aluminum in the coating, indicating the presence of less-protective oxides on the surface.

Degradation of the aluminide coating has previously been discussed and is reviewed in figure 2. Generally, total depletion of the γ' and β phases occurs before coating failure.

The cyclic oxidation lives of the LPPS NiCoCrAlY coated specimens were less than expected. Figure 3 shows a comparison of the weight change of LPPS—coated specimens and the bulk LPPS coating. The coated U-700 specimens exhibit a significant weight loss after 500 1-hr cycles at 1100 °C. Visual examination

of the cylindrical specimens after cyclic oxidation revealed considerable oxidation and spallation of the coating, especially near the ends of the cylinders (fig. 4). The coating failure which occurred after cyclic oxidation can be compared with a fully intact, protective coating that has undergone isothermal oxidation (also shown in fig. 4). Microstructural examination of coating and substrate cross sections before cyclic oxidation exposure revealed very little porosity at the coating/interface (fig. 5, as-sprayed plus 4-hr argon anneal at 1080 °C); whereas examination of specimens after cyclic oxidation showed extensive porosity formation at the coating/substrate interface (fig. 5 to 7). Apparently, the porosity formed and grew with increasing coating/substrate interdiffusion and is probably the result of a vacancy flux imbalance (ref. 4) caused by unequal atomic transport across the coating/substrate interface. The coatings eventually delaminated and spalled near the cylinder ends, most probably due to a lack of contact with the substrate. Extensive oxidation then occurred at the coating/substrate interface via the interconnected porosity (fig. 5 to 7) causing rapid coating degradation and massive coating spallation. As expected, the higher the temperature, the more rapid the formation of the porosity and the shorter the time to coating failure.

There was poor agreement between the observed weight change and that predicted by the cyclic oxidation/spalling model for the LPPS NiCoCrAlY coated U-700. Two causes for this poor agreement were evident. First, the fraction of spalled oxide measured after the isothermal test (i.e., approximately 0.01 at 1100 °C) and input to the spalling model was an order of magnitude larger than expected for Al_2O_3 scales (ref. 2). The discrepancy between the spall fractions has not been completely resolved due to the difficulty in measuring the extremely small amount of Al_2O_3 that spalls after oxidation at 1050 to 1150 °C. Second, the spalling model assumes only external formation of Al_2O_3. Significant oxide formation within the porosity at the coating/substrate interface, massive coating spallation (especially at the coating ends), and formation of less-protective oxides were observed experimentally. To estimate the oxidation-limited coating life using the diffusion model, the spall fraction input to the spalling model was estimated so that the predicted weight change was similar to that for the LPPS coating on U-700 (fig. 8). The spalling model was then used to predict the weight of aluminum consumed (fig. 9) and the rate of aluminum consumption (fig. 10), the latter being input to the diffusion model.

The aluminum concentration measured after 300 1-hr cycles at 1100 °C and the aluminum profiles predicted by the diffusion model are shown in figure 11. The diffusion model does not predict the γ' or β phases remaining in the coating. The predicted concentration profile contains less aluminum in the coating and more in the substrate than measured in the test specimen. The rate of aluminum consumption predicted by the spalling model was probably too high due to the poor spalling resistance of the coated specimens. In addition, the diffusion coefficients input to the diffusion model (ref. 4) were measured on single-phase Ni-Cr-Al alloys and may not be appropriate for the complex, multiphase superalloys. Based on the cyclic oxidation behavior of the LPPS coating on U-700 at shorter times, the diffusion model predicts the life of the coating to be in excess of 1500 hr at 1100 °C. Experimentally, massive coating spallation was observed between 500 to 1000 1-hr cycles at 1100 °C. Obviously, the formation of the porosity and the oxidation within the pores significantly decreased coating life.

FUTURE WORK

Measurement of concentration/distance profiles in several of the coated specimens after various cyclic oxidation exposures will permit a more extensive verification of the predictive capability of the diffusion model. Continued burner rig testing should provide oxidized specimens which, although containing porosity at the coating/substrate interface, may eliminate oxide formation within the porosity and the resultant massive coating spallation. Premature coating failure may therefore be eliminated and permit an accurate test of the life-predictive ability of the diffusion model. A computer model is also under development to simulate §' and β depletion during degradation of aluminide coatings. This aluminide diffusion model should be capable of predicting coating life. Measured concentration/distance profiles after cyclic oxidation of the aluminide coated U-700 will be compared with those predicted by the diffusion model to determine the accuracy and usefulness of the model. Predicted and measured coating lives will also be compared. It is anticipated that the conclusion of this work will result in an improve methodology for predicting the oxidation life of both overlay and aluminide coatings.

DUAL CYCLE ATTACK

An experimental study has recently been initiated to investigate the effect of aging in a corrosive environment (900 °C, 0.5 ppm Na) on the oxidation life of the two coatings discussed above in this paper. An attempt will be made to develop an empirical model to relate coating life to combined oxidation/hot corrosion cyclic exposure. The approach this study will take is schematically shown in figure 12. Burner rig testing in the oxidizing environment has been initiated.

REFERENCES

1. Goward, G. William: Protective Coatings foe High Temperature Alloys: State of Technology. Source Book on Material for Elevated-Temperature Applications, Elihu F. Bradley, ed., American Society for Metals, 1978, pp. 369-386.

2. Lowell, C. E. ; Smialek, J.L.; and Barrett, C.A.: Cyclic Oxidation of Superalloys. High Temperature Corrosion, Robert A. Rapp, ed., National Association of Corrosion Engineers, 1983, pp. 219-226.

3. Nesbitt, J. A.; and Heckel, R. W.: Modeling Degradation and Failure of Ni-Cr-Al Overlay Coatings. NASA TM-83672, 1984.

4. Nesbitt, James A.: Overlay Coating Degradation by Simultaneous Oxidation and Coating/Substrate Interdiffusion. NASA TM-3738, 1984.

OXIDATION-LIMITED COATING LIFE PREDICTION

OBJECTIVE: TO DEVELOP AN IMPROVED METHODOLOGY FOR PREDICTING THE OXIDATION LIFE OF METALLIC COATINGS
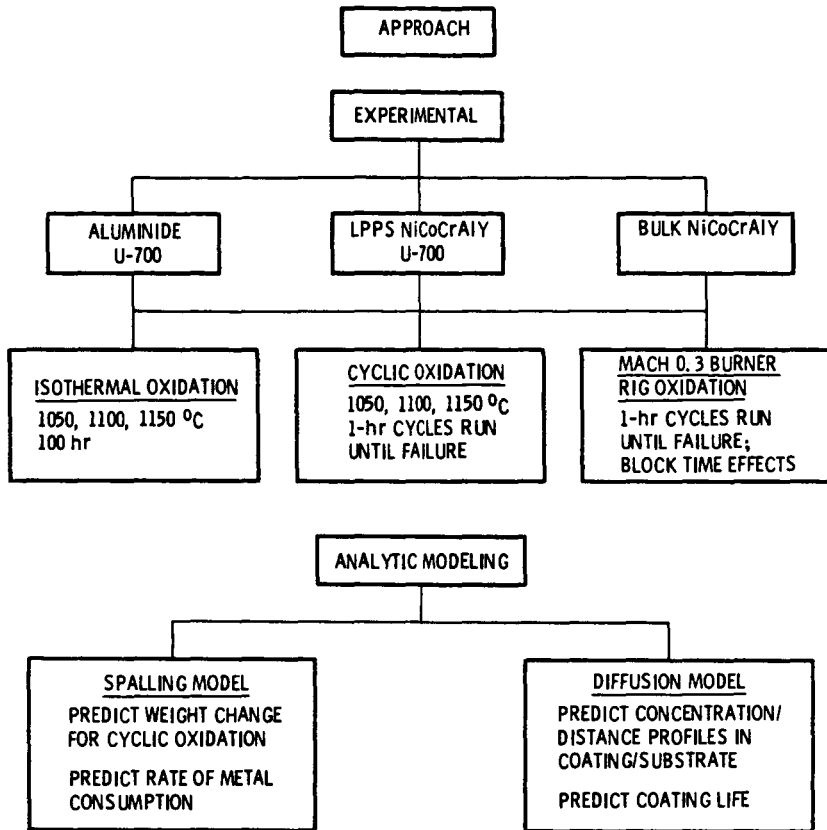
Figure 1

CYCLIC FURNACE OXIDATION OF ALUMINIDE COATED U-700
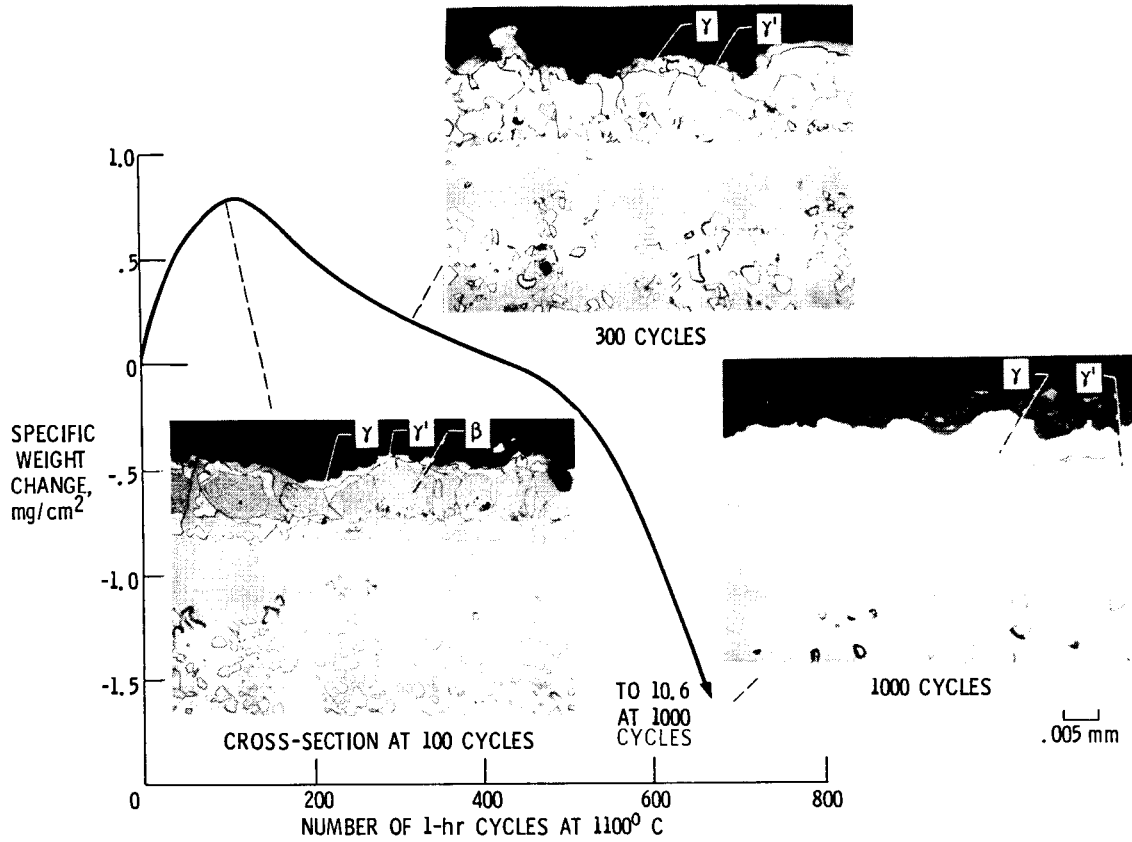
Figure 2

CS-83-3417

CYCLIC FURNACE OXIDATION OF LPPS NiCoCrAlY OVERLAY COATING
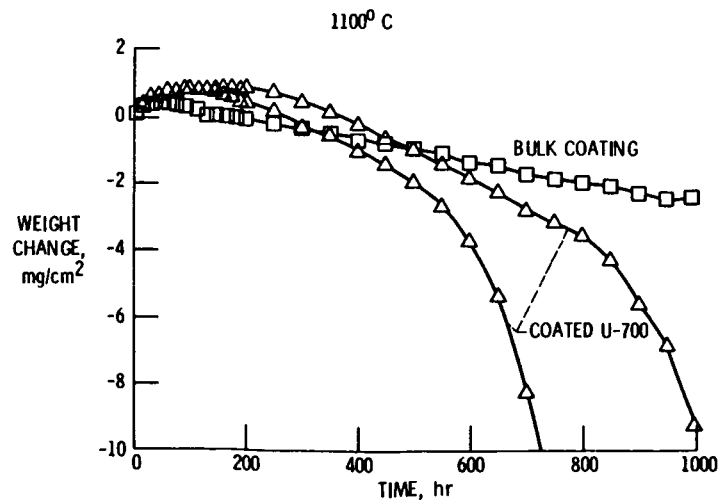
Figure 3

MACROSCOPIC COATING FAILURE

100 hr ISOTHERMAL AT 1150° C

1000 1-hr CYCLES AT 1100° C

0.635 cm
0.25 in

100 1-hr CYCLES AT 1150° C

250 1-hr CYCLES AT 1150° C
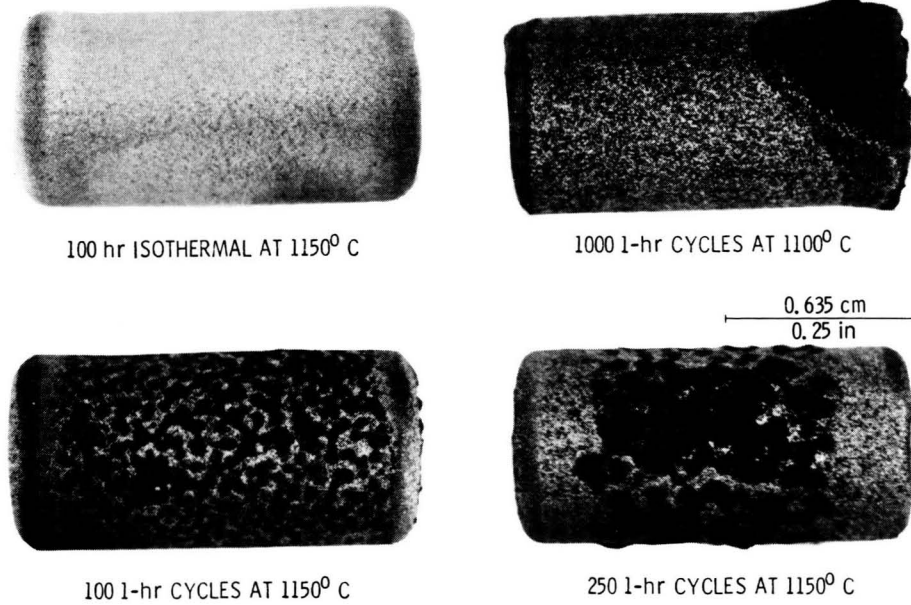
Figure 4

CS-84-3971

MICROSCOPIC COATING FAILURE

1150° C

AS-SPRAYED PLUS 4-hr ARGON ANNEAL AT 1080° C

THIRTY 1-hr CYCLES

100 1-hr CYCLES

250 1-hr CYCLES

100 μm
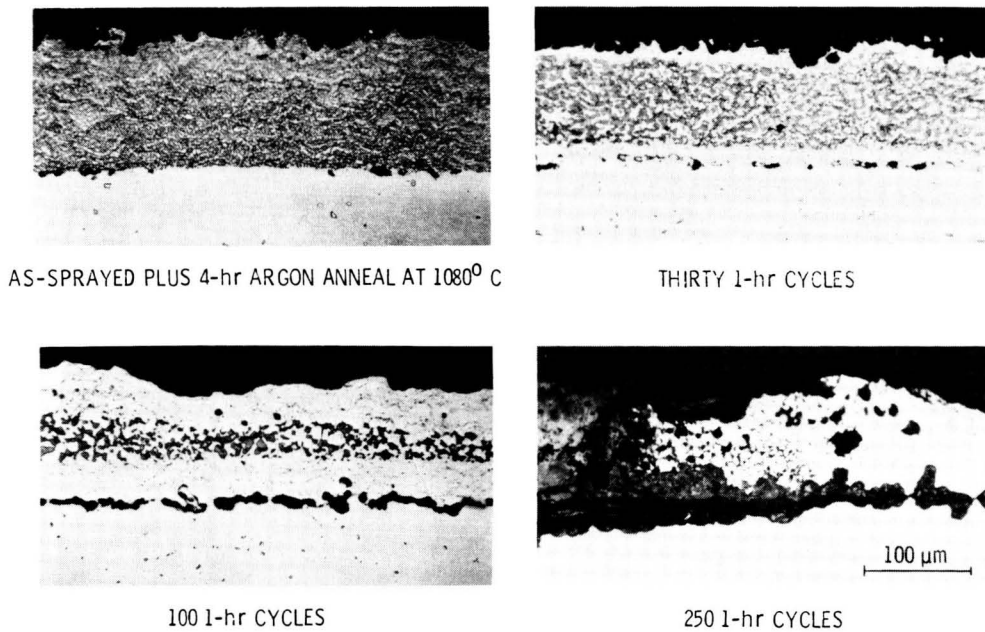
Figure 5

CS-84-3972

MICROSCOPIC COATING FAILURE
1100° C

100 1-hr CYCLES

300 1-hr CYCLES

NO COATING REMAINING

100 μm

2000 1/2-hr CYCLES
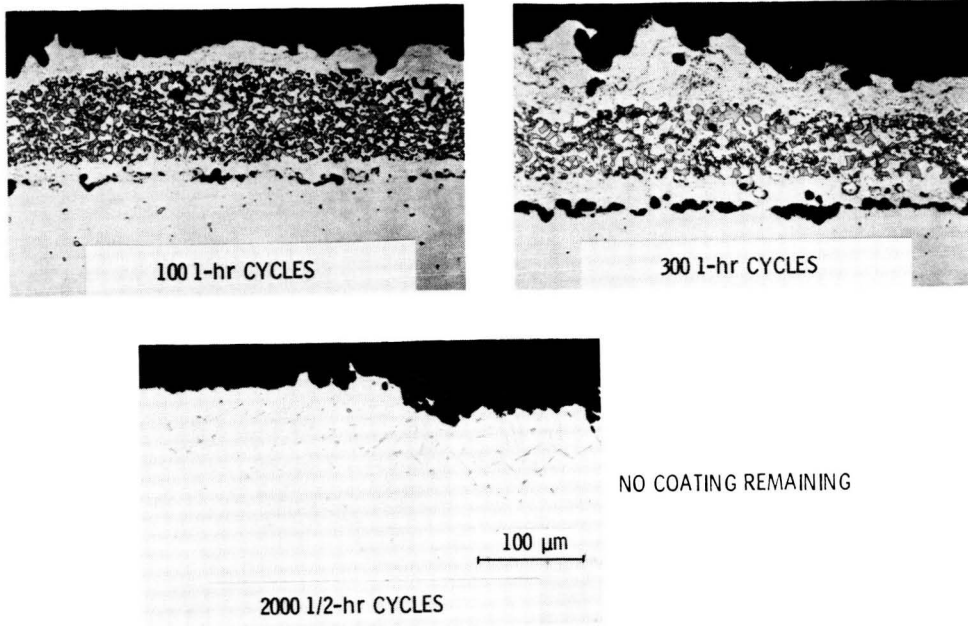
CS-84-3973

Figure 6

MICROSCOPIC COATING FAILURE
1050° C
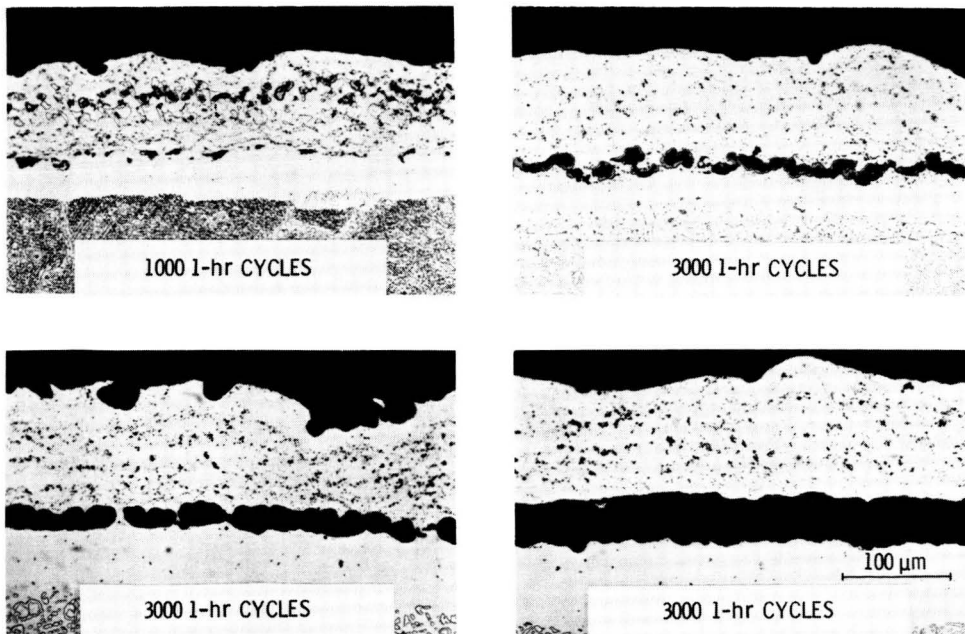
1000 1-hr CYCLES

3000 1-hr CYCLES

3000 1-hr CYCLES

3000 1-hr CYCLES

100 μm

CS-84-3974

Figure 7

144

CYCLIC FURNACE OXIDATION OF LPPS NiCoCrAlY COATING ON U-700

1100° C

WEIGHT
CHANGE,
mg/cm^2

EXPERIMENTAL ☐

ISOTHERMAL (BASED ON 100 hr TEST)

SPALLING MODEL, $Q_0 = 0.001$

TIME, hr
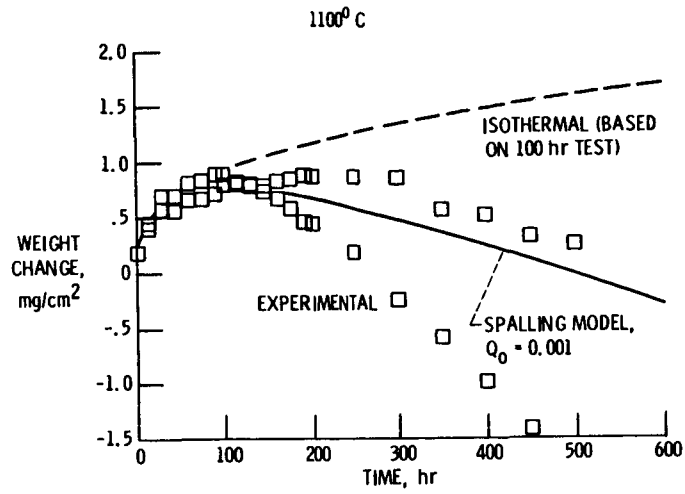
Figure 8

ALUMINUM CONSUMPTION PREDICTED BY SPALLING MODEL

ALUMINUM
CONSUMPTION,
mg/cm^2

LPPS COATING ON U-700; 1100° C; $Q_0 = 0.001$

TIME, hr

Figure 9

145

RATE OF Al CONSUMPTION PREDICTED BY SPALLING MODEL

LPPS COATING ON U-700; 1100° C; Q_0 = 0.001

Figure 10

ALUMINUM CONCENTRATION PREDICTED BY DIFFUSION MODEL

LPPS NiCoCrAlY COATING ON U-700; 300 1-hr CYCLES 1100° C

Figure 11

146
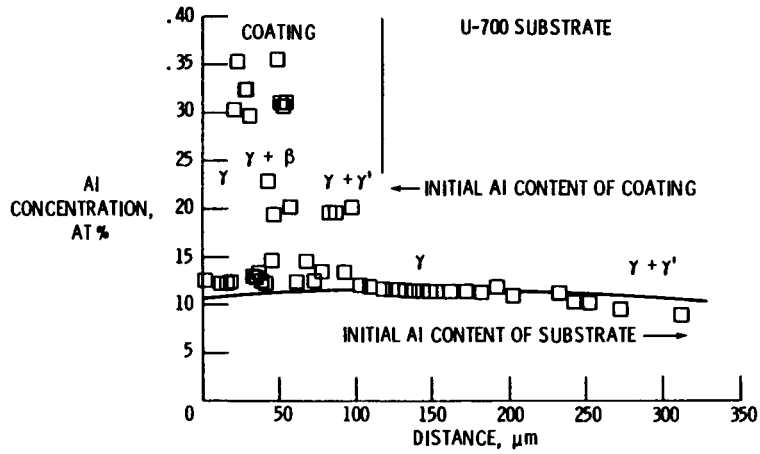
DUAL CYCLE ATTACK

OBJECTIVE: TO CHARACTERIZE THE EFFECT OF COMBINED OXIDATION AND HOT
CORROSION CYCLIC EXPOSURE ON COATING LIFE

```
                        ┌──────────────┐
                        │   APPROACH   │
                        └──────┬───────┘
                               │
                        ┌──────────────┐
                        │ EXPERIMENTAL │
                        └──────────────┘
               ┌───────────────┴────────────────┐
      ┌────────────────┐              ┌────────────────────────────┐
      │   ALUMINIDE    │              │   LPPS NiCoCrAlY U-700     │
      │    U-700       │              │ (125 AND 625 μm THICKNESSES)│
      └────────────────┘              └────────────────────────────┘
               └───────────────┬────────────────┘
                    ┌────────────────────────────┐
                    │  MACH 0.3 CYCLIC BURNER RIG │
                    └────────────────────────────┘
```
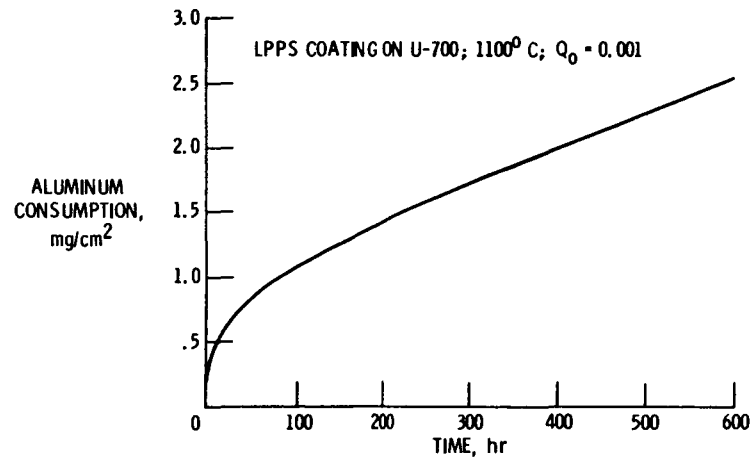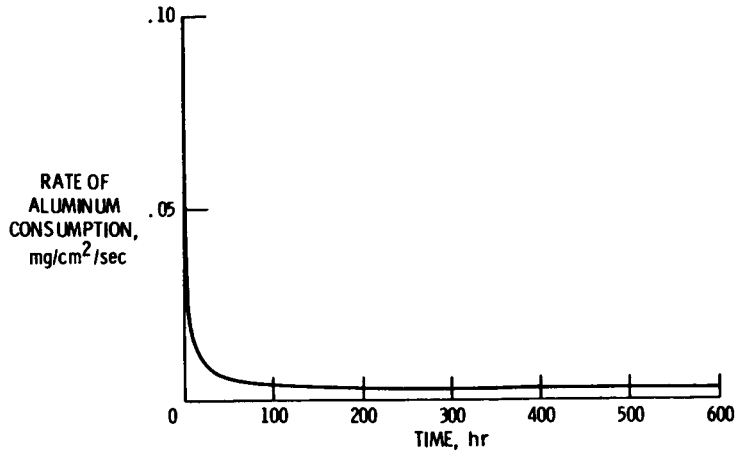
HOT CORROSION AGING	OXIDATION AGING	
900 °C, 0.5 ppm NaCl <1/3 OF HOT CORROSION LIFE	1100 °C 10, 100, 300, 600 hr	G.E. CONTRACT (NAS2-3936)

OXIDATION	HOT CORROSION
1100 °C < 3000 hr	900 °C, 0.5 ppm NaCl < 1000 hr

EMPERICAL DAMAGE MODEL
EFFECT OF HOT CORROSION AGING ON
OXIDATION COATING LIFE

VERIFICATION
DUAL TEMPERATURE MACH 0.3 BURNER RIG
HOT CORROSION AND OXIDATION INCLUDING
BLOCK TIME EFFECTS

Figure 12

147

INTRODUCTION TO LIFE MODELING OF THERMAL BARRIER COATINGS

Robert A. Miller
National Aeronautics and Space Administration
Lewis Research Center

INTRODUCTION

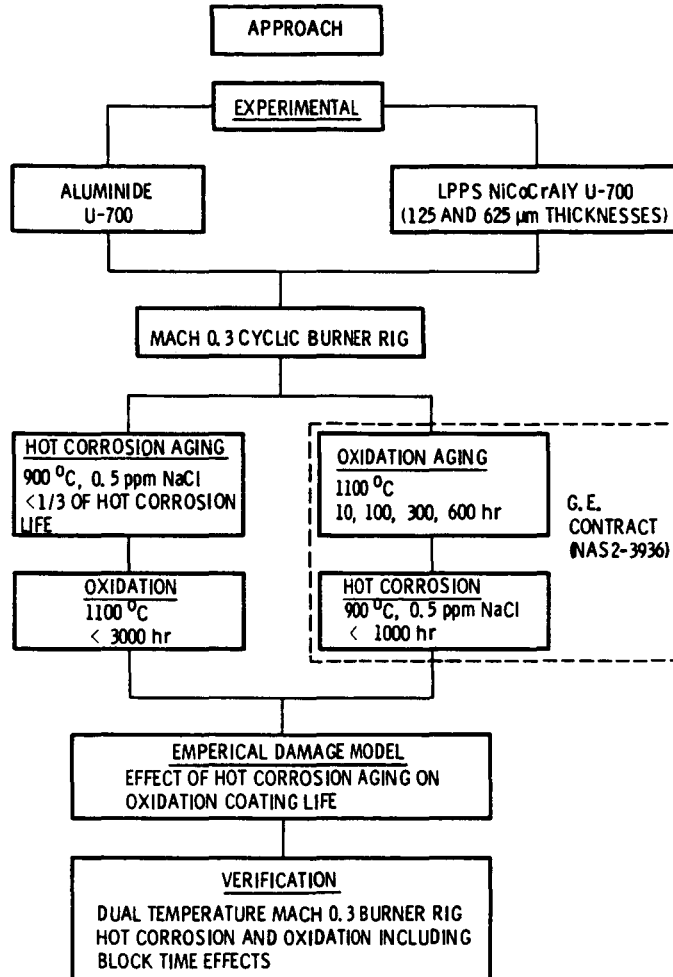Thermal barrier coatings may be applied to air-cooled turbine section air foils to insulate such components from hot gases in the engine. The coatings, which typically consist of about 0.01 to 0.04 cm of zirconia-yttria ceramic over about 0.01 cm of NiCrAlY or NiCrAlZr alloy bond coat, allow increased gas temperatures or reduced cooling air flows. This, in turn, leads to marked improvements in engine efficiency and performance. However, certain risks are associated with designing for maximum benefits, and eventually a point is reached where coating loss would immediately jeopardize the underlying component. Therefore, designers must be able to accurately predict the life of a given bill-of-material coating in any particular design.

This paper will outline the results to date of an in-house aeronautics, base R&T program which is designed to provide the first step towards developing mission-capable life-prediction models. This work directly effects several HOST-supported contractual efforts.

FAILURE MECHANISMS AND MODEL DEVELOPMENT

Coating failure has been correlated with thermal expansion mismatch strains encountered on cooling plus additional strains arising from bond-coat oxidation (ref. 1). Figure 1(a) shows, in cross section, a thermal barrier coating system which has failed on the first cooldown after having been heated in air for 20 hr at 1250 °C. The failure morphology is typical in that a delamination crack has formed in the ceramic just above the irregular interface with the bond coat. Also, oxide layers have grown both at the interface and internally at the splat boundaries of the air-plasma-sprayed bond coat. Figure 1(b) shows that, if a duplicate specimen is heated for the same time and temperature in a shop-argon environment, little oxidation occurs and failure is not observed. This and other work (see ref. 1) demonstrates that bond-coat oxidation plays a major role in coating failure.

Figure 2 shows a specimen which is identical in composition to the coating systems in figure 1, but differs because the bond coat has been plasma sprayed at low pressure. Splat boundary oxidation has been eliminated in this specimen. However, the failure morphology of this specimen, which has been exposed to twenty-two 20-hr cycles in air at 1100 °C in a furnace is still essentially the same as that in figures 1(a) and 1(b). The cycling has led to additional, vertical cracking of the ceramic which extends from the delaminated region to the surface. When a specimen is exposed in a burner rig, failure again initiates by delamination, but subsequent cycling leads to spalling of the delaminated region (ref. 1). In either event failure initiates in the same manner (i.e., delamination on cooling) whether a specimen is tested in a furnace or a burner rig and whether the bond coat has been prepared at low pressure or atmospheric pressure.

PRECEDING PAGE BLANK NOT FILMED

A simple model was proposed to account for thermal barrier coating failure. First, bond-coat oxidation was assumed to be the only important time-at-temperature effect. Next, cyclic strains were assumed to promote slow crack growth in the ceramic. These strains are assumed to arise from thermal expansion mismatch between the metallic and ceramic layers and from additional strains associated with oxidation. These oxidative strains may arise when oxygen from the atmosphere is inserted into the bond coat as oxide scale, or they may be related to oxidation-induced changes in the mechanical properties of the bond coat.

A crack in the ceramic was assumed to grow according to a growth law of the type

$$\frac{da}{dN} = A \, \epsilon_e^b a^d \tag{1}$$

where da/dN is the crack growth rate, ϵ_e is an effective strain, and a is the crack length. The expression for the effective strain caused by the combined effects of thermal expansion mismatch and oxidation was taken to be

$$\epsilon_e = (\epsilon_f - \epsilon_r)(w/w_c)^m + \epsilon_r \tag{2}$$

where ϵ_r represents the mismatch strain (which for convenience is discussed only in terms of the radial component), ϵ_f is that strain which would fail an unoxidized specimen in a single cycle, w is the oxidative weight gain, and w_c is that weight gain which would cause failure in a single cycle. Expression (2) is plotted schematically in figure 3 for three values of m; note that if effective strain is directly proportional to weight gain then m is unity. Inserting expression (2) into (1) and then rearranging and integrating gives

$$\int_0^{N_f} \left[(\epsilon_f - \epsilon_r)(w_N/w_c)^m + \epsilon_r \right]^b dN = 1/a \int_{a_i}^{a_c} a^{-d} da \tag{3}$$

where N_f is cycles to failure, a_i is an initial crack length, and a_c is critical crack length. The subscript N has been affixed to the weight gain term to emphasize that the weight at the end of each cycle is being taken as the important life-controlling factor. This weight gain is a function of time at temperature t which is given by

$$t = N\tau \tag{4}$$

where τ is the length of each heating cycle. The weight gain is also a strong function of temperature.

The initial and critical crack lengths a_i and a_c, which serve as the integration limits to expression (3), are difficult to obtain. However, it is not necessary to evaluate these terms if one recognizes that expression (3) may be set to a constant which may be evaluated at $N_f = 1$ and $w_1 = w_c$; the constant is equal to ϵ_f^b. Also, the integration may be replaced by a summation and, after rearranging, the final expressions for coating life is

$$\sum_{N=1}^{N_f} \left[(1 - \epsilon_r/\epsilon_f)(w_N/w_c)^m + \epsilon_r/\epsilon_f \right]^b = 1 \tag{5}$$

MODEL VERIFICATION

Initial verification of the model is discussed in references 2 and 3. In those studies the coating system consisted of a layer of air plasma sprayed ZrO_2 - 8 percent Y_2O_3 ceramic over either air-plasma-sprayed NiCrAlY or NiCrAlZr or a low-pressure plasma-sprayed NiCrAlZr. All of the coated specimens were furnace tested at about 1100 °C for cycle lengths of 1, 6, or 20 hr. The number of cycles to failure for the low-pressure plasma-sprayed NiCrAlZr system (labeled batch LZ1 in ref. 2) is plotted as functions of cycle length in figure 4. Experimental values are represented by the open symbols and modeled values by the solid symbols. These points were calculated from expression (5) using the experimental values of w_N, which were first fit to arbitrary functions, and the following parameters:

$$b = 17.00 \qquad\qquad m = 1.00$$

$$\epsilon_r/\epsilon_f = 0.38 \qquad\qquad w_c = 2.4 \text{ mg/cm}^2$$

It should also be emphasized that the model parameters appear to be mathematically correlated with each other, so that no one set of four parameters can be obtained from the data. Details of the experiment and the calculation are given in reference 3. As shown in figure 3 an increase in the heating cycle length from 1 to 20 hr caused the number of cycles to failure to decrease by over one order of magnitude. The model accounted for these changes quite well.

CONCLUDING REMARKS

The model discussed above represents the first step in the development of a mission-capable model for predicting the lives of thermal barrier coatings applied to turbine airfoils. Although the model has been based on simple assumptions, the results to date have been encouraging. Much more work will be required to further verify the validity of this approach, to extend it to engine operation, or to develop alternate approaches. Two important factors which must be investigated are the effect of changes in the test temperature and the effect of complex cycles. It will also be necessary to determine whether the model remains valid for specimens exposed to high heat fluxes which are typical of those encountered in gas turbine engines.

REFERENCES

1. Miller, Robert, A.; and Lowell, Carl, E.: Failure Mechanisms of Thermal Barrier Coatings Exposed to Elevated Temperatures. Thin Solid Films, vol. 95, 1982, pp. 265-273.

2. Miller, Robert A.: Oxidation Based Model for Thermal Barrier Coating Life. J. Am. Ceram. Soc., vol. 67, 1984, pp. 517-521.

3. Miller, Robert A.; Agarwal, P.; and Duderstadt, E. C.: Life Modelling of Atmospheric and Low Pressure Plasma Sprayed Thermal Barrier Coatings. Ceram. Eng. Sci. Proc.

TBC'S FAIL IN OXIDIZING ENVIRONMENT
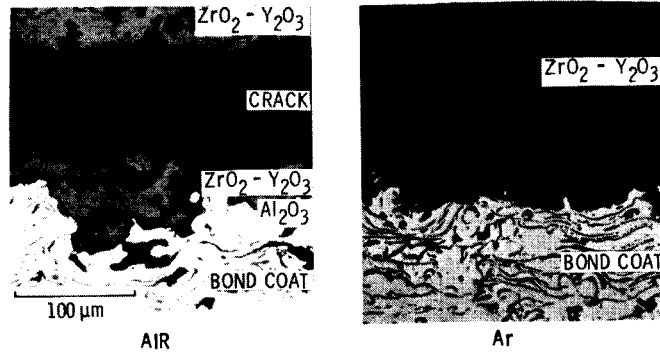ZrO_2 - Y_2O_3/NiCrAlZr; TUBE FURNACE; 20 hr CYCLES AT 1250 °C

AIR

Ar

Figure 1

TBC FAILURE IN FURNACE TEST
ZrO_2 - $8Y_2O_3$ (NASA, APPS)/
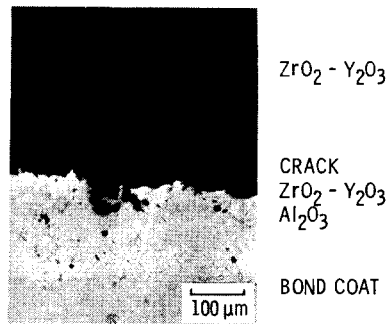NiCrAlZr (GE, LPPS)/ B1900; 22 20-hr
CYCLES BETWEEN 1100 AND 25 °C

Figure 2

152

RELATIONSHIP FOR EFFECTIVE STRAIN

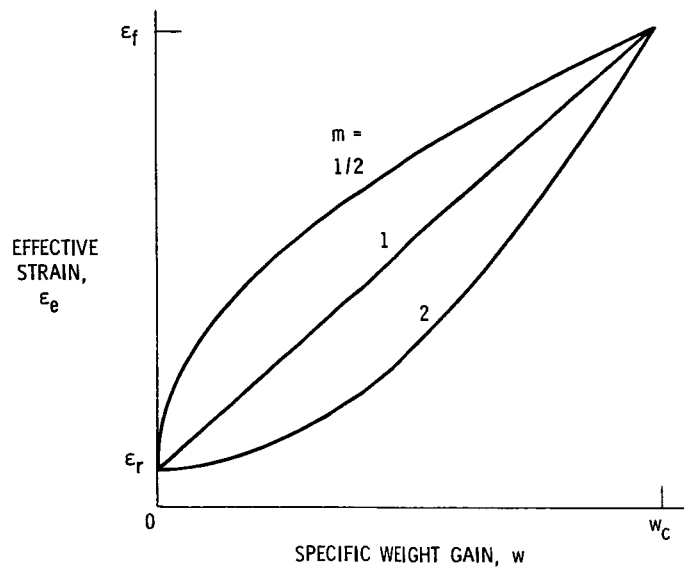$$\epsilon_e = (\epsilon_f - \epsilon_r)\ (w/w_c)^m + \epsilon_r$$

[Figure: plot of EFFECTIVE STRAIN, ϵ_e versus SPECIFIC WEIGHT GAIN, w. Three curves labeled m = 1/2, 1, 2 connecting ϵ_r at origin to ϵ_f at w_c.]

$$\epsilon_f$$

$$m = 1/2$$

$$1$$

$$2$$

EFFECTIVE
STRAIN,
ϵ_e

$$\epsilon_r$$

0   SPECIFIC WEIGHT GAIN, w w_c

Figure 3

MEASURED AND MODELED TBC LIVES

$ZrO_2 - 8Y_2O_3$ (NASA, APPS, BATCH 1)/NiCrAlZr (GE, LPPS)/B1900; 1100 °C CYCLIC FURNACE

[Figure: log plot of CYCLES TO FAILURE, N_f versus HEATING CYCLE LENGTH, τ, hr, with open and closed symbols at approximately 1, 6, and 20 hr.]

b = 17.00
m = 1.00
w_c = 2.4 mg/cm^2
ϵ_r/ϵ_f = 0.38
OPEN SYMBOLS DENOTE MEASURED
CLOSED SYMBOLS DENOTE MODELED

CYCLES
TO
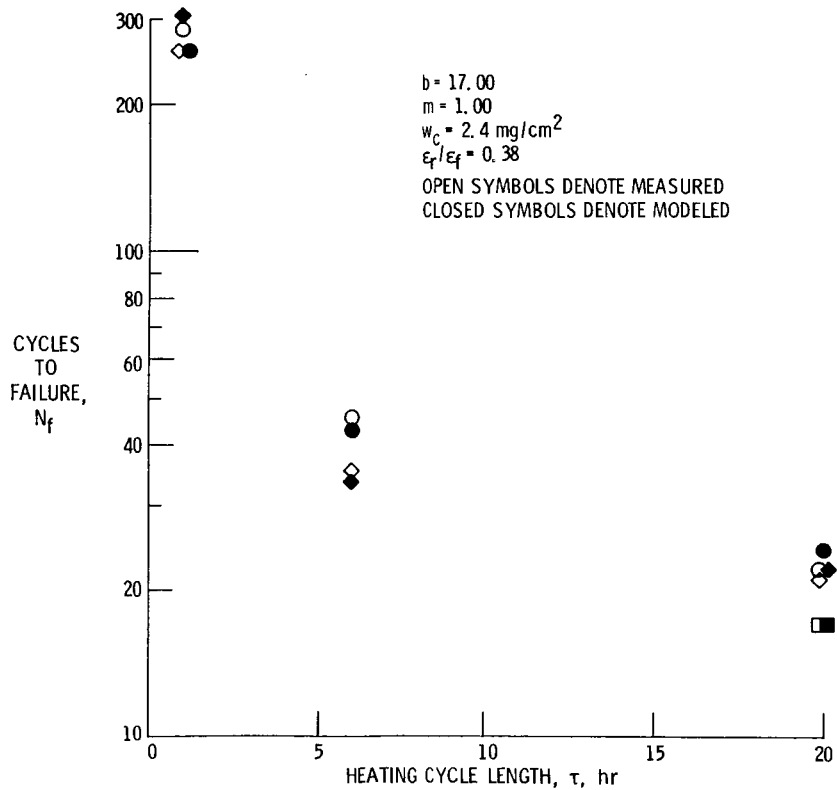FAILURE,
N_f

HEATING CYCLE LENGTH, τ, hr

Figure 4

153

MECHANICAL BEHAVIOR OF THERMAL BARRIER COATINGS FOR GAS TURBINE BLADES*

Christopher C. Berndt ** , Woraphat Phucharoen and George C. Chang
Cleveland State University

ABSTRACT

Plasma-sprayed thermal barrier coatings (TBC's) will enable turbine components to operate at higher temperatures and lower cooling gas flow rates; thereby improving their efficiency. Future developments are limited by precise knowledge of the material properties and failure mechanisms of the coating system. Details of this nature are needed for realistic modelling of the coating system which will, in turn, promote advancements in coating technology.

The present work details complementary experiments and analytical modelling which has been undertaken in order to define and measure the important failure processes for plasma-sprayed coatings. The experimental portion includes two different tests which have been developed to measure coating properties. These are termed as "tensile adhesion" and "acoustic emission" tests. The analytical modelling section details a finite element method which was used to calculate the stress distribution in the coating system. Some preliminary results are presented.

1. INTRODUCTION

In the tensile adhesion test (TAT) a fixture is glued to the coating surface and the assembly subjected to a tensile force (ref. 1). The tensile strength of the coating is usually referred to as the bond strength. Two major criticisms of the TAT which are relevant to this work should be kept in mind. The forces imposed on the coating in a direction perpendicular to the substrate do not necessarily duplicate the forces which the coating experiences during its service life. Also the failure mode of the coatings, Fig. 1, cannot be controlled during a TAT and the coating will always fail at the weakest point under tension. This fracture mode may not be the same as failures experienced during the service life of the coating. In many cases mixed mode failure occurs and this makes it very difficult to exactly ascertain the failure mechanisms of coatings.

Thermally induced failure processes were also monitored during acoustic emission (AE) tests. The time and temperature dependent cracking processes gave rise to noise. Since failure of the thermal protection system is progressive then catastrophic failure occurs at some stage when there is a transformation from the microcrack to a macrocrack network.

The objective of the analytical work is to determine the distribution of stresses and strains for a model TBC system. Therefore the mechanical property measurements may be used in the analytical studies. These, in turn, will provide an

---

understanding from the structural engineering viewpoint of the failure morphologies exhibited by coatings.

2. EXPERIMENTS

2.1 Tensile Adhesion Tests

The tensile adhesion tests were carried out on disc shaped specimens which were 32mm (1.25in) in diameter and 6mm (0.25in) in thickness with an edge radius of 3mm (0.125in). Thus the test surfaces of interest were 25.4mm (1.00in) in diameter and conformed to the ASTM standard test geometry (1). Bond coatings of NiCrAlY or NiCrAlZr were plasma-sprayed to a thickness of about 0.13mm (0.005in) at a power level of 13kW (450 amps and 29 volts). The ceramic overlay for all of the TAT specimens consisted of zirconia - 8wt% yttria which was plasma-sprayed at a power level of 17kW (550 amps and 31 volts) to an additional thickness of about 0.38mm (0.015in). These specimens will be identified as the Y bond coated and the Zr bond coated specimens.

The metal and ceramic deposits were approximately the same thickness over the entire specimen surface. This allowed the oxidative weight gain to be ascertained during preconditioning of the specimen by heat treatment. It should be noted that this study also examined batch variations during the processing of coatings. Thus the batch histories of the specimens are reported but they are not discussed in any detail.

The specimen was then incorporated into a tensile adhesion test configuration as depicted in Fig. 2 (ref. 2). It was necessary to include a collar into this arrangement, prior to specimen fabrication, so that tensile forces could be applied. Two pairs of knife edges were glued to the support bar and the collar so that extensometers could be attached to the specimen. These were in a back-to-back configuration and permitted the slightly non-axial forces imposed on the coating to be taken into account.

2.2 Thermal Cycling Tests

The specimens for the thermal cycling work consisted of 12.7mm (0.5in) diameter superalloy rods (U-700) which were plasma-spray coated over a length of 25mm near one end. The coating of 0.38mm (0.015in) zirconia - 12wt%yttria was sprayed either directly onto the substrate or onto 0.1mm (0.005in) of plasma-sprayed NiCrAlZr bond coat. Some poor coatings were also produced by spraying onto substrates which were preheated in excess of the optimum deposition temperature and these are termed as "preheated coatings". All specimens were cantilever supported so that they could be inserted into the hot zone of a tubular furnace.

The AE emitted from the sample was monitored during a heating and cooling cycle that ranged from 55°C to 1200°C. Most noise was emitted on cooling to below 550°C. The threshold level of the AE equipment was adjusted by running calibration experiments so that no AE counts were evolved from oxidation of the substrate. The results which are reported here therefore measure AE processes which originate from the plasma-spray coating process. The AE (measured as either accumulative counts or count rate) was subsequently processed to reveal any trends dependent on temperature or coating process conditions.

2.3 Finite Element Modelling

The analytical modelling was also carried out on duplex coatings of 0.13mm (0.005in) bond coat with 0.38mm (0.015in) ceramic overlay. The coatings were assumed

to be applied to cylindrical specimens of 12.7mm (0.5in) in diameter and 76mm (3in) in length. The length to diameter ratio of the cylinder is sufficiently large that the numerical problem can be approximated by a two dimensional plain strain case. Figure 3 illustrates a slice of unit length from this cylinder which was considered for finite element analysis. The initial general approach to breaking up the unit slice into symetrical wedges is shown in figure 4. The interfacial region between the bond coat and ceramic coating was approximated by a sinusoidal function along the circumferential line where the radius is 6.48mm (0.255in), fig. 5. The peak-to-peak amplitude and period of this interfacial region was 0.05mm (0.002in). For the present study it has been assumed that the interface between the bond coat and substrate is smooth.

The three materials comprising the substrate, the bond coat, and the ceramic layer are treated as being homogeneous, isotropic, and linearly elastic. Each material possesses its own temperature dependent parameters, such as Young's modulus, Poisson's ratio, and thermal expansion coefficient. The values which were chosen for the preliminary analysis reported in this work are shown in Table 1. This simplified material model represents the first step towards obtaining a detailed solution to the complex TBC problem on hand. The finite element model paid attention to distinguishing elements in the vicinity of the sinusoidal interface. The only "load" applied to the model is one of uniform temperature and this simulates a temperature drop during the cooling cycle. The coating/substrate system was assumed to be stress free at 800°, for the purposes of this work, and the stress was found after a 100° drop.

Table 1. Material Data for Thermal Barrier Coatings.

	Substrate	Bond Coat	Ceramic Coating
Young's Modulus (GPa)	179.0	138.0	13.8
(psi x 10^6)	25.5	20.0	2.0
Poisson's Ratio	0.25	0.27	0.25
Density (kg/m^3)	37,590	33,830	27,390
(pci)	0.280	0.252	0.204
Thermal Expansion Coefficient (m/m/$^{\circ}$C x 10^{-6})	13.8	15.2	10.0
(in/in/$^{\circ}$F x 10^{-6})	7.73	8.42	5.56

3. RESULTS

The change in tensile adhesion strengths with respect to oxidative weight gain are summarized in Fig. 6. All of the preoxidized Y and Zr bond coated specimens exhibited lower bond strengths than the as-sprayed Y bond coated specimens. The locus of failure was different for each sample preparation and coating system. The preoxidized Zr coated samples failed in a cohesive (C) manner, within the ceramic, whereas the as-sprayed Zr bond coated specimens exhibited failure at the substrate-bond coat interface (S). This adhesive type of failure within the as-sprayed coating is indicative of a poorly prepared coating. Nevertheless this bond strength value represents a minimum value of the cohesive mode which is observed during the service failure of coatings. On the other hand the Y bond coated samples did not exhibit either purely cohesive or any failure at the substrate-bond coat interface. All of

these preoxidized samples failed adhesively (A) whereas the as-sprayed coatings failed either adhesively or with a mixed mode A-C failure. Only one of these samples exhibited failure within the epoxy.

The Y bond coated specimens (Fig. 6a) revealed a general trend where the strength decreased with the specific weight gain. These failures also mostly incorporated an adhesive component. The bond strength results of Zr bond coated specimens (Fig. 6b) were ambiguous since the failure modes were not similar. The outlier of the Zr bond coated specimen (batch 1 as distinguished in Fig. 6) which exhibited the greatest weight gain also showed comparable bond strength to the other two preoxidized samples. The substrate interfacial-adhesive mode does not duplicate the cohesive failure mode experienced under service conditions. Therefore the values which have been obtained represent a minimum bond strength and the overall trend in bond strength may be to decrease with an increase in specific weight gain. The as-sprayed Y bond coated and preoxidized Zr bond coated samples most closely replicated the failure mode which was experienced in service.

The tensile tests measured the extension at two positions which were 180° apart and thus the force versus average extension curve can be established. The average extension followed an approximately linear relationship with respect to the force until the failure point. Any fine detail on this curve has not yet been analysed. It was possible to calculate the compliance and elongation at fracture of these samples.

The AE tests indicated when cracking processes occurred within the specimen. Figure 7 shows the count rate data for the single component YSZ coatings. Acoustic emission is generated immediately upon cooling at 1200°C. This gradually decreases at a temperature of about 800°C. Acoustic emission signals are again generated at lower tempertures and the count rate increases to a maximum at approximately 100°C before gradually decreasing to a temperature of 55°C. Then the next thermal cycle commences. For convenience this AE behavior is termed the "systematic response regime". In all cases there are small random fluctuations in the signal about the systematic trend. However in many cases there are also large erratic signals superimposed on the AE response curves. This AE behavior is referred to as the "stochastic response regime". These large count rates are thought to represent macro-cracking processes such as interlamellar cracking or coating delamination. They may also arise from prior-formed cracks which interact by sliding in a haphazard and irregular fashion. The processes which give rise to the systematic and stochastic regimes occur at higher temperatures for the preheated YSZ coating.

The duplex coating systems also exhibited the same trends. Examination of the first cycle (Fig. 8) shows that these coatings were less responsive, in terms of AE behavior, than the single component coatings which were examined above. The non-preheated coatings did not exhibit the stochastic noise distribution which was observed for the single component coatings. The non-preheated coatings commenced AE activity at temperatures less than 600°C which may be compared to 1200°C for all the other coating systems. The preheated duplex coatings displayed significant AE activity at temperatures greater than 1100°C. These samples also displayed more systematic and stochastic activity at temperatures less than 500°C than the optimally sprayed duplex coating.

The second thermal cycle (not shown in this report) was different from the initial cycles. Both the systematic and stochastic distributions of AE increased and this resulted in a greater accumulative count. On the third cycle there was a further increase in the stochastic behavior so that the continuous behavior was

masked. It is difficult to discern real trends which may be associated with the initiation temperature of AE because these temperatures are all grouped within the 500-600°C temperature band.

The initial finite element calculations revealed that upon cooling compressive stresses developed in the ceramic parallel to the interface (in the Y direction) and mixed compressive and tensile stresses built up perpendicular to the interface (in the X direction). Shear stresses and the stresses in the X direction are localized near the interface (fig. 9). Stresses in the Y direction of the bond coat are compressive at the tips of the asperities and positive elsewhere. In the X direction the stresses are positive within the asperities and mixed elsewhere. Again shear stresses and the stresses in the X direction maximize near the bond coat - ceramic coating interface. It should be emphasized that these results are preliminary since these initial calculations have shown that a more refined mesh will be required in the vicinity of the interface.

4. DISCUSSION

The marked difference in failure mechanisms of the specimens makes comparison of the bond strengths difficult. It should be emphasized that the failure morphology which is observed during tensile adhesion testing does not always replicate the failure mode which is observed during furnace or burner rig tests. One other study (ref. 3) has examined the fracture modes of specimens in relation to the bond strength. It was found, in this earlier work, that bond strength increased as the locus of failure changed from the interface between the metal and ceramic to entirely within the coating. It is generally observed that the distribution of different modes of failure is not the same over the entire cross-sectional area of specimen. This may be explained in terms of different stresses and stress gradients across the specimen due to stress concentrations from a free edge (ref. 4). Other workers (ref. 5) have found difficulty in obtaining reproducible TAT data and several works (ref. 6,7) have proposed that tensile tests on notched bars may be used as a basis to obtain fracture mechanics values of coatings.

The Zr bond coated samples exhibited both a higher compliance and a greater net extension at failure than the Y bond coated specimens. The compliance, measured in mN^{-1}, can be considered as the reciprocal of the effective Young's modulus if the thickness of the coating (0.51mm or 0.020in) is also taken into account. Thus E = $1/(C \times t)$ where E is Young's modulus, C the compliance and t is the thickness of both the bond and ceramic coatings. Therefore the <u>average</u> Young's modulus of the coating system measured in tension is in the range of 170 to 720 GPa. This is an over-simplification because deformation over the thickness of a duplex system would not be expected to be isotropic.

Coatings which exhibited the highest compliance (or lowest Young's modulus) may be expected to also reveal the greatest elongation at failure if it can be assumed that failure occurs by the same mechanism. However the failure mode is varied, being either adhesive, cohesive, substrate interfacial or of mixed mode. A few tentative relationships can be seen from the mechancial property determinations. The compliance of 75% of the Zr bond coated samples was greater than that of the Y bond coated samples. The average compliance of the Y bond coated specimens was 5.1×10^{-9} mN^{-1} whereas that of the Zr bond coated specimens was 8.3×10^{-9} mN^{-1}.

A number of experimental conditions should be remembered with regard to the acoustic emission tests. The heating and cooling rates of the specimen do not

represent practical operating conditions of a thermal barrier coating. However failure is still thought to occur on cooling in higher heat flux Mach 0.3 tests (ref. 8); and at higher heat fluxes, such as those in an engine, the cooling mode of failure is still likely to be important. Thus coating failure, for the present case, results from thermal expansion mismatch stresses between the coating and substrate as well as any oxidation effects of the bond coat and/or substrate.

The AE is assumed to correspond to cracking processes which occur as a result of the plasma-spray deposition process. Thus higher count rates, such as are observed from the stochastic regime, can be related to macrocracking processes and this has been supported by the observation of delamination during the first cycle for some specimens. Also the finite element studies indicate that the greatest stress build-up at the bond coat-ceramic coating interface most probably arises from shearing stresses.

Two different types of AE distributions can be observed by examining the count rate responses and both cracking processes are inter-related. The systematic response distribution is thought to represent the progressive growth and interaction of microcracks (i.e., subcritical crack growth) and possibly the spalling and interaction of oxidation products. The number of these events and their growth increases with decreasing temperature and therefore the AE count rate generation increases. The large count rates are presumed to evolve from uncontrolled macrocracking processes (i.e., critical crack growth). Thus macrocracking was observed to occur near the substrate-coating interace where stresses are greatest.

5. CONCLUDING REMARKS

A testing technique has been established which permits the properties of the coating only to be measured. The tensile properties of plasma-sprayed thermal barrier coating systems have been measured by a modified tensile adhesion test. The elongation at failure and the average compliance of the Zr bond coated specimens were both greater than those for the Y bond coated specimens. The average bond strength of the as-sprayed coatings was greater than that of the preoxidized specimens and this effect was most clear for the Y bond coated samples. Also the failure loci of the Y and Zr bond coated specimens were different.

The processing conditions, coating system structure (single versus duplex) and the number of thermal cycles influenced the AE response. The different cracking processes were distinguished by qualitative examination of the AE count rate data. The stochastic response, that is macrocracking processes, increased upon preheating of the coating and upon subjecting the specimen to increased thermal cycling. The stochastic response decreased when using a duplex coating instead of a single component coating.

Several experimental improvements can be offered in the light of the AE tests. The specimen geometry should permit 100% coverage of the plasma-sprayed coating system. In this manner AE events which arise from incomplete surface coverage, such as from edge effects, can be avoided. There is also the benefit that oxidative weight gains can be measured. Future tests shall control the furnace temperature gradient so that it is linear over the entire temperature range of experimentation. In this way temperature effects and change in temperature effects will not be confounded.

This work has been exploratory with the aim of using tensile adhesion test methods, AE techniques, and finite element modelling for examination of the

mechanical properties of plasma-sprayed coatings. It is anticipated that development of these methods can lead to a detailed understanding of the failure mechanisms and properties of coatings.

6. REFERENCES

1. ASTM, American Society for Testing and Materials,: "Standard C633-69 Method of Test for Adhesion or Cohesive Strength of Flame-Sprayed Coatings", (1969).
2. Berndt, C. C.; and Miller, R. A.: "Mechanical Property Measurements of Plasma-Sprayed Thermal Barrier Coatings Subjected to Oxidation", Ceram. Eng. Sci. Proc., Vol.5, (1984).
3. Levine, S. R.: "Adhesive/Cohesive Strength of a ZrO_2.12 w/o Y_2O_3/NiCrAlY Thermal Barrier Coating", NASA TM-73792, May 1978, 24 pages.
4. Sickfeld, J.: "Pull-Off Test, an Internationally Standardized Method for Adhesion Testing - Assessment of the Relevance of Test Results", in "Adhesion Aspects of Polymeric Coatings", pp.543-567, Ed. K.L.Mittal, Pub. Plenum Press, (1983).
5. Hermanek, E. S.: "Determining the Adhesive and Cohesive Strengths of Thin Thermally Sprayed Coatings", Welding J., 57 (1970) 31-35.
6. Pabst, R. F.; and Elssner, G.: "Adherence Properties of Metal-to-Ceramic Joints", J. Mater. Sci., 15 (1980) 188-196.
7. Berndt, C. C.: "Tensile Adhesion Test Measurements on Plasma-Sprayed Coatings", 6th. Inter. Conf. on Fracture, 4-10 Dec., 1984, New Delhi, India.
8. Miller, R. A.; and Lowell, C. E.: "Failure Mechanisms of Thermal Barrier Coatings Exposed to Elevated Temperatures", Thin Solid Films, 95 (1982) 265-273.

(a) INITIAL SETUP — plug, adhesive, ceramic, bond coat, substrate

(b) EPOXY FAILURE (establishes a minimum value)

(c) COHESIVE FAILURE (within coating)

(d) ADHESIVE FAILURE (at metal-ceramic interface)

(e) SUBSTRATE-INTERFACIAL FAILURE
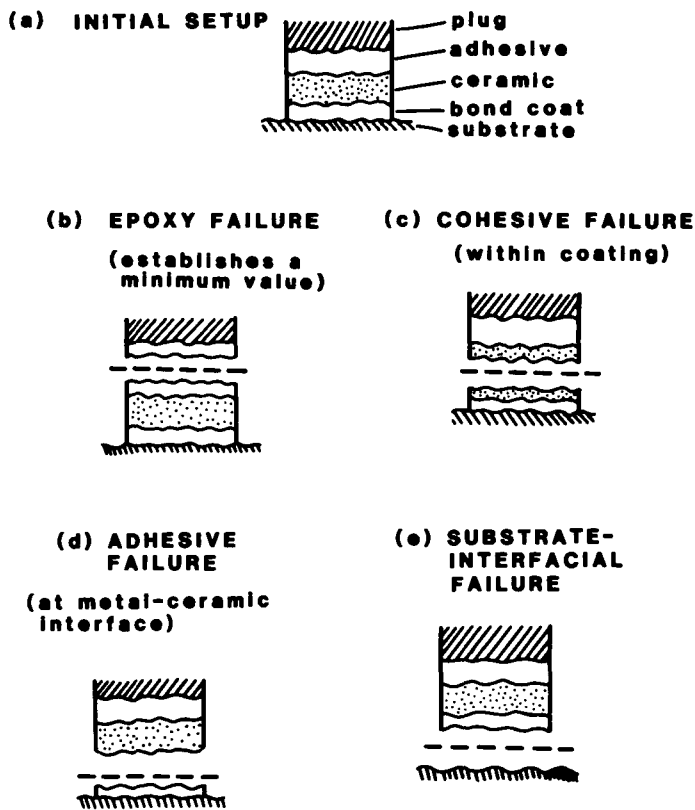
Figure 1. Modes of tensile adhesion test failures for plasma-sprayed coatings. Cohesive failure in the text is referred to as "C", adhesive failure as "A", and substrate-interfacial failure as "S".
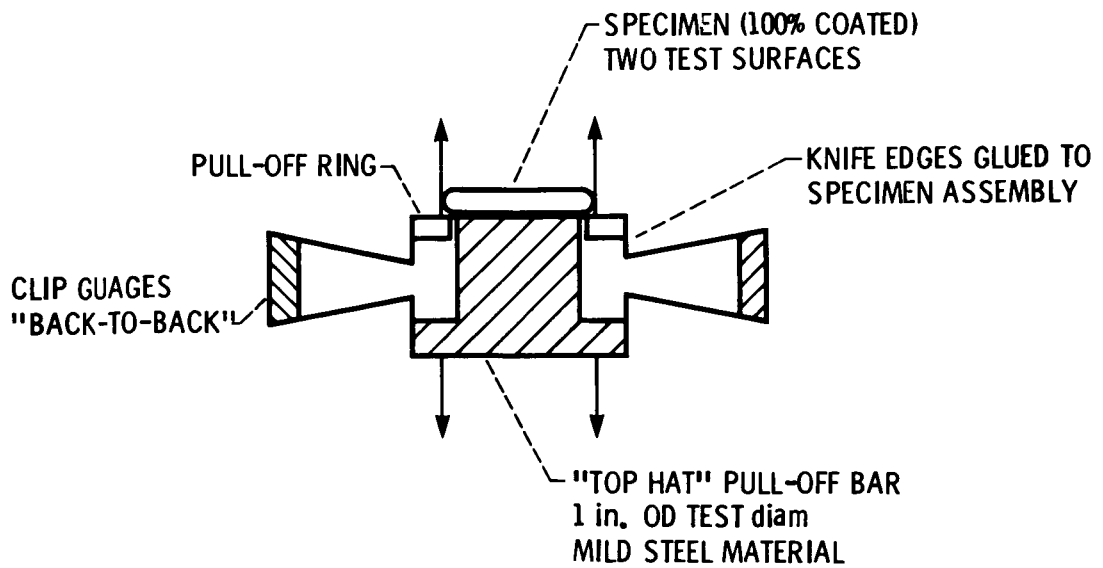
Figure 2. Specimen arrangement for carrying out tensile adhesion tests on plasma-sprayed coatings.
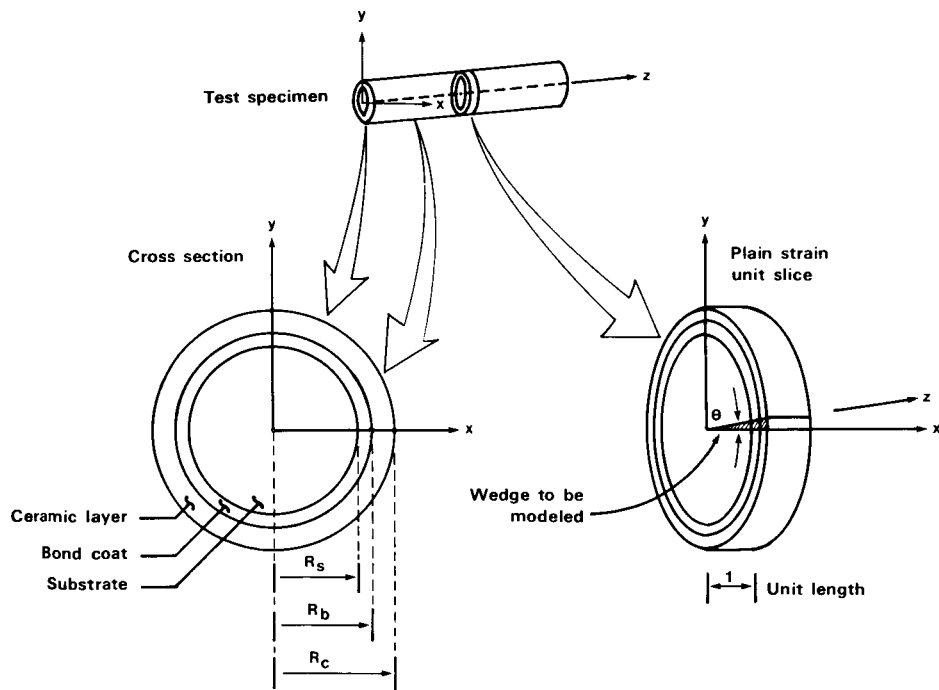
Figure 3. Cylindrical test specimen used for finite element modelling.
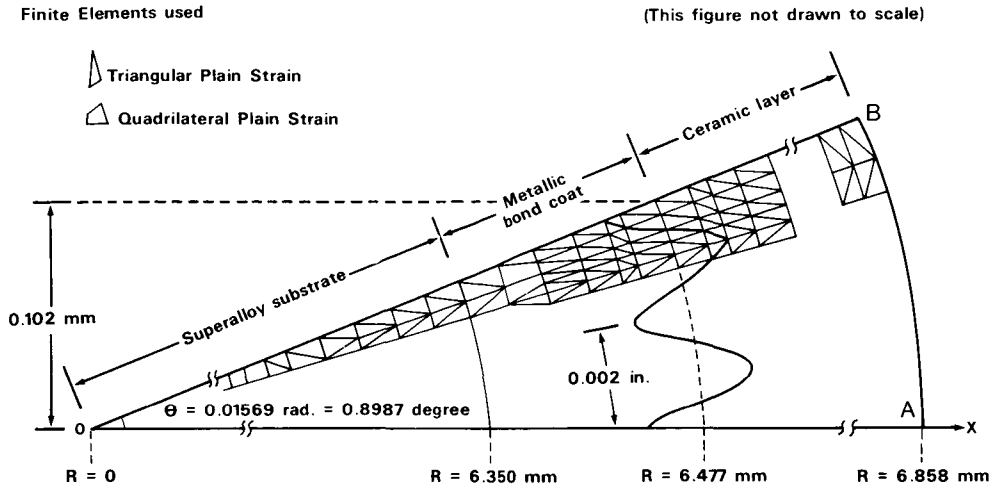
Figure 4. Schematic of the basic finite element model used for thermal barrier coatings.
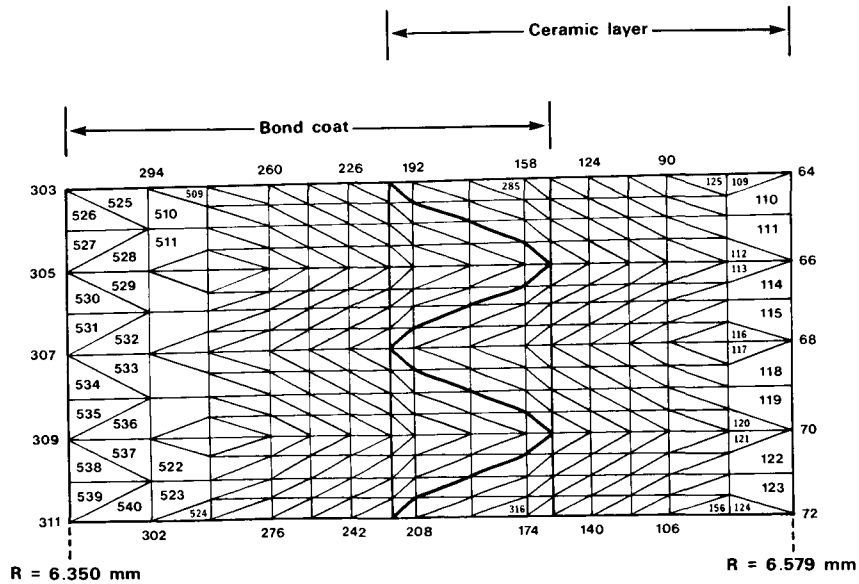

Figure 5. Details of the finite element model for thermal barrier coatings in the vicinity of the bond coat – ceramic coating interface.
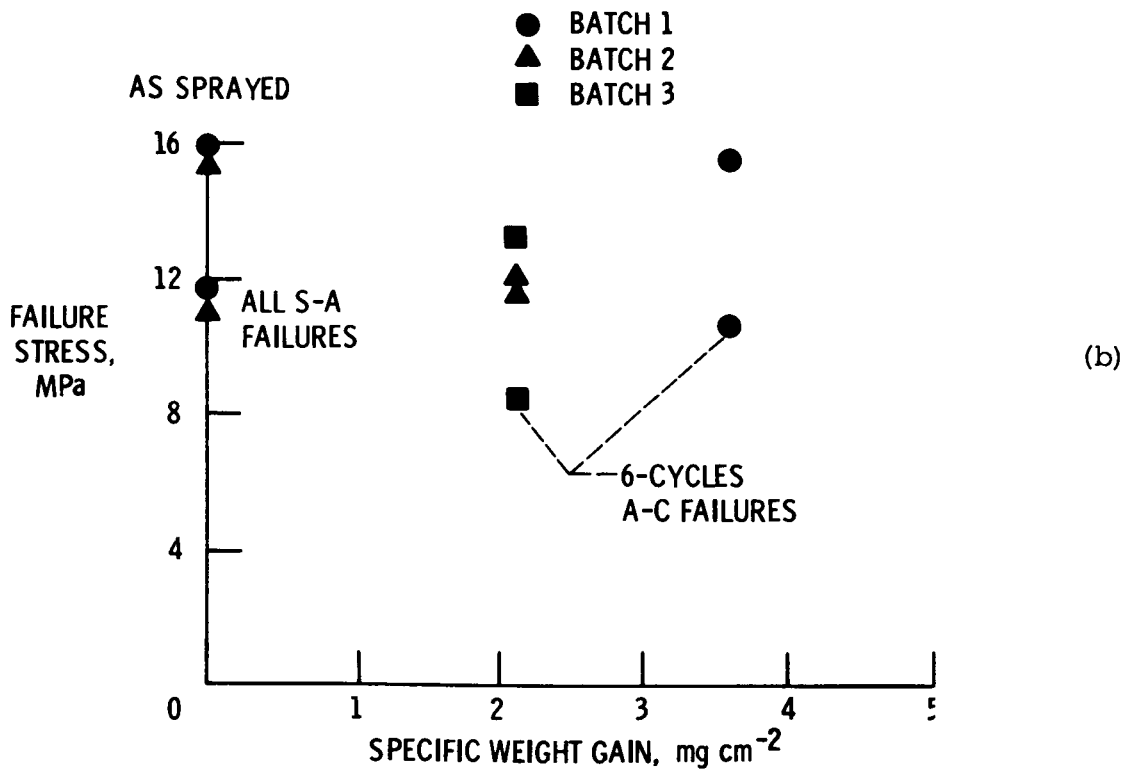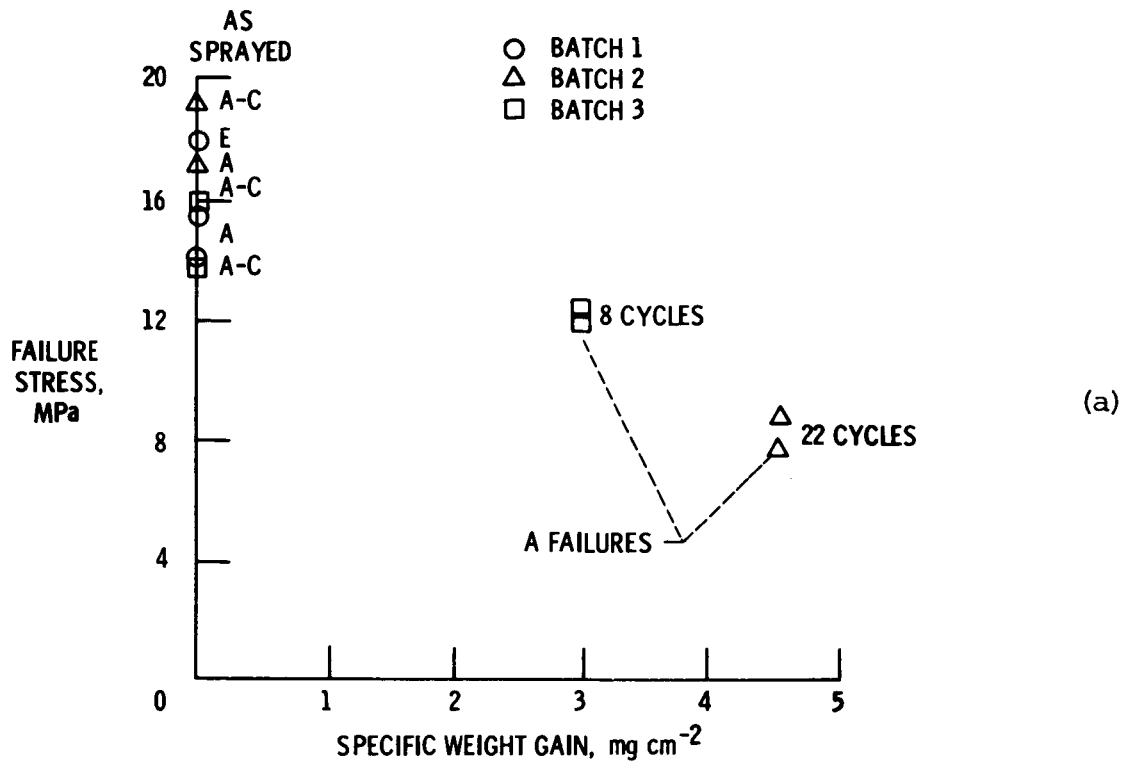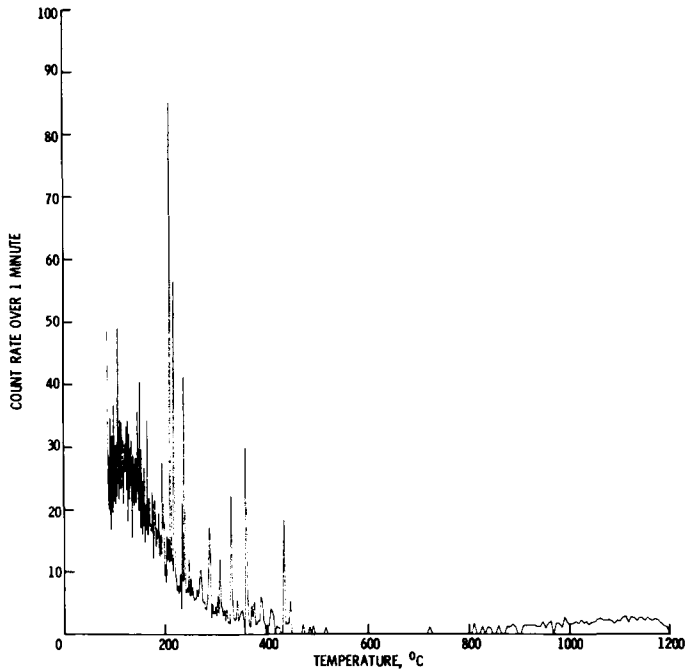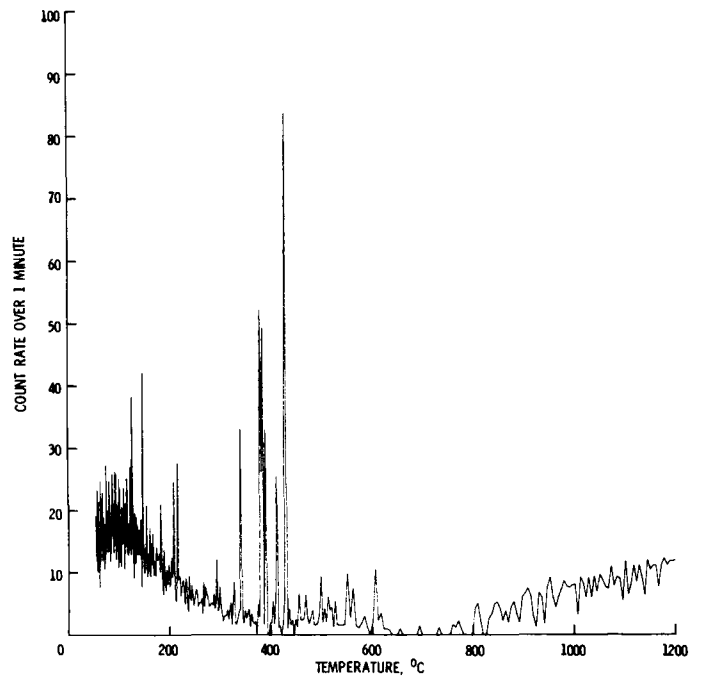
Figure 6.   Bond strength of coatings with respect to specific oxidative weight   gain.
The modes of failure are also indicated.
(a) NiCrAlY bond coated.   (b) NiCrAlZr bond coated.

164

(a)

(b)

Figure 7. Acoustic emission response of single component coatings. (a) non-preheated coating. (b) preheated coating.
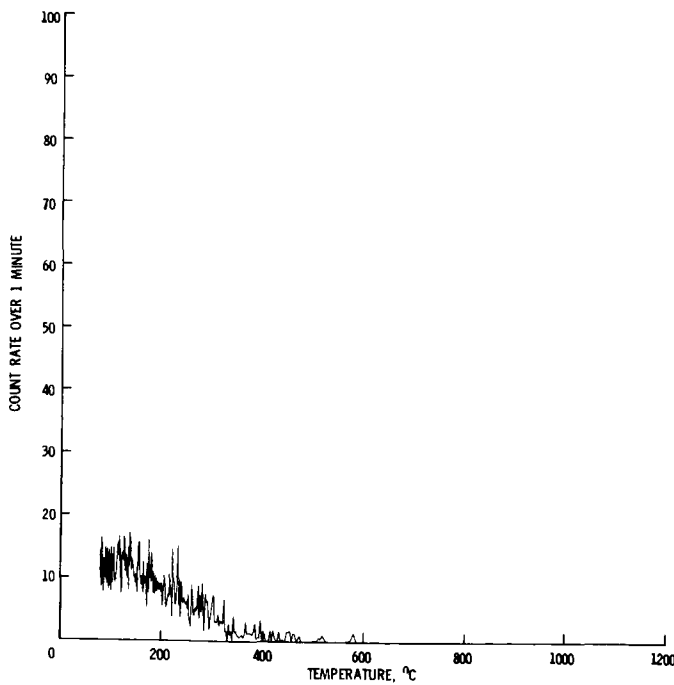
(a)
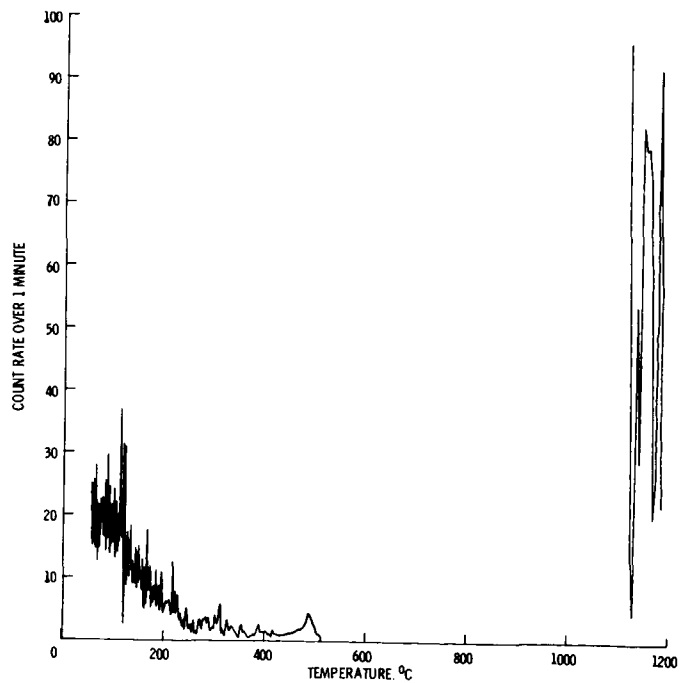
(b)

Figure 8. Acoustic emission response of duplex coatings. (a) nonpreheated coating. (b) preheated coating.
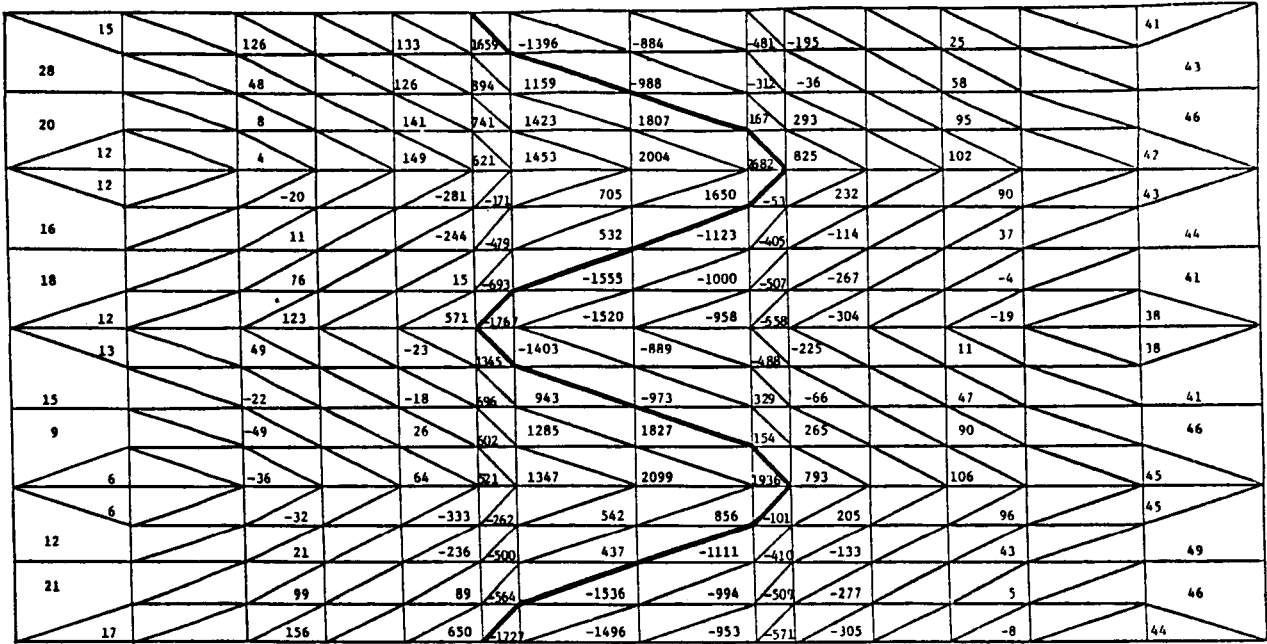
Figure 9a. Results from initial finite element modelling for the normal stresses in the X direction, refer to fig. 3. The numerical values are given in units of "psi". The bond coat is on the left hand side of the figure while the ceramic coating in on the right side.

Figure 9b. Results from initial finite element modelling of the shearing stresses. The numerical values are given in units of "psi". The bond coat is on the left hand side of the figure while the ceramic coating is on the right hand side.

166

THERMAL BARRIER COATING LIFE PREDICTION
MODEL DEVELOPMENT

T.E. Strangman
Garrett Turbine Engine Company

Thermal barrier coatings (TBC) for turbine airfoils in high-performance engines represent an advanced materials technology that has both performance and durability benefits. Foremost of the TBC benefits is the reduction of heat transferred into air-cooled components. As indicated in Figure 1, cooling air requirements can be reduced by one-third or the airfoil creep life can be increased by a factor of five with the successful application of a 125μm thick zirconia coating.

In order to achieve these benefits, however, the TBC system must be reliable. Mechanistic thermochemical and thermomechanical life models and statistically significant design data are therefore required for the reliable exploitation of TBC benefits on gas turbine airfoils. Garrett's NASA-Host Program (NAS3-23945) is designed to fulfill these requirements.

This program is focused on predicting the lives of two types of strain-tolerant and oxidation-resistant TBC systems (Figure 2) that are produced by commercial coating suppliers to the gas turbine industry. The plasma sprayed TBC system, composed of a low-pressure plasma spray (LPPS) applied oxidation resistant NiCrAlY bond coating and an air-plasma-sprayed yttria (8 percent) partially stabilized zirconia insulative layer, is applied by both Chromalloy (Orangeburg, New York) and Klock (Manchester, Connecticut). The second type of TBC is applied by the electron beam-physical vapor deposition (EB-PVD) process by Temescal (Berkeley, California).

Key elements of Garrett's TBC life prediction strategy include the following:

● Development of mission-analysis capable TBC life models

● Development of rapid TBC life computation approaches for preliminary and final design analysis

● Calibration of TBC life models with affordable tests

● Establishment of NDE feasibility for TBCs

● Interative engine testing to validate TBC life analysis

Burner rig oxidation and hot corrosion test data will be used to establish the thermochemical life model. Anticipated results are indicated in Figure 3, multi-temperature tests will also be performed to facilitate the development of a cumulative damage model, which is required for an engine mission-analysis capability.

Tensile and compressive spalling strain and fracture toughness test data are being obtained to quantify the width of the TBC's strain-tolerant envelope as a function of flaw size, exposure temperature and time. Anticipated results are provided in Figure 4.

A low-cost modified bond strength test with an artificial penny-shaped flaw at the ceramic-metal interface or within the zirconia layer has been developed to provide a quantitative estimate of the fracture toughness. Post-test examination of the fracture surface provides detailed information with respect to location of the fracture path and elements present on the fracture surface.

Non-destructive evaluation techniques, such as eddy current, photothermal radiometric imaging and scanning photoacoustic microscopy, are also being investigated in this program. These technologies will be assessed for their capability to quantify a TBC's thickness, flaw size and insulative capability.

Lives of all the TBC systems will be predicted for TFE731 high pressure turbine blades for factory engine test, business aircraft and maritime surveillance missions. Complementary engine validation tests are planned.

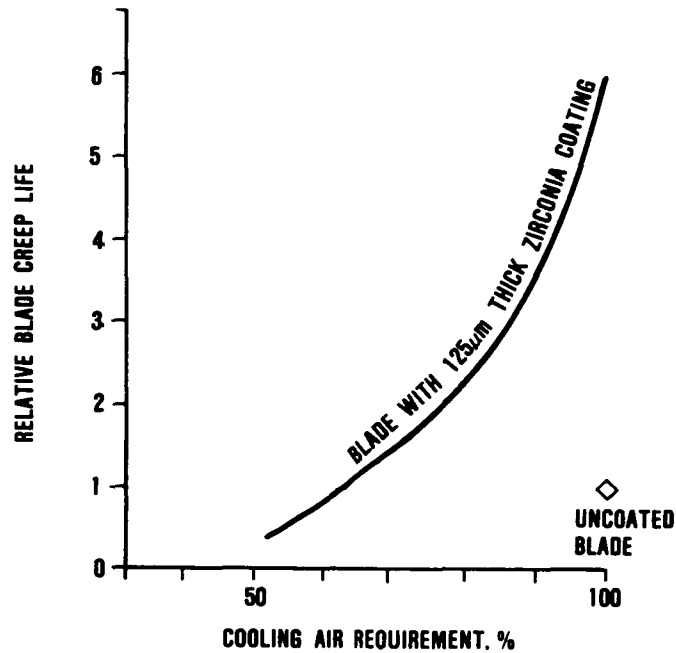This program has just been initiated. Specimen procurement is in progress.

RELATIVE BLADE CREEP LIFE (y-axis)

COOLING AIR REQUIREMENT, % (x-axis)

BLADE WITH 125μm THICK ZIRCONIA COATING

UNCOATED BLADE

Figure 1. TBCs Improve Creep Life and Reduce Cooling Air Requirements for Garrett High-Pressure Turbine Blade.

PLASMA SPRAY

ELECTRON BEAM –

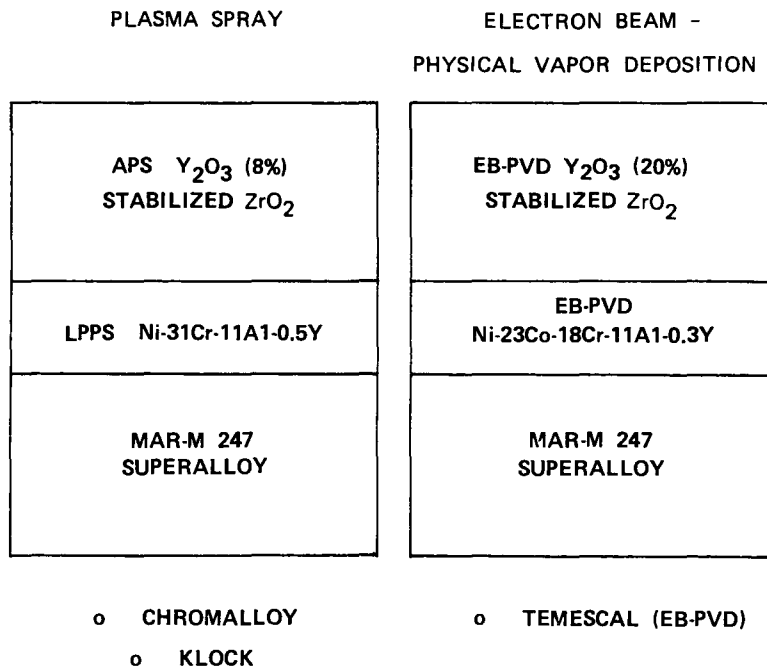PHYSICAL VAPOR DEPOSITION

APS Y_2O_3 (8%) STABILIZED ZrO_2	EB-PVD Y_2O_3 (20%) STABILIZED ZrO_2
LPPS Ni-31Cr-11A1-0.5Y	EB-PVD Ni-23Co-18Cr-11A1-0.3Y
MAR-M 247 SUPERALLOY	MAR-M 247 SUPERALLOY

o   CHROMALLOY

o   KLOCK

o   TEMESCAL (EB-PVD)

Figure 2. Life Prediction Models Are Being Developed For Plasma-Sprayed and EB-PVD TBC Systems.
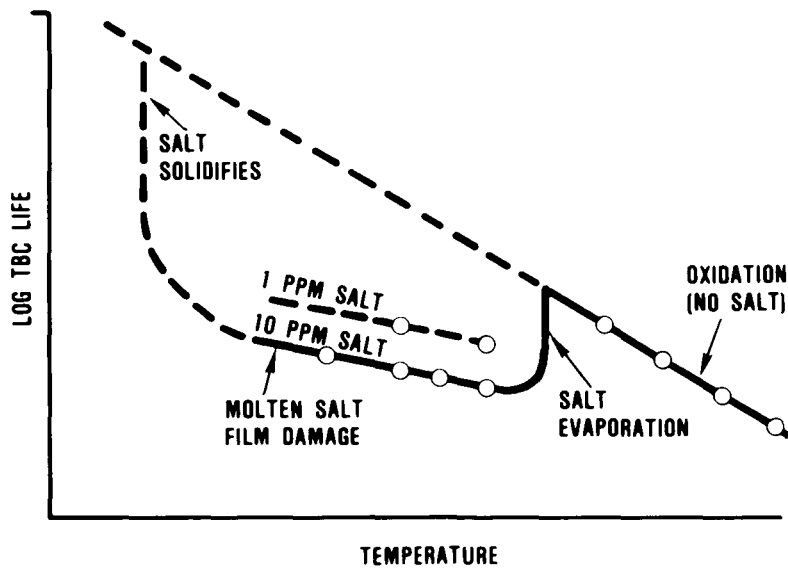
Figure 3. Burner Rig Tests Will Be Used To Develop and Calibrate Thermochemical TBC Life Model.
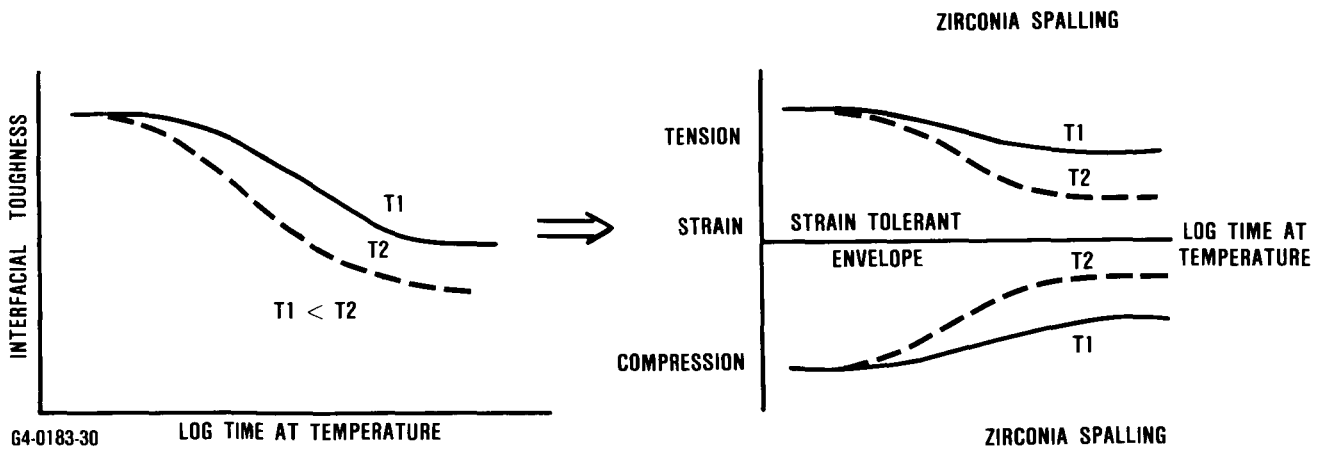
Figure 4. Interfacial Toughness Data Will Be Used To Extrapolate Spalling Strain Data With Respect To Exposure Time and Temperature.

THERMAL BARRIER COATING LIFE PREDICTION MODEL DEVELOPMENT

R. V. Hillery
General Electric Company

The effort to increase engine efficiency has received added impetus in recent years because of the sharp increase in fuel cost. Several generations of superalloys have been developed over the years to permit increases in turbine inlet gas temperatures to increase engine efficiency, but the practical temperature limits make this increasingly difficult and expensive. The use of thermal barrier coatings has potential to increase engine efficiency by permitting increased gas inlet temperatures at present metal temperatures, or maintaining current gas inlet temperatures and reducing coolant requirements and the efficiency penalties associated with cooling air usage. Alternatively, TBCs can be utilized to reduce metal temperatures and extend life.

Thermal barrier coatings are now commonly used on combustors, afterburner flameholders, and other low-risk applications, and extend the useful lives of those components significantly. Also, TBCs have been successfully tested on several high pressure turbine (HPT) nozzles and blades. The occasional loss of some of the ceramic insulating layer of the TBC from combustors and flameholders is not unduly harmful to engine operation or life, and the ability to predict coating life in such applications is not essential. On the other hand, the reliability of coatings used on HPT components is critical. Loss of the coating from such components has the potential to shorten life to less than that of uncoated parts, particularly if cooling air has been reduced to obtain engine efficiency. Thus the long-term use of TBCs on HPT hardware under engine operating conditions where safe metal temperatures must be maintained requires absolutely predictable coating performance. At the present time, the ability to quantitatively predict TBC life does not exist.

In order to fully exploit thermal barrier coatings on turbine components and achieve the maximum performance benefit, the knowledge and understanding of TBC failure mechanisms must be increased and the means to predict coating life developed. The proposed program will determine the predominant modes of TBC system degradation and then develop and verify life prediction models accounting for those degradation modes. The successful completion of the program will have dual benefits: the ability to take advantage of the performance benefits offered by TBCs, and a sounder basis for making future improvements in coating behavior.

The program is composed of eight technical tasks as described briefly below.

Task I - Failure Mechanism Determination

The work in this task will consist of designing and performing experiments to determine the relative importance of various potential failure modes of a plasma sprayed TBC system and to conduct additional tests to confirm that the identified failure modes are correct. The TBC system will consist of a low pressure plasma sprayed (LPPS) Ni-22Cr-10Al-0.3Y (wt. %) bond coat and a plasma sprayed yttria partially stabilized zirconia (ZrO_2-8%Y_2O_3) top

coat on conventionally cast Rene' 80 alloy substrate. Bond coat thickness will be 0.005 inch+0.001 inch, and the zirconia thickness will be 0.010+0.002 inch.

Task II - Major Mode Life Prediction Model

The objective of this task is to develop life prediction models for those predominant failure models determined in Task I. This will be accomplished by designing a suitable set of experiments and concommitant analyses, thus creating a life prediction model by means of a combined analytical experimental program.

Task III - Model Verification

The plan for this Task is to use instrumented burner rig testing of TBC coated Rene' 80 specimens to verify the life model under conditions which are generally simulative of turbine blade conditions. The variables to be covered are: 1) strain (TMF) cycle, 2) peak cycle temperature, and 3) cycle duration.

Task V - Thermomechanical Life Models

The stress analysis and life modeling to be conducted in this and following tasks will require the knowledge of several coating properties (thermal/physical properties, deformation properties, failure characteristics), some of which will be determined in the program.

The primary objective of this Task is to develop a "continuum" mechanics life prediction model by applying a structural analysis code based on publicly available heat transfer and stress analyses codes modified to deal with the thermal barrier coating problem.

Task VI - Thermochemical Failure Modes

In this task, oxidation and hot corrosion failure models will be developed. Assuming that oxide scale growth on the bond coat surface is found to be a predominant factor in TBC failure, and further that the relationship between scale thickness and stress is determined in earlier tasks, then the effort in this task will be to determine the rate of oxide scale growth at various anticipated use temperatures. Thus, it should be possible to develop a model for predicting TBC life at various operating temperatures or combinations of temperatures.

Task VII - Exceptional Failure Modes

A data base on erosion and foreign object damage will be developed in this Task for use in predicting anticipated erosion and foreign object damage to thermal barrier coated components.

Task VIII - Comprehensive Model Development

The objective of this task is to develop a comprehensive life prediction model. This model will include four activities:

o   Structural Analysis - Determination of the mechanical and thermal fields in the structure for a given flight profile.

o   Continuum Analysis - Evaluation of potential for crack initiation through appropriate mechanisms as well as gross structural instabilities; for example, creep or buckling.

o   Exceptional Failure Modes Analysis - Evaluation of those events which require external agents to produce failure, e.g., FOD or erosion.

o   Fracture Mechanics Analysis - Determination of the structural life once a dominant crack is formed.

Task IX - Life Prediction Model Verification

The test plan developed in Task VIII to test the dominant features of the model will be conducted. Details of conditions, data, analysis, etc., will depend on each particular test to be defined at that point in the program.

_____   _____

This contract began in April of this year and work to date has been exclusively in Task I. A literature search has been completed and preliminary experiments aimed at definition of predominant failure modes are underway.

THERMAL BARRIER COATING LIFE PREDICTION
MODEL DEVELOPMENT

Jeanine DeMasi
Keith Sheffler
United Technologies Corporation
Pratt & Whitney

The objective of this program is to develop an integrated life prediction model accounting for all potential life-limiting Thermal Barrier Coating (TBC) degradation and failure modes including spallation resulting from cyclic thermal stress, oxidative degradation, hot corrosion, erosion, and foreign object damage (FOD). This overall program objective will be accomplished in two phases. The goal of the first phase will be to determine the mechanisms and relative importance of the various degradation and failure modes, and to develop and verify the methodology to predict predominant mode failure life in turbine airfoil applications. Phase I will employ an empirically based correlative model relating coating life to parametrically expressed driving forces such as temperature and stress. The effort in this phase will be accomplished in three tasks: failure mode determination (Task I), modeling (Task II), and substantiation testing (Task III). This Phase currently is in the material procurement, specimen preparation and initial testing stages. Phase II will experimentally verify Phase I models and develop an integrated, mechanistically based life prediction model including all relevant failure modes.

The two-layer TBC system being investigated, designated PWA264, currently is in commercial aircraft revenue service. It consists of an inner low pressure chamber plasma-sprayed NiCoCrAlY metallic bond coat underlayer (4-6 mils) and an outer air plasma-sprayed 7 w/o Y_2O_3 - ZrO_2 (8-12 mils) ceramic top layer. The TBC system is shown in figure 1. The composition and structure of this coating are based in part on effort conducted under previous NASA sponsored programs (ref. 1 and 2).

Phase I, Task I - Failure Mechanism Determination

The Phase I, Task I investigation is designed to evaluate the relative importance of various thermomechanical and thermochemical failure modes, focusing on thermal stress cycling, oxidative degradation, and their potential interaction. The primary experimental method to be employed in this investigation is cyclic burner rig testing. Static furnace exposure tests also will be included to evaluate the relative importance of oxidation and other thermal exposure effects. At the conclusion of this task, a preliminary life prediction model will be developed on the basis of the experimental data generated.

Phase I, Task I - Experimental Design and Test Plan

The experimental plan for this Task is based on a thorough review of the literature pertaining to thermal barrier coating degradation and failure modes, and on careful evaluation of damage observed on laboratory and engine-exposed thermal barrier coated hardware. This review identified ceramic spallation resulting from formation of a dominant crack in the ceramic phase, parallel to and adjacent to, but not co-incident with, the metal-ceramic interface, as the primary mode of thermal barrier coating failure. This cyclic cracking failure mode clearly is influenced by thermal exposure effects, as shown by results of experiments conducted to study

thermal pre-exposure and thermal cycle-rate effects (ref. 3 through 6). Various mechanisms have been proposed to account for these thermal exposure effects, including oxidation, time-dependent bond coat flow, ceramic sintering, changes of ceramic phase distribution, etc. Oxidation is important, as shown by comparison of inert environment and air pre-exposure effects and by the observation of significant oxidative degradation on failed laboratory test specimens. However, it is also interesting that significantly less oxidation degradation is observed on failed engine test components than on laboratory specimens. Evaluation of engine exposed coatings also shows essentially no ceramic sintering.

The Task I test plans shown in figures 2, 3, and 4 are designed to identify the relative importance of the various potential thermal barrier coating degradation modes discussed above. Included in this test plan are static furnace and cyclic burner rig thermal exposure tests, with the cyclic tests being conducted with both clean and contaminated fuels to assess the relative importance of hot corrosion induced ceramic spallation (ref. 7 through 10). Static furnace tests will be conducted both in air and in a non-oxidizing environment to separate the influence of oxidation from other potential thermal exposure effects. To determine the relative importance of thermal exposure and cyclic thermal stress effects, cyclic burner rig tests will be conducted at two cycle rates, on as-fabricated coatings, and on coatings pre-exposed in oxidizing and non-oxidizing environments. The influence of cyclic thermal stress level will be studied by varying peak test temperature, transient heating rate, and ceramic thickness. Also included in this plan is a fractional exposure test which will involve destructive examination of unfailed coatings exposed for various fractions of the anticipated ceramic spalling life. These observations will provide information about the nature and rate of coating damage accumulation.

Phase I, Task I - Instrumentation and Coating Property Measurements

The design of the specimen to be employed for cyclic burner rig testing is shown in figure 5. To provide temperature distributions required for Task I preliminary life prediction modeling, an instrumented specimen will be run at the beginning of each Task I burner rig test. The design of this instrumented specimen, presented in figure 6, provides for temperature measurement at the ceramic surface and at a location approximately 10 mils below the metal-ceramic interface in five equally distributed circumferential locations. These temperature measurements will provide boundary values for transient thermal and structural finite element analyses of coating temperature and strain (stress) distribution.

To provide necessary material properties for thermal and stress analyses, selected mechanical, thermomechanical and physical property tests will be conducted in Task I. These tests will be conducted on bulk ceramic or metallic (bond-coat composition) specimens fabricated by plasma application of thick coating deposits on mild steel panels. These panels will be machined to remove the steel substrate and to form "thick coating" blanks to required test specimen dimensions. Initial ceramic test panels have been fabricated; as shown in figure 7, the structure produced in these panels provides a relatively good approximation of the desired thin coating structure shown in figure 1.

Phase I, Task I - Analysis and Verification Testing

To assess the relative importance of various failure modes studied in the Task I experimental plan, empirically-based correlative life prediction models will be developed to independently predict life for each mode. Using a typical engine mission cycle, these models will be applied to independently predict mission cycle coating life for each failure mode. Predicted lives will be compared to determine the importance of each failure mode.

Based on results of this assessment an interactive prediction model will be developed to account for the predominant modes of coating degradation and failure. This preliminary life prediction system will be based on relatively simple interactive modes such as linear or damage summation.

To verify the preliminary prediction model, additional burner rig tests will be conducted using test parameters and methods which are different from those used to generate the data on which the model in based. The test method will involve exposure of a single rotating specimen located in the center of the burner rig spindle. This will improve and simplify temperature measurement and control, and will eliminate circumferential thermal gradients which are inherent to the multiple specimen configuration used earlier in this task. To improve the simulation of airfoil conditions the specimen will be hollow and incorporate internal cooling, thus providing a steady state thermal gradient across the TBC. Three sets of test parameters will be selected to simulate typical airfoil mission cycles. The specimen geometry has a 1-inch outside diameter (O.D.), with a 1/2-inch inside diameter (I.D.) and is approximately 5 inches long. The specimen geometry is shown in figure 8.

Phase I, Task II - Major Mode Life Prediction Model

The Task II objective is to design, conduct and analyze experiments to obtain data for major mode life prediction model development. Design of the experiments will be based on results of Task I. Test parameters will cover the range of parameters anticipated on thermal barrier coated turbine components. Transient thermal and stress analyses will be conducted for each test condition. The results will be used to construct life prediction models for the predominant failure modes. For this task a minimum of 20 single-specimen, cooled burner rig tests will be conducted to obtain major mode life prediction model development.

The test method will be the same as for Task I verification testing. This method involves clean fuel or ducted burner rig testing of a single tube rotating about its axis, with internal cooling and external burner heating (figure 8). Variables to be studied include maximum surface temperature, thermal gradients, cycle duration, transient rates, ceramic thickness, virgin and pre-exposed ceramic, and clean fuel versus corrosive environment. Test parameters will be varied to cover the range of parameters anticipated on thermal barrier coated turbine components. A combination of thermocouple data and thermal analysis will establish the transient temperature distribution for each combination of test parameters.

Transient thermoelastic analysis will be used to develop a correlative model. Utilizing the MARC program, transient thermal analysis as well as stress analysis will be developed and modified for the rotating tube specimen test. MARC provides elastic, elastic-plastic, creep, large displacement, buckling and heat transfer analysis capabilities. Dimensional analysis of parameters which characterize the

C-3

data base (loading, specimen geometry, material properties, and number of cycles to failure) will be conducted. Multiple linear and nonlinear regression techniques are to be used to obtain the best correlation between the established parameter groups. Analytical studies of the stress increase in the ceramic layer due to oxidation of the bond layer will be conducted to account for the effects of oxidation. Multiple linear and nonlinear regression will be conducted to correlate parabolic oxidation of the bond layer and time to spallation of ceramic as functions of temperatures of bond layer and ceramic. Also, a unified correlation model will be developed so that all failure modes and their ranges are accounted for, with thermal cyclic stress as the main failure mode. Creep and long time exposure, with some periodic cyclic effects, will also be incorporated.

Phase I, Task III - Model Verification

The validity of models developed in Task II will be assessed in Task III through a series of approved benchmark engine mission simulation tests. The basis for judgment of model validity will be how closely the model predicts TBC life for each benchmark engine simulation test. If necessary, recommendations for further research or refinement required for satisfactory engine life prediction methodology will be made.

Phase II - Design Capable Life Models

Phase II objectives (Tasks V through IX) are to develop and verify integrated design-capable life prediction models accounting for all important contributions to coating failure. Continuum and fracture mechanisms life prediction models based on material properties and analysis of load resulting from the coating system, including the effects of thermal exposure on component properties, will be done in Task V. Task VI will develop oxidation and hot corrosion failure models under both steady state and simulated engine conditions. Task VII will generate a data base from which erosion and FOD life prediction models can be developed. Task VIII and IX develop and verify integrated design, causal life prediction models using correlation, continuum mechanics and fracture mechanics methodologies.

REFERENCES

1. Sheffler, K.D.; Graziani, R.A.; and Sinko, G.C.: JT9D Thermal Barrier Coated Vanes. NASA CR 167964, April 1982.

2. Anderson, N.P; and Sheffler, K.D.: Development of Strain Tolerant Thermal Barrier Coating Systems. Final Report, Contract NAS3-22548. 1982.

3. McDonald, G.; and Hendricks, R.C.: Effect of Thermal Cycling on $ZrO_2-Y_2O_3$ Thermal Barrier Coatings. Thin Solid Film. V.73, 1980, p. 491.

4. Gedwill, M.A.: Burner Pig Evaluation of Thermal Barrier Coating Systems for Nickel-Base Alloys. NASA-TM 81685, February 1981.

5. Miller, R.A.; and Lowel, C.E.: Failure Mechanisms of Thermal Barrier Coatings Exposed to Elevated Temperatures. NASA TM 82905, April 1982.

6. Miller, R.A.: Oxidation-Based Model for Thermal Barrier Coating Life. Ceramic Journal. 1984, pp. 83-87.

7. Grisaffe, S.J.; and Levine, S.R.: Proceedings of First DOE/EPRI Conference on Advanced Materials for Alternative Fuel Capable Directly Fired Heat Engines. Castine, ME. 1979, p. 680.

8. Bratton, R.J.; et. al.: Evaluation of Present Day Thermal Barrier Coatings for Industrial/Utility Applications. Thin Solid Films. 73, 1980, p. 429.

9. Hodge, P.E.; et. al.: Evaluation of the Hot Corrosion Behavior of Thermal Barrier Coatings. Thin Solid Films. 73, 1980, p. 447.

10. Bevan, C.E.: Development of Advanced Plasma Sprayed Ceramic Coatings for Industrial Gas Turbine Engines. Final Report, Contract B-A0747-A-Z. PWA 5906, July 1982.

TABLE I
TASK I COATING PROPERTY TESTS

	As Deposited Ceramic	As Deposited Bond Coat
Elastic Constants	4 temperatures (1000°F, 1300°F) (1600°F, 2100°F)	
Thermal Conductivity	3 temperatures (1000°F, 1600°F, 2100°F)	3 temperatures (1000°F, 1600°F, 2100°F)
Specific Heat	3 temperatures (1000°F, 1600°F, 2100°F)	3 temperatures (1000°F, 1600°F, 2100°F)
Stress Rupture (4 point bend)	4 stress/temperature combinations (1000°F, 1300°F) (1700°F, 2100°F)	--
Creep (4 point bend)	9 stress/temperature combinations (1000°F, 1600°F, 2100°F)	-- --
Sintering Shrinkage	2 temperatures (1000°F, 2100°F)	2 temperatures (1000°F, 2100°F)
Isothermal LCF	-------	9 temperature/strain range combinations (1000°F, 1400°F, 2100°F)
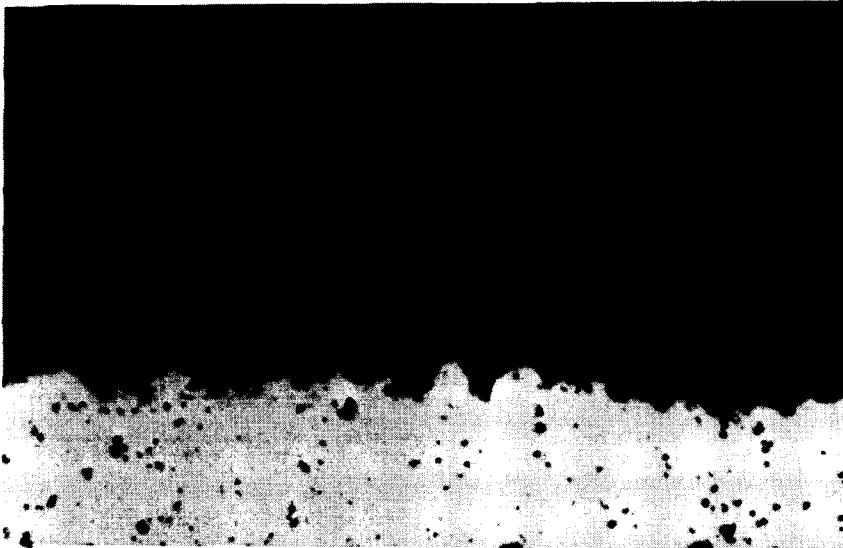
Figure 1   Light Photomicrograph Showing PWA264 Microstructure 200X

TEMPERATURE	OXIDIZING ATMOSPHERE		NON-OXIDIZING ATMOSPHERE	
	STATIC FAILURE	FRACTIONAL EXPOSURE	STATIC FAILURE	FRACTIONAL EXPOSURE
2200°F (T_3)	① B	② ✕	③ ✕	④ ✕
2100°F (T_2)	⑤ A_1	⑥ C	⑦ A_2	⑧ ✕

MINIMUM OF TWO (2) COUPONS PER BLOCK

TEST CONDITIONS SHOWN THUS: ⬚✕   NOT TO BE EVALUATED

Inspection Interval		Hours
B	=	10
A_1	=	10
A_1	=	80
A_2	=	80

Figure 2   Task I Furnace Exposure Test Plan to Evaluate Thermal Barrier
Coating Static Failure Life

181

MAXIMUM CYCLE TEMPERATURE	TRANSIENT HEATING RATE	SHORT CYCLE		LONG CYCLE	
		CYCLE TO FAILURE	FRACTIONAL EXPOSURE	CYCLE TO FAILURE	FRACTIONAL EXPOSURE
2050°F (T_2)	FAST (60 SEC.)	(9) D_1	(10) G	(11) F	(12) X
	SLOW (180 SEC.)	(13) E	(14) X	(15) X	(16) X
1950°F (T_1)	FAST (60 SEC.)	(17) D_2	(18) X	(19) X	(20) X
	SLOW (180 SEC.)	(21) X	(22) X	(23) X	(24) X

CONDITION D,E,F — 12 SPECIMENS PER TEST:

4 — 10 MIL VIRGIN CERAMIC ("BASELINE" COATING)
2 — 5 MIL VIRGIN CERAMIC
2 — 15 MIL VIRGIN CERAMIC
2 — 10 MIL AIR PRE-EXPOSED CERAMIC
2 — 10 ARGON PRE-EXPOSED CERAMIC
12 TOTAL

CONDITION G: FRACTIONAL EXPOSURE TEST — See Text For Explanation.

Figure 3   Cyclic Burner Rig Test Matrix

	LOW CORRODANT LEVEL	HIGH CORRODANT LEVEL
CYCLE TO FAILURE	(25) J	(26) H
FRACTIONAL EXPOSURE	(27) X	(28) K

Figure 4   Cyclic Hot Corrosion Testing Matrix

182
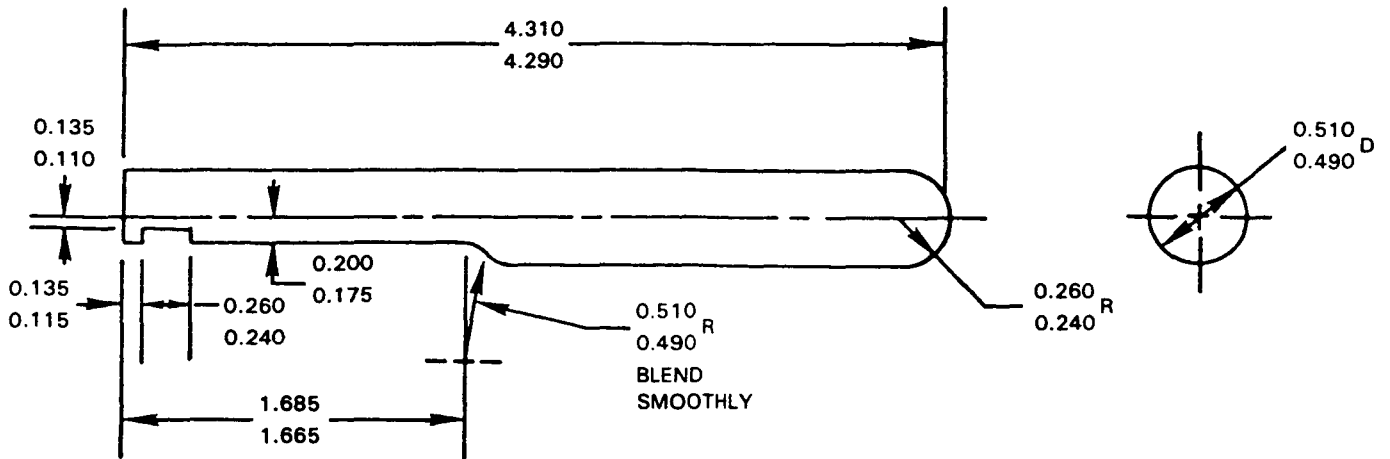
All Dimensions Shown In Inches

Figure 5 Cyclic Burner Rig Specimen
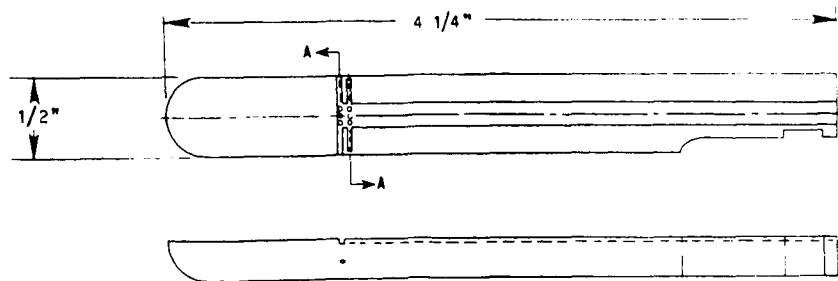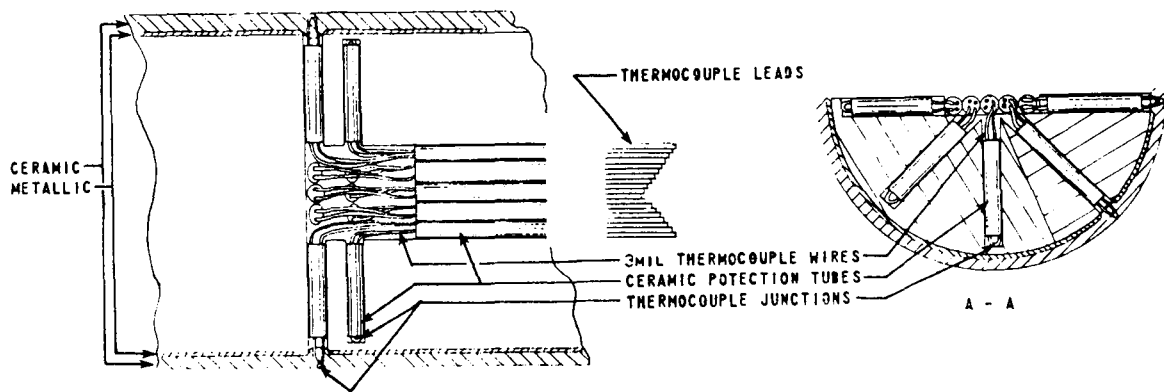
Figure 6 Thermocoupled Calibration Specimen Geometry
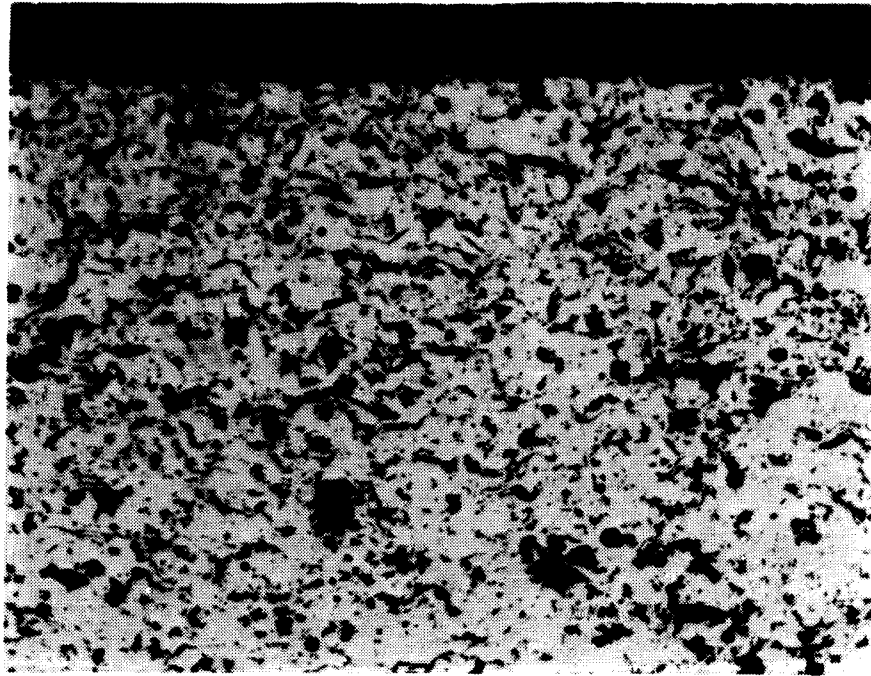
Figure 7   Bulk Specimen Microstructure 200X

All Dimensions Shown In Inches

$\frac{1.010}{0.090}$ DIA

$\frac{0.150}{0.490}$ DIA

$\frac{5.020}{4.080}$ REF
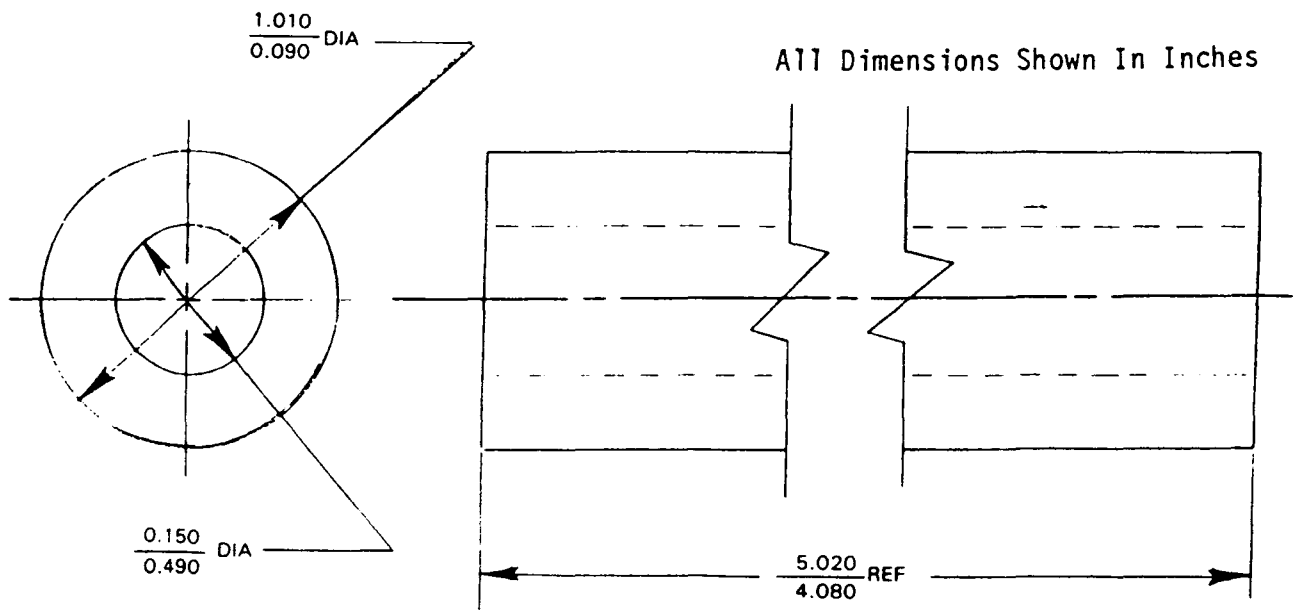
Figure 8   One-Inch Hollow Single Rotating Internally Specimen Geometry

184

AEROTHERMAL MODELING PROGRAM - PHASE II

Edward J. Mularz
NASA Lewis Research Center
Propulsion Laboratory, USARTL

Aircraft gas-turbine engine manufacturers have achieved substantial increases in performance of their engines in recent years. These performance increases are due largely to the use of advanced component designs and materials. The use of materials with higher temperature capabilities and the use of advanced liner cooling schemes have allowed the operation of the combustor at higher exit plane temperatures. Incorporating these improvements into the turbine engine has resulted in the hot-section parts being exposed to increasingly higher temperature and pressure levels. These levels produce an environment that is increasingly hostile to the hot-section components.

While the hot-section components account for only 20 percent of the engine's total weight, they account for nearly 60 percent of the engine's maintenance costs. The components most susceptible to damage have been shown to be the combustor liner and turbine airfoils. Clearly, the engine designer must increase efforts to reduce maintenance costs of these engine components if the United States engine manufacturers are to maintain their place in the competitive world aerospace market.

The predominant failure mode of aircraft gas-turbine combustors of sheet metal louver design has been identified as creep, low-cycle fatigue interaction or cracking. This cracking is caused by the thermal cycling of sections of the combustor liner where a large temperature gradient exists. To alleviate this failure mode, the thermal gradients within the entire combustor liner assembly must be significantly reduced. These gradients are generated by the local radiative and convective heat fluxes within the combustor. Therefore, a thorough understanding and characterization of these fluxes must be developed in order to determine current stress and temperature gradient limits and to design advanced, near-isothermal combustor liners.

To be able to predict the aerodynamic flow field of the combustor, the local heat fluxes, and, therefore, the liner life, several physical phenomena must be better understood. First, the aerothermal model chosen to analytically simulate the combustor must accurately predict the combustor's aerodynamic flow field. The previous, phase I effort of this program documented that current models can qualitatively predict the complex three-dimensional flow fields within a combustor. Quantitative modeling of these flows, however, requires the reduction of both computer execution times and the removal of numerical diffusion in the calculations. As more efficient numerical schemes appear, one can then effectively investigate areas such as scalar transport in the interaction of various flow streams and such as the development of the fuel spray and its interaction with the surrounding airstream.

The phase II effort is directed at improving the accuracy and validity of the analysis methods needed by designers of gas-turbine combustors. Following the successful development and validation of these improved analysis methods, the United States engine manufacturers can then proceed with confidence to incorporate these

methods into their design systems. The use of these improved design systems should result in United States produced gas-turbine engines of superior performance and durability in the 1990's.

The overall objective of the Hot-Section Technology Aerothermal Modeling Program - Phase II is to improve the accuracy and utility of current aerothermal models for gas-turbine combustors. Three thrusts are identified:

(1) <u>Improved numerical methods for turbulent viscous recirculating flows</u>. - The three contractors from phase I all stated that improvements in accuracy and speed of convergence of combustor analytical models is necessary before the codes can become capable of producing quantitative, rather than qualitative, predictions of the combustor flow fields. In this effort improvements are being sought in both solution algorithms and differencing schemes. Present hybrid-upwind finite difference schemes possess excessive numerical diffusion errors which preclude accurate quantitative calculations. The advanced numerical techniques being considered should have improved efficiency (smaller error for the same computational time) over present codes.

(2) <u>Flow interaction experiment</u>. - The philosophy adopted in phase I was to assess the gas-turbine combustor aerothermal models using the constituent flow approach, that is, to evaluate submodels separately against simple flows which could be identified as relevant to the gas-turbine combustor. Among the examples of constituent flows against which the models were assessed were swirling flows and jets in crossflow. Although the performance of the models suggested that improvements are needed, notably with regard to eliminating false diffusion in three-dimensional calculations, it also was deemed appropriate to pursue a flow interactions experiment, with suitably defined and measured boundary conditions, against which state-of-the art and improved models could be evaluated. Consideration of the gas-turbine combustor suggests that the interaction of jets in a confined crossflow with a swirling flow would be an appropriate experiment in that this interaction is a characteristic of, and is expected to be important in, current and future gas-turbine engine combustion chambers. Such an experiment is underway with analytical modeling used to predict the results. Improvements to the physical model will be considered after the numerical and experimental results are analyzed.

(3) <u>Fuel injector-air swirl characterization</u>. - Fuel injection plays an important part in the design of combustors for gas-turbine engines. Durability can be reduced by nonuniformities produced at the fuel injector. Nonuniformities can produce hot streaks that overheat sections of turbine vanes, adversely affecting their life. Nonuniformities can also produce rich zones that increase soot and the radiative heat load that reduce the durability of the combustor liner. The ability to understand and model the fuel injection process plays a critical part in the design of high-performance, durable engines. Fuel injection is a complex phenomena, and initial formation of a fuel spray cannot be predicted or modeled in the vicinity of the fuel injector with the present analytical computer models. The sheets or ligaments of fuel break up into droplets downstream of the fuel injector. It is at this point that the two-phase flow field can begin to be modeled. To assess these models, however, a well-controlled experiment is needed to provide the benchmark data. Modern gas-turbine combustors typically use an air swirler-fuel injector combination to create an efficient burning zone. Previous fuel-injection experimental and analytical efforts have not included the interaction of the air swirler with the fuel injector. It is the purpose of this effort to perform experimental research on two-phase flow interactions to support analytical modeling of the dome region of the combustor. To establish that the experiments and data are appropriate, a sensiti-

vity analysis of the major variables is to be made using a state-of-the art model. After the sensitivity analysis, the experimental program will be carried out to generate data for an improved model. Should the experiment include taking data with unproven instrumentation (for example, individual droplet velocities with laser anemometry), an additional task will be to verify those measurements. Improvements to the physical model will be considered after the numerical and experimental results are analyzed.

MASS AND MOMENTUM TURBULENT TRANSPORT EXPERIMENTS

B. V. Johnson and R. Roback
United Technologies Research Center

INTRODUCTION

An experimental study of mixing downstream of axial and swirling coaxial jets is being conducted to obtain data for the evaluation and improvement of turbulent transport models currently employed in a variety of computational procedures used throughout the propulsion community. The nonswirling coaxial jet study was completed under Phase I and is reported in Reference 1. The swirling coaxial jet study was conducted under Phase II of the contract and is reported in Reference 2. A TEACH code was acquired, checked out for several test cases, and is reported in Reference 3. A study to measure length scales and to obtain a limited number of measurements with a blunt trailing edge inlet is being conducted under Phase III of the contract and HOST sponsorship. Results from Phases I and II have also been presented in References 4, 5 and 6.

PHASE III OBJECTIVES

The Phase III effort was directed toward (1) the aquisition of length scale and dissipation rate data that will provide more accurate inlet boundary conditions for the computational procedures and a data base to evaluate the turbulent transport models in the near jet region where recirculation does not occur and (2) the acquisition of mass and momentum turbulent transport data with a blunt inner-jet inlet configuration rather than the tapered inner-jet inlet employed in Phases I and II.

Mass and momentum turbulent transport data was obtained downstream of the blunt inner-jet inlet configuration, using the laser velocimeter/laser induced fluoresence measurement techniques employed in the previous experiments with swirling and nonswirling flow conditions. The velocities, concentrations, mass turbulent transport and momentum turbulent transport results obtained downstream of the blunt inner-jet inlet configuration for the nonswirling flow condition were not significantly different from those obtained with the tapered inner-jet inlet. The results will be presented and compared with the Reference 1 results in the forthcoming Phase III interim summary report.

The measurement technique generally used to obtain approximate integral length and micro scales of turbulence and dissipation rates was recently computerized at UTRC. This computerized data aquisition and reduction procedure was then used to obtain length scale and dissipation rate data for three test configurations. The data and results obtained with the tapered inner jet inlet configuration and the nonswirling flow condition will be discussed in the following sections.

LENGTH SCALE AND DISSIPATION RATE MEASUREMENTS

Data Analysis Formulation

With Taylor's hypothesis, the temporal variation of a one dimensional velocity fluctuation is related to a spatial variation by the convective velocity, U. This is also referred to as the frozen-turbulence approximation (Ref. 7). The auto-correlation is defined

$$R(\tau) = u(t) \; u(t+\tau)/u'^2$$

An integral scale and an approximate micro scale of turbulence and an eddy dissipation rate are related to the autocorrelation. The integral scale of turbulence is:

$$L1 = U \int_0^\infty R(\tau) \, d\tau$$

A second integral scale of turbulence is also obtained directly from spectrum (Ref. 7)

$$L2 = (U/4) \lim_{n \to 0} [E(n)/u'^2]$$

The microscale length of turbulence, λ, is defined as the intercept of the parabola that matches $R(\tau)$ at $\tau = 0$, i.e.,

$$R(\tau) = 1 - (\tau U/\lambda)^2$$

The dissipation rate, ϵ, is related to the microscale of turbulence, the rms velocity and the fluid kinematic viscosity, :

$$\epsilon = 30 \; \nu u'^2/\lambda^2$$

Although the autocorrelation/microscale relations shown above will lead to a dissipation rate, the determination of the curvature of $R(\tau)$ at $\tau = 0$ is often difficult and sometimes ambiguous. Another relationship for the dissipation rate is obtained directly from the one-dimensional velocity turbulent energy spectra

$$1/\lambda^2 = (2\pi)/(U^2 u'^2) \int_0^\infty n^2 \, E(n) \, dn$$

where $E(n)$ is the turbulent kinetic energy per frequency cycle of one velocity component at frequency n. Thus the approximate dissipation rate is more easily obtained with an independent spectrum measurement.

An autocorrelation for the spectral data is also constructed from the Fourier transform of the energy spectral distribution using a computer routine which is part of the data reduction program. The Fourier transform which produces the spatial correlation is

$$R(\tau) = \int_0^\infty e^{i\tau\omega} \, E(\omega) \, d\omega$$

The information flow chart for the computerized length scale measurement technique is shown in Figure 1.

Test Conditions and Apparatus

The length scale and dissipation rate measurements were conducted in the UTRC coaxial flow facility (Figure 2) using water as the working fluid. The flow conditions and geometries were identical to those employed in Reference 1, i.e. U (inner) = 0.52 m/s and U (annular) = 1.66 m/sec and with a Reynolds number of 35,000 based on the duct diameter and the average velocity.

A sketch of the inlet and measurement locations is shown in Figure 3. The swirler was not installed for the measurements discussed herein. Mean, fluctuating and spectral measurements of the axial velocity were obtained in the regions without recirculation at z = -41, 5, 51 and 102 mm from the inlet plane. Mass and momentum turbulent transport data was obtained at the latter three locations during Phase I (Reference 1). Standard hot film constant resistance measurement procedures were used to aquire the data. The water was filtered to prevent particles in the water from attaching to the probe and altering the probe calibration curve.

Results

The mean and fluctuating axial velocity measurements obtaining at the four axial locations are presented in Figures 4 and 5 and compared with results from Reference 1 obtained with a laser velocimeter. The agreement between the two sets of measurements is excellent. The conclusion from this comparison is that the hot film data aquisition and reduction procedure for obtaining mean and fluctuating velocities reproduces the previous results with acceptable accuracy.

The dissipation rate distributions for the four axial locations are presented in Figure 6. Note the dissipation rates at the center of the inner jet and the annular jets are approximately the same at z = -41 and 5 mm from the inlet plane. At z = 5.1 mm, the dissipation rate across the inlet varies by 2 1/2 orders of magnitude. This radial variation decreases to less than one order of magnitude (by increasing the lower dissipation rates and decreasing the higher dissipation rates) at z = 102 mm from the inlet plane. As expected the locally high and low dissipation rates are associated with high and zero axial velocity shear rates, respectively.

The integral length and micro scales of turbulence are presented in Figure 7. The integral scales L1 and L2, defined on the figure, were both determined as part of the computerized data reduction procedure. Note that the integral scales determined by both methods are in generally good agreement. The largest difference between the two scales is about 20 percent and occured at z = 102 mm. This is a location with long wave length eddies occuring over a moderate frequency range. The differences between the two integral length scales are generally less than ten percent with the integral scale determined from the integration of the auto correlation always being greater. The integral scales of turbulence in the inner jet inlet were 9 to 12 mm, approximately half the tube diameter and compatible with length scales reported in Reference 7 for previous work by Laufer.

The micro scales of turbulence ,λ, were 15 to 40 percent of the integral length scales. The ratio of micro scale to integral scale inside the inlet duct (z = -41 mm) was somewhat greater than measured by Laufer for a two-dimensional duct, i.e. : 15 percent of the UTRC circular duct diameter compared to 10 percent of the Laufer 2-d slot height. Thus, the present results in the duct appear to be reasonably

191

compatable with previous studies. The micro scale of turbulence does not vary much
(1 < λ < 3.8mm) compared to the integral scale of turbulence. For the two
measurement locations downstream of the inlet, the ratio of the maximum to minimum
microscales (2< λ <4mm) is only half the ratio of the integral length scales
(4.2<L <19).

REFERENCES

1.   Johnson, B. V. and J. C. Bennett: Mass and Momentum Turbulent Transport
Experiments with Confined Coaxial Jets. NASA Contractor Report CR-165574 (Interim
Summary Report), November 1981.

2.   Roback, R. and B. V. Johnson: Mass and Momentum Turbulent Transport Experiments
with Confined Swirling Coaxial Jets. NASA Contractor Report CR-168252 (Interim
Summary Report), August 1983.

3.   Chiapetta, L. M.: User's Manual for a TEACH Computer Program for the Analysis of
Turbulent, Swirling Reacting Flow in a Research Combustor.   UTRC Report
R83-915540-27 prepared under NASA Contract NAS3-22771, September 1983.

4.   Johnson, B. V. and J. C. Bennett: Mass and Momentum Turbulent Transport
Experiments with confined Coaxial Jets.   Presented at Fourth Symposium on Turbulent
Shear Flows, Karlsruhl, September 12-14, 1983.

5.   Johnson, B. V. and J. C. Bennett: Statistical Characteristics of Velocity,
Concentration, Mass Transport and Momentum Transport for Coaxial Jet Mixing in a
Confined Duct.   ASME Journal of Engineering for Gas Turbines and Power. Vol. 106, p.
121-127, January 1984.

6.   Johnson, B. V. and R. Roback: Mass and Momentum Turbulent Transport Experiments
with Confined Swirling Coaxial Jets: Part I.   AIAA Preprint 84-1380.   Presented at
20th Joint Propulsion Conf. Cincinnati, Ohio. June 11 - 13, 1984.

7.   Hinze, J. O.: Turbulence, McGraw-Hill, 1959

FIG. 1

INFORMATION FLOW CHART FOR COMPUTERIZED
LENGTH SCALE MEASUREMENT TECHNIQUE

TSI

MODEL 1050
HOTWIRE
ANEMOMETER

MODEL 1052
LINEARIZER

RMS
METER

TSI MODEL
1210 – 20
HOT FILM
SENSOR

U, u˙

SPECTRAL DYNAMICS
MODEL SD340
MICRO FFT ANALYZER

SAICOR
MODEL 42
CORRELATOR AND
PROBABILITY ANALYZER

DEC
MODEL PDP 11/23S
COMPUTER

PLOTTER

DECWRITER III

R(τ)

E(n)

U, u˙

R(τ), λ, L_e, ϵ

$\int_0^\infty$ E(n) dn
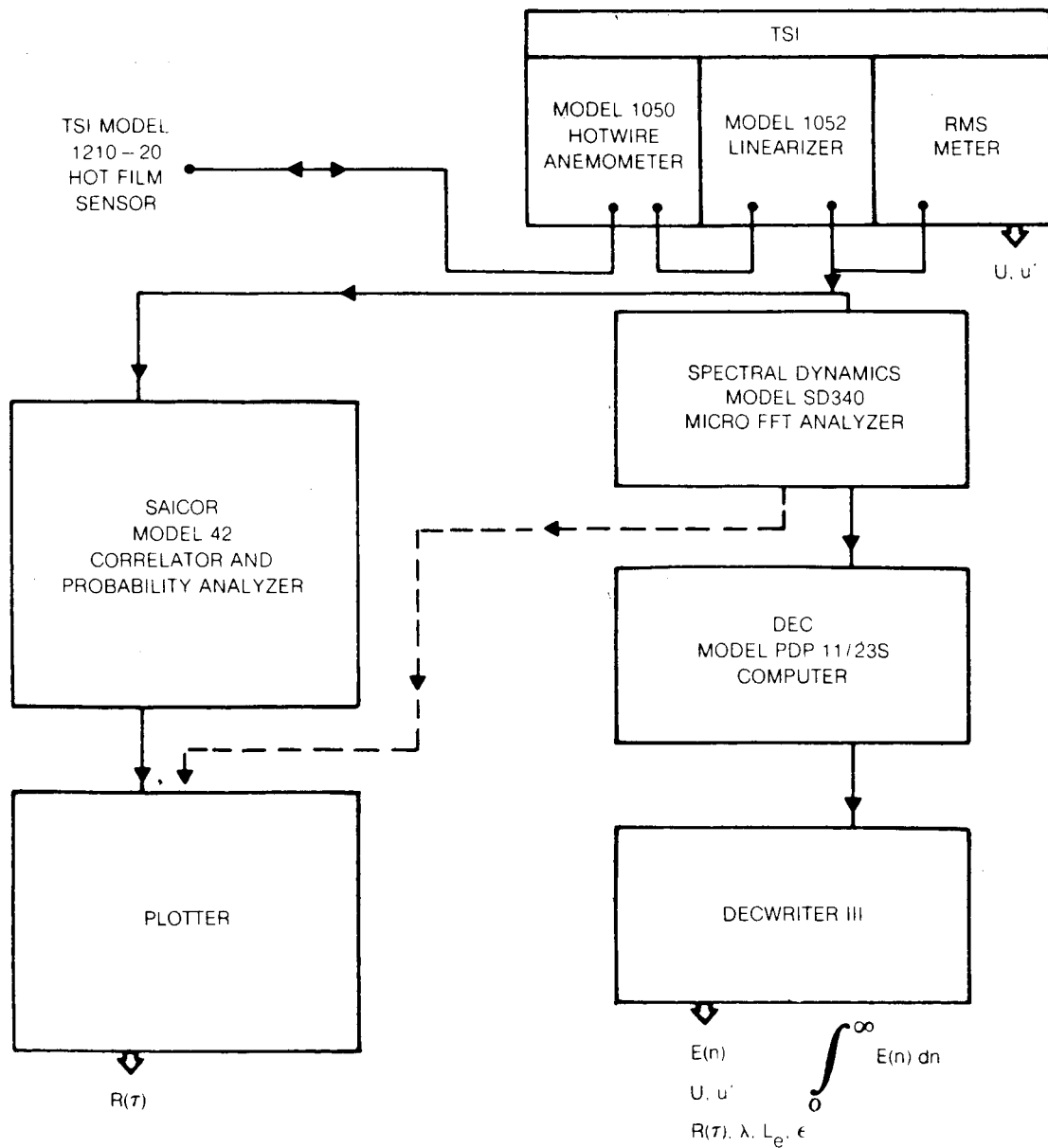
FIG. 2

SKETCH OF COAXIAL FLOW FACILITY

TEST SECTION
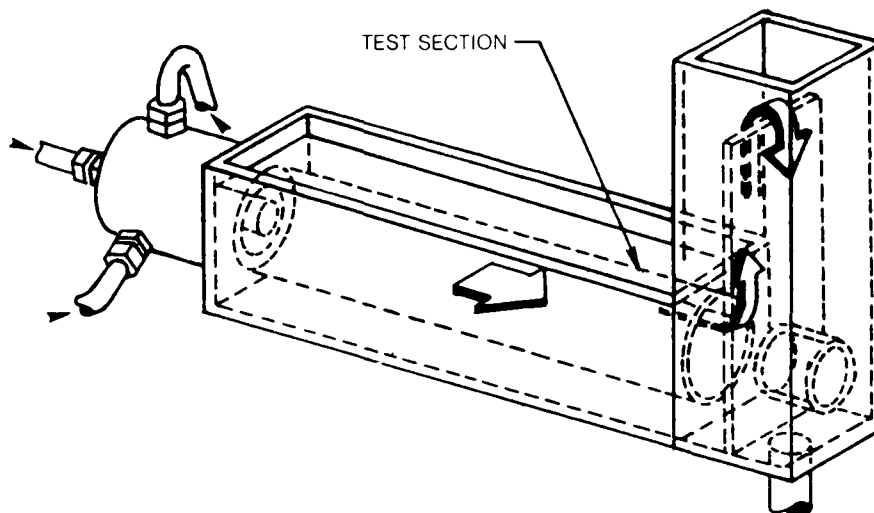
FIG. 3

SKETCH OF LENGTH SCALE MEASUREMENT ARRANGEMENT

SWIRLER EXIT PLANE

MEASUREMENT LOCATIONS

– 51   – 41

5

Z

51   102mm

TSI 1210w
HOT FILM
PROBE

OUTER FLOW

INNER FLOW
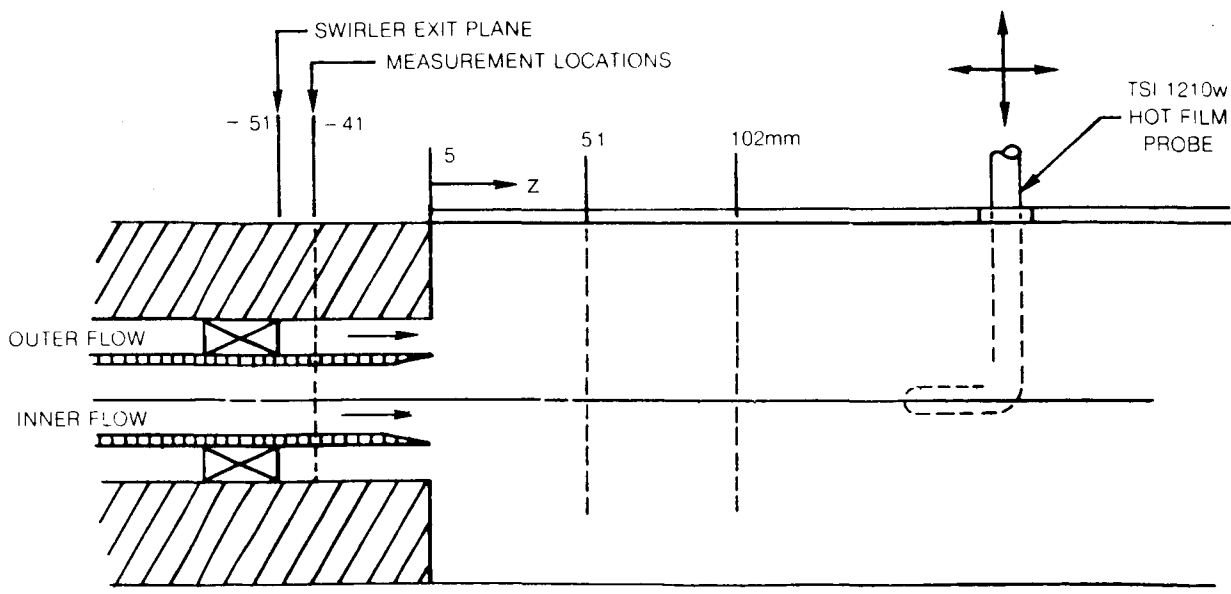
FIG. 4

MEAN AXIAL VELOCITY PROFILES FOR NONSWIRLING FLOW
WITH TAPERED INNER JET INLET

○ HOT FILM
□ LASER VELOCIMETER

z = −41.4mm(−1.63in.)

z = 5.1mm(0.2in.)—HOT FILM
z = 13mm(0.5in.) − LV

RADIUS RATIO, r/R_O

z = 51mm(2.0in.)

z = 102mm(4.0in.)

RADIUS RATIO, r/R_O

MEAN AXIAL VELOCITY, U − m/sec
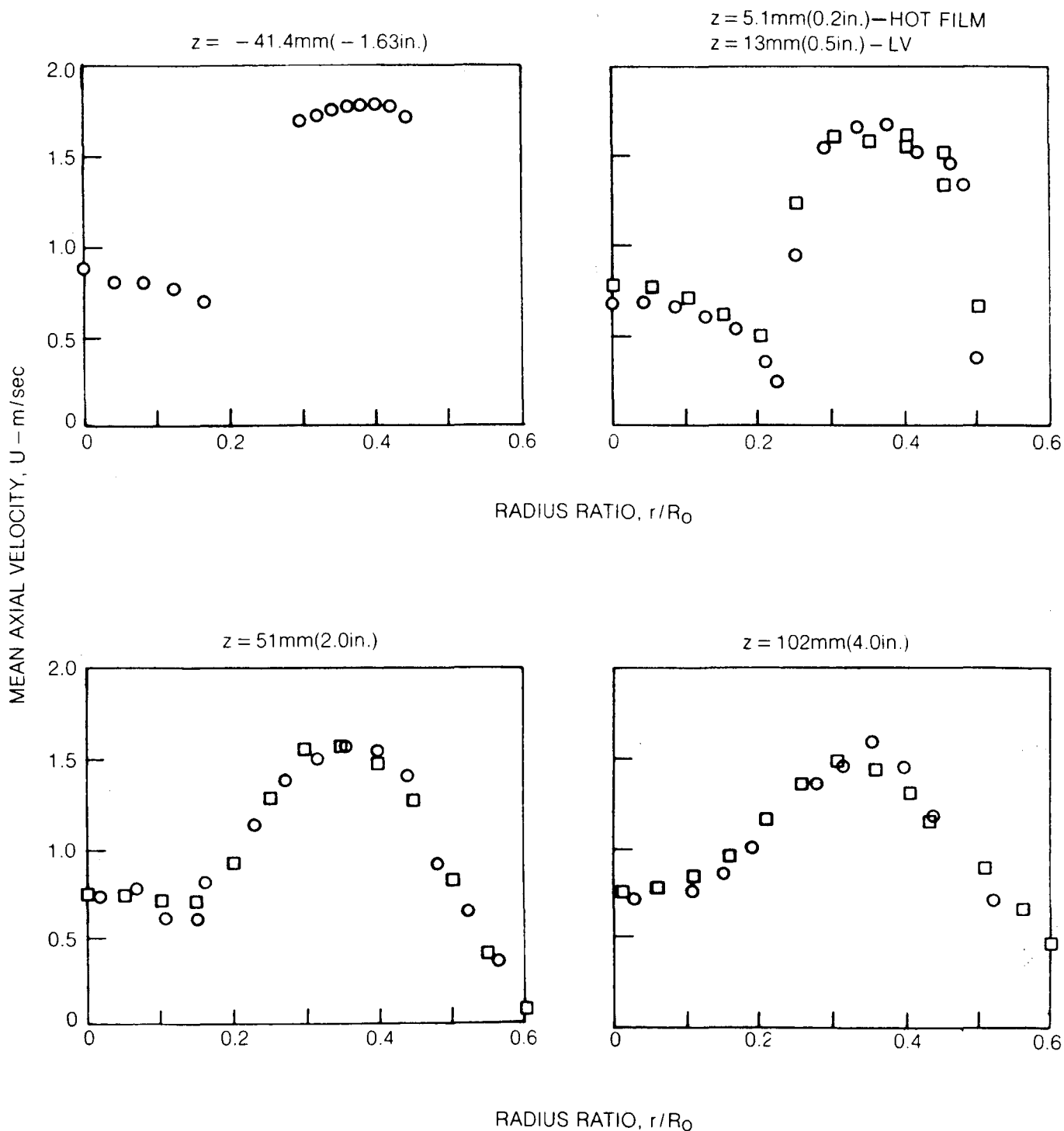
FIG. 5

**FLUCTUATING AXIAL VELOCITY PROFILES FOR NONSWIRLING FLOW
WITH TAPERED INNER JET INLET**

○ HOT FILM
□ LASER VELOCIMETER

z = −41.1mm(−1.63in.)

z = 5.1mm(0.2in.) − HOT FILM
z = 13mm(0.5in.) − LV

RADIUS RATIO, r/R_O

FLUCTUATING AXIAL VELOCITY, u′ − m/sec

z = 51mm(2.0in.)

z = 102mm(4.0in.)

RADIUS RATIO, r/R_O
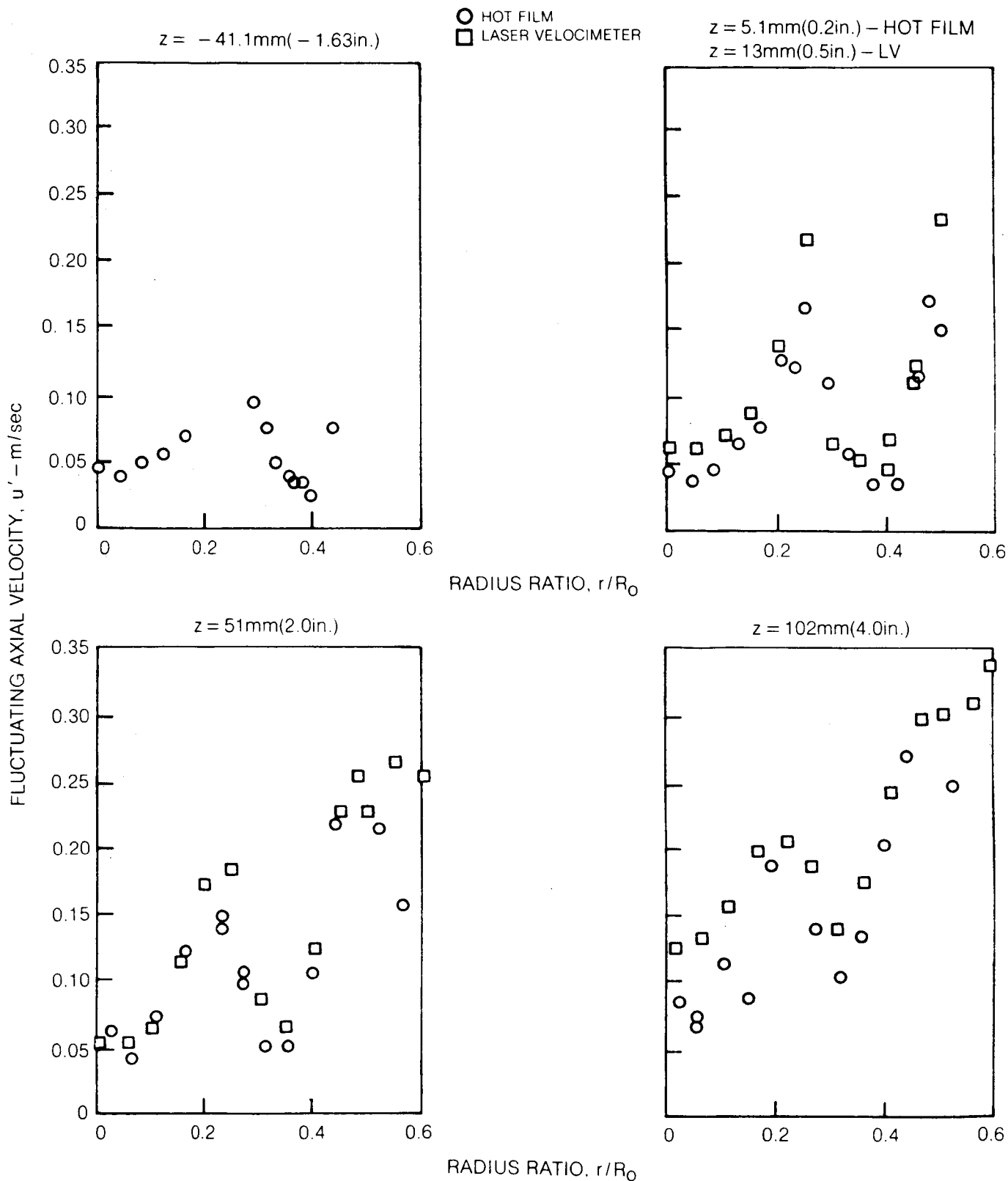
FIG. 6

DISSIPATION RATE FOR NONSWIRLING FLOW WITH TAPERED INNER JET INLET
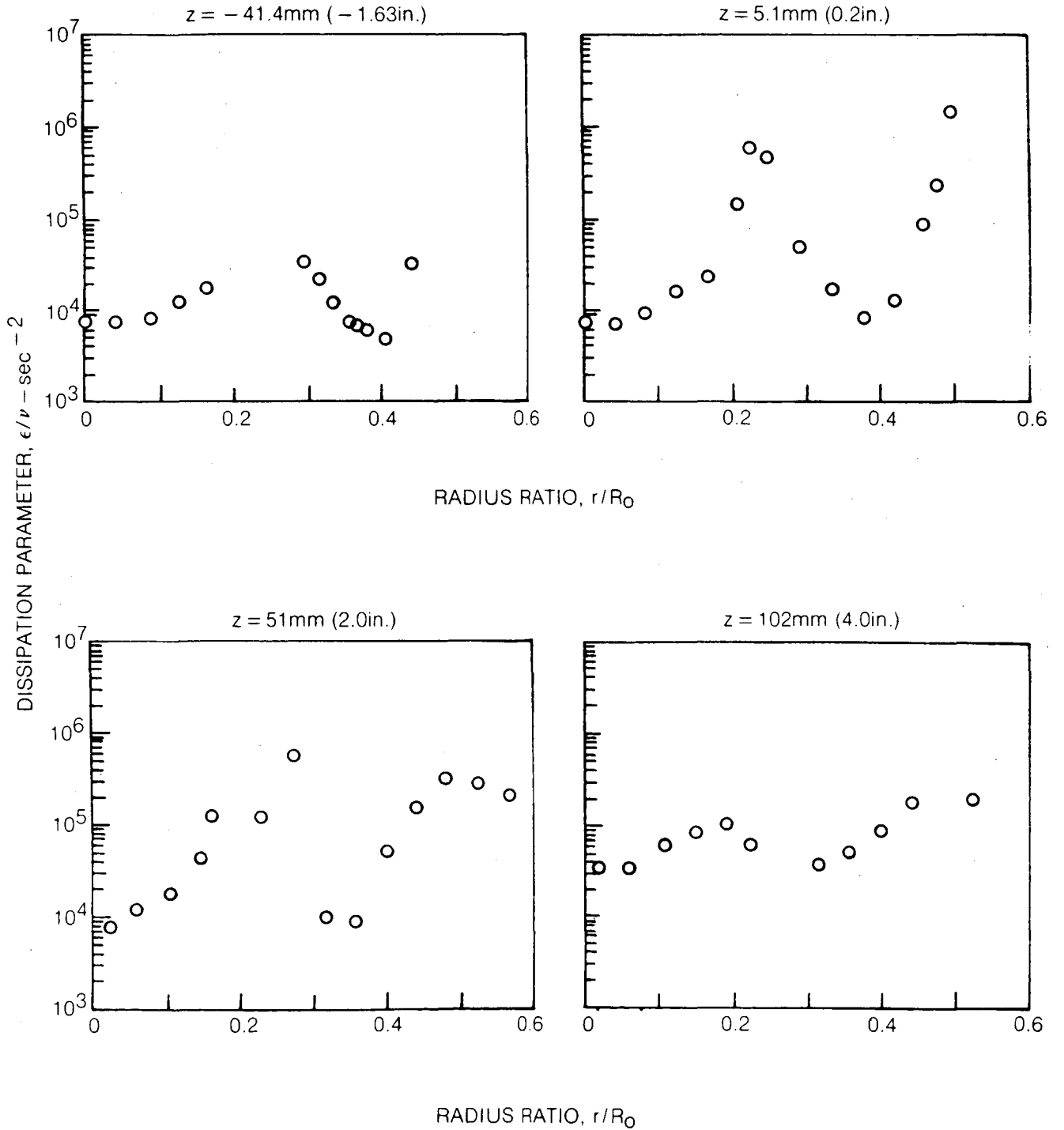
FIG. 7

LENGTH SCALE DISTRIBUTION FOR NONSWIRLING
FLOW WITH TAPERED INNER JET INLET

O MICROSCALE. $\lambda = U u' / [2\pi \int_0^\infty dn\, n^2\, E(n)]^{1/2}$

△ INTEGRAL SCALE. L1 $= U \int_0^\infty R(\tau)\, d\tau$

□ INTEGRAL SCALE. L2 $= (U/4) \lim_{n \to 0}(E(n)/u'^2)$

z = −41.4mm(−1.63in.)

z = 5.1mm(0.2in.)

RADIUS RATIO, r/R$_0$

z = 51mm(2.0in.)

z = 102mm(4.0in.)

LENGTH SCALE – mm

RADIUS RATIO, r/R$_0$
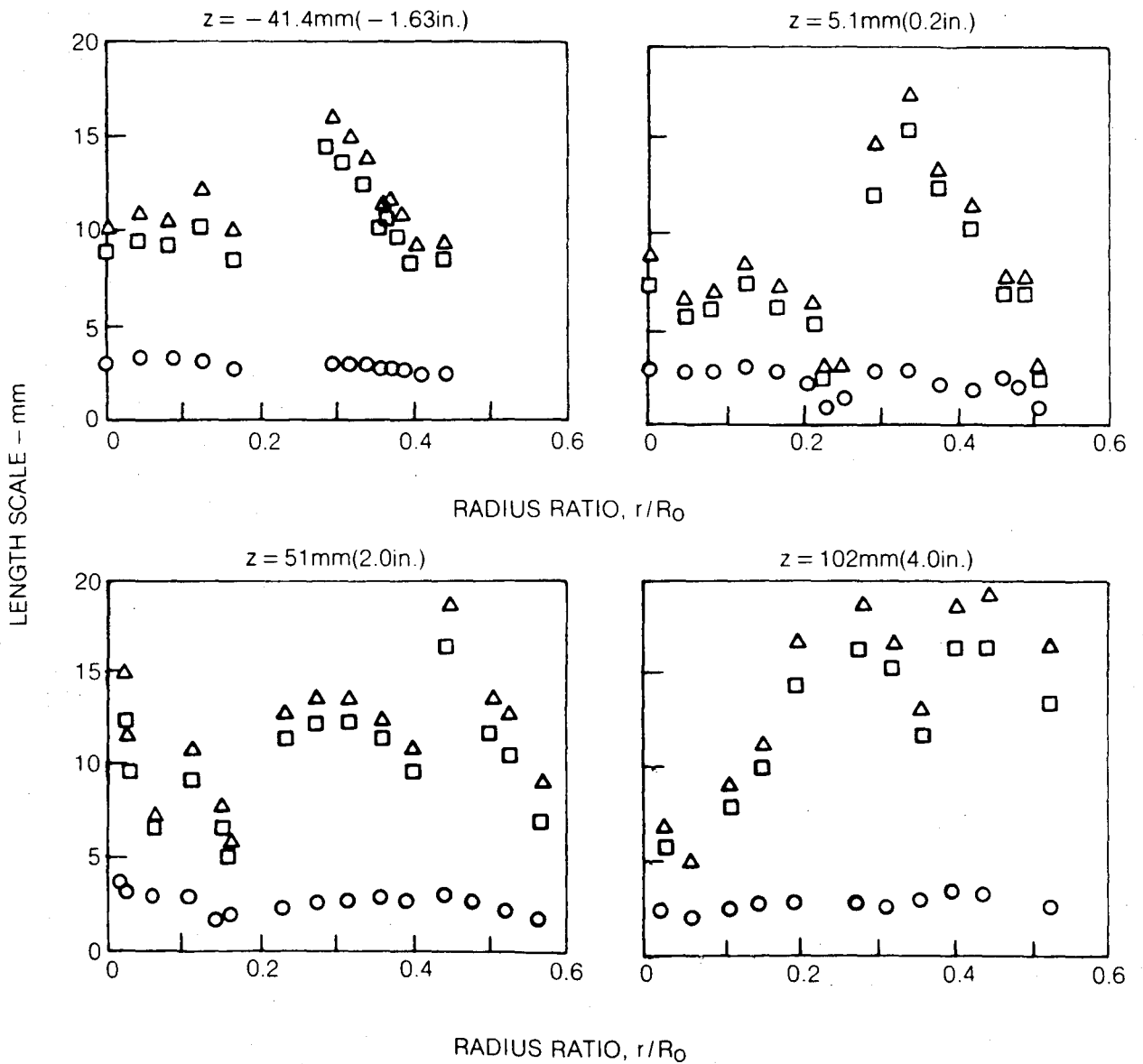
NASA DILUTION JET MIXING - PHASE III

R. Srinivasan, G. Myers, and C. White
Garrett Turbine Engine Company

Many of the gas turbine combustors in operation use multiple rows of dilution jets, and some of them have geometries that are different from circular holes. The data base available in the literature is generally applicable to a single row of circular holes.

On the basis of the data obtained in References 1, 2, and 3, empirical correlations have been developed (References 2, 3, and 4) that provide a very useful design tool. However, these correlations are applicable only within the range of the generating test conditions.

The objectives of the Phase III program are to:

- Extend the data base on mixing of a single-sided row of jets with a confined cross flow.

- Collect data base on mixing of multiple rows of jets with confined cross flow.

- Develop empirical jet mixing correlations.

- Perform limited 3-D calculations for some of these test configurations.

The test portion of Phase III has been completed. The tests were performed with uniform mainstream conditions for several orifice plate configurations. A schematic of the test section and the orifice configurations are shown in Figure 1. The orifice plate plenum has provisions to supply independently controlled air flows to each of the rows of jets. The orifice air supply and the main air supply lines have perforated plates to ensure uniform flow distribution. Temperature and pressure measurements were made in the test section at 4 axial and 11 transverse stations. These measurements were made with a 60-element rake probe. The test results for some of these cases are discussed in this paper.

RESULTS AND DISCUSSION

The temperature field results are presented in three-dimensional oblique views of temperature difference ratio, THETA:

$$THETA = \frac{(T_m - T)}{(T_m - T_j)}$$

where:

T_m = Mainstream Temperature

T_j = Jet Temperature

T = Local Temperature

Figure 2 provides a comparison between the theta distributions for streamlined slots at a jet-to-cross-stream momentum flux ratio, J, of 6.6 and those with equivalent area circular holes at comparable momentum flux ratio. The streamlined slots have deeper jet penetration at X/H_O = 0.5 and 1.0 compared with circular holes. However, at X/H_O = 2.0, both orifice configurations produce very similar temperature distribution. At moderate momentum flux ratios, the streamlined slots overpenetrate to the opposite duct wall, followed by enhanced mixing (Figure 3). The temperature distributions for this case are quite different from those of circular jets at comparable momentum flux ratio.
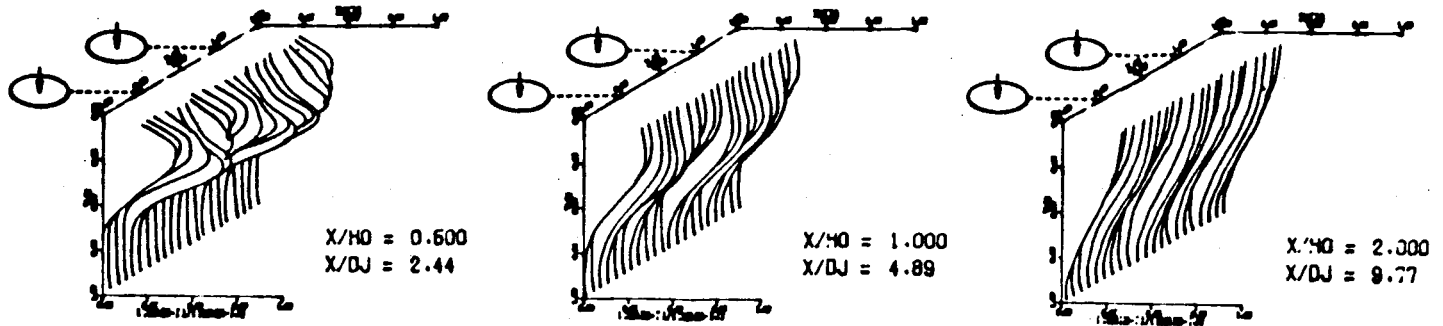
Figure 4 presents a comparison of temperature distributions between bluff and streamlined slots at comparable momentum flux ratios. At X/H_O = 0.5, the streamlined slots have deeper jet penetration than bluff slots. However, at X/H_O = 2.0, both of these orifice configurations show similar, completely mixed temperature distributions.

Figure 5 compares the temperature distribution for two in-line rows of jets with A_j/A_m = 0.049 for each row at J = 6.5, with an equivalent area circular hole having the same S/H_O ratio, at comparable momentum flux ratio. The two configurations have very similar temperature distributions. At a higher momentum flux ratio of 26.3, similar characteristics are observed (Figure 6).

Figure 7 presents the temperature distributions for a double row of jets, with the first row having A_j/A_m = 0.049 and S/H_O = 0.25. In the figure, these results are compared with those for a single row of jets having the same total geometric area at comparable momentum flux ratio. At X/H_O = 0.5, the double row of jets show a flatter peak theta distribution than the single row of jets. But beyond X/H_O = 1.0, the two orifice configurations have very similar temperature profiles. In Figure 8, the temperature distributions of these two orifices are compared at moderate momentum flux ratios. For this case, the double row of jets have mixing rates (in both vertical and transverse directions) comparable to the single row of jets with equivalent area.

The following conclusions can be made from these results:

● The effects of orifice shapes are significant only in the regions close to the jet injection plane ($X/H_O<1$). The temperature distributions in regions beyond X/H_O = 1 are similar to those with equivalent area circular holes.

- At the same S/H_O and momentum flux ratio, double rows of in-line jets have temperature distributions similar to a single row of jets with equivalent area.

REFERENCES

1. Walker, R. E.; and Kors, D. L.: Multiple Jet Study Final Report. NASA CR-121217, June 1973.

2. Srinivasan, R.; Berenfeld, A.; and Mongia, H.: Dilution Jet Mixing Phase I Report. Garrett Turbine Engine Co., Phoenix, AZ, Garrett Report 21-4302, November 1982 (NASA CR-168031).

3. Srinivasan, R.; Coleman, E.; Johnson, K.; and Mongia, H.: Dilution Jet Mixing Program Phase II Report. Garrett Report 21-4804, December 1983 (NASA CR-174624).

4. Holdeman, J. D.; and Walker, R. E.: Mixing of a Row of Jets with a Confined Crossflow. AIAA Journal, vol. 15, no. 2, February 1977, pp. 243-249 (AIAA Paper 76-48; NASA TM-71821).

Figure 1. Schematic of the test section and orifice plates

TEST RIG GEOMETRY
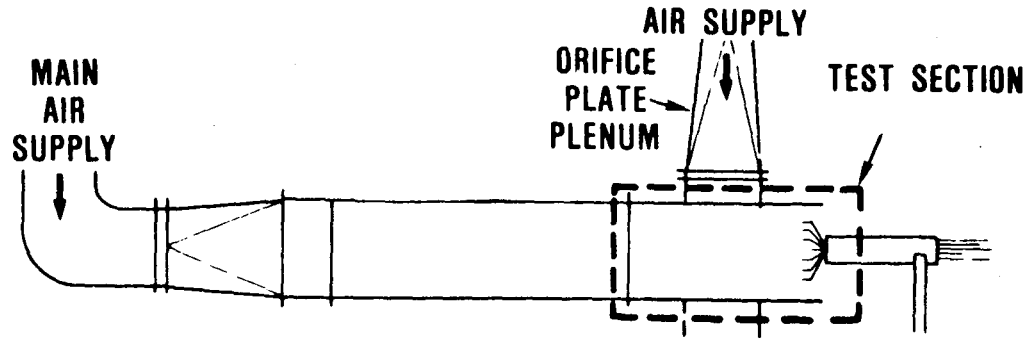
ORIFICE CONFIGURATIONS
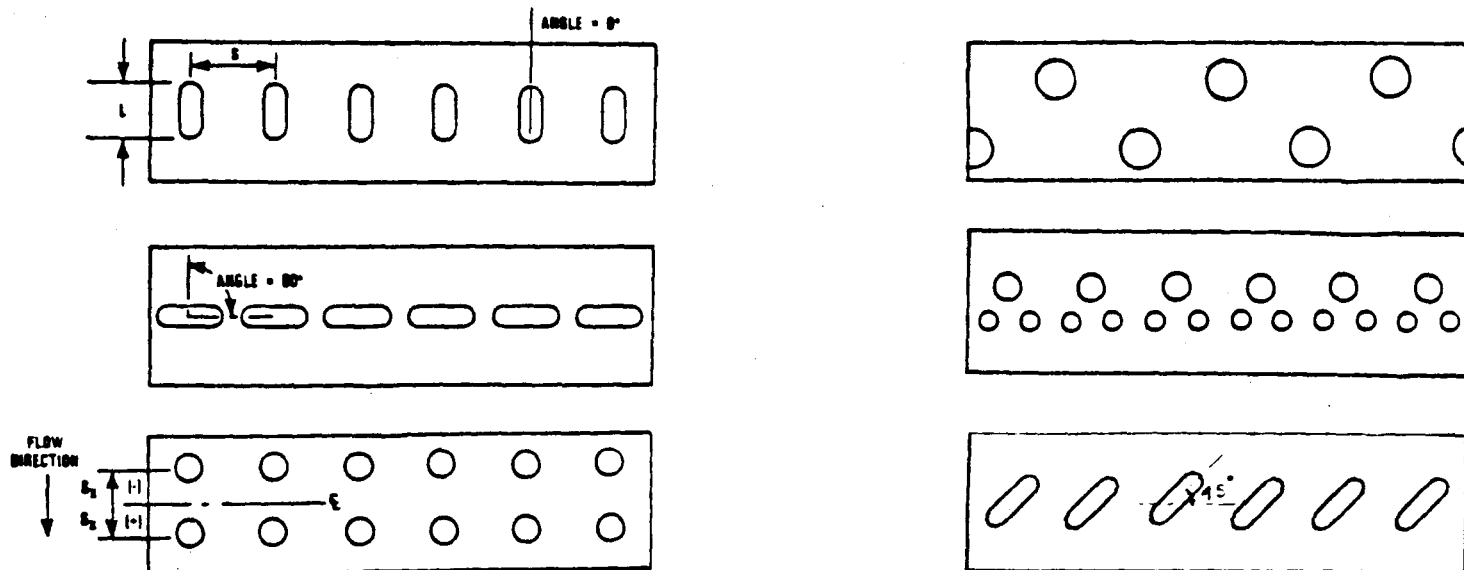
Figure 2. Comparison of temperature distributions between streamlined slots and circular holes at low momentum flux ratios.
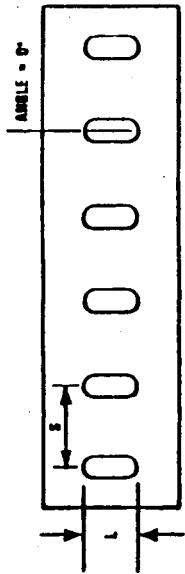
STREAMLINED SLOT, A_j/A_m=0.098, S/H_o=0.5, J=6.6

X/HO = 0.500
X/DJ = 2.29

X/HO = 1.000
X/DJ = 4.58

X/HO = 2.000
X/DJ = 9.15

CIRCULAR HOLE, A_j/A_m=0.098, S/H_o=0.5, J=5.0

X/HO = 0.600
X/DJ = 2.44

X/HO = 1.000
X/DJ = 4.89

X/HO = 2.000
X/DJ = 9.77
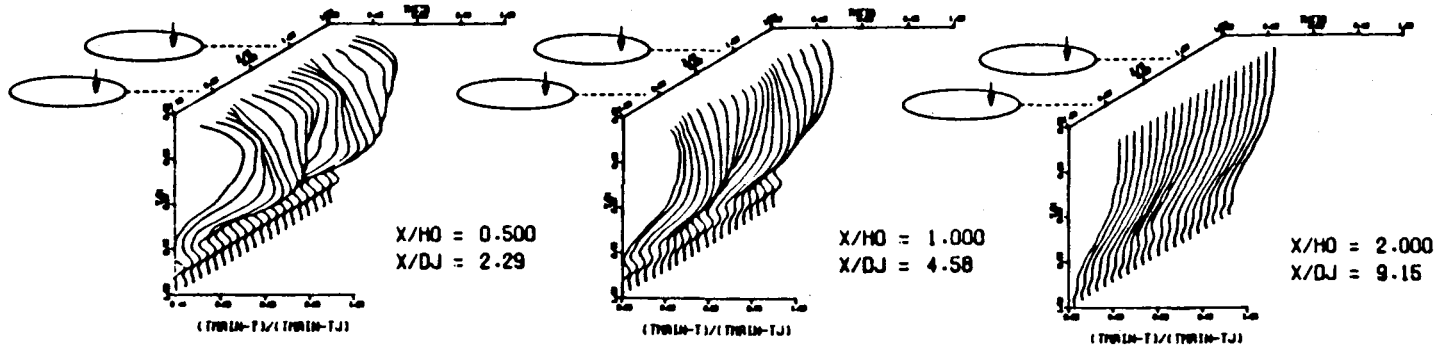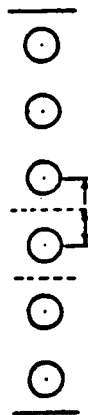
Figure 3. Comparison of temperature distributions between streamlined slots and circular holes at moderate momentum flux ratios.

STREAMLINED SLOT, A_j/A_m=0.098, S/H_o=0.05, J=26.5

X/HO = 0.500
X/DJ = 2.38

X/HO = 1.000
X/DJ = 4.76

X/HO = 2.000
X/DJ = 9.52

CIRCULAR HOLE, A_j/A_m=0.098, S/H_o=0.5, J=18.6

X/HO = 0.500
X/DJ = 2.58

X/HO = 1.000
X/DJ = 5.16

X/HO = 2.000
X/DJ = 10.33
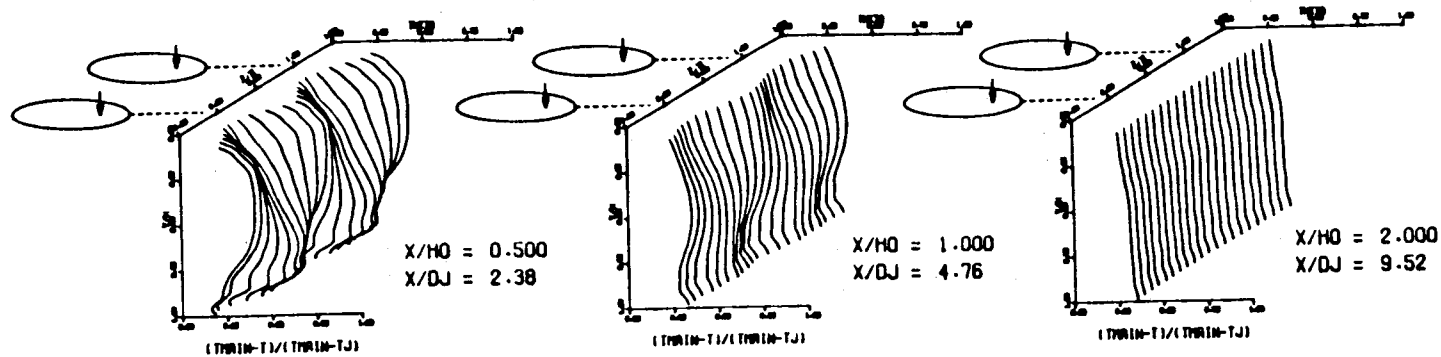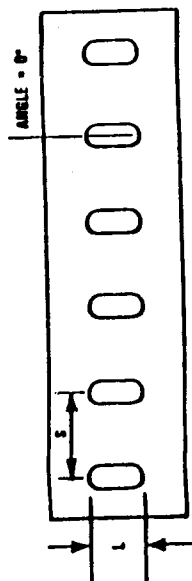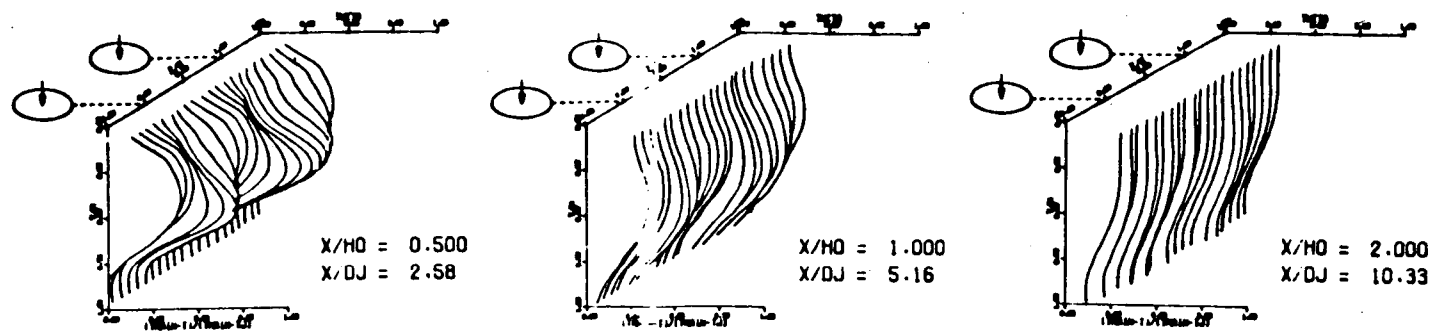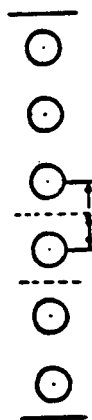
Figure 4. Comparison of temperatures distributions between bluff and streamlined slots at moderate momentum flux ratios.
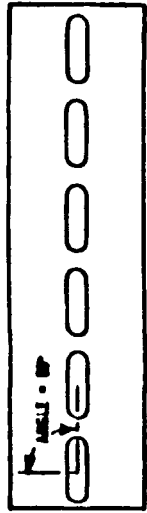
BLUFF SLOTS, A_j/A_m=0.098, S/H_o=0.5, J=26.6
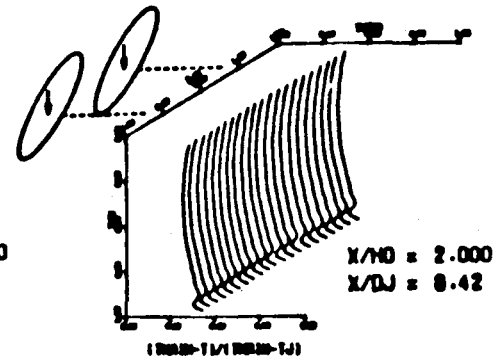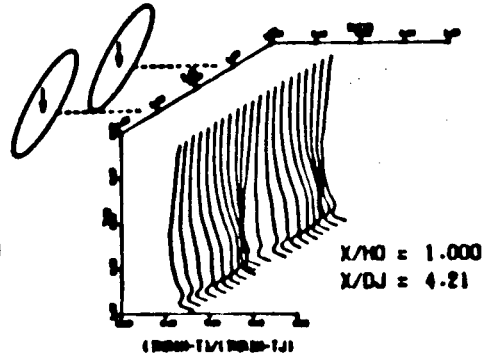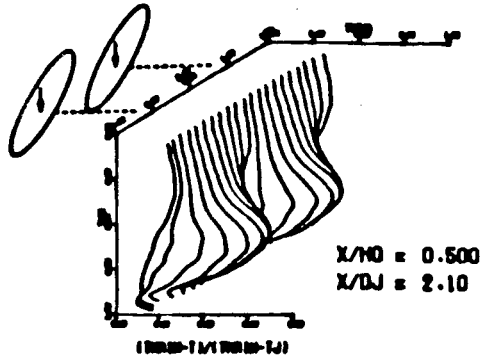
STREAMLINED SLOTS, A_j/A_m=0.098, S/H_o=0.5, J=26.5
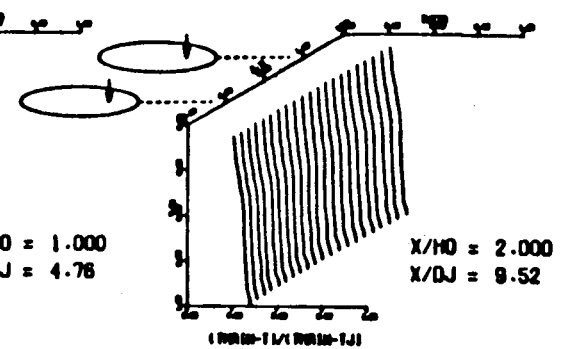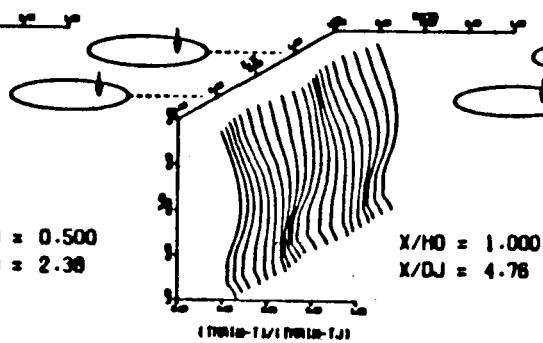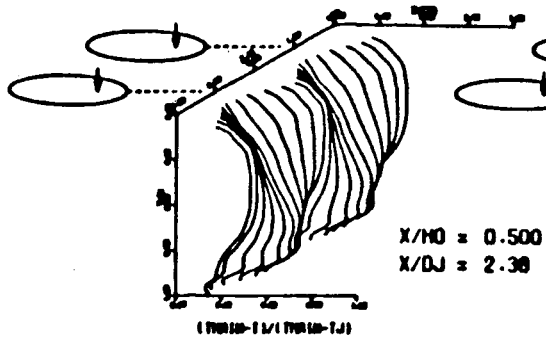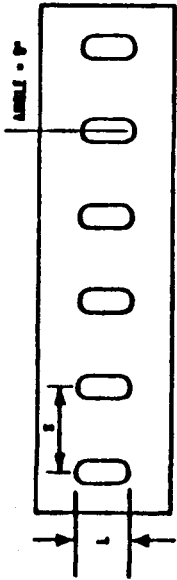
Figure 5. Comparison of temperature distributions between two rows
of jets and an equivalent single row of jets.

DOUBLE ROW, A_j/A_m=0.098, S/H_o=0.5, J=6.7

X/HO = 0.500
X/DJ = 3.48

X/HO = 0.750
X/DJ = 5.21

X/HO = 1.000
X/DJ = 6.95

(THRIN-T)/(THRIN-TJ)

SINGLE ROW, A_j/A_m=0.098, S/H_o=0.5, J=5.0

X/HO = 0.500
X/DJ = 2.44

X/HO = 0.750
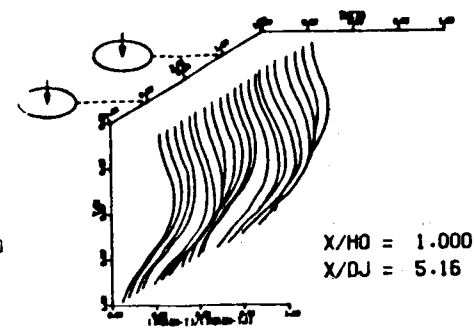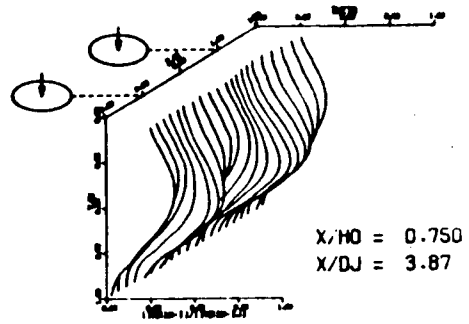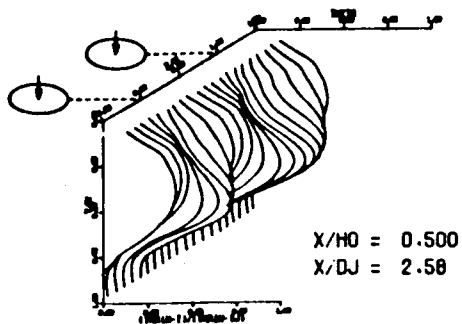X/DJ = 3.67

X/HO = 1.000
X/DJ = 4.89
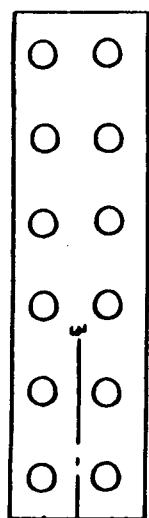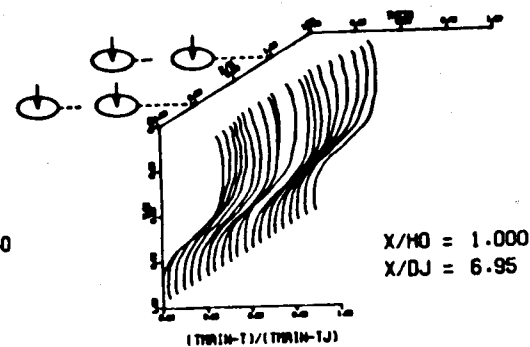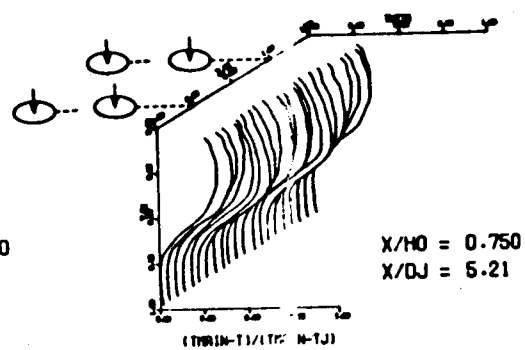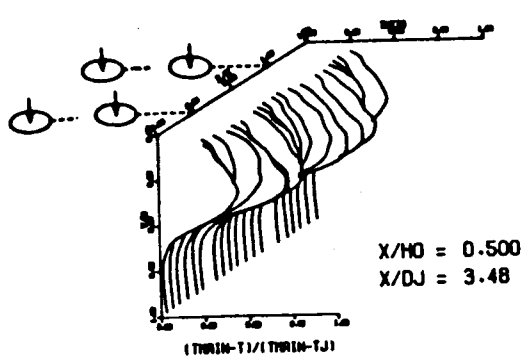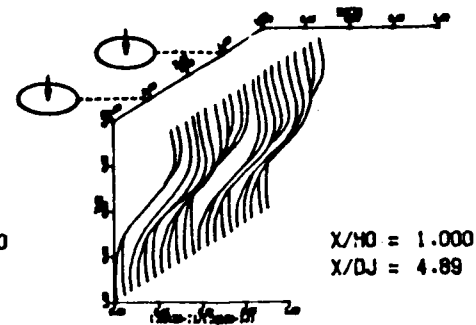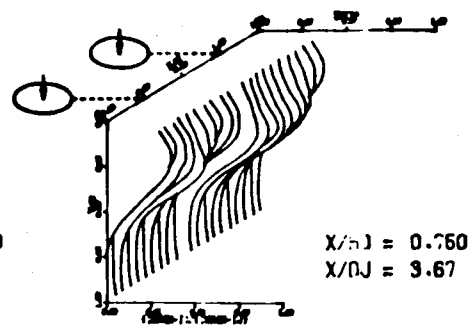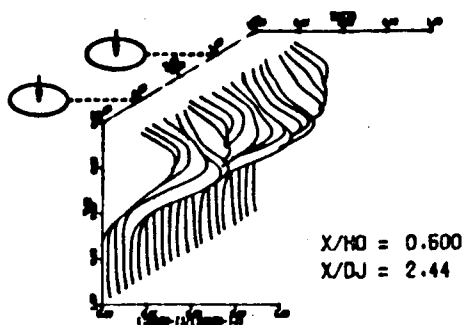
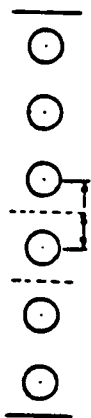Figure 6. Comparison of temperature distributions between single and double rows of jets, $S/H_o=0.5$

DOUBLE ROW OF JETS, $A_j/A_m=0.098$, $J=26.3$

X/HO = 0.500
X/DJ = 3.51
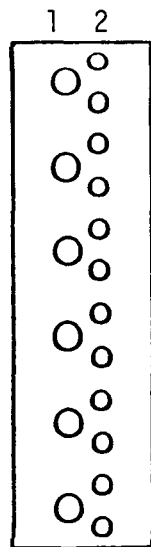
(THRIN-T)/(THRIN-TJ)

X/HO = 0.750
X/DJ = 5.26

(THRIN-T)/(THRIN-TJ)

X/HO = 1.000
X/DJ = 7.02

(THRIN-T)/(THRIN-TJ)
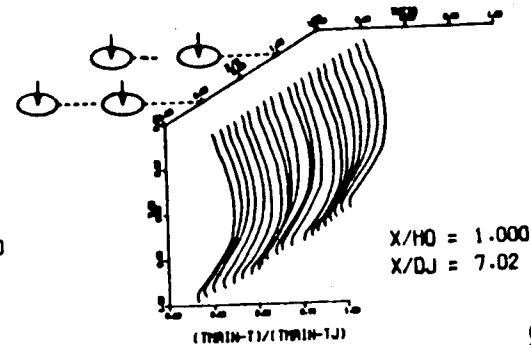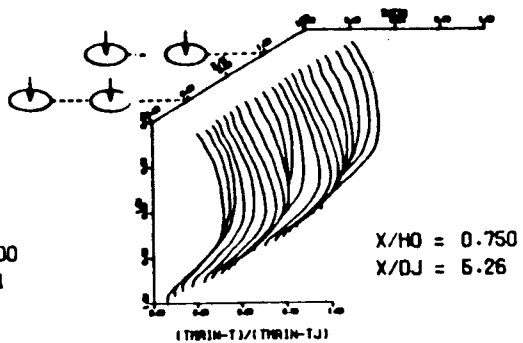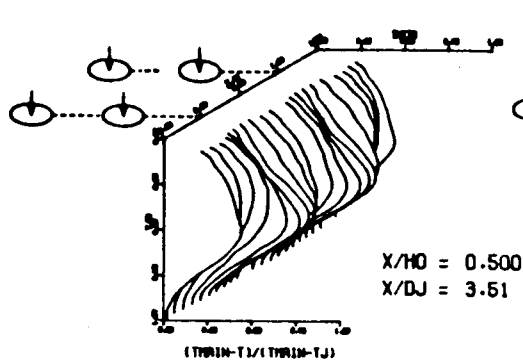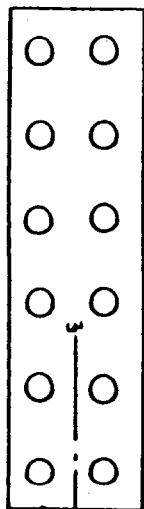
SINGLE ROW OF JETS, $A_j/A_m=0.098$, $J=18.6$

X/HO = 0.500
X/DJ = 2.58

X/HO = 0.750
X/DJ = 3.87

X/HO = 1.000
X/DJ = 5.16

Figure 7. Comparison of temperature distributions between a double row
of dissimilar holes and a single row of equivalent holes at
low momentum flux ratio.

DOUBLE ROW OF JETS, $A_{j1}/A_m=0.049$, $S/H_o=0.5$, $J_1=6.7$
$A_{j2}/A_m=0.049$, $S/H_o=0.5$, $J_2=6.7$

X/HO = 0.500
X/DJ = 3.28

X/HO = 1.000
X/DJ = 6.56

X/HO = 2.000
X/DJ = 13.12

SINGLE ROW OF JETS, $A_j/A_m=0.098$, $S/H_o=0.5$, $J=5.0$

X/HO = 0.500
X/DJ = 2.44

X/HO = 1.000
X/DJ = 4.89

X/HO = 2.000
X/DJ = 9.77
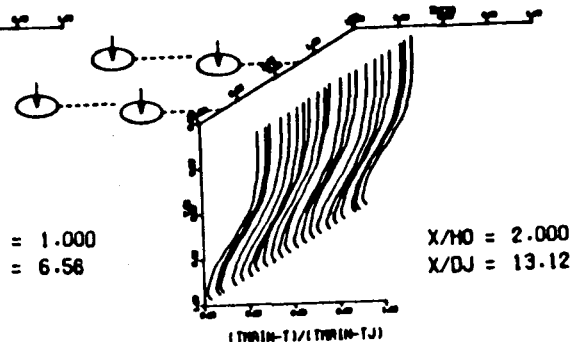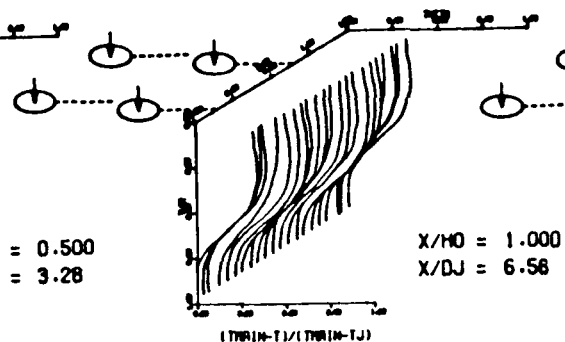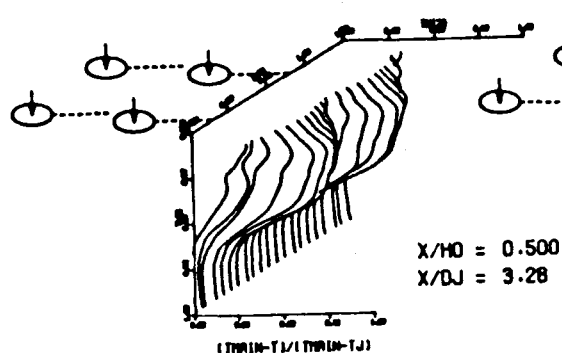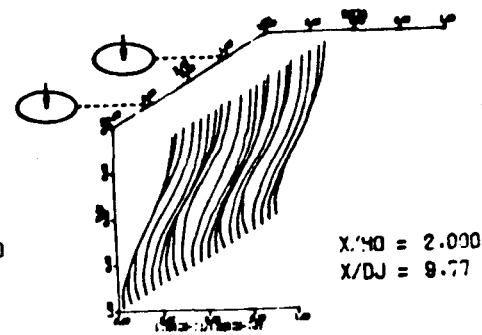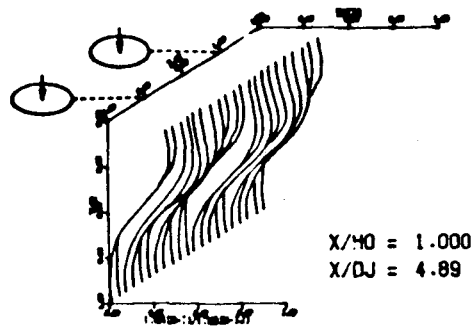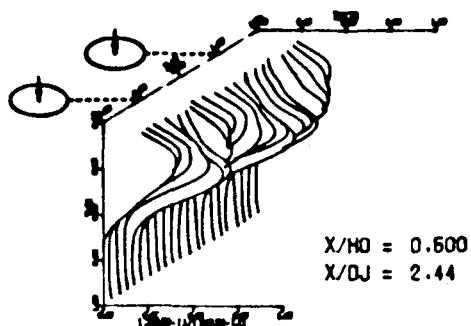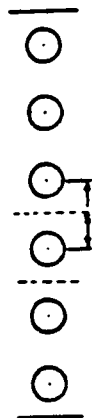
Figure 8. Comparison of temperature distributions between a double row of dissimilar holes and a single row of equivalent holes at moderate momentum flux ratio.

DOUBLE ROW OF JETS, A_{j1}/A_m=0.049, S/H$_o$=0.5, J_1=26.8
A_{j2}/A_m=0.049, S/H$_o$=0.5, J_2=26.6

X/HO = 0.500
X/DJ = 3.42

X/HO = 1.000
X/DJ = 6.83

X/HO = 2.000
X/DJ = 13.67

SINGLE ROW OF JETS, A_j/A_m=0.049, S/H$_o$=0.5, J=18.6

X/HO = 0.500
X/DJ = 2.58

X/HO = 1.000
X/DJ = 5.16

X/HO = 2.000
X/DJ = 10.33
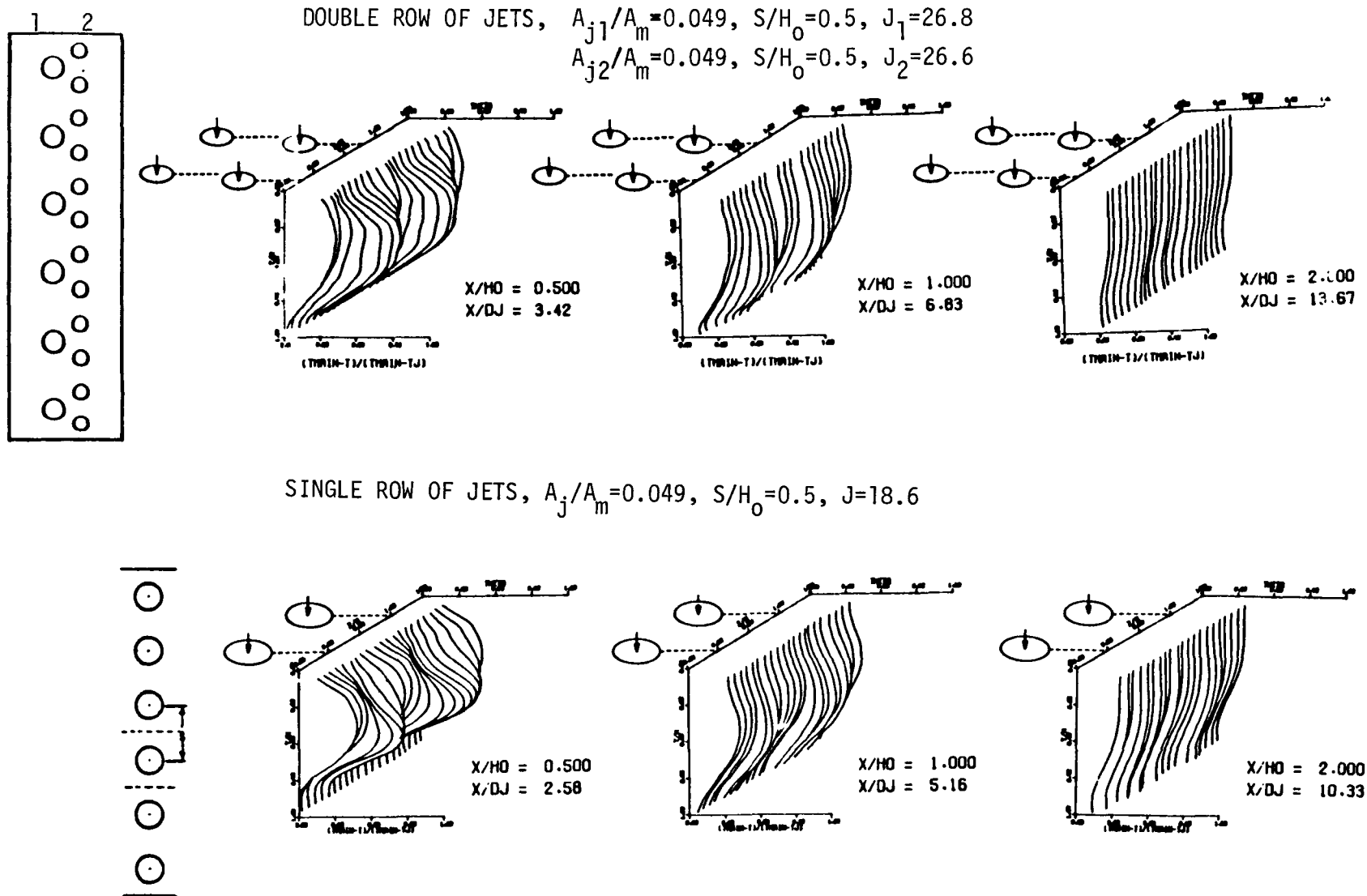
LATERAL JET INJECTION INTO
TYPICAL COMBUSTOR FLOWFIELDS

David G. Lilley
Oklahoma State University

A three-year research program is underway which deals both experimentally and theoretically with the problem of primary and dilution lateral jet injection into typical combustor flowfields in the absence of combustion. Parameter variations to be systematically investigated include: lateral jet size and velocity, main inlet-to-combustor expansion ratio, combustor inlet swirl strength, downstream contraction nozzle, multijet injection, and jet inlet angle. Helium bubble and smoke flow visualization, five-hole pitot probe time-mean velocity measurements, and one-wire and two-wire hot-wire normal and shear stress turbulence data are to be obtained in the experimental program. A fully three-dimensional computer code simulation is to be used in the theoretical contribution. The basic aim is to characterize the time-mean and turbulence flowfield, recommend appropriate turbulence model advances, and implement and exhibit results of flowfield predictions.

Recently, experimental and theoretical research has been completed on 2-D axisymmetric geometries under low speed, nonreacting, turbulent, swirling flow conditions, in the absence of any lateral jets (ref. 1). The flow enters the test section and proceeds into a larger chamber (the expansion D/d = 2) via a sudden or gradual expansion (side-wall angle α = 90 and 45 degrees). A weak or strong nozzle may be positioned downstream to form a contraction exit to the test section. Inlet swirl vanes are adjustable to a variety of vane angles with values of ϕ = 0, 38, 45, 60 and 70 degrees being emphasized. The objective was to determine the effect of these parameters on isothermal flowfield patterns, time-mean velocities and turbulence quantities, and to establish an improved simulation in the form of a computer prediction code equipped with a suitable turbulence model.

The principal aim of the new research program is to investigate the trajectory, penetration and mixing efficiency of lateral air jet injection into typical combustor flowfields in the absence of combustion, so as to characterize the time-mean and turbulence flowfield for a variety of configurations and input parameters, recommend appropriate turbulence model advances, and implement and exhibit results of flowfield predictions. A combined experimental and theoretical approach is to be followed, in a modified version of the test facility, equipped initially with one and two lateral jets, located one test-section diameter downstream of the inlet. A recent research paper (ref. 2) describes some of the earlier studies. Parameters to be systematically investigated include:

1. lateral jet size and velocity,

2. main inlet-to-combustor expansion ratio,

3. combustor inlet swirl strength,

4. downstream contraction nozzle,

5. multijet injection,

6. jet inlet angle,

and their effects on the subsequent flowfield are to be observed and characterized. The specific objectives of the proposed research are:

1. To **exhibit** the flowfield characteristics utilizing appropriate flow visualization technques, so as to define clearly areas for later detailed study.

2. To **measure** the time-mean flowfield and normal and shear turbulent Reynolds stresses for a variety of flow conditions, so providing a direct comparision with results of nondiluted experiments previously obtained. Main and lateral airflow inlet conditions will be carefully recorded with emphasis on those parameters of interest in associated computational flow studies.

3. To **present** results of interest in combustor design, illustrating the **effects** of many parameters (lateral jet size and velocity, main inlet-to-combustor expansion ratio, combustor inlet swirl strength, downstream contraction nozzle, multijet injection, and jet inlet angle) **on** subsequent flowfield patterns, like streamlines, time-mean velocities, and normal and shear turbulent Reynolds stresses.

4. To **characterize** the turbulence flowfield in a general sense, leading to the **recommendation** of suitable turbulence modeling advances.

5. To **develop** a fully 3-D computational technique and **evaluate** its predictive capability using the determined turbulence model, for a variety of input parameter variations.

References

1. Lilley, D. G., "Investigations of Flowfields Found in Typical Combustor Geometries", NASA CP-2309, 1984, pp. 139-151.

2. Ferrell, G. B., Abujelala, M. T., Busnaina, A. A., and Lilley, D. G., "Lateral Jet Injection into Typical Combustor Flowfields", Paper AIAA-34-0374, Reno, Nevada, January 9-12, 1984.

LATERAL JET INJECTION INTO TYPICAL COMBUSTOR FLOWFIELDS

David G. Lilley

Contents

1. Introduction

1.1 The Test Facility
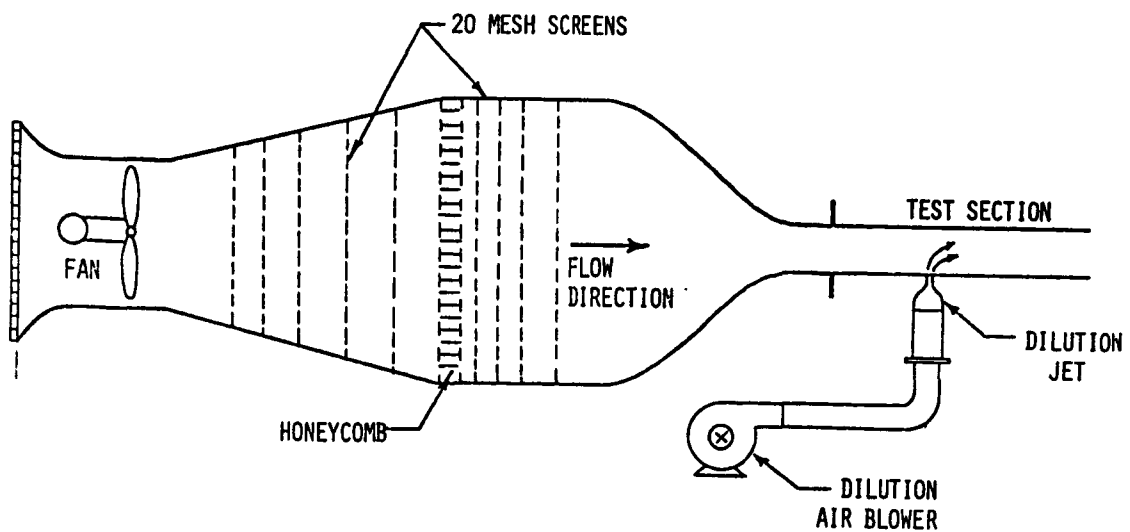
Initial Proposed Test Apparatus

1.2 Objectives

To determine the effect of

    1.   inlet swirl strength

    2.   inlet to test section expansion ratio

    3.   lateral jet size and velocity

    4.   downstream contraction nozzle size and location

    5.   number, location and injection angle of lateral jets

on

    1.   isothermal flowfield patterns

    2.   time-mean velocities

    3.   turbulence quantities

1.3 Approach

    1.   Time-mean flowfield characterization by five-hole pitot probe measurements and by flow visualization.

    2.   Turbulence measurements by a variety of single- and multi-wire hot-wire probe techniques.

    3.   Flowfield computations using the computer code developed during the previous year's research program and/or other codes.

2. Facilities and Techniques

2.1 Facilities

1. wind tunnel,

2. one variable-angle vane swirler,

3. three plexiglass text sections of diameters 30, 22.5 and 15 cm,

4. expansion blocks of 90 and 45 deg., for each of the three test sections,

5. weak and strong downstream contraction nozzles, for each of the three test sections.

2.2 Recent Studies with No Lateral Jets

1. Flow visualization using neutrally-buoyant helium-filled soap bubbles.

2. Time-mean velocities with a five-hole pitot probe for a full range of swirl strengths.

3. Turbulence measurements using a six-orientation single-wire hot-wire technique.

4. An advanced computer code has been developed to predict corresponding confined swirling flows to those studied experimentally.

5. Tentative predictions have now been supplemented by predictions made from realistic inlet conditions.

2.3 Lateral Jet Nozzle Details
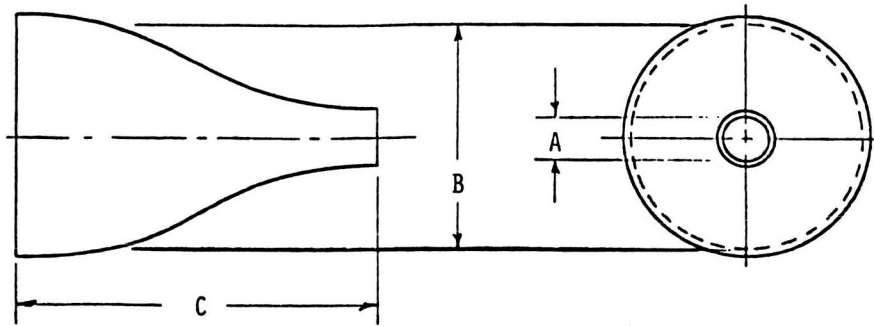
$A_{COMB.}/A_{JET}$	A	B	C
50	2.12	10.00	20.00
100	1.50	10.00	20.00
150	1.22	10.00	20.00

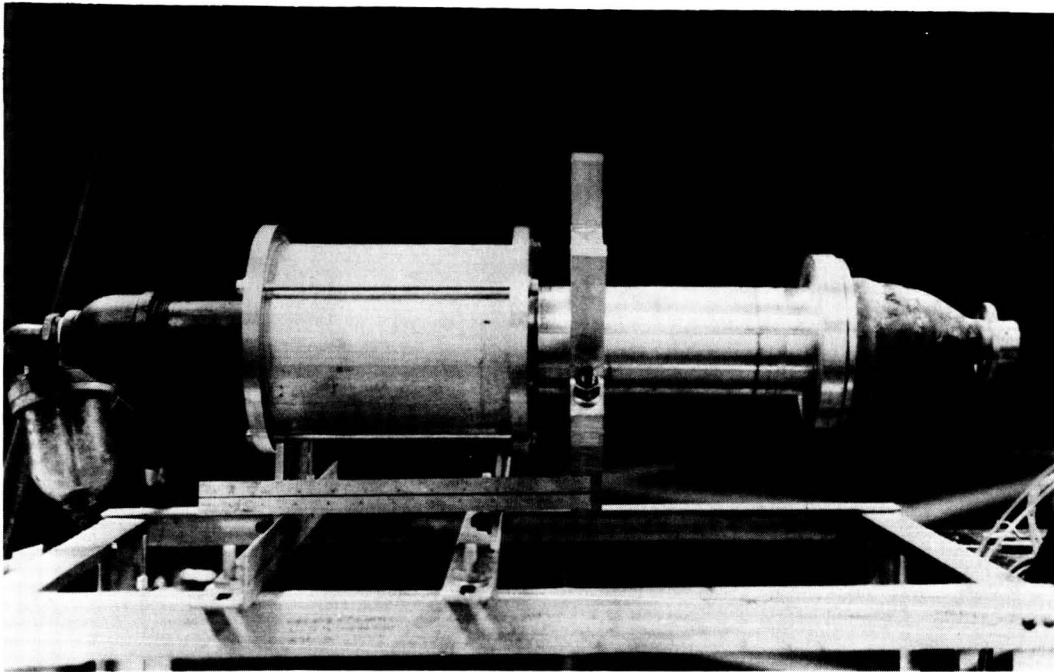NOTE: ALL DIMENSIONS IN CM

Lateral Jet Nozzle Details

3. Progress

3.1 Test Facility
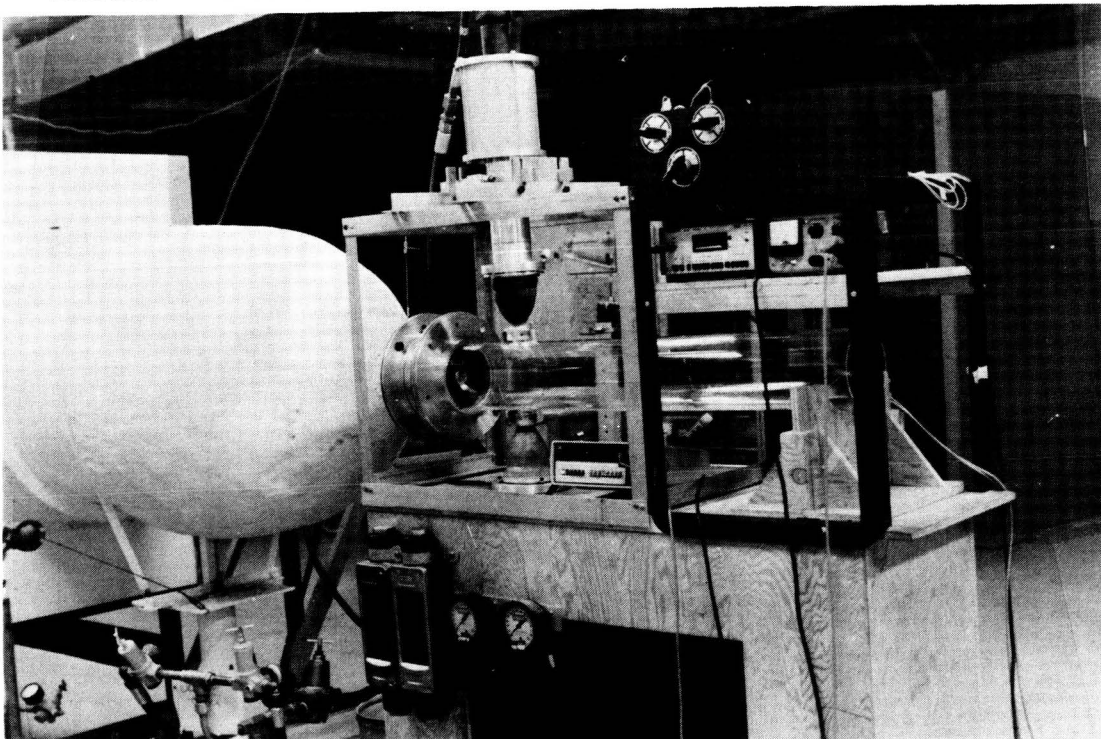
3.2 Lateral Jet Assembly

3.3 Approach

1. Experimental and theoretical program

2. 14-task approach

3. Phase 1 - detailed experimentation

4. Phase 2 - simulation

5. Phase 3 - parametric investigations

TABLE 1. Program Tasks and Time Schedule

	Year 1	Year 2	Year 3
Phase 1 - Detailed Experimentation			
Task 1 - Basics	▭		
Task 2 - Flow Visualization	▭		
Task 3 - Time-Mean Measurements	▭		
Task 4 - Turbulence Measurements		▭	
Phase 2 - Simulation			
Task 5 - Standard Computer Code	▭		
Task 6 - Development of Advanced Turbulence Models		▭	
Phase 3 - Parametric Investigations			
Task 7 - Lateral Jet Size and Velocity Effects	▭		
Task 8 - Main Flow Swirl Effects		▭	
Task 9 - Main Inlet-to-Combustor Expansion Ratio Effects		▭	
Task 10 - Downstream Nozzle Effects		▭	
Task 11 - Multijet Injection Effects		▭	
Task 12 - Lateral Jet Injection Angle Effects		▭	
Task 13 - Detailed Investigation of Nine Specific Flow Configurations	▭		▭
Task 14 - Documentation	▭ ▭	▭	▭

3.4 Flow Visualization

One jet with R = 4

φ = 0°

φ = 45°
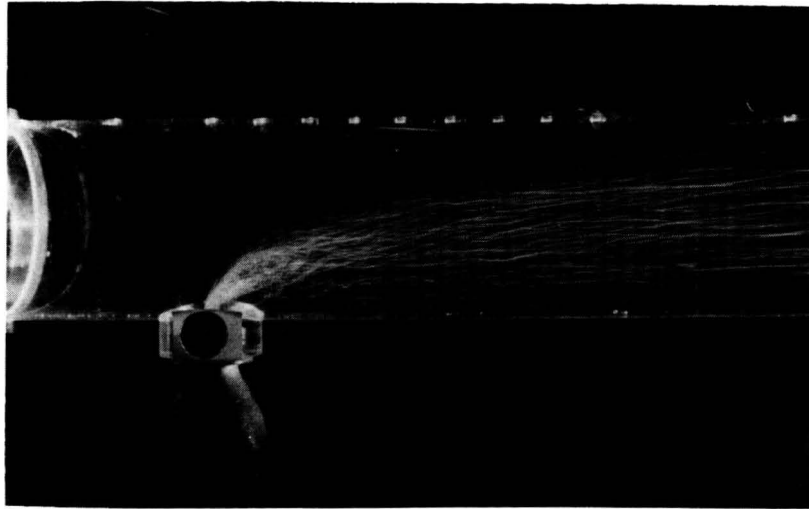
φ = 70°
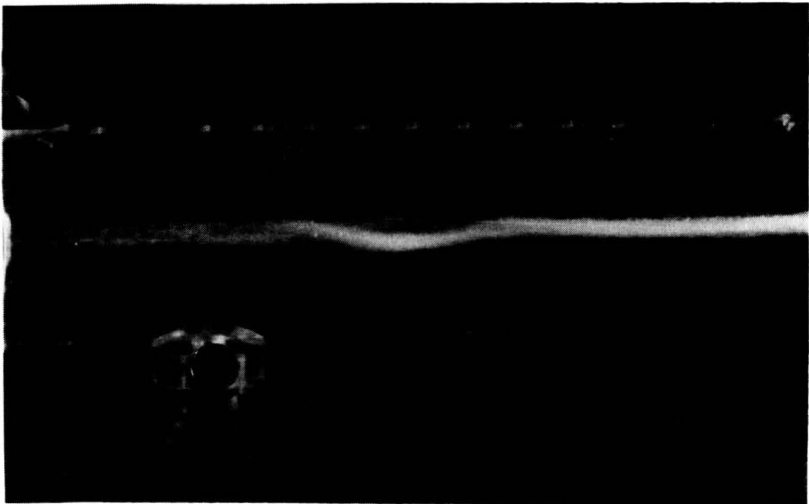
3.5 Flow Visualization

Two jets with R = 4

$\phi = 0^{\circ}$

$\phi = 45^{\circ}$

$\phi = 70^{\circ}$

4. <u>Closure</u>

1. Lateral multi-jet injection into typical combustor flowfields - round-sectioned crossflow with swirl.

2. Measurements of effects of many input parameters on flowfield patterns.
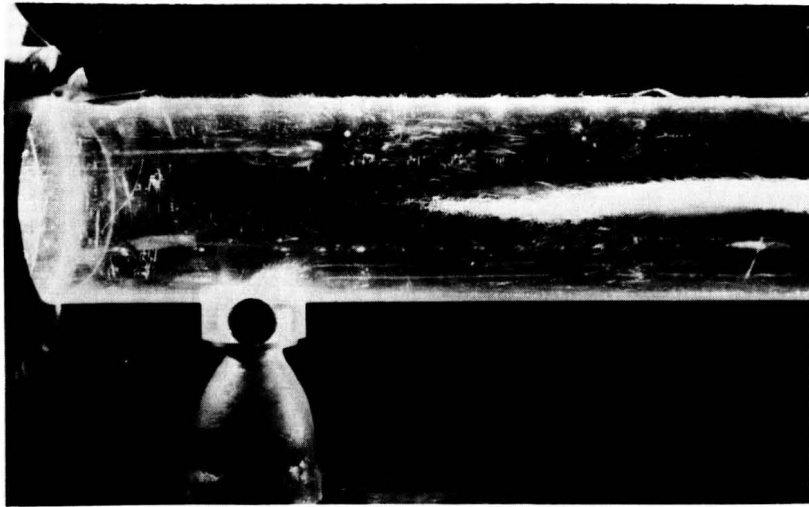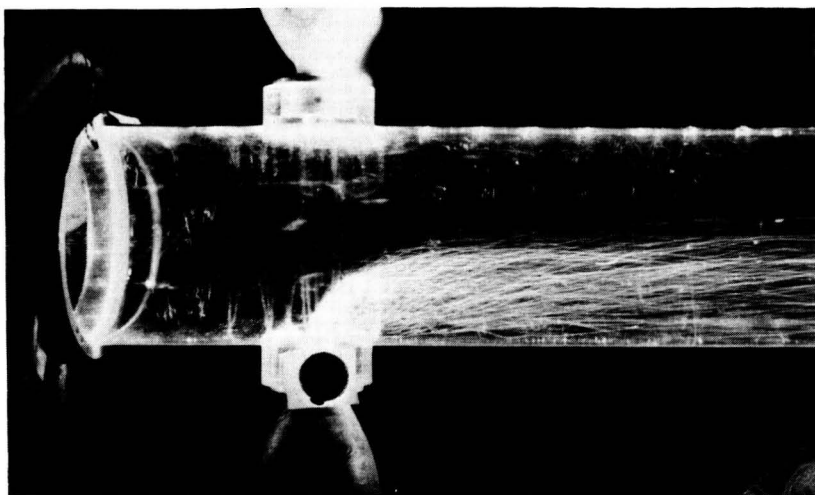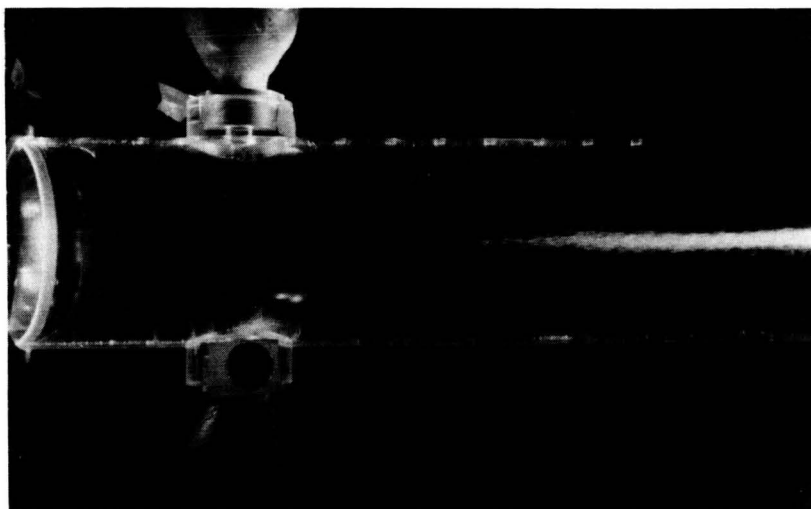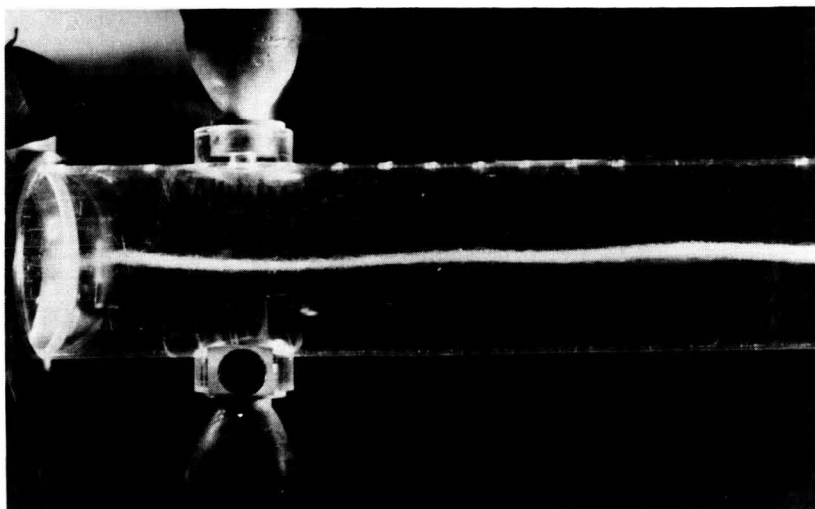
3. Computer prediction and turbulence modeling of associated phenomena.

FLAME RADIATION

J. D. Wear
National Aeronautics and Space Administration
Lewis Research Center

INTRODUCTION

The objectives of this in-house program were to obtain total radiation and heat flux data incident on a combustor liner by advanced instrumentation. If the results obtained by the special instrumentation are considered to be representative of the total radiation and heat flux, then the effect of variation of engine operating parameters and of fuel type can be more easily obtained.

INSTRUMENTATION

The special instrumentation used for these investigations consisted of five total radiometers (Medtherm) and two total heat flux gages (Gardon type). The radiometers were arranged axially and circumferentially through sliding air seals in the outer liner. The two heat flux gages were welded in the outer liner between two circumferential radiometers. Static pressures were obtained on both the cold and the hot side of the outer liner in the area of the heat flux gages. Liner metal temperatures were also obtained.

OPERATING CONDITIONS AND FUELS

The combustor inlet pressure was varied over a nominal range of 0.5 to 2.07 MPa, inlet air temperature from 550 to 670 K, and fuel-air ratio from about 0.015 to 0.040. The nominal gas temperatures for these fuel air ratios are 1120 and 1950 K, respectively. Two fuels were used for a majority of the tests, ASTM Jet A and a fuel designated as ERBS V. The ERBS fuel had about twice the aromatic content of the Jet A and a boiling end point about 50 K higher.

RESULTS

The results presented show the output from some of the special instrumentation and the effects of combustion pressure, fuel type, and fuel-air ratio.

A statement of approach to the investigations is as follows:

(1) Measure flame radiation and liner heat flux in an annular combustor at pressures to 20 atmospheres and fuel-air ratios to 0.040.

(2) Conduct research with a standard fuel, Jet A, and an experimental fuel, ERBS V.

(3) Evaluate the effects of pressure, fuel-air ratio, and fuel type on radiation and liner heat flux.

A cross-sectional sketch of the combustion system is shown in figure 1. Fuel was injected by two rows of counterswirl low-injection-pressure fuel modules. Figure 2 shows the position of the radiometers. In figure 3 the positions of four of the radiometers and the two heat flux gages are shown on the hot gas side of the outer liner.

Comparison of total radiation and total heat flux obtained at two fuel-air ratios and over a combustor pressure range is shown in figure 4 for Jet A fuel. At a fuel-air ratio of 0.04 and a pressure of 0.5 MPa, total radiation was about 46 percent of total heat flux. As the combustor pressure was increased to 1.6 MPa, total radiation increased to about 92 percent of total heat flux.

The radiation values obtained from the three radiometers positioned axially along the liner using Jet A are shown in figure 5. As the combustion pressure increased, the rate of radiation increase with pressure was greater for the radiometer closest to the fuel modules (4.6 cm from injection plane) than for the other two radiometers (9.7 and 15.1 cm from the injection plane).

A comparison of a few of the characteristics of the Jet A and ERBS V fuels used in the investigations (table I) indicates that the aromatic content of the ERBS V is about twice that of the Jet A. Also the final boiling point of the ERBS V is about 50 K greater than that of Jet A.

Figure 6 is a plot of total radiation data obtained from the three in-line radiometers using ERBS V fuel. Again, the radiation obtained from the radiometer closest to the fuel modules was greater than that obtained from the other two radiometers.

Comparison of the radiation data obtained from the three in-line radiometers for the two fuels is presented in figures 7 to 9. Figure 7 shows data for the closest position, 4.6 cm from the fuel injection plane; figure 8, 9.7 cm; and figure 9, 15.1 cm. As shown in figure 7, the radiation data obtained with Jet A are somewhat greater than those obtained with ERBS V, at the two values of fuel-air ratio. The difference is more pronounced at the higher pressure levels. At the 9.7- and 15.1-cm positions, the values obtained with the two fuels were similar, except at the low combustor pressure condition, where the Jet A fuel showed higher radiation than with the ERBS V.

Liner differential temperatures (liner metal temperature minus inlet air temperature) as shown in figure 10 are slightly higher with the ERBS V fuel than with Jet A at the higher fuel-air ratio of 0.04. Temperatures were similar at a fuel-air ratio of 0.015.

Figures 11 and 12 present smoke number (SN) data for the two fuels at three fuel-air ratios of 0.02, 0.03, and 0.04 over the pressure range. The smoke numbers obtained with the ERBS V fuel were generally greater than those obtained with Jet A. The highest SN obtained was 25, with ERBS V fuel, 2.07 MPa pressure, and a fuel-air ratio of 0.04.

SUMMARY OF RESULTS

1. At a fuel-air ratio of 0.040, total radiation increased from about 46 percent of total heat flux at a pressure of 0.5 MPa to 92 percent of total heat flux at 1.6 MPa pressure.

2. The rate of total radiation increase with increase in pressure was greatest at the sample position closest to the fuel injection plane (4.6 cm).

3. Total radiation measured at the 4.6 cm position was slightly greater with Jet A than with ERBS V over the pressure range.

4. Smoke numbers obtained with ERBS V were somewhat greater than those obtained with Jet A over the pressure range.

FUEL PROPERTIES

	ASTM JET A	ERBS V
GRAVITY, °API	43.1	36.6
AROMATICS, (D1319), vol.%	15.5	30.2
H/C RATIO, wt.	0.161	0.147
NET HEAT OF COMBUSTION, (D1405) kJ/kg	43.27	42.44
ASTM DISTILLATION (D86), K		
INITIAL BOILING POINT	433	444
50 PERCENT EVAPORATED	483	486
FINAL BOILING POINT	547	594

Table I

CROSS-SECTIONAL SKETCH OF HIGH-PRESSURE COMBUSTOR AND LINER

Figure 1

RADIATION INSTRUMENTATION
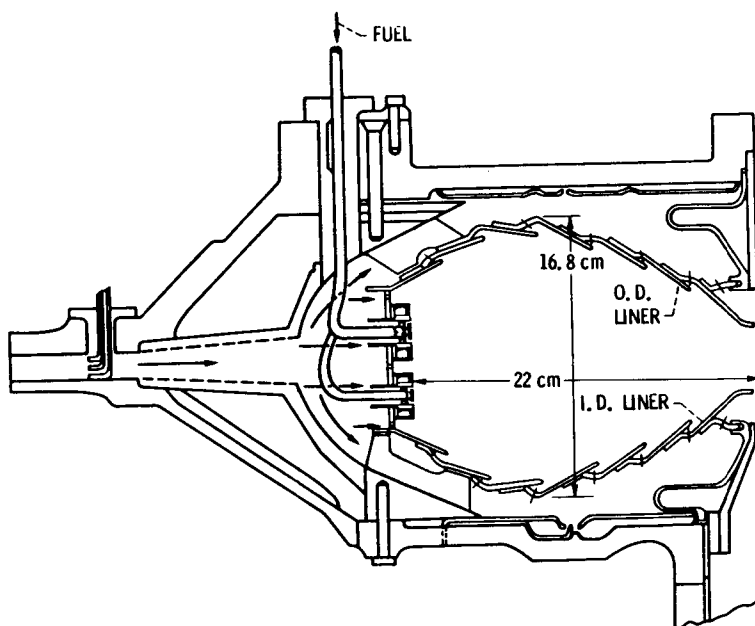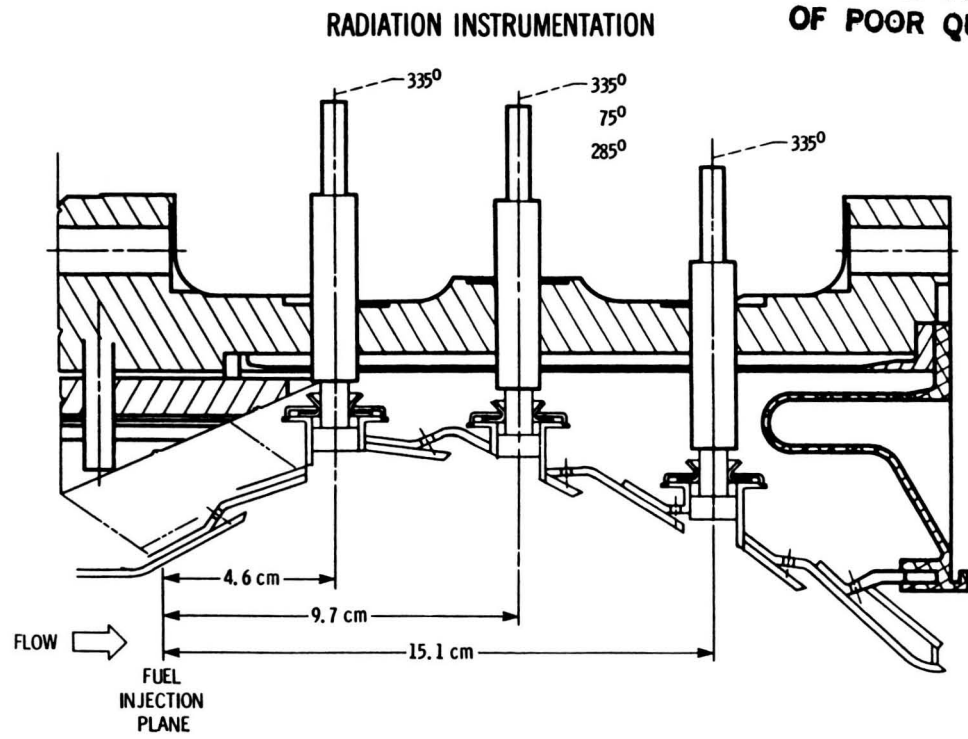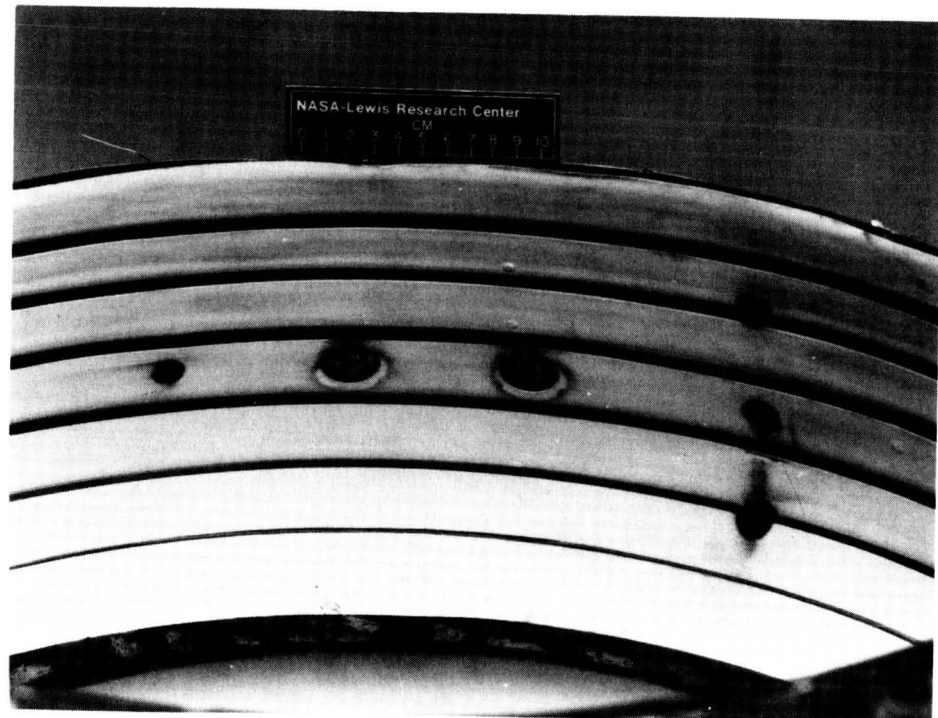
Figure 2

CS-84-3966

Figure 3

TOTAL RADIATION AND HEAT FLUX
FUEL, ASTM JET A
INLET-AIR TEMPERATURE, 550/670 K
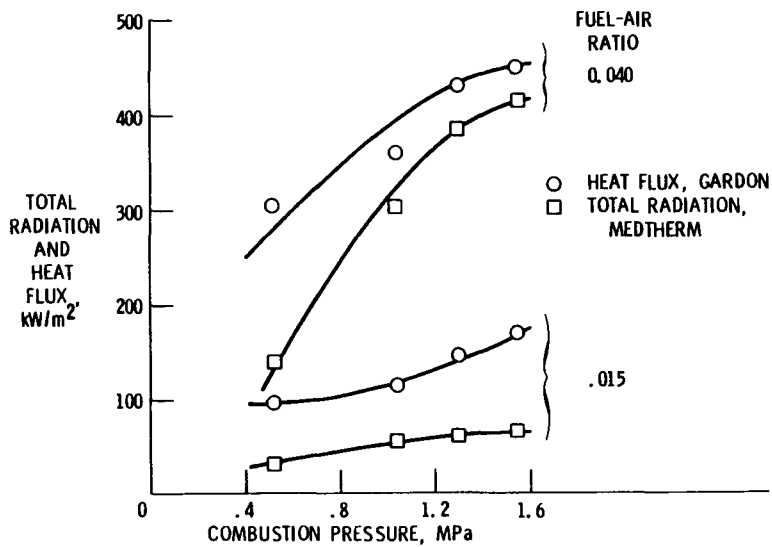
Figure 4

TOTAL RADIATION
FUEL, ASTM JET A
INLET-AIR TEMPERATURE, 550/670 K

Figure 5

228
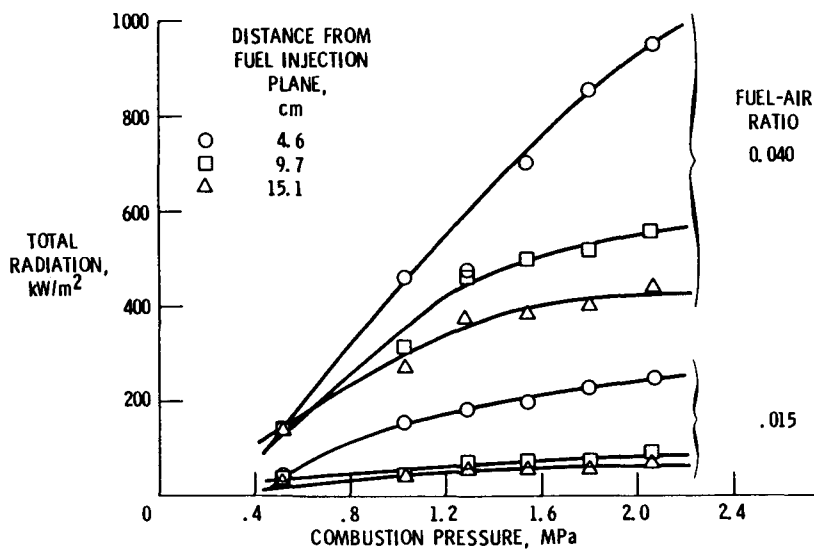
TOTAL RADIATION

FUEL, ERBS V

INLET-AIR TEMPERATURE, 550/670 K
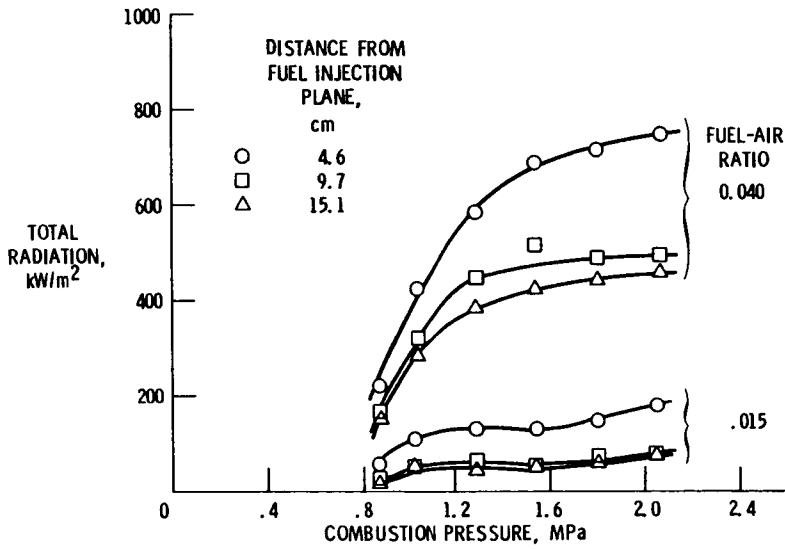
Figure 6.

TOTAL RADIATION

INLET-AIR TEMPERATURE, 550/670 K

DISTANCE FROM FUEL INJECTION PLANE, 4.6 cm
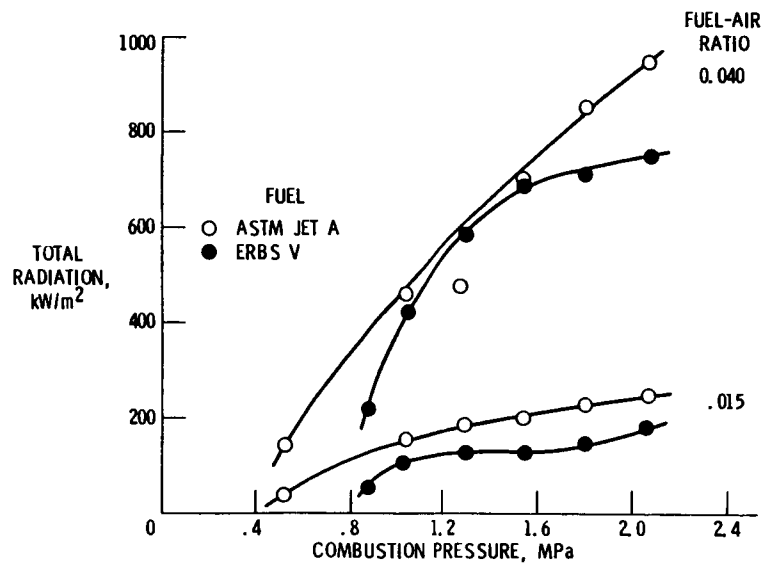
Figure 7

TOTAL RADIATION

INLET-AIR TEMPERATURE, 550/670 K

DISTANCE FROM FUEL INJECTION PLANE, 9.7 cm
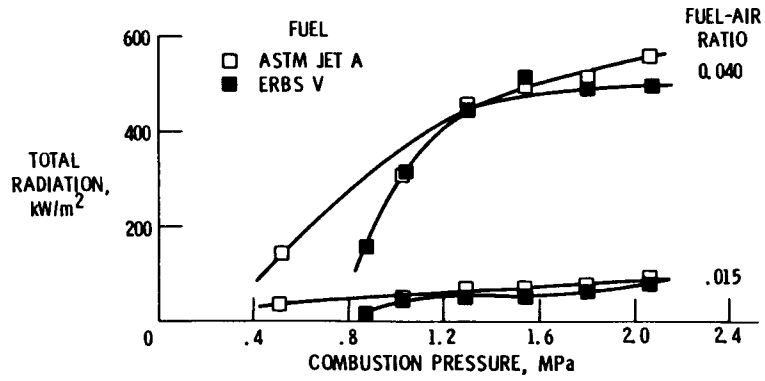
Figure 8.

TOTAL RADIATION

INLET AIR TEMPERATURE, 550/670 K

DISTANCE FROM FUEL INJECTION PLANE, 15.1 cm

Figure 9

230
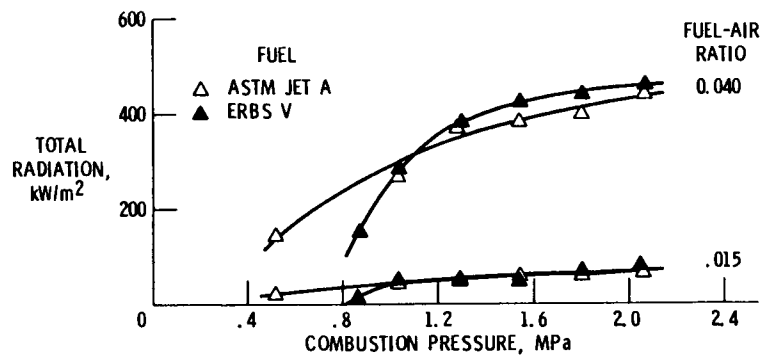
COMBUSTOR LINER TEMPERATURE
INLET-AIR TEMPERATURE, 550/670 K

DIFFERENTIAL TEMPERATURE, LINER METAL AVERAGE MINUS INLET AIR TEMPERATURE, K

○ ASTM JET A
● ERBS V

FUEL-AIR RATIO
0.040

.015

COMBUSTION PRESSURE, MPa
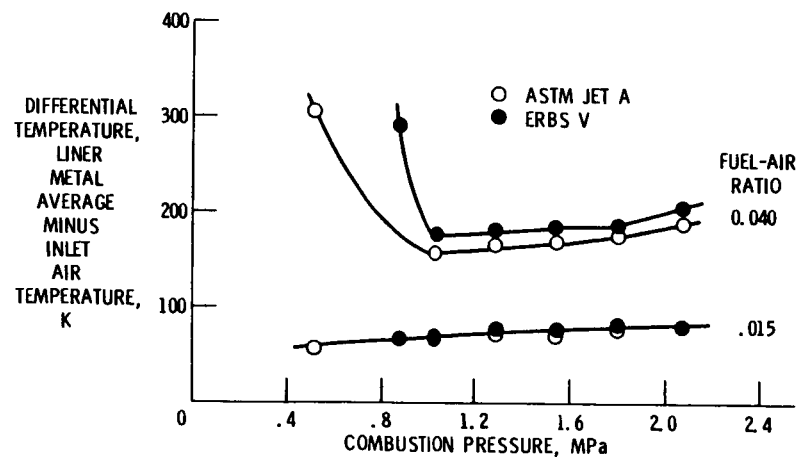
Figure 10.

SMOKE NUMBER
INLET-AIR TEMPERATURE, 550/670 K

SMOKE NUMBER, SN

FUEL-AIR RATIO
0.030

FUEL
○ ASTM JET A
● ERBS V

.020

COMBUSTION PRESSURE, MPa

Figure 11

231

SMOKE NUMBER
INLET-AIR TEMPERATURE, 550/670 K

Figure 12

BURNER LINER THERMAL/STRUCTURAL LOAD MODELLING

R. J. Maffeo
General Electric Company
Aircraft Engine Business Group

The objective of this program is to develop a thermal data transfer computer program module for the Burner Liner Thermal/Structural Load Modelling Program. This will be accomplished by (1) reviewing existing methodologies for thermal data transfer and selecting three heat transfer codes for application in this program, (2) evaluating the selected codes to establish criteria for developing a computer program module to transfer thermal data from the heat transfer codes to selected stress analysis codes, (3) developing the automated thermal load transfer module, and (4) verifying and documenting the module.

In aircraft turbine engine hot section components, cyclic thermal stresses are the most important damage mechanism. Consequently, accurate and reliable prediction of thermal loads is essential to improving durability. To achieve this goal, a considerable effort over the past 20 years has been devoted to the acquisition of engine temperature test data, as well as the development of accurate, reliable, and efficient computer codes for the prediction of steady-state and transient temperatures and for the calculation of elastic and inelastic cyclic stresses and strains in hot section components. There is a need for continued development of these codes, because the availability of more accurate analysis techniques for complex configurations has enabled engine designers to use more sophisticated designs to achieve higher cycle efficiency and reduce weight.

It has become apparent in recent years that there is a serious problem of interfacing the output temperatures and temperature gradients from either the heat transfer codes or engine tests with the input to the stress analysis codes. With the growth in computer capacity and speed and the development of input preprocessors and output postprocessors, the analysis of components using hundreds and even thousands of nodes in the heat transfer and stress models has become economical and routine. This has exacerbated the problem of manual transfer of output temperatures from heat transfer nodes to stress analysi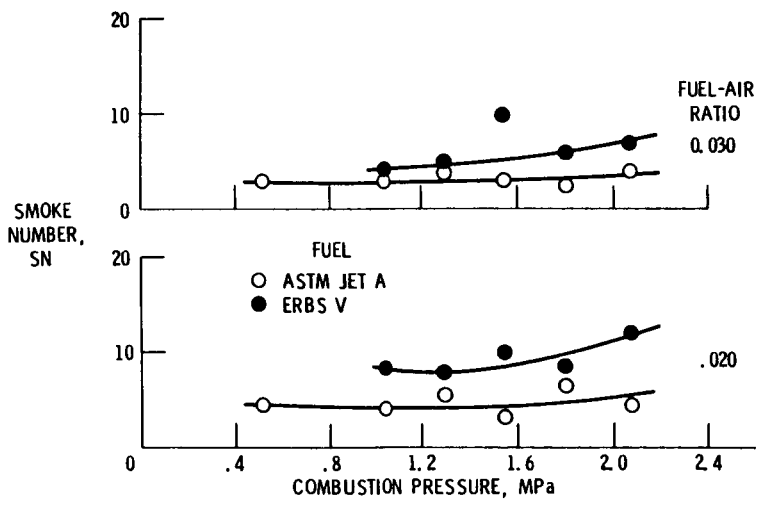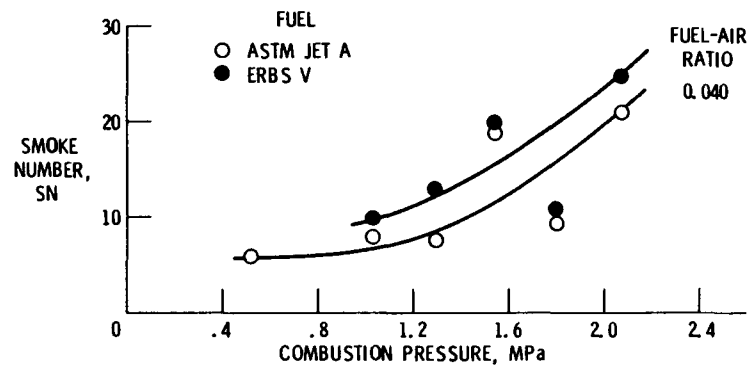s input to where the engineering effort required is comparable to that required for the remainder of the analysis. Furthermore, a considerable amount of approximation has been introduced in an effort to accelerate the process. This tends to introduce errors into the temperature data which negates the improved accuracy in the temperature distribution achieved through use of a finer mesh. There is, then, a strong need for an automatic thermal interface module.

The overall objectives of this thermal transfer module are that it handle independent mesh configurations, finite difference and finite element heat transfer codes, perform the transfer in an accurate and efficient fashion and that the total system be flexible for future applications.

Based on our study of existing thermal transfer modules, and our experience with our two-dimensional in-house transfer code, three levels of program development criteria were identified.

Level I contains the general criteria which must be satisfied for a usable product. These include:

- Independent Heat Transfer and Stress Model Meshes
- Accurate Transfer of Thermal Data
- Computationally Efficient Transfer
- User Friendly Program
- Flexible System

Level II contains specific criteria which must be satisfied to meet requirements associated with gas turbine applications, such as:

- Internal Coordinate Transformations
- Automatic Exterior Surfacing Techniques
- Geometrical and Temporal Windowing Capability

Level III has criteria which are desirable but not necessary. Total automation of these could be accomplished in future enhancements of the transfer code. Items that fall in this area include:

- Automatic Scaling of Temperatures Based on Engine Power Setting
- Altered Stress Geometry
- Automatic Handling of Temperature Discontinuities

All of the Level I and Level II criteria have been developed and implemented into the thermal load transfer code. This code is being used at General Electric and has been used in conjunction with a three-dimensional model of a combustor liner for the verification phase of this contract. In the verification phase of the contract, 3D heat transfer and stress analysis models of combustor liners and turbine blades were used to validate the mapped temperature produced by the transfer module. Verification cases were made for both finite element and finite difference heat transfer codes. The existing transfer module can process heat transfer results directly from the MARC and SINDA programs and will output temperature information in the forms required for MARC and NASTRAN. The input and output routines in the module are very flexible and could easily be modified to excent data from other heat transfer codes and format data to other stress analysis codes. A user manual for the code has been written and is available.

This thermal load transfer module has been shown to efficiently and accurately transfer thermal data from dissimilar heat transfer meshes to stress meshes. The fundamental part of the code, the 3D search, interpolation and surfacing routines, have much more potential. They form an outstanding foundation for automatic construction of embedded meshes, local element mesh refinement, and the transfer of other mechanical type loading.

3-D
TITAN
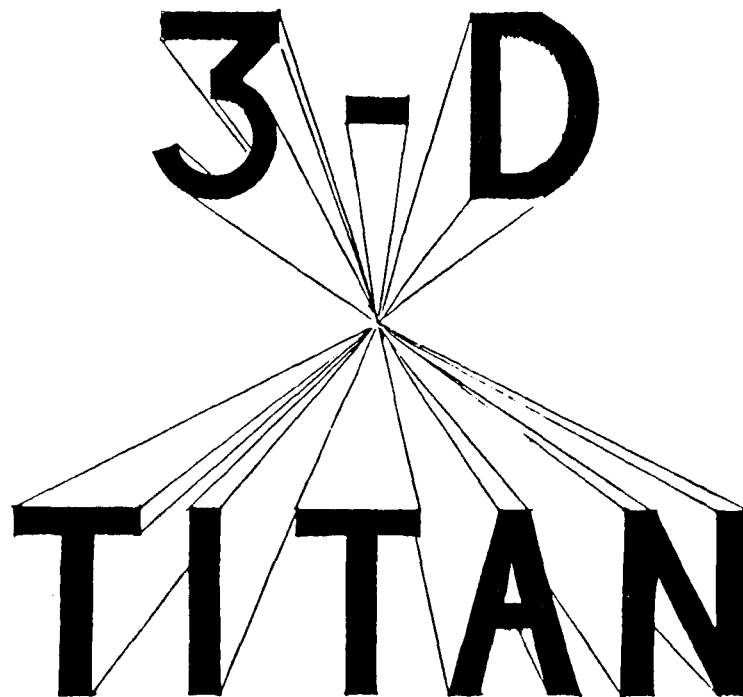
PROBLEM :

- LARGE HEAT TRANSFER/STRESS MODELS

- DIFFERENT MESH DENSITIES

- FINITE DIFFERENCE VS. FINITE ELEMENT CODES

- THERMAL TRANSFER TIME CONSUMING AND ERROR PRONE

Objectives

- Transfer Temperatures from a Heat Transfer Study
  To a Stress Analysis

    - Independent Meshes

    - Accurate/Efficient Transfer

    - Flexible

Thermal Transfer Module
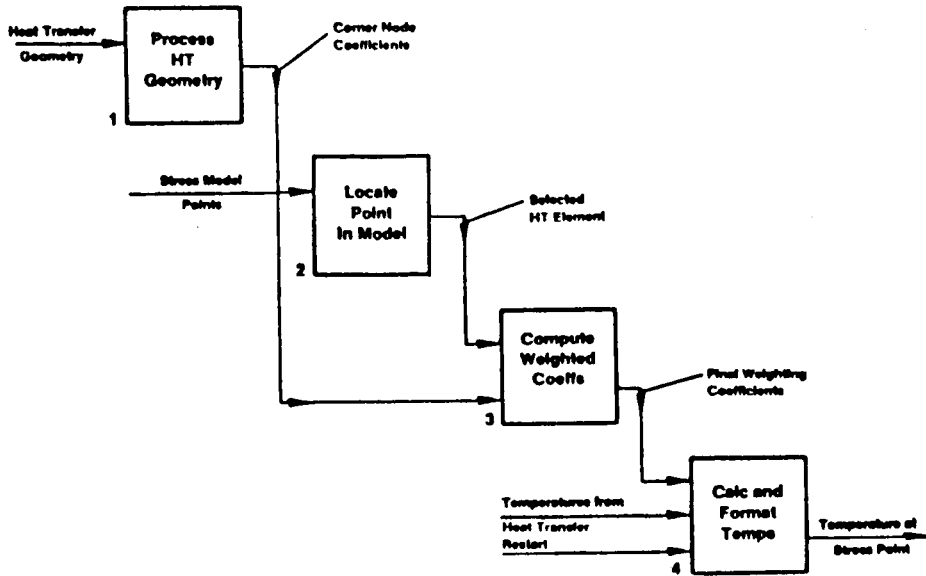
Overall System

Enhanced Program Features

Verification Study

- 415 Heat Transfer Elements
- 827 Corner Nodes

Verification Model

**Temperature Verification Plots
Convex Side Mid Section
Large Model (Airfoil)**

□ Heat Transfer Result
○ Heat Transfer Result
△ Thermal Transfer Module

Temperature

Distance
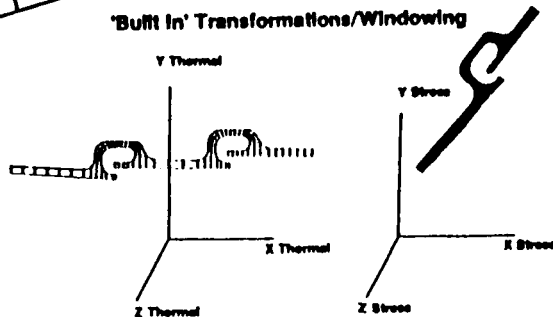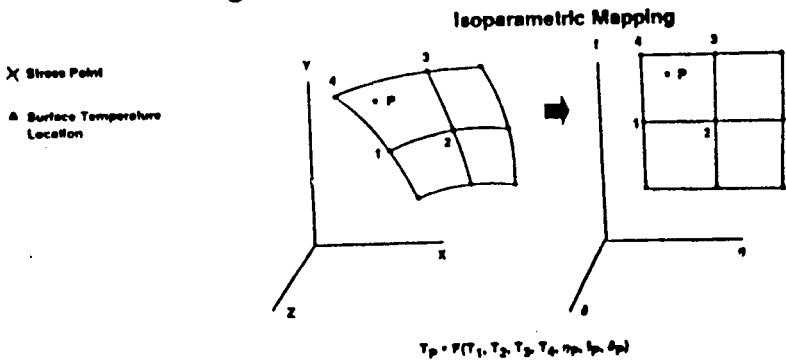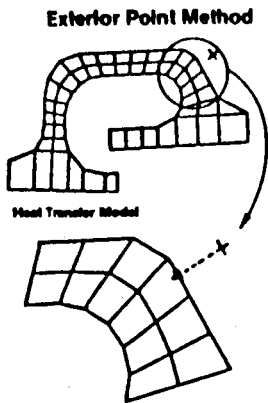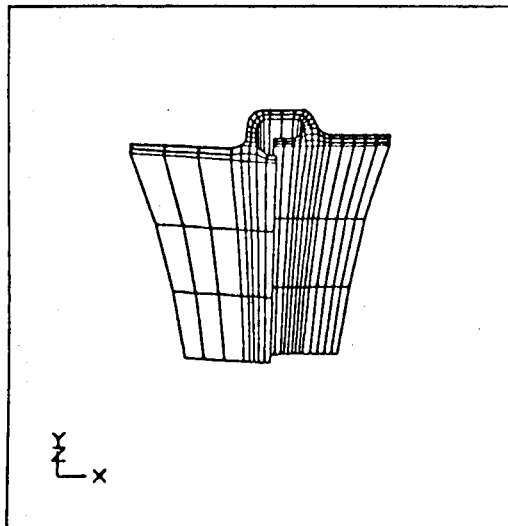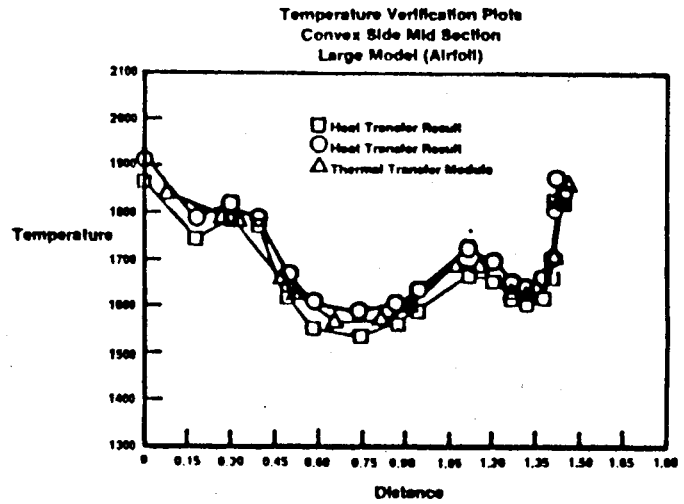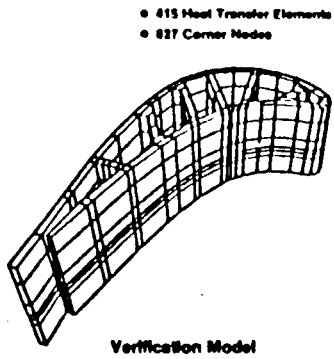
HEAT TRANSFER MODEL
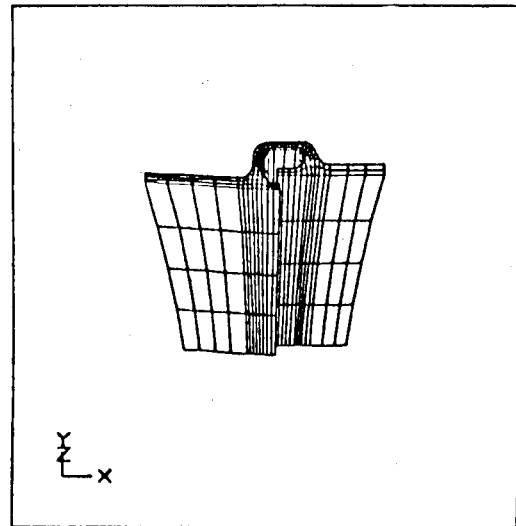
STRESS MODEL
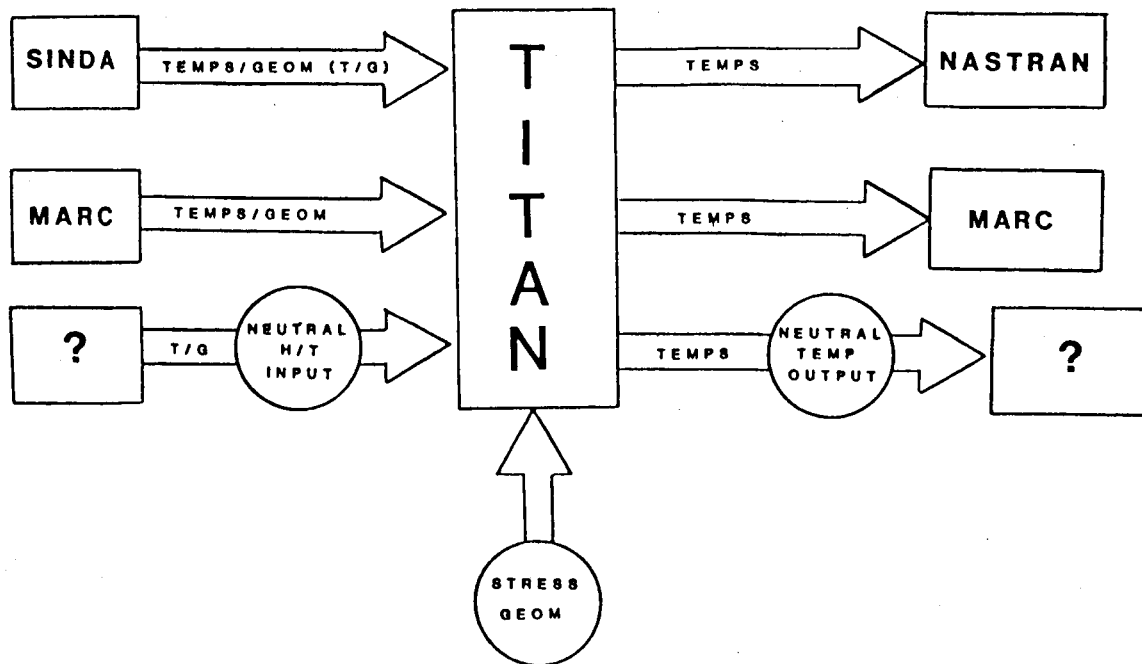
TITAN SCHEMATIC

Future Applications

Automatic Boundary Condition Assignment
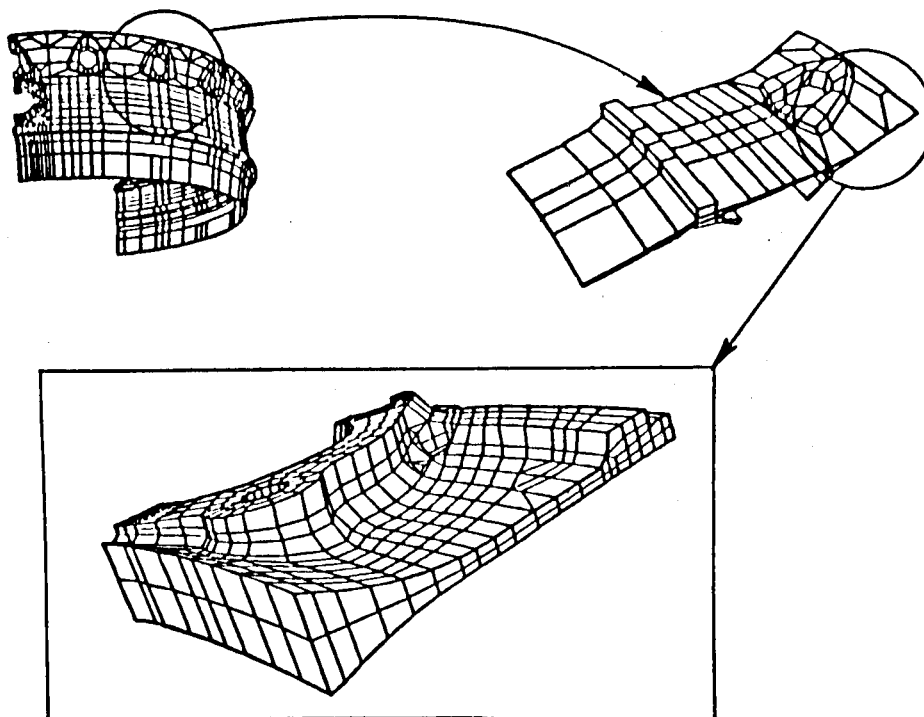
3D INELASTIC ANALYSIS METHODS FOR HOT SECTION COMPONENTS

M.L. Roberts, R.L. McKnight, L.T. Dame & P.C. Chen
General Electric Company
Aircraft Engine Business Group

INTRODUCTION

The objective of this research is to develop analytical tools capable of economically evaluating the cyclic time-dependent plasticity which occurs in hot section engine components in areas of strain concentration resulting from the combination of both mechanical and thermal stresses. The techniques developed must be capable of accommodating large excursions in temperatures with the associated variations in material properties including plasticity and creep.

The overall objective of this research program is to develop advanced 3-D inelastic structural/stress analysis methods and solution strategies for more accurate and yet more cost-effective analysis of combustors, turbine blades, and vanes. The approach will be to develop four different theories, one linear and three higher order with increasing complexities including embedded singularities.

The objective will be achieved through a four-phase program consistent with the NASA Statement of Work.

In Task I, a linear formulation theory is being developed. These consist of three linear formulation models in which stress, strain, and temperature are linear functions of the spatial coordinates; and the increments in loading, temperature, and time are linear. Three constitutive relations are being developed for these linear formulation models each capable of predicting elastic, plastic, thermal, and creep strains and cyclic effects. One constitutive relation will be approximate, one will be of the current genre, and one will be a unified theory.

In Task II, the polynomial formulation theory is being developed. These consist of three polynomial formulation models in which stress, strain, and temperature are polynomial functions of the spatial coordinates, and the increments in loading temperature and time are quadratic. They will also accommodate two-intersecting embedded discontinuities. Three constitutive relations are associated with these polynomial formulation models.

In Task IV, the special functions theory will be developed. These will consist of three special function formulation models in which stress, strain, and temperature are special functions of the spatial coordinates and the increments in loading, temperature, and time are special functions. These models will accommodate eight intersecting embedded similar discontinuities and have three associated constitutive relations.

In Task V, the general functions theory will be developed. These will consist of three general function formulation models in which stress, strain, and temperature are general functions of the spatial coordinates and the increments in loading, temperature, and time are general functions.

These models will accommodate eight intersecting embedded different discontinuities and have three constitutive relations associated with them. One of the constitutive relations will be more complex than those used for the special functions theory.

Task III and VI are reporting requirements.

The above approach will provide the hot section designer/analyst with a wide variety of tools in his nonlinear toolbox. Each of these tasks will produce a matrix of constitutive models and formulation models of varying complexity. There will be three constitutive models (simple, classical, unified) coupled with a mechanics of materials model, a special finite element, and an advance formulation model. This will allow the selection of that tool which best fits the problem to be solved with the appropriate combination of accuracy and cost.

Three constitutive models have been developed in conjunction with the Task I linear theory. These consist of a simple model, a classical model, and a unified model. The simple model will perform time-independent inelasticity analyses using a bilinear stress-strain curve and time-dependent inelasticity analyses using a power-law creep equation. The second model will be the classical model of Professors Walter Haisler and David Allen (Reference 1) of Texas A&M University. The third model will be the unified model of Bodner, Partom, et. al. (Reference 2). All of these models have been customized for a linear variation of loads and temperatures.

The three formulation models for Task I are a nine-noded shell element, a twenty-noded brick element both with and without time embedment, and a boundary integral model. The nine-noded shell element is obtained by "degenerating" a 3D isoparametric solid element and then imposing the necessary kinematic assumptions in connection with the small dimension of the shell thickness (References 3 and 4). This nine-noded Lagrangian formulation overcomes the shear-locking problem experienced by the lower order elements as the element size versus thickness aspect ratio becomes very large. Lobatto quadrature is being used with this element to effectively provide the equivalent of upper and lower surface nodes and for recovery of stresses/strains at the node points.

In the conventional format, the 20 noded brick element will use Gaussian quadrature to develop the stiffness and mass matrices and the right hand side load vectors; however stresses/strains will be recovered at the nodal points. This element will also be implemented in a time-embedded format. This will add an extra degree-of-freedom at each node-time.

The boundary element method linear formulation consists of an eight noded, curved surface compatible with the 20 noded brick element. In this element, inelastic behavior is treated as a body force and its effect is determined by integrating over the volume. Stresses and strains can then be found at any point by performing a differentiation of the integral equations.

REFERENCES

1. Allen, D.H., and Haisler, W.E., "A Theory of Thermoplastic Materials", Computers and Structures, Vol. 13, pp. 129-135, 1981.

2. Bodner, S.A., Partom, I., and Partom, Y., "Uniaxial Cyclic Loading of Elastic-Viscoplastic Material," ASME J. Appl. Mech. $\underline{46}$, p. 805, 179.

3. Chang, T.Y. and Sawamiphakdi, K., "Large Deformation Analysis of Shells by Finite Element Method," Comp. & Struct., $\underline{13}$, pp. 331-340 (1981).

4. Chang, T.Y. and Sawamiphakdi, K., "Nonlinear Finite Element Analysis of Shells with Large Aspect Ratio," presented at the Nonlinear Structural Analysis Workshop, NASA Lewis Research Center, April 19 & 20, 1983.

COMPONENT SPECIFIC MODELING

M. L. Roberts
General Electric Company
Aircraft Engine Business Group

1. INTRODUCTION

Modern jet engine design imposes extremely high loadings and temperatures on hot section components. Fuel costs dictate that minimum weight components be used wherever possible. In order to satisfy these two criteria, designers are turning toward improved materials and innovative designs. Along with these approaches, however, they must also have more accurate, more economical, and more comprehensive analytical methods.

Numerous analytical methods are available which can, in principle, handle any problem which might arise. However, the time and expense required to produce acceptable solutions is often excessive. This program addresses this problem by developing specialized software packages, which will provide the necessary answers in an efficient, user-oriented, streamlined fashion. Separate component-specific models will be created for burner liners, turbine blades, and turbine vanes using fundamental data from many technical areas.

2. OBJECTIVE

The overall objective of this program is to develop and verify a series of interdisciplinary modeling and analysis techniques which have been specialized to address three specific hot section components: combustor burner liners, hollow air-cooled turbine blades, and air-cooled turbine vanes. These techniques will incorporate data as well as theoretical methods from many diverse areas, including cycle and performance analysis, heat transfer analysis, linear and nonlinear stress analysis, and mission analysis. Building on the proven techniques already available in these fields, the new methods developed through this contract will be integrated to predict temperature, deformation, stress, and strain histories throughout a complete flight mission.

3. APPROACH

The work breakdown structure and tasks were discussed in detail at the Second HOST Workshop last year, and will not be repeated here. Three major development activities make up the Base Program. These are:

1. The Thermodynamic Engine Model,

2. The Thermomechanical Loads Model, and

3. The Three Component Specific Models:

- Combustor liner,

- Turbine blade, and

- Turbine vane.

Thermodynamic Engine Model

The Thermodynamic Engine Model provides a decomposition/synthesis approach to compute, at any point in a mission, the engine rotor speeds and the gas path dynamic variables (velocity, temperature, pressure, density and Mach number) at any station along the combustor liner and high pressure turbine flow path. With this capability it is possible to synthesize the gas path variable history at any station of the burner liner, blade or vane for a complete mission, without computing the complete engine cycle for all mission points.

To develop the model, the engine cycle deck was run at 148 cycle points covering the complete engine operating range shown in Figure 1. From this data an engine performance cycle map and an interpolation scheme were developed to compute the gas path parameters at a chosen engine station, given the engine operating conditions specified in terms of altitude, free stream Mach number and engine power level. This also was discussed in more detail at last year's Workshop. Results for a typical commercial airline flight: altitude, Mach number, thrust, core rotor speed, compressor discharge temperature and turbine inlet temperature, are shown in Figures 2 through 7. It is not necessary to run complete missions. Segments can be run separately and joined to synthesize alternate missions.

Thermomechanical Loads Model

The Thermomechanical Loads Model accepts as input variables the rotor speeds and the gas path temperatures and pressures at one or more engine stations and computes component metal temperatures and surface pressures. Again, a decomposition/synthesis approach is used.

A typical commercial engine combustor liner, for which the loads model was developed, is shown in Figure 8. The correlation for the burner liner temperature, T_{liner}, was developed in terms of the cooling effectiveness factor, η_c:

$$\eta_c = \frac{T_4 - T_{liner}}{T_4 - T_3}$$

where

T_3 = compressor discharge temperature, and

T_4 = combustor exit temperature.

Using both engine test data and analytic results, a correlation of cooling effectiveness with combustor length was developed for a single combustor panel (Figure 9). For a realistic picture of liner temperatures, both average temperature and the hot streak temperature associated with the fuel nozzles were correlated. The effects of pressure and of altitude on cooling effectiveness were examined separately. Both were small enough to be neglected. To account for the temperature gradient through the metal thickness, an expression was derived from cooling effectiveness, compressor discharge temperature and pressure, and combustor exit temperature. By correlating test data against combustor pressure, a representative expression for temperature gradient through the metal thickness was obtained at five typical points along the length of the combustor liner. This completed the work on the combustor liner Thermomechanical Loads Model.

A common approach was taken for the cooled high pressure turbine blade and vane. Cooling effectiveness was again used as the correlating factor. The initial step was to correlate cooling effectiveness as a function of engine operating conditions at the 50% span station. Cross sections at 50% span of the typical blade and vane configurations are shown in Figures 10 and 11. A typical correlation of cooling effectiveness with gas path temperature and power level at the 50% span station on the turbine vane is shown in Figure 12. Both test data and analytical predictions are shown. The trend of the data is quite similar to the combustor data; however, there is some disagreement between the analytical and test values of n_c. This was not unexpected because of: (1) differences between nominal values of design variables (T_{gas}, $T_{coolant}$, wall thicknesses and thermal properties) and actual values; (2) uncertainties in calculating the gas side and coolant side heat transfer coefficients, the radiation heat flux, film cooling effectiveness, etc., (3) measured temperature errors due to uncertainties in thermocouple measurements, flow checking measurements, etc. As a result the test data was used to validate the trend lines, and the analytic predictions were used for the correlation.

From data of the type shown in Figure 12, a correlating equation was developed to predict cooling effectiveness at the 50% span station as a function of operating conditions:

$$\frac{1-n_c}{1-n_{c,Ref}} = \left(\frac{T_3}{T_{3,Ref}}\right)^{0.04} \left(\frac{T_{4.1,Ref}}{T_{4.1}}\right)^{0.04}$$

where $\eta_{c,Ref}$, $T_{3,Ref}$ and $T_{4.1,Ref}$ denote the reference values and conditions of Figures 10 and 11.

To predict the metal temperatures at other points on the blades, the cooling effectiveness factors at other spanwise stations were correlated against the values at the 50% span station, $_{50\%}$. This was done at eight chordwise stations on both the suction and pressure surfaces. Thus, using the gas path temperatures T_3 and $T_{4.1}$ for any engine operating condition, the reference data shown in Figures 10 and 11, and the correlating equation for η_c, the Thermomechanical Loads Model can be used to predict the metal temperatures over the complete blade and vane surfaces.

To establish the general procedure for predicting the static gas pressure distributions along the airfoil surfaces of the blade and vane, typical design gas pressure distributions were collected and normalized. Figure 13 shows the typical turbine normalized vane gas static pressure distribution.

With the completion of the Thermomechanical Loads Model, the capability exists for synthesizing a mission, determining the hot section flow path gas properties for the complete mission, and, from these, the metal temperature and pressure histories for the combustor and turbine blade and vane.

Component Specific Model Development - Geometric Modeling

The approach taken to model the three components is to select typical components, identify the key input parameters and develop master regions from these parameters. The finite element mesh can then be overlaid on each master region. Figure 14 shows a typical combustor nugget, some of the physical input parameters, and the master region definition based on those parameters. Figure 15 shows representative 2D and 3D models generated from these master regions. Modeling of the other two components, the blade and vane, is currently progressing.

4. CONCLUSION

When completed, this program will provide a non-linear stress analysis system for hot section engine parts that will allow the component designer to evaluate quickly the effects of mission variations on component life. It will be easy to use, cost effective, and make a significant contribution to assessing hot section durability.

246
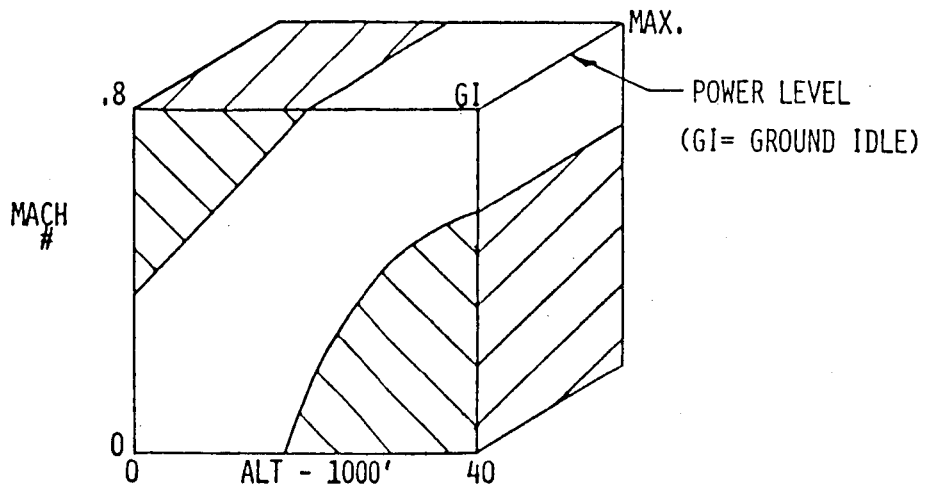
FIGURE 1. ENGINE OPERATING RANGE
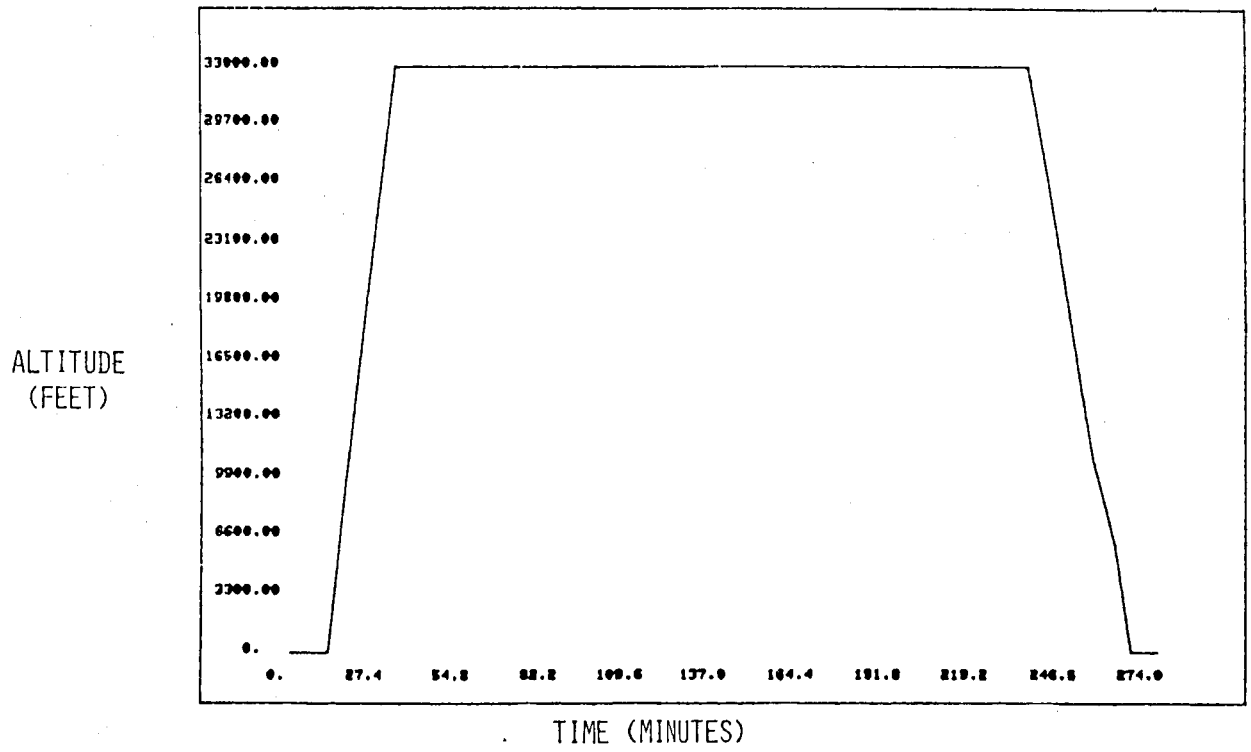
TIME (MINUTES)

FIGURE 2. ALTITUDE VS. TIME

ORIGINAL PAGE IS
OF POOR QUALITY
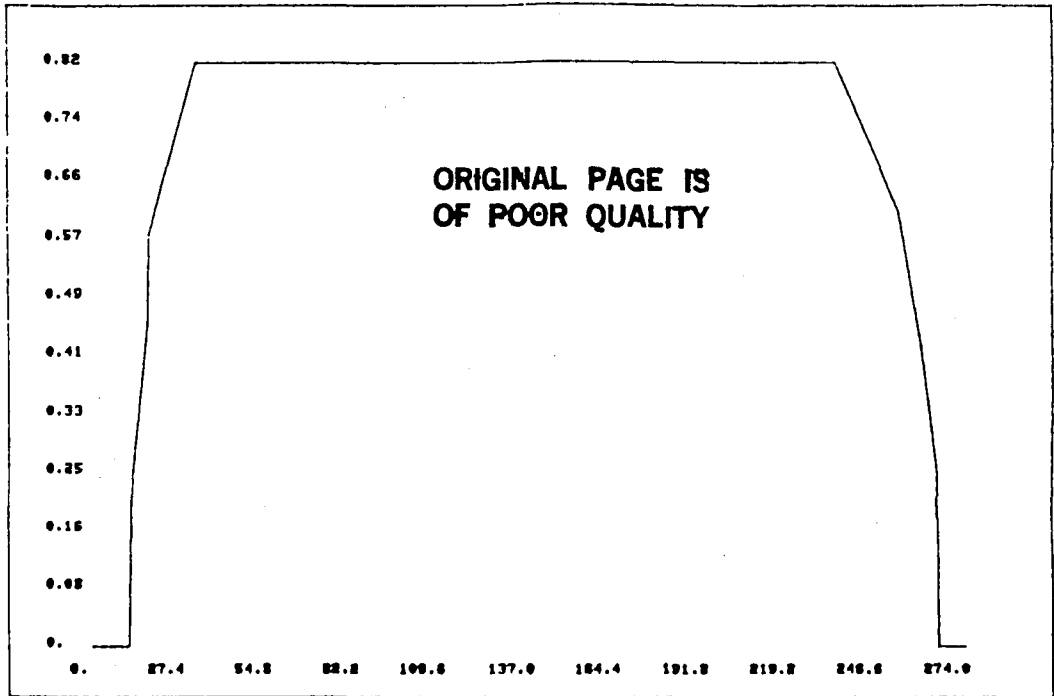
MACH NO.

TIME (MINUTES)

FIGURE 3. MACH NO. VS. TIME

THRUST
(POUNDS)
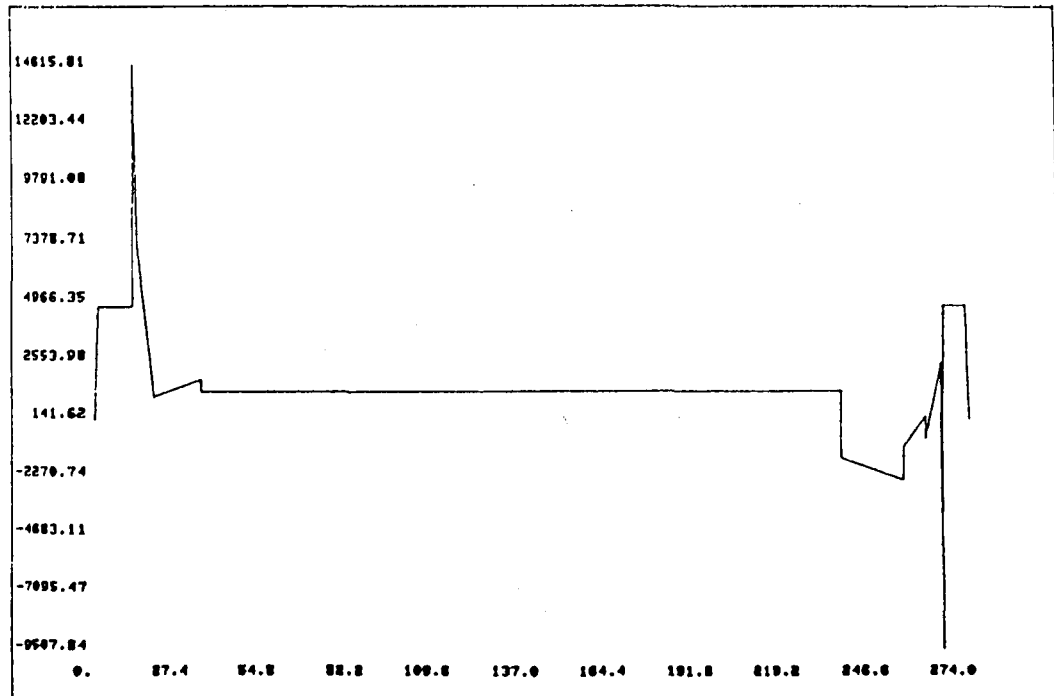
TIME (MINUTES)

FIGURE 4. THRUST VS. TIME

248

CORE
ROTOR
SPEED
(RPM)

TIME (MINUTES)
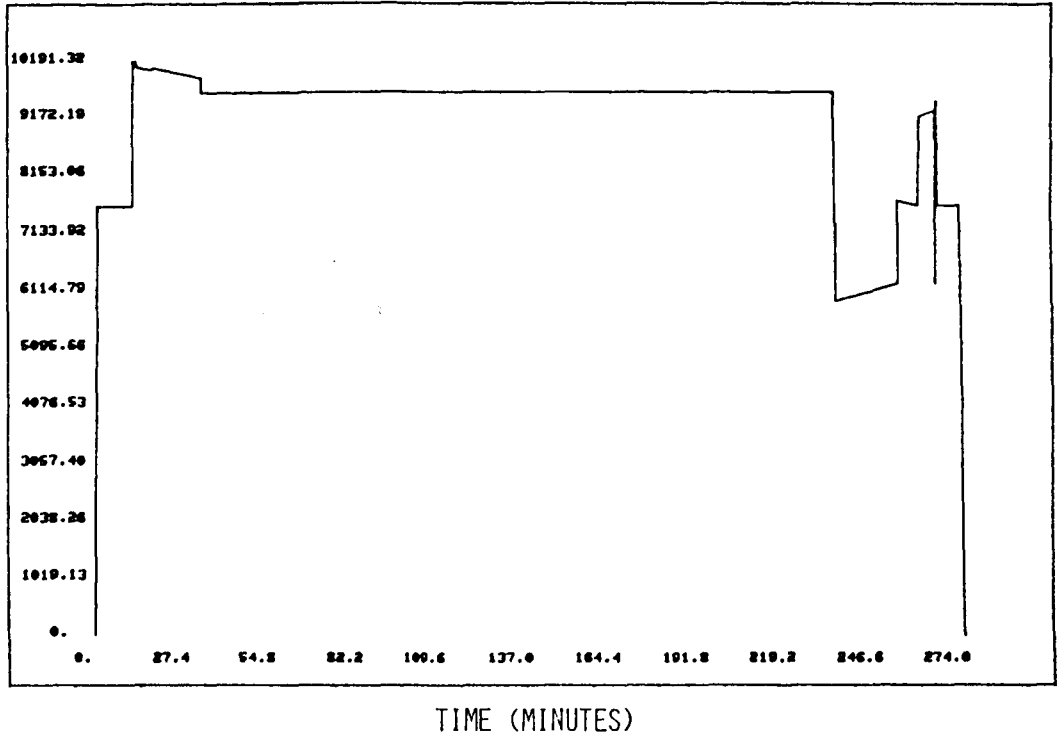
FIGURE 5. CORE ROTOR SPEED VS. TIME

COMPRESSOR
DISCHARGE
TEMPERATURE
(°F)

TIME (MINUTES)
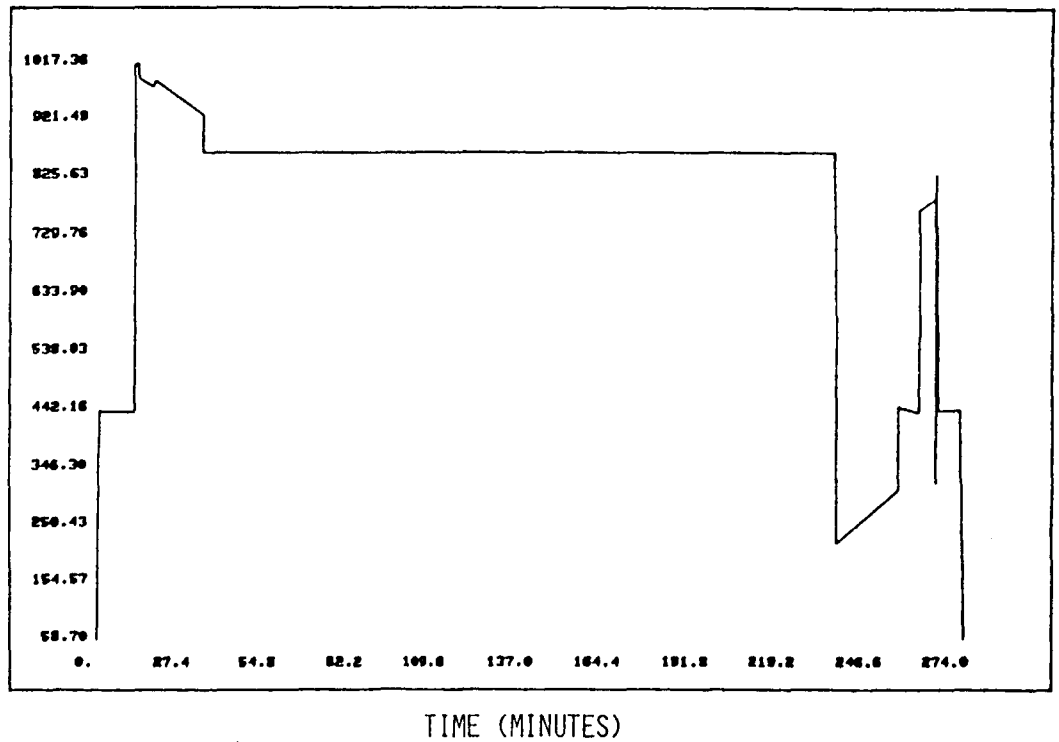
FIGURE 6. COMPRESSOR DISCHARGE TEMPERATURE VS. TIME
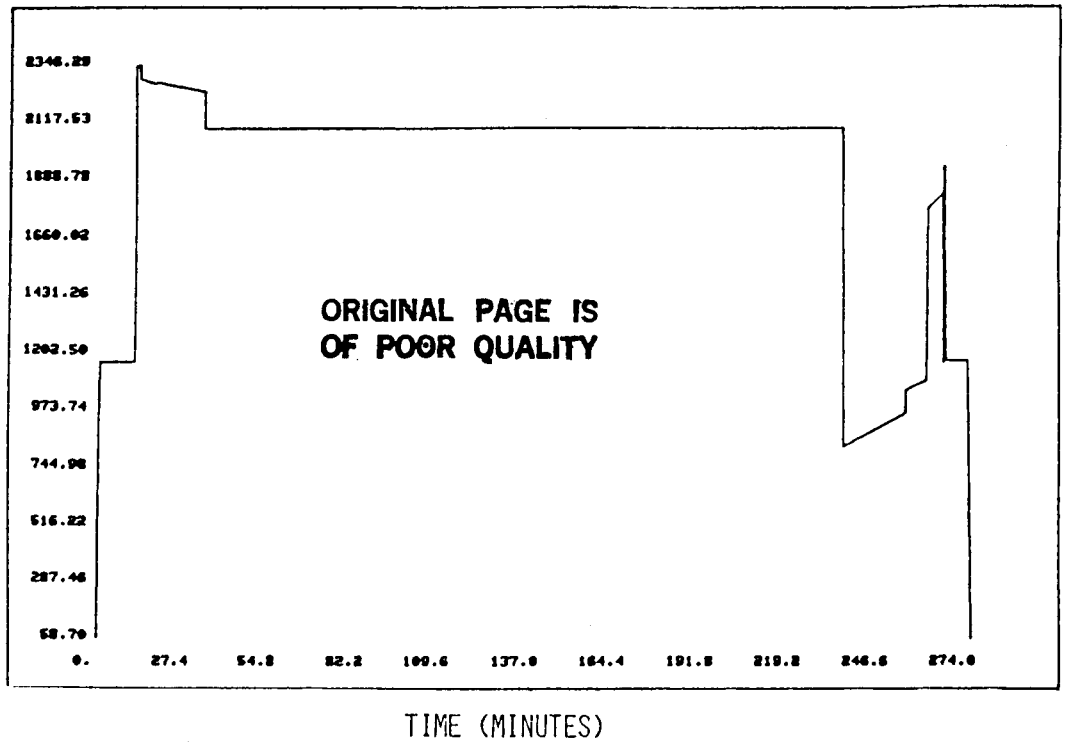
FIGURE 7. TURBINE INLET TEMPERATURE VS. TIME

Pressure Tap Locations

1. Dome Upstream
2. Dome Downstream
3. Inner Passage, Upstream
4. Inner Passage, Downstream
5. Outer Passage, Downstream
6. Combustor Downstream
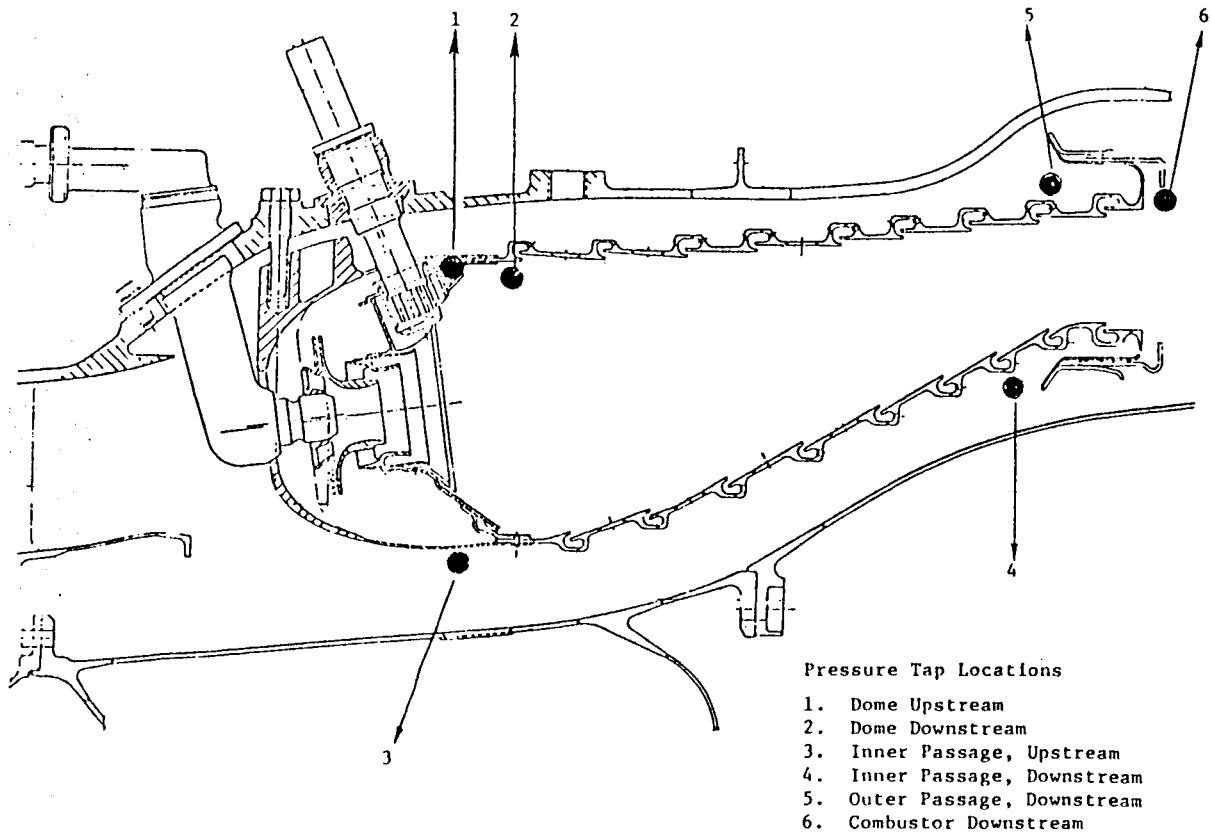
FIGURE 8. CF6-50 ROLLED RING COMBUSTOR

250
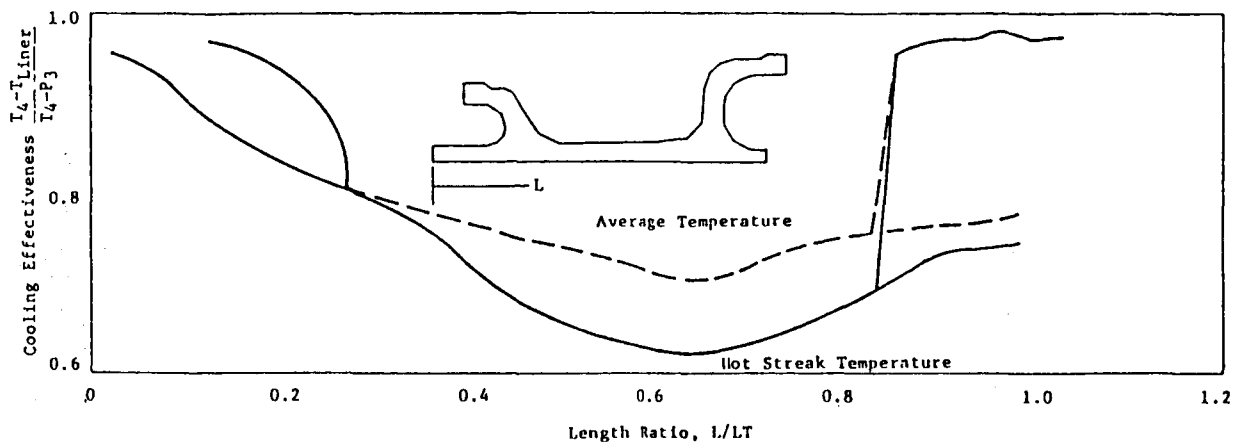
FIGURE 9. COOLING EFFECTIVENESS DISTRIBUTION, PANEL 7
OUTER

$$\eta_c = \frac{T_{41} - T_m}{T_{41} - T_j}$$

$\eta_{c, Bulk} = 0.592$ at Pitch Line
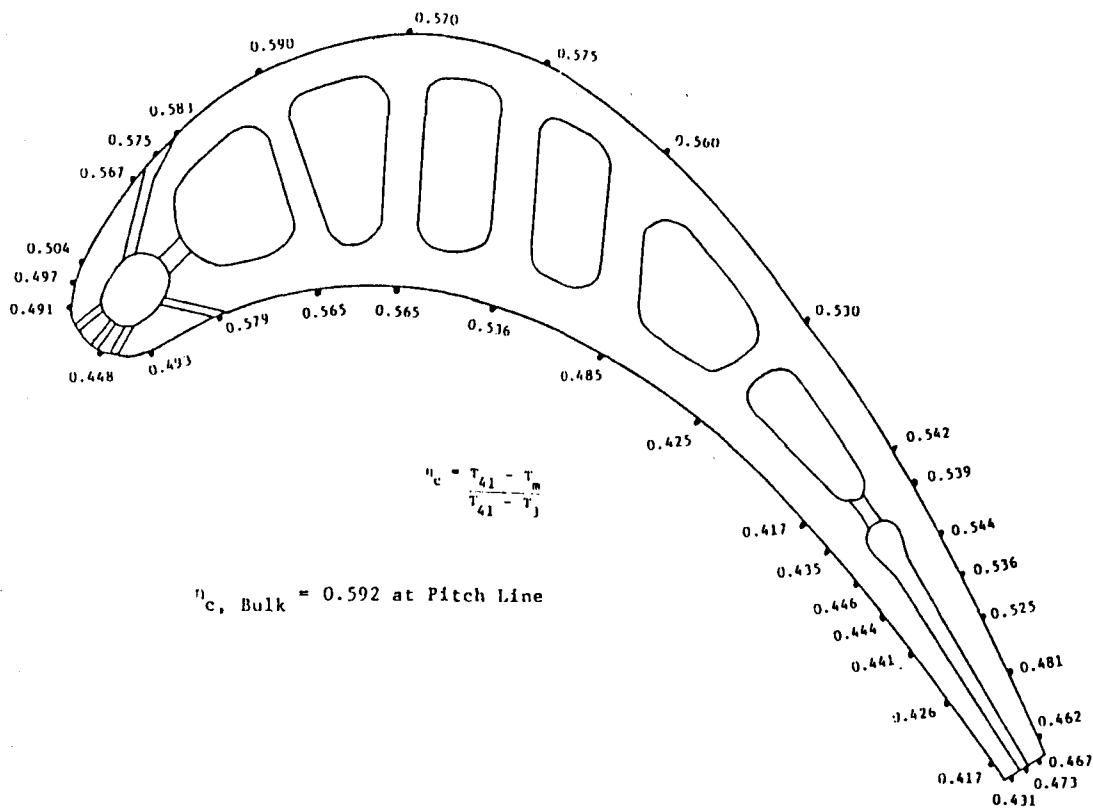
FIGURE 10. TURBINE BLADE SECTION WITH LOCAL GENERALIZED
COOLING EFFECTIVENESS (η_c)

251

FIGURE 11. TURBINE VANE SECTION WITH LOCAL GENERALIZED COOLING EFFECTIVENESS (η_c)

$$\eta_c = \frac{T_{41} - T_m}{T_{41} - T_3}$$

$\eta_{c, \text{Bulk}} = 0.592$ at Pitch Line
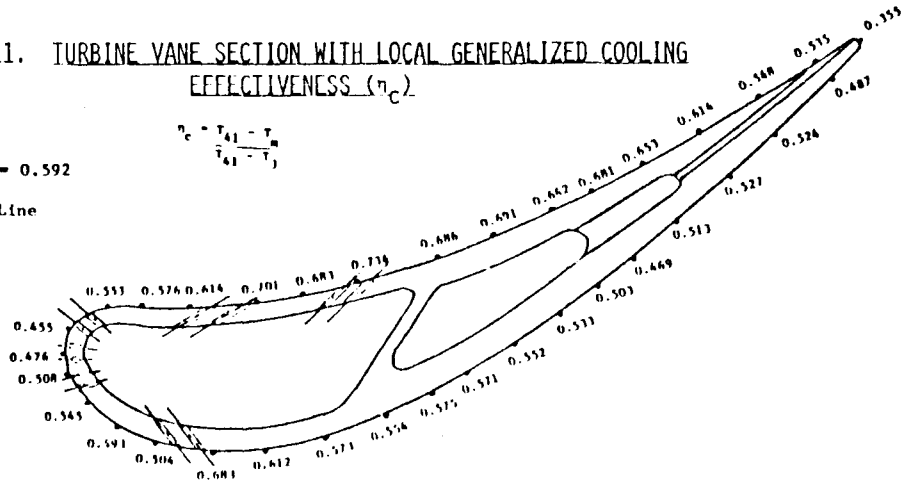
FIGURE 12. VANE COOLING EFFECTIVENESS AT 50% SPAN

$$\eta_c = \frac{T_{41} - T_m}{T_{41} - T_3}$$

252
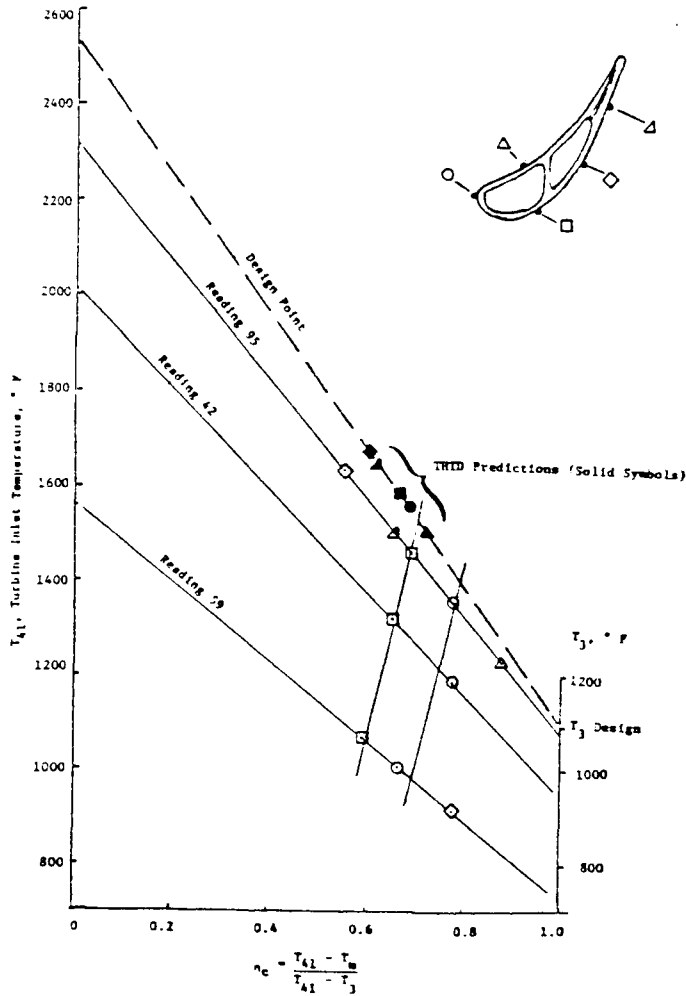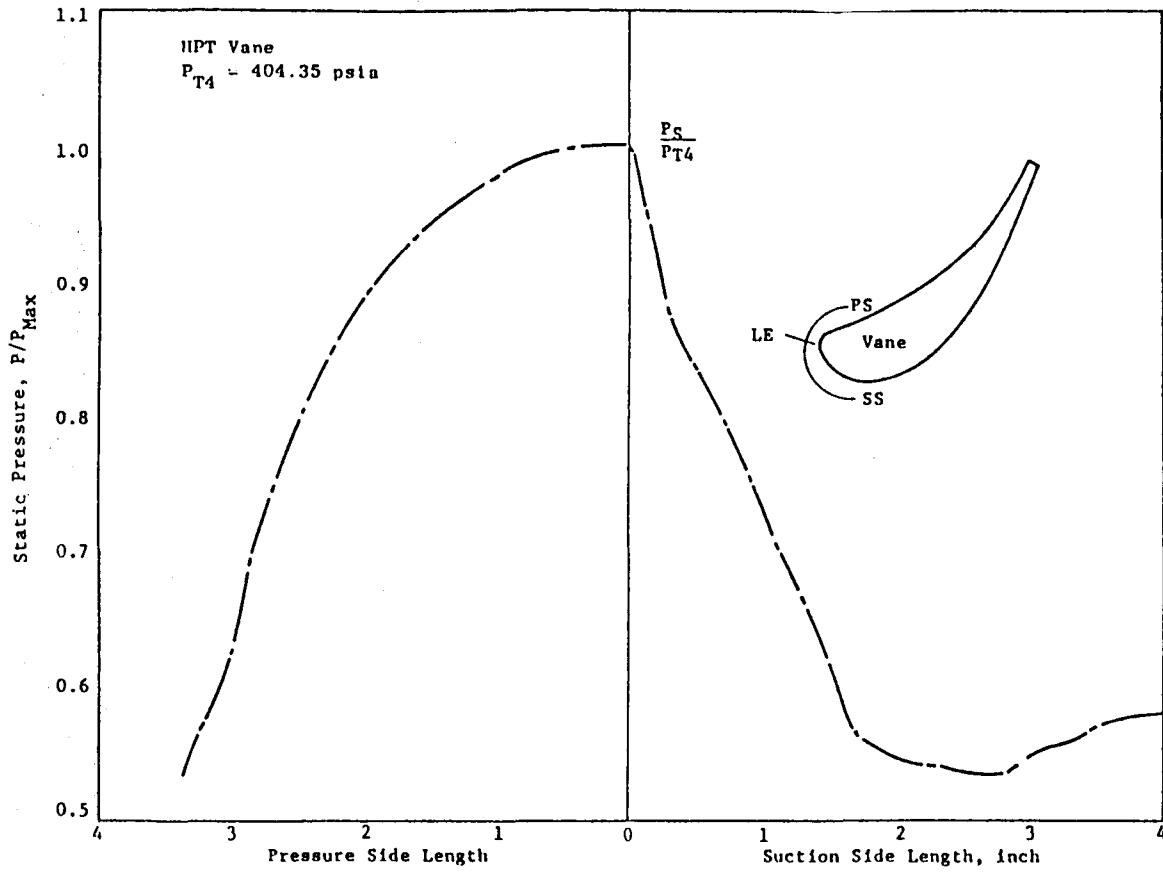
FIGURE 13. GAS STATIC PRESSURE DISTRIBUTION ALONG VANE SURFACE
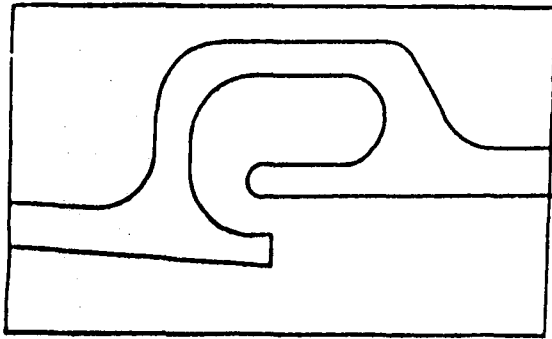
Typical Nugget
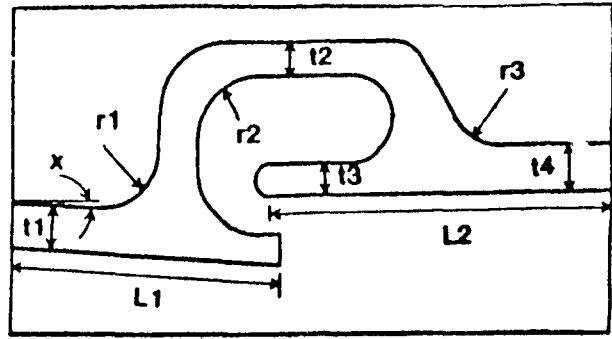
Physical Input Parameters
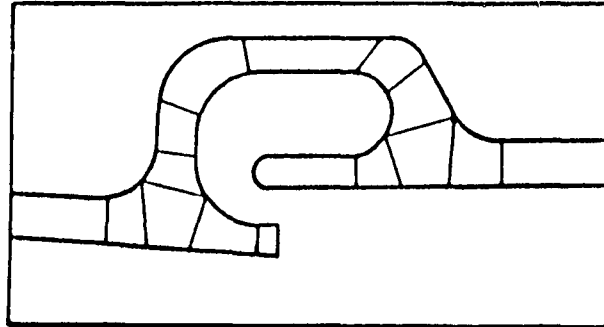
Master Region Definition

FIGURE 14. COMBUSTOR MODELING PROCESS
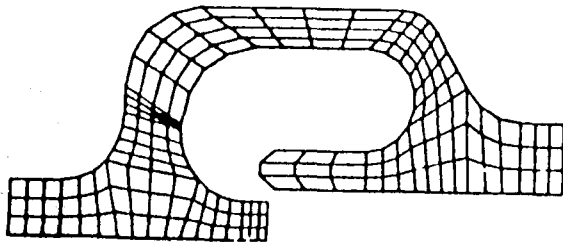
2 D Model
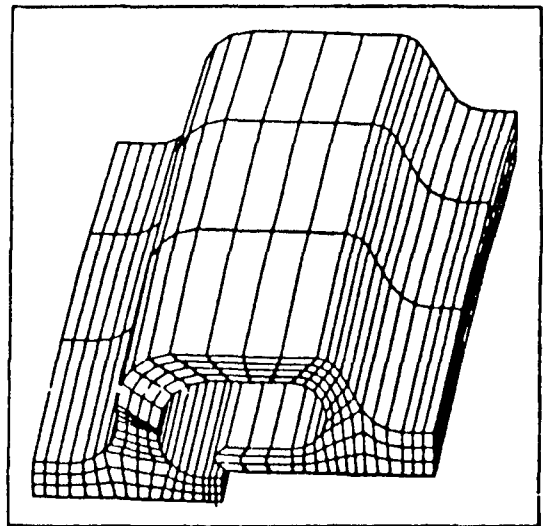
3 D Model

FIGURE 15. COMBUSTOR NUGGET FINITE ELEMENT
MODELS

3-D INELASTIC ANALYSIS METHODS
FOR HOT SECTION COMPONENTS (BASE PROGRAM)

E. S. Todd
United Technologies Corporation
Pratt & Whitney

The objective of this program is to produce a series of new computer codes that permit more accurate and efficient three-dimensional inelastic structural analysis of combustor liners, turbine blades, and turbine vanes. Each code embodies a progression of mathematical models for increasingly comprehensive representation of the geometrical features, loading conditions, and forms of nonlinear material response that distinguish these three groups of hot section components.

Software in the form of stand-alone codes and modules for use in general purpose structural analysis programs is being developed by Pratt & Whitney (P&W) with assistance from three uniquely qualified subcontractors: MARC Analysis Research Corporation (MARC), United Technologies Research Center (UTRC) and State University of New York at Buffalo (SUNY-B). Special finite element models are being constructed by MARC, while mechanics of materials models and constitutive models are being assembled by UTRC. Development of advanced formulation (boundary element) models is being shared by P&W and SUNY-B. Verification of the various analysis packages is being done by P&W.

The technical effort of the Inelastic Analysis Methods program is divided into two 24-month segments: a base program, and an optional program to be exercised at the discretion of the government. The first year (Task I) of the base program dealt with linear theory in the sense that stresses or strains and temperatures in generic modeling regions are linear functions of the spatial coordinates, and solution increments for load, temperature and/or time are extrapolated linearly from previous information. Three linear formulation computer codes, hereafter referred to as MOMM (Mechanics of Materials Model), MHOST (MARC-HOST), and BEST (Boundary Element Stress Technology), have been developed and delivered to Lewis Research Center.

Three increasingly sophisticated constitutive models are employed by MOMM, MHOST, and BEST to account for inelastic material behavior (plasticity, creep) in the elevated temperature regime. The simplified model assumes a bilinear approximation of stress-strain response and glosses over the complications associated with strain rate effects, etc. The state-of-the-art model partitions time-independent (plasticity) and time-dependent (creep) in the conventional way, invoking the Von Mises yield criterion and standard (isotropic, kinematic, combined) hardening rules for the former, and a power law for the latter. Walker's viscoplasticity theory (ref. 1), which accounts for the interaction between creep/relaxation and plasticity that occurs under cyclic loading conditions, has been adopted as the advanced constitutive model.

In brief, MOMM is a stiffness method finite element code that utilizes one-, two- and three-dimensional arrays of beam elements to simulate hot section component behavior. Despite limitations of such beam model representations, the code will be useful during early phases of component design as a fast, easy to use, computationally efficient tool. All of the structural analysis types (static, buckling, vibration, dynamics), as well as the three constitutive models mentioned above, are provided by MOMM. Capabilities of the code have been tested for a variety of simple

problem discretizations (ref. 2). Work is in progress to establish modeling guidelines for simulation of two- and three-dimensional behavior.

The MHOST code employs both shell and solid (brick) elements in a mixed method framework to provide comprehensive capabilities for investigating local (stress/strain) and global (vibration, buckling) behavior of hot section components. Over the last decade, in order to support their commercially available software, the MARC Corporation has accumulated a great deal of technical expertise creating new, improved algorithms that will significantly reduce CPU (central processing unit) time requirements for three-dimensional analyses. The MHOST code development has taken advantage of this expertise. First generation (Task I) MHOST code is operational and has been tested with a variety of academic as well as engine-related configurations (ref. 2).

Successful assembly of the all new BEST code is possibly the most important accomplishment of the Task I effort. The challenge of extending basic theory and algorithms to encompass inelastic dynamic effects in three-space was met by combining the special skills and efforts of the research and programming teams at SUNY-B and P&W. As with MOMM and MHOST, the initial version of BEST is executable and has been exercised with both small and large test cases (ref. 2). While MHOST and BEST are currently viewed as complementary, they are also competitors; and overall performance on large inelastic models will be watched with interest as the codes mature.

Experimental data from the Benchmark Notch Test program (ref. 3) is being used to verify the stress analysis capabilities of the Inelastic Methods codes. Nominal dimensions of the benchmark notch specimen are shown in figure 1. Finite element and boundary element meshes for one-quarter of the specimen gage section are shown in figure 2. Measured notch root stress-strain behavior for initial uploadings of several specimens is summarized in figure 3. Correlation between the MHOST predictions and the measured strains is very good (fig. 4). Modest mesh refinement/optimization in the vicinity of the notch (fig. 2) is expected to bring the BEST calculations into close agreement with the data.

The existing models will be extended to include higher-order representations of deformations and loads in space and time to deal effectively with collections of discontinuities such as cooling holes and cracks. This will be accomplished during the second half of the base program (Task II) and the optional program (Tasks IV and V). Work on Task II (polynomial theory) is under way and will be described at the Fourth Annual HOST Workshop.

REFERENCES

1. Walker, K. P.: Research and Development Program for Nonlinear Structural Modeling With Advanced Time-Temperature Dependent Constitutive Relationships. NASA CR-165533, November 25, 1981.

2. Wilson, R. B.; Bak, M. J.; Nakazawa, S.; and Banersee, P. K.: 3-D Inelastic Analysis Method for Hot Section Components (Base Program): First Annual Status Report. NASA CR-174700, February 1984.

3. Domas, P. A.; Sharpe, W. N.; Ward; M.; and Yau, J.: Benchmark Notch Test for Life Prediction. NASA CR-165571, June 1982.

71.12
(2.80)
Radius

7.11
(0.28)
Radius

2.54
(0.10)

12.95
(0.51)

B

Sym. Centerline

24.13
(0.95)

R

19.05
(0.75)
Radius

19.05
(0.75) Dia.

Sym. Centerline

50.80
(2.00)

254.00
(10.00)

25.40
(1.00) Dia.

PO No.	B	R
1	17.958 (0.707)	4.902 (0.193)
2	24.13 (0.95)	-

Dimensions in mm (inches)
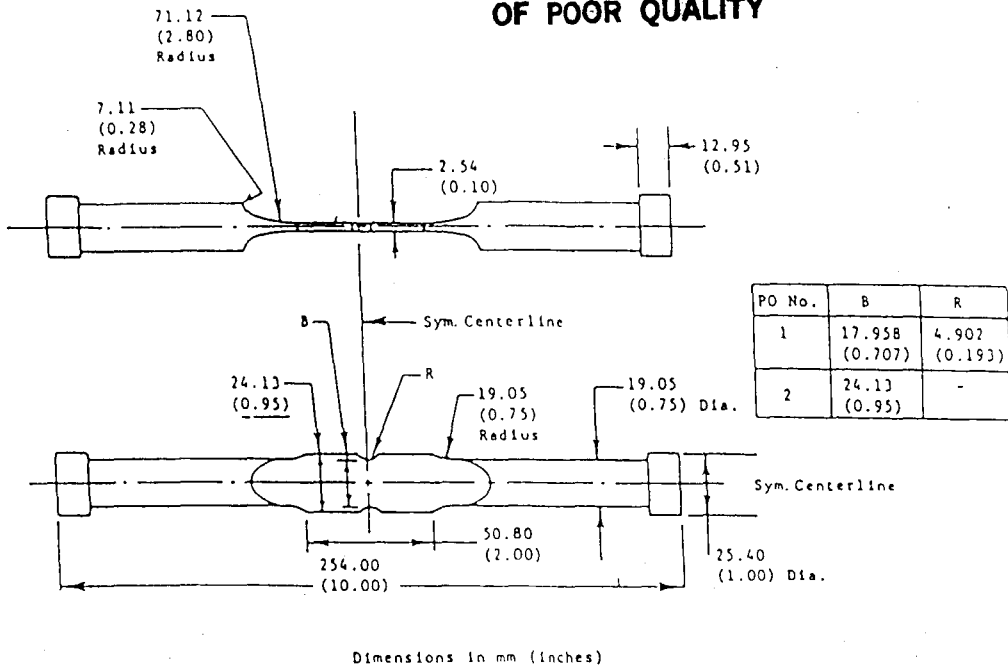
Figure 1   Benchmark Notch Specimen

FINITE ELEMENT MODEL
FINE MESH

FINITE ELEMENT MODEL
COARSE MESH

BOUNDARY ELEMENT MODEL
MIXED VARIATION
L - LINEAR
Q - QUADRATIC
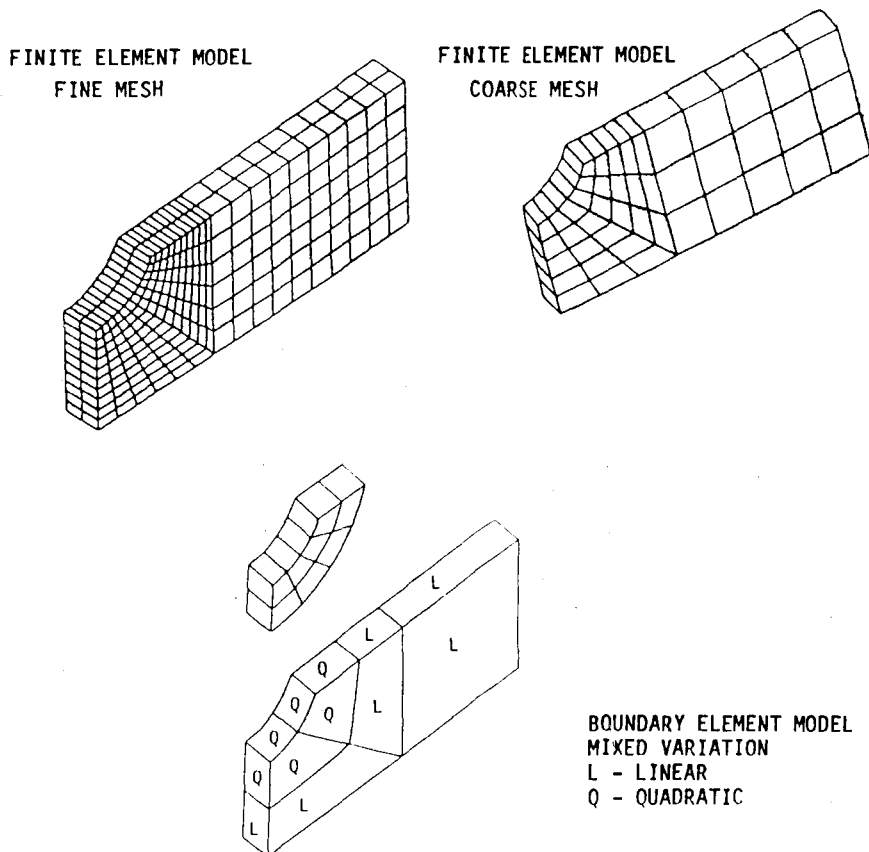
Figure 2   Meshes Used in Benchmark Notch Analysis
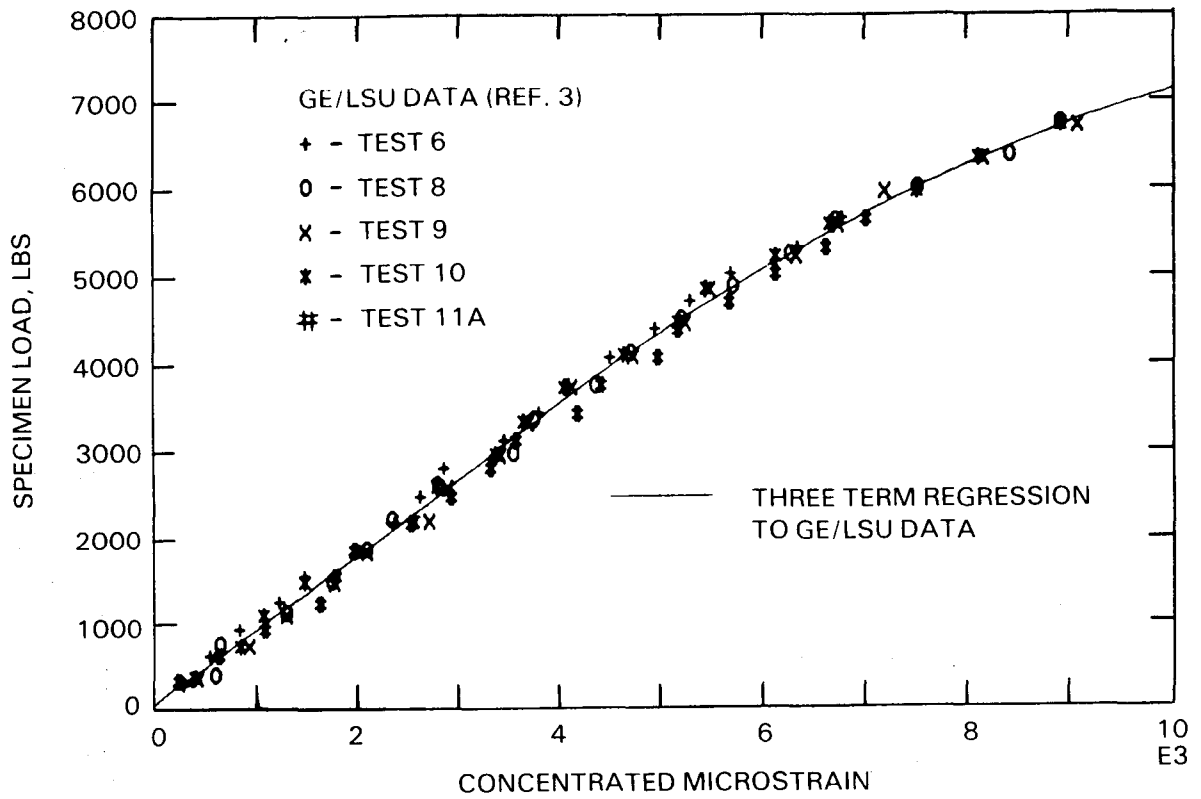
Figure 3   Notch Strain Vs. Load - First Quarter Cycle
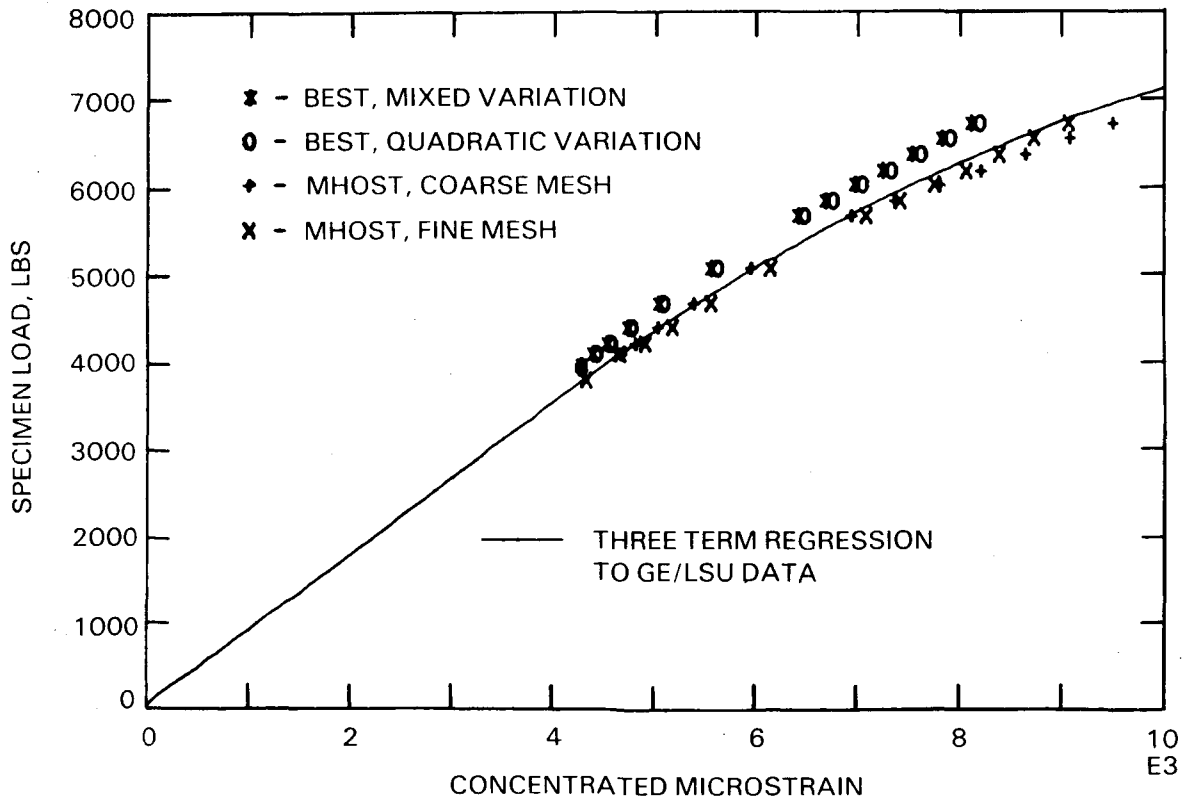
Figure 4   Benchmark Notch - Calculated Vs. Measured Strains

HIGH TEMPERATURE STRESS-STRAIN ANALYSIS

Robert L. Thompson
National Aeronautics and Space Administration
Lewis Research Center

INTRODUCTION

The objectives of the HOST Burner Liner Cyclic Rig Program are threefold:
(1) to assist in developing predictive tools needed to improve design analyses and
procedures for the efficient and accurate prediction of burner liner structural
performance and response; (2) to calibrate, validate, and evaluate these predictive
tools by comparing the predicted results with the experimental data; and (3) to
evaluate existing as well as advanced temperature and strain measurement instrumen-
tation, through both contact and noncontact efforts, in a simulated turbine engine
combustor environment. As the predictive tools, as well as the tests, test methods,
instrumentation, and data acquisition and reduction methods are developed and evalu-
ated, a proven, integrated analysis/experiment method will be developed that will
permit the accurate porediction of the cyclic life of a burner liner.

TEST RIGS

The above objectives will be partially accomplished with two experimental rigs,
one a bench-top rig to test 8- by 5-in flat plates under thermal cycling conditions
and the other an annular rig to test 20-inch diameter cylindrical test specimens.
Figure 1 shows the major components and the installation of the bench-top rig which
is about 90 percent complete. Four quartz lamps (6 kW each) are used to heat the
plate specimens. Water and/or air cooling are used to cool the fixture, lamps, and
test plate. Cooling air to the plate can be preheated. A viewing port provides for
visual inspection of the plate and data acquisition with an infrared (IR) camera
system. Provisions for instrumentation include 30 thermocouples and 10 strain
gauges.

Figure 2 shows the annular rig installation which is about 75 percent complete.
Shown also is the stacked-ring louver burner liner to be tested first. Simpler
liners as well as advanced liners will also be tested, primarily deformation testing
and some fatigue testing will be done. The quartz lamp heating system supplied by
Research, Inc., under contract to Pratt & Whitney Aircraft (P&WA) is shown in figure
3. This rig and program are a cooperative effort between NASA Lewis and P&WA. P&WA
supplied the test section, which includes the heating system, and is supplying
technical assistance to the program. NASA Lewis is providing the test facility and
operators and other technical expertise. The heat source is 112 quartz lamps (6 kW
each) configured circumferentially in 16 sectors each having 7 lamps. Water and/or
air are used to cool the fixture, lamps, and test specimen. Cooling air to the
specimen can be preheated. A natural gas and air mixture will be burned to preheat
the air to about 500 °F. Cooled viewing ports are provided for visual inspection of
the specimen, and thermal data acquisition with an infrared system. Seven quick-
disconnect instrumentation panels provide for 99 thermocouples, 28 strain gauges,
and 21 pressure transducer connections.

TESTS

To verify the feasibility of the test and the bench-top rig design and to identify potential test problems and analysis/experimental complications, a limited number of steady-state and transient tests were conducted. Structural analyses were performed on the 5- by 8- by 0.05-in Hastelloy-X flat plate specimen tested. Figure 4 shows the steady-state temperatures of the Hastelloy-X plate heated at various power levels for three cooling airflows to the plate. The maximum plate temperature is plotted as a function of the applied power level. The cooling air to the plate was varied in steps from 0 to 0.05 to 0.1 lb/sec. The solid points show the effect of preheating the cooling air to the plate to about 430 °F. Note that a 60 percent power level results in a maximum plate temperature of about 1800 °F (maximum normal temperature of a Hastelloy-X combustor liner), while cooling the plate reduces the maximum temperature of the plate appreciably.

Figures 5 to 7 show the cold-side steady-state plate temperatures. Seven thermocouples are used to measure plate temperature. Their locations are shown in the sketch in figure 5. Steady-state temperatures are plotted as functions of the plate centerline temperatures in the horizontal and vertical directions for several applied power levels. With no plate cooling (fig. 5), the heating of the plate for the four power levels is nonuniform, with the lower right quadrant of the plate being much cooler than the others. This is attributed to uneven plate oxidation, the different lamps used, and cooling shelf on which the specimen rests. Figures 6 and 7 show the effect of cooling air on the plate temperatures. These curves show that the axial temperature distribution on the plate can be controlled by varying the cooling airflow. Hot-side plate temperatures were also measured. Through the thickness temperature gradients of 20 to 30 F° were obtained.

Some results of thermal cycling of a test plate are shown in figures 8 and 9. The power was varied cyclically from 5 to 100 percent and back down to 5 percent with a 148/sec cycle time as shown in figure 8(a). The maximum plate temperature for this cycle is shown in figure 8(b). Cooling air flow to the plate was at its maximum at 0.1 lb/sec. The preheater was used to preheat the cooling air to the plate to about 430 °F. Figure 9 shows the maximum temperature of the plate as a function of the number of thermal cycles. The minimum temperature at 5 percent power is also shown for the same location. After the first thermal cycle the temperatures were very repeatable. A specified temperature history can also be run, in which case the power is the dependent variable. No data are shown for this case. A programmable microprocessor is used to run the tests in either the power control mode or the temperature control mode.

Cold-side plate temperatures are measured with both thermocouples and a computer-controlled infrared camera system. The major components of the IR system are shown in figure 10. Typical calibration curves for the system are shown in figure 11 where intensity is plotted against thermocouple temperature. Curves like these are used to obtain temperatures from a thermal image and also to determine the emissivity of Hastelloy-X plates. The emissivity of Hastelloy-X was determined to be about 0.88 to 0.90 and was not found to be a function of temperature.

Thermal images of the plate, viewed through the quartz window, for a typical thermal cycle are shown in figure 12. The thermal images obtained from the tests are recorded on a VHS tape recorder, with an image recorded every 1/30 of a second. The thermal images recorded are processed and analyzed following the test using the computer. The processed temperature data are then saved on a magnetic tape for further processing and analysis on the Lewis IBM 370 mainframe computer. This

capability has not been fully demonstrated. The capability also exists to monitor in real time the plate temperature at any point within the field of view of the IR camera. Another use of the IR system is as a diagnostic tool.

Figures 13 and 14 show a comparison of the infrared data with thermocouple data. The thermocouple data and other research and facilities data are acquired with the ESCORT II data acquisition system and stored on the mainframe computer. Steady-state temperatures are compared in figure 13 for a 90 percent power level with cooling air to the plate. There is good agreement between the thermocouple and infrared temperature data, with the maximum difference being about 5 percent. Figure 14 shows a comparison of IR data with thermocouple data for a thermal cycle. Figure 15 illustrates a temperature distribution of the plate obtained from the IR and thermocouple data, to be saved for further analysis.

The experience gained from the bench-top rig operation is and will be carried over to the annular rig. For example, a noncontact strain measurement device will be tested on the bench-top rig. If it is successful, it will be used on the annular rig. Also, lamp durability tests are underway on the bench-top rig. The data and information obtained from these tests will be applied to the annular rig.

The installation of the annular rig is nearing completion. An evaluation of the vitiated preheater for the annular rig has been completed. Air and natural gas were burned in a modified GE J-47 combustor can. Performance results of these tests were the average exit air temperature varied from 400 to 600 °F (500 °F was the nominal design temperature); the pattern factor ranged from 0.009 to 0.053; air-flow rate was varied from 3.5 to 8.0 lb/sec (design conditions); the maximum liner temperature was 700 °F; and no smoke or soot was emitted. The heating system is being installed. Checkout of the water coolant system for the heater is scheduled for October 1984 and checkout of the complete rig is set for November. Testing of the stacked-ring louver liner could begin in December with the testing of simpler as well as advanced liners to follow.

ANALYSIS

The objectives of this program will be partially accomplished with the structural analysis of specimens. A structural analysis of a flat-plate specimen was performed using MARC, a general purpose nonlinear finite-element structural analysis program. The Walker, the Miller, and the Krieg, Swearengen, and Rhode (KSR) viscoplastic constitutive models have been incorporated into MARC. These models can account for the interaction between creep and plastic deformations and strain-rate effects, among others, critical to a burner liner design.

The plate was analyzed using a four-node plane stress element. The mesh configuration is shown in figure 16. The configuration is doubly symmetric and thus only a quarter of the plate is modelled. The finite-element model of frame and plate is also shown where the frame is modelled with bar elements.

For the structural analysis, uniform temperatures were assumed for the plate and frame, with about a 20-percent temperature difference between the plate and frame as shown in figure 17. The maximum principal strains in the plate for the assumed temperature history are shown in figure 18 for the three viscoplastic models. The comparison shows no difference in the prediction of the strains. However, a comparison of the maximum stress component S_x for the three viscoplastic models shows considerable differences (fig. 19). The Miller and KSR models give similar

stresses, while the Walker model gives higher stresses. Figure 20 shows hysteresis loops (maximum stress versus strain) for the three viscoplastic models. No direct comparisons have yet been made between the analysis and experiment because of the nonuniformity of plate temperatures obtained from experiments. However, the structural analysis of plates with nonuniform temperatures obtained from experimental data is underway. Also underway are structural analyses of two-dimensional axisymmetric and three-dimensional burner liner models.

SUMMARY

The preliminary tests conducted with the bench-top rig have demonstrated that the desired plate temperatures, temperature gradient (through the thickness and axially), and repeatable temperature histories can be achieved, although near uniform plate temperatures have yet to be achieved. Finite-element models of plates have been generated and structural analyses of these plates with uniform plate temperatures have been performed using three viscoplastic models. Structural analysis of plates with nonuniform temperatures is underway as are two- and three-dimensional analyses of burner liners.

It has been demonstrated on the bench-top rig that the temperature data obtained from the thermocouples can be collected with the ESCORT II data acquisition system and that these data can then be stored on the Lewis IBM 370 computer for further processing, reduction, and analysis. It has also been demonstrated that the IR camera system can provide accurate temperature maps of the flat plate and can also be used as a diagnostic tool. The system to transfer thermal information from the IR system to the mainframe is in place but has not been demonstrated fully. The experience gained from the bench-top rig installation and operation is being carried over to the annular rig.

The annular rig installation is nearing completion and will provide data on cylindrical tubes and subelements of burner liners. Tests run with the vitiated preheater on the Annular rig were successful.

Structural analyses will be performed to predict the material stress-strain response of plates and burner liners using measured temperature distributions. These analyses will provide a basis for comparing analytical predictions, for example, using several viscoplastic constitutive models, with experimental data for validation and subsequent selection of improved analysis methods to predict accurate and efficient structural responses of burner liners.

BENCH TOP QUARTZ LAMP FLAT PLATE TEST RIG

- QUARTZ LAMPS
- AIR LINES
- WATER LINES
- IR CAMERA
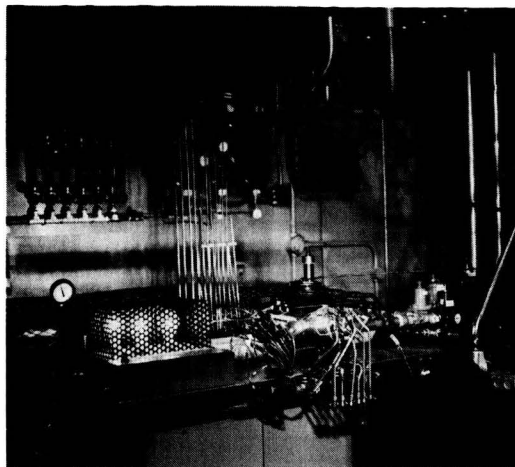
- VIEWING PORT AND COVER
- DIFFUSOR PLATE
- LAMP-OUT DETECTION SYSTEM

CS 84-3985

Figure 1

ANNULAR QUARTZ LAMP COMBUSTOR TEST RIG
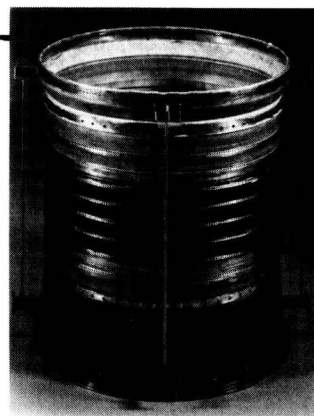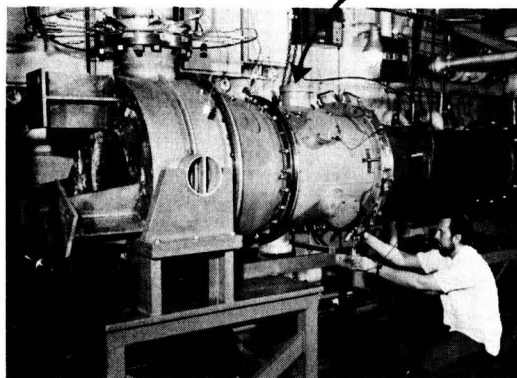
STACKED RING LOUVER LINER

CS 84-3984

Figure 2

QUARTZ LAMP CYCLIC COMBUSTOR TEST RIG SCHEMATIC
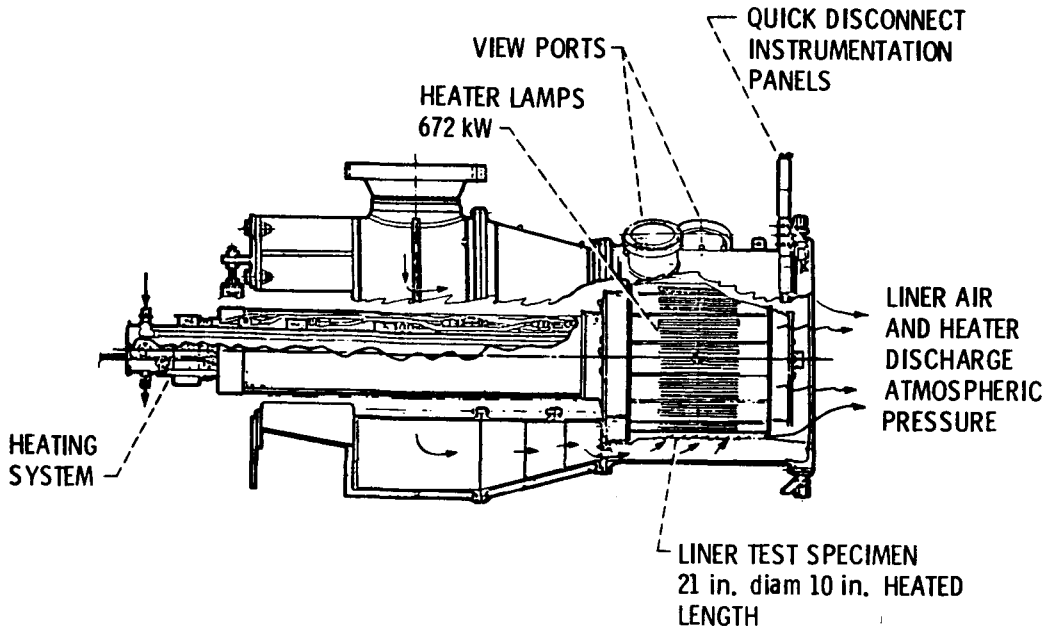
Figure 3

HASTELLOY—X FLAT PLATE HEATED TO STEADY—STATE CONDITIONS
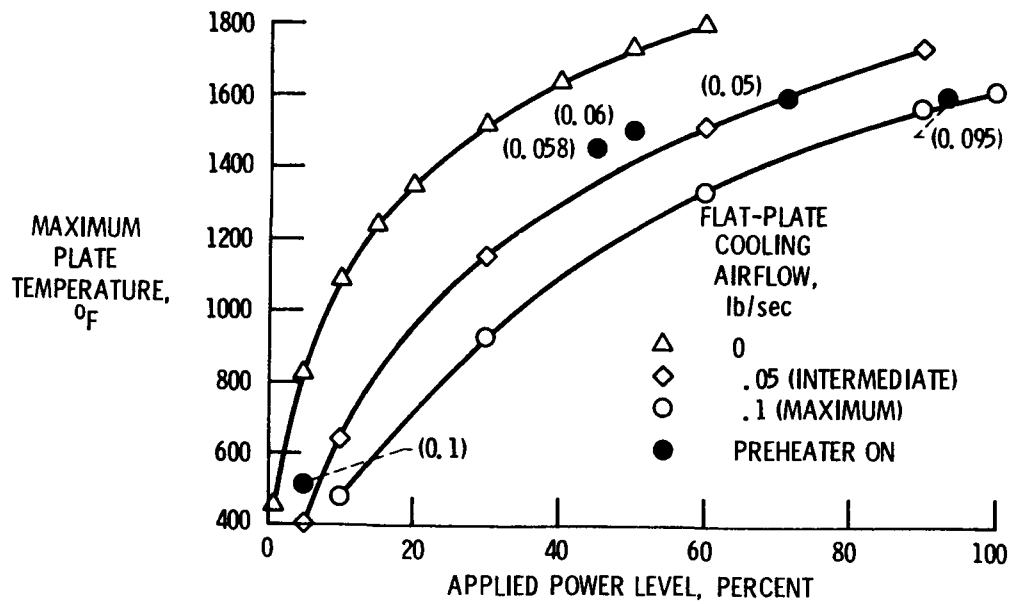
Figure 4

COLD-SIDE PLATE TEMPERATURES FOR NO PLATE COOLING

HORIZONTAL   VERTICAL
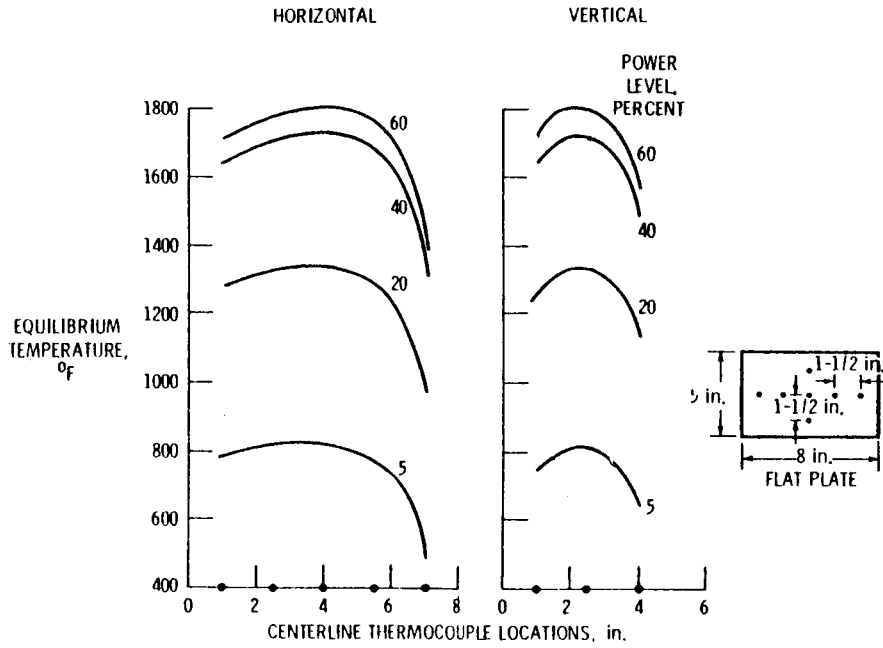
Figure 5

COLD-SIDE PLATE TEMPERATURES FOR INTERMEDIATE PLATE COOLING

HORIZONTAL   VERTICAL
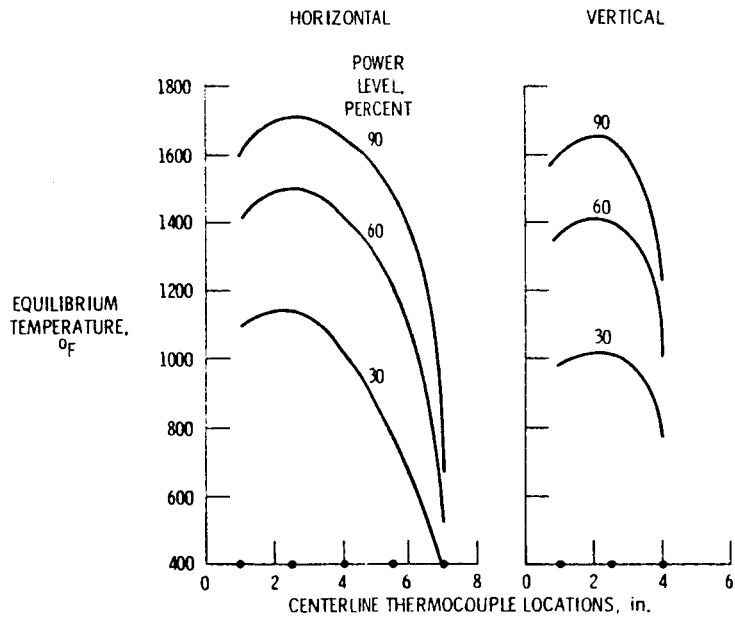
Figure 6

COLD-SIDE PLATE TEMPERATURES FOR MAXIMUM PLATE COOLING

HORIZONTAL

VERTICAL

POWER LEVEL, PERCENT

90

60

30

90

60

30

EQUILIBRIUM TEMPERATURE, °F

CENTERLINE THERMOCOUPLE LOCATIONS, in.
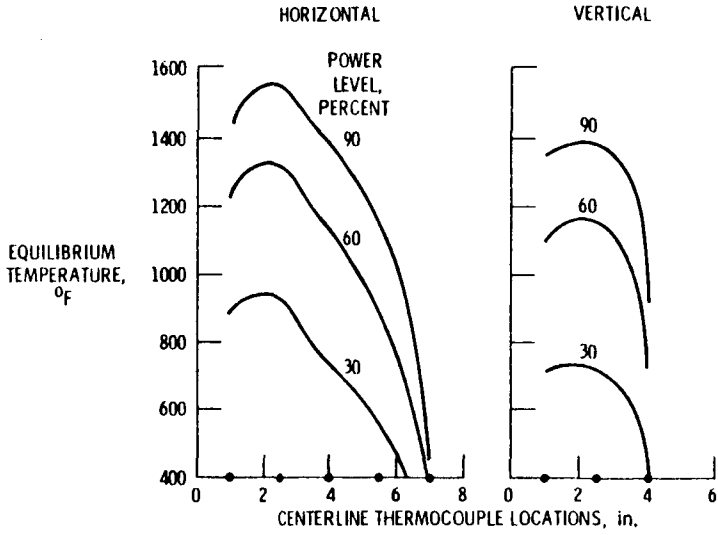
Figure 7

THERMAL CYCLING OF FLAT PLATE

MAXIMUM PLATE TEMPERATURE RESULTING FROM APPLIED POWER HISTORY

MAXIMUM PLATE COOLING, PREHEATER ON

PLATE TEMPERATURE, °F

SPECIFIED POWER HISTORY

APPLIED POWER LEVEL, PERCENT

TIME, sec
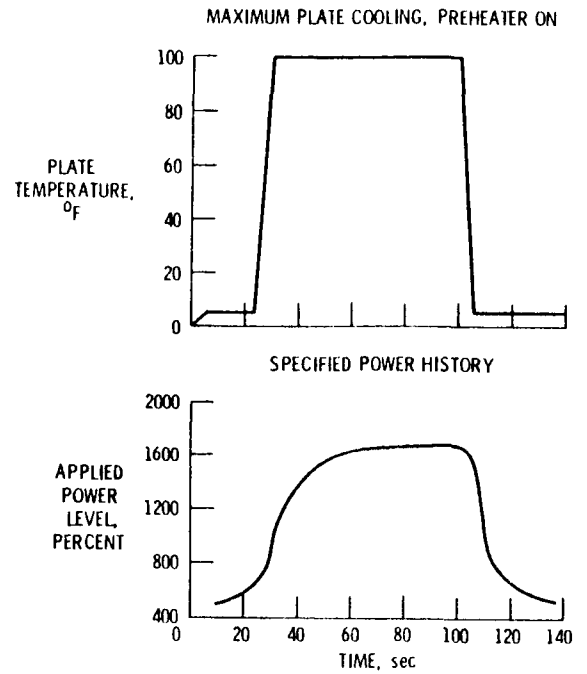
Figure 8

CYCLIC HEATING OF TEST PLATE

MAXIMUM PLATE COOLING; PREHEATER ON

TEMPERATURE, °F

MAXIMUM PLATE TEMPERATURE DURING THERMAL CYCLE AT 100-PERCENT POWER LEVEL

MINIMUM PLATE TEMPERATURE DURING THERMAL CYCLE AT 5-PERCENT POWER LEVEL
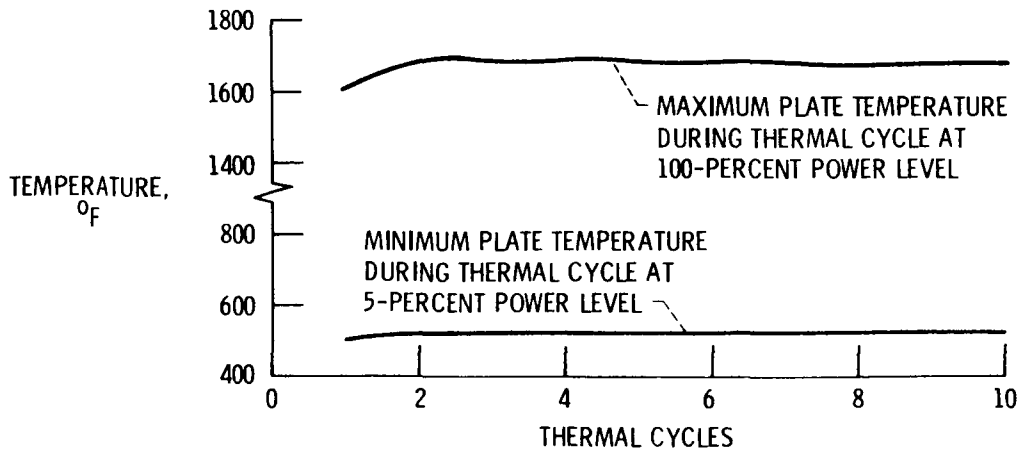
THERMAL CYCLES

Figure 9

INFRARED THERMOVISION SYSTEM INSTALLATION
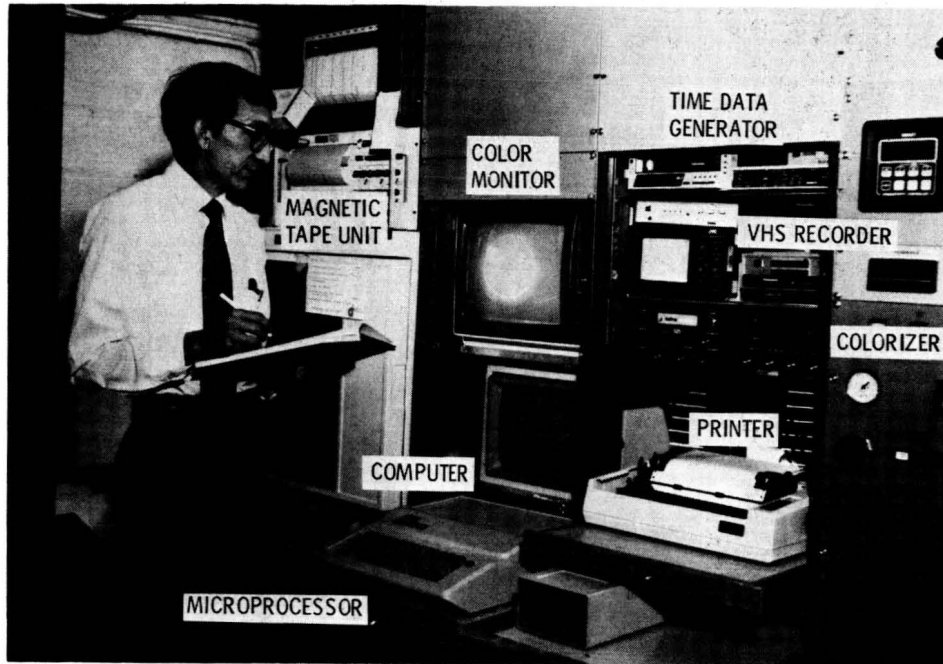
Figure 10

CS 84-3983

CALIBRATION CURVES FOR INFRARED CAMERA
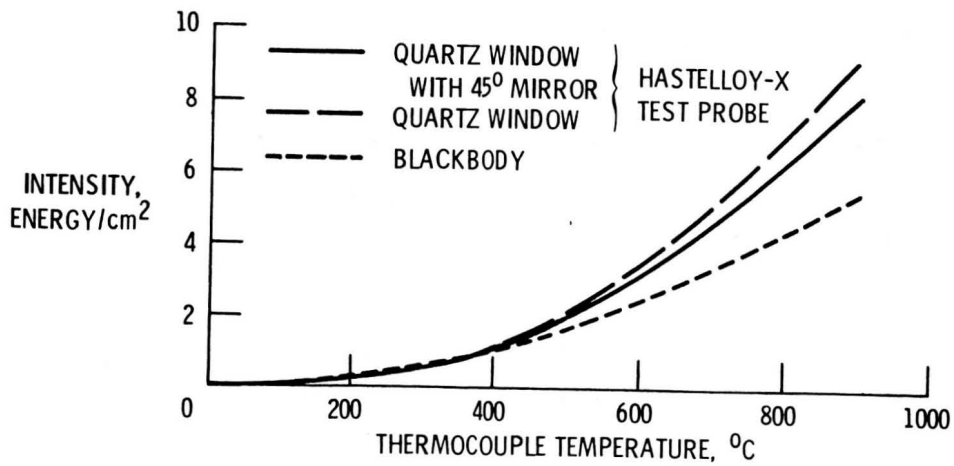
Figure 11

THERMAL IMAGES OF HASTELLOY—X PLATE FOR TYPICAL THERMAL CYCLE

50 sec

60 sec

70 sec

80 sec

CS 84-3986

0 sec

20 sec

30 sec

40 sec

CS 84-3987
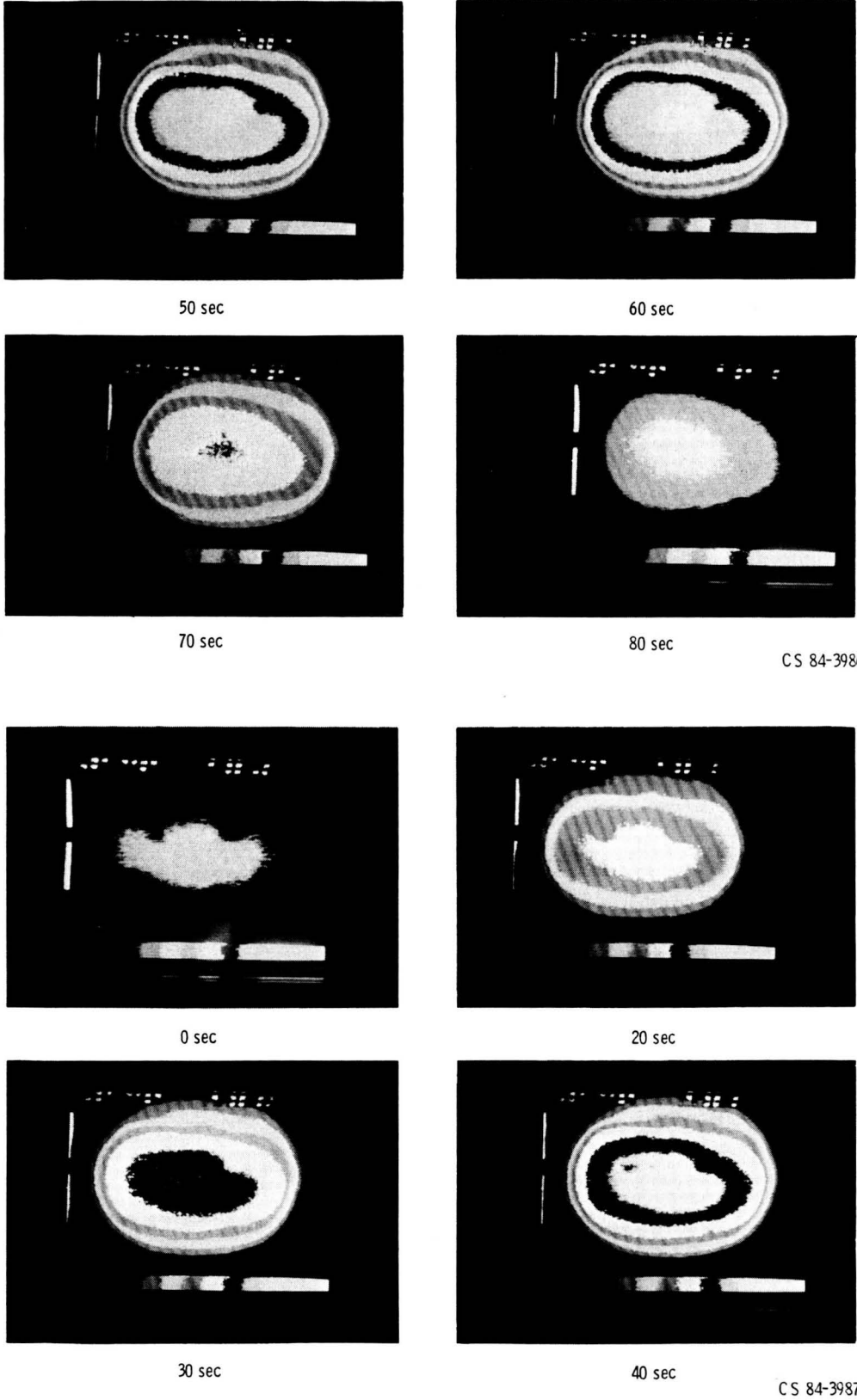
Figure 12

C-4

STEADY–STATE COMPARISON OF IR CAMERA AND THERMOCOUPLE DATA

90-PERCENT POWER LEVEL COOLED PLATE
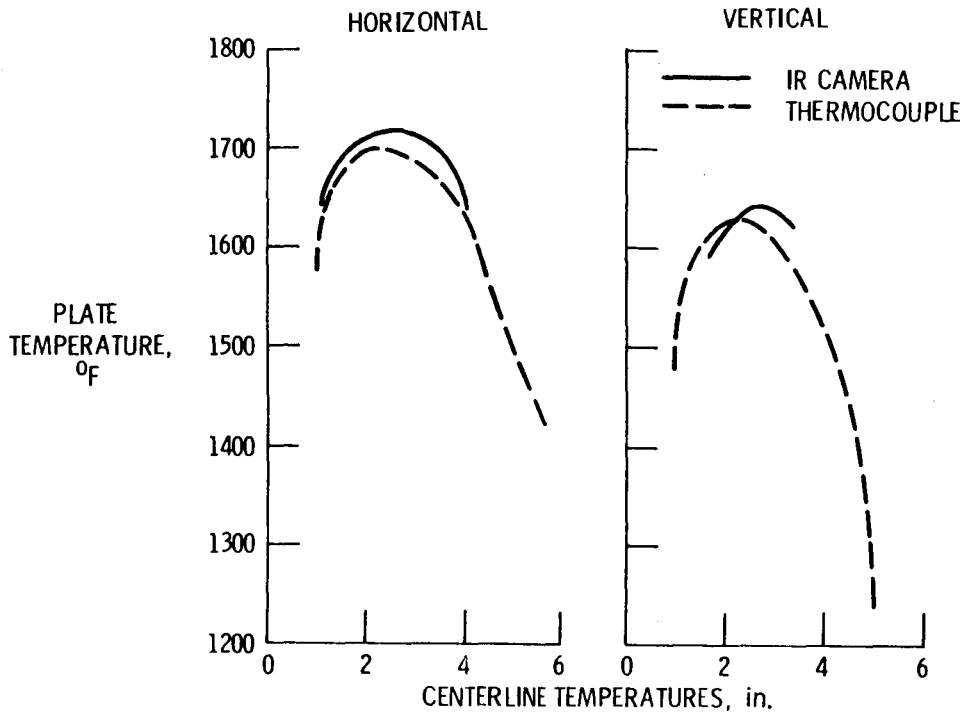
Figure 13

COMPARISON OF IR CAMERA AND THERMOCOUPLE DATA
FOR ONE THERMAL CYCLE
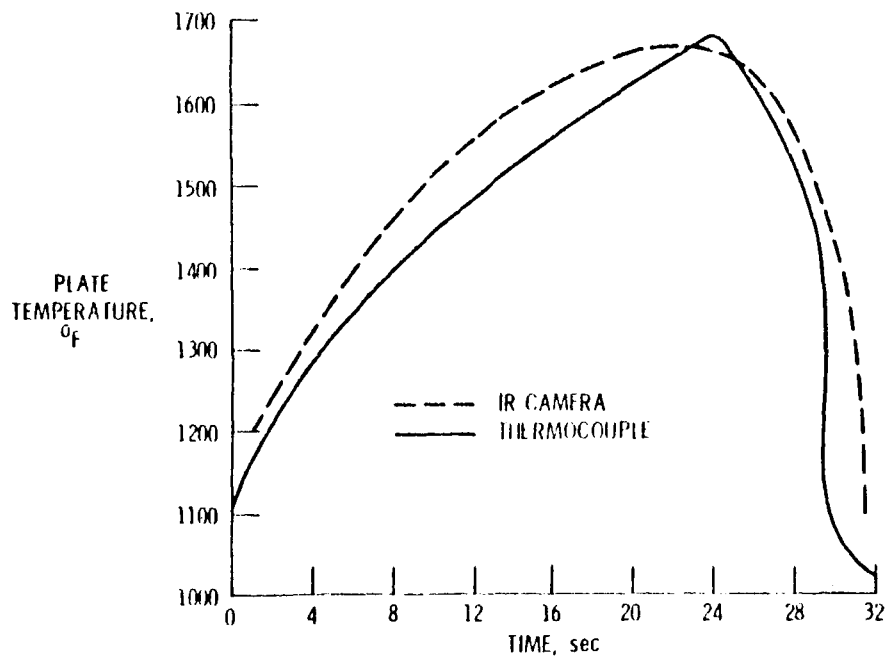
Figure 14

REPRESENTATIVE TEMPERATURE DISTRIBUTION ON 8 x 5 in. FLAT PLATE

60-PERCENT POWER; NO PLATE COOLING

1500	1520	1590	1610	1600	1570	1510	1410
1510	1530	1640	1640	1620	1590	1530	1430
1520	1560	1670	1670	1650	1610	1550	1450
1560	1610	1720	1700	1690	1650	1520	1420
1530	1580	1690	1670	1660	1600	1500	1400
1520	1550	1640	1640	1640	1560	1480	1390

Figure 15

FINITE–ELEMENT MODELS

PLATE SPECIMEN

FRAME AND PLATE

1/4 MESH; SOLID PLATE

1/4 MESH

Figure 16

270
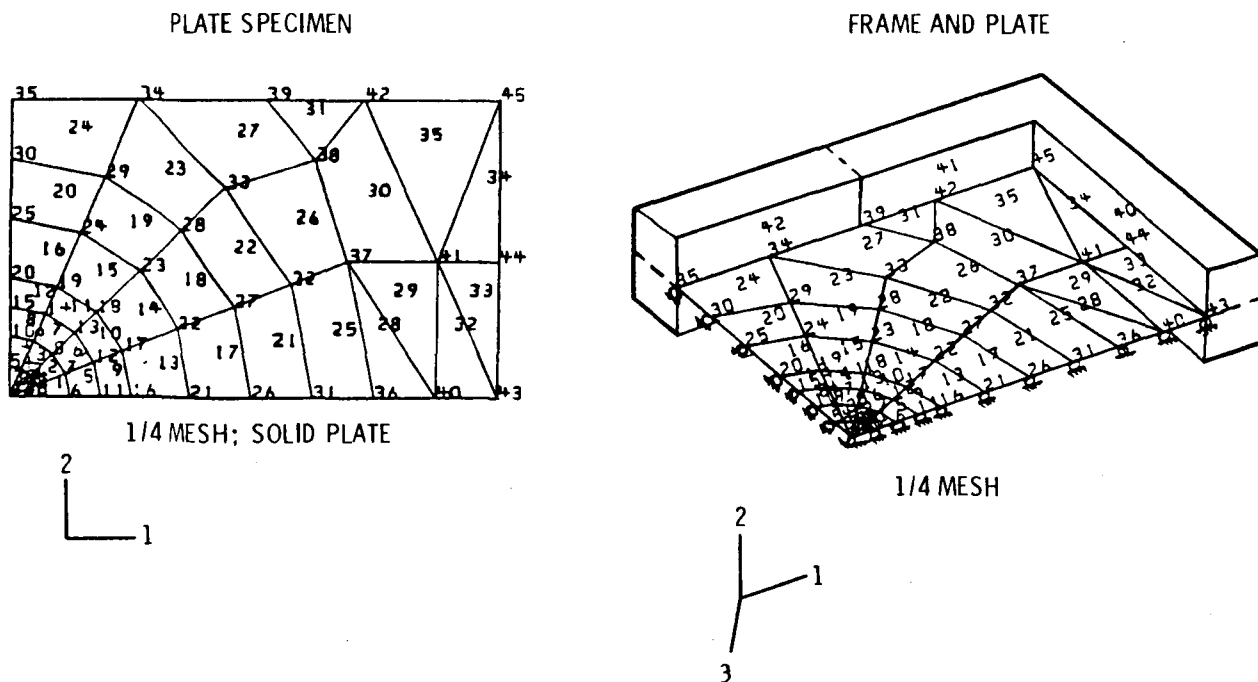
UNIFORM TEMPERATURE HISTORY OF PLATE AND FRAME
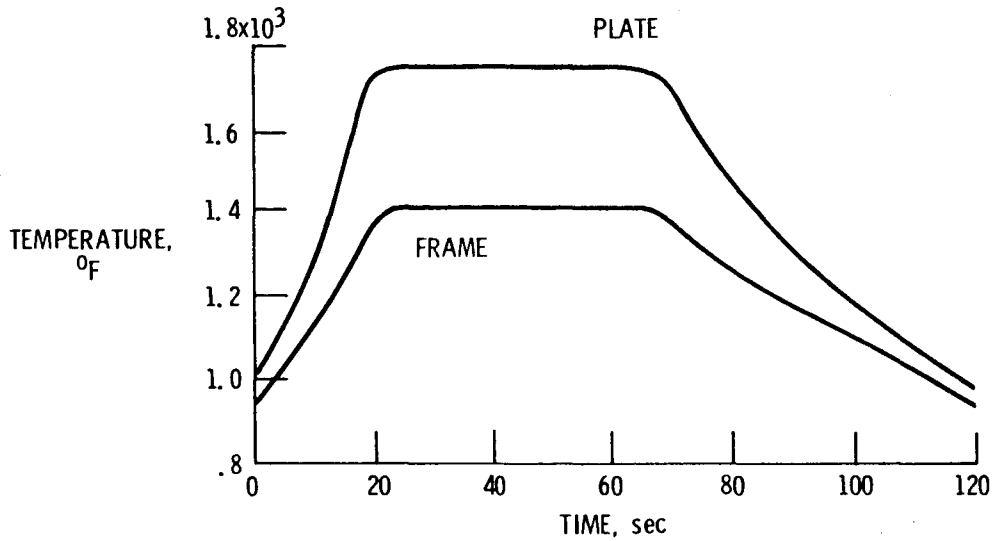
Figure 17

COMPARISON OF THREE VISCOPLASTIC THEORIES

Figure 18

271
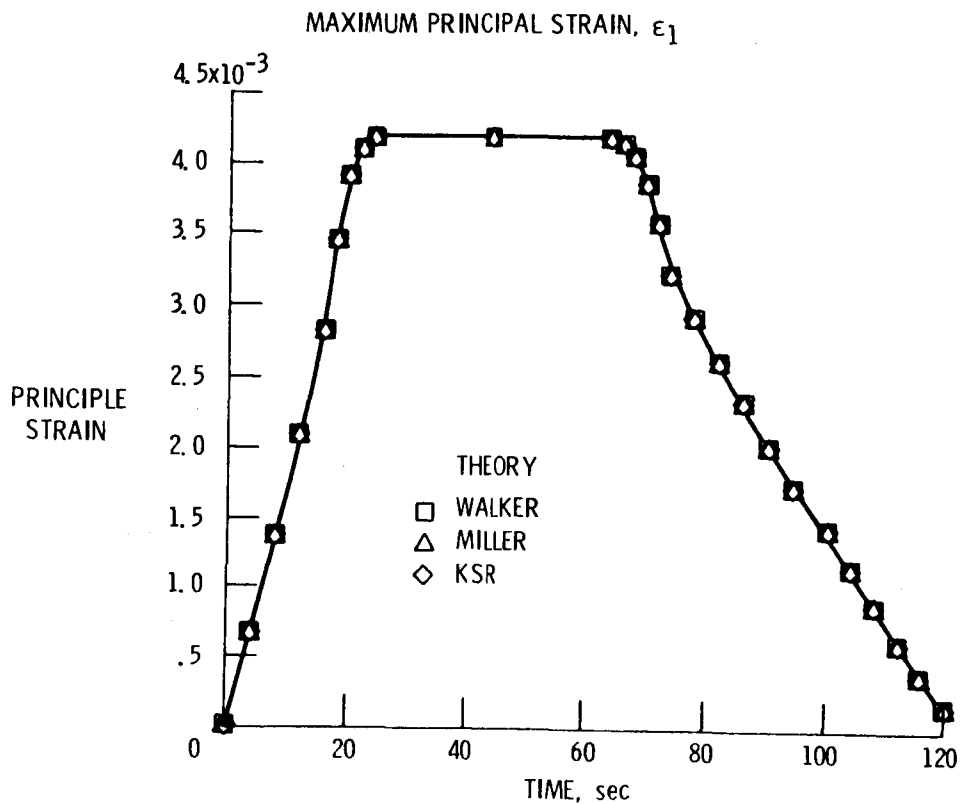
COMPARISON OF THREE VISCOPLASTIC THEORIES
STRESS COMPONENT, Sx
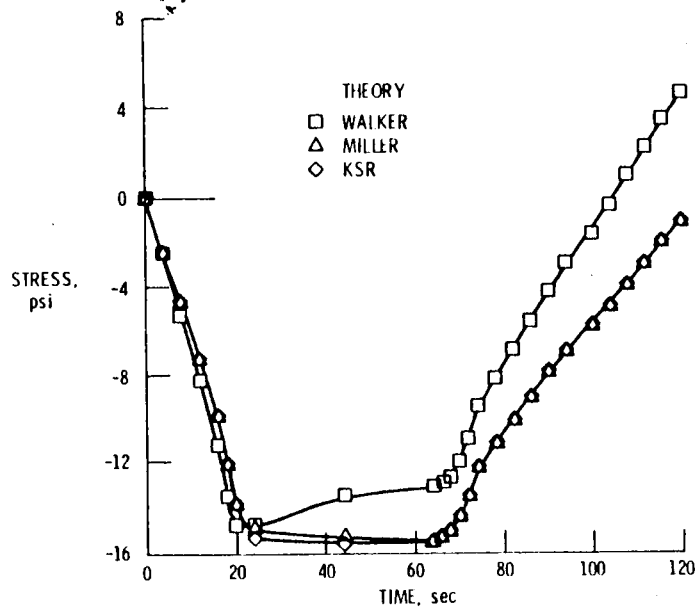
Figure 19

COMPARISON OF THREE VISCOPLASTIC THEORIES
HYSTERESIS LOOPS

Figure 20

272
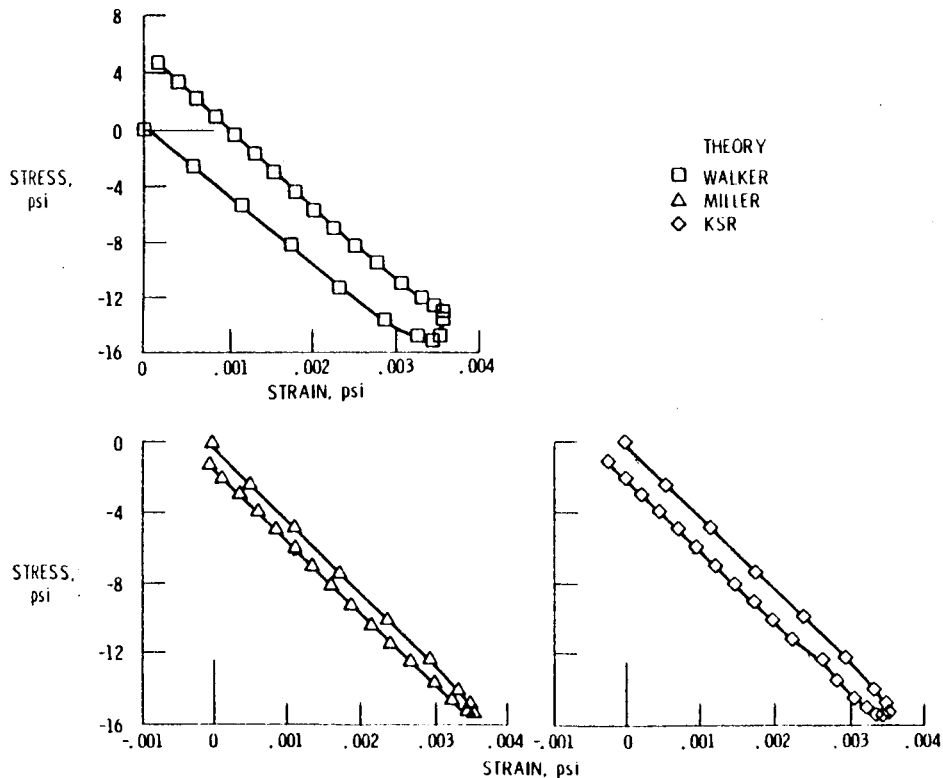
HIGH-TEMPERATURE CONSTITUTIVE MODELING*

D. N. Robinson and J. R. Ellis
University of Akron

INTRODUCTION

Thermomechanical service conditions for high-temperature structural components, e.g., hot-section aircraft engine and nuclear reactor components, involve temperature levels, thermal transients and mechanical loads severe enough to cause measurable inelastic deformation. Although inelastic strain per cycle is small in many applications (in the order of elastic strain) as cycling occurs in the absence of shakedown inelastic strain can accumulate monotonically (ratchetting) or alternate repeatedly (fatigue). In any case, the seat of failure clearly resides in the occurence of continued inelastic deformation. Structural analysis in support of the design of high-temperature components - leading to the stress, strain and temperature fields upon which life predictions are ultimately based - therefore depends strongly on accurate mathematical representations (constitutive equations) of the nonlinear, hereditary, inelastic behavior of structural alloys at high temperature, particularly in the relatively small strain range. To be generally applicable, constitutive equations must be expressed in multiaxial form and be appropriate for all modes of mechanical and thermal loading to be experienced by the elevated temperature components (e.g., cyclic, non-isothermal, non-radial, etc.).

In contribution to the overall program in constitutive equation development sponsored by the HOST project, the in-house NASA/LeRC effort is concentrating mainly on three fundamental areas of research:

1) Multiaxial experimentation to provide a much needed rational basis for high-temperature multiaxial constitutive relationships.

2) Nonisothermal testing and theoretical development toward a complete thermo-mechanically path dependent formulation of viscoplasticity - including the influence of thermally induced metallurgical changes.

3) Development of viscoplastic constitutive models accounting for strong initial anisotropy.

Current activities, progress and future directions in these areas of research are indicated in the following sections.

MULTIAXIAL EXPERIMENTATION IN SUPPORT OF CONSTITUTIVE EQUATION DEVELOPMENT

Thoughtful exploratory experimentation must go hand-in-hand with the formulation of constitutive theories and furnish guidance for their development. Without close interaction between experimentalist and theoretician physically unrealistic and ad hoc constitutive models often result that may not be used with confidence even slightly outside the specific conditions addressed by their data base.

A particularly glaring deficiency in terms of elevated temperature testing is that regarding multiaxial behavior. A major reason for this has been the lack of extensometry for accurately measuring multiaxial strain at high-temperature. Only through recent developments in extensometry (e.g., ref.1) has it become possible to do meaningful multiaxial testing at relevant temperatures on relevant materials.

The necessity of conducting fundamental multiaxial tests is best recognized in the context of classical plasticity theory. In that constitutive theory the concept of a yield surface plays a central role. A description of the yield surface, at a fixed inelastic state, together with the concept of normality is precisely that which allows a consistent multiaxial plastic flow law to be expressed. An appropriate description of the yield surface and a demonstration of the validity of the concept of normality can only be realized through multiaxial testing.

At high temperature, alloys of interest are strongly time-dependent (viscoplastic) and the concept of a yield surface, in the classical sense, breaks down. However, concepts have been postulated for time-dependent inelastic behavior that have an analogous geometrical interpretation to that of yield surfaces (e.g., Odqvist (ref.2) and Drucker (ref. 3)). Such a concept was introduced by Rice (ref. 4), Ponter and Leckie (ref. 5) and Ponter (ref. 6) in the form of a flow potential function of the applied stress σ_{ij} and the internal (back) stress α_{ij} *

$$\Omega(\sigma_{ij}, \alpha_{ij}) \qquad (1)$$

from which the viscoplastic flow and evolutionary laws are derivable, i.e.

$$\dot{\varepsilon}_{ij} = \frac{\partial \Omega}{\partial \sigma_{ij}} \qquad (2)$$

$$\dot{\alpha}_{ij} = -h(\alpha_{kl}) \frac{\partial \Omega}{\partial \alpha_{ij}} \qquad (3)$$

Here, $\dot{\varepsilon}_{ij}$ is the inelastic strain-rate and h is a scalar function of the internal stress. Experimental evidence for the existence of a potential function was found in a preliminary way by Brown (ref.7) and Robinson (ref. 8) and recently and more comprehensively by Oytana, Delobelle and Mermet (ref. 9).

Robinson (refs. 10,11) has adopted a potential function of the general form:**

$$\Omega = \frac{1}{2\mu} \int f(F) dF + \frac{R}{H} \int g(G) dG \qquad (4)$$

---

* As the tests described here are isothermal, the development in this section is similarly limited to isothermal conditions. Also, isotropic hardening effects are taken to be saturated out.

** The complete model utilizes a discontinuous pontential function that allows analytically different governing equations in various "regions of the state space." These aspects of the model will not be discussed here.

in which μ, R and H are material constants (or, under non-isothermal conditions, functions of temperature) and the stress dependence enters through the functions

$$F(\sigma_{ij}, \alpha_{ij}) \text{ and } G(\alpha_{ij}) \tag{5}$$

The flow equation (2) then becomes

$$2\mu\dot{\epsilon}_{ij} = f(F) \frac{\partial F}{\partial \sigma_{ij}} \tag{6}$$

which can be interpreted geometrically in a superimposed stress and inelastic strain-rate space (fig. 1) as indicating normality of the inelastic strain-rate (vector) to the hypersurfaces

$$F(\sigma_{ij}, \alpha_{ij}) = \text{const.} \tag{7}$$

The internal stress α_{ij}, denoting the inelastic state, is taken fixed. The surface F = 0 is considered by Robinson to correspond to a threshold (Bingham-Prager) stress below which the inelastic strain-rate vanishes.

Experimental determination of the function F is analogous to the determination of the yield function (or a yield surface) in classical plasticity. Specification of F at constant inelastic states permits the definition of a consistent multi-axial form of the viscoplastic flow law, and provides information concerning an evolutionary law for the inelastic state variable α_{ij}.

For isotropic alloys it is reasonable to further specialize F and G to be dependent on the principal invariants of the applied and internal stress. In the spirit of v.Mises, Robinson has taken

$$F(J_2) = \frac{J_2}{K^2} - 1 \quad \text{and} \quad G(\hat{J}_2) = \frac{\hat{J}_2}{K^2} \tag{8}$$

as depending on only the second principal invariants

$$J_2 = \frac{1}{2} \Sigma_{ij}\Sigma_{ij} \tag{9}$$

$$\hat{J}_2 = \frac{1}{2} a_{ij}a_{ij} \tag{10}$$

The first of equations (8) plays the role of a (Bingham) yield condition with K denoting the magnitude of the threshold Bingham shear stress.

In equation (9) the effective stress

$$\Sigma_{ij} = S_{ij} - a_{ij} \tag{11}$$

is taken as the difference of the applied deviatoric stress S_{ij} and the internal stress deviator a_{ij}. The choice of stress dependence in equation (8) is consistent with the experimental observations reported in reference 9.

With these choices, equations (2) and (3) give

$$2\mu\dot{\varepsilon}_{ij} = f(F)\Sigma_{ij} \tag{12}$$

and

$$\dot{a}_{ij} = h(G)\dot{\varepsilon}_{ij} - r(G)a_{ij} \tag{13}$$

with

$$\frac{r}{h} = \frac{R}{H}g(G) \tag{14}$$

Evidently, the evolutationary equation (13) is of the physically accepted Bailey-Orowan form.

Squaring both sides of the equation (12) we get

$$4\mu^2 I = f^2 J_2 = \hat{F}(J_2) \tag{15}$$

where

$$I = \frac{1}{2}\dot{\varepsilon}_{ij}\dot{\varepsilon}_{ij} \tag{16}$$

is a measure of the magnitude of the inelastic strain-rate. Equation (15) states (see Fig. 2) that surfaces of constant J_2 in stress space (at a fixed inelastic state) are surfaces of constant inelastic strain-rate I. Further, the strain-rate vectors are normal to these surfaces. Constant inelastic strain-rate surfaces are the counterparts of yield surfaces (surfaces of constant inelastic strain) in time-dependent plasticity.

In general, these surfaces change position and size through changes in the internal stress, threshold stress and time as inelastic deformation and recovery occurs. A complete understanding of the nature and behavior of these surfaces under virgin conditions and conditions subsequent to inelastic deformation (creep, cyclic plasticity, etc.) is prerequisite to formulating a consistent description of multiaxial viscoplastic behavior.

Computer controlled experiments for directly determining the loci of constant inelastic strain rate at fixed inelastic state are included in the test plan for the currently expanding Structures Division laboratory. In the interim period, before that laboratory if fully operational, preliminary tests of this type are being conducted under subcontract to Oak Ridge National Laboratory.

NONISOTHERMAL TESTING AND THERMOMECHANICAL MODELING

Essentially all of the important structural problems related to the design of aircraft engine hot-section components are nonisothermal. Inelasticity does not occur in these components as a result of mechanical loading alone but is generally induced through thermal transient cycles and thermal gradients. Nevertheless, the constitutive equations and life prediction models used in structural analysis and design are almost always based completely on experimental data collected under isothermal conditions. Isothermal tests are commonly conducted over the temperature and then "fit" as functions of temperature across the temperature range to furnish a "nonisothermal" representation. This traditional approach leads to "nonisothermal" models that do not reflect the strong thermomechanical path dependence observed in, for example, the cyclic hardening behavior of some alloys of interest - particularly in the presence of metallurgical changes.

Cyclic hardening of some common structural alloys within their temperature range of interest is believed to be influenced by the phenomenon of dynamic strain aging. Strain aging occurs in solid solutions where solute atoms (e.g., carbon, nitrogen, etc.) are particularly free to diffuse through the parent lattice. It is

energetically preferable for these solute atoms to occupy sites in the neighborhood of mobile dislocations where their presence immobilizes the dislocations or at least makes their movement difficult, thus causing strengthening.

Isothermal cycling at temperatures where such metallurgical changes occur might therefore be expected to show abnormal hardening, i.e., higher hardening rates and greater saturation strengths than at temperatures both lower and higher. Macroscopic evidence of strain aging in three common alloys (i.e., Hastelloy X and types 304 and 316 stainless steel) is shown in figures 3 through 5. In each case the hardening rate and the stress range at "saturation", peak at an intermediate temperature in the range. This hardening peak is interpreted as a manifestation of dynamic strain aging. At lower temperatures the mobility of solute atoms is far less and strain aging cannot occur; at higher temperatures normal recovery precesses, e.g., climb of edge dislocations, take over.

In the aging process described dislocations can, under some circumstances, break away from their solute atmospheres becoming mobile again. Although temporarily freed, dislocations can again be immobilized as solute atoms gradually diffuse back to them. As the thermally activated process of diffusion is involved and solute atoms are migrating to dislocations which themselves are moving under the applied stress, it is expected that the ensuing inelastic deformation (cyclic hardening in particular) has a complex dependence on thermomechanical history.

Phenomenological evidence of thermomechanical path dependence under cyclic conditions is seen in the results of the simple nonisothermal tests reported in figures 3 and 4 (dotted curves). In these tests cycling is initiated at one temperature and after some cycling the temperature is changed and cycling resumed.

Figure 3 shows the results of two nonisothermal tests on Hastelloy X cycled over a strain range at constant strain rate. In one, the specimen is cycled at 800F for five cycles; the temperature is then changed to 1000F and cycling is continued to apparent saturation, at about one hundred cycles. In the second, this history is repeated up to thirty cycles where the specimen is then brought back to 800F and cycling continued. Results of a similar test on type 304 stainless steel are shown in figure 4 (dotted line).

The features of these test results that reflect thermomechanical history dependence are : 1) The change in strength (stress range) with temperature at a fixed number of cycles is always negative, i.e., an increase in temperature always produces a decrease in strength and vice versa, contrary to the implication of the isothermal data; 2) The current strength, in particular the "saturation" strength, depends on the temperature-strain history. Evidently, the information contained in the isothermal data is not sufficient for a complete nonisothermal description of the cyclic deformation in the temperature range of interest. In fact, the data suggests that, with accompanying metallurgical changes, the materials retain a full memeory of their thermomechanical history to cyclic saturation. Similar observations have been made on two-phase alloys (ref.12) presumably arising from microstructural changes associated with precipitation of the γ' phase.

Characterization of isotropic cyclic hardening effects requires that a constitutive model contain a scalar state variable (e.g., K) and a corresponding evolutionary law describing its rate of change with thermomechanical history. A proposed form of evolutionary law appropriate for cyclic stressing (in the absence of thermal recovery) is

$$\dot{K} = \tilde{F}(P,T)\dot{P} + \tilde{G}(P,T)\dot{T} \tag{17}$$

in which

$$P = \int (\dot{\varepsilon}^P_{ij} \dot{\varepsilon}^P_{ij})^{1/2} \tag{18}$$

277

is a measure of the accumulated plastic strain and T is the temperature. The current value of K (or equivalently the stress range) is determined from equation (17) only if the thermomechanical path is known.

Information for characterizing the function $\tilde{F}$ can be obtained from ordinary isothermal tests, however, nonisothermal tests must be conducted to supply information about $\tilde{G}$. Candidate tests for this purpose have been identified and will be conducted as the nonisothermal testing facilities become available in the Structures Division laboratory.

Using preliminary information about the function $\tilde{G}$ an appropriate evolutionary law having the form of equation (17) has been adopted for use with the Robinson viscoplastic model described in references 10 and 11. Predictions made by this nonisothermal model give excellent qualitative agreement with the experimental results of figures 3 through 5.

A VISCOPLASTIC MODEL FOR TRANSVERSE ISOTROPY

The need for increased efficiency in energy systems places greater demands on the high-temperature structural alloys used for system components. As higher operating temperatures are sought, advanced materials are being developed to meet these demands. Good examples of such materials are the directionally solidified polycrystalline alloys finding application in turbine blades of aircraft engines. The directional properties of these metals render them highly anisotropic relative to conventional alloys. This introduces additional complexity in understanding and mathematically representing their mechanical behavior over and above the already enormous complexities associated with elevated temperature.

Here, we discuss a means of extending the isotropic viscoplastic model discussed in the first section and fully described in references 10 and 11 to be applicable to materials with initial anisotropy (ref.13) arising from directionally solidified grain growth.

The direction of grain solidification at each point can be characterized by a field of unit vectors $d_i(x_k)$. The mechanical behavior must then depend not only on the stress and deformation history at the point but also on the local preferential direction. It follows that equation 5 must be replaced by

$$F(\Sigma_{ij}, d_i d_j) \quad \text{and} \quad G(a_{ij}, d_i d_j) \tag{19}$$

In the case of full isotropy F and G were taken as depending on the (second) principal invariants of Σ_{ij} and a_{ij} (eg. (8)). Here instead, we take F and G to depend on invariants that reflect the appropriate anisotropy. The theory of tensorial invariants (ref. 14) requires that for form-invariance under arbitrary rigid-body rotations F and G must be expressible in terms of the principal invariants of their respective tensorial arguments and invariants involving various products of these tensors. Here, we take the functions F and G as depending on subsets of these invariants. We denote I_1, I_2 and I_3 as the invariant arguments of the function F and $\hat{I}_1$, $\hat{I}_2$, $\hat{I}_3$ as those for G.

That is, we take

$$F(I_1, I_2 I_3) = \frac{I_1}{K^2} + \left(\frac{1}{K_d^2} - \frac{1}{K^2} \right)(I_2 - I_3^2) - 1 \tag{20}$$

and

$$G(\hat{I}_1, \hat{I}_2, \hat{I}_3) = \frac{\hat{I}_1}{K^2} + \left(\frac{1}{K_d^2} - \frac{1}{k^2} \right)\left(\hat{I}_2 - \hat{I}_3^2 \right) \tag{21}$$

where

$$I_1 = \frac{1}{2} \Sigma_{ij}\Sigma_{ji} \qquad\qquad \hat{I}_1 = \frac{1}{2} a_{ij}a_{ji}$$

$$I_2 = d_i d_j \Sigma_{jk}\Sigma_{ki} \qquad\qquad \hat{I}_2 = d_i d_j a_{jk}a_{ki} \tag{22}$$

$$I_3 = \frac{1}{2}d_i d_j \Sigma_{ji} \qquad\qquad \hat{I}_3 = \frac{1}{2} d_i d_j a_{ji}$$

As before, the flow and evolutionary equations are obtained by taking the appropriate derivatives as indicated in equations (2) and (3). This results in

$$2\mu\dot{\varepsilon}_{ij} = f(F)\left[\Sigma_{ij} + \left(\frac{K^2}{K_d^2} - 1\right)\left(d_j d_k \Sigma_{ki} + d_k d_i \Sigma_{jk} - \frac{1}{2} d_p d_k \Sigma_{kp}(\delta_{ij} + d_i d_j)\right)\right] \tag{23}$$

for the flow law, and

$$\dot{a}_{ij} = h(G)\dot{\varepsilon}_{ij} - r(G)\left[a_{ij} + \left(\frac{K^2}{K_d^2} - 1\right)\left(d_j d_k a_{ki} + d_k d_i a_{jk}\right.\right.$$
$$\left.\left. - \frac{1}{2} d_p d_k a_{kp}(\delta_{ij} + d_i d_j)\right)\right] \tag{24}$$

for the evolutionary law.

As earlier, K denotes the threshold (Bingham) shear stress transverse to the preferential material direction. K_d denotes the same for shear along the material direction. For $K = K_d$, indicating no difference in shear strength across and along the direction d_i, equations (23) and (24) reduce to their respective isotropic counterparts eqs. (12) and (13).

Equations 20 through 24 have been applied in several structural problems involving creep and cyclic plasticity. The predictions give good qualitative agreement with existing experimental results on the directionally solidified (DS) alloy MAR-M-247 as reported in reference 14. Quantitative comparisons are delayed until characterization tests on a DS alloy furnish specific values of the material parameters in the viscoplastic model.

Additional studies are continuing concerning the adoption of other sets of invariants (integrity bases) reflecting higher degrees of anisotropy, e.g., orthotropy and cubic symmetry.

REFERENCES

1. Ellis, J.R., "A Muliaxial Extensometer for Measuring Axial, Torsional and Diametral Strains at Elevated Temperature", ORNL/TM 8760, (1983).

2. Odqvist, F.K.G., "Recent Advances in Theories of Creep of Engineering Materials", Applied Mechanics Reviews, 7, pp. 517-519, (1954).

3. Drucker, D.C., "On Time-Independent Plasticity and Metals Under Combined Stress at Elevated Temperature", Brown University Report NONR 562(20)/46, (1965).

4. Rice, J.R., "On the Structure of Stress-Strain Relations for Time-Dependent Plastic Deformations in Metals", J. Appl. Mech., Trans, ASME 37, Series E. No. 3, 728-37, (1970).

5. Ponter, A.R.S. and Leckie, F.A., "Constitutive Relationships for the Time-Dependent Deformation of Metals", J. Eng. Mater, Technol., Trans. ASME 98, 47-51 (1976).

6. Ponter, A.R.S., "Convexity and Associated Continuum Properties of a Class of Constitutive Relationships", J. de Mecanique 15 (4), 527-42 (1976).

7. Brown, G.M., "Inelastic Deformation of an Aluminum Alloy Under Combined Stress at Elevated Temperature", J. Mech. Phys. Solids 18, 383-396 (1970).

8. Robinson, D.N., "On the Concept of a Flow Potential and the Stress-Strain Relations of Reactor Systems Metals". ORNL/TM 5571, (1976.

9. Oytana, C., Delobelle, P., and Mermet, A., "Constitutive Equations Study in Biaxial Stress Experiments", J. of Eng'r. Materials and Tech., Vol. 104, pp. 1-11, (1982.

10. Robinson, D.N., "A Unified Creep-Plasticity Model for Structural Metals at High Temperature". ORNL/TM 5969, (1978.

11. Robinson, D.N. and Swindeman, R.W., "Unified Creep-Plasticity Constitutive Equations for 2-1/4 CR-1 Mo Steel at Elevated Temperature." ORNL/TM 8444, (1982).

12. Cailletaud, G. and Chaboche, J.-L, "Macroscipic Description of the Microstructural Changes Induced by Varying Temperature: Example of IN 100 Cyclic Behavior", ICM, 3, Vol. 2 (1979).

13. Robinson, D.N., "Constitutive Relationships for Anisotropic High-Temperature Alloys", NASA Technical Memorandum 83437, presented at the International Post-Conference Seminar on Inelastic Analysis and Life Prediction, Chicago, (1983).

14. Sink, S.W., Hoppin, G.S. and Fuji, M., "Low Cost Directionally-Solidified Turbine Blades", Vol. 1, NASA CR-159464 (1979).
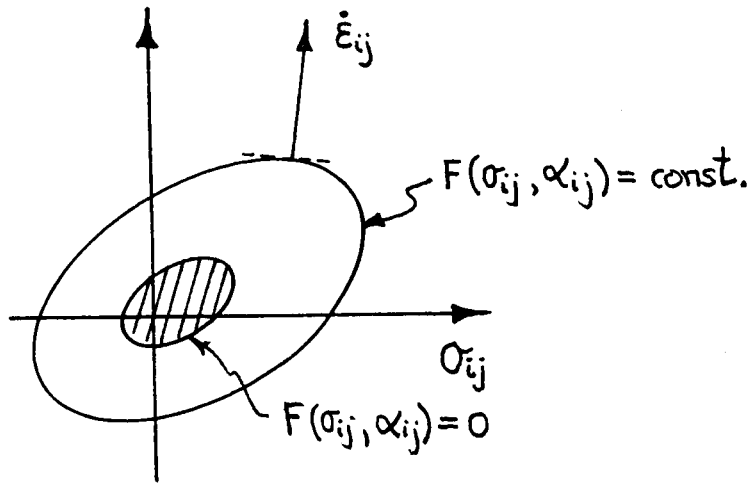
Figure 1 Flow potential surfaces in stress space showing normality of inelastic strain rate vectors.
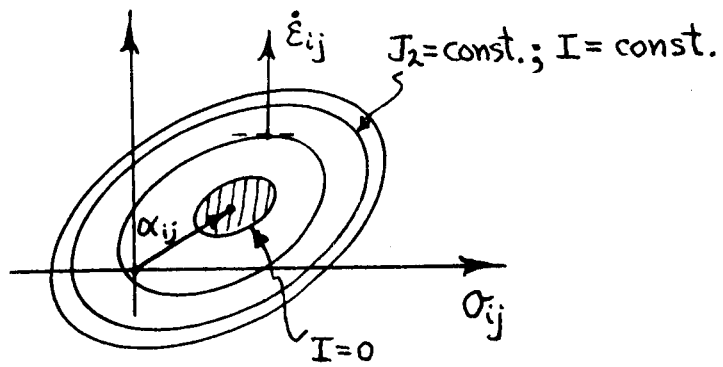
Figure 2 For an isotropic J_2 material ,surfaces of constant inelastic strain rate are surfaces of J_2 = constant.

281
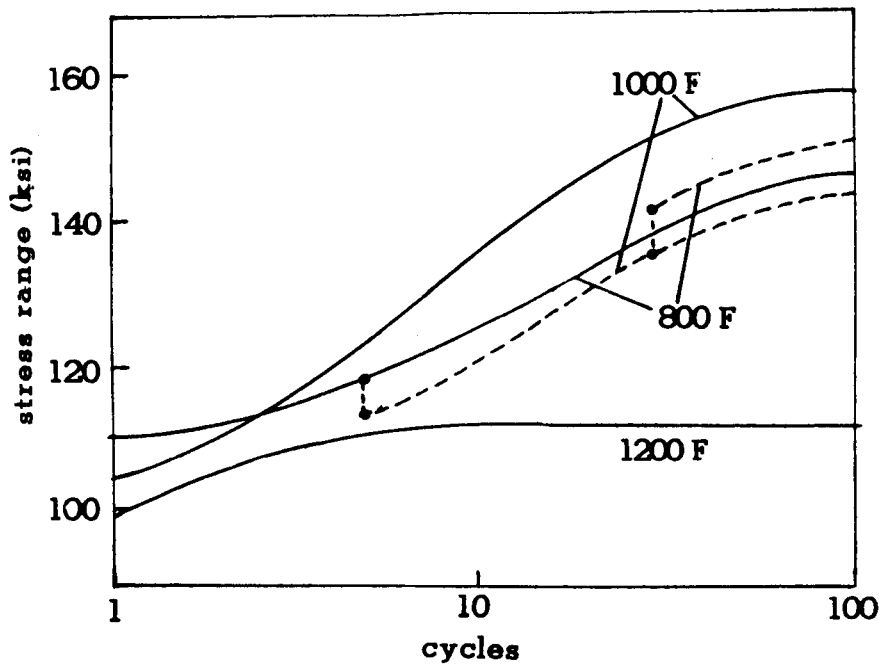
HASTELLOY X

Figure 3 Isothermal(solid)and nonisothermal(dotted)
cyclic hardening curves for Hastelloy X.

304 SS
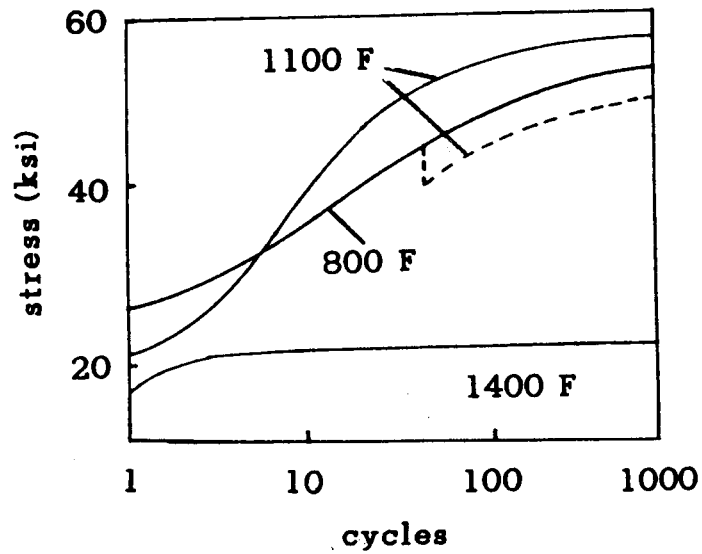
Figure 4 Isothermal(solid)and nonisothermal(dotted)
cyclic hardening curves for type 304 Stainless Steel.

316 SS
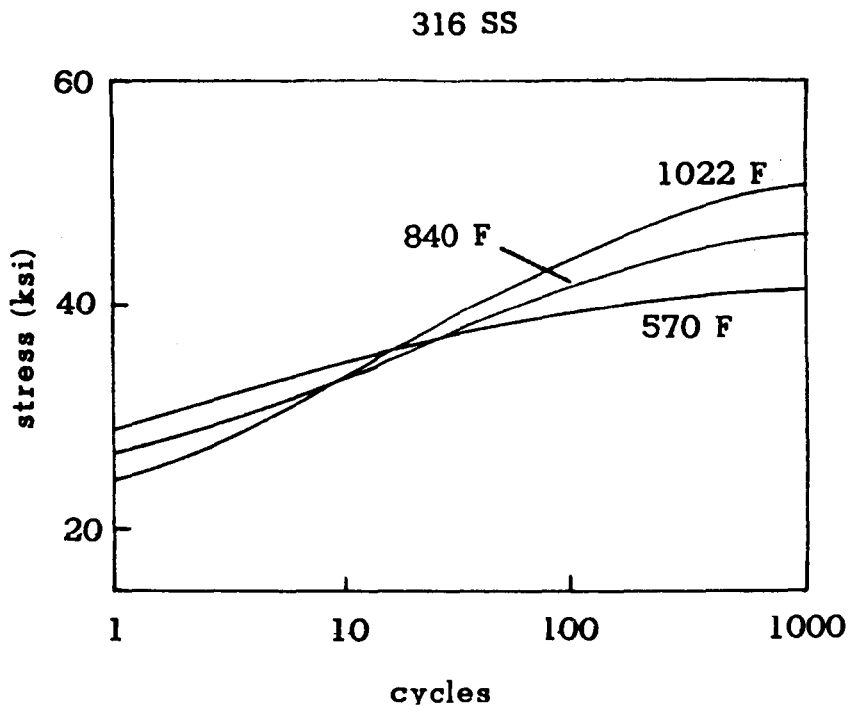
Figure 5 Isothermal cyclic hardening curves for type
316 Stainless Steel.

CONSTITUTIVE MODELING FOR ISOTROPIC MATERIALS

Ulric S. Lindholm
Southwest Research Institute

INTRODUCTION

This report presents results of the first year of effort on a program with the objective to develop a unified constitutive model for finite-element structural analysis of turbine engine hot section components. The program is a joint effort between Southwest Research Institute and Pratt & Whitney Aircraft.

The initial two year program includes a state-of-the-art review of applicable constitutive models with selection of two for detailed comparison with a wide range of experimental test. The experimental matrix contains uniaxial and biaxial tensile, creep, stress relaxation and cyclic fatigue tests at temperatures to 1093°C and strain rates from 10^{-7} to 10^{-3} sec^{-1}. Some non-isothermal TMF cycles will be run also. The constitutive models will be incorporated into the MARC finite element structural analysis program with a demonstration computation made for an advanced turbine blade configuration. In the code development work, particular emphasis is being placed on developing efficient integration algorithms for the highly non-linear and stiff constitutive equations. Another area of emphasis is the appropriate and efficient methodolgy for determining constitutive constants from a minimum extent of experimental data.

CONSTITUTIVE MODELS

An extensive review of currently available unified constitutive models was made from which a review is given in references 1 and 2. In a "unified" theory, the inelastic strain rate term, $\dot{\varepsilon}^P$, is considered to include all strains that are not elastic; i.e., the difference between the total strain and the elastic strain, $\dot{\varepsilon} - \dot{\varepsilon}^e$. Thus, unified implies that all aspects of inelastic behavior such as plastic flow, creep and stress relaxation are included in the single function, $\dot{\varepsilon}^P$, and are simply representative response characteristics for different loading histories. In such theories, inelastic behavior may be described with or without the use of a yield function or concept of plastic potential. Those chosen here for further study do not employ a yield criteria and are based on internal variables to describe "yielding" and strain or work hardening behavior.

Two particular constitutive models were chosen for detailed study and comparison with experimental data. These were developed by Bodner and Partom (B-P) (ref. 3) and by Walker (WK) (ref. 4). Both models had considerable prior application to high-temperature alloys used in gas turbine components. Most unified models are of the basic form

$$\frac{\underset{\sim}{\sigma} - \underset{\sim}{X}_1}{\underset{\sim}{X}_2} = f(\dot{\underset{\sim}{\varepsilon}}^P, T) \tag{1}$$

here σ, $\dot{\varepsilon}^P$ and T are stress, inelastic strain rate and temperature, respectively. Generally, two independent internal variables are used, $\underset{\sim}{X}_1$ a tensor quantity describing directional material hardening (often referred to as a back stress, equilibrium stress, or kinematic hardening variable) and X_2 a scalar measure of the magnitude of isotropic hardening. The evolutionary equations for both internal variables are usually of the hardening-recovery form,

$$\dot{X}_i = h(X_i) \, \dot{M} + r(X_i, T) \tag{2}$$

where M is a physical measure of hardening and h and r are hardening and recovery functions.

The WK model uses a power law for the kinetic term, $f(\dot{\varepsilon}^P, T)$, and plastic strain as the measure of hardening M. The B-P model uses an exponential form in the kinetic term and plastic work for M. The other major difference between the two models is that B-P avoids the use of the back stress $\underset{\sim}{X}_1$ and encorporates both isotropic and directional hardening in a partitioning of $\underset{\sim}{X}_2$. For a more detailed comparison see references 1 and 2.

EXPERIMENTAL PROGRAM

An extensive test program is underway to generate a comprehensive set of data which is to be compared with model predictions. A cast nickel base alloy, B1900+Hf, with grain size of ASTM No. 1 to 2 is used for the specimens shown in figure 1. As indicated, tensile, creep, isothermal cyclic, thermomechanical cyclic and biaxial (tension-torsion) tests are being performed. To date the tensile, creep and isothermal cyclic tests are complete. Sample results, including correlations with the B-P model, are given in figures 2-5 (correlations with the WK model are being generated also but were not available as of this writing). All model correlations are made with a single set of material constants.

Figure 2 shows the correlation for tensile curve at three temperatures. In the process of determining the constants associated with work hardening in the B-P model, the experimental hardening data was plotted as in figure 3 where $\gamma = d\sigma/dW_p = d\sigma/\sigma \, d\varepsilon^P$. Analysis shows that the data at each strain rate can be closely approximated as the sum of two linear curves, whose slopes and intercepts yield the coefficients for the isotropic and kinematic hardening terms. Thus, it appears possible to predict cyclic behavior from monotonic stress-strain curves. This conclusion needs further verification but holds potential for reducing the testing required for constitutive constant determinations. Another observation from figure 3 is that a change in strain rate does not change the hardening rate (slope) in agreement with the separation of kinetic and hardening terms in equation (1). The slopes do change with temperature because of thermal recovery of hardening (eq. (2)).

Figure 4 shows the small strain ($0.2\%\varepsilon^P$) flow stress over the range of temperature and strain rate studied. Inflections in the curves at the intermediate temperatures result from the influence of thermal recovery at lower rates and higher temperatures. At low temperatures and high rates, thermal recovery is not significant.

An example of initial and saturated cyclic loops at 538°C is given in figure 5. Agreement between experiment and theory is reasonable in this and other cases examined considering the same constants are used for figures 2, 4 and 5. More complex loops with creep or relaxation holds during a cycle will be correlated during the second year along with cyclic biaxial data.

IMPLEMENTATION IN F.E. CODE

Both models are being implemented for use with the MARC finite element code. The code will subsequently be used to analyze a notched tensile round test specimen used as a benchmark experiment and also an advanced turbine blade configuration. The latter will be a numerical demonstration only. Several numerical methods are being studied for implementing the models in the MARC code. Integration methods for viscoplastic theories to be examined include:
   (1)   Explicit Euler integration with both a fixed and self-adaptive time step
   (2)   The implicit noniterative, selfcorrecting solution (NONSS) method of Miller and Tanaka (ref. 5)
   (3)   Implicit integration of the integral form of the equations.
It is expected that each theory will be coded with at least two numerical intergration algorithms.

SUMMARY

The work to date is encouraging with respect to the ability of unified constitutive theories to predict with reasonable accuracy quite complex time and temperature dependent inelastic material behavior. Also encouraging, at this point, is the possibility of determining all necessary constitutive constants from perhaps as little as monotonic tensile curves at several temperatures and strain rates. Such data is generally available for alloys of interest. For implementation of the models in finite element codes and efficient structural analysis, optimum numerical integration schemes need further development.

REFERENCES

1.   Chan, K. S.; Bodner, S. R.; Walker, K. P.; and Lindholm, U. S.: A Survey of Unified Constitutive Theories.   Second Symposium on Nonlinear Constitutive Relations for High Temperature Applications, Cleveland, Ohio, June 1984.

2.   Lindholm, U. S.: Constitutive Modeling for Isotropic Materials.   First Annual Report, NASACR-174718, May 1984.

3.   Bodner, S. R. and Partom, Y.:   ASME J. of Applied Mechanics, Vol. 42, 1975, p. 385.

4.   Walker, K. P.:   NASA Contract Report NASA CR 165533, 1981.

5.   Tanaka, T. G.:   Deformation of Metals and Alloys.   Ph.D. Thesis, Stanford University, 1983.
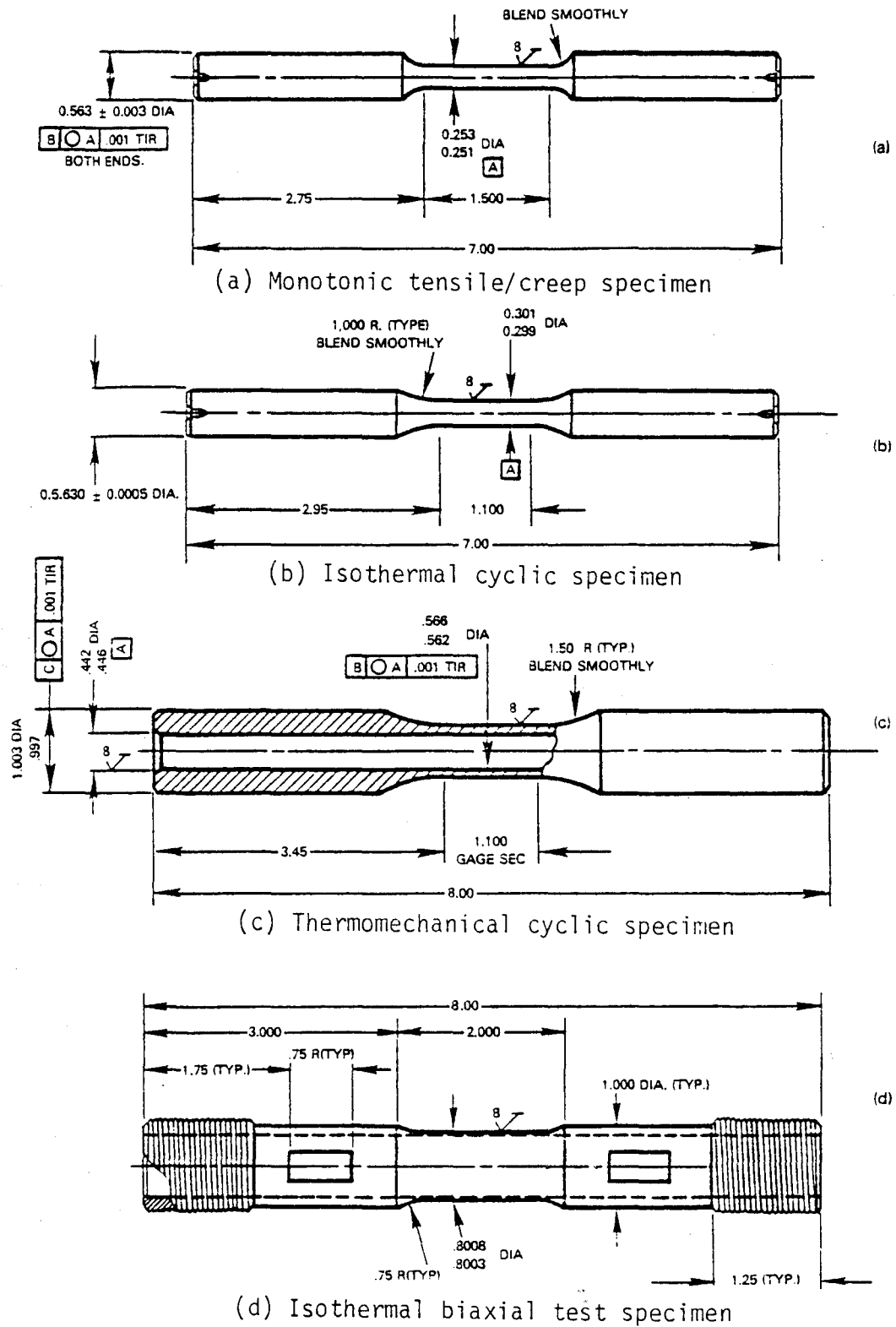
Figure 1. Specimen Designs Utilized in Various Constitutive Tests.

288
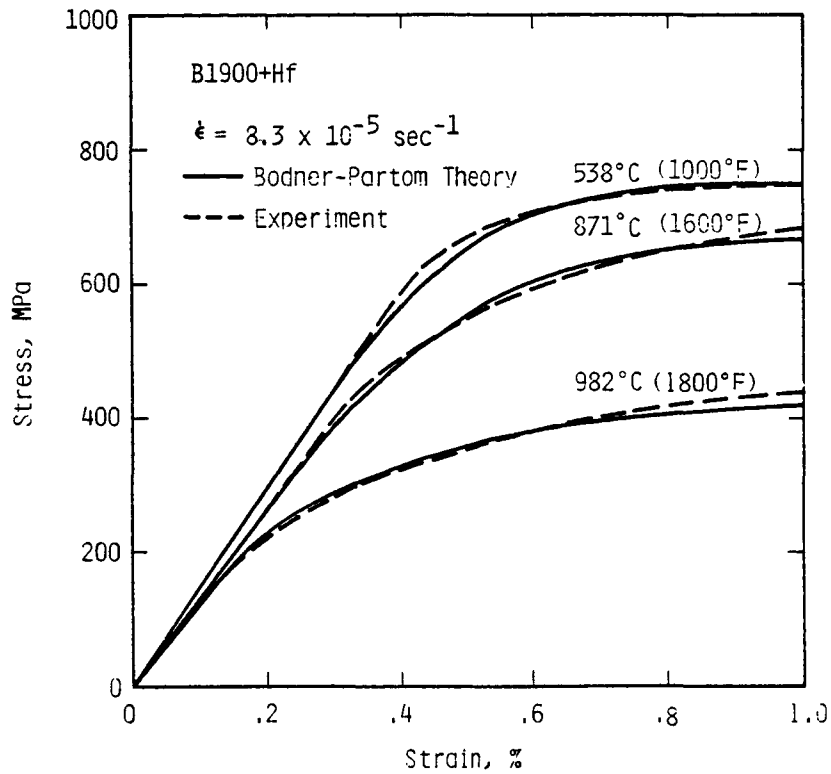
Figure 2.   A Comparison of the Calculated (Bodner–Partom Theory) and the Experimental Stress–Strain Curves of B1900+Hf at 538, 871 and 982°C.
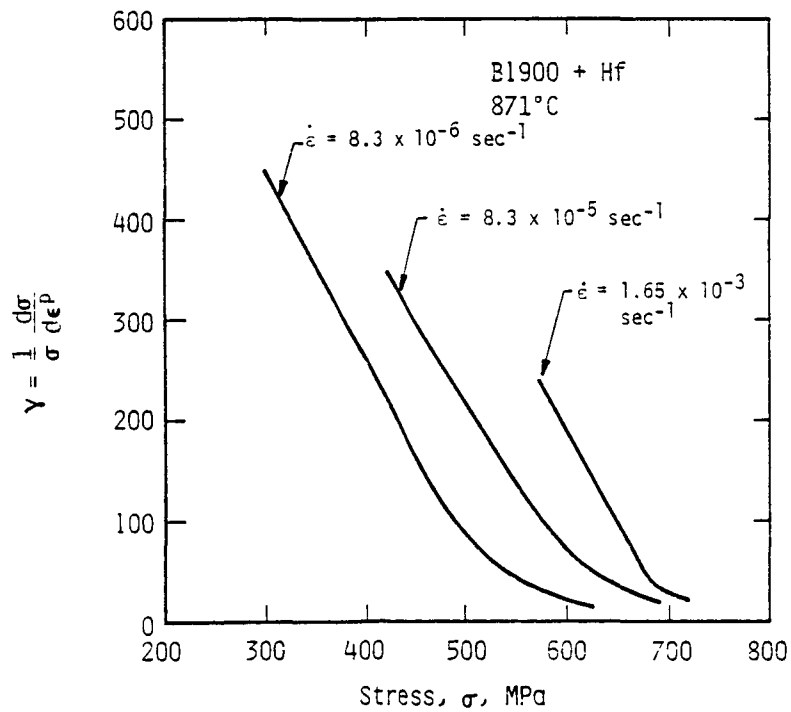
Figure 3.   Work Hardening Behavior of B1900+Hf at Three Strain Rates and 871°C.

289
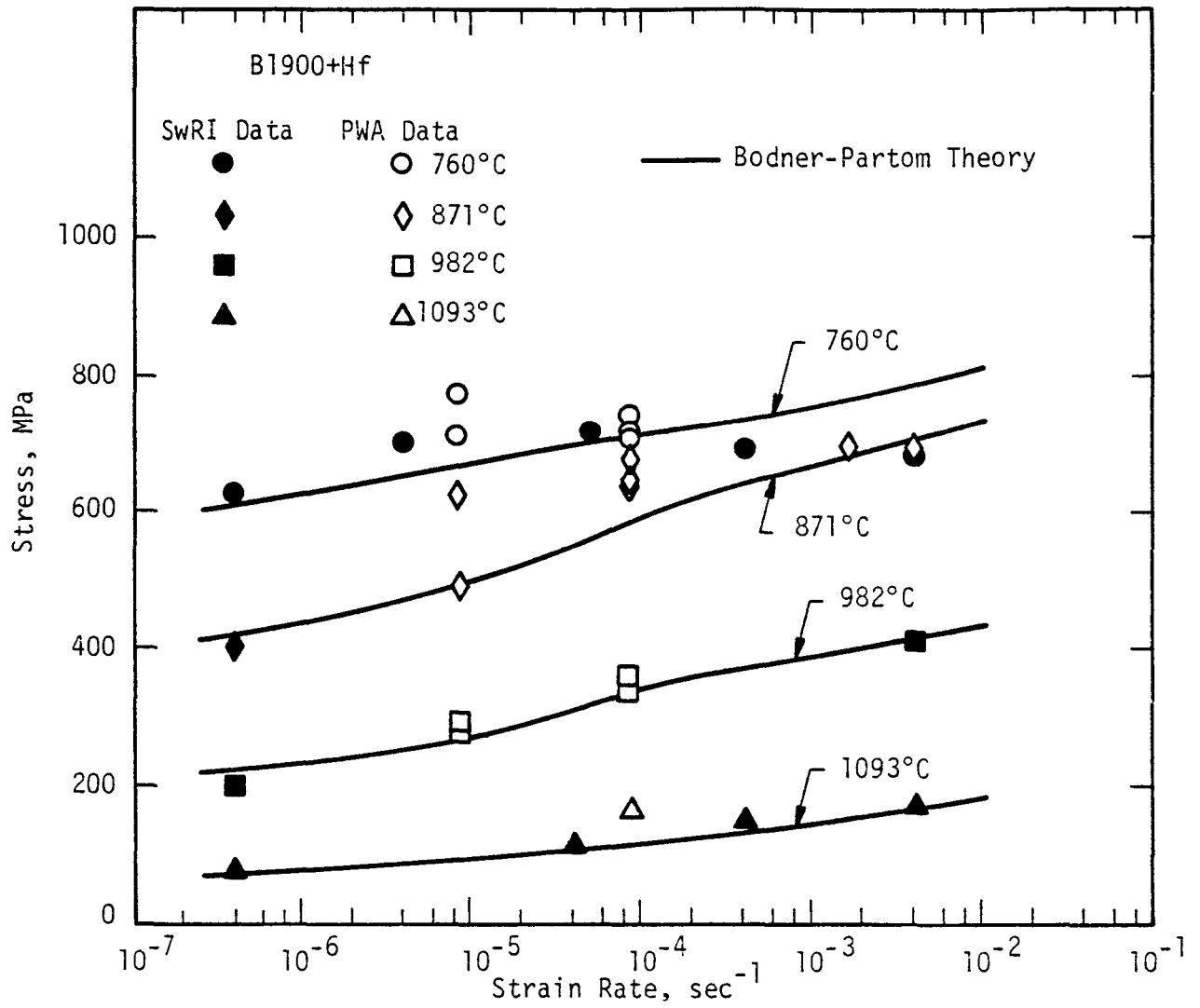
Figure 4.   Temperature and Strain-Rate Dependence of 0.2%
            Offset Yield Stress for B1900+Hf.
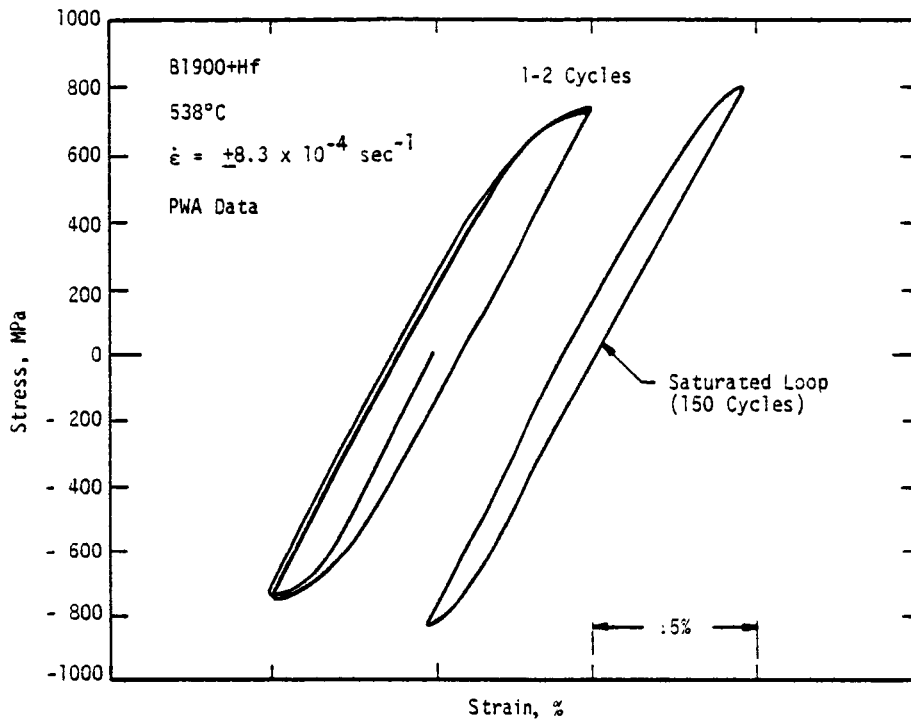
(a) Experiment
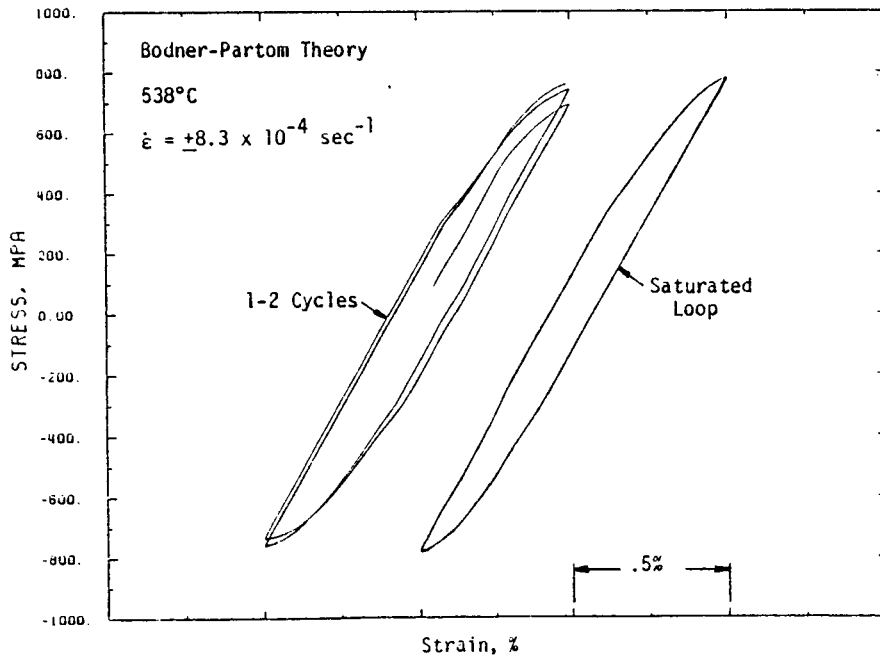
(b) Bodner-Partom Theory

Figure 5. A Comparison of the Calculated (Bodner-Partom Theory) and
the Experimental Hysteresis Loops After 1-2 Cycles and at
Cyclic Saturation.

291

CONSTITUTIVE MODELING FOR ISOTROPIC MATERIALS

V.G. Ramaswamy, R.H. Van Stone, L.T. Dame, J.H. Laflen
General Electric Company
Aircraft Engine Business Group

INTRODUCTION

Accurate analysis of stress-strain behavior is of critical importance in the evaluation of life capabilities of hot section turbine engine components such as turbine blades and vanes. The constitutive equations used in the finite element analysis of such components must be capable of modeling a variety of complex behavior exhibited at high temperatures by cast superalloys. The classical separation of plasticity and creep employed in most of the finite element codes in use today is known to be deficient in modeling elevated temperature time dependent phenomena. Rate dependent, unified constitutive theories can overcome many of these difficulties and may be more suitable for the analysis of the complex behavior of high temperature superalloys. However, many aspects of the unified theories have not been fully evaluated. There is an urgent need for a comprehensive evaluation and further refinement of the capabilities of unified constitutive models for analysis of high temperature superalloy behavior.

OBJECTIVE

It is the purpose of this contract (NAS3-23927) to thoroughly evaluate the unified constitutive theories for application to typical isotropic cast nickel base superalloys used for air-cooled turbine blades and vanes. The specific modeling aspects evaluated are: uniaxial, monotonic, cyclic, creep, relaxation, multiaxial, notch and thermomechanical behavior. Further development of the constitutive theories to model thermal history effects, refinement of the material test procedures, evaluation of coating effects and verification of the models in an alternate material will be accomplished in a follow-on for this base program.

APPROACH

The scope of the overall program covers several aspects of the development of constitutive models for material behavior. The objectives of the base program is being accomplished through a two year combined analytical and experimental program. This is divided into several tasks, each task focusing on a specific objective. First an extensive literature survey was made to identify possible constitutive models for detailed evaluation. Based on the detailed evaluation, two models have been selected for implementation into a finite element code. A comprehensive uniaxial smooth specimen material test program is defined so as to investigate the constitutive behavior patterns of Rene' 80, which is the base material. These experimental results are being used for both the determination of the material parameters and further evaluation of the predictive capabilities of the two models.

The models will be evaluated for multiaxial analysis capabilities, based on multiaxial test data. Two types of multiaxial tests are being performed - tension-tension type at a notch root using an extended ISG technique at Michigan State University (MSU) (Ref. 1) and tension-torsion type on hollow tubes at the General Electric Turbine Technology Laboratories. The notch root behavior prediction capability of the models will be evaluated based on several benchmark notch verification experiments. This part is similar to the work conducted by General Electric on the NASA sponsored Benchmark contract (Ref. 2).

The capability of the constitutive models to analyze the behavior of an actual engine component will be verified by performing a finite element analysis of a turbine blade tip, similar to that described in Reference 3.

PROGRESS

A. MODEL EVALUATION AND SELECTION

A comprehensive survey of various unified constitutive theories available in the literature has been completed. From the 13 models surveyed, 5 theories were selected for detailed evaluation. They are the models of (1) Bodner et. al., (2) Krieg, Swearengen, Rohde (3) Miller (4) Robinson and (5) Walker (References 4, 5, 6, 7, 8). Each of these models was programmed as subroutines in a computer program, which performs a simple numerical integration of the basic equations. All these models involve a number of material parameters. For the purpose of evaluation of the theories, constants available for different materials and temperature in the published literature were used. Each model was subjected to a variety of appropriate loading conditions, so as to evaluate their ability to model several basic aspects of high temperature superalloy behavior. These include: (1) strain rate sensitivity (2) creep (3) stress relaxation (4) history dependence (5) cyclic hardening/softening (6) anelasticity. In addition, the models were evaluated in terms of their complexities in numerical implementation and material parameter evaluation.

During the course of this detailed evaluation, several generic features of the models have become more evident, such as the roles played by the backstress and drag stress. The numerical difficulties special to each of the models have also become apparent. Based on this evaluation process, two models were selected for further detailed investigation. These were (1) the Bodner Model and (2) a generic backstress/drag stress model. In the generic backstress/drag stress model, the specific functional forms are being chosen based on the behavior observed in the Rene' 80 test program.

B. EXPERIMENTAL PROGRAM

All specimens used in this program are cast as solid specimens and machined to the desired configuration. Because of the desire to determine thin wall constitutive relationships applicable to airfoils, the specimens are tubular, with approximately .030 in. wall thickness. Tables 1a and 1b

show all the monotonic tests and creep tests completed to date. Table 1c shows all the isothermal cyclic tests that have been performed. The tests cover a range of strain rates from .002 in/in/min to .2 in/in/min and the temperature range from 538C (1000F) to (982C) 1800F.

The tests are specially designed to meet the needs of constitutive model development. At the same time, efforts were taken to maximize the types of data obtained. For example, at the end of the strain rate controlled monotonic tests, a stress relaxation test is performed. The cyclic tests have an automatic data acquisition system, which is capable of getting up to 200 data points for each hysteresis loop. Some examples of this can be seen in Fig. 4.

The tension-tension multiaxial tests are being done by Prof. J.F. Martin at MSU. These tests utilize an axisymmetric notched round bar with three indentations at the notch root. Both the hoop and axial strains will be measured using the interferometric strain gage, similar to that used in the benchmark test program (Ref. 2).

Data reduction procedures also reflect the special needs of constitutive model development. For each test, the elastic modulus is first determined, based on the initial stress-strain readings. Then the inelastic strain is calculated. Since time is recorded at each data point, the time derivatives of all measured quantities is calculated. Thus stress rate and inelastic strain rate is calculated at each point using a 7 point sliding polynomial technique. All the results are stored in a computer file which can be directly used as input in material parameter evaluation.

C. EVALUATION OF MATERIAL PARAMETERS

It has been widely recognized that one of the major sources of difficulty in the use of unified constitutive theories is the determination of the material parameters. No generalized procedures of determining these material parameters are currently available. Considerable effort has been made to develop such a method in the present contract.

The approach that is adopted is to develop a computer program which directly uses the various test results as input and generates the various material parameters as output. The computer program developed is kept as flexible as possible, so that different functional forms can be used. Such an approach also assures consistency in the treatment of the various test data. However, it should also be noted that, while conceptually simple, such an approach can be very challenging, mainly due to the non-linear equations involved. Such a computer program has been developed for a generic backstress-drag stress model.

The generic backstress-drag stress model is described by the following set of equations for the uniaxial case:

$$\dot{\varepsilon}^I = (\frac{\sigma - \Omega}{Z})^N \; \text{sgn} \; (\sigma - \Omega) \qquad\qquad 1$$

$$\dot{\Omega} = f_1 \dot{\varepsilon}^I - f_2 |\dot{\varepsilon}^I| \Omega - R_1 \qquad\qquad 2$$

$$\dot{Z} = g_1 \dot{\varepsilon}^I - g_2 |\dot{\varepsilon}^I| Z - R_2 \qquad\qquad 3$$

In the above,

$\dot{\varepsilon}^I$ = Inelastic strain rate
Ω = Backstress
Z = Drag stress

R_1 and R_2 are static thermal recovery functions.

f_1 and g_1 are the hardening functions.

f_2 and g_2 are the dynamic recovery functions.

Equations 1, 2 and 3 are a set of coupled non-linear differential equations. The specific forms for the various hardening and recovery functions are significantly different for the various models that have been published. The approach taken in this project is to choose those forms that appear most appropriate for Rene' 80 behavior. To determine the various material parameters involved, an iterative approach is used. In this, a set of starting assumptions are made which are subsequently relaxed. Then successive non-linear optimizations are performed in equations 1, 2 and 3 using the experimentally measured quantities as the basis.

Rene' 80 test data at 982C (1800F) has been analyzed in detail using a computer program incorporating the procedure described above. Some of the notable results are as follows:

(1) f_1 = constant, f_2 = constant appears to work reasonably well for this case. The constants in R_1 have been found using slow strain rate monotonic and creep tests. However, the overall contribution of the above term seems extremely small, as compared to the hardening and dynamic recovery terms.

(2) Fig. 1a shows the results of the iteration procedure after 5 iterations, using only the high $\dot{\varepsilon}$ monotonic test (.2 in/in/min). It appears that parameters determined using the computer program can reproduce the stress strain behavior reasonably well. Fig. 1b shows the same result, but using only the small strain rate monotonic test (.002 in/in/min). The constants for these two strain rates are significantly different.

(3) The monotonic based constants are not able to predict the cyclic behavior. Fig. 2a and 2b show the cyclic loop predictions using monotonic based constants. Fig. 3a indicates that softening is continuing. In the model, the drag stress equation constants control cyclic softening.

(4) Fig. 3 shows the results of using constants based on all monotonic tests. It is seen that these parameters overpredict the high $\dot{\varepsilon}$ tests and underpredict the low $\dot{\varepsilon}$ tests. Thus, although the model appears good for a specific strain rate, it does not seem capable of representing the entire strain rate spectrum used here (0.002 in/in/min to 0.2 in/in/min).

(5) Fig. 4a shows the comparison of the test data and model prediction for a cyclic test at .2 in/in/min. The result shown is for the 96th cycle. The initial hardening shown in the plot is to be disregarded, because the prediction was made for only 2 cycles and not the entire 96 cycles. Fig. 4b shows similar results as above for the 0.002 in/in/min cyclic test. Both Fig. 4a and 4b indicate that the procedure works well for each strain rate. However, the material parameters are significantly different for the two cases. Here again, the difference is believed to be caused by the drag stress equation parameters, as in the monotonic case. This points to the limitations of the particular model in representing a wide range of strain rate behavior.

Current work is evaluating the Bodner model, and extending the analysis to lower temperatures where less strain rate sensitivity is anticipated.

(D) FINITE ELEMENT CODE IMPLEMENTATION

The 2-D finite element code containing Bodner's constitutive model has been completed and tested. The 2-D finite element code utilizes two dimensional constant strain triangles and an incremental initial strain iteration technique. To facilitate the simulation of arbitrary load histories, the load history is partitioned into piecewise linear segments with steady state thermal conditions during each segment. In order to simplify input, reduce convergence problems and minimize cost, a dynamic time stepping procedure is incorporated. The 3-D finite element code using 20 noded isoparametric bricks is currently being developed.

In order to verify the 2-D finite element code with Bodner's model a number of uniaxial test cases were run and compared with published results. (References 9-11). In addition, a large two dimensional model (Fig. 5a) of the benchmark notch specimen (Reference 2) was constructed

and run with three different loading histories and compared with published experimental results. An example of these comparisons can be seen in Figure 5b. The overall performance of the finite element code with Bodner's model was quite good. The cost of running the code is comparable to one using a conventional uncoupled plasticity and creep constitutive model.

REFERENCES

1. Bofferding, C.H. III, "A Study of Cyclic Stress and Strain Concentration Factors at Notch Roots Throughout Fatigue Life", M.S. Thesis, Michigan State University, 1980.

2. Domas, P.A., Sharpe, W.N., Ward, M. and Yau, J., "Benchmark Notch Test for Life Prediction" NASA CR-165571, June 1982.

3. McKnight, R.L., Laflen, J.H., and Spamer, G.T., Turbine Blade Tip Durability Analysis, NASA CR 165268, 1982.

4. Bodner, S.R. and Partom, Y., "Constitutive Equations for Elastic Viscoplastic Strain-Hardening Materials," ASME Journal of Applied Mechanics, ASME, June 1975.

5. Krieg, R.D., Swearengen, J.C., Rohde, R.W., "A Physically Based Internal Variable Model for Rate Dependent Plasticity" Proceedings of ASME/CSME PVP Conference, 1978.

6. Miller, A., "An Inelastic Constitutive Model for Monotonic, Cyclic and Creep Deformation (Part I and II)", Journal of Engineering Materials and Technology, April 1976.

7. Robinson, D.N., Swindeman, R.W., "Unified Creep-Plasticity Constitutive Equations for 2 1/4 Cr-1 Mo Steel at Elevated Temperature" ORNL/TM-8444.

8. Walker, K.P. "Research and Development Program for Nonlinear Structural Modeling with Advanced Time-Temperature Dependent Constitutive Relationships" NASA CR-165533.

9. Stouffer, D.C., Bodner, S.R., "A Relationship Between Theory and Experiment For a State Variable Constitutive Equation," Mechanical Testing for Deformation Model Development, ASTM STP 765, 1982.

10. Bodner, S.R., "Representation of Time Dependent Mechanical Behavior of Rene' 95 by Constitutive Equations", AFML-TR-79-4116, November 1978.

11. Stouffer, D.C. "A Constitutive Representation for In100" AFWAL-TR-81-4039, June 1981.

TABLE I

(a) TENSILE SPECIMEN TEST MATRIX

Test Temperature C (F)	Strain Rate			
	0.002 Min^{-1}	0.02 Min^{-1}	.06 Min^{-1}	0.2 Min^{-1}
538 (1000)	T	T + SR		T + SR
649 (1200)		T + SR		
760 (1400)		T + SR		
871 (1600)		T + SR		
982 (1800)	T + SR	T + SR	T	T + SR

T indicates a constant strain rate tension test terminated at a strain of 0.03.

SR is a stress relaxation test to be performed at a constant strain of 0.03.

(b) CREEP SPECIMEN TEST MATRIX

Test Temperature C (F)	Initial Applied Stress Levels mPa (ksi)
982 (1800)	110 (16.0)
982 (1800)	217 (31.5)
982 (1800)	303 (44.0)
871 (1600)	493 (71.5)
871 (1600)	414 (60.0)
871 (1600)	312 (45.3)
760 (1400)	554 (80.3)
760 (1400)	685 (99.3)
760 (1400)	634 (92.0)
1093 (2000)	114 (16.6)

(c) UNI-AXIAL FATIGUE SPECIMEN TEST MATRIX

$(|\epsilon_{max}|$ or $|\epsilon_{min}| = 0.0015, 0.0030, 0.0045)$

Continuously Cycled Tests (Strain Controlled)

Test No.	Temperature - C (F)	Aϵ	ϵ (ϵmin^{-1})
1	538 (1000)	∞	0.2
2	871 (1600)	∞	0.2
3	982 (1800)	∞	0.2
4	538 (1000)	∞	0.002
5	871 (1600)	∞	0.002
6	982 (1800)	∞	0.002
7	538 (1000)	+1	0.2
8	538 (1000)	+1	0.002
9	871 (1600)	+1	0.2
10	871 (1600)	-1	0.2
11	982 (1800)	-1	0.2
12	982 (1800)	-1	0.002

Hold Time Tests (A$_\epsilon$ = ∞, ϵ = 0.2 min^{-1}, strain controlled)

Test No.	Temperature - C (F)	Maximum or Minimum Strain Hold	Hold Time (Sec)
13	538 (1000)	Maximum	12
14	538 (1000)	Maximum	120
15	871 (1600)	Maximum	12
16	871 (1600)	Maximum	120
17	871 (1600)	Minimum	12
18	871 (1600)	Minimum	120
19	982 (1800)	Minimum	12
20	982 (1800)	Minimum	120
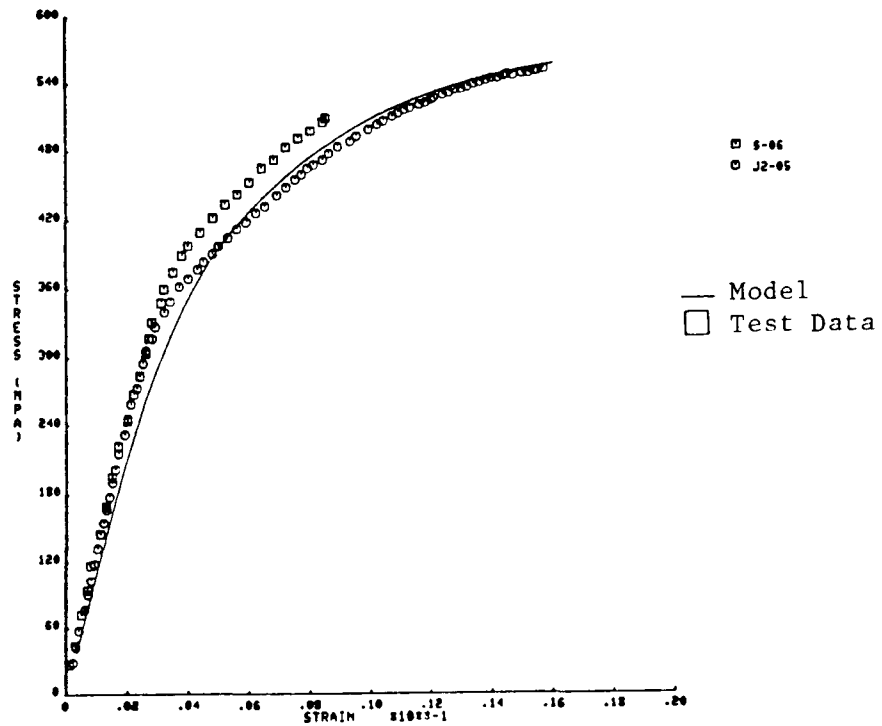
Figure 1a. Rene 80 982 C (1800 F) Monotonic Test at 0.2 in/in/min.
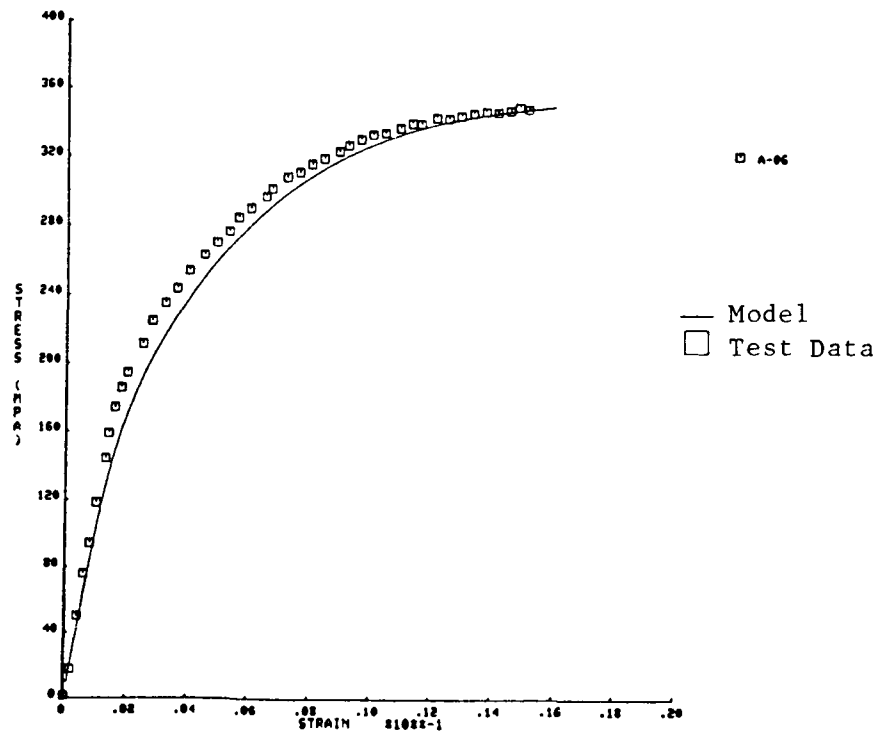
Figure 1b. Rene 80 982 C (1800 F) Monotonic Test at 0.002 in/in/min.

300
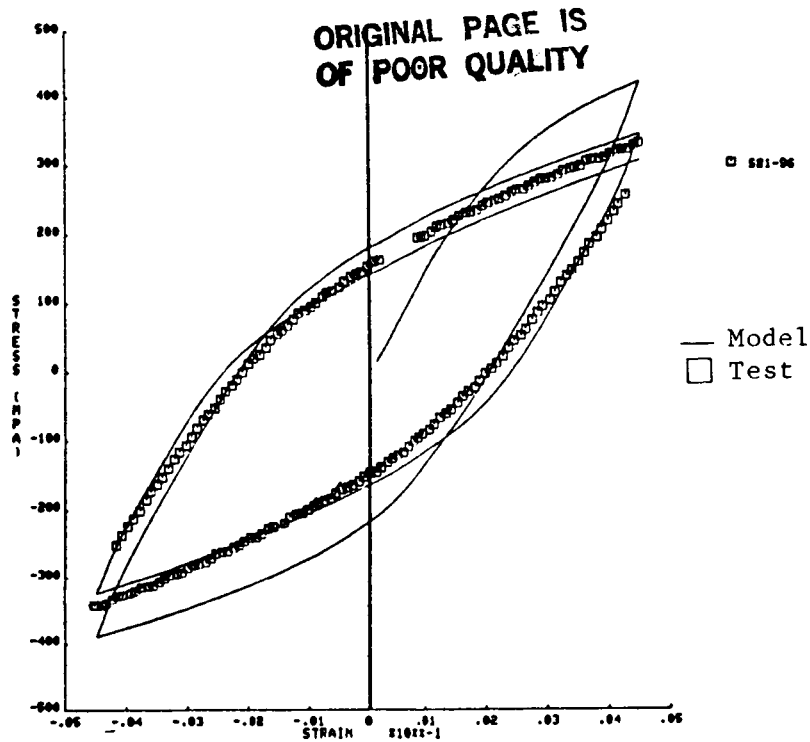
Figure 2a.   Rene 80 982 C (1800 F) 0.2 in/in/min Cyclic Test.
             Model Prediction Using Monotonic Based Material Parameters.
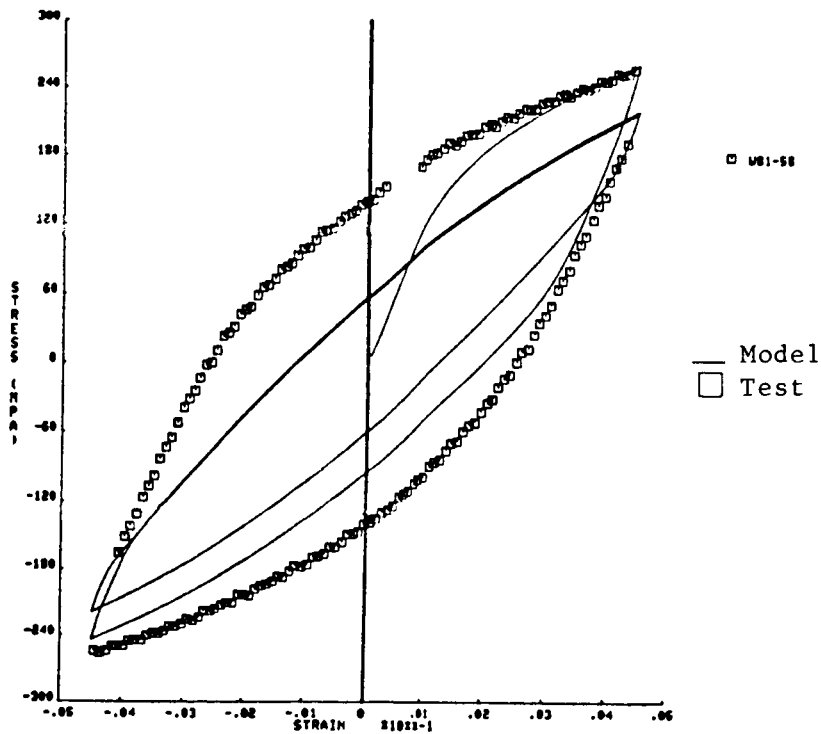
Figure 2b.   Rene 80 982 C (1800 F) 0.002 in/in/min Cyclic Test.
             Model Prediction Using Monotonic Based Material Parameters.
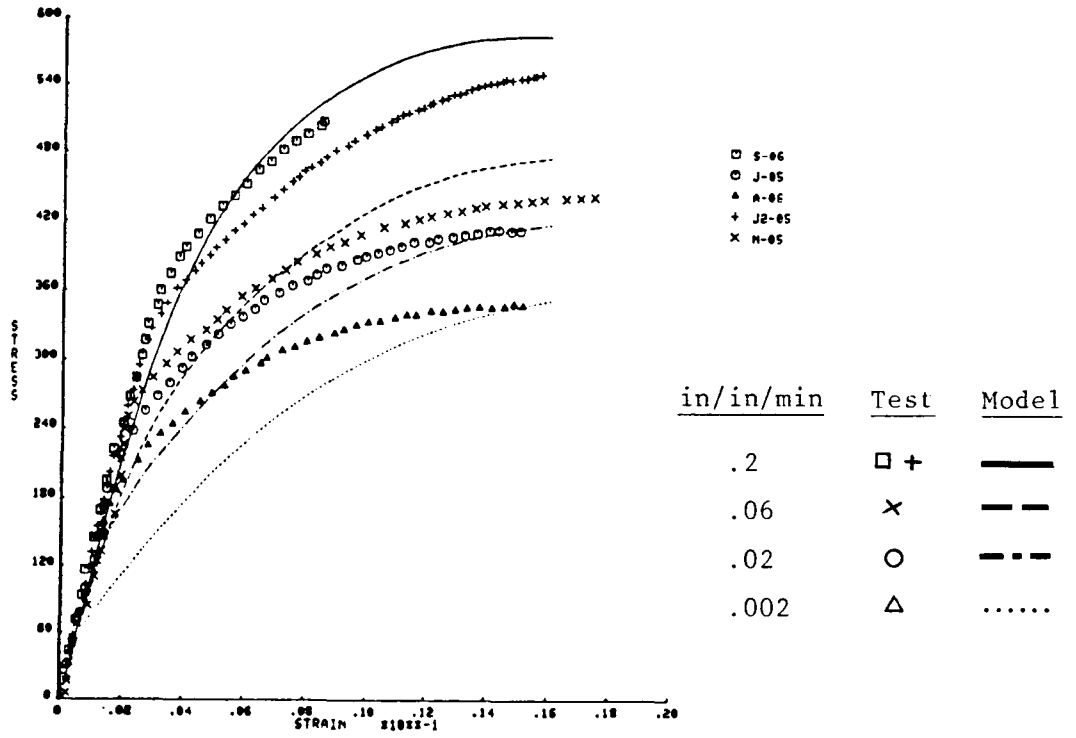
Figure 3.   Rene 80 982 C (1800 F) Monotonic Tests.

302
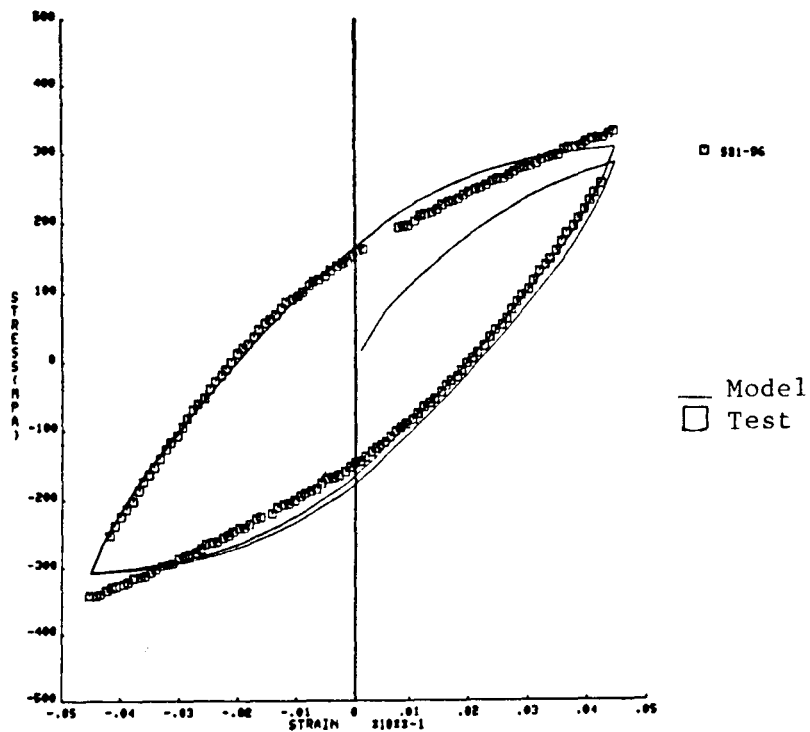
Figure 4a. Rene 80 982 C (1800 F) Cyclic Test 0.2 in/in/min, 96th Cycle.
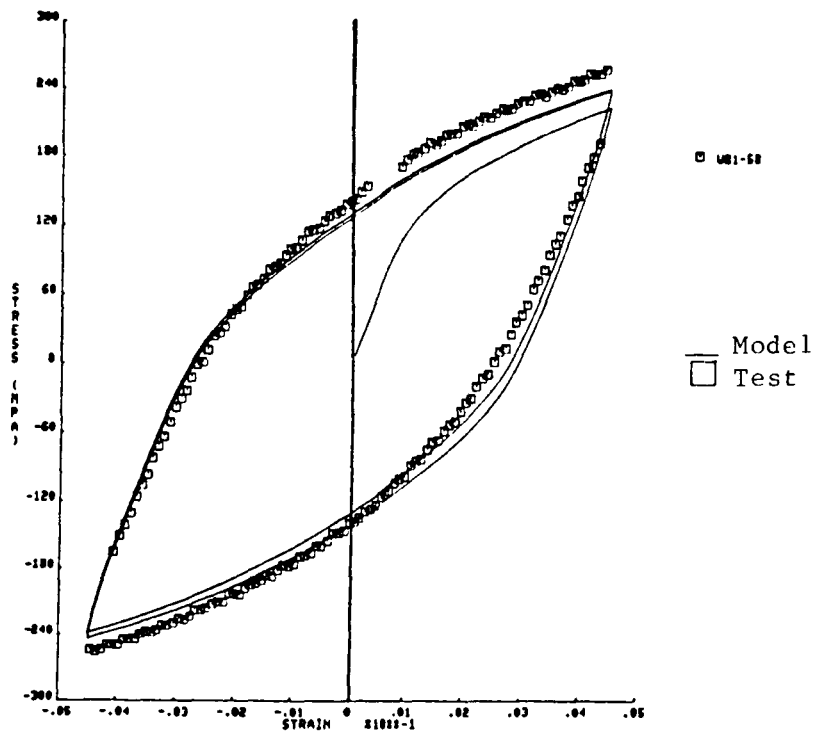
Figure 4b. Rene 80 982 C (1800 F) Cyclic Test 0.002 in/in/min, 58th Cycle.

303
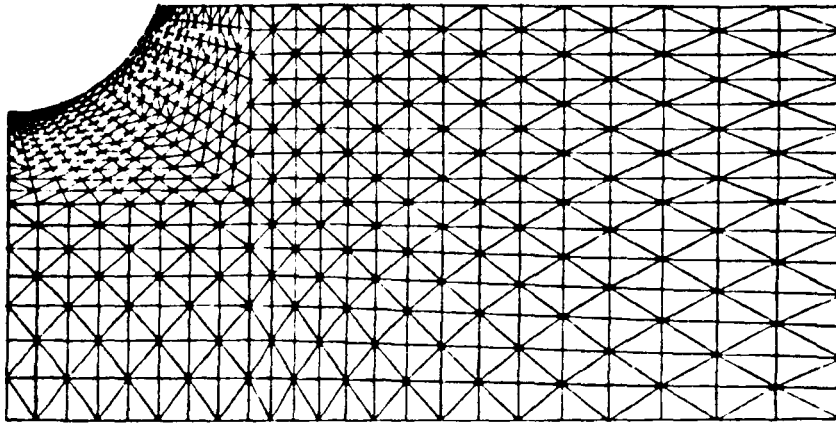
Figure 5a. Finite Element Mesh for Benchmark Notch Specimen.
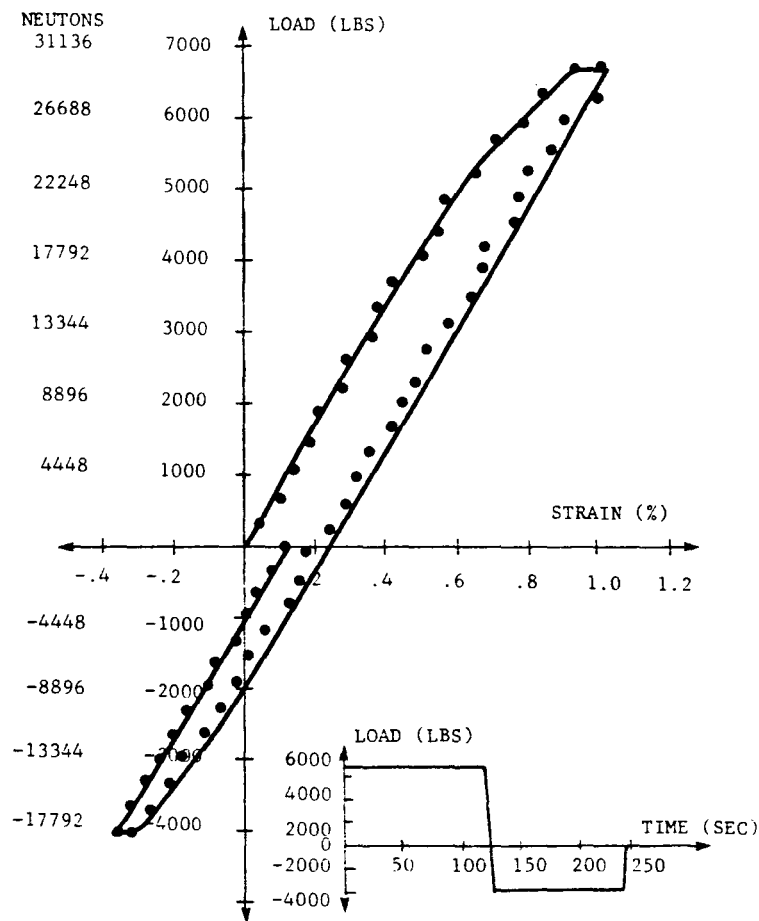
Figure 5b. Bodner Model Predictions for Benchmark Notch Specimen.

304

CREEP FATIGUE LIFE PREDICTION FOR ENGINE HOT SECTION
MATERIALS (ISOTROPIC) - TWO YEAR UPDATE[1]

Vito Moreno
United Technologies Corporation
Pratt & Whitney

INTRODUCTION

Requirements for increased durability of gas turbine hot section components have placed a greater degree of importance on accurate structural analysis and life prediction. The development of improved life prediction technology for structures operating at elevated temperatures is one of the objectives of the NASA Hot Section Technology (HOST) program. As part of HOST, the current contract will investigate fundamental approaches to high temperature life prediction, identify modeling strategies and develop specific models for component relevant loading conditions.

This contract is a 5-year, 2-part effort (2-year base program, plus a 3-year optional program) and includes two isotropic hot section materials and protective coating systems. The recently completed base program concentrated on the investigation of various life prediction approaches for high temperature applications and the selection and development of basic models for simple-cycle, isothermal loading conditions. The optional program will consider the development of models to address thermo-mechanical cycling, multi-axial conditions, cumulative loading, environmental effects and cyclic mean stress. Verification tests of models on an alternate material and coating system will also be conducted.

TECHNICAL PROGRESS SUMMARY

Base Program Material and Testing

Monotonic tensile, creep, and cyclic fatigue tests were conducted on specimens fabricated from a single heat of cast B1900+Hf material. Casting parameters were selected to produce a small, uniform grain size of approximately 0.018 cm (0.007 in.) to 0.025 cm (0.010 in.) throughout the test specimen gage sections to provide an isotropic nature to the crack initiation process. The fatigue tests were conducted in an axial strain-controlled mode at temperatures between 538°C (1000°F) and 982°C (1800°F). These tests investigated effects on initiation life of strain range, strain rate, mean strain, and compressive and tensile strain dwell periods. In all tests, crack initiation was defined as the occurrence of a 0.075 cm (0.30 in.) surface crack, as determined by replication. A total of approximately 150 tests were run in the base program.

---

[1]NASA Contract NAS3-23288.

Screening of Candidate Life Prediction Approaches

During the base program, various life prediction approaches were reviewed to assess their accuracy and practicality for elevated temperature life prediction. Approaches and representative models included correlation of macroscopic parameters (strain range, mean stress, etc.), inelastic strain (SRP), strain rate (Majumdar, ref. 1), work (Ostergren, ref. 2), damage accumulation (ductility exhaustion) and fracture mechanics models. The following observations were made:

1. A "ductility exhaustion" format provides a workable means of incorporating the most desirable features of the models reviewed.

   (a) The ductility can be considered a loading history-dependent parameter. This allows prediction of loading path effects, such as mean strain or overload, without including this data in the base regression for the model constants. Separate ductilities can be estimated for the grain and the grain boundaries to potentially include the mode of initiation (transgranular versus intergranular) in the prediction.

   (b) The damage (ductility exhaustion) parameter can be formulated to include time-independent and time-dependent components. For the B1900 + Hf fatigue tests conducted in this program, the two-damage components provided an improvement in the predictive capability for a range of strain rates and hold times as compared to a single-damage parameter formulation.

   (c) The required information to determine the specific damage parameter of a loading cycle is obtained from rapid cycle fatigue testing, the stress response of the cycle being predicted, and the cycle period (time).

2. Less desirable features of other models limited their applicability and increased the required analytical input. Some of these features include:

   (a) Inelastic strain or strain rate (ϵ_{pl} or $\dot{\epsilon}_{pl}$) is difficult to calculate accurately and relatively small for the loading cycles considered in this program.

   (b) Use of a crack growth model to predict initiation requires small crack growth data which is relatively difficult to obtain. Furthermore, the current level of development of time-dependent inelastic crack-tip parameters (e.g. J, C*) is such that the prediction and application to a surface-initiated crack under complex loading is not clearly defined for an immediately useable life model.

   (c) A number of the models evaluated showed good predictive capability but required various types of fatigue tests (strain rate, hold times) in the initial model data base to evaluate the necessary constants. This was considered an expensive requirement for development of a model. The applicability of the models is also limited to those materials where the data is available or planned.

306

From these observations, the damage model discussed below is considered as the approach having the greatest predictive capability with the most practical data base requirements. It becomes a good starting point for the additional loading cycles to be considered in the optional program.

Fatigue Model Development and Evaluation

The proposed model assumes that fatigue cracks are initiated when a measure of the grain cyclic capability is exhausted by the cycle damage and is expressed as:

$$\boxed{\begin{array}{c}\text{GRAIN CYCLIC DAMAGE}\\ \text{CAPABILITY (DUCTILITY)}\end{array}} - \boxed{\dfrac{\text{DAMAGE}}{\text{CYCLE}}} \quad \text{X} \quad \text{CYCLES} = 0 \qquad (1)$$

The grain cyclic ductility is determined at higher temperatures (>760°C (>1400°F)) as the amount of primary creep strain that could have been generated if the maximum stress on the first loading cycle was held constant. At lower temperatures, the cyclic ductility is determined as the amount of tensile elongation. The cycle damage function is determined as the product of a reference damage rate, (from fully reversed tests) and the ratios of tensile stress, stress range and period.

Assuming that the cycle damage is composed of time-independent and time-dependent components, the equation for initiation is written as:

$$\bar{\epsilon}_p - \int_0^N \frac{dD}{dN_R} \left\{ \left(\frac{\sigma_T}{\sigma_{TR}}\right)\left(\frac{\Delta\sigma}{\Delta\sigma_R}\right) + \left[\left(\frac{\Delta\sigma_R}{\Delta\sigma}\right)\left(\frac{\sigma_T}{\sigma_{TR}}\right)\right]^b * \left[\left(\frac{t}{t_R}\right)^c - 1\right]\right\} dN = 0 \qquad (2)$$

Where:
$\bar{\epsilon}_p$ $\equiv$ grain cyclic capability for specific test condition being predicted

dD/dN_R $\equiv$ damage rate from fully reversed testing

$\Delta\sigma$ $\equiv$ stress range

σ_T $\equiv$ maximum tensile stress

t $\equiv$ 1/2 cycle period

R $\equiv$ reference condition

b_1,c $\equiv$ constants determined from monotonic creep tests

Here the integration reflects the fact that the stress response varies during the cycling.

Application of equation (2) to the prediction of B1900 + Hf 871°C (1600°F) fatigue tests produced the results shown in figure 1. The prediction of rapid cycle tests at various mean strains (-0.25, +0.25, +0.50%) is shown in figure 1A. The trend of longer life with decreasing mean strain is clearly predicted. The prediction of slower strain rate and hold time tests is shown in figure 1B. The trends and the prediction in life relative to the fully reversed baseline data (not shown) are also predicted.

Prediction of mean strain and strain rate effects is also demonstrated at 537°C (1000°F) and 982°C (1800°F) in figure 2. The model predicts the reduction in life associated with a positive mean strain at 537°C (1000°F) (fig. 2A). Time-dependent damage is not included, so the trend in life is associated only with the time-independent term. At 982°C (1800°F) (fig. 2B) the correct trend in life at lower strain rates is also shown.

REFERENCES

1. Majumdar, S.; and Maiya, P.S.: A Mechanistic Model For Time Dependent Fatigue. Jour. of Materials & Technology. January 1980, Vol. 102, pp. 159-167.

2. Ostergren, W.J.: A General Damage Equation For Low Cycle Fatigue Life Prediction at Elevated Temperatures. Rensselaer Polytechnic Institute. Zerox University Microfilm, Ann Arbor, Mich. No. 76-27,203. 1976.
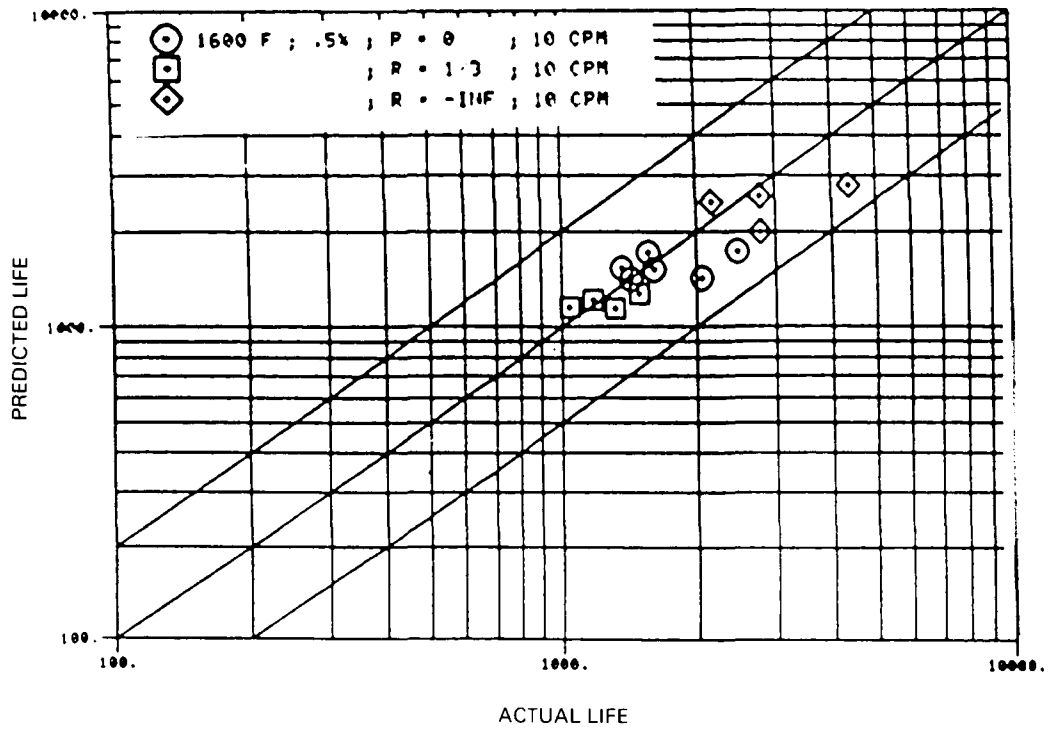
(A)
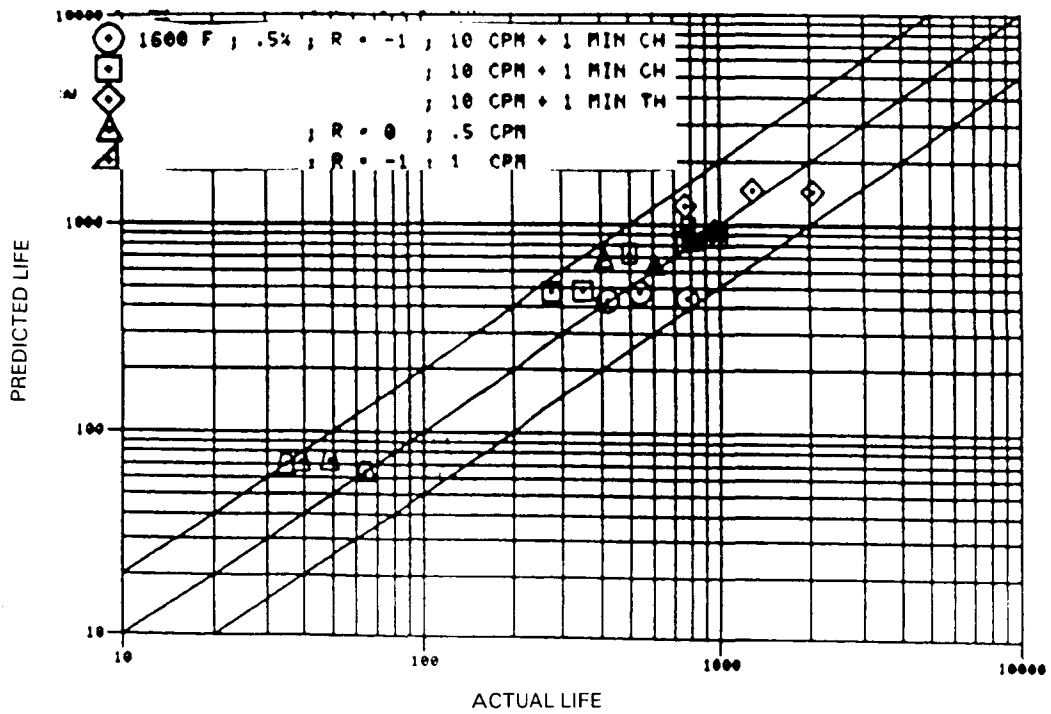
(B)

Figure 1   Mean Strain and Rate Effects Predicted at 871°C (1600°F) - Model
Verification Tests
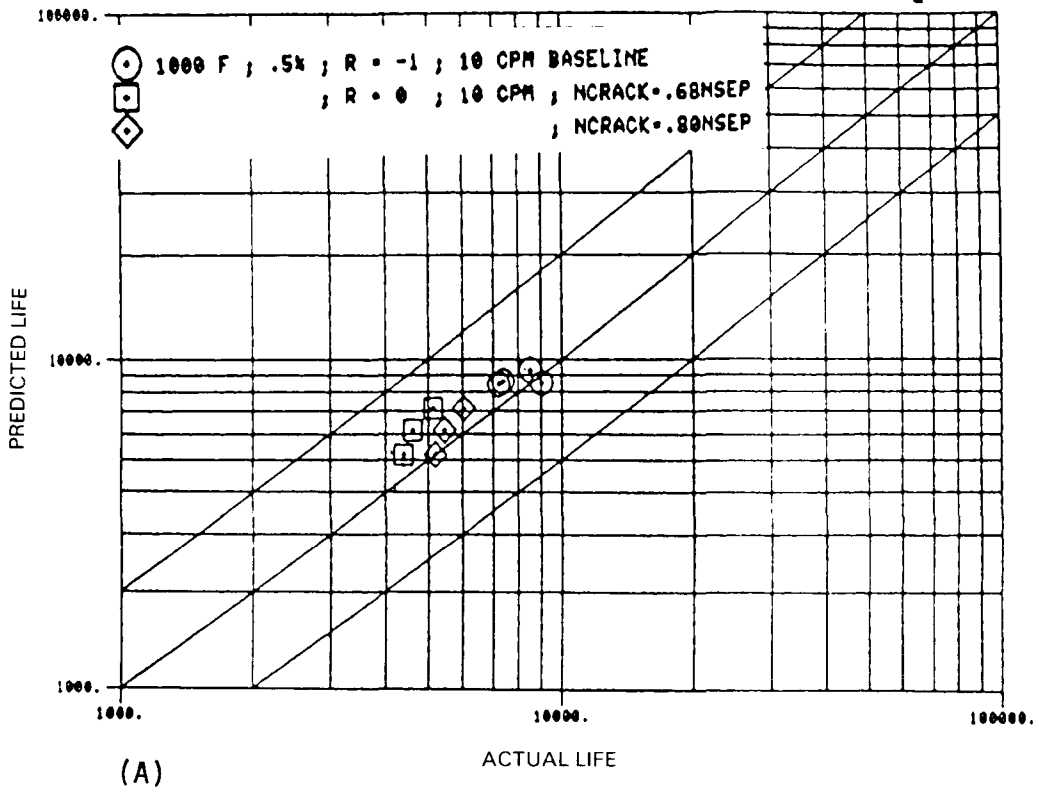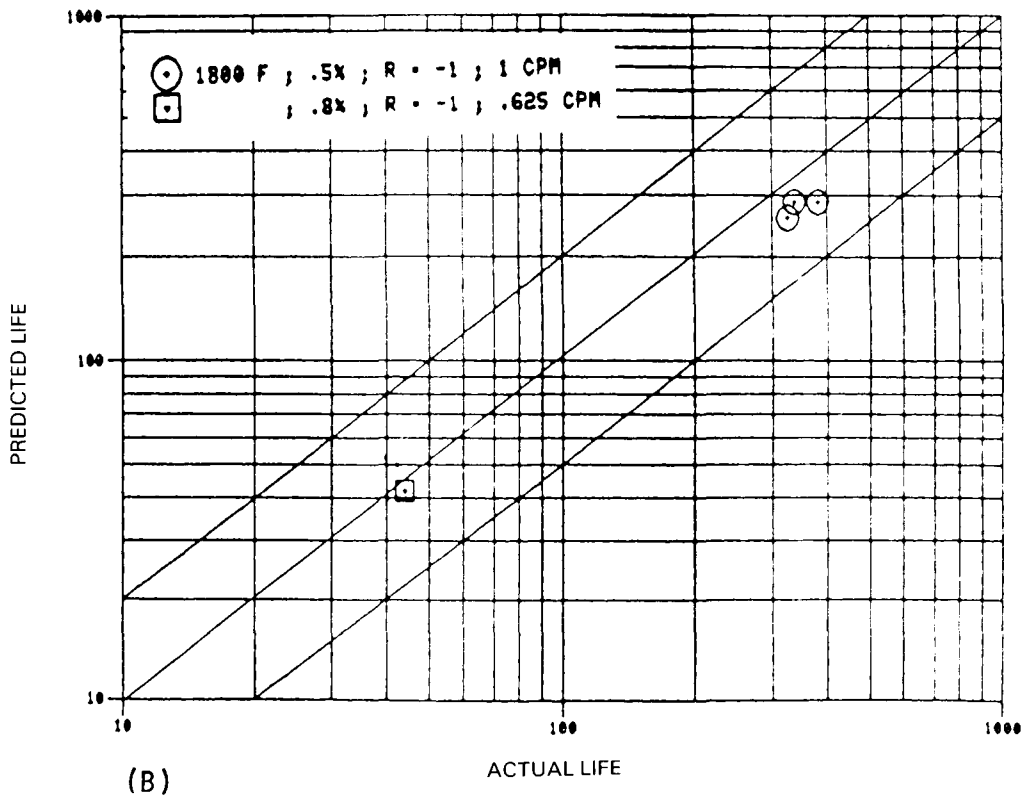
Figure 2   Similar Predictive Capability Displayed at Other Temperatures

ELEVATED TEMPERATURE CRACK GROWTH

K.S. Kim
J.F. Yau
R.H. Van Stone
J.H. Laflen
General Electric Company
Aircraft Engine Business Group

1. INTRODUCTION

Critical gas turbine engine hot section components such as blades, vanes, and combustor liners tend to develop minute cracks during the early stages of operation. These cracks may then grow under conditions of fatigue and creep to critical size. Current methods of predicting growth rates or critical crack sizes are inadequate, which leaves only two extreme courses of action. The first is to take an optimistic view with the attendant risk of an excessive number of service failures. The second is to take a pessimistic view and accept an excessive number of "rejections for cause" at considerable expense in parts and downtime. Clearly it is very desirable to develop reliable methods of predicting crack growth rates and critical crack sizes.

To develop such methods, it is necessary to relate the processes that control crack growth in the immediate vicinity of the crack tip to parameters that can be calculated from remote quantities, such as forces, stresses, or displacements. The most likely parameters appear to be certain path-independent (P-I) integrals, several of which have already been proposed for application to high temperature inelastic problems. A thorough analytical and experimental evaluation of these parameters needs to be made which would include elevated temperature isothermal and thermomechanical fatigue, both with and without thermal gradients.

In any investigation of fatigue crack growth, the problem of crack closure must be addressed in order to develop the appropriate crack growth model. Analytically, this requires the use of gap elements in a nonlinear finite element code to predict closure loads. Such predictions must be verified experimentally through detailed measurements; the best method for measuring crack closure has not been established in previous studies.

It is the purpose of this contract (NAS3-23940) to determine the ability of currently available P-I integrals to correlate fatigue crack propagation under conditions that simulate the turbojet engine combustor liner environment. The utility of advanced fracture mechanics measurements will also be evaluated and determined during the course of the program. These goals will be accomplished through a two year, nine task, combined experimental and analytical program. To date, an appropriate specimen design and a crack displacement measurement method

have been determined. Alloy 718 has been selected as the analog material based on its ability to simulate high temperature behavior at lower temperatures in order to facilitate experimental measurements. Available P-I integrals have been reviewed and the best approaches are being programmed into a finite element postprocessor for eventual comparison with experimental data. These experimental data will include cyclic crack growth tests under thermomechanical conditions and, additionally, thermal gradients.

2. A REVIEW OF P-I INTEGRALS

The utility of the J integral as a parameter for predicting crack growth in the elastic-plastic regime is rather limited. The theoretical basis of the J integral does not allow the extension of its usage to nonproportional loading and unloading in the plastic regime, nor can it be utilized in the presence of a temperature gradient and material inhomogeneity. A typical example where all these limiting factors are operative would be the hot section components of a gas turbine in mission cycles.

In recent years there has been a considerable effort to modify or reformulate the P-I integral. Consequently, a number of new P-I integrals have emerged in the literature. These include the J^*, $\hat{J}$, J_Θ, ΔT_p, ΔT_p^* integrals and two thermoelastic integrals, J_W and J_G (see Appendix for definition of these). These P-I integrals have been critically reviewed in this program. The theoretical background has been examined with particular attention to whether or not the path-independence is maintained in the presence of nonproportional loading; unloading in the plastic regime; and a temperature gradient and material inhomogeneity. The relation among the P-I integrals, salient features and limitations were investigated. The physical meaning, the possibility of experimental measurement, and the computational ease were also examined. The summary of the review is presented in Table 1. In view of the requirements associated with performing the forthcoming tasks in this program the following conclusions were made:

i) The J^*, $\hat{J}$, ΔT_p and ΔT_p^* integrals maintain the path-independence under the thermomechanical cycles which will be used in the tests in this program and will be simulated numerically in subsequent tasks. Although the physical meaning of these P-I integrals needs to be further pursued, they would be the logical choices for further evaluation in this program.

ii) The J, J_W, J_G and J_Θ integrals have limited capabilities. The J_W and J_G integrals are usable only for thermoelastic problems with homogeneous material properties. These integrals may be useful for prediction of crack growth in a rather small temperature gradient field and under small scale yielding conditions. The J_Θ integral is a modified version of J to include the thermal strain. Therefore, it cannot be used with substantially

nonproportional loading and unloading in the plastic regime. It would be worthwhile, however, to investigate the utility of operationally defined J and possibly J_Θ for the test cycles in this program.

3. NUMERICAL COMPUTATION

All selected P-I integrals have been implemented in a postprocessor to the General Electric nonlinear finite element program, CYANIDE. Numerical values of the integrals will be evaluated and examined for cracks subjected to various situations such as monotonic/cyclic loadings, uniform/non-uniform temperature distributions, stationary/propagating cracks, etc. Best formulations suitable for all situations will be selected and used to correlate with the test results. The relationship between the analytical CTOD (or CMOD) displacements and the values of P-I integrals will be established to identify the displacement which must be measured to determine operational P-I integral.

In computation, an integration path is first selected which should start from a node on one side of the crack surface, extend along edges of elements, and end at a node on the other side of the crack surface. The path can be selected by either providing all nodal numbers to be included in the path, or simply inputing only a few key nodes and letting the program search for a proper path. Once the path is defined, the program will identify whether a element is inside or outside the path, thus, computation of the area integral can be performed. Displacement, stress, and strain data required for computation are to be read directly from random CYANIDE output files. Each integral is to be set up in an individual calling subroutine thus addition of other new integrals can be easily done without affecting the entire program structure. The program is in the FORTRAN format and to be run in the timesharing mode. Options are provided for selecting types of integrals, an integration path, and load cases. The basic structure of the program has been established and successfully tested through the computation of the conventional J integral. The results for an elastic compact tension problem have shown very stable trend of path independence and are about four percent different from a handbook solution. For the plastic case, however, the results were shown to be increasingly deviating from the referenced one as the load increased. This may be due to the fact that crack tip blunting was not simulated in the analysis which used triangular elements, while the blunting effect was reportedly included in developing the handbook curves.

Implementation of other P-I integrals has been completed and further checkouts are in progress. Algorithms for the integral forms from Blackburn, Ainsworth, Kishimoto, and Atluri have been implemented. Example results for the same compact tension specimen problem are compared in Figure 2 along with the solution from the conventional J integral. It was found that for isothermal monotonic loading condition, several relationships exist between P-I integrals

$$J \text{ (Rice)} = J_\Theta \text{ (Ainsworth)}$$

313

$$\Sigma \Delta T_p^* (\text{Atluri}) = J^* \quad (\text{Blackburn})$$

$$\Sigma \Delta T_p (\text{Atluri}) = J \quad (\text{Rice})$$

The first equation is theoretically verifiable, but the second and third equations are pertinent to the particular geometry and loading condition under consideration. Examining path independence for the integrals, it was revealed that most integrals showed a drastic drop in results evaluated in the crack tip region, and a slightly increasing trend as the integration path was further removed from the crack tip. Except for Kishimoto's integral, contribution from the area integral term are significantly smaller than the line integral. Both the ΔT_p and ΔT_p^* integrals were computed for a complete loading/unloading cycle. The trend for the results (Figure 3) computed from a remote path agrees well with Nagakaki's findings. However, it was also found that both ΔT_p and ΔT_p^* from the near field path were gradually losing the characteristics of path independence as the unloading proceeds further down. This may be due to the use of large unloading increments in the analysis. The capabilities of all integrals for problems with temperature gradients, varying material properties and propagating cracks are yet to be investigated.

In a parallel work, the proposed single edge crack specimen is being analyzed using the three-dimensional elastic-plastic finite element method. Stress and displacement distributions at some remote location in the gauge section for a cracked specimen subjected to displacement boundary conditions at the buttonhead were obtained. The purpose of this analysis is twofold: (1) to provide guidelines for experimental set-up and data measurement, and (2) to provide necessary boundary conditions for further analysis of local details.

In another effort, a mesh generation program has been developed to generate finite element mesh for crack problems. The program allows gradual transitioning of the mesh arrangement from a relatively coarse mesh in the remote field to very fine one near the crack area. Two basic types of mesh arrangement, namely, the fan type and square type, are options. The fan mesh is currently used in all the preliminary analyses, while, the square mesh will be extensively used for simulating crack growth behavior and crack closure phenomenon.

APPENDIX

The P-I integrals reviewed in this program are presented here. The index notation was used. The common variables are: σ_{ij} = stress tensor, ε_{ij} = strain tensor, u_i = displacement vector, t_i = traction vector, Θ = relative temperature, α = thermal expansion coefficient, μ and λ = Lame's constants. For integration paths and areas the reader is referred to Figure 1.

Rice's J-Integral [1]

$$J = \int_\Gamma (n_1 W - t_i u_{i,1}) \, ds$$

where $W = \int_0^{\varepsilon_{ij}} \sigma_{ij} \, d\varepsilon_{ij}$

Wilson and Yu's Thermo-Elastic Integral [2]

$$J_W = \int_\Gamma (n_1 W - t_i u_{i,1}) ds - \alpha(3\lambda + 2\mu) \int_A [\tfrac{1}{2}(\Theta \epsilon_{ii})_{,1} - \epsilon_{ii}\Theta_{,1}] dA$$

where

$$W = \tfrac{1}{2}\sigma_{ij}\epsilon_{ij},$$

Gurtin's Thermo-Elastic Integral [3]

$$J_G = \int_\Gamma \left| n_1 W - t_k u_{k,1} - \frac{\alpha^2(3\lambda+2\mu)^2}{2(\lambda+\mu)} \Theta^2 n_1 + \frac{\alpha\mu(3\lambda+2\mu)}{(\lambda+\mu)} \left(\Theta \frac{\partial u_1}{\partial n} - u_1 \frac{\partial \Theta}{\partial n} \right) \right| ds$$

where

$$\frac{\partial}{\partial n} = n_j \frac{\partial}{\partial x_j}$$

and

$$W = \mu \epsilon_{ij} \epsilon_{ij} + \frac{\lambda}{2}(\epsilon_{kk})^2$$

The J_Θ- Integral by Ainsworth et. al [4]

$$J_\Theta = \int_\Gamma (n_1 W - t_i u_{i,1}) ds + \int_A \sigma_{ij}\epsilon_{ij,1} dA$$

where

$$W(\epsilon'_{ij}) = \int_0^{\epsilon'_{ij}} \sigma_{ij} d\epsilon'_{ij} \quad, \quad \text{and} \quad \epsilon'_{ij} = \epsilon_{ij} - \epsilon^\Theta_{ij}$$

The J^*-Integral by Blackburn [5]

$$J^* = \int_{\Gamma+\Gamma_C} (\tfrac{1}{2}\sigma_{ij}u_{i,j}dx_2 - t_i u_{i,1} ds) + \int_A (\tfrac{1}{2}\sigma_{ij}u_{i,j1} - \tfrac{1}{2}\sigma_{ij,1}u_{ij}) dA$$

The $\hat{J}$-Integral by Kishimoto, Aoki and Sakata [6]

$$\hat{J} = - \int_{\Gamma+\Gamma_C} t_i u_{i,1} ds + \int_A \sigma_{ij}\epsilon_{ij,1} dA$$

The ΔT-Integrals by Atluri et. al [7]

$$\Delta T^*_p = \int_{\Gamma+\Gamma_C} \left| n_1 \Delta W - (t_i + \Delta t_i)\Delta u_{i,1} - \Delta t_i u_{i,1} \right| ds$$

$$+ \int_A \left| \Delta\sigma_{ij}(\epsilon_{ij,1} + \tfrac{1}{2}\Delta\epsilon_{ij,1}) - \Delta\epsilon_{ij}(\sigma_{ij,1} + \tfrac{1}{2}\Delta\sigma_{ij,1}) \right| dA$$

$$\Delta T_p = \int_{\Gamma+\Gamma_C} \left| n_1 \Delta W - (t_i + \Delta t_i)\Delta u_{i,1} - \Delta t_i u_{i,1} \right| ds$$

$$+ \int_{A_s - A_\Gamma} \left| (\sigma_{ij,1} + \tfrac{1}{2}\Delta\sigma_{ij,1})\Delta\epsilon_{ij} - (\epsilon_{ij,1} + \tfrac{1}{2}\Delta\epsilon_{ij,1})\Delta\sigma_{ij} \right| dA$$

where

$$\Delta W = (\sigma_{ij} + \tfrac{1}{2}\Delta\sigma_{ij})\Delta u_{i,j} \quad,$$

and A_s is the total area and A_Γ is the area in Γ.

REFERENCES

1. Rice, J. R., "A Path-Independent Integral and the Approximate Analysis of Strain Concentration by Notches and Cracks," Journal of Applied Mechanics, Vol. 35, 1968, pp. 379-386.

2. Wilson, W. K. and Yu, I. W., "The Use of the J-Integral in Thermal Stress Crack Problems," International Journal of Fracture, Vol. 15, 1979, pp. 377-387.

3. Gurtin, M. E., "On a Path-Independent Integral for Thermoelasticity," International Journal of Fracture, Vol. 15, 1979, pp. R169-R170.

4. Ainsworth, R. A., Neale, B. K., and Price, R. H., "Fracture Behavior in the Presence of Thermal Strains," Proceedings of Institute of Mechanical Engineers' Conference on Tolerance of Flaws in Pressurized Components, London, 1978, pp. 171-178.

5. Blackburn, W. S., "Path-Independent Integrals to Predict Onset of Crack Instability In An Elastic Material," International Journal of Fracture Mechanics, Vol. 8, 1972, pp. 343-346.

6. Kishimoto, K., Aoki, S., and Sakata, M., "On the Path-Independent Integral-$\hat{J}$," Engineering Fracture Mechanics, Vol. 13, 1980, pp. 841-850.

7. Atluri, S.N. Nishioka, T., and Nakagaki, M., "Incremental Path-Independent Integrals in Inelastic and Dynamic Fracture Mechanics," Georgia Institute of Technology Report No. GIT-CACM-SNA-83-27, May 1983.

Table 1: Summary of P-I Integrals

P-I Integral	Measure of Crack Tip Severity	Physical Meaning[5]			Capability to Handle				Computation (Integrals involved)	Experimental Measurement [1]
		Elastic	Thermo-elastic	Plastic	Prop. loading	Nonprop. & Loading Unloading (plastic regime)	Thermal Strain	Material Inhomogenity		
J	Yes	$-\frac{\partial P}{\partial a}$	-	$-\frac{\partial P}{\partial a}$	Yes	No	No	No	Line	Yes
J_w	Yes	$-\frac{\partial P}{\partial a}$	$-\frac{\partial \Phi}{\partial a}$	-	No	No	Yes	No	Line + Area	Yes
J_G	Yes	$-\frac{\partial P}{\partial a}$	$-\frac{\partial \Phi}{\partial a}$	-	No	No	Yes	No	Line	Yes
J_Θ	Yes	$-\frac{\partial P}{\partial a}$	$-\frac{\partial \Phi}{\partial a}$	$-\frac{\partial P}{\partial a}$[2]	Yes	No	Yes	No	Line + Area	Yes
J^*	Yes	$-\frac{\partial P}{\partial a}$	$-\frac{\partial \Phi}{\partial a}$	Unknown	Yes	Yes	Yes	Yes	Line + Area	No
$\hat{J}$	Yes	Rate of work done to crack tip by surrounding material (3)			Yes	Yes	Yes	Yes	Line + Area	No
ΔT_p^*	Yes	$-\frac{\Delta \Pi}{da}$ for prop. loading[4]			Yes	Yes	Yes	Yes	Line + Area	No
ΔT_p	No	$-\frac{\Delta \Pi}{da}$ for prop. loading[4]			Yes	Yes	Yes	Yes	Line + Area	Yes

Note: (1) Yes if it can be expressed as the rate of a potential or if it has only line integrals.

(2) $-\frac{\partial \Phi}{\partial a}$ for thermoplastic proportional loading

(3) With the assumption of a rigid fracture process zone at the crack tip independent of the crack size

(4) Further study is needed for the case of thermomechanical loading

(5) P = Potential energy, Φ = Global thermodynamic potential, $\Delta \Pi$ = Incremental potential
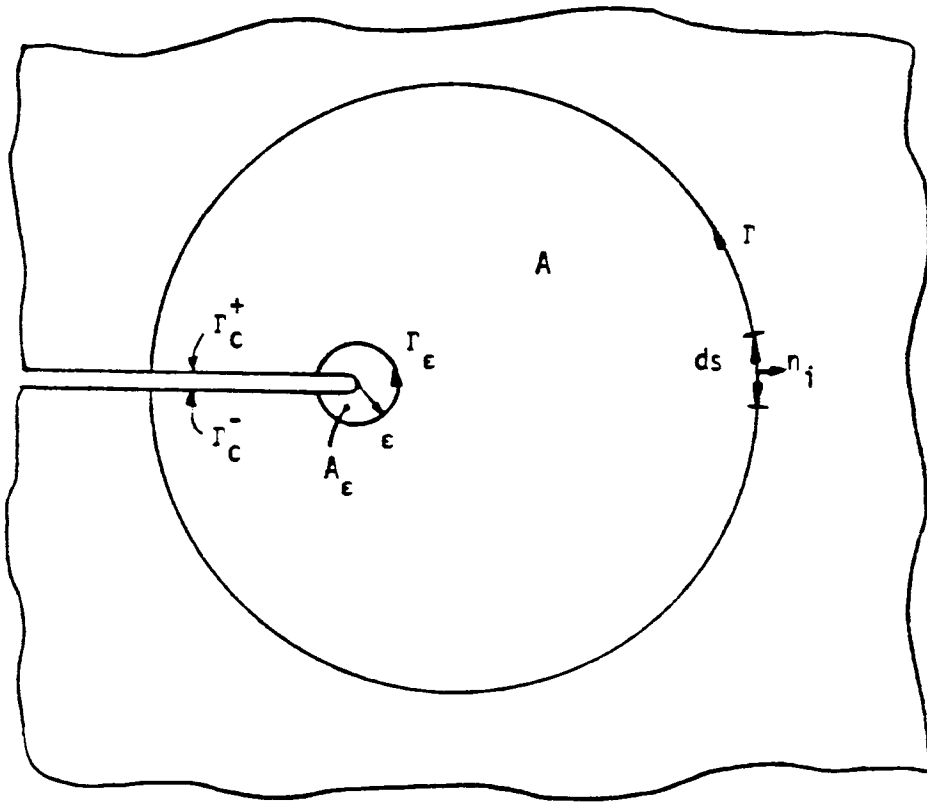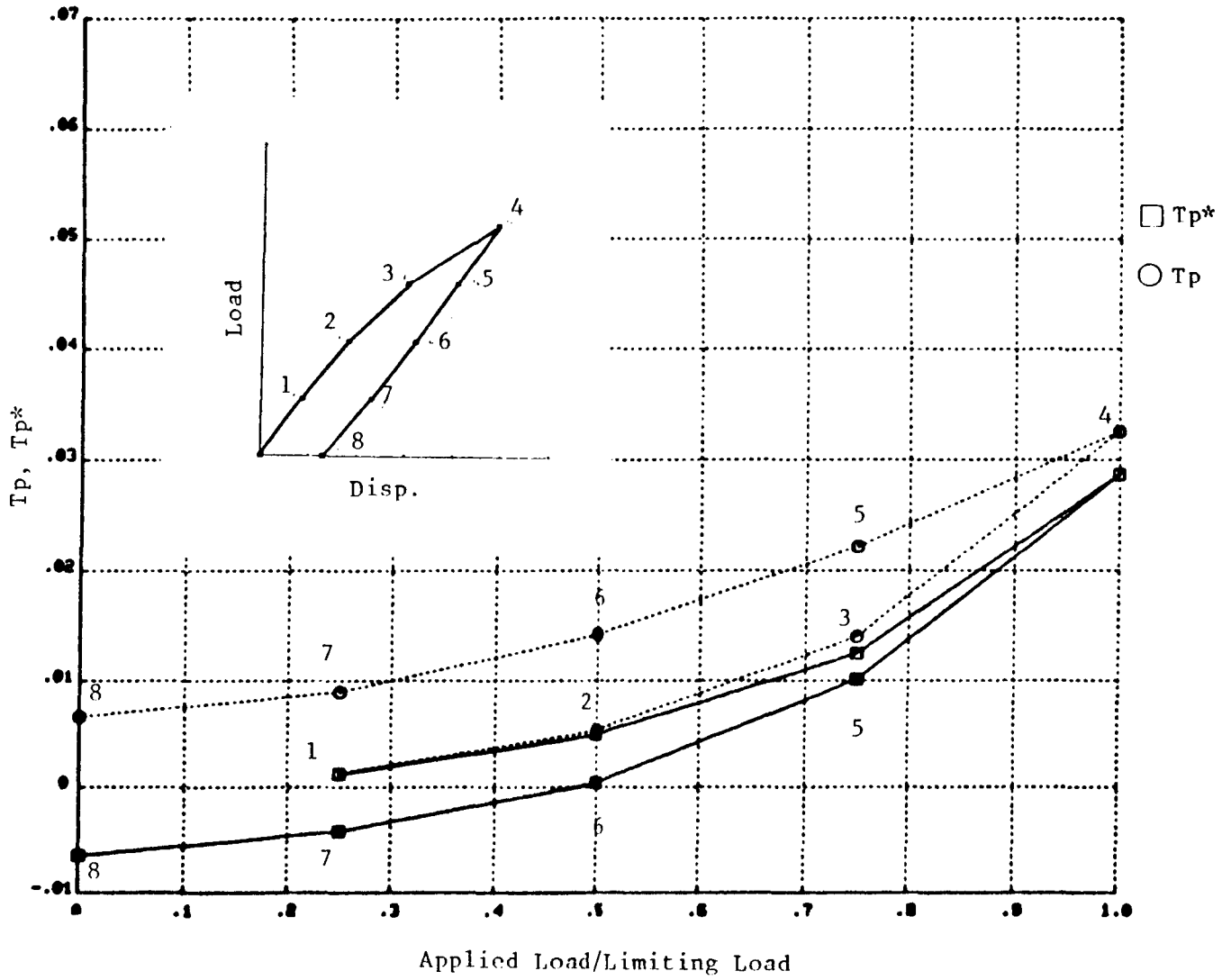
317

Figure 1: Integration Paths and Areas

318

Figure 2. Comparison of Atluri's Tp and Tp* Integrals for a Complete Load Cycle.
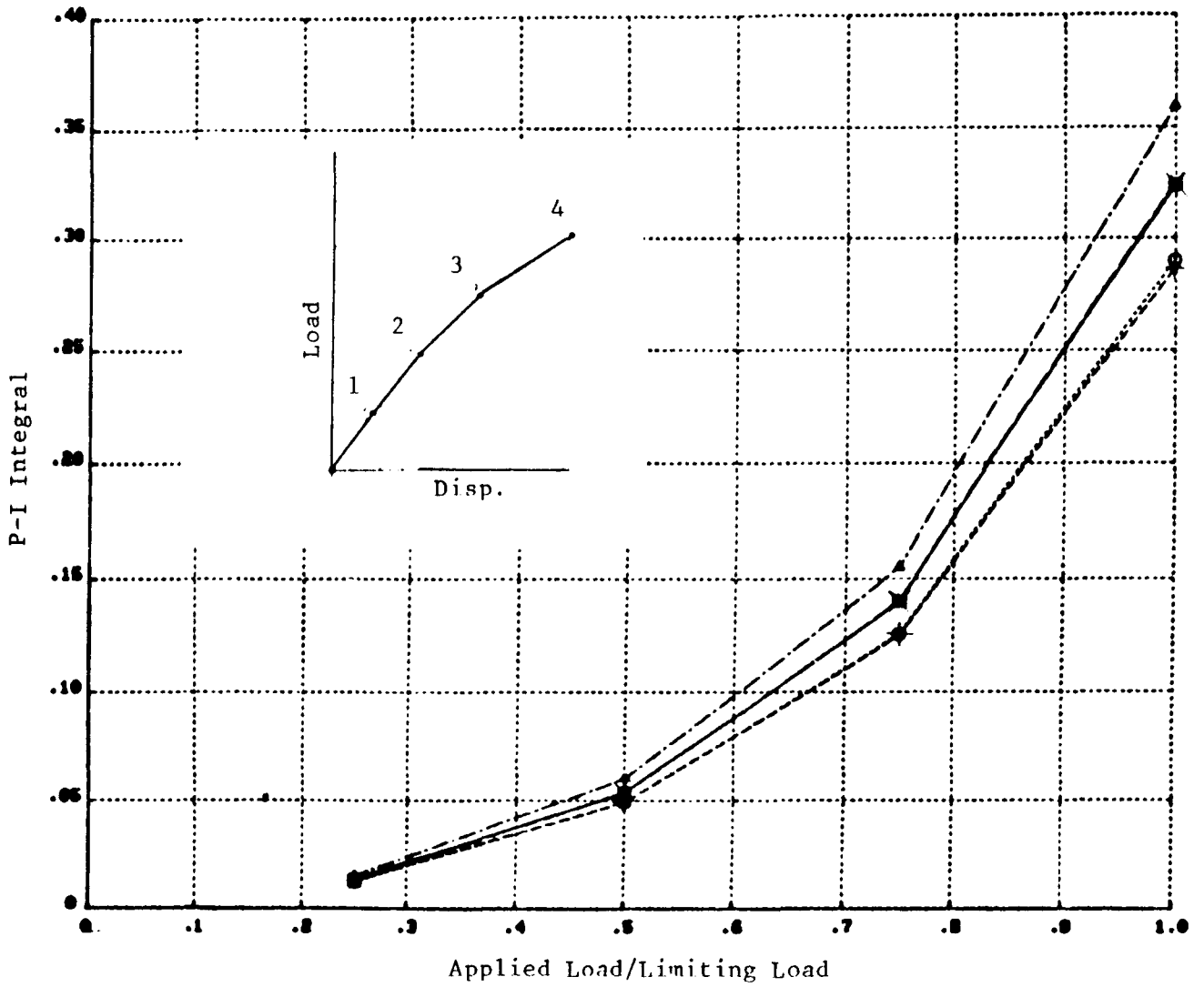
Figure 3. Comparison of Various P-I Integral results for a Compact Tension Specimen Problem.

Oxidation and Low Cycle Fatigue Life Prediction
Yoshiki Oshida and Hao-Wen Liu
Department of Mechanical Engineering
Syracuse University

When a metallic material is exposed to a high temperature in an ambient atmosphere, oxidation takes place on the metallic surface. The formed oxides (both surface and grain boundary oxides) are mechanically brittle so that if the stress is high enough the oxides will be cracked. This oxide crack will become the nucleus of a fatigue crack if the allpied ΔJ is larger than ΔJ_{th}. Therefore oxidation may reduce high temperature low cycle fatigue life.

Grain Boundary Oxidation

The grain boundary oxide formation in TAZ-8A nickel-base superalloy was studied. The effect of oxide crack nucleus on low cycle fatigue life will be analyzed. TAZ-8A was subjected to high temperature oxidation tests in air under the stress-free condition. The oxidation temperatures were 600°, 800°, and 1000°C. The oxidation time varied from 10 to 1000 hours. The temperatures were controlled within $\pm$ 8°C.

Figure 1 shows the measured weight gain per unit area of exposure, ΔW [mg/cm^2] as a function of exposure time for three different test temperatures. If oxidation of TAZ-8A obeys the parabolic rate law, the square of ΔW should relate linearly to oxidation time as shown in figure 2. Many other superalloys and refractory materials have exhibited the parabolic rate law for oxidation. The parabolic oxidation rate indicates that oxidation is controlled by diffusion kinetics.

The slope of these straight lines is called parabolic rate constant, a. Figure 3 shows the relationship between parabolic rate constants and inverse absolute temperatures for a number of superalloys. TAZ-8A shows a superior oxidation resistance than Rene 41 and Mar-M200. The data seem to follow two line segments similar to Mar-M200. This change of the slope might be related to the change in diffusion mechanism. At the higher temperatures (i.e., between 800° and 1000°C), oxidation is mainly controlled by outward diffusion of Cr.

Grain boundary oxidation is faster and penetrates deeper. Therefore the grain boundary oxide cracks are larger and they are more critical in reducing the low cycle fatigue life. The oxidation rate was measured in terms of weight gain, and the oxidation penetration was measured by direct optical observation. One of the main objectives of the current research program is to separate the grain boundary oxidation from the total oxidation. The weight gain (ΔW_T) was measured, and it is simply the sum of weight gain due to surface oxidation (ΔW_S) and the weight gain due to grain boundary oxidation (ΔW_G). ΔW_S and ΔW_G can be easily separated by calculating $\Delta W_S = V_S \times \rho_S$, where V_S is the total volume of surface oxide layer of a test coupon, and ρ_S is the specific gravity of surface oxides. The calculated results are shown in figure 4. This approach for separation of ΔW_S and ΔW_G is based on the assumption of homogeneous surface oxide layer thickness.

A second way to separate ΔW_S and ΔW_G is by calculating weight gain due to grain boundary oxidation by morphological measurements of width (GPW) and depth (GPD) of grain boundary oxide penetration. Figure 5 is one example of the results of this morphological study on oxidized coupon (1000°C x 960 hr). The shape of grain boundary oxides can be classified into two groups (round-edge and sharp-edge). This figure shows the size as well as the shape of the grain boundary oxides. The frequencies of the observed oxide size and shape are indicated by the size and shape of the data points in the figure. The data have considerable scatter in the GPW vs. GPD relationships. Based on the morphological analysis that the average value of the aspect ratio (GPW/GPD) of grain boundary oxides is close to 1.0; so only the data point on the 45 degree dashed line are used for calculation of grain boundary oxide weight. Each of the numbers on the 45 degree dashed line is the percentage of the number of the data points for the

morphology over the total number of all of the data points along this dashed line. Let us call these numbers as distribution percentage, p_i. The weight gain due to grain boundary oxidation (ΔW_G) can be estimated as

$$\Delta W_G = N \times \rho_{GO} \times \sum_{i=1}^{n} V_{GOi} \times p_i$$

where V_{GOi} is the volume of grain boundary oxide per grain at the ith morphology in figure 5, $\sum_{i=1}^{n} V_{GOi} \times p_i$ is the average volume of grain boundary oxide per grain

N is the total number of grains on the surface of the test coupon which was obtained as the total surface area of a coupon divided by average grain size area, and ρ_{GO} is the specific gravity of grain boundary oxides which is assumed to be equal to ρ_S. V_{GOi} can be calculated from the GPW, GPD, and the shape. The calculated results of ΔW_G and ΔW_S (= $\Delta W_T - \Delta W_G$) based on this morphological approach are also plotted in figure 4. Except in the early stage of oxidation, both approaches for separation of grain boundary oxidation from total oxidation are satisfactory.

Figure 6 shows both the calculated results of ΔW_G according to the surface homogeneous oxide layer and ΔW_G based on the morphological approach for grain boundary oxides at three different oxidation temperatures. These two measurements agree reasonably well with each other.

In figure 7, the data on total oxidation are exactly the same as those shown in figure 3. Of interest is that (i) grain boundary oxidation rate, in terms of its parabolic rate constant, is 10^2 time larger than the total oxidation and the surface oxidation, and (ii) in both grain boundary and surface oxidation, the similar breaking points at 800°C were found as that for the total oxidation.

The application of the statistical theory of extreme values to the analysis of maximum pit depth due to pitting corrosion was successfully introduced by Aziz (ref.1) and Hawn (ref.2). For some high temperature alloys, low cycle fatigue (LCF) cracks at elevated temperatures were often initiated as grain boundary oxides, and the maximum grain boundary oxide depth will control the LCF crack initiation period as well as the early stage of crack propagation period. Therefore the most important measure of "damage" to a specimen is grain boundary oxide penetration depth. This is analogous to the maximum pit depth of Aziz (ref.1). Aziz found that the maximum pit depth obeys the Poisson's distribution. The oxidized coupons were sectioned, and the cross sectional surface was examined under an optical microscope and the maximum grain boundary oxide penetration depth, a_0, of this surface was recorded. After approximately 50 μm of the surface layer was removed another maximum a_0 was recorded. A coupon was machined and examined repeatedly layer after layer. All together 12 data points were collected for each of the three coupons oxidized at different temperatures. Assuming a Poisson's distribution, figure 8 shows the results for 800°C oxidation temperature at four different oxidation times. The straight lines are drawn by the least square fit. Suppose the surface area ratio of a real component to the test coupon is 100, the extrapolated a_0 value can be read on the line at the return period = 100. For example in the case of 800°C x 960 hr oxidation, on the small test coupon area, the deepest a_0 is 120 μm, whereas on a surface area 100 times larger, the likely a_0 is 158 μm. According to Aziz(ref.1), "rather than considering the return period, it is equally worthwhile to consider the frequencies" on the left side of the figure. The probability of obtaining an a_0 of 158 μm is 0.990. Therefore there is only one chance in a hundred to have a_0 deeper than 158 μm on the total surface area of the 12 layers of the tested coupon oxidized at 800°C for 960 hrs. This should be equivalent to the test of 12 sectioned surfaces of 12 separate coupons.

Because of the brittle property of oxides, a crack might be initiated at a grain boundary oxide. Once a crack is initiated and if the applied cyclic stress is high enough, the crack will propagate by the fatigue loading. Therefore the grain boundary oxides can be considered as a crack nucleus. It is reasonable to expect that the rates of both surface oxidation and grain boundary oxidation will be accelerated by mechanical stress, and that the grain boundary oxide penetration depth will be increased by a high enough applied stress.

Grain Boundary Oxide Crack and Low Cycle Fatigue Life - A Preliminary Analysis

Fatigue life consists of crack nucleation and crack propagation periods. Fatigue crack nucleation period is relatively shorter at higher stresses. Low cycle fatigue crack nucleation period might even be shortened by severe environmental attack, such as oxidation. In this case, fatigue life consists mainly of crack propagation period.

For general-yielding cyclic-loading, Dowling and Begley (ref.3) have shown that fatigue crack growth rate correlates well with ΔJ; and near the threshold, da/dN can be written in the form (ref.4 and 5).

$$\frac{da}{dN} = A \frac{\Delta J_{th}}{\sigma_{YC}} \left(\frac{\Delta J}{\Delta J_{th}} - 1 \right)^m \tag{1}$$

Zheng and Liu (ref.5) have shown that for a small crack in a large solid,

$$J = [\eta_1 DW + \eta_2 \sigma_Y \varepsilon_Y]a \tag{2}$$

DW is deformation work density. For cyclic loading, it is related to the applied stress and strain ranges.

$$DW = \left[\frac{\Delta\sigma^2}{8E} + \sigma_{YC}\Delta\varepsilon_p \right] \tag{3a}$$

$$= \alpha\left[\frac{\Delta\sigma}{2}\left(\Delta\varepsilon_p + \frac{\Delta\varepsilon_e}{2}\right) \right] \tag{3b}$$

where $\Delta\sigma$, $\Delta\varepsilon_e$, and $\Delta\varepsilon_p$ are the applied stress, elastic strain, and plastic strain ranges. E and σ_{YC} are Young's modulus and cyclic yield strength.

Fatigue life can be obtained by integrating equation (1) (ref.5).

$$(DW)^m N_f = \frac{\sigma_{YC}}{A(m-1)\eta_1^m} \left(\frac{\Delta J_{th}}{a_i} \right)^{m-1}$$

$$= C \, a_i^{(1-m)} \tag{4}$$

where a_i is the crack nucleus size. Fatigue life, N_f is related to the size of the crack nucleus a_i.

Figures 9 and 10 show the correlations of low cycle fatigue lives of an aluminum alloy with these two parameters of deformation work density (equations 3a and 3b). In figures 9 and 10, fatigue lives of both smooth and pre-cracked specimens are plotted. The size of the pre-cracks, a_o is larger than a_i. According to eq.(4), the fatigue lives of the smooth and the pre-cracked specimens (N_f and N_{fo}) are related.

$$\frac{N_{fo}}{N_f} = \left(\frac{a_o}{a_i} \right)^{1-m} = constant \tag{5}$$

Therefore, the log-log plots of the fatigue lives of the smooth and pre-cracked specimens are parallel as shown in figures 9 and 10.

323

The grain boundary oxide cracks can be considered as pre-cracks. Therefore the fatigue lives of oxidized specimens will have a similar relation.

As shown by the data in figures 5 and 8, the oxide crack size may have a substantial statistical scatter; and it is expected that this statistical scatter will be reflected in the fatigue lives of the oxidized specimens.

It should be emphasized that the analysis on the fatigue lives of oxidized specimens is preliminary. However, it can serve as the guide for the future study.

References

(1) P.M.Aziz; Corrosion, 12(10), 1956, pp.495A-506A.
(2) D.E.Hawn; Materials Performance, 1977, pp.29-32.
(3) N.E.Dowling and J.A.Begley; ASTM STP Vol.590, 1976, pp.80-103.
(4) H.W.Liu and Dai Liu; Scripta Met., 18, 1984, pp.7-12.
(5) M.Zheng and H.W.Liu; Technical Report NASA Grant No. NAG3-348 "Crack Tip Field and Fatigue Crack Growth in General Yielding and Low Cycle Fatigue", 1984.
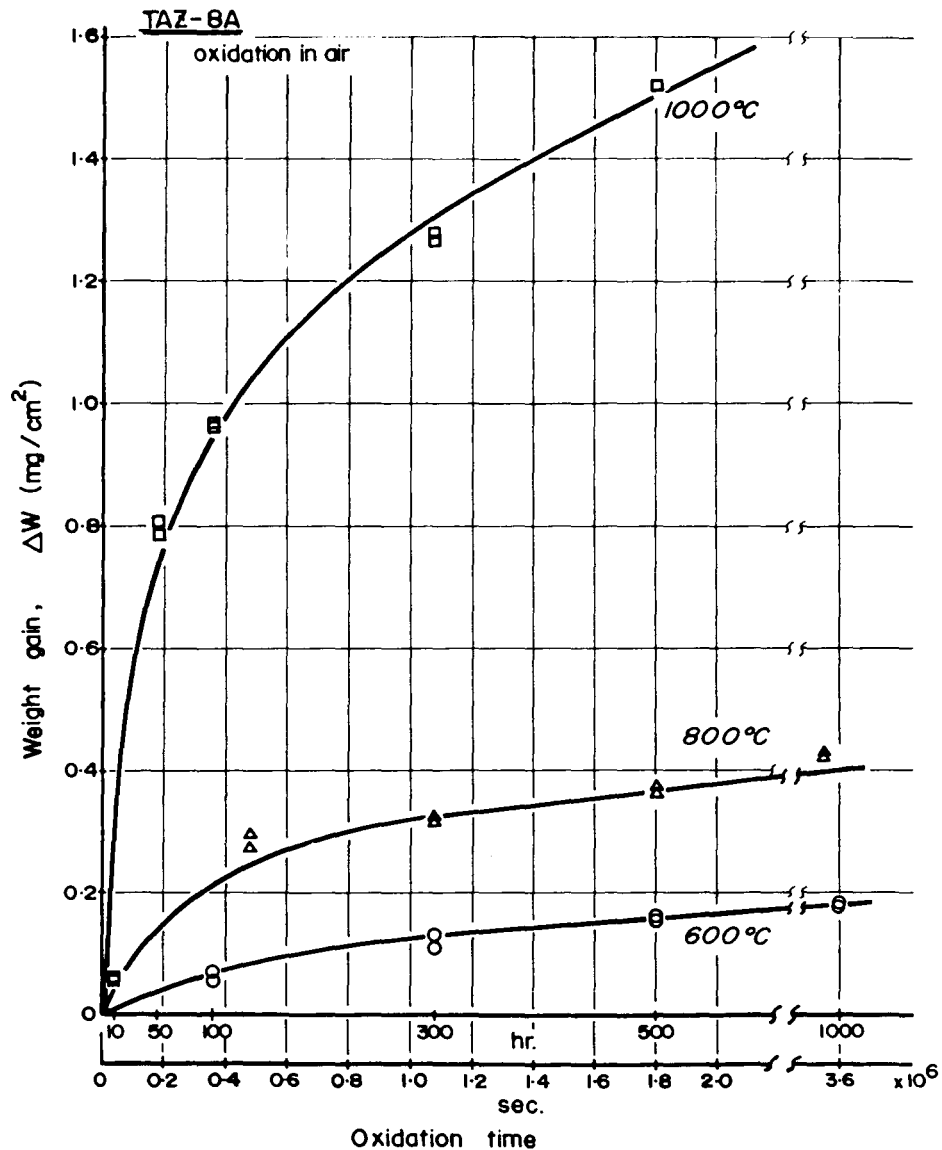
Fig. 1   Total weight gain vs. oxidation time

324
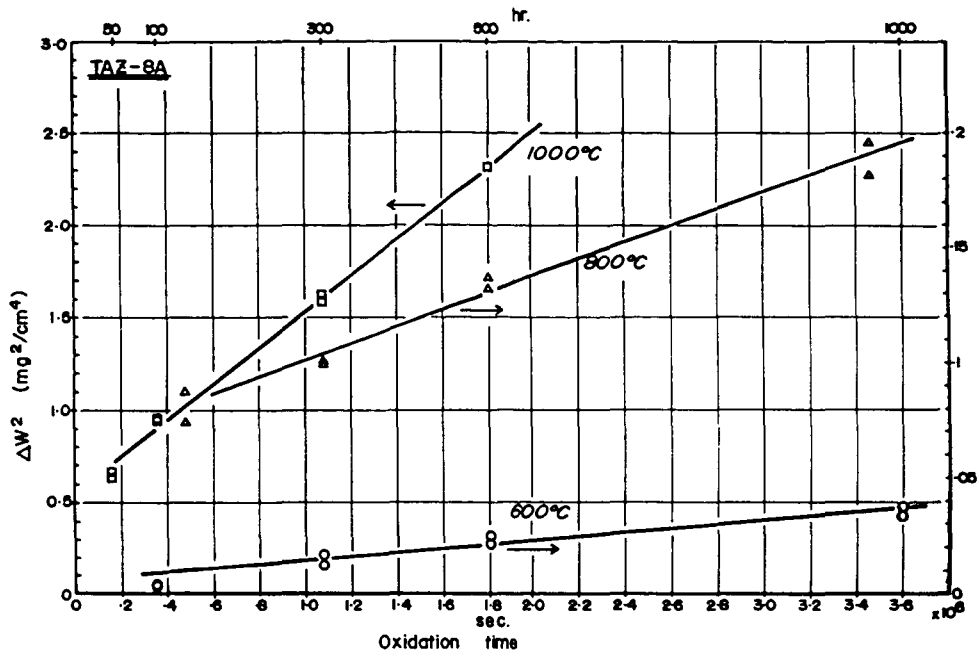
Fig. 2   Square of total weight gain vs. oxidation time
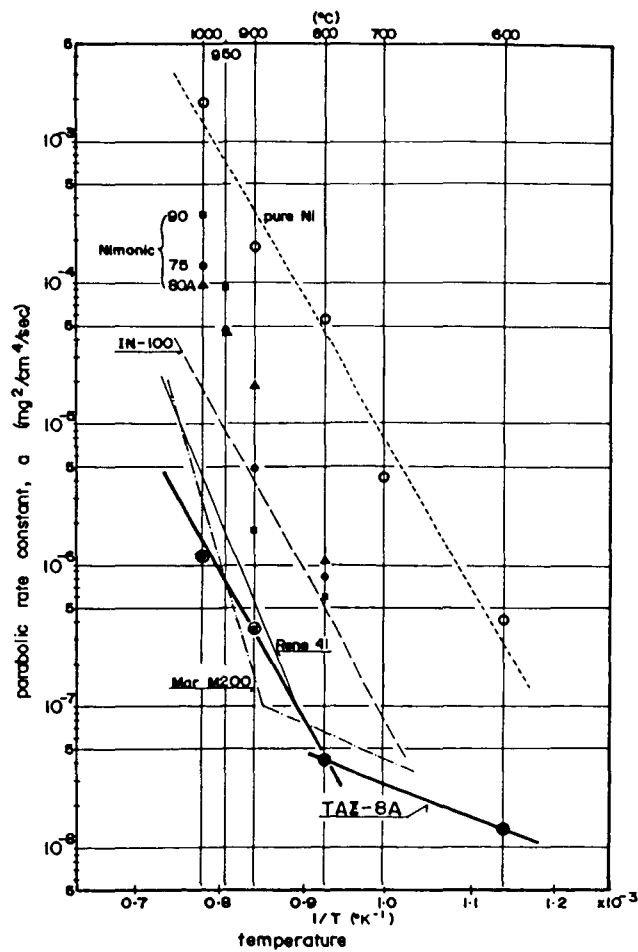
Fig. 3   Parabolic rate constant vs. inverse absolute temperature

325
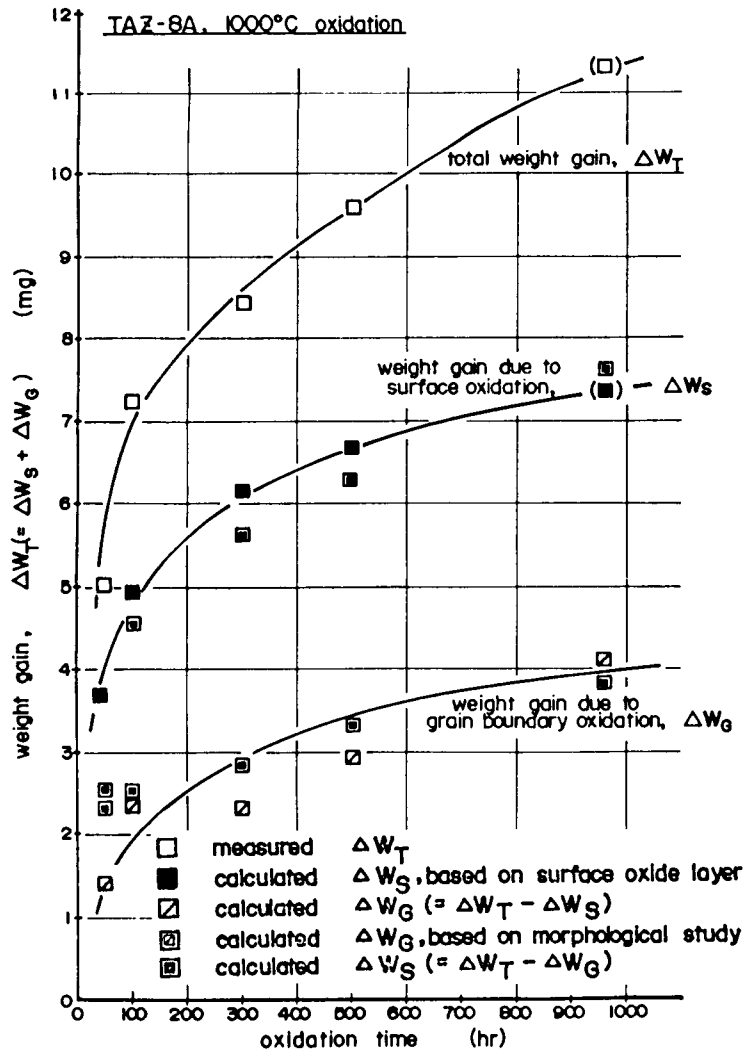
Fig. 4 Weight gain (total, surface oxidation, and grain boundary oxidation) vs. oxidation time
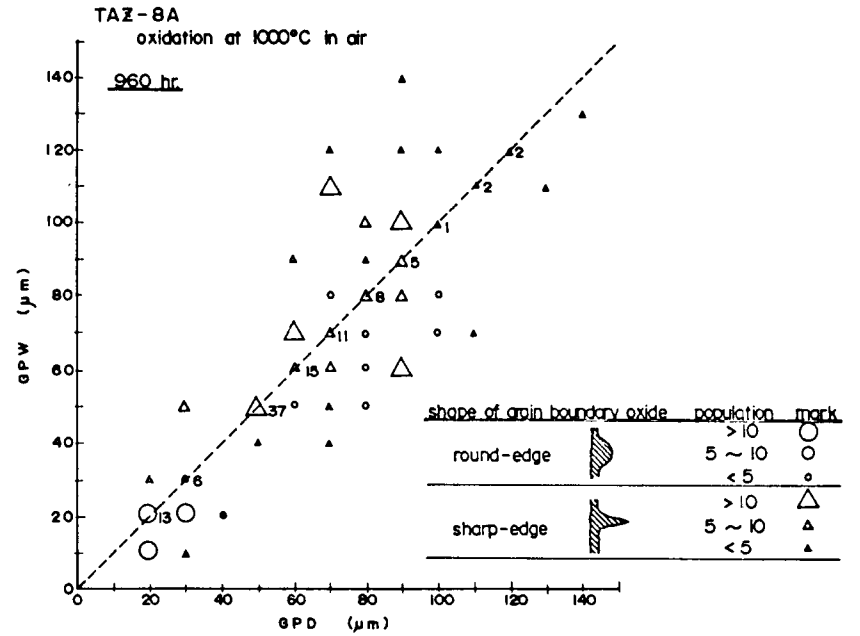
Fig. 5 Results of morphological study on grain boundary oxide
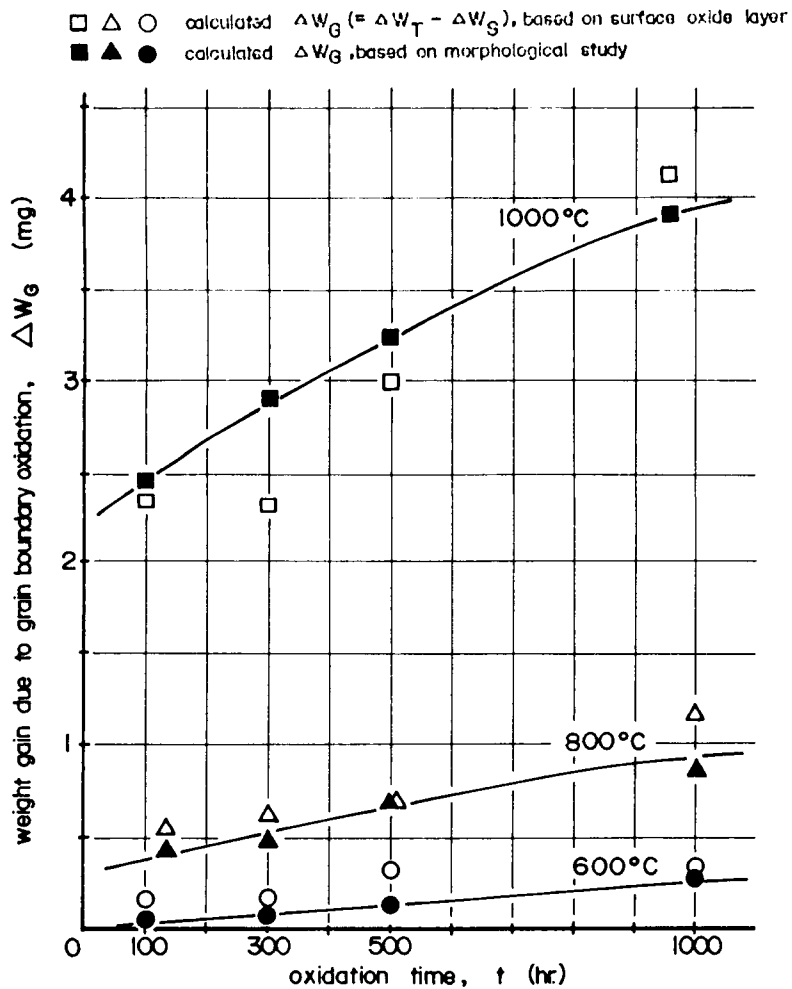
Fig. 6   Weight gain due to grain boundary oxidation vs. time
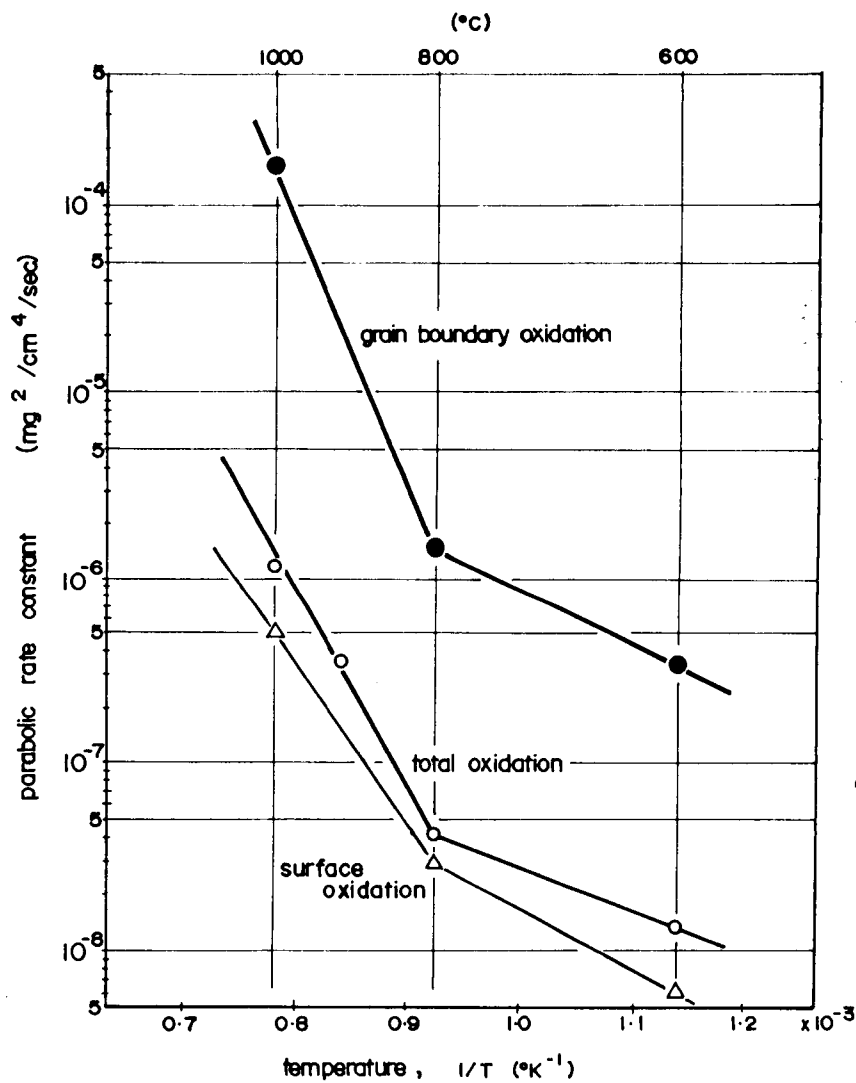
Fig. 7   Parabolic rate constants of total oxidation and grain boundary oxidation vs. inverse absolute temperature
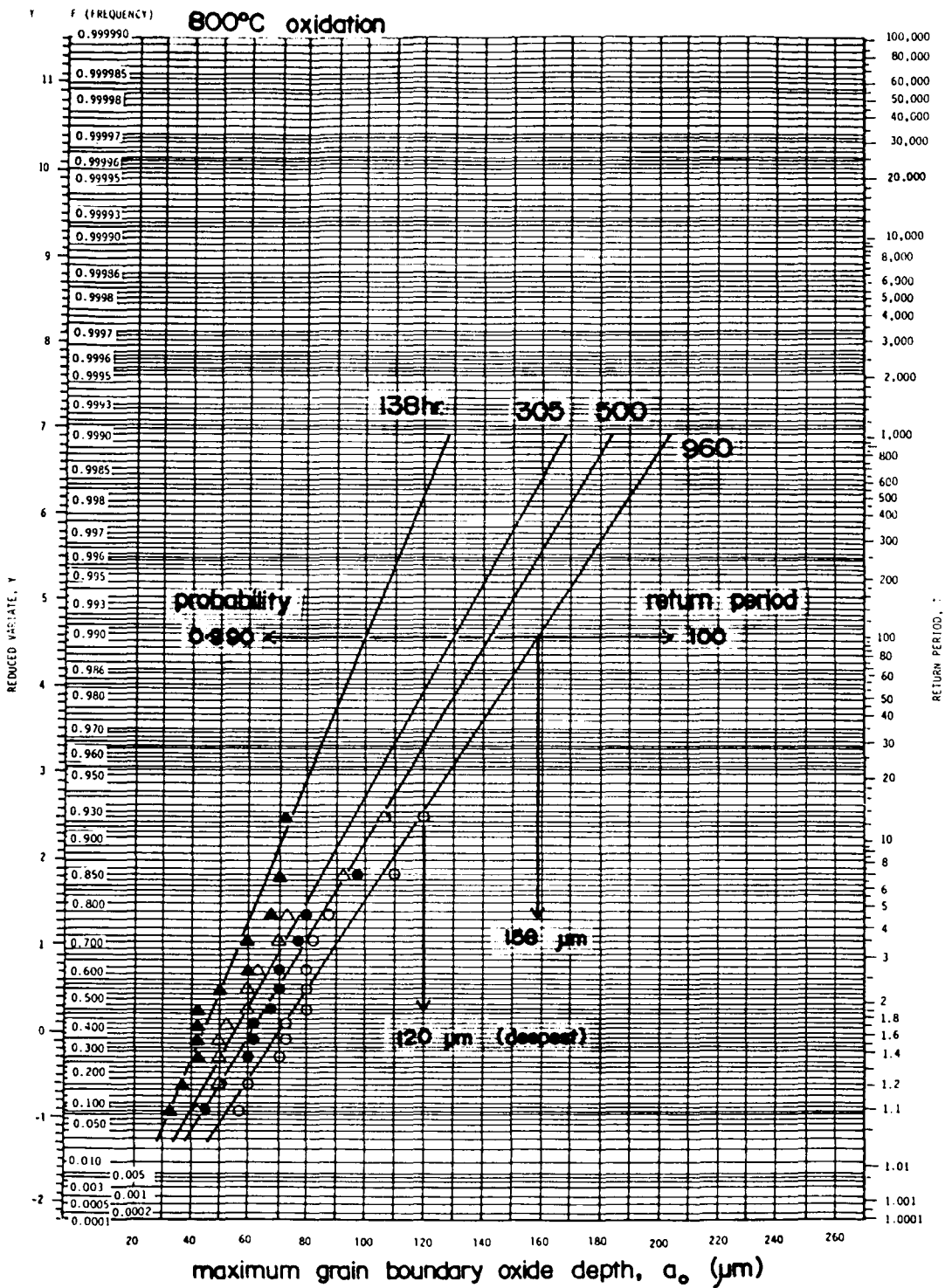
Fig. 8   Maximum grain boundary oxide depth vs. frequencies
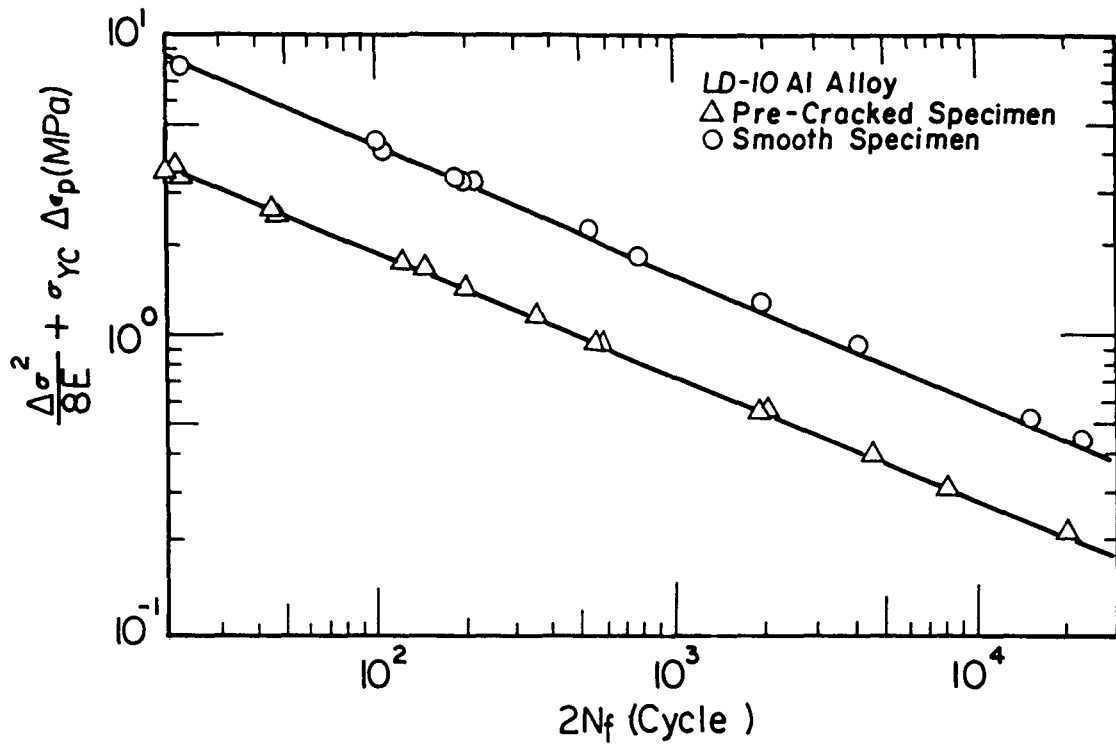
Fig. 9   Correlation of $(\frac{\Delta\sigma^2}{8E} + \sigma_{YC}\Delta\varepsilon_p)$ versus $(2N_f)$ for LD-10 aluminum alloy.
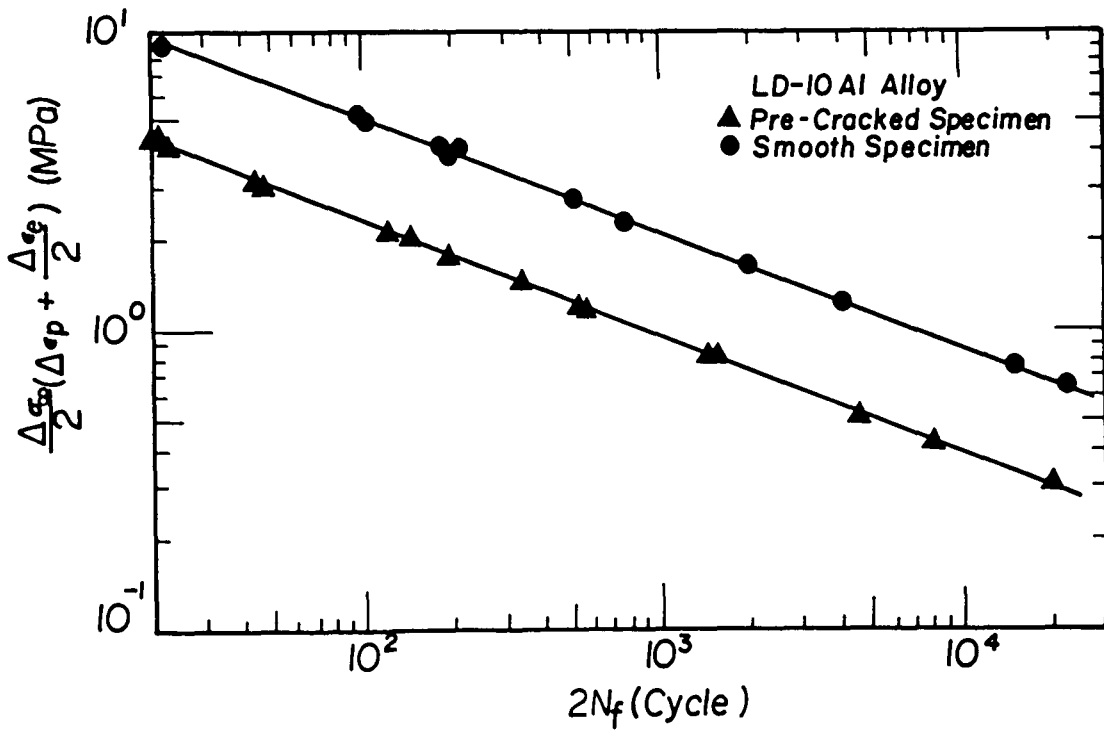
Fig. 10   Correlation of $[\frac{\Delta\sigma_\infty}{2}(\Delta\varepsilon_p + \frac{\Delta\varepsilon_e}{2})]$ versus $(2N_f)$ for LD-10 aluminum alloy.

CONSTITUTIVE MODELING OF INELASTIC ANISOTROPIC

MATERIAL RESPONSE

D.C. Stouffer
Department of Aerospace Engineering and Engineering Mechanics
University of Cincinnati

INTRODUCTION

The broad objective of this research program is to develop a constitutive equation to predict the inelastic thermomechanical response of single crystal superalloys. These equations are essential for developing accurate finite element models of hot section components and contribute significantly to the understanding and prediction of crack initiation and propagation. The specific goal is to develop a WORKABLE constitutive equation for single crystal turbine blades that can be used in a finite element model for structural analysis.

The method used in this program is limited to unified state variable constitutive equations. Unified equations are valid over the entire deformation history and do not require separate representations for loading and unloading. State variables are employed in an attempt to characterize to essential features of changes in the material microstructure during the deformation history.

Two approaches to developing an anisotropic constitutive equation have been reviewed in detail. One approach is to apply the Stouffer-Bodner [1,2] representation for deformation induced anisotropy to materials with an initial anisotropy such as single crystals. This representation is developed in the eigenspace of the stiffness or compliance matrix to eliminate coupling so that one component of stress produces only one component of strain rate. The second approach is to determine the global inelastic strain rate from the contribution of the slip in each of the possible crystallographic slip systems (Pasley et al [3,4]). In each of these representations the model of Bodner et al [5,6,7] for isotropic materials is used to characterize the fundamental slip mechanisms. This representation is based on the Prandtl-Reuss flow equation an has one state variable to characterize both strain hardening and thermal recovery. A three dimensional finite element is being developed with a variable constitutive equation link that can be used for constitutive equation development and to predict the response of an experiment using the actual specimen geometry and loading conditions.

THE EIGENSPACE APPROACH

The form of the deformation rate equation used in [1,2] was an extension of the Prandtl-Reuss flow equation of classical plasticity to allow anisotropy. The equation related the inelastic strain rate vector, $\dot{\varepsilon}_\alpha^I$, to the deviatoric stress vector, S_α, by a six dimensional second order linear transform whose components are functions of stress and stress history; i.e.,

$$\dot{\varepsilon}_\alpha^I = \lambda_{\alpha\beta} S_\beta \qquad (\alpha,\beta = 1 \text{ to } 6) \qquad (1)$$

where $\lambda_{\alpha\beta}$ is constrained to satisfy incompressibility. Equation (1) reduces to the isotropic flow rate if $\lambda_{\alpha\beta}$ is replaced by a scalar material function.

In general, the flow equation (1) has both normal and shear stress coupling. That is, one component of stress can produce six components of inelastic strain rate. However, if Equation (1) is transformed to the eigenspace of the compliance tensor; i.e., $\lambda_{\alpha\beta}$ is diagonal, then the coupling is eliminated. This implies that one component of stress will only produce one component of inelastic strain rate. The technique produces an extremely simple and mathematically convenient flow rule. Further, the eigenspace formulation has been used to propose a number of different hardening rules.

However, the transformation matrix that carries $\lambda_{\alpha\beta}$ into the eigenspace must also be determined as part of the constitutive formulation. In general it is expected that this transformation matrix would contain information of the anisotropy of the material and, therefore, depend upon the deformation history. Thus, in a material with initial cubic symmetry, for example, it is expected that the deformation itself will alter the cubic response through cross hardening and the Bauschinger effects. In this case the initial cubic symmetry cannot be imposed during the entire response. Calculations have shown that for an incompressible cubic material the transformation between the physical space and eigenspace is constant and independent of the material parameters; however, for more complex symmetry, such as orthotropic the transformation matrix depends on the deformation. Thus, the components of the transformation matrix must also be determined from the experimental data. This has caused some difficulty because the material parameters (transformation matrix components) are mathematically motivated rather that physically motivated.

THE CRYSTALLOGRAPHIC APPROACH

The orientation, temperature and stress dependence of the deformation of single crystal superalloys can also be modeled by analyzing the deformation on each of the crystallographic slip planes and summing the results. This approach can be developed from the actual deformation mechanisms present in the material and should lead to a better understanding of underlying physical phenomena.

The typical microstructure of a nickel-base single crystal superalloy, Mar M200 for example [8], contains fcc γ^1 distributed in a fcc γ solid solution matrix. The microstructure also contains MC carbides and micropores in the interdendritic regions. The matrix can exhibit both <110> and <112> slip on the octahedral planes, [111], and the γ^1 can exhibit slip on both the octahedral and cubic, [100], planes. Further planer and wavy glide and dislocation climb have been observed in at the temperature range of interest. Thus, several slip systems and several deformation mechanisms can be active in the range of thermomechanical loading present in gas turbines.

An appropriate starting point is to base the modeling on Schmid's law; i.e., the slip in a crystallographic slip direction on a slip plane is a function of the shear stress component in that slip direction. This is a valid assumption for <011> slip on the octahedral planes in Mar M 200 at 760°C but not at 870°C, [8]. The relationship should also depend on the current material microstructure and temperature to include the important response properties. Schmid's law has been formulated in a mechanics context by Pasley et al [3,4]. In this work the total inelastic strain rate tensor is constructed by transforming the strain rate on each

of the slip directions into the crystallographic basis and summing over all slip directions. The linear superposition is valid since strain can be represented by a linear transform. Modifications to this approach include replacing the simple creep representation used in [3,4] by a constitutive equation [5,6,7] to include history dependence. It is also necessary to determine the active slip systems and deformation mechanisms as a function of temperature and strain rate to correctly characterize the material. Methods must also be included to account for cross hardening within each material phase and the interaction between the γ and γ^1 material phases. Finally the phenomena associated with thermal cycling must be identified and modelled.

FINITE ELEMENT MODEL

A finite element code is being developed that incorporates a time dependent constitutive model based on octahedral and cube slip. There are a number of possible flow rules, hardening rules and cross hardening rules. These are being incorporated into the FEM code so that they can be studied in various combinations in depth. An important part of the constitutive model development will involve an experimental – finite element analysis – constitutive model verification loop. Since a limited amount of instrumentation is possible during specimen testing an important part of constitutive model verification will involve a comparison between the deformed specimen dimensions and the FEM analysis.

The finite element code being developed uses twenty noded isoparametric bricks and an initial strain iterative procedure. The inelastic response is computed at each of the order two Gauss quadrature points. Since relatively small inelastic strains are expected in actual material applications small strain and small displacement theory is used. Additional features of the finite element code are the ability to model piecewise linear load histories and a dynamic time incrementing procedure.

As it is now being developed this finite element code is intended for use as a tool in constitutive model development. However, with a few relatively minor modifications the code should be useful as an analysis and design tool.

PLANS AND PROBLEMS

During the next year we plan to continue development of the constitutive models with emphasis on the crystallographic approach. It is hoped that these studies may also provide some insight into determining the material functions in the eigenspace approach. Further success depends on our ability to identify the active slip systems and deformation mechanisms present in the material. For example, at the present time three slip systems containing a total of 30 slip directions have been identified. Assuming positive and negative slip to be different gives 60 stress and strain rate variables. If each slip system can exhibit three mechanisms then nine sets of constitutive parameters are required. Thus, an extensive number of variables and material parameters can be brought into the formulation. To avoid curve fitting a careful plan must be established to evaluate and assemble the constitutive model. This should include an experimental program at the crystallographic level to identify the active slip systems and deformation mechanisms in the material system of interest and use these results to determine atleast some of the constitutive parameters.

REFERENCES

1. Stouffer, D.C. and Bodner, S.R., A Constitutive Model for the Deformation Induced Aniostropic Flow of Metals, Int. J. Engineering Science, 17, pp 757-764 (1979).

2. Bodner, S.R. and Stouffer, D.C., "Comments on Anisotropic Plastic Flow and Incompressibility," Int. J. Engineering Science, 21, pp. 211-215 (1983).

3. Paslay, P.R., Wells, C.H. and Leverant, G.R., "An Analysis of Primary Creep of Nickel-Base Superalloy Single Crystals," ASME Journal of Applied Mechanics, 37, pp 759-764 (1970).

4. Pasley, P.R, Wells, C.H., Leverant, G.R. and Burck L.H., "Creep of Single Crystal Nickel-Base Superalloy Tubes under Biaxial Tension, Journal Applied Mechanics, 38, pp 623-627 (1971).

5. Bodner, S.R. and Partom, Y., "A Large Deformation Elastic Viscoplastic Analysis of Thick-walled Spherical Shells," Journal of Applied Mechanics, Vol. 39, pp. 751-757 (1972).

6. Bodner, S.R. and Partom, Y., "Constitutive Equations for Elastic Viscoplastic Strain Hardening Materials," Journal of Applied Mechanics, Vol. 42, pp. 385-389 (1975).

7. Bodner, S.R., Partom, I. and Partom, Y., "Uniaxial Loading of Elastic-Viscoplastic Materials, J. Applied Mechanics, Vol. 46, pp 805-810 (1979).

8. Milligan, W.M., Jayaraman, N. and Bill, R.C., "Low Cycle Fatigue of Mar M200 Crystals at 760°C and 870°C," in review, Dept. of Material Science, University of Cincinnati, Cincinnati, Ohio, (1984).

Biaxial Constitutive Equation Development

Eric H. Jordan and Kevin P. Walker
University of Connecticut and Engineering Science Software, Inc.

INTRODUCTION

Some current production gas turbine engines utilize large scale single crystal super-alloy hot section components. Structural analysis of these components requires a valid stress-strain-temperature relation, often referred to as a constitutive equation. At present this behavior can only be represented by elastic constitutive equations or pure creep equations. The actual application involves viscoplastic strain cycles that are not represented well by either of these types of equations. The goal of the work described in this report is to develop and verify viscoplastic constitutive equations for superalloy single crystals and directionally solidified alloys.

In developing the constitutive equations an interdisciplinary approach is being pursued. Specifically, both metallurgical and continuum mechanics considerations are recognized in the formulation. Experiments will be utilized to both explore general qualitative features of the material behavior that need to be modeled and to provide a means of assessing the validity of the equations being developed. The model under development explicitly recognizes crystallographic slip on the individual slip systems. This makes possible direct representation of specific slip system phenomena previously studied by metallurgists.

GENERAL FEATURES OF THE PROPOSED MODEL

Viscoplastic constitutive equations currently used for describing the high temperature structural behavior of isotropic superalloys make use of a state variable concept. These viscoplastic equations are basically rate-dependent creep equations in which the creep or inelastic strain rate depends not only of the state of stress, but also on two state variables. These state variables represent the effect of prior inelastic deformation history on the current creep response of the material.

Constitutive equations for describing the anisotropic creep behavior of superalloy single crystals were developed by Paslay, Wells and Leverant [1] in 1971. The present constitutive formulation takes the anisotropic creep theory developed in Reference [1] and incorporates two state variables into the model to account for the effect of prior inelastic deformation history on the current rate-dependent response of the material. This is done in a manner analogous to the isotropic development of viscoplastic state variable models.

SIMULATIONS WITH THE MODEL

Figure 1 shows a numerical simulation of a single crystal superalloy which can exhibit slip on its four octahedral 111 planes in twelve 110 type directions. The single crystal bar specimen is pulled along its axis under load control with the direction of the load axis inclined at various angles to the crystallographic axes. Curve 1 shows the response obtained by loading the bar specimen along its axis under fully reversed load control to a value of ±207 MPa (±30Ksi) at a constant load rate magnitude of 6.9 MPa (1 Ksi) per second. Curves 2 to 6 show the effect of inclining the specimen axis and corresponding load direction by angles of 0 = 9°, 18°, 27°, 36° and 45° to the crystallographic axes in a plane containing two of the crystallographic axes. The increasing angles correspond to moving along the [001] - [011] side of the stereographic triangle. Curve 7 corresponds

to the [Ī11] vertex of the stereographic triangle.

According to Schmid's law [2] the yield stress decreases from its maximum values at the [001] and [011] vertices of the stereographic triangle to a minimum value at 0=22.5° halfway between the [001] and [011] vertices. The increased plasticity in the loop for curves 3 and 4 corresponding to 0=18° and 0=27° reflect this minimum behavior. Symmetry between the loops equidistant from the minimum at 0=22.5° is not achieved with the present formulation because Young's modulus for the single crystal bar specimen increases from the [001] vertex to the [001] vertex and from the [011] vertex to the [Ī11] vertex of the stereographic triangle. This increasing value of Young's modulus is reflected in the increasing slope of the curves labeled 1 to 7 in Figure 1.

Figure 2 shows the effect of strain rate on a bar specimen oriented along the [001] direction corresponding to one of the crystallographic axes. The specimen was pulled along its axis under strain control at constant strain rate magnitudes of 10^{-3} to 10^{-6} per second and shows the usual type of positive strain rate sensitivity in which the "yield" stress increases with increasing strain rate.

Octahedral slip on the four 111 planes in the twelve [112] slip directions and cube slip along the planes containing the crystallographic axes are also being coded into the FORTRAN subroutine to provide a constitutive model which can exhibit different types of slip behavior in different temperature ranges.

CONSIDERATIONS RELATING THEORY AND EXPERIMENT

In experiments on isotropic materials involving hollow tube biaxial specimens it is relatively straight forward to calculate from the measured load and torque values using "strength of materials" formulae. Unfortunately, these simple formulae cannot, in general, be used with anisotropic materials. Instead, the specimen must be analyzed as a structure. It is essential to make the analysis of the specimen computationally efficient if simulation of the measured load-displacement histories is to be practical. The approach taken in this investigation is to solve for the stress distribution in the specimen using a specially constructed finite element program written in FORTRAN on the IBM PC-XT computer. This program represents the tubular specimen as a single high order finite element whose shape function includes terms which reflect the spatial symmetry corresponding to the cubic symmetry of the superalloy single srystal. The code for this finite element model has been written and is currently undergoing numerical experiments.

Experiments performed on single crystal superalloys [3-5] have shown that there is a tension-compression asymmetry in the flow stress. This has been accounted for by metallurgists by assuming that the applied stress constricts the Shockley partials during cross slip. Asymmetric flow stress behavior may be incorporated into the model in many ways. The specific manner chosen to incorporate this asymmetry will be chosen in accordance with the constriction stress explanation put forth by metallurgists. Specifically, the drag stress state variable in the constitutive model will be assumed to depend on the constriction stress component.

PROPOSED EXPERIMENTAL PROGRAM

Biaxial experiments with tubular specimens will be conducted at 1600°F on a combined tension-torsion machine. The biaxial setup used to conduct these experiments was developed previously with partial support from NASA grant NAG-3-160. The setup

includes a servo-hydraulic tension-torsion machine and a capacitance probe based extensometer shown in Figure 3. This extensometer utilizes four high temperature non-contacting capacitance probes that do not require cooling. Two probes per channel are used to cancel out cross-talk between extension and rotation. In order to heat the specimen to 1600°F an audio frequency heater has been purchased and is undergoing operation trials.

Gripping a tubular tension-torsion specimen at high temperatures is problematical. To accomplish this the single crystal tube has Hastelloy-X extensions which are vacuum brased onto the specimen. These extensions are welded into disposable 304 stainless steel flanges that bolt to the tension-torsion machine. This procedure eliminates both the need to cool the grips and the need to machine complicated end shapes on the single crystals. The first three specimens have recently been received and are ready for testing.

The testing machine is controlled by a microcomputer. The microcomputer also places the load-displacement results from the tension-torsion machine onto a diskette which can be read by the IBM PC-XT computer and compared with the theoretical predictions from the constitutive model without manual manipulation of the experimental data. This is necessary due to the large volume of data generated in multiaxial testing. In controlling the test machine the digital-to-analog converter sends voltages to a special, highly stable, analog integrator that generates straight line voltage time segments. Without the integrator the command signal would only be stepwise continuous and would involve undefined strain rates between the steps.

The test program is divided into two broad classes of experiments. Specific features of the response which need modeling will be addressed in the first class of experiments, while the second class of experiments is designed to produce target verification tasks for the model. Early experiments will investigate the possibility of removing the effects of prior cycling by stress-free high temperature hold times or by steady cycling. If this can be demonstrated many independent experiments can be performed on one specimen.

Two types of experiments can be performed to assess the values of the two state variables comprising the constitutive model. The value of the scalar drag stress state variable can be determined from experiments in which the strain rate is changed very rapidly, since the proposed equations are such that the stress increment or decrement due to a sudden change in strain rate depends only on the drag stress and not on the tensorial equilibrium stress state variable. To study the value of the tensorial equilibrium stress state variable, creep tests can be performed at various points on a steady state hysteresis loop, searching for the load that gives zero initial creep rate corresponding to the equilibrium stress value. This procedure was used in Reference [6], while the tests involving sudden changes in strain rate have previously been used by Krempl in Reference [7].

REFERENCES

1. Paslay, P.R., Wells, C.H., and Leverant, G.R.: "An Analysis of Primary Creep of Nickel Base Superalloy Single Crystals," J. Appl. Mech., pp. 759-764, 1970.

2. Schmid, E. and Boas, W.: "Plasticity of Crystals with Special Reference to Metals," Chapman and Hall, London, 1968.

3. Umakoshi, Y., Pope, D.P., and Vitek, V.: "The Asymmetry of $Ni_3(Al,Ta)$ Single crystals," Acta Met., Vol. 32, No. 3, pp. 449-456, 1984.

4. Paidar, V., Pope, D.P., and Vitek, V.: "A Theory of the Anomalous Yield Behavior of $L1_2$ Ordered Alloys," Acta Met., Vol. 32, No. 3, pp. 435-448, 1984.

5. Shah, D., and Lin, L., J. Metals, Vol. 32, No. 8, p. 62, 1980.

6. Walker, K.P.: NASA CR-165533, 1981.

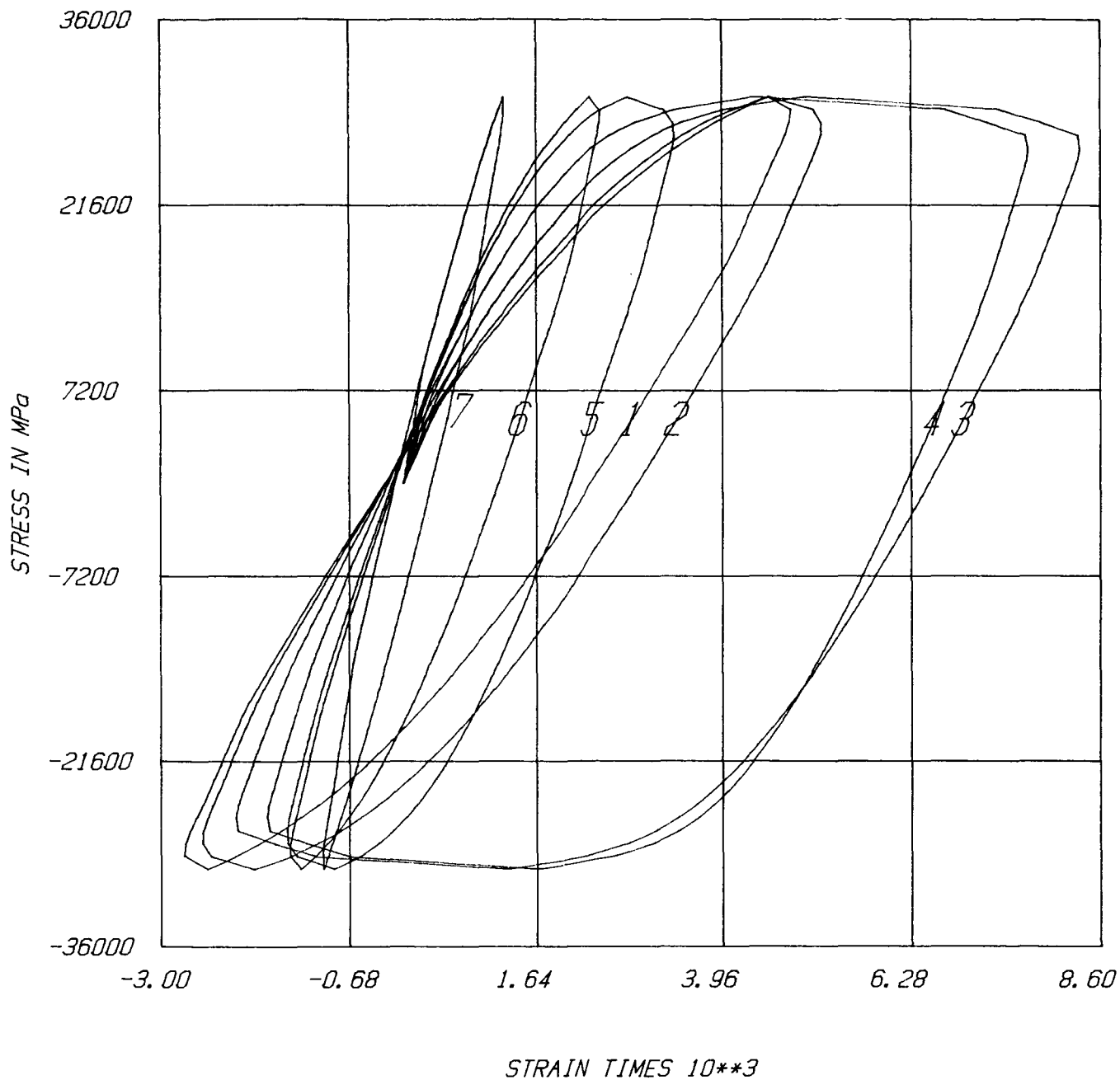7. Krempl, E.: RPI Report No. RPI CS 78-5, 1978.
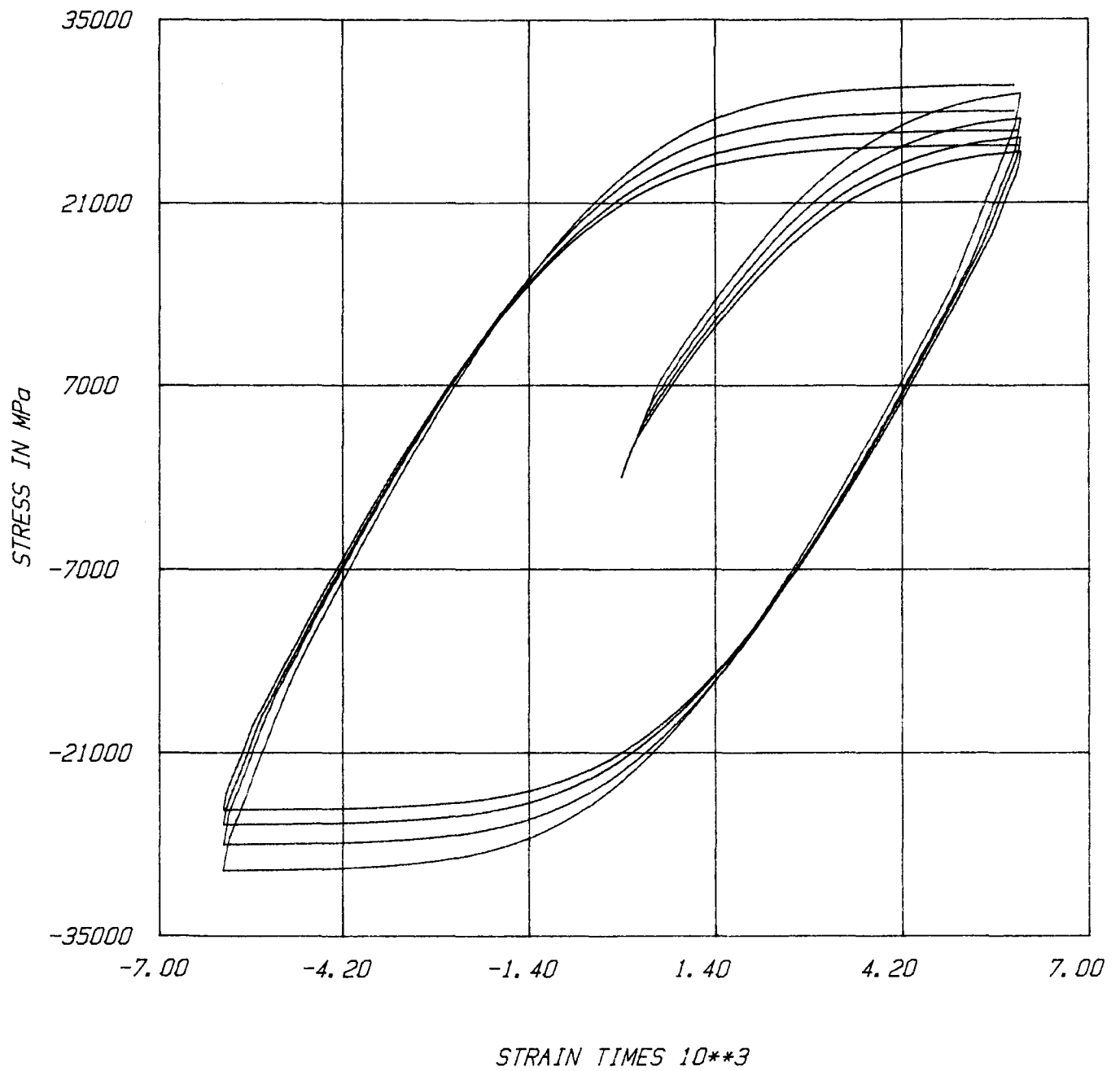
Figure 1.   Orientation Dependence of Hysteresis Loops

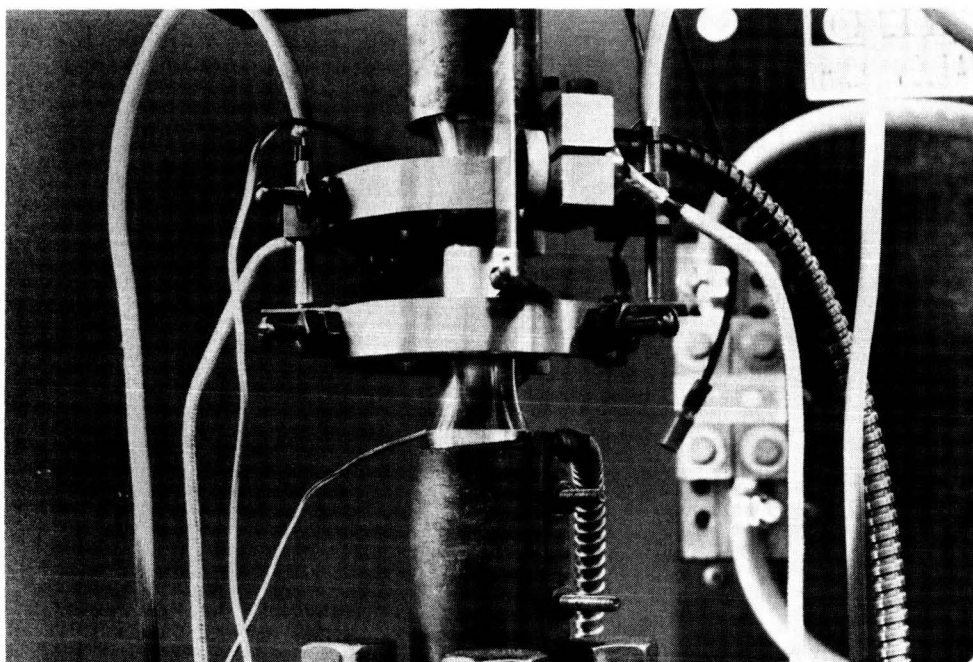Figure 2.   Strain Rate Dependence of Hysteresis Loops

Figure 3: Capacitance Probe Based High Temperature Biaxial Extensometer

LIFE PREDICTION AND CONSTITUTIVE MODELS FOR ENGINE HOT SECTION ANISOTROPIC MATERIALS

GUSTAV A. SWANSON
Pratt & Whitney
United Technologies Corporation

INTRODUCTION

The development of directionally solidified and single crystal alloys is perhaps the most important recent advancement in hot section materials technology. By reducing or eliminating grain boundaries in superalloys, the high temperature strengths have been substantially improved. Metallurgists have developed the alloy chemistries and casting processes so that they are now in practical use. However, the life limits of gas turbine parts, under complex loading conditions, are still not well known or understood. The objective of this program is to develop that knowledge to enable the designer to improve anisotropic gas turbine parts to their full potential.

Program Overview

The base program, which is followed by two options (fig. 1), will concentrate on coated turbine blade airfoil conditions. The coating, which is added to turbine airfoils to improve their oxidation and corrosion life, plays a major role in fatigue initiation. For this reason coated specimens are used extensively in this program. The materials have been selected, specimen fabrication is underway, the literature search is completed and Task III testing has begun. Table I shows the task breakdown of the base program.

Material Selection

The two single crystal alloys selected are PWA 1480 and Alloy 185. Table II lists the composition of these alloys. PWA 1480 was selected because it is the single crystal alloy most widely used today in gas turbine engines. Furthermore, it is representative of other practical single crystal alloys. Alloy 185 was selected because of differences between it and PWA 1480. These differences include a high volume fraction of γ' due to the higher aluminum content, a large γ/γ' misfit due to the high molybdenum content, and a higher level of creep anisotropy at higher temperatures. Contrast between the two alloys will provide a good test of the generality of any life prediction and constitutive models developed in this program.

The coatings selected are an overlay coating, PWA 286, and an aluminide diffusion coating, PWA 273. Coating chemistries are listed in Table III. These widely used coatings represent two basic classes.

Test Specimens

The constitutive specimens are solid and cylindrical; the fatigue specimens are hollow and cylindrical. The latter geometry is particularly applicable to thermomechanical fatigue (TMF) specimens. The thin wall facilitates thermal transient responses at reasonably fast rates. In addition, compressive stresses can be achieved

with minimum risk of buckling. The crystallographic orientation of the specimens for both the constitutive and life prediction program will include <100>, <110>, <111>, and <123>. Under tensile loading, the first two orientations produce slip along the orthogonal planes; the third along cuboidal planes, and the forth a mixture of the two.

Test specimens for the coatings' tensile, constitutive, and life properties required special preparation. The plasma-sprayed specimens were fabricated by two methods; some were machined from HIPed bulk powder. The others were sprayed with a 1.5 mm (0.060 in.) layer of coating on a metal substrate which was subsequently removed by machining. On turbine blades the plasma-sprayed coating is about 0.4 mm (0.015 in.) thick and finished with shot peen. Metallographically the two specimens bracket the actual porosity of airfoil coating (see fig. 2).

Diffusion coating properties are impossible to measure directly. The strategy in this program will be to utilize two thicknesses of substrate. Specimens of both thicknesses will be coated and then tested for tensile, creep and fatigue properties. The results will then be plotted versus substrate thickness and extrapolated to zero thickness to obtain the values for the coating alone.

Models to be Evaluated

An extensive literature search has been completed for both the constitutive and life prediction models. The bulk of the past work has been done on isotropic materials. This research will be adapted to anisotropic materials whenever possible. For example, the life prediction models may use maximum resolved shear strain ranges on the active slip planes in place of principle strain ranges. The constitutive models to be considered will include macroscopic continuum theories of Hill (ref. 1), and Lee and Zaverl (ref. 2 and 3), or a unified visco-plastic formulation such as that of Walker and Cassenti (ref. 4 and 5). The unified theory is currently being extended by Walker to recognize specific slip systems of nickel-based single crystal alloys. Stouffer, in a parallel program (ref. 6), is also developing a constitutive model for single crystal alloys. All of these models will be evaluated utilizing the test data generated in this program.

Life prediction models under consideration include a number of isotropic models: linear time-cycle fraction (ref. 7), ductility exhaustion (ref. 8 and 9), frequency modified life (ref. 10, 11 and 12), frequency separation (ref. 13 and 14), Ostergren's method (ref. 15), strain range partitioning (ref. 16), damage mechanics, (ref. 17 and 18), continuous damage (ref. 19 and 20), and cumulative damage approach (ref 21). All of these models will be evaluated utilizing resolved shear stress and/ or strain on active slip planes. A model to study the interaction of the coating and substrate is being developed.

Test Results

Because the test program is in its early stages evaluation of the results would be premature. One interesting preliminary result, however, is a comparison of the fracture surfaces of tensile specimens of PWA 1480 pulled in the <001> direction shown in figure 3. Note that the faceting at 760°C (1400°F) is pronounced and that

the number of active slip planes is small. However, as the test temperature is increased to 1093°C (2000°F), the number of faceting planes becomes more numerous and the fracture surface appears more normal to the tensile load.

Plans

By October 1985, we plan to complete the Task III tests and to have a preliminary evaluation of the constitutive and life prediction models.

REFERENCES

1. Hill, R.: A Theory of the Yielding and Plastic Flow of Anisotropic Metals. Proc. Royal Society of London, Ser. A., Vol. 193, pp. 281-297, 1948.

2. Lee, D.; Zaverl, F. Jr.; Shih, C. F.; and German, M. D.: Plasticity Theories and Structural Analysis of Anisotropic Metals. Report No. 77CRD285, General Electric Corporate Research and Development Center. Schenectady, New York, 1977.

3. Lee, D.: Anisotropic Yielding Behavior of a Fiber-Reinforced, Directionally Solidified Eutectic Alloy. Metallurgical Transactions A, Vol. 9A, pp. 1477-1481, 1978.

4. Walker, K. P.: Research and Development Program for Nonlinear Structural Modeling With Advanced Time-Temperature Dependent Constitutive Relationships. NASA CR-165533, November 1981.

5. Cassenti, B. N.: Follow on program to Reference 4. NASA Lewis Contract, NAS3-23273.

6. Stouffer, D.: Evaluation of Constitutive Modeling Method for Single Crystal Superalloys. Third Annual Workshop, Turbine Hot Section Technology (HOST) Project, NASA Lewis Research Center, Cleveland, Ohio, Oct. 23-24, 1984.

7. Class 1 Components in Elevated Temperature Service, Class III. ASME Boilers and Pressure Vessel Code, Case Interpretations. Code Case 1592, American Society of Mechanical Engineers, N. Y.

8. Sach, G.; Gerberich, W. W.; Weiss, V.; and Lavorre, J. V.: Proc. ASTM, V. 60, 1961, pp. 512-529.

9. Polhemus, J. F.; Spaeth, C. E.; Vogel, W. H.: Ductility Exhaustion Model Prediction of Thermal Fatigue and Creep Interaction. Fatigue at Elevated Temperature, ASTM STP520, American Society for Testing and Materials, 1973, pp. 625-636.

10. Coffin, L. F. Jr.: Fatigue at High Temperature. Fatigue at Elevated Temperatures, ASTM STP 520, American Society for Testing and Materials, 1973, pp. 5-34.

11. Coffin, L. F., Jr.: Fatigue at High Temperature Prediction and Interpretation. James Clayton Lecture, Institute of Mechanical Engineers, Vol. 188, 1974, pp. 109-127.

12. Coffin, L. F., Jr.: The Effect of Frequency on Cyclic Strain and Fatigue Behavior of Cast Rene at 1600°F. Metallurgical Transactions, Vol. 5, May 1974, pp. 1053-1060.

13. Coffin, L. F.: The Concept of Frequency Separation in Life Prediction for Time-Dependent Fatigue. Symposium on Creep Fatigue Interaction, 1976, pp. 349-363.

14. McKnight, R. L.; Lafen, J. H.; and Spmer, G. T.: Turbine Blade Tip Durability Analysis. National Aeronautics and Space Administration Report, NASA CR-165268.

15. Ostergren, W. J.: A Damage Function and Associated Failure Equation for Predicting Hold Time and Frequency Effects in Elevated Temperature, Low Cycle Fatigue. Journal of Testing and Evaluation, JTEVA, Vol. 4., No. 5, September 1976, pp. 327-339.

16. Manson, S. S.; Halford, G. R.; and Nachtigall, A. C.: Separation of the Strain Components for Use in Strain Range Partitioning. Symposium on Advances in Design for Elevated Temperature Environment, American Society for Mechanical Engineers, 1975, pp. 17-28.

17. Chaboche, J. L.: Thermodynamic and Phenomenological Description of Cyclic Visco-Plasticity with Damage. European Space Agency Technical Translation, May 1979.

18. Lemaitre, J.; and Chaboche, J. L.: A Nonlinear Model of Creep Fatigue Damage and Accumulation and Interaction. Symposium at IUTAM, Sur La Mecanique Des Milieux et Des Corp Viscoelastiques, Gothenburg, Sweden, September 2-6 1974.

19. Majumdar, S.; and Miaya, P. S.: Wave Shaped Effects in Elevated Temperature Low-Cycle Fatigue on Type 304 Stainless Steel. T. Y. Change and E. Krempl (EDS.), Inelastic Behavior of Pressure Vessel and Piping Components, PVP-PD-028, ASME, New York, pp. 43-54.

20. Majumdar, S.: Designing Against Low Cycle Fatigue at Elevated Temperature. Nuclear Engineering and Design, Vol. 63, 1981, pp. 121-135.

21. Moreno V.: NASA Contract NAS 3-23288

TABLE I

BASE PROGRAM TASKS

    I Material/Coating Selection and Acquisition

   II Selection of Candidate Life Prediction
      and Constitutive Models

  III Level 1 Experiments

   IV Correlation of Models With Level 1 Single
      Crystal Experiments

    V Level 2 Single Crystal Experiments

   VI Final Selection of Life Prediction and Con-
      stitutive Models

  VII Subcomponent Verification For Primary Sin-
      gle Crystal Material

 VIII Alternate Single Crystal Material Charac-
      terization For Airfoil Applications

   IX Model Verification On Alternate Single
      Crystal Material

    X Delivery of Computer Code to NASA

TABLE II

SINGLE CRYSTAL ALLOY COMPOSITION

(Weight Percent)

Alloy	Ni	Cr	Co	Ti	Al	Ta	W	Mo	Nb	C	B	Zr	Hf	Y
PWA 1480	Bal*	10.0	5.0	1.5	5.0	12.0	4.0	--	--	--	--	--	--	--
Alloy 185	Bal	--	--	--	6.8	--	6.0	14.0	--	0.04	--	--	--	--

* Balance

347

TABLE III

COATING MATERIALS

Coating	Composition	Deposition Process
Overlay PWA 286	NiCoCrAlY + Si +Hf	Vacuum Plasma Spray
Diffusion PWA 273	Aluminide/ Outward Diffusion	Gas Phase

PROGRAM OUTLINE

1984	1985	1986	1987	1988

BASE

COATED AIRFOIL CONDITIONS

TWO SINGLE CRYSTAL ALLOYS
PWA 1480 & ALLOY 185

TWO COATINGS
OVERLAY (PWA 286)
DIFFUSION (PWA 273)

OPTION 1

BLADE ROOT CONDITIONS

TWO SINGLE CRYSTAL ALLOYS
SAME AS ABOVE

COATINGS
NONE

OPTION 2

AIRFOIL & ROOT CONDITIONS

ONE DSR MATERIAL
(DIRECTIONALLY SOLIDIFIED
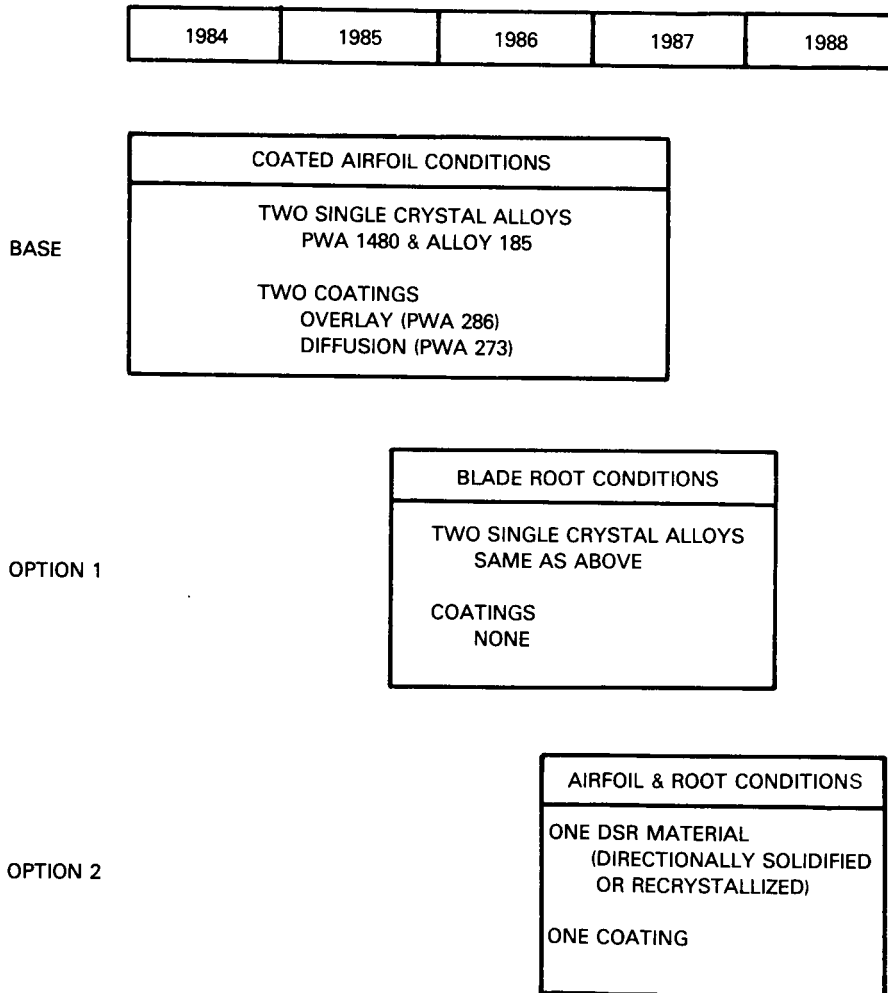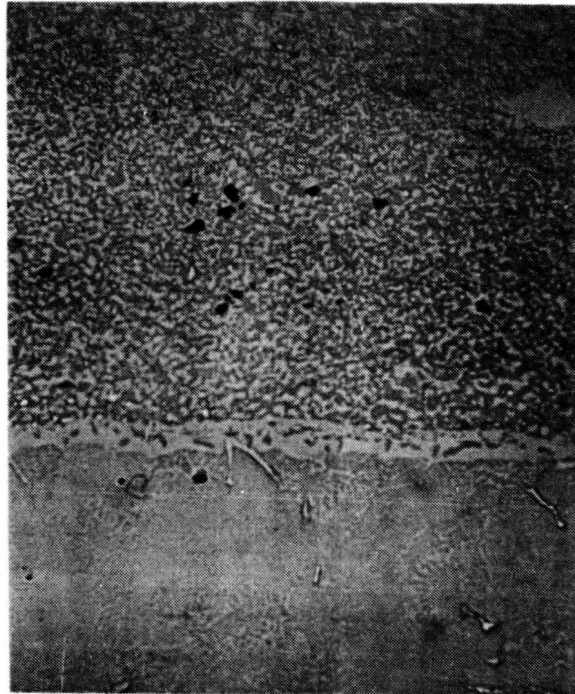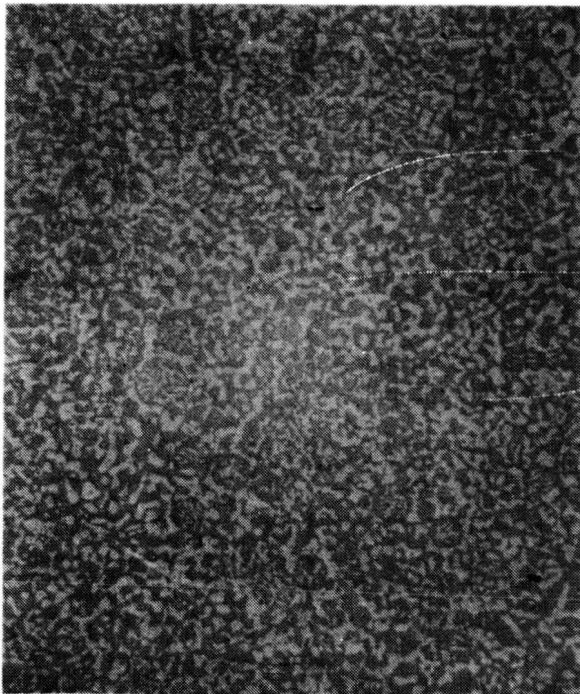OR RECRYSTALLIZED)

ONE COATING

Figure 1

348

PWA 286 OVERLAY COATING STRUCTURE: STAND-ALONE vs PRODUCTION

ORIGINAL PAGE IS
OF POOR QUALITY

TYPICAL PRODUCTION COATING   500X
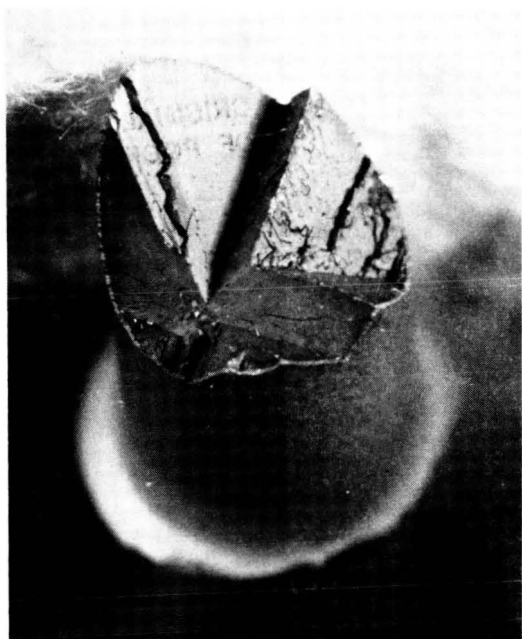HEAT TREATED & PEENED

HIPed BULK POWDER   500X

THICK PLASMA SPRAY   500X
HEAT TPEATED & PEENED

Figure 2

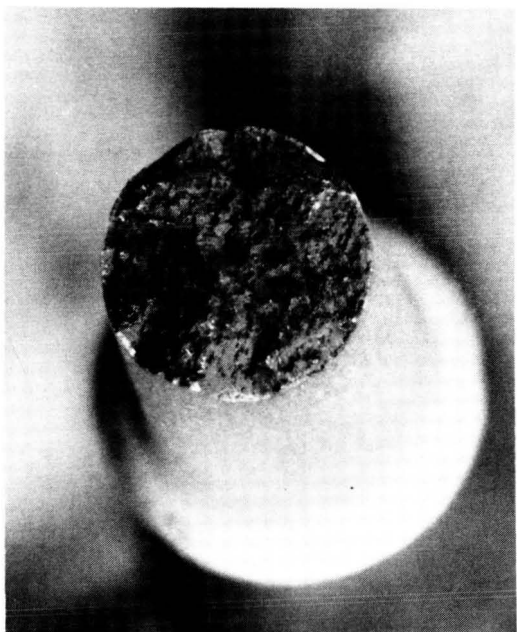FRACTURE SURFACE OF PWA 1480 TENSILE SPECIMENS

760°C (1400°F)

871°C (1600°F)

982°C (1800°F)

1093°C (2000°F)

Figure 3

350

TURBINE AIRFOIL GAS SIDE HEAT TRANSFER*

Edward R. Turner

Allison Gas Turbine Division
General Motors Corporation

ABSTRACT

Work is currently underway to develop and characterize an analytical approach, based on boundary layer theory, for predicting the effects of leading edge (shower-head) film cooling on downstream gas side heat transfer rates. Parallel to this work, experiments are being conducted to build a relevant data base for present and future methods verification.

INTRODUCTION

In a previous work (NAS3-22761), the emphasis was placed on developing more accurate analytical models for predicting local gas side heat transfer rates on modern non-film-cooled turbine vane geometries. Analytical and experimental results of that program are detailed in Reference 1. However, it is recognized that as future core turbine designs move towards higher turbine inlet temperatures, some degree of surface film cooling will be required to meet projected performance and durability goals. Therefore, the purpose of this work is to initiate an in-depth analytical/experimental characterization of heat transfer phenomena associated with film cooling by first considering a specific film cooling configuration commonly used in practice.

In particular, it has been demonstrated that multiple hole (showerhead) film cooling of the critical vane leading edge region can significantly enhance the long-term durability of vanes which otherwise are internally cooled by combination of convection and jet impingement techniques. While experiments and analyses have been reported that address the heat transfer problem within the showerhead array itself (e.g., Refs 2 to 5), there has been little systematic effort aimed at characterizing local downstream effects on highly loaded airfoil surfaces operating at realistic Mach number, Reynolds number, wall-to-gas, and coolant-to-gas temperature ratios.

The primary objective of this work is to develop a designer useable analytical method for predicting local heat transfer rate differences that exist between non-film-cooled and leading edge film-cooled airfoil designs in regions downstream of the showerhead array. In support of this objective, experiments are being conducted to build a realistic data base for developing and verifying modeling assumptions.

What follows first is a summary of the completed experimental program. This is followed by a discussion of some experimental results that illustrate important physical attributes of the leading edge film-cooled heat transfer problem that are receiving the most attention in the current methods development effort. Finally, the overall analytical program is summarized in terms of general approach and remaining tasks.

EXPERIMENTAL PROGRAM

The experimental technique used for determining local heat transfer coefficient distributions downstream of a showerhead array follows exactly that used for the non-film-cooled experiments reported in Reference 1 and summarized by Figure 1. As Figure 1 illustrates, a local surface heat transfer coefficient distribution is determined by experimentally measuring steady-state aerothermal boundary conditions and then numerically solving the heat conduction equation to calculate the airfoil internal temperature distribution. Once done, a local heat transfer coefficient can be formed using locally calculated surface normal temperature gradient, measured wall and gas temperatures, and material conductivity.

The film-cooled leading edge heat transfer experiments were conducted utilizing a two-dimensional (2-D) linear cascade of three vanes. The vane profile used in this work was identical to that referred to as the C3X vane in Reference 1. The leading edge for a new C3X test vane was designed and fabricated to include five rows of staggered holes to simulate a plenum-fed showerhead array. Geometric details of the actual array are summarized in Table I. The C3X profile used in both the non-film-cooled and film-cooled experiments is shown in Figure 2. This figure also indicates that the only difference between the non-film-cooled and film-cooled leading edge vane test hardware is in the details of the leading edge region. As nearly as possible, the present film-cooled experimental program was structured to directly extend the non-film-cooled C3X data base (Ref 1) with minor changes in technique and hardware. A photograph of one-half of the actual film-cooled C3X test vane that illustrates the structural configuration of the leading edge array is shown in Figure 3.

Experiments were conducted to simulate the case where all leading edge holes are supplied by a common plenum. This reflects the situation that exists for the majority of real designs. Aerodynamic and heat transfer data were obtained at two cascade exit Mach number (M_2) levels and three exit Reynolds number (Re_2) levels. At each exit Mach number/Reynolds number operating condition, plenum coolant-to-mainstream total pressure ratio, P_c/P_t (blowing strength), and plenum coolant-to-mainstream total temperature ratio, T_c/T_g (cooling strength), were systematically varied. A total of 45 heat transfer data sets were obtained within the experimental program. The ranges of test operating conditions for the four parameters varied are summarized in Table II.

EXPERIMENTAL RESULTS

In presenting the experimental heat transfer results, the goal is to isolate the differences between non-film-cooled and leading edge film-cooled heat transfer phenomena downstream of the showerhead array. This can be accomplished by ratioing the experimentally determined local Stanton number for cases where coolant is being ejected from the leading edge to the local Stanton number determined for the case where no coolant is added.

Rather than simply form the film-cooled Stanton number-to-non-filmed-cooled Stanton number ratio (St_{FC}/St_{NFC}), which would take on values about a "no difference" value of unity, an alternate parameter referred to as Stanton number reduction (SNR) is used. SNR is defined as

$$SNR = 1 - St_{FC}/St_{NFC} \qquad (1)$$

Therefore, SNR=0 implies "no difference" and positive or negative values imply reduced or increased heat transfer levels respectively. Forming SNR values along the entire test surface gives the actual SNR distribution for the airfoil. In addition, St_{FC}/St_{NFC} is determined using data obtained at equivalent M_2 and Re_2 conditions, so SNR is approximately equal to the actual heat transfer coefficient reduction.

Figures 4 and 5 are used to illustrate the formation and type information given by vane surface SNR distributions. All data shown in these figures were obtained at fixed operating conditions; i.e., $M_2 = 0.90$, $Re_2 = 2.0 \times 10^6$, $T_c/T_g = 0.8$. Variable blowing strengths ($P_c/P_t = 1.0, 1.02, 1.05, 1.10$) were set to at these conditions and heat transfer data taken. The four different surface heat transfer coefficient distributions determined from the cascade data at the four P_c/P_t conditions are shown in Figure 4. A value of $P_c/P_t = 1.0$ signifies a no coolant ejection condition and $P_c/P_t > 1.0$ signifies coolant is being ejected. Using the results of Figure 4 and the SNR definition given by equation (1), surface SNR distributions can be constructed. These are shown in Figure 5. Since each SNR distribution only shows the difference between a given film and baseline non-film-cooled condition, a SNR data presentation is useful for discussing phenomena unique to the film-cooled problem. This can be demonstrated by concentrating on some of the more important findings of the experimental program. Note first that the SNR results in Figure 5 indicate that the major difference in heat transfer level occurs on the suction surface between 20 and 40 percent surface distance ($0.2 < S < 0.4$). This region corresponds to what is considered to be the suction surface transition zone (see Figure 4). Therefore, over the range of blowing strengths represented by the data in Figures 4 and 5, the primary effect of leading edge film cooling is to increase the pre-turbulent boundary layer heat transfer levels (SNR < 0).

This pre-turbulent increase is similar in character to what would be anticipated by increasing the free-stream turbulence intensity. Thus, it appears that the discrete injection process acts as a turbulence promoter and/or simulated boundary layer trip device. Although the pressure surface seems to be unaffected in view of

the results shown in Figures 4 and 5, the same suction surface phenomenon is present but only to a lesser degree. This statement is supported by the results shown in Figure 6. SNR data shown in Figure 6 were obtained at the same fixed operating conditions (M_2, Re_2, T_c/T_g) as those in Figures 4 and 5 but at higher blowing strengths (P_c/P_t = 1.3-1.7).

Figure 6 clearly illustrates the so-called pre-turbulent increase in heat transfer (SNR < 0) associated with the discrete injection process on both the suction and pressure surfaces. Quantitative differences may be explained in part by differences in surface static pressure levels and/or gradient between the two surfaces. C3X test vane measured and predicted surface static-to-inlet total pressure distributions (P_s/P_t) are shown for reference in Figure 7.

Representative SNR data, indicative of differences associated with exit Reynolds number (Re_2) variation (M_2, T_c/T_g, P_c/P_t fixed), are shown in Figure 8. The main qualitative difference in the results is the location of the zone of negative SNR (increased heat transfer) on the suction surface. Figure 8 indicates that since transition zone location changes as Reynolds number is varied, the pre-turbulent region most affected by the injection process would be shifted. The progressively earlier location of minimum suction surface SNR with increasing Reynolds number is consistent with what would be expected in terms of transition origin versus Reynolds number models. The absence of a definitive trend difference on the pressure surface suggests a less well defined (understood) transition process.

One of the questions posed prior to this work was whether there were any benefits to be extracted from leading edge injection in terms of recovery region surface protection. To partially answer this question, Figure 9 is referred to. Data shown was obtained at variable plenum coolant-to-mainstream total temperature ratios (T_c/T_g = 0.7,0.8,0.9) at fixed M_2, Re_2, P_c/P_t conditions. The general overall increase in SNR (decreased heat transfer) as T_c/T_g is decreased indicates the positive effect that results from diluting the hot free-stream fluid with the colder leading edge ejectant. However, as the pressure surface results indicate, the favorable dilution phenomenon is offset by the adverse turbulence generation mechanism associated with the discrete injection process (see Figure 5). The net result is that even for T_c/T_g = 0.7, SNR is still negative immediately downstream of the showerhead on the pressure surface.

Figure 9 also indicates that the dilution versus turbulence generation mechanisms are at work on the suction surface. However, SNR results shown in Figure 6 indicate that in the fully turbulent region (S > 0.4) no significant effect is expected (i.e., SNR ≈ 0 for S > 0.4) as a result of the leading edge injection process. Therefore, Figures 6 and 9 together support the notion that in pre-turbulent zones the SNR result obtained is governed by the competing dilution/turbulence generation mechanisms, while in the fully turbulent zones the SNR result is determined by dilution strength only. If this is the case, then it can be argued that leading edge film cooling by itself cannot be used to always offset high near recovery region heat loads even though far recovery region loads are reduced.

Finally, one curious result concerning suction surface transition behavior is illustrated in Figures 4 and 5. Studying the suction surface heat transfer coefficient data of Figure 4 first, note that transition in the thermodynamic boundary layer sense appears to complete near S = 0.6 or the location where the heat transfer coefficient appears to level off. However, SNR data of Figure 5 indicate that the upstream disturbance (leading edge discrete injection in this case) causes no change beyond S = 0.4. Therefore, it would seem that the S = 0.4 location distinctly delineates pre- and post-transition zones in terms of disturbance phenomena. But the fact that between S = 0.4 and S = 0.6 the heat transfer coefficient is still increasing (Figure 4) contradicts the above statement.

It is theorized that perhaps the apparently contradictory trends in Figures 4 and 5 actually are indicative of transition rate differences between the hydrodynamic and thermodynamic boundary layers. That is, since the SNR data of Figure 5 show the type results that would be obtained by introducing a simulated boundary layer trip, then the "no difference" result beyond S = 0.4 might imply that the untripped hydrodynamic boundary layer had completed transition near S = 0.4. However, heat transfer coefficient data of Figure 4 indicate that both the disturbed and undisturbed thermodynamic boundary layers complete transition further downstream nearer S = 0.6. Since parallel measurements of the developing hydrodynamic boundary layer state were not made (e.g., surface wall shear stress distributions), it is impossible to conclusively quantify the implied differences between hydrodynamic and thermodynamic transition phenomena suggested here.

ANALYTICAL PROGRAM

The overall objective of the analytical methods development program is to develop a computational technique, based on boundary layer theory, to predict the SNR type results shown in Figures 5, 6, 8 and/or 9. Work towards this objective is currently in progress.

The basic approach being taken is to develop a modified version of the finite difference boundary layer code, STAN5, for predicting within regions downstream of the showerhead array where it is assumed that a boundary layer would re-form. The initial task as far as this approach is concerned is to develop a method for generating appropriate starting location velocity and thermal profiles that reflect experimental results in terms of wall gradient quantities (initial location heat flux or heat transfer coefficient.) For this effort, a previously developed non-blown similarity solution technique (Refs 1 and 5) is being modified to account for the turbulence generation and dilution mechanism phenomenon associated with a discrete injection process.

Following this work, the final task will be to develop a suitable model for tracking the disturbance decay through transition. This is perhaps the more difficult problem since the success of this effort depends in part on having a reliable, undisturbed (non-blown) transition model. It can be argued that a consistently reliable, non-film-cooled airfoil transition model does not yet exist. However, if at a minimum the important qualitative trends present in the experimental results are captured, then the final prediction code will be of value to the turbine cooling designer interested in obtaining a more correct evaluation of the overall heat transfer benefits or penalties associated with leading edge film-cooled airfoil geometries.

REFERENCES

1. Hylton, L.D.; Mihelc, M.S.; Turner, E.R.; Nealy, D.A.; and York, R.E: Analytical and Experimental Evaluation of Heat Transfer Distribution Over the Surfaces of Turbine Vanes. NASA CR 168015, 1983.

2. Luckey, D.W.; and L'Ecuyer, M.R.: Stagnation Region Gas Film Cooling--Spanwise Angled Injection from Multiple Rows of Holes. NASA CR 165333, 1981.

3. Bonnice, M.A.; and L'Ecuyer, M.R.: Stagnation Region Gas Film Cooling--Effects of Dimensionless Coolant Temperature. NASA CR 168197, 1983.

4. Stepka, F.S.; and Gaugler, R.E.: Comparison of Predicted and Experimental External Heat Transfer Around a Film Cooled Cylinder in Crossflow. ASME Paper No. 83-GT-47, 1983.

5. Miller, K.L.; and Crawford, M.E: Numerical Simulation of Single, Double, and Multiple Row Film Cooling Effectiveness and Heat Transfer. ASME Paper No. 84-GT-112, 1984.

6. Kwon O.K.; Turner, E.R.; and Kou, Y.M.: Prediction of Stagnation Flow Heat Transfer on Turbomachinery Airfoils. AIAA Paper No. 83-1173, 1983.

Table I.
Film-cooled leading edge geometry.

Geometric parameters	Value
Rows of holes*	5
Hole pitch-to-diameter ratio (P/D)	4.0
Hole spacing-to-diameter ratio (S/D)	7.5
Hole slant angle (α)--deg	45
Hole skew angle (β)--deg	90

*Centered about location of maximum surface
 static pressure

Table II.
Range of parameters varied in film-cooled experiments.

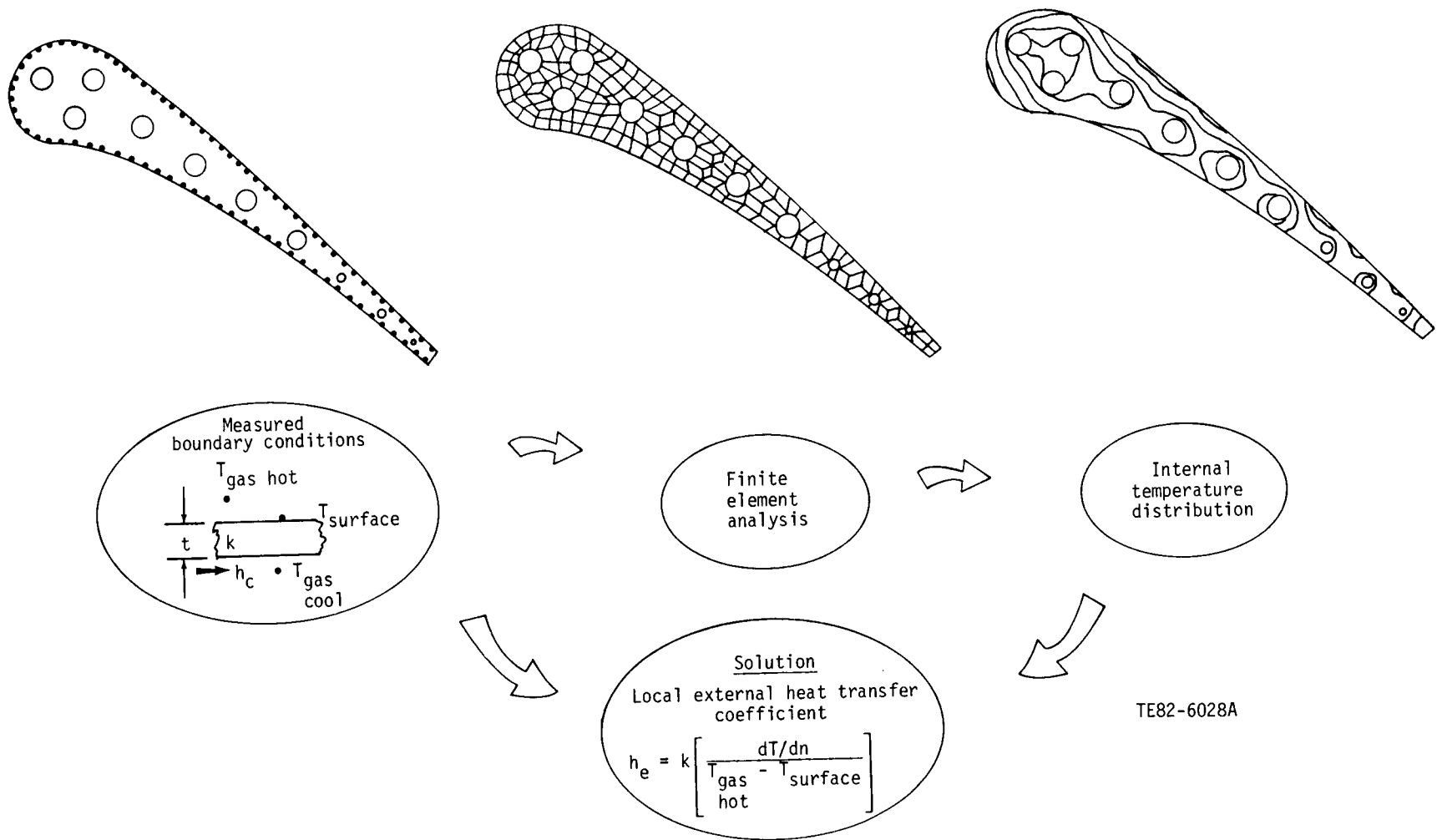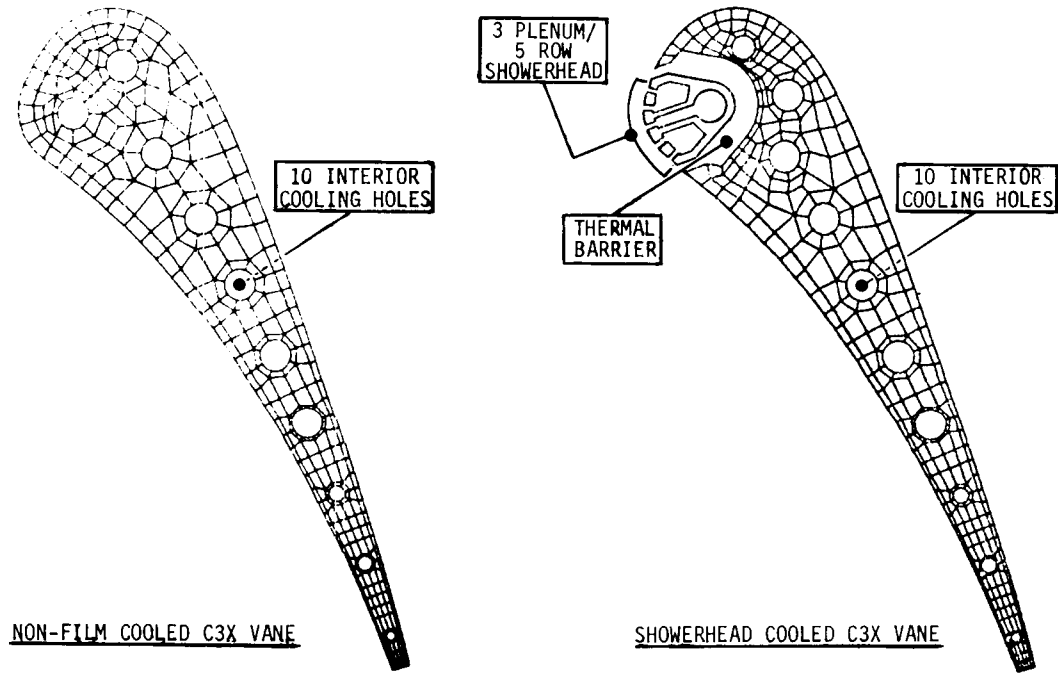| Parameter	Range
Exit Mach number, M_2	0.90-1.05
Exit Reynolds number, Re_2	$1.5 \times 10^6 - 2.5 \times 10^6$
Plenum coolant-to-mainstream total pressure ratio, P_c/P_t	1.0-1.7
Plenum coolant-to-mainstream total temperature ratio, T_c/T_g	0.6-0.9

Figure 1. Heat transfer data reduction technique.

3 PLENUM/
5 ROW
SHOWERHEAD

10 INTERIOR
COOLING HOLES

THERMAL
BARRIER

10 INTERIOR
COOLING HOLES
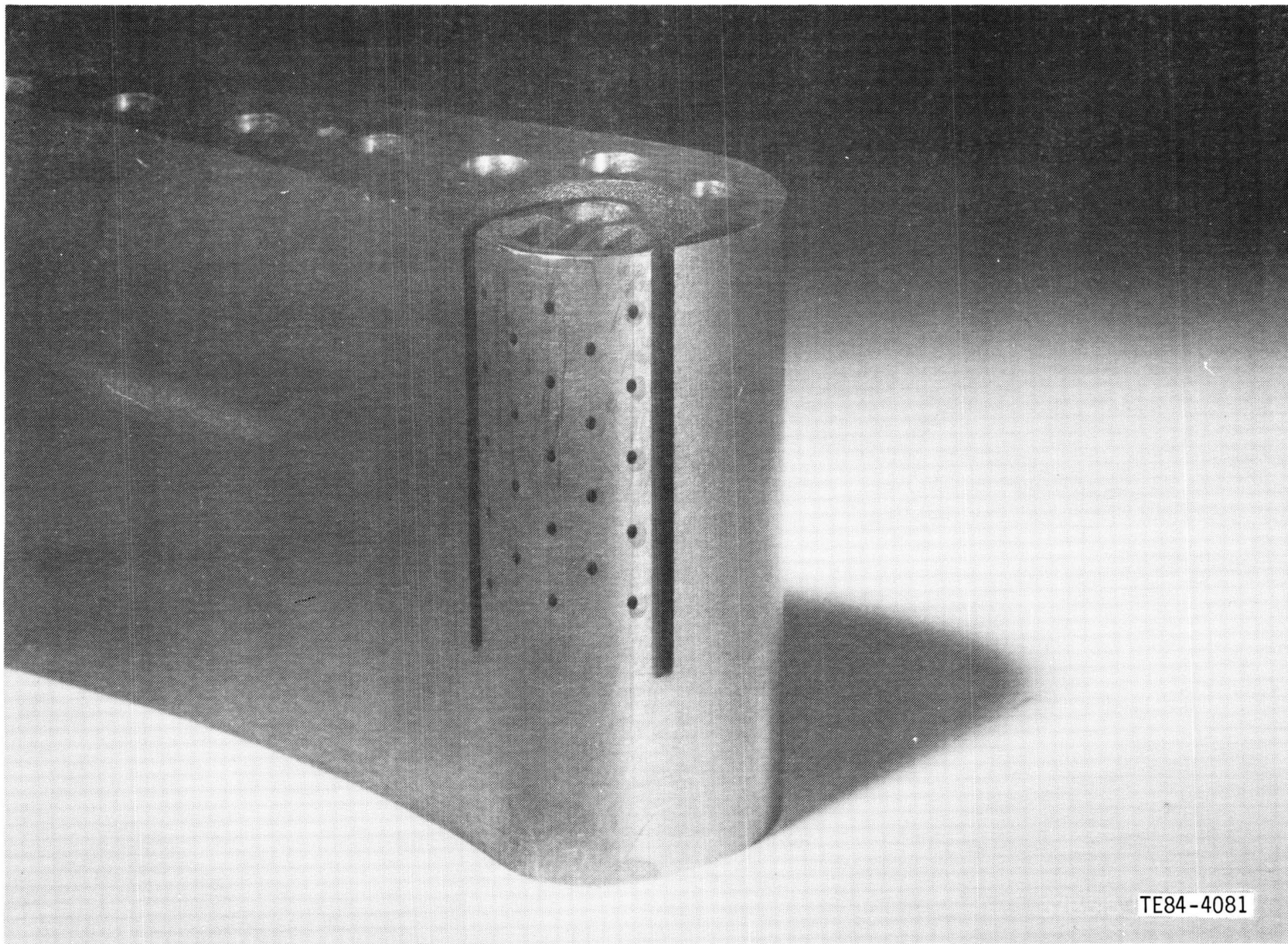
NON-FILM COOLED C3X VANE

SHOWERHEAD COOLED C3X VANE

TE84-4080

Figure 2.   Cross section of C3X vanes for heat transfer experiments.

TE84-4081

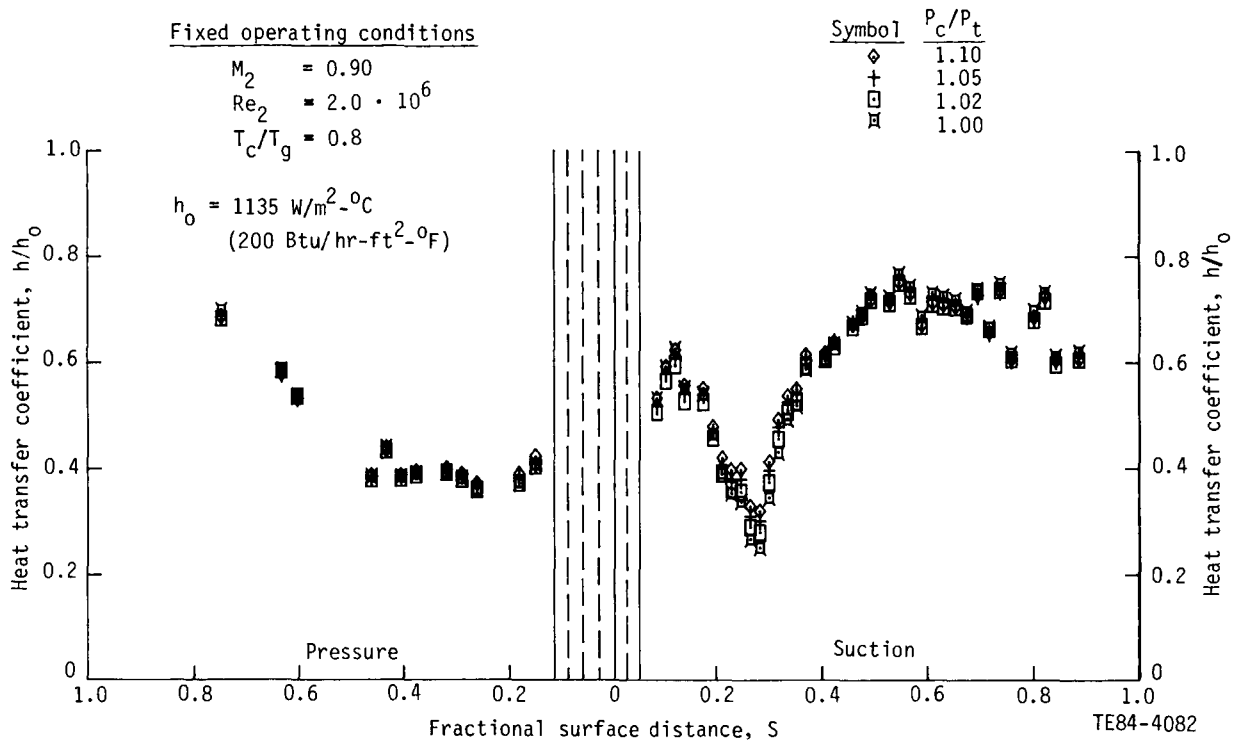Figure 3. Film-cooled C3X vane half prior to instrumentation.

Figure 4. Variable blowing strength heat transfer coefficient data.
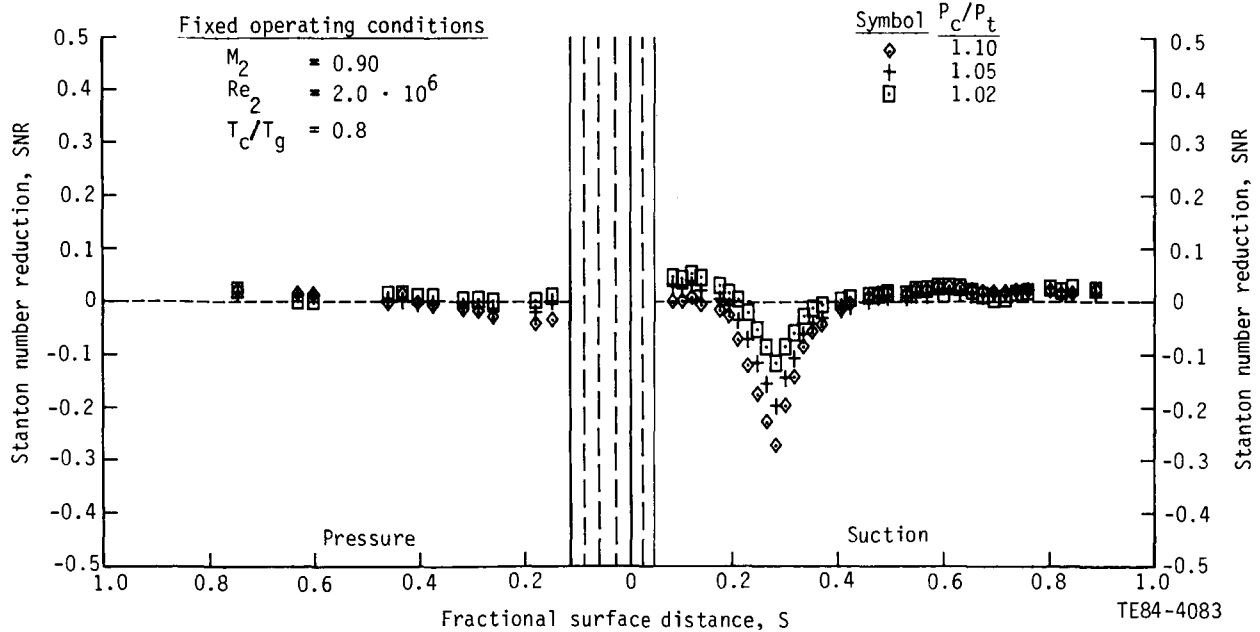

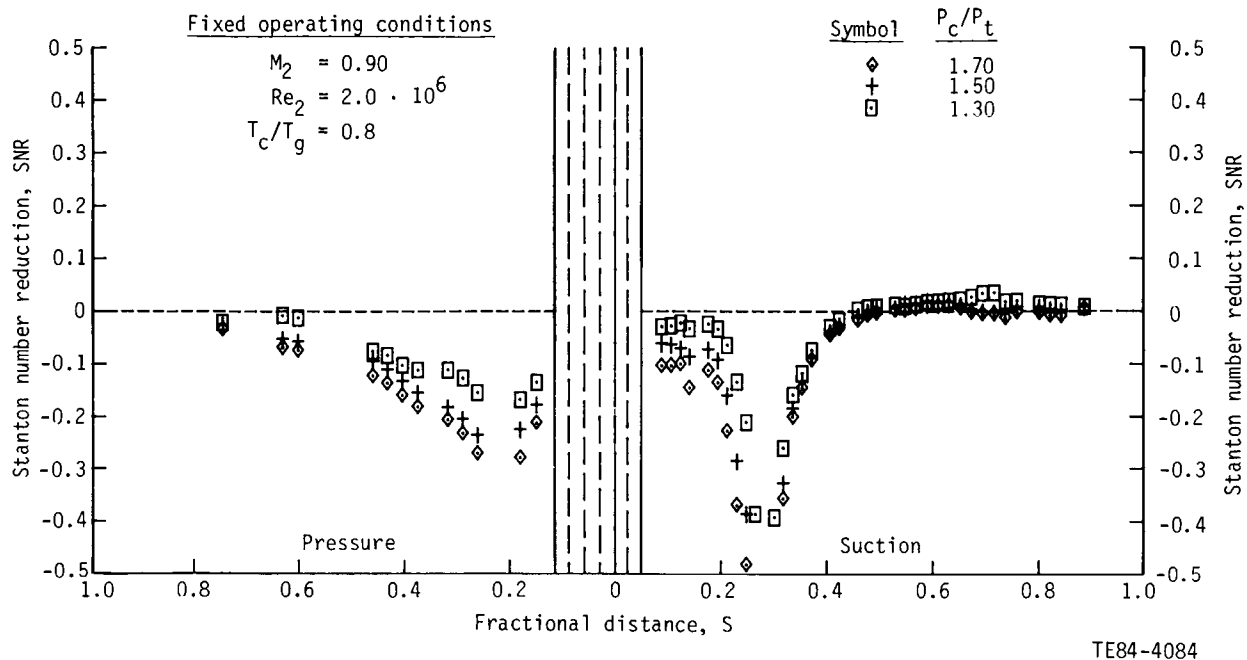Figure 5. Effect of blowing strength variation.

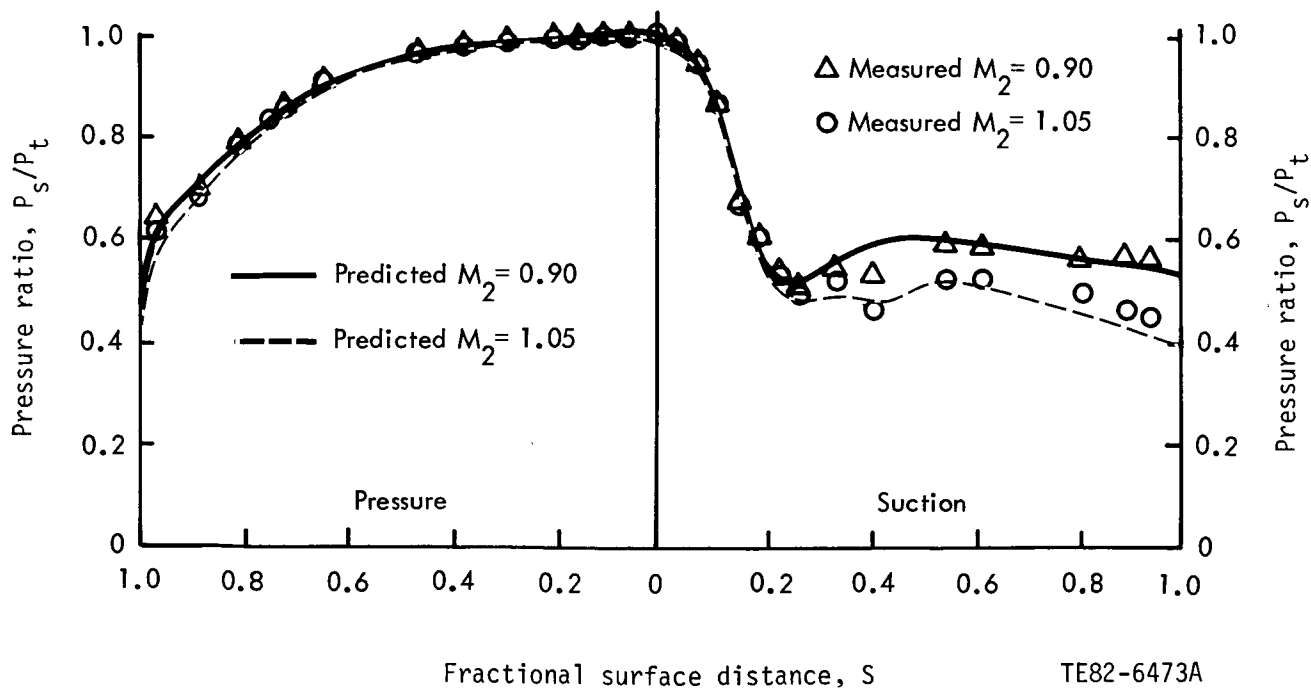Figure 6. Effect of blowing strength variation.

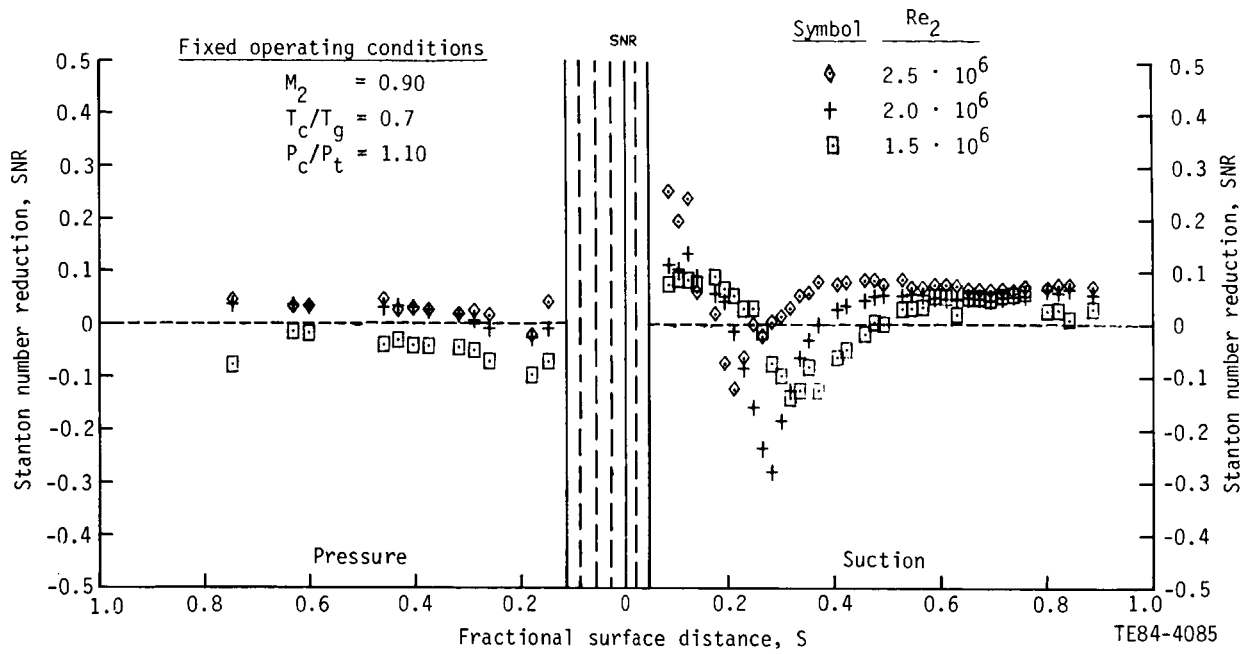Figure 7. Surface static-to-inlet total pressure distributions.

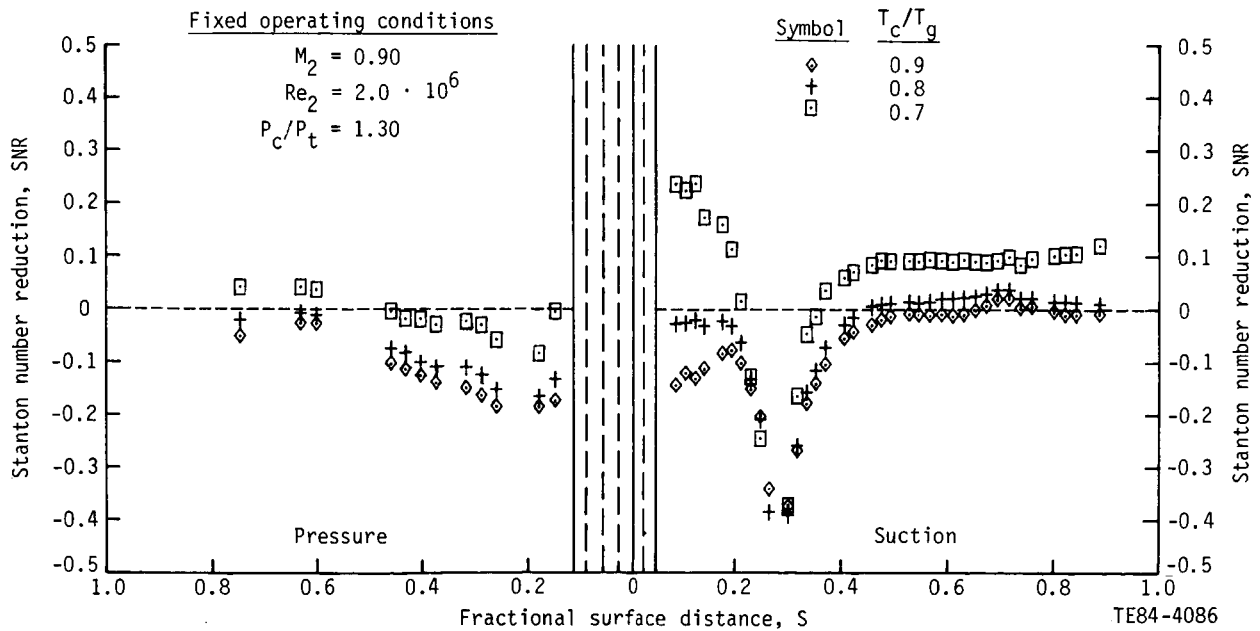Figure 8.   Effect of Reynolds number variation.

Figure 9.   Effect of coolant temperature variation.

363

CALCULATION OF TWO- AND THREE-DIMENSIONAL TRANSONIC CASCADE FLOW FIELD USING THE NAVIER-STOKES EQUATIONS*

B. C. Weinberg, R.-J. Yang, S.J. Shamroth and H. McDonald
Scientific Research Associates, Inc.

INTRODUCTION

Major objectives of the HOST program have been to improve hot section performance and life. Of specific interest here is the turbine, and in order to achieve the HOST objectives, accurate determinations of turbine blade pressure distributions and associated heat transfer rates are required. Over the years, substantial efforts have been expended in developing reliable and efficient computational procedures for predicting the flow field and accompanying heat transfer characteristics within turbine passages.

At the present time there are three possible approaches to the prediction of turbine flow fields, i.e. (i) inviscid analyses, (ii) inviscid analyses with boundary layer corrections, and (iii) full Navier-Stokes flow field analyses. The first approach is only useful in computing blade loading, and limited by the need to assume airfoil circulation to obtain a unique flow field, and the inability to account for viscous effects. The second approach can be used to obtain heat transfer rates and viscous losses by using either a viscous-inviscid interaction model or a non-interactive technique. The non-interactive technique is viable if viscous displacement effects are small. If the viscous displacement effects are large, then an interaction model should be used. However, this approach is subject to the principal difficulties that the boundary layer approximations may not be valid, and the division between viscous and inviscid regions could be unrealistic. This may be a particular problem in three-dimensional transonic flow where the local pressure distribution and shock location become very sensitive to small changes in the effective passage area. The third approach using the full Navier-Stokes equations solves the flow field using a single set of governing equations requiring no interaction model or approximations in separated regions.

APPROACH

The present work applies a Navier-Stokes analysis [1] employing the time-dependent Linearized Block Implicit scheme (LBI) of Briley and McDonald [2] to two-dimensional and three-dimensional transonic turbulent cascade flows. In general, the geometrical configuration of the turbine blade impacts both the grid construction procedure and the implementation of the numerical algorithm. Since modern turbine blades of interest, e.g. the Allison C3X turbine cascade shown in Fig. 1, are characterized by very blunt leading edges, rounded trailing edges and high stacking angles, a robust grid construction procedure is required that can accomodate the severe body shape while resolving regions of large flow gradients. A constructive 0-type grid generation technique, suitable for cascades with rounded trailing edges, has been developed

and used to construct the C3X turbine cascade coordinate grid shown in Fig. 1. The C3X was selected in view of the extensive heat transfer measurement program being undertaken on this airfoil by Allison as part of the HOST program.

Another aspect of the numerical algorithm that is addressed is the setting of boundary conditions; on the body, upstream and downstream boundaries and the periodic surfaces. In particular in the transonic regime, where the pressure on the blade is sensitive to the upstream and downstream conditions proper boundary condition specification is crucial in obtaining accurate predictions. Two-dimensional calculations were performed employing the Navier-Stokes procedure for the C3X turbine cascade, and the predicted pressure coefficients and heat transfer rates were compared with the experimental data generated under the HOST program by Hylton, et al [3]. In addition, the corresponding three-dimensional rectilinear C3X turbine cascade was considered in which blade-endwall effects are present. Three-dimensional Navier-Stokes calculations also were performed. Some results of both the two- and three-dimensional calculations are briefly discussed below.

Figure 1 shows the 0-type grid generated by the constructive technique for the C3X blade. The features of the techniques are: (a) the actual physical shape of blade is maintained, (b) regions of large flow gradients are resolved, (c) upstream and downstream boundaries are placed far from the blade surface so that boundary conditions can be more easily implemented, and (d) the coordinate intersection angles are controlled so that metric data associated with the coordinate system are smooth. The coordinate system for two-dimensional calculations consists of 30 points in the pseudo-radial direction and 120 points in the pseudo-azimuthal direction. The upstream boundary is placed at 2.25 axial chords upstream of the leading edge and the downstream boundary is placed at 2.65 axial chords downstream of the trailing edge. High radial resolution is obtained near the surface of the blade, with the first coordinate line located at a distance of 1.0×10^{-6} axial chords from the surface which is within the turbulent boundary layer viscous sublayer. In addition, high pseudo-azimuthal resolution is obtained at both leading and trailing edges.

RESULTS

In Fig. 2 the computed pressure distribution for a sample case (ratio of upstream total to downstream static pressure $P_o/P_{exit} = 1.66$, exit Mach number $M_{exit} = 0.9$, exit Reynolds number $Re_{exit} = 2.43 \times 10^6$, ratio of averaged blade surface temperature to inlet gas total temperature $T_w/T_g = 0.75$, and averaged inlet turbulence intensity $T_u = 6.5\%$, is shown and compared with the Allison experimental data corresponding to case 144 in Ref. 3 and inviscid calculations [4]. There is excellent agreement between the present calculations and the experimental data. Mixing length and k-ϵ two-equation turbulence models were employed, and (as expected) the results of calculations indicate very little difference in the prediction of the pressure coefficient. Due to the small viscous displacement effect, the inviscid calculations show close agreement with the present computed results. Also shown in this figure are the data from cases 148 and 158 which were run under nominally identical conditions (cf. Ref. 3) to indicate the relationship between the predictions and the experimental scatter.

In Fig. 3 the distribution of the computed heat transfer coefficient is shown for case 144 with both film-cooling and non-film-cooling options. For the non-film-cooling option, with the local surface temperature distribution given in [3], a mixing length turbulence model in conjunction with a transition model was employed in which laminar flow was assumed in the region $X/C_x < 0.2$ followed by a transitional zone and thereafter by fully turbulent flow. The predictions obtained with the model compare very well with the experimental data taken with no film cooling present.

366

Following this initial calculation, the film cooling option in the code was activated with air injected at 30° to the suction sie over $0.8 < x/c_x < 0.9$ at a velocity of 7% of freestream. The local surface temperature was kept fixed at the same value as the non-film-cooling option. Although no data is available for comparison the calculation does demonstrate the effect of film-cooling. From the onset of injection to the trailing edge the heat transfer rate drops to nearly zero. This behavior is a consequence of the buffer region of constant temperature cool gas which protects the blade surface from the hotter fluid in the cascade passage. The comparison of the pressure distribution for both film cooling and non-film-cooling options is shown in Fig. 4. The effect of blowing on the pressure distribution is clear, i.e. the adverse pressure gradient that is generated, the resulting upstream influence, and the subsequent favorable pressure gradient that follows it.

For the three-dimensional rectilinear C3X turbine cascade, the configuration consisted of a C3X cascade situated in the azimuthal- radial plane (see Fig. 1), and bounded in the transverse direction by an endwall and a symmetry plane. For the three-dimensional calculation a grid was constructed consisting of 100 x 25 x 15 grid points in the pseudo-azimuthal, pseudo-radial and transverse directions, respectively. For this demonstration case laminar conditions were assumed. The height of the blade above the endwall (to the symmetry plane, midspan) was set to be one axial chord, while the inlet boundary layer thickness was 20% of that value. The computed pressure distribution at different heights above the endwall are shown in Fig. 5. The pressure side is minimally affected by the endwall, remaining at or near the two-dimensional value run on the same spanwise cross-sectional grid, while the suction side, which shows as much as 15% change over the two-dimensional value near the 30% axial chord location, approaches the two-dimensional value at 26% span above the endwall. The differences from the two-dimensional value are due to the effects of secondary flow generated by horseshoe and passage vortices. The results are consistent with the expected physics (Refs. 5, 6). In Fig. 6, the velocity vector plots are presented for the forward portion of the C3X cascade at two different planes above the endwall. Very near the endwall (within 2.95% spanwise plane) a saddle point exists as indicated in the picture. This saddle point moves toward the leading edge and disappears beyond 2.95% spanwise plane. A stagnation point forms on the nose of the blade surface beyond 2.95% spanwise plane. Further results and a detailed discussion will be presented in the final report, now in preparation.

PLANS

The demonstration three-dimensional calculations completes the technical effort under the subcontract. Future efforts have been proposed and these include continued code development (incorporating the effect of rotation), further validation, improvements in numerical methodology, application to specialized design problems and developing user-oriented input output routines.

REFERENCES

1. Shamroth, S.J., McDonald, H. and Briley, W.R.: Prediction of Cascade Flow Fields Using the Averaged Navier-Stokes Equations. ASME Journal of Engineering for Gas Turbines and Power, Vol. 196, pp. 383-390, 1984.

2. Briley, W.R. and McDonald, H.: Solution of the Multidimensional Compressible Navier-Stokes Equations by a Generalized Implicit Method. Journal of Computational Physics, Vol. 24, pp. 372-397, 1977.

3. Hylton, L.D., Mihelc, M.S., Turner, E.R., Nealy, D.A. and York, R.E.: Analytical and Experimental Evaluation of the Heat Transfer Distribution Over the Surface of Turbine Vanes. NASA-CR-168015, May 1983.

4. Delaney, R.A.: Time Marching Analysis of Steady Transonic Flow in Turbomachinery Cascades Using the Hopscotch Method. ASME Journal of Engineering for Power, Vol. 105, pp. 272-279, 1983.

5. Langston, L.S., Nice, M.L. and Hooper, R.M.: Three-Dimensional Flow Within a Turbine Cascade Passage. ASME Journal of Engineering for Power, Vol. 99, pp. 21-28, 1977.

6. Sieverding, C.H. and Van den Bosche, P.: The Use of Colored Smoke to Visualize Secondary Flows in a Turbine-Blade Cascade. Journal of Fluid Mechanics, Vol. 134, pp. 85-89, 1983.
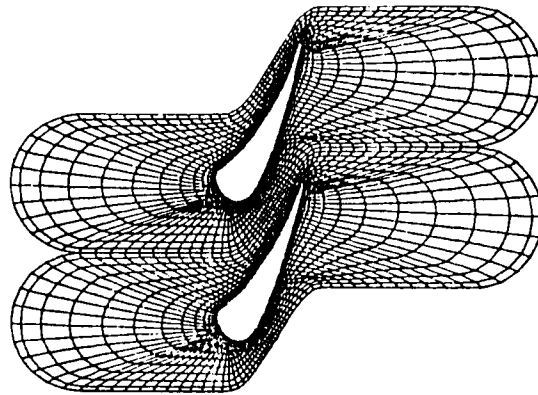
C3X TURBINE BLADE "O"-GRID MESH

FIGURE 1

PRESSURE COEFFICIENT DISTRIBUTION

CASE 144 $M_{exit} = 0.90$ $Re_{exit} = 2.43 \times 10^6$
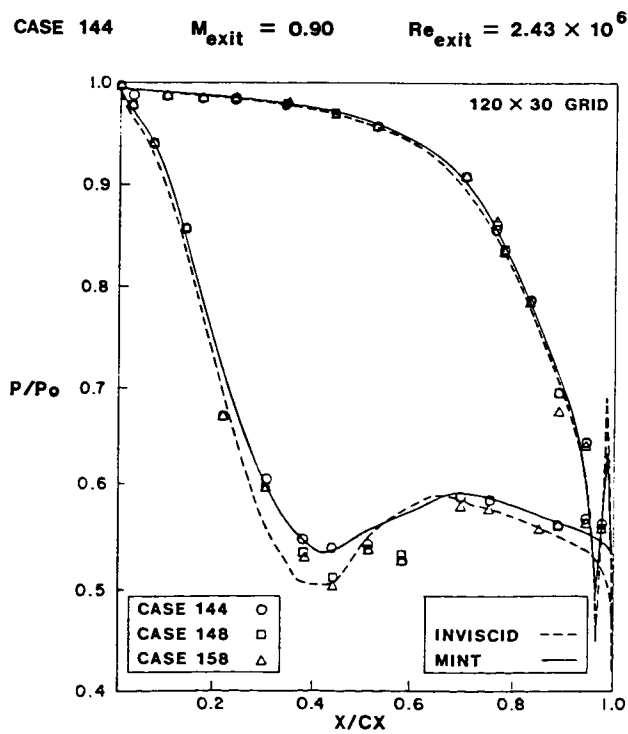

FIGURE 2

369

HEAT TRANSFER COEFFICIENT

CASE 144 $M_{exit} = 0.90$ $Re_{exit} = 2.43 \times 10^6$ $T_w / T_g = 0.75$
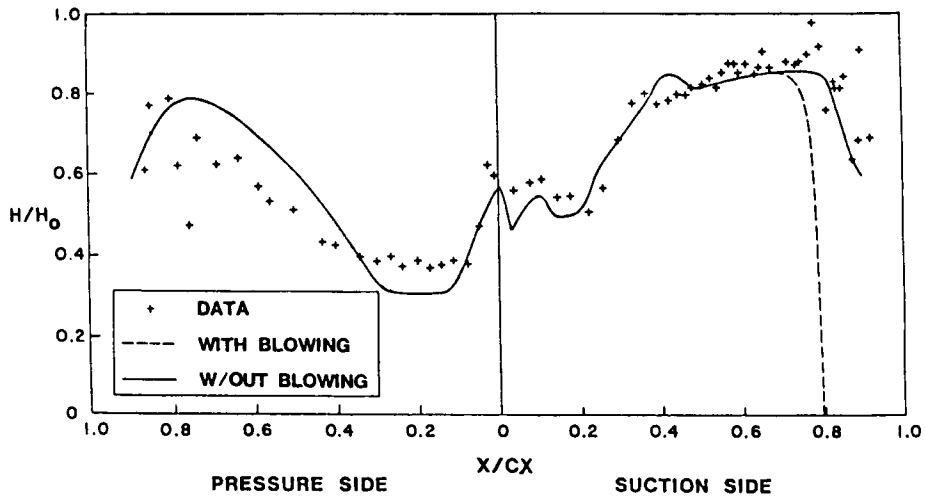

FIGURE 3

PRESSURE COEFFICIENT DISTRIBUTION

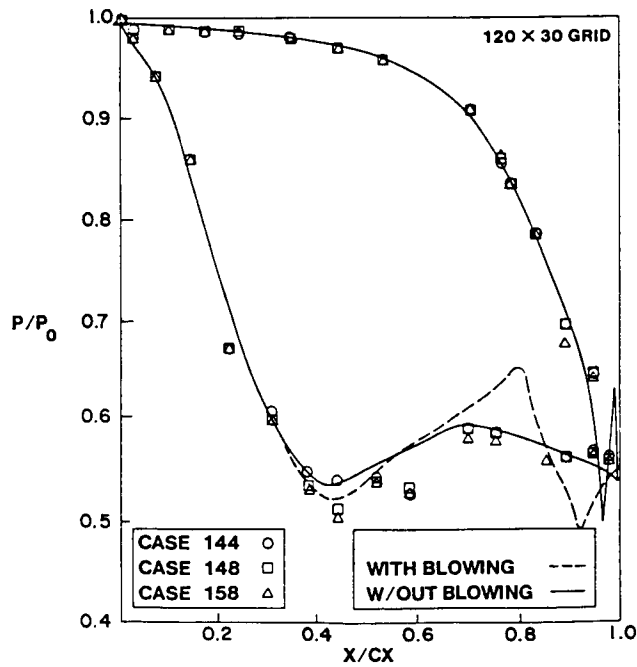CASE 144 $M_{exit} = 0.90$ $Re_{exit} = 2.43 \times 10^6$

FIGURE 4

370

C3X 3-D RECTILINEAR CASCADE
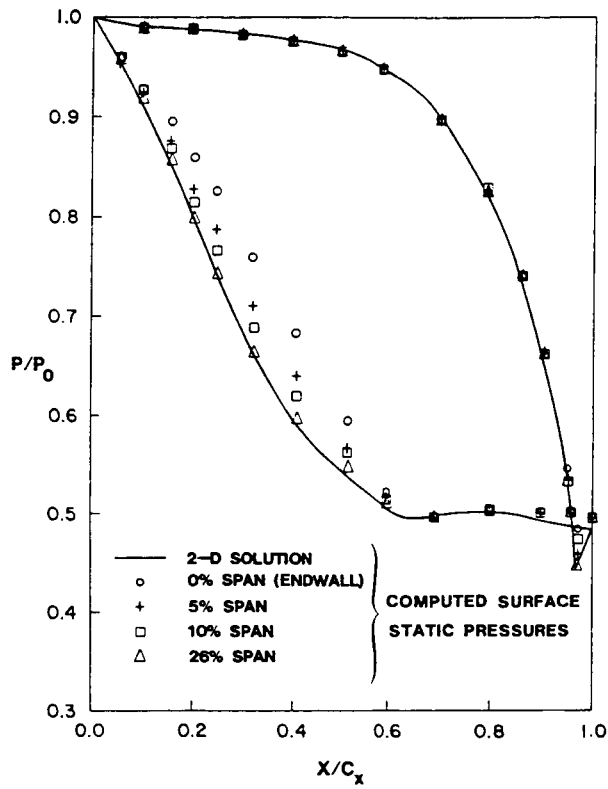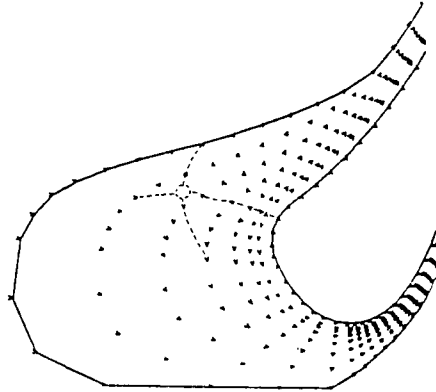## PRESSURE COEFFICIENT DISTRIBUTION
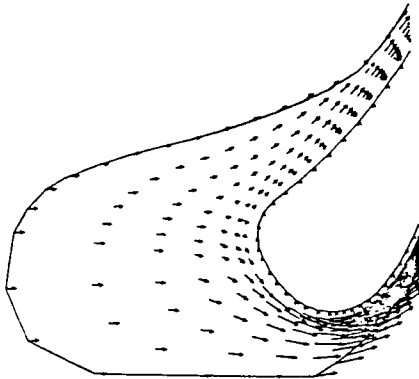

FIGURE 5

(a) VECTOR PLOT ON 0.135% SPANWISE PLANE

(b) VECTOR PLOT ON MIDSPAN PLANE

FIGURE 6

MEASUREMENT OF AIRFOIL HEAT TRANSFER
COEFFICIENTS ON A TURBINE STAGE

Robert P. Dring
Michael F. Blair
United Technologies Research Center

INTRODUCTION

The primary basis for heat transfer analysis of turbine airfoils is experimental data obtained in linear cascades. These data have been very valuable in identifying the major heat transfer and fluid flow features of a turbine airfoil. The question of major interest is how well all of these data translate to the rotating turbine stage. It is known from the work of Lokay and Trushin (ref. 1) that average heat transfer coefficients on the rotor may be as much as 40 percent above the values measured on the same blades non-rotating. Recent work by Dunn and Holt (ref. 2) supports the conclusion of ref. 1. What is lacking is a set of data from a rotating system which is of sufficient detail as to make careful local comparisons between static cascade and rotor blade heat transfer. In addition, data is needed in a rotating system in which there is sufficient documentation of the flow field to support the computer analyses being developed today. Other important questions include the impact of both random and periodic unsteadiness on both the rotor and stator airfoil heat transfer. The random unsteadiness arises from stage inlet turbulence and wake generated turbulence and the periodic unsteadiness arises from blade passing effects. A final question is the influence, if any, of the first stator row and first stator inlet turbulence on the heat transfer of the second stator row after the flow has been passed through the rotor.

OBJECTIVES

The first program objective is to obtain a detailed set of heat transfer coefficients along the midspan of a stator and a rotor in a rotating turbine stage (Fig 1.) These data are to be such that the rotor data can be compared directly with data taken in a static cascade. The data are to be compared to some standard analysis of blade boundary layer heat transfer which is in use today. In addition to providing this all-important comparison between rotating and stationary data, this experiment should provide important insight to the more elaborate full three-dimensional programs being proposed for future research. A second program objective is to obtain a detailed set of heat transfer coefficients along the midspan of a stator located in the wake of a full upstream turbine stage. Particular focus here is on the relative circumferential location of the first and second stators. Both program objectives will be carried out at two levels of inlet turbulence. The low level will be on the order of 1 percent, and the high level on the order of 10 percent, which is more typical of combustor exit turbulence intensity. The final program objective is to improve the analytical capability to predict the experimental data.

Heat transfer measurements will be obtained in this study using low conductivity rigid foam castings of the test airfoils. A uniform heat flux will be generated on the surface of the foam test airfoils using electrically heated metal foil strips attached to the model surface. Local heat transfer coefficients around the airfoils will be determined using thermocouples to measure the temperature difference between the heated metal skin and the free stream.

Photographs of the First Stage Rotor Model at various steps of fabrication are presented in Fig. 2. The first stage of the fabrication process consisted of developing a metal "master airfoil". An aluminum rotor blade, chosen at random from the Large Scale Rotating Rig (LSRR) rotor, was carefully inspected to determine locations with surface waviness. These slight deviations from a perfectly "developable" surface (a surface with no compound curvature) are an inherent characteristic of the "multiple radial station contour tracing" machining process used to manufacture the aluminum airfoils. Despite the fact that this surface waviness only consists of depressions a few thousandths of an inch deep at their maximum, they do present a problem unique to this method of instrumentation. The metal foil which will be glued to the exterior surface of the airfoil is extremely intolerant of surface waviness. Even miniscule depressions on the airfoil translate to "wrinkles" or "lumps" on the finished, assembled foil surface. For this reason it was necessary that any depressions be filled to produce as nearly a "developable" surface as possible. This filling procedure consisted of a trial-and-error/inspection iteration towards the finished airfoil. An airfoil was accepted as a "master" only after a completely wrinkle-free "test" metal foil could be glued to its entire surface. An inviscid flow computation of the velocity distribution around the finished "master" airfoil indicated that the maximum change in local velocity produced by the surface filling (measured maximum filling thickness) was only 1/4 percent. A photograph of the completed "metal master airfoil" is presented in Fig. 2.

The next step in the model fabrication process (not shown in Fig. 2) consisted of casting a concrete mold of the master airfoil. Special low shrinkage gypsum cement (USG Hydrocal) was used to produce a smooth airfoil surface and a precise geometrical reproduction.

A steel skeleton (Fig. 2.) was fabricated for each of the test airfoils to ensure adequate strength to endure both the aerodynamic and centrifugal forces of the test environment. The skeleton provided a secure location to attach the foam airfoil to either the rotor hub or the stator case. The photograph of the first stage rotor skeleton presented in Fig. 2. shows the attachment "button" for fastening the blade to the hub.

The rotor airfoil was cast in rigid foam with the steel skeleton mounted in the concrete mold. A special fixture ensures that the mounting button on the skeleton was precisely located at the same position relative to the concrete mold as was the botton on the original "metal master

airfoil". Photographs of the suction and pressure surfaces of the cast foam rotor blade are shown in Fig. 2. For this particular model the suction surface was instrumented and the pressure surface was the "backside" through which the instrumentation was routed. The suction surface view shows the pattern of holes to be used for installation of themocouples. The holes in the suction surface were evenly spaced at one inch increments at the midspan location for the demonstration test. The pressure surface view shows the trenches cut into that surface for routing of thermocouple leads, the copper buss bars for connecting to the foil skin and the electric power leads. The copper buss bars ensure that the voltage along each end of the foil strip is uniform, producing a uniform current over the entire foil surface.

The rate of heat transfer varies strongly with location near the leading edge of an airfoil. Measurement of these extreme gradients in heat transfer requires a dense grid of thermocouples in this region. In an attempt to obtain accurate measurements in the leading edge region for the present test airfoils, a new high density thermocouple installation technique has been assessed. Shown in Fig. 3. is a photograph of the leading edge array installed in this particular rotor model. The photograph shows the backside of the leading edge region of the foil before it was installed on the airfoil. Also shown are a specially fabricated template for accurately locating thermcouple beads and a thin "transfer template" which is shown attached directly to the backside of the foil. This "transfer template" was removed following the completion of the thermocouple installation. Shown in the photograph are 20 thermocouples located at 0.050 in. apart within an estimated accuracy of $\pm$ 0.005 in.

The next photograph of Fig. 3. shows the rotor model with the heater foil installed on the suction surface only. In this photograph the thermocouples have been welded to the backside of the heater foil and routed through the trenches to the support botton. The third photograph of Fig. 3. shows the model with the foil attached to the pressure surface and connected to the buss bars. At this stage the instrumentation cavity was refilled with urethane foam to conform to the original pressure surface contour. The final photograph of Fig. 3. shows the completed test model coated with flat black paint. This paint coating ensures a uniform, known emissivity so that a slight ($\approx$3 percent) but accurate radiation correction can be incorporated into the data reduction routine.

A demonstation of the rotor heat transfer measurement technique has been successfully carried out. This test showed: (1) that the instrumented Urethane foam heat transfer models could survive the centrifugal loading in the rotating frame of reference, (2) that the instrumenation within the heat transfer model, and specifically the dense array of thermocouples around the leading edge, could survive the centrifugal loading, and finally (3) that the slip-ring unit provides a reliable and effectively noise-free method of acquiring thermocouple data in the rotating frame of reference. The actual test airfoils (first stator, rotor, and second stator) each have typically 95 thermocouple sites with 60 at midspan and 20 concentrated near the leading edge of each airfoil. The instrumentation diagram for the first stage rotor is shown in Figure 4 as an example.

REFERENCES

1. Lokay, V.I., and Trushin, V.A.: Heat Transfer from the Gas and Flow-Passage Elements of a Rotating Gas Turbine. Heat Transfer - Soviet Research, Vol. 2., No. 4, July 1970.

2. Dunn, M.G., and Holt, J.L.: The Turbine Stage Heat Flux Measurements. Paper No. 82-1289, AIAA/ASME 18th Joint Propulsion Conference, 21-23, June 1982, Cleveland, Ohio.

OBJECTIVES

- Turbine first stator and rotor heat transfer data
- Rotor-stator interaction (ΔX)
- Free stream turbulence
- Comparison with cascade data
- Second stator heat transfer data
- Stator-stator interaction (ΔCirc)
- Quasi-steady and/or unsteady boundary layer analysis
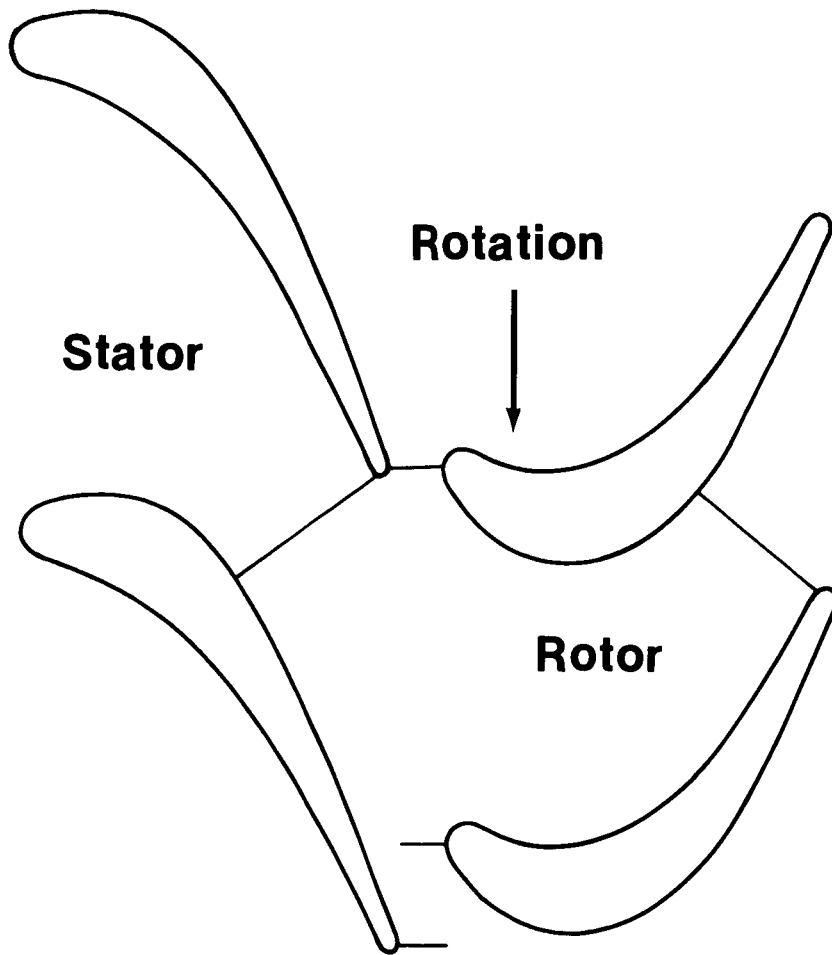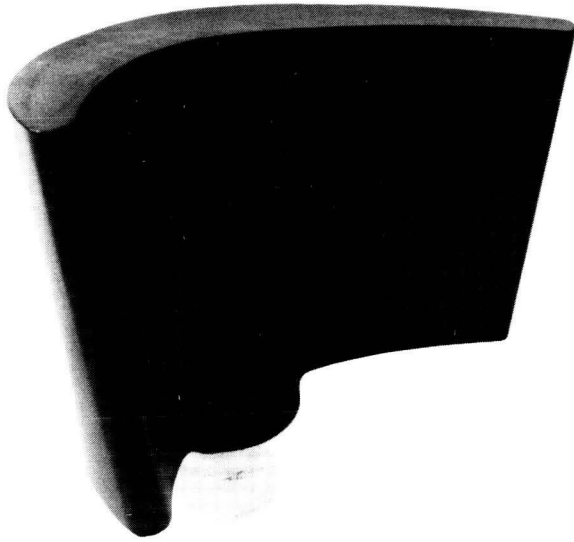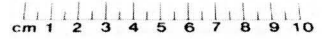
TURBINE STAGE AT 15% AXIAL GAP

FIG. 1

STAGES OF FABRICATION FOR THE FIRST STAGE ROTOR
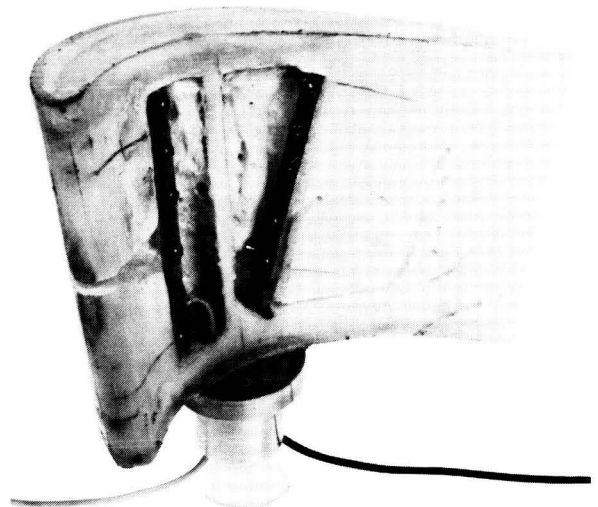

METAL MASTER AIRFOIL

STEEL SKELETON

SUCTION SURFACE OF CAST AIRFOIL

PRESSURE SURFACE OF CAST AIRFOIL

FIG .2

84—2—25—2

378

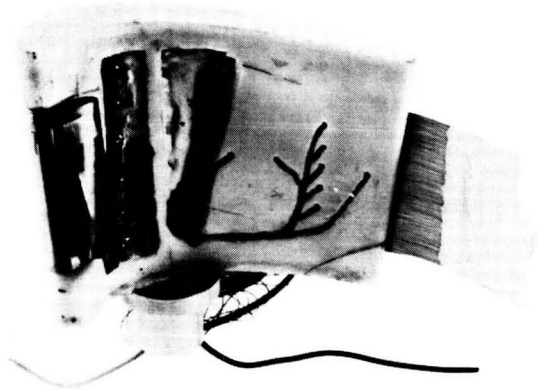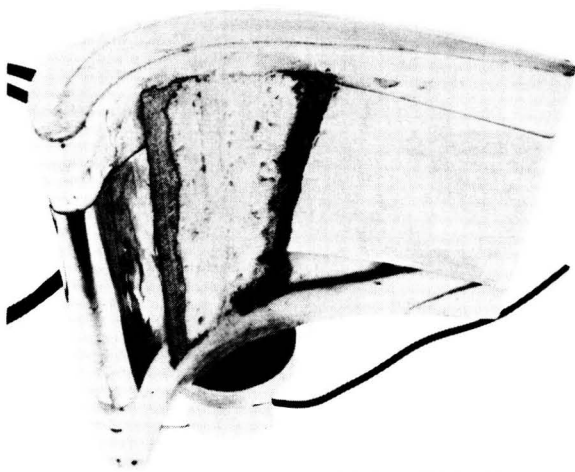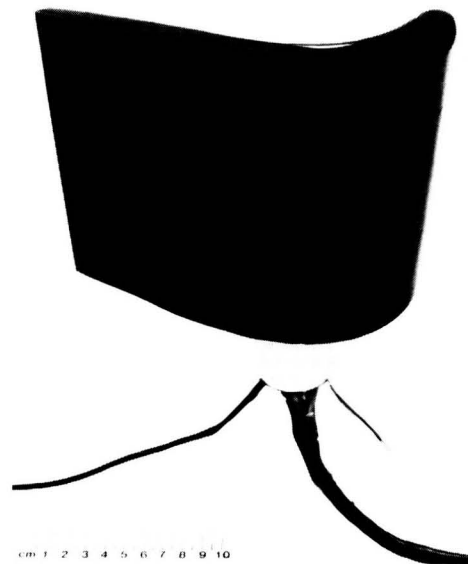**STAGES OF FABRICATION FOR THE FIRST STAGE ROTOR**
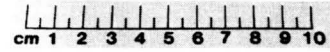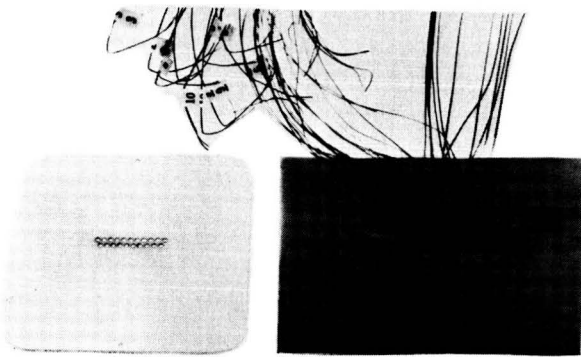
LEADING EDGE THERMOCOUPLE GRID
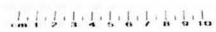
AIRFOIL WITH FOIL PARTIALLY INSTALLED
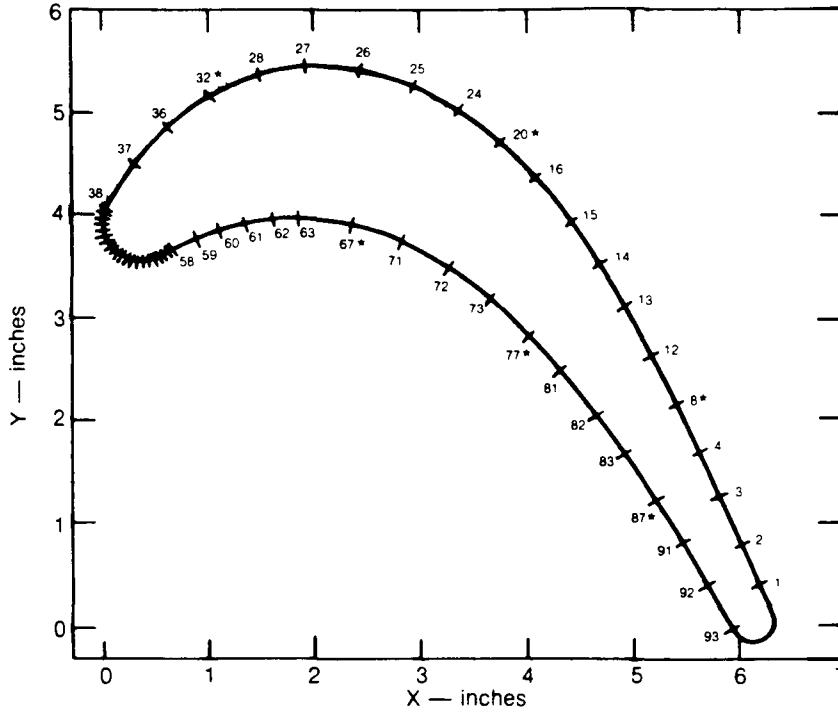
AIRFOIL WITH INSTRUMENTATION CAVITY CLOSED

COMPLETED TEST AIRFOIL

FIG. 3

84—2—25—1

379

INSTRUMENTATION DIAGRAM FOR THE FIRST STAGE ROTOR

$B_x = 6.341$ in.   TOTAL ARC LENGTH = 18.753 in.

NOTE — ORIGIN OF ARC LENGTH (S) IS THE AXIAL TRAILING EDGE
(MAXIMUM X), S INCREASES MOVING COUNTERCLOCKWISE
SUCTION SURFACE AIRFOIL TC's 1-58
PRESSURE SURFACE AIRFOIL TC's 38-93

T.C.#	X/B$_x$	S/B$_x$
1	0.975	0.069
2	0.945	0.148
3	0.912	0.227
4	0.878	0.306
8*	0.845	0.385
12	0.811	0.463
13	0.773	0.542
14	0.735	0.621
15	0.692	0.700
16	0.643	0.779
20*	0.588	0.858
24	0.525	0.936
25	0.456	1.015
26	0.382	1.094
27	0.303	1.173
28	0.226	1.252
32*	0.155	1.331
36	0.095	1.410
37	0.044	1.488
38	0.003	1.567

T.C.#	X/B$_x$	S/B$_x$
39	0.001	1.575
40	0.000	1.583
41	0.000	1.591
42	0.002	1.599
43	0.004	1.607
44	0.007	1.615
45	0.012	1.622
46	0.017	1.630
47	0.023	1.638
48	0.030	1.646
49	0.037	1.654
50	0.044	1.662
51	0.052	1.670
52	0.061	1.678
53	0.068	1.686
54	0.076	1.693
55	0.083	1.701
56	0.090	1.709
57	0.096	1.717
58	0.103	1.725

T.C.#	X/B$_y$	S/B$_y$
59	0.139	1.764
60	0.172	1.804
61	0.211	1.843
62	0.251	1.883
63	0.290	1.922
67*	0.371	2.000
71	0.445	2.080
72	0.513	2.159
73	0.574	2.237
77*	0.629	2.316
81	0.680	2.395
82	0.730	2.474
83	0.774	2.553
87*	0.820	2.632
91	0.858	2.711
92	0.899	2.789
93	0.940	2.868

* AT THESE AXIAL STATIONS T.C.s LOCATED
AT 50% SPAN AND ±8.3, 16.6 AND 25%
AWAY FROM MIDSPAN

FIG. 4

EFFECTS OF VERY HIGH TURBULENCE ON CONVECTIVE HEAT TRANSFER

Robert J. Moffat and Paul K. Maciejewski
Thermosciences Division, Department of Mechanical Engineering
Stanford University

INTRODUCTION

In spite of all the effort expended on heat-transfer research over the past 30 years, gas-turbine designers must still use significantly large "experience factors" for each family of engines to "adjust" predictions based on laboratory data. We believe that turbulence effects may be an important contributor to this situation.

Gas-turbine blade and vane heat-transfer situations are characterized by high free-stream turbulence (20% or more) of large scale compared to boundary-layer thickness, but nearly all of the data in the literature is from tests with little or no turbulence. In fact, it is a point of pride to "clean up" a tunnel until the free-stream turbulence is less than 0.25% before taking data "for record"! By itself, this is evidence that we believe turbulence is important. When turbulence is introduced, it is nearly always "grid-generated" turbulence—in part because its characteristics are reasonably predictable.

In the present research, we are studying the effects of high-intensity, large-scale turbulence on turbulent boundary-layer heat transfer. We are producing flow fields with turbulence intensities up to 40% and length scales up to several times the boundary-layer thickness. In addition, we plan to compare three different types of turbulence (i.e., turbulence generated by three different devices) to see whether they have the same effect on the boundary layer. The three are: (1) the far field of a free jet, (2) flow downstream of a grid, and (3) flow downstream of a simulated gas-turbine combustor.

To characterize the turbulence produced in these different flow fields, we shall use two different hot-wire anemometer systems. High relative turbulence is difficult to measure with conventional hot-wire anemometry. For measurements at a point, we plan to use a real-time triple-wire system developed in our laboratory for recording the instantaneous velocity components u, v, and w. This system has the capability of reporting the measurements of u, v, and w in real time, properly in phase, at up to 10 kHz per channel. It has also demonstrated the ability to measure the velocity components within ± 5% up to 20° angle of incidence of the instantaneous velocity, which corresponds to a very high relative turbulence intensity. For length-scale measurements, two single-wire probes will be used with a correlator. We plan to characterize each turbulence field by several measures: intensity (by component), scale, and spectrum.

Heat transfer will be measured on a 2.5-m-long, 0.5-m-wide flat plate using an energy-balance technique. The same plate will be used in each of four flow fields: a low-turbulence tunnel for baseline data, and the three flow situations mentioned earlier.

By this research, we hope to determine how many descriptors of the system are needed to specify the system well enough to get repeatable heat transfer.

PREVIOUS WORK

A representative collection of experiments on the effects of free-stream turbulence is given in the works of Kestin [ref. 1], Kearney et al. [ref. 2], Slanciauskaus and Pedesius [ref. 3], Brown and Burton [ref. 4], Bradshaw and Simonich [ref. 5], and Blair [ref. 6].

Kestin reported no effect of turbulence level on a constant-velocity turbulent boundary layer. Kearney et al. reported no effect on the constant-velocity boundary layer and also no effect when a strong acceleration was applied to the flow (K = 2.5 × 10^{-6}) for a grid-generated turbulence level of 4%. Slanciauskaus and Pedesius found effects of 10% to 15% with turbulence intensities up to 8%, but obtained a 20% increase when the turbulence intensity rose to 14%. Part of this increase was attributed to changes in the mainstream flow as a consequence of the boundary-layer growth. Brown and Burton confirmed Kestin's results; but then, in 1978, Simonich and Bradshaw reported an increase in Stanton number in response to free-stream turbulence. In a more recent study, Blair (1983) reported increases as much as 20% for grid-generated free-stream turbulence of 7%.

Kestin's (1966) found that the principal effect of free-stream turbulence of 3.8% was to move the transition location upstream. He concluded that there was no effect on the fully developed turbulent layer. This study was followed by Kearney et al., at Stanford. Their data are shown in Fig. 1. Kearney's test section consisted of a duct with a flat-plate floor and a top wall which could be adjusted to produce either a uniform velocity flow or an acceleration at a constant value of K. A uniform velocity section followed the accelerating section. Data were taken in all three sections of the plate, for a low-velocity (6-18 m/s) flow in the tunnel.

Kearney's data for low (0.7% and moderate (3.9%) turbulence show no effect on Stanton number. The two data sets are well aligned with each other and agree with the constant-velocity correlation in the approach section. The STAN5 program was fitted with a turbulence kinetic-energy closure and produced results which matched the data: no effect on Stanton number for 4% turbulence. Computer runs for 10% free-stream turbulence, however, indicated a small increase in Stanton number, about 5%. An important aspect of Kearney's work is his use of an enthalpy-thickness Reynolds number to focus on local response, in order to isolate the effect of free-stream turbulence on turbulent boundary-layer heat transfer from its effect on moving the location of transition.

Slanciauskaus and Pedesius tested over a wider range of turbulence levels (1.1% to 13.5%) but tested only the constant-velocity case. Their data are shown in Fig. 2. The effect of turbulence level is clearly discernible and orderly, and suggest an effect approaching 20% on Stanton number. These were the first data to suggest a significant effect due to turbulence.

Simonich and Bradshaw report the largest effects, as shown in Fig. 3. Their data for heat-transfer coefficient represent average values over a flat plate of relatively large size, placed on the centerline of a wind tunnel. It is possible that increasing the turbulence caused a change in the location of the transition zone on the plate. If this occurred, one would expect high turbulence levels to cause the transition location to move upstream, raising the average heat coefficient on the plate by exposing more of the plate to a turbulent boundary layer. If this occurred, it would account for the rather large effects observed.

In 1979, Consigny et al. confirmed that the principal effect of turbulence is to alter the location and extent of transition. Their data showed that changes in turbulence intensity from 1% to 3.6% shifted the transition zone upstream from its original location at x-Reynolds number of 250,000 to a final location at x-Reynolds number of 100,000. This caused drastic changes in the values of h at locations which were originally laminar and finally turbulent, but did not significantly alter the behavior of the already-turbulent region.

In a carefully controlled and documented study, Blair reported that free-stream turbulence has a significant effect on heat transfer for fully turbulent boundary-layer flow. His data (Fig. 4) clearly show both the effect of free-stream turbulence on transition location and on Stanton number in the fully turbulent region. Observe that in the fully turbulent region with free-stream turbulence levels of 4 to 6%,

Stanton number is significantly higher than the correlation given by Kays [ref. 7] (Blair's Ref. 23), for low levels of free-stream turbulence.

At the present writing, it appears likely that free-stream turbulence levels up to 10% cause a proportional increase in heat transfer for constant velocity and for accelerating turbulent boundary layers. Large effects on the average values may result if the turbulence affects the location of transition and if the heat-transfer data are compared (with and without turbulence) at constant x-Reynolds numbers or constant positions on the surface. There is a suggestion (Brown and Martin, 1979) that scale or frequency of the turbulence may be as important as intensity in determining the effect. This suggestion remains to be investigated.

THE PRESENT VIEWPOINT

We treat turbulence as a separate property of the flow, measured by a set of attributes such as its intensity components, scale components, spectra, etc. The hypothesis is that, whenever the free-stream turbulence can disrupt the innermost region of the boundary layer, it will affect the heat transfer. Our expectation is that small-scale and large-scale turbulence may act by quite different means to affect surface heat transfer: small-scale turbulence by diffusion and large-scale by pressure and shear interactions in the near-wall region. To illustrate the hypothesis, consider the following situation: A cubical box whose bottom face is a heat-transfer measuring face and which is provided with some means of violently agitating the air inside the box in a purely random manner. A small amount of electric power provided to the bottom plate, will heat it slightly above the surrounding temperature, not enough to cause any significant buoyant effect, but enough to allow the heat-transfer coefficient to be measured. For the first data point in this thought experiment, the air inside the box is at rest. The situation is one of low-Grashof-number free convection, and one would expect a low value of h. For the second data point, the air is agitated moderately. The random motions of small packets of air near the surface will cause the surface heat transfer coefficient to increase. If the scale of the turbulent motions produced is small compared with the size of the box and the events are randomly distributed inside the box, the average heat-transfer coefficient (over some characteristic length) will be uniform over the entire surface. The average h will increase as the vigor of the mixing inside the box is increased.

It seems reasonable to assume that the process discussed above would have an upper asymptote, determined by the no-slip condition and a Couette flow analysis for very high shear rates on a local area of the surface. As a consequence, the variation in h with turbulence intensity might look like that shown in Fig. 5.

Consider, now, an extension of the tests in which the left and right walls of the box are porous, allowing flow through the box. If the turbulence is zero, the heat-transfer coefficient will be a function of position and velocity given by the usual Reynolds number correlation. Figure 6 represents a typical distribution of heat-transfer coefficient with position along a flat plate for a constant velocity parallel to the plate. The laminar region, the transitional region, and the turbulent region are shown. Figure 7 shows the heat-transfer coefficient (turbulent) at a particular location x as the velocity increases. Both Figures 6 and 7 must be kept in mind while visualizing how the heat-transfer coefficient might vary with turbulence level, position, and velocity.

Now consider a compound case where the turbulence intensity and the free-stream velocity are independent variables. In this case, turbulence is described absolutely in terms of turbulence kinetic energy per unit mass rather than as a fraction of free-stream velocity. Figure 8 shows an operating surface describing the variation of heat-transfer coefficient with turbulence intensity per unit volume and position along a plate for a constant velocity. The individual cases already considered form the bounding planes for this operating surface, and the surface itself is sketched in

with the assumption that the heat-transfer coefficient is a smoothly varying function of two variables, all other factors being held constant. Physical arguments lead to the heat-transfer coefficient asymptotically approaching a uniform high value at very high turbulence. The technical literature contains ample evidence that h asymptotically approaches the zero-turbulence state for the fully turbulent boundary layer. The primary effect of low turbulence levels is to advance the location of transition towards the laminar region, a feature not shown in Fig. 8.

There are important engineering applications of heat transfer corresponding to each of the asymptotic states shown on these operating-surface diagrams. In piston engines, the heat transfer to cylinder walls, piston tops, and cylinder heads corresponds quite closely to a case with high turbulence intensity and zero mean convective velocity. There is evidence in work done by the General Motors Research Laboratories linking the value of the measured heat-transfer coefficient to the turbulence kinetic energy measured within the cylinder. These results generally support the shape shown in Fig. 1 for the effect of turbulence in the absence of mean velocity. At the other extreme, years of research on heat transfer in low-turbulence tunnels have produced data along the "front" face of the operating surface in Fig. 8. The modern gas-turbine engine provides an example of a situation in which there are both very high turbulence intensities and high free-stream velocities. The structure of the typical gas-turbine combustion chamber, even in the absence of turbulence generated by the combustion process itself, produces extremely high turbulence intensities in the gas path which are not related to the mean speed in the throughflow direction in the usual way. Typically, air enters the combustion chamber at high velocity perpendicular to the engine axis to enhance mixing. This induces large-scale, high-intensity turbulence, which is then convected downstream by the mean speed. It seems reasonable to expect that the turbulence components (the fluctuating components of velocity) are not so much related to the mean speed as they are to the pressure drop in the combustion chamber and the heat release rate per unit volume. If this is the case, then, in the first stage stator and rotor in particular, a situation exists in which very high fluctuation velocities and large scales could be encountered. The scale of the turbulence at this location is not that dictated by a well-developed channel flow, but is rather the leftover scale from the injection process and the combustion process.

THE PRESENT EXPERIMENTS

Figure 9 shows the test plate ready for installation in HMT-2, a low-turbulence heat-transfer wind tunnel. This plate will be subjected to the four flow fields described in our introduction. It consists of seven 31.12 cm × 31.75 cm aluminum sections thermally isolated from each other by 0.16 cm balsa strips. Each section has five type J thermocouples embedded in its underside to ensure axial and spanwise temperature uniformity. The sections are individually powered by 30.48 × 30.48 cm Electrofilm patch heaters capable of delivering 10 W/m². The heated sections are preceded by a 50.8 cm unheated leading edge. The entire plate is to be operated to maintain a constant temperature difference between the plate and the free stream while we measure the power required by each section to determine local average h. Turbulence characteristics will be measured by the anemometry systems already discussed. Once our plate has been baseline tested in HMT-2, we plan to test it in the far field of a free jet.

In a free jet, the turbulence intensity and length scale vary differently with position, and a wide range of combinations can be found by sampling different radial and axial positions. Large-scale structures are present in the outer regions of the jet, and the local relative intensities are very high. Positioning a flat plate parallel to the local mean velocity at different radial locations results in a family of related flow fields. As our free-jet test proceeds, we shall design and build our combustor liner simulators.

In our combustor simulators, we plan to achieve independent control of the intensity and scale of the turbulence by using generators which produce an array of high-velocity jets at right angles to the mean flow. We are particularly interested in large-scale turbulent structures (on the order of the boundary-layer thickness or greater) and highly energetic ones. These structures will closely resemble the secondary injection holes used in most gas-turbine combustion chambers. It would be simplistic to say that we are simply going to put a scaled-up burner liner in our tunnel and see what it does to the heat transfer, but that is what it will look like.

REFERENCES

1. Kestin, J., "The Effect of Free-Stream Turbulence on Heat-Transfer Rates," Advances in Heat Transfer, 1966, pp. 31-32.

2. Kearney, D. W., Kays, W. M., and Moffat, R. J., "The Effect of Free-stream Turbulence on Heat Transfer to a Strongly Accelerated Turbulent Boundary Layer," Proc. of the 1970 Heat Transfer and Fluid Mechanics Institute," edited by T. Sarpkaya (Stanford University Press), pp. 3-14 (1970).

3. Slanciauskaus, A., and Pedesius, A., "Effect of Free-stream Turbulence on the Heat Transfer in the Turbulent Boundary Layer," Paper FC(1)-5, Academy of Sciences of the Lithuanian SSR Institute of Physical and Technical Problems of Energetics, Kaunos, USSR (1977).

4. Brown, A., and Burton, R. C., "The Effects of Free-Stream Turbulence Intensity and Velocity Distribution on Heat Transfer to Curved Surfaces," Jour. of Engrg. for Power, Vol. 100, 1978, pp. 159-168.

5. Bradshaw, P., and Simonich, P., "Effect of Free-Stream Turbulence on Heat Transfer through a Turbulent Boundary Layer," J. of Heat Trans., No. 100, No. 4, 1978.

6. Blair, M. F., "Influence of Free-Stream Turbulence on Turbulent Boundary-Layer Heat Transfer - Part I and Part II," ASME Jour. Heat Transf., February 1984.

7. Kays, W. M., Convective Heat and Mass Transfer, McGraw-Hill, New York, 1966, pp. 22 and 224.
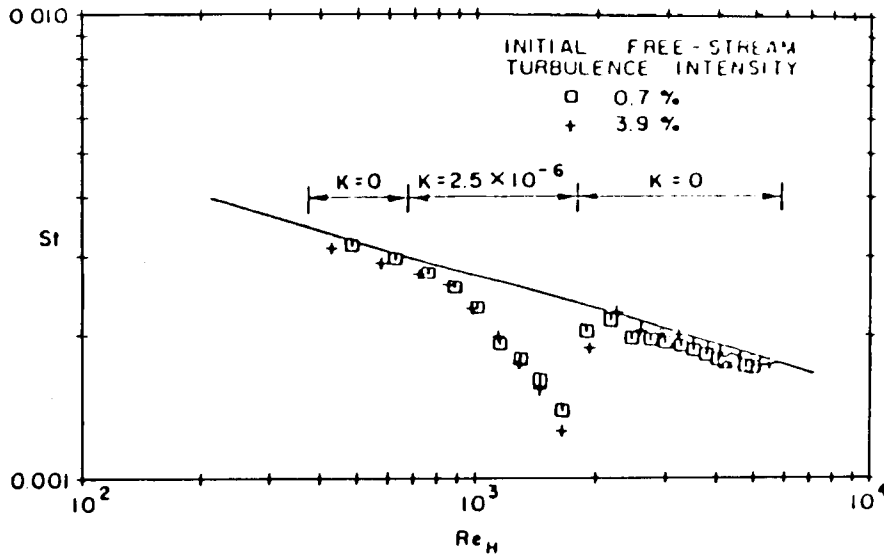
Fig. 1. Effect of free-stream turbulence on heat transfer through turbulent boundary layer with strong acceleration (Kearney et al., 1970).
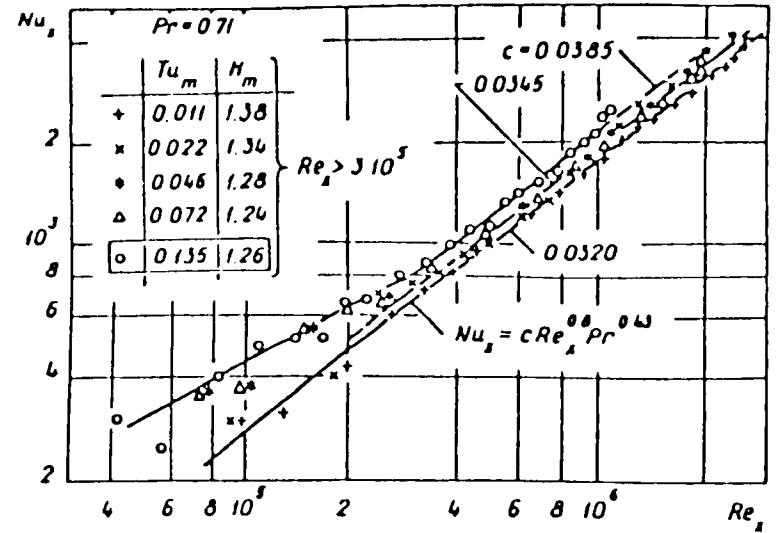

Fig. 2. The effect of free-stream turbulence on heat transfer with no pressure gradient (Slanciauskaus & Pedesius, 1977).
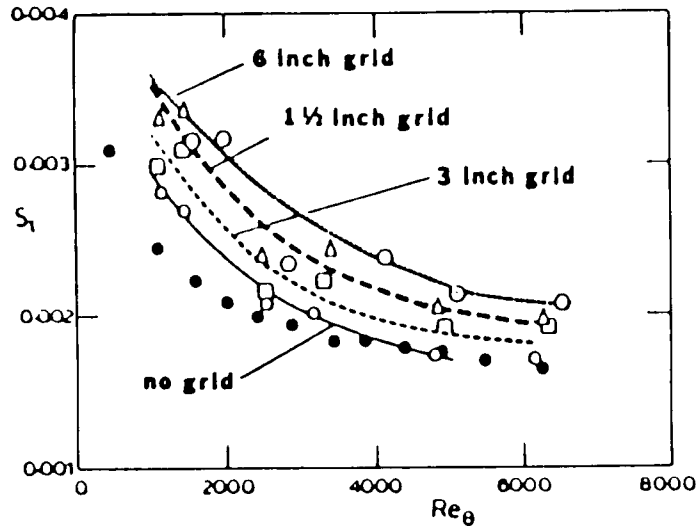

Fig. 3. Simonich & Bradshaw (1978) results concerning the effects of turbulence on heat transfer.
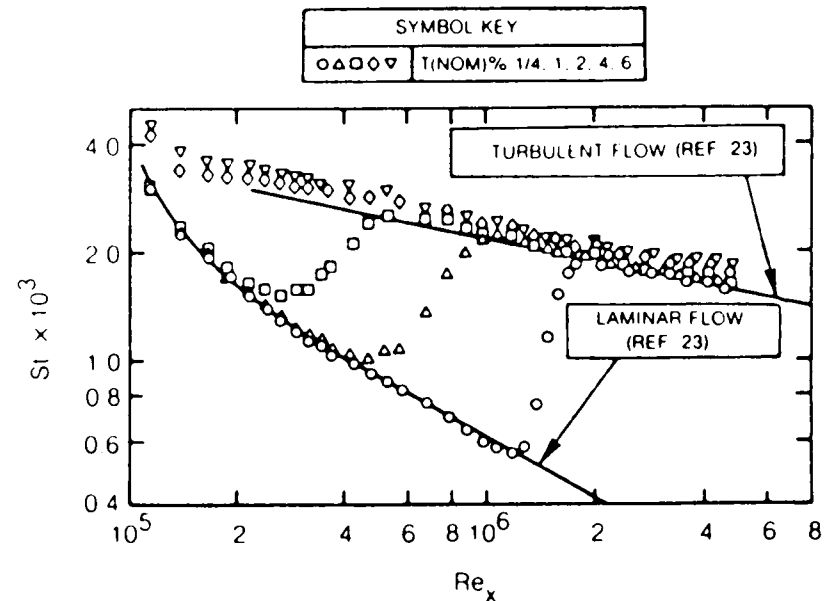

Fig. 4. Heat transfer distributions along a flat plate for five free-stream turbulence levels (Blair, 1983).
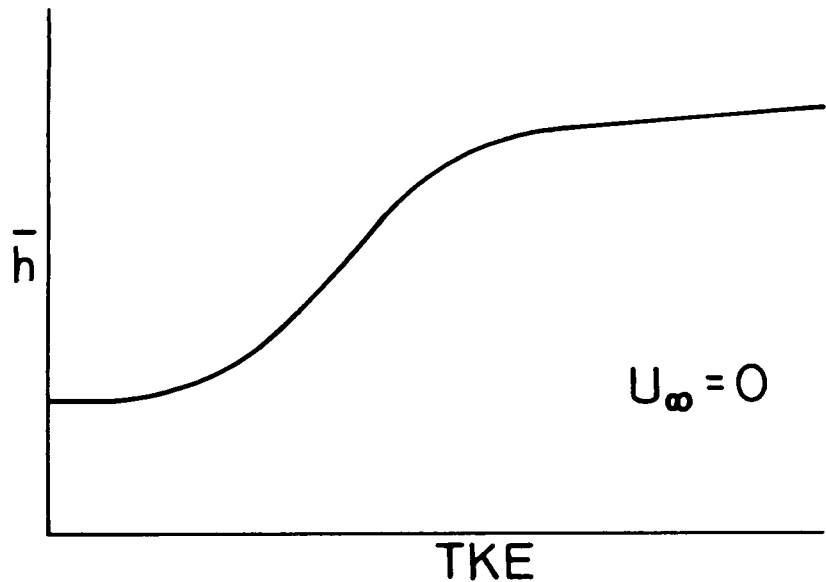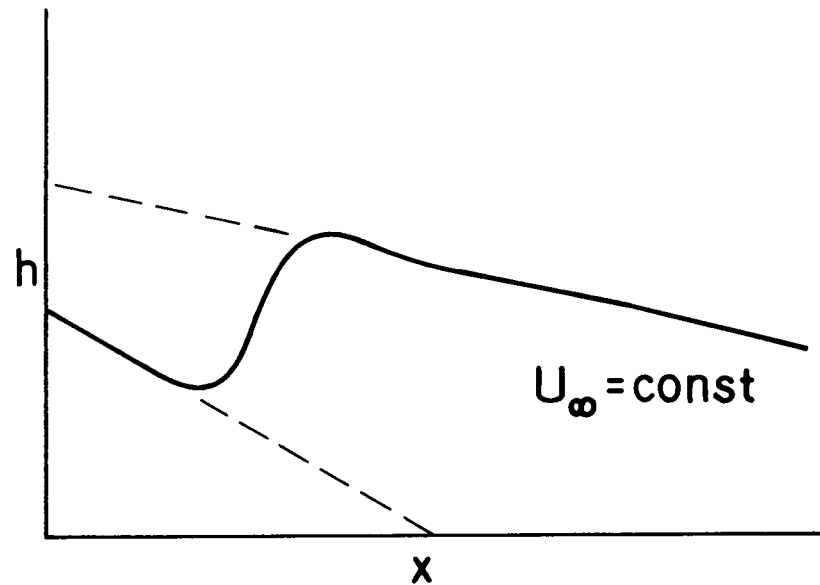
Fig. 5. Sketch of h vs. TKE for $U_\infty = 0$.
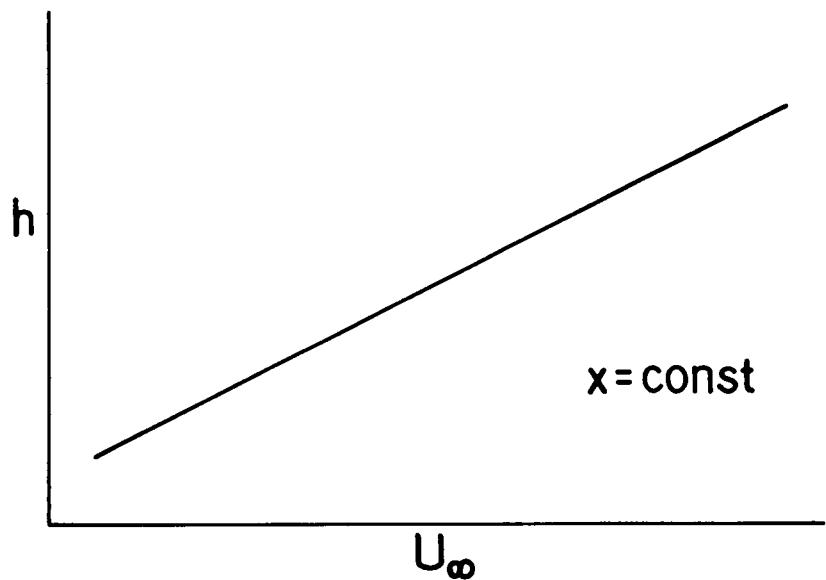

Fig. 6. Sketch of h vs. x for U_∞ = const.
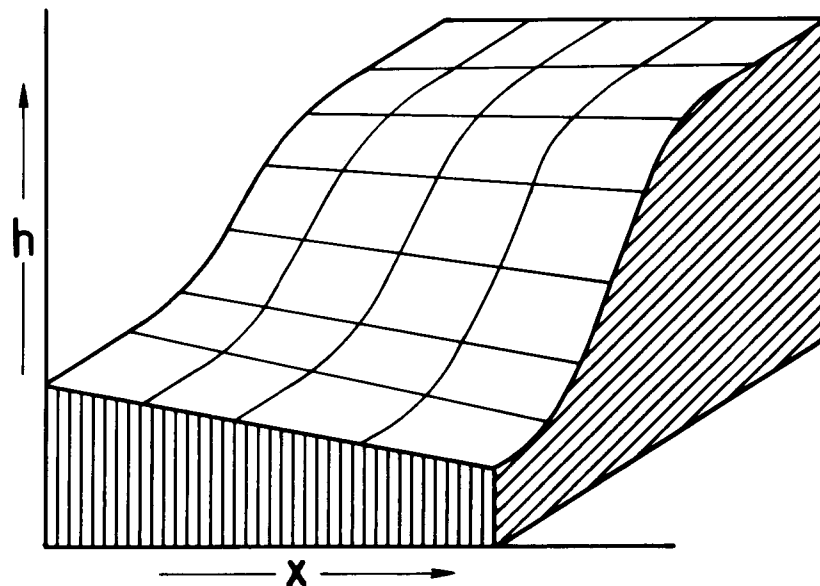
Fig. 7. Sketch of h vs. U_∞ for x = const.

Fig. 8. Sketch of the operating surface h vs. x and TKE at constant free-stream velocity.

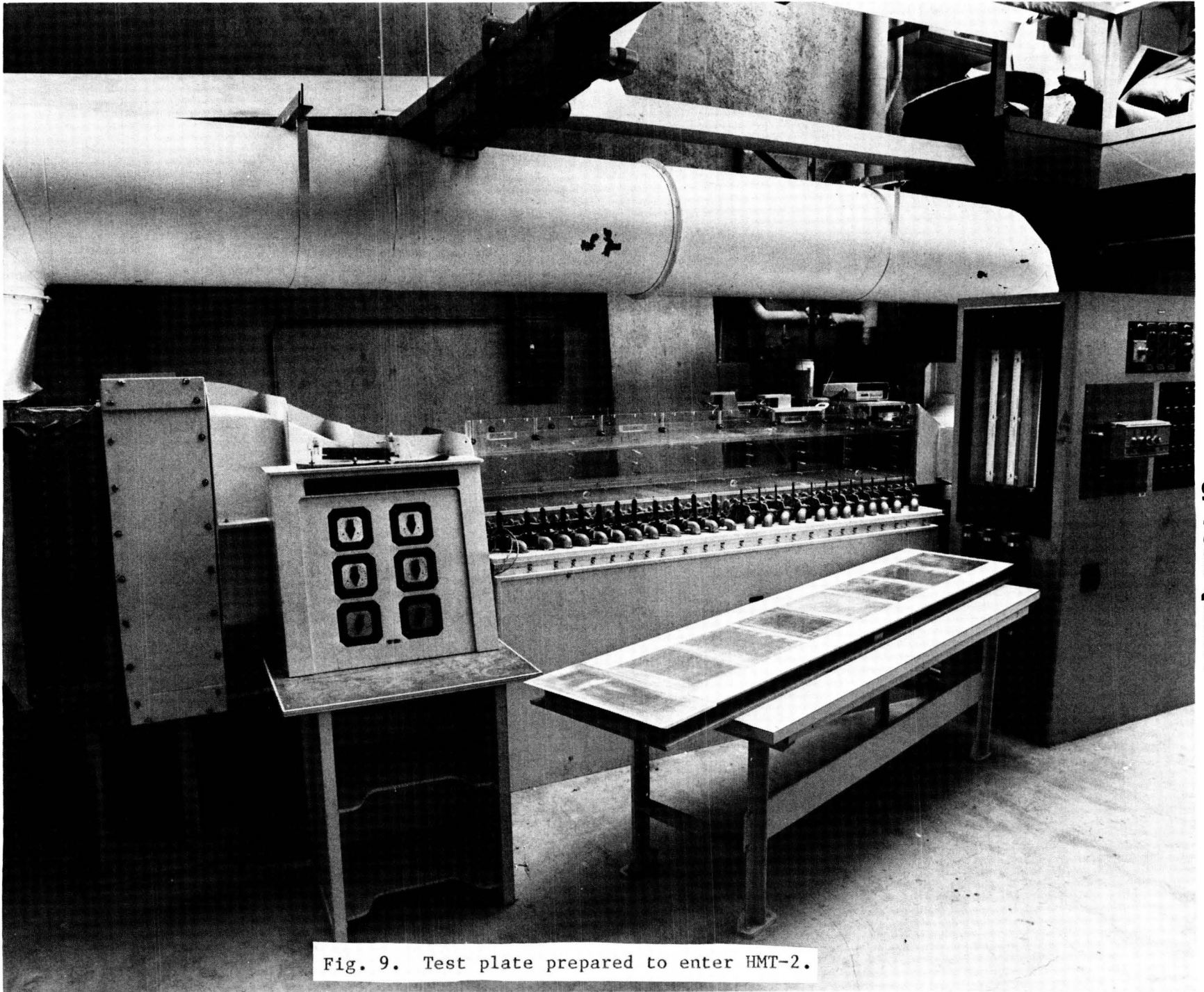Fig. 9. Test plate prepared to enter HMT-2.

GAS FLOW ENVIRONMENTAL AND HEAT TRANSFER NONROTATING 3D PROGRAM*

R. A. Crawford
University of Tennessee Space Institute

N87-11223

OBJECTIVES

The experimental contract objective is to provide a complete set of "benchmark" quality data for the flow within a "large" rectangular turning duct. These data are to be used to evaluate and verify three-dimensional internal viscous flow models and computational codes. The analytical contract objective is to select such a computational code and define the capabilities of this code to predict the experimental results. Details of the proper code operation will be defined and improvements to the code modeling capabilities will be formulated. Separate but coordinated experimental and analytic approaches are in progress to attain the contract objectives.

APPROACH, EXPERIMENTAL

The experimental facility design features modular tunnel components which allow flow measurements every 15° in the 90° bend. The 25.4 cm (10 in) square cross section tunnel is designed with a 13 to 1 area ratio bell mouth contoured to provide uniform flow velocity and is powered by a variable speed, six-bladed fan. The tunnel is designed for incompressible flow and will produce tunnel velocities of 6 to 20 m/sec (20 to 65 ft/sec). These two flow conditions provide laminar and fully turbulent boundary layer profiles at the entrance to the 90° bend. Corresponding Reynolds numbers based on tunnel width of $Re_d = 98 \times 10^3$ at 6 m/sec and $Re_d = 328 \times 10^3$ at 20 m/sec are significantly higher than the Reynolds number values from NASA-CR-3367 by Taylor, Whitelaw and Yianneskis. Thus the boundary layer thickness in this investigation was also significantly less (1/3) than that reported in NASA-CR-3367. This investigation provides baseline curved duct flow data which is closer to real turbine cascade Reynolds numbers and Dean numbers than previously obtained.

The primary instrumentation is designed for non-intrusive flow measurements utilizing a three-dimensional, laser velocimeter (LV) and wall static pressure gages. The LV utilizes two color beams and Bragg diffraction beam splitting/frequency shifting to separate the three simultaneous, orthogonal, vector velocity components. The LV signal processors determine the digital values of velocity from the seed particles crossing the laser beam probe volume. To improve and speed up digital data acquisition, the LV processors are designed around an S-100 bus Z-80 microprocessor which provides on-line, near-real time data reduction. This on-line data as it is acquired and recorded for off-line detailed analysis. To qualify the measurements as "benchmark" data, the LV data will be compared with both pitot probe and hot wire anemometer measurements for flow conditions which permit comparisons.

RESULTS, EXPERIMENTAL

Following careful checkout and calibration of the experimental facility and instrumentation the curved duct was surveyed with the 3D LV system at six stations (inlet, 0°, 30°, 60°, 90°, exit). Extensive tunnel flow quality surveys were completed in the inlet section following "benchmark" calibration of the LV system, pitot-static, and hot wire anemometer. All three measurement systems were calibrated against reference standards and were found to agree within $\pm$ 1% on the entrance section velocity. The LV system was calibrated with a spinning disk reference velocity

---

at 20 m/sec. The pitot-static pressures were read on a precision slant manometer with 13mm of H_2O full scale. The hot-wire system was calibrated in a reference nozzle flow at 30.5 m/sec.' Velocity surveys taken 50.8 cm (20 in) behind the bell mouth exit showed flat velocity profiles $\pm$ 0.5% mean velocity outside of the boundary layer. The mill bed traverse system has demonstrated repeated accuracy of $\pm$ 0.1mm on all three axis movement. Both LV and probe positions are controlled by the computer driven mill bed.

Development and operation of a satisfactory flow seeding system remained a problem during the experimental investigation. Phenolic micro-ballons of equivalent 2-5 micron size were successfully seeded in a water-alcohol slurry and in a fluidized bed air seeder. However the phenolic spheres would become staticly charged and collect on screens and tunnel walls. The operational problems of using the micro-ballons were greater than their advantages of small particle lag. Water droplets were selected because of their good scattering characteristics, clean properties and low cost. However water droplet seed must be in the 2-5 micron size range to prevent serious particle lag problems. It is very difficult to control droplet size as temperature, relative humidity and atmospheric dust influence water droplet size. At high tunnel speeds, 20 m/sec, the influence of centrifugal forces caused some particle lag problems in the Y-component velocity measurements.

The experimental investigation is complete with 3-D velocities surveys at six flow stations, 600 spatial points per station, for two bulk flow velocities of 6 m/sec and 20 m/sec. Since each of the 600 point surveys took several days to accomplish, the complete data set was non-dimensionalized on bulk velocity to eliminate small variations in tunnel speed during the testing. Sample results are shown in Figures 1 and 3 for the 60° station. Due to the thinness of the entrance boundary layer the axial and crossflow velocity developments in the turn are driven primarily by the pressure forces.

APPROACH, ANALYTICAL

The analytical approach involves, first, selecting a computer code capable of solving the Navier Stokes equations with turbulence models for three dimensional internal flow, and adapting it to the experimental geometry and flow conditions. After this, calculations are to be made for laminar flow conditions for unheated flow. Analysis of these calculations will define the grid size and stretching factors required for adequate resolution as well as the values of time steps and smoothing factors required for convergence. Also, any output and graphics capability required for comparison with data is to be developed during this phase. The adequacy of the code with respect to the differencing scheme, adaptability and convergence will be decided in this phase, by comparisons with published experimental and computational data and by grid sensitivity studies. After the grid refinement studies to determine grid sensitivity are completed, computations on the curved duct at conditions corresponding to the UTSI experiment will be performed. The analytic results from these computations will be used in detailed comparisons with experimental data.

RESULTS, ANALYTICAL

The code selected was based on the Beam-Warming algorithm. It is fully elliptic with all inertial terms retained. Both cross-stream viscous terms are retained, and only the stream-wise viscous term is neglected. The code, developed by P.D. Thomas, uses generalized coordinates and was easily adapted to the curved duct case. Extensive comparisons were made with the analytic results published by Briley and McDonald and with experimental data published by Whitelaw et. al. The comparisons were made for laminar flow to avoid uncertainties due to turbulence modeling. Grid refinement comparisons involving doubling the number of points did not significantly effect the

downstream results for the inlet boundary layer profile selected. If a much thinner entrance boundary layer is input the fine grid results may differ from the course grid results.

For the turbulent cases simulating the curved duct experiment, an algebraic eddy viscosity model was used. The sensitivity to initial boundary layer thickness was investigated by comparative runs with 13mm (0.5 in), 25mm (1.0 in) and 51mm (2.0 in) profiles. The 13mm and 25mm solutions were very similar but the 51mm boundary layer was large compared to the tunnel half height and the solution was different. The similarity of the two thin boundary layer solutions especially near the end of the curved duct may indicate an axial numerical diffusion of the boundary layer which would not occur experimentally.

Comparison of the cross-flow and stream-wise velocities at the 60° station from the analytic and experimental cases shows a significant difference. Although the general flow pattern is similar the experimental results show much thinner boundary layers and larger velocity gradients. Figures 1 and 2 compare crossflow velocities at the 60° station. Figures 3 and 4 compare stream-wise velocities at the 60° station. A significant effort remains to complete analysis of all data and explain the differences in theoretical and experimental results.
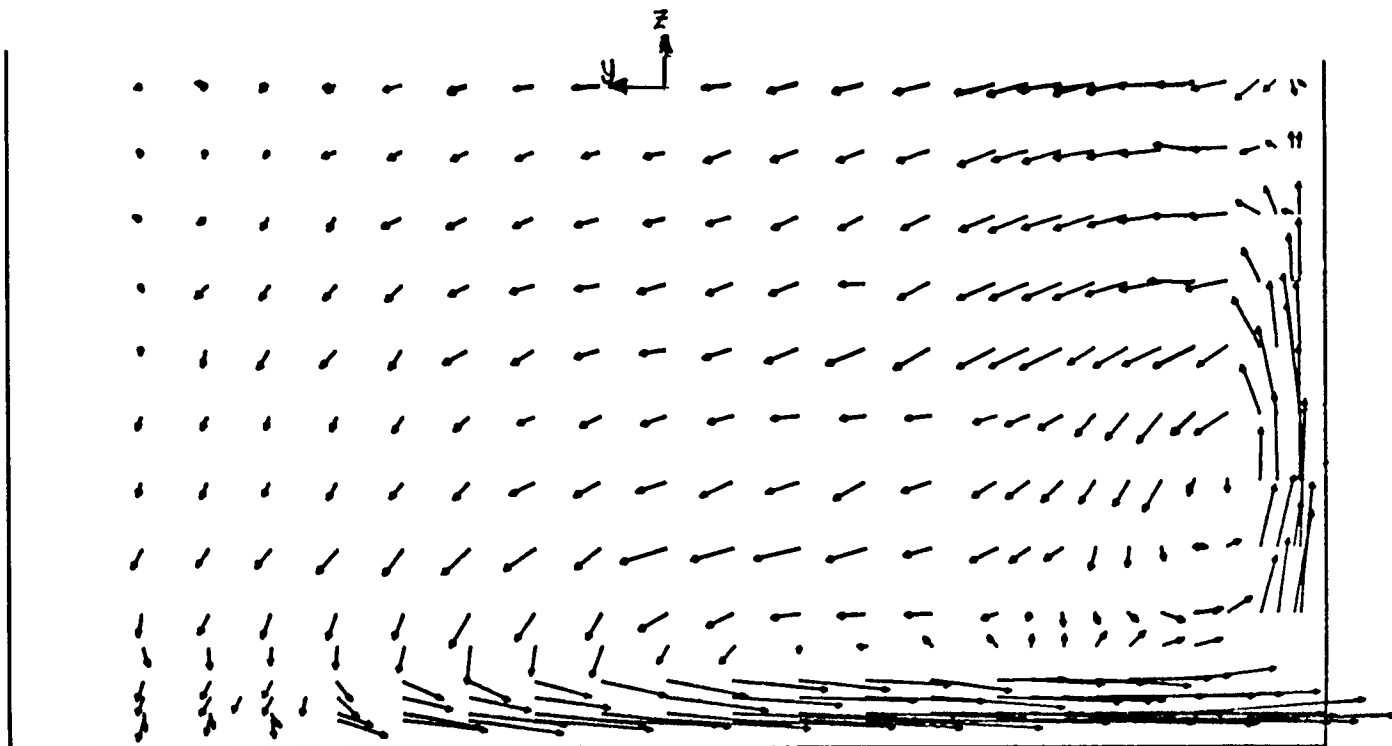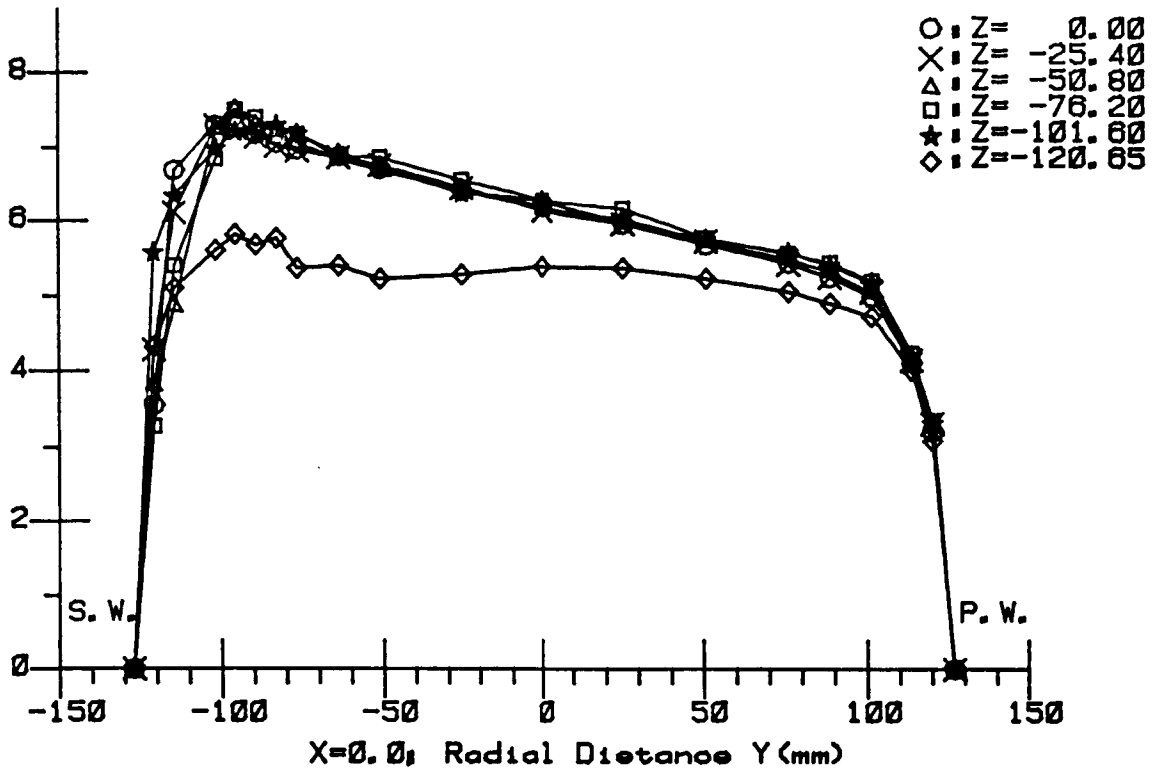
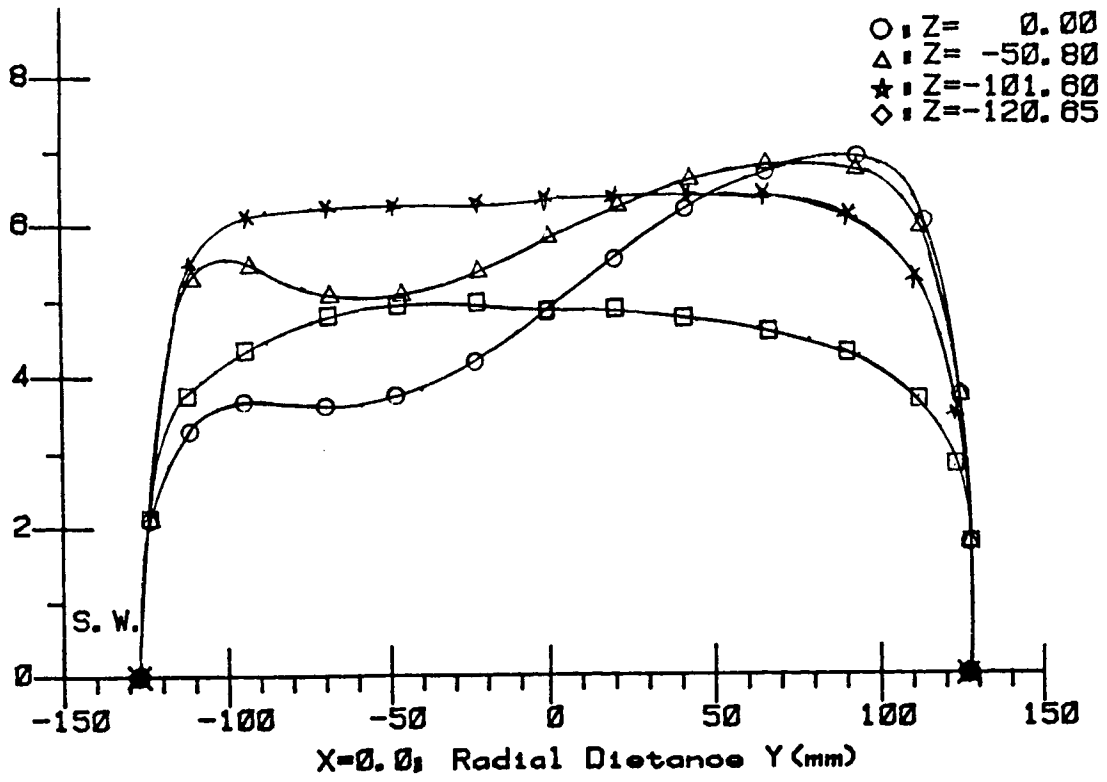EXPERIMENTAL CROSSFLOW VELOCITY, 60° STATION
FIGURE 1.
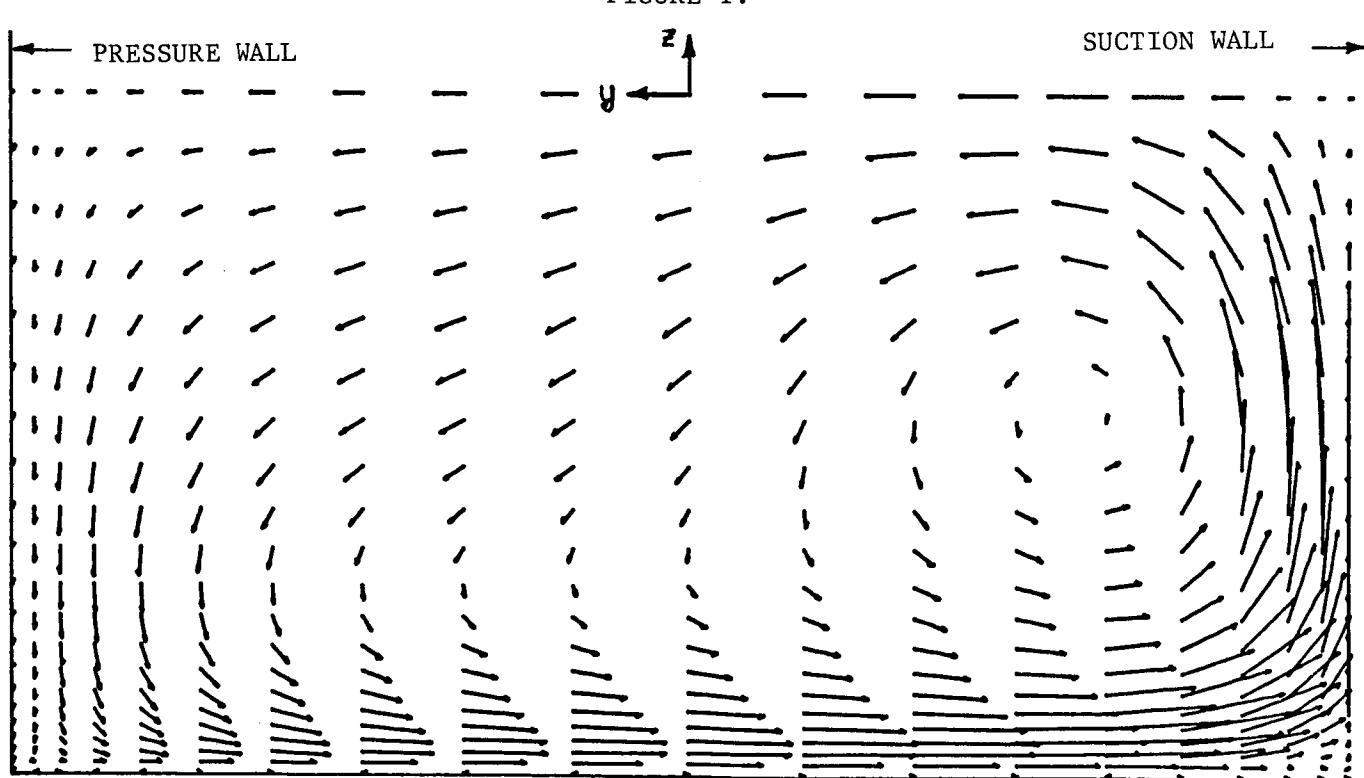
ANALYTIC CROSS FLOW VELOCITY, 60° STATION
FIGURE 2

EXPERIMENTAL AXIAL VELOCITY, 60° STATION
FIGURE 3

ANALYTIC AXIAL VELOCITY, 60° STATION
FIGURE 4

Assessment of a 3-D Boundary Layer Code to Predict Heat Transfer and Flow Losses in a Turbine*

Olof L. Anderson

N87-11224

United Technologies Research Center

The prediction of the complete flow field in a turbine passage is an extremely difficult task due to the complex three-dimensional pattern which contains separation and attachment lines, a saddle point and a horseshoe vortex (Fig. 1). Whereas, in principle such a problem can be solved using full Navier-Stokes equations, in reality methods based on a Navier-Stokes solution procedure encounter difficulty in accurately predicting surface quantities (e.g. heat transfer) due to grid limitations imposed by the speed and size of the existing computers. On the other hand the overall problem is strongly three-dimensional and too complex to be analyzed by the current design methods based on inviscid and/or viscous strip theories. Thus there is a strong need for enhancing the current prediction techniques through inclusion of 3-D viscous effects. A potentially simple and cost effective way to achieve this is to use a prediction method based on three-dimensional boundary layer (3-DBL) theory. The major objective of this program is to assess the applicability, using the data in Ref. 1, of such a 3-DBL approach for the prediction of heat loads, boundary layer growth, pressure losses and streamline skewing in critical areas of a turbine passage. A brief discussion of the physical problem addressed here along with the overall approach and some calculated results is presented in the following paragraphs.

In the present investigation, zonal concepts are utilized to delineate regions of application of 3-DBL theory -- these being the endwall surface, suction surface and pressure surface as shown by the shaded regions of Fig. 1. The zonal concept employed in this investigation implies that there exists a thin region near the surface dominated by wall pressure forces and friction forces so that boundary layer theory is valid provided that the proper inflow conditions and boundary layer edge conditions are applied. Although the pressure surface boundary layer shows weak three dimensional effects on a stationary blade, the endwall surface boundary layer shows strong three dimensional effects due to sweeping of the boundary layer across the passage from the pressure to the suction surface, and the suction surface boundary layer shows strong effects due to the nearby passage vortex which sweeps the boundary layer away from the endwall. These strong three dimensional effects should provide a rigorous test of the zonal application of 3-D boundary layer theory to this problem.

The zonal approach requires three distinct analyses (See Fig. 2). A modified version of the 3-DBL code (Ref. 2), named "TABLET" (Three-Dimen - sional Algorithm for Boundary Layer Equations in Turbulent Flow) is used to analyze the boundary layer flow. This modified code solves the finite difference form of the compressible 3-DBL equations (including the energy equations) in a nonorthogonal surface coordinate system which includes coriolis forces produced by coordinate rotation. These equations are solved using an efficient, implicit, fully coupled finite difference procedure. The nonorthogonal surface coordinate system (including the metrics and direction cosines) is calculated using a general analysis based on the transfinite mapping of Gordon (Ref. 3) which is valid for any arbitrary surface. Experimental data is used to determine the boundary layer edge conditions. In this study the boundary layer edge conditions (free stream velocity and velocity gradients) are determined by integrating the boundary layer edge equations, which are the Euler equations at the edge of the boundary layer, using the known experimental wall pressure distribution. Starting solutions along the two inflow boundaries are estimated by solving the appropriate limiting form of the 3-DBL equations.

Test cases were selected from an experimental study by Graziani et.al.(Ref. 1) of a large scale turbine blade cascade. The solution of the boundary layer flow on the endwall surface is shown on Fig. 3. This solution, which is for the thick boundary layer case of Ref. 1, was started using locally similar solutions of the boundary layer equations along the two inflow boundaries assuming that the cross flow velocity can be neglected. The computational domain extends from just downstream of the saddle point to the blade trailing edge. Fig. 3 shows a comparison of the measured and calculated limiting streamlines, where the calculated streamlines are represented by the direction of the local wall shear force vector. A comparison of the measured and calculated local Stanton number was presented at a previous HOST workshop. Although the inflow conditions along the upstream boundary are not duplicated precisely because of the saddle point, the overall prediction of the flow direction and heat transfer (Stanton number) is encouraging.

The second test case is for the suction surface, described in (Ref. 1) and the results are shown on Figs. 4 through 7. Fig. 4 shows the surface coordinates used in this calculation generated by the coordinate analysis. The computational domain extends from a point downstream of the blade leading edge to the blade trailing edge and from the endwall to the midplane (which is a plane of symmetry). Again, local similarity solutions were used for the inflow boundaries, and the boundary layer edge conditions were obtained from the experimental pressure distribution. Fig. 5 shows the boundary layer edge conditions calculated by the boundary layer edge analysis using the experimental pressure distribution. The plotted velocity vectors show a strong crossflow produced by the passage vortex and no flow across the plane of symmetry. Fig. 6 shows a comparison of the measured wall limiting streamlines with the calculated wall shear force vector. Again the strong cross flow near the blade trailing edge is shown. The magnitude of the wall shear force vector indicates a boundary layer approaching separation near the trailing edge. A comparison of the measured and calculated heat transfer (Stanton number) is shown on Fig. 7. The predictions of flow angle are very encouraging. The predictions of heat transfer are more sensitive to inflow conditions and turbulence modeling and need further refinement.

It is planned to use this analysis for predicting the wall limiting streamlines and heat transfer on the pressure surface of a rotating turbine blade, which includes coriolis forces, to complete this preliminary assessment of the applicability of 3-DBL theory for analysis of viscous flow in a turbine passage using the zonal concept.

References
1. Graziani, R. A., Blair, M. F., Taylor, J. R. and Mayle, R. D.: An Experimental Study of Endwall and Airfoil Surface Heat Transfer in a Large Scale Turbine Blade Cascade, Trans. ASME, J. of Eng. for Power, Vol. 102, No. 2, April, 1980, pp. 257-267.

2. Vatsa, V. N. and Davis, R. T.: The Use of Levy-Lees Variables in 3-D Boundary Layer Flows. NASA CR-112315, January, 1973.

3. Gordon, J. W. and Thiel, L. C.: Transfinite Mappings and Their Application to Grid Generation; Numerical Grid Generation, F. Thompson Ed., Elsevier Science Publishing Co. Inc., 1982.
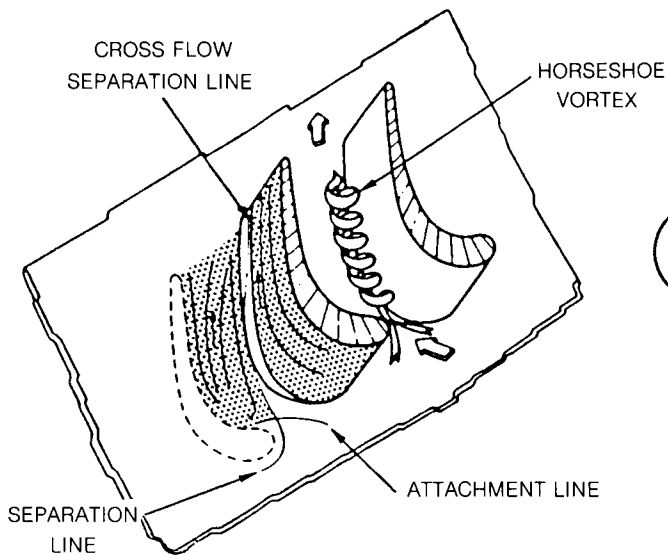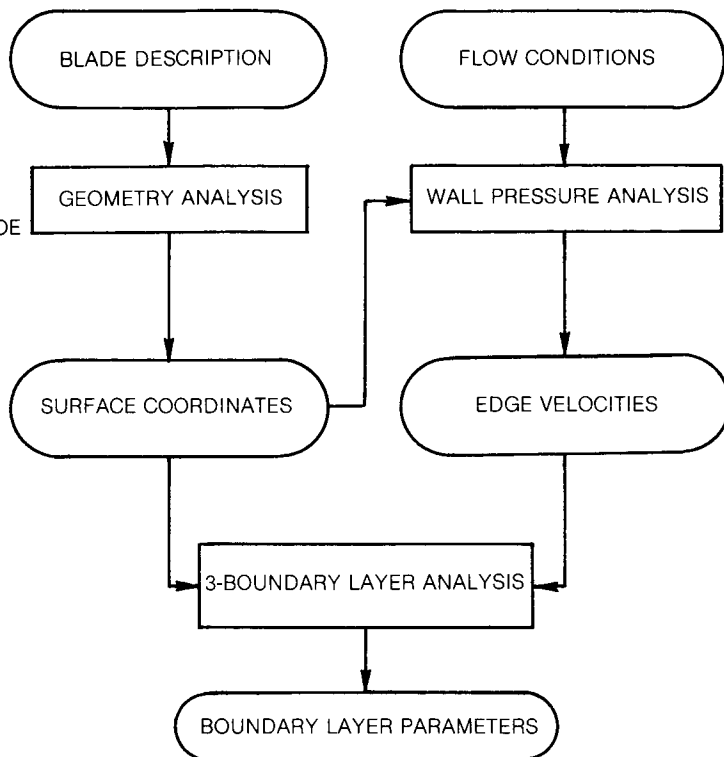
Fig. 1 Flow in a Turbine Passage

Fig. 2 Flow Chart of Geometry, Wall Pressure and 3-D Boundary Layer Analysis

$$Re_{bx} = 5.5 \times 10^5$$

1.5in. INLET BOUNDARY LAYER

MEASURED   CALCULATED

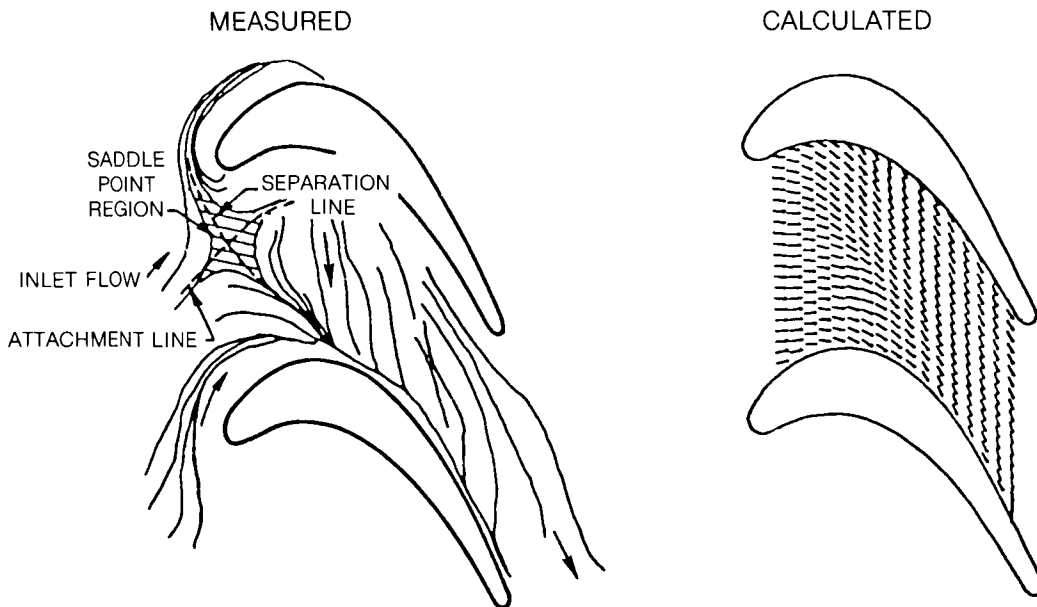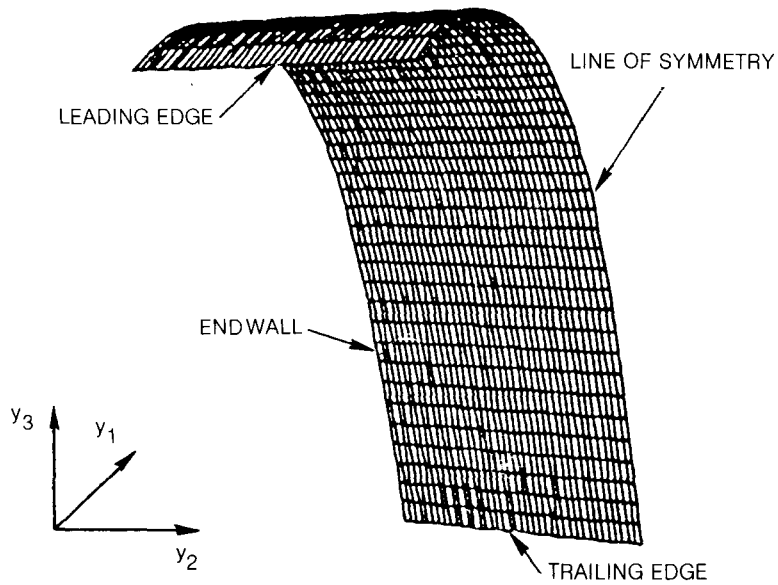**Fig. 3 Comparison of Measured and Calculated Endwall Limiting Streamlines**

Fig. 4 Coordinate System Calculated for Suction Surface
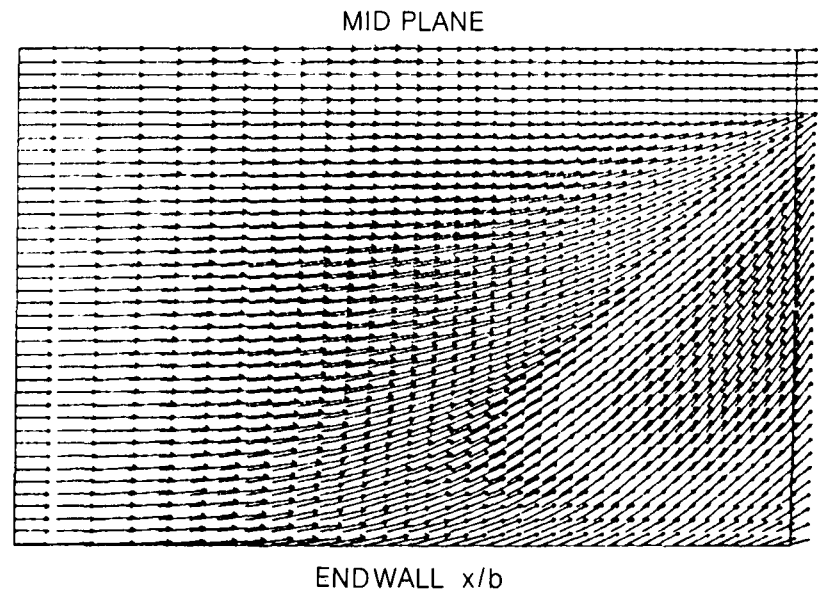

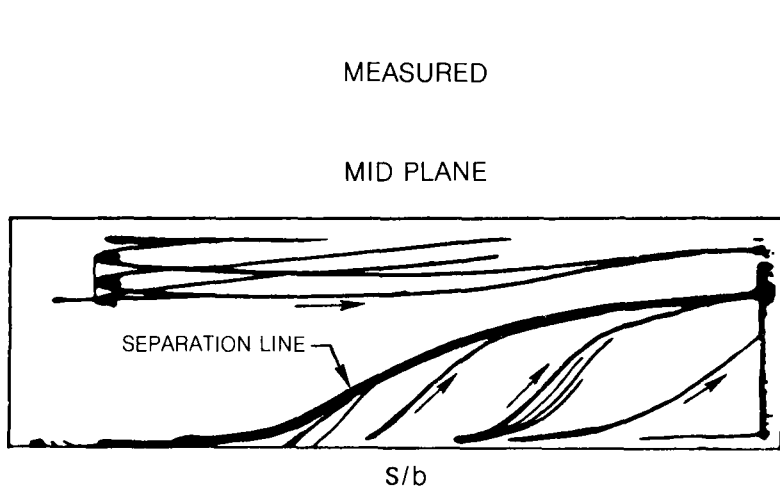**Fig. 5 Calculated Boundary Layer Edge Conditions**

Fig. 6 Measured and Calculated Suction Surface Limiting Streamline

MEASURED
MID PLANE

CALCULATED
MID PLANE

S/b

x/b
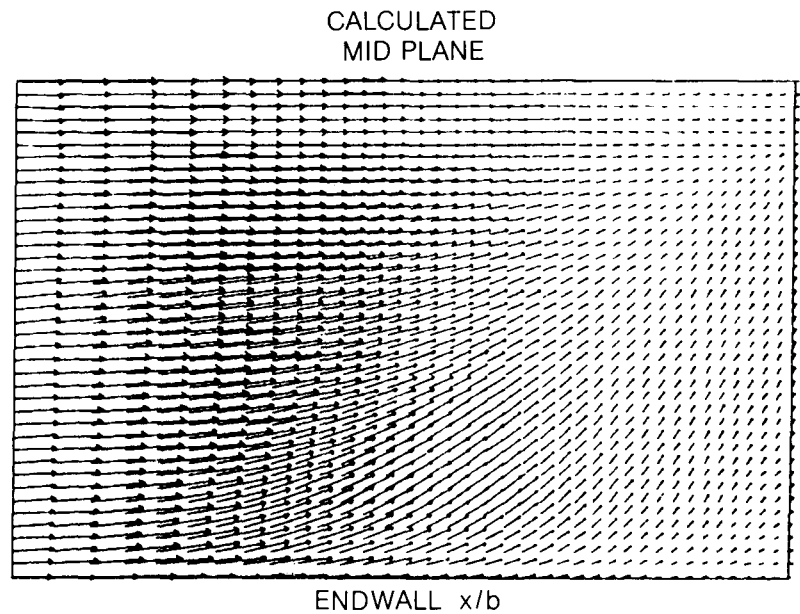
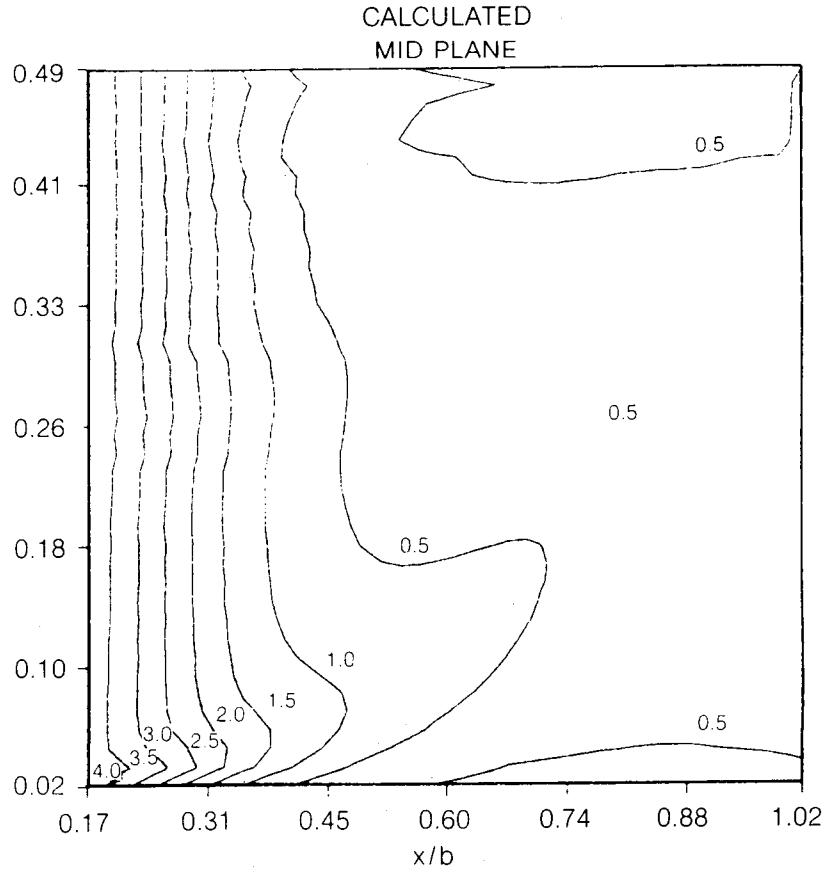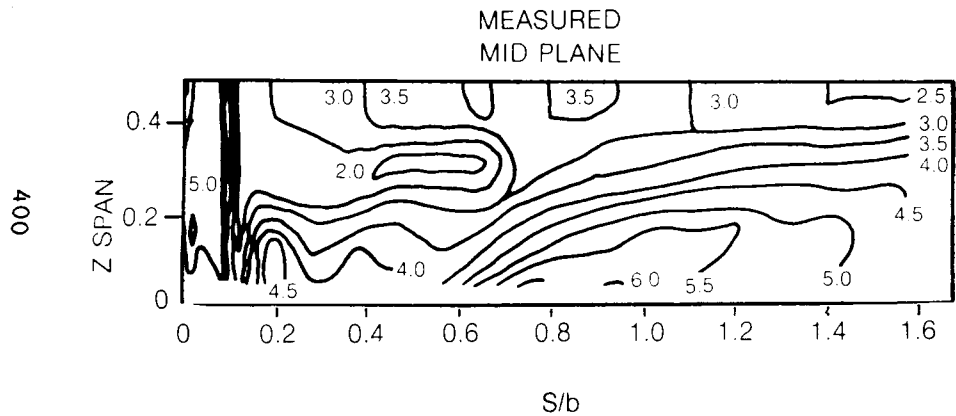**Fig. 7 Measured and Calculated Suction Surface Stanton No. Contours**

COOLANT PASSAGE HEAT TRANSFER WITH ROTATION
A PROGRESS REPORT

F. C. Kopper
United Technologies Corporation
Pratt & Whitney

INTRODUCTION

In current and advanced turbofan engines, increased cycle pressure and temperature are employed to achieve reduced specific fuel consumption and increased thrust/weight ratios. As a result, turbine airfoils are subjected to increasingly higher heat loads which escalate the cooling requirements in order to satisfy life goals. If high turbine efficiency is to be achieved, cooling flow requirements must be kept as low as as possible and the anticipated significant effect on the local metal temperatures (and ultimately on airfoil life) must be evaluated. One way to keep the quantity of cooling air bounded would be to develop more efficient internal cooling schemes. Also, development of reliable methods for predicting the thermal and aerodynamic performance of these schemes would eliminate the necessity of maintaining a safety margin surplus of cooling air.

To predict local metal temperatures, and ultimately blade life, the turbine designer faces the problem of accurately evaluating the local heat transfer from the hot gas to the blades and from the blades to the coolant flowing within the internal passages of the airfoil. Furthermore, for an acceptable design, the heat transfer must be tailored to reduce gradients while at the same time maintaining an appropriate overall level of metal temperature. To accomplish these design goals, the designer must be able to predict local boundary conditions both on the external hot gas side and the internal coolant side of the airfoil walls. These boundary conditions, which consist of the external gas driving temperature (Tg), external heat transfer coefficient (h_{ex}), internal heat transfer coefficient (hc), and internal coolant temperature (Tc), are input to computer prediction codes that solve the heat conduction-structural aspect of the airfoil analysis, subsequently arriving at a life prediction.

To predict local coolant side heat transfer coefficients and coolant temperature rise in the cooling passages of current and advanced turbine blades is difficult because of the complex geometry of the passages and the turbulence-promoting devices that are used to achieve high levels of airfoil cooling effectiveness. Currently the design analysis of airfoil internal passage heat transfer and pressure drop relies on correlations derived for the most part from testing models in a static (non-rotating) environment. Executing tests with rotation is difficult and costly and, as a consequence, there are almost no data in the literature that a turbine designer can use with confidence to account for the effects of rotation on the internal heat transfer coefficients and pressure loss in typical turbine blade designs. Some data are available for smooth tubes over a limited range of relevant parameters, but application of these data to the complicated flow passages of a turbine airfoil would not be appropriate. As a consequence, adjustment factors are generally applied to the static test derived correlations to bring them into nominal correspondence with engine experience. This, in theory, accounts for rotation effects. Design application of computer codes to predict 3D viscous passage flow has been limited because the computer codes are in an early stage of evolution. These codes, however, offer the potential for analyzing arbitrary geometries accounting for all real-world effects.

OBJECTIVE

The objective of this 36-month experimental and analytical program is to develop a heat transfer and pressure drop database, computational fluid dynamic techniques and correlations for multi-pass rotating coolant passages with and without flow turbulators. The experimental effort will be focused on the simulation of configurations and conditions expected in the blades of advanced aircraft high pressure turbines so that the effects of Coriolis and buoyancy forces on the coolant side flow can be rationally included in the design of turbine blades.

EXPERIMENTAL MODEL

The coolant passage heat transfer model features a four-pass serpentine arrangement designed to reflect the passages in a gas turbine blade. A photograph of the partially assembled model is shown in figure 1. The radial passages have a square cross section with 12.7 by 12.7 mm (0.5 by 0.5 in.) dimensions. The model test section surfaces consist of copper segments, 10.7 by 49.3 mm (0.42 by 1.94 in.), which are heated with thin film electrical heaters. The copper segments are separated from each other with 1.5 mm (0.060 in.) strips of G-11 composite material. The copper segments are held in place with a frame constructed of G-10 composite material. G-10 and G-11 were chosen because of the low thermal conductivity and high strength.

The heat transfer coefficients on the test section surfaces are obtained from (a) heat balances on the copper segments and (b) thin film heat flux gages mounted on the segments. Pressure measurements are obtained along the straight sections and in the turns. The model instrumentation with 64 heated segments and 16 pressure measurement locations, is shown in figure 2. The 12 heat flux gages are positioned to determine local heat transfer gradients in the inlet region and on the walls downstream of the first two turns. The electrical leads from the heaters, thermocouples and heat flux gages are brought through hermetically-sealed connectors and sliprings to a computer-based data acquisition system. The pneumatic leads are brought through a leak-tight connector to 16 differential pressure transducers (ZOC model by Scanivalve) and a reference pressure transducer. The electrical signals from these pressure transducers are also routed through the sliprings to the data acquisition system.

DATA REDUCTION

Data acquisition/analysis consists of three general categories: equipment calibration, model heat loss measurement, and heat transfer coefficient calculations. The equipment calibration follows standard experimental procedures.

Next, model heat losses are determined experimentally. The model is brought up to a constant wall temperature, steady-state operating condition with no coolant flow. The energy needed to maintain constant wall temperatures then equals the energy conducted through the model walls to the environment. These values are normalized by the temperature difference between the heated copper walls and the model exterior to account for slight variations in environmental conditions during testing. This difference represents the driving gradient for conduction losses and is measured for each test.

For each copper element the net energy convected to the fluid is calculated by subtracting the electrical line losses and conducted heat losses from the total energy supplied. Bulk fluid temperatures are then calculated based on an energy balance for each flow path section as follows:

$$T_{b_{out}} = \frac{q_{net, \, 4 \, walls}}{\dot{m}c_p} + T_{b_{in}}$$

where the model inlet bulk temperature is measured. Once bulk fluid temperatures are determined, heat transfer coefficients are calculated from the equation

$$h = \frac{q_{net, \, wall}}{A \, (T_w - T_b)}$$

where T_b is the average of the inlet and exit bulk temperatures. Thus heat transfer coefficients are calculated for each individual copper wall element. This quantifies local heat transfer processes and helps isolate local effects of rotation.

RESULTS

To date experimental heat transfer and pressure drop results have been obtained for stationary conditions (no model rotation). This data will serve as the baseline for assessing the impact of rotation and buoyancy effects. Figure 3 presents the heat transfer results obtained for a Reynolds number of 25,000 which is a representative nominal value for airfoil cooling passages. This figure shows that the heat transfer downstream of the entrance and turns decays monotonically to approximately the level (marked by arrows) for fully developed flow in a square duct as established by Lowdermilk, et al. (ref. 1). The expected periodicity from pass-to-pass is achieved.

Heat transfer in the turns is approximately 2 to 2 1/2 times that of fully developed flow levels. There is no heat transfer data in the literature with which to directly compare the current results. Sahm and Metzger (ref. 2) have found heat transfer levels around 2 to 2 1/2 times fully developed values for 180-degree square cornered bends. This is in agreement with the current results. Figure 4 compares the entry length behavior for the current data with results from the literature. For the first outward straight passage the four data points (solid circles) include the guard heater region and the following three straight segments. As the flow enters the channel from the plenum it passes through a screen and begins boundary layer development. Previous measurements just downstream of the screen showed the velocity profile of the core flow to be similar to fully developed turbulent flow. Because the near wall shear flow characteristics would be similar to those of developing flow, it would be expected that the entry length heat transfer behavior be in reasonable agreement with results for combined hydrodynamic and thermal boundary layer development. This is supported by the comparisons of figure 4 (Boelter et al, ref. 3, and Aladyev, ref. 4 for pipe flow; Yang and Liao, ref. 5, for square duct flow). Heat transfer levels downstream of the first bend would be expected to be lower than for the first passage. This, again, is in agreement with observation. A creditable correlation for the effects of the bend secondary flows on the downstream heat transfer is not available.

Pressure drop measurements are shown in figure 5 for a non-heated stationary test condition at the same Reynolds number as for the heat transfer results but at a lower pressure. The results indicate a negligible pressure drop in the straight sections which is in agreement with predictions and about 0.8 dynamic heads pressure drop through each turn. This agrees with a value of 0.71 dynamic heads determined from reference 6 for connected 90-degree square elbows. The slightly higher loss for the model is believed to result from the diffusions and accelerations the flow experiences as it negotiates the area variations in the turns.

THREE-DIMENSIONAL VISCOUS FLOW COMPUTATIONS

Computation of heat transfer and pressure drop for the reported experimental conditions employing a generalized aerothermal fluid dynamic solver for three-dimensional elliptic, turbulent, steady flows has been started; results are currently not available.

TESTING WITH ROTATION

Table I defines the planned test points for the first phase (smooth passage investigation) of this program and reflects the domain of interest for turbine blade coolant passages.

REFERENCES

1. Lowdermilk, W.H.; Weiland, W.F.; and Livingood, I.N.: Measurement of Heat-Transfer and Friction Coefficients For Flow of Air in Noncircular Ducts at High Surface Temperatures. NACA Research Memorandum RME53J07, January 25, 1954.

2. Sahm, M.K.; and Metzger, D.E.: Effects of Turn Geometry Parameters on Heat Transfer Around Smooth Wall 180° Turns in Rectangular Ducts of Aspect Ratio 1.0 to 3.0. Technical Report ERC-R-83029, Mechanical and Aerospace Engineering, Arizona State University, July 1983.

3. Boelter, L.M.K.; Young, O.; and Iversen, H.W.: NACA TN1451, Washington, July 1948.

4. Aladyev: I.T. Experimental Determination of Local and Mean Coefficients of Heat Transfer For Turbulent Flow in Pipes. NACA Technical Memorandum 1356, 1954.

5. Yang, J.W.; and Liao, N.: An Experimental Study of Turbulent Heat Transfer in Converging Rectangular Ducts. Paper No. 73-WA/HT-27. ASME Journal of Heat Transfer. November 1973.

6. American Society of Heating Refrigeration and Air Conditioning Engineers: Handbook of Fundamentals, 1972, p. 472.

TABLE I

Test Matrix

Test No.	Basic Dimensionless Parameters				Secondary Dimensionless Parameters				Comments
	R_e	R_o	$\frac{\Delta T}{T_{in}}$	$\frac{H}{d}$	$\frac{\Delta\rho}{\rho}$	$\frac{\Omega H}{V}$	$\frac{Gr}{Re^2}$	$Gr_{max} \times 10^{-8}$	
1	25,000	0	0.14	--	0	0	0		⎫
2	12,500	0	0.14	--	0	0	0		⎬ Nonrotating
3	50,000	0	0.14	--	0	0	0		⎭
4	25,000	0.210	0.14	52	1.53	0.32	2.01		Baseline
5	12,500	0.210	0.14	52	1.53	0.32	0.50		⎫ R_e Varied
6	50,000	0.210	0.14	52	1.53	0.32	8.03		⎭
7	25,000	0.420	0.14	52	3.06	1.28	8.03		⎫ R_o Varied
8	25,000	0.105	0.14	52	0.76	0.08	0.50		⎭
9	25,000	0.210	0.07	52	1.53	0.16	1.00		⎫ $\Delta T/T$ Varied
10	25,000	0.210	0.21	52	1.53	0.48	3.01		⎭
11	25,000	0.210	0.14	34	1.00	0.21	1.31		H/d Varied
12	25,000	0.210	0.14	52	1.53	0.32	2.01		⎫ α Varied
13	25,000	0.210	0.14	52	1.53	0.32	2.01		⎭

Dimensionless Parameters

Reynolds number, Re	$\rho V d_H/\mu = V d_H/\nu = \dot{m} d_H/(A\mu)$
Rotation number, Ro	$\Omega d_H/V$
Density or temperature ratio	$\Delta\rho/\rho$, $\Delta T/T$
Radius ratio	H/d_H
Rotational Grashof number, Gr	$Ro^2 Re^2 (\Delta T/T)(H/d_H)$

PHOTOGRAPH OF UNINSTRUMENTED COOLANT PASSAGE HEAT TRANSFER MODEL

TRAILING EDGE (+ Ω) PLANE TEST SECTIONS REMOVED
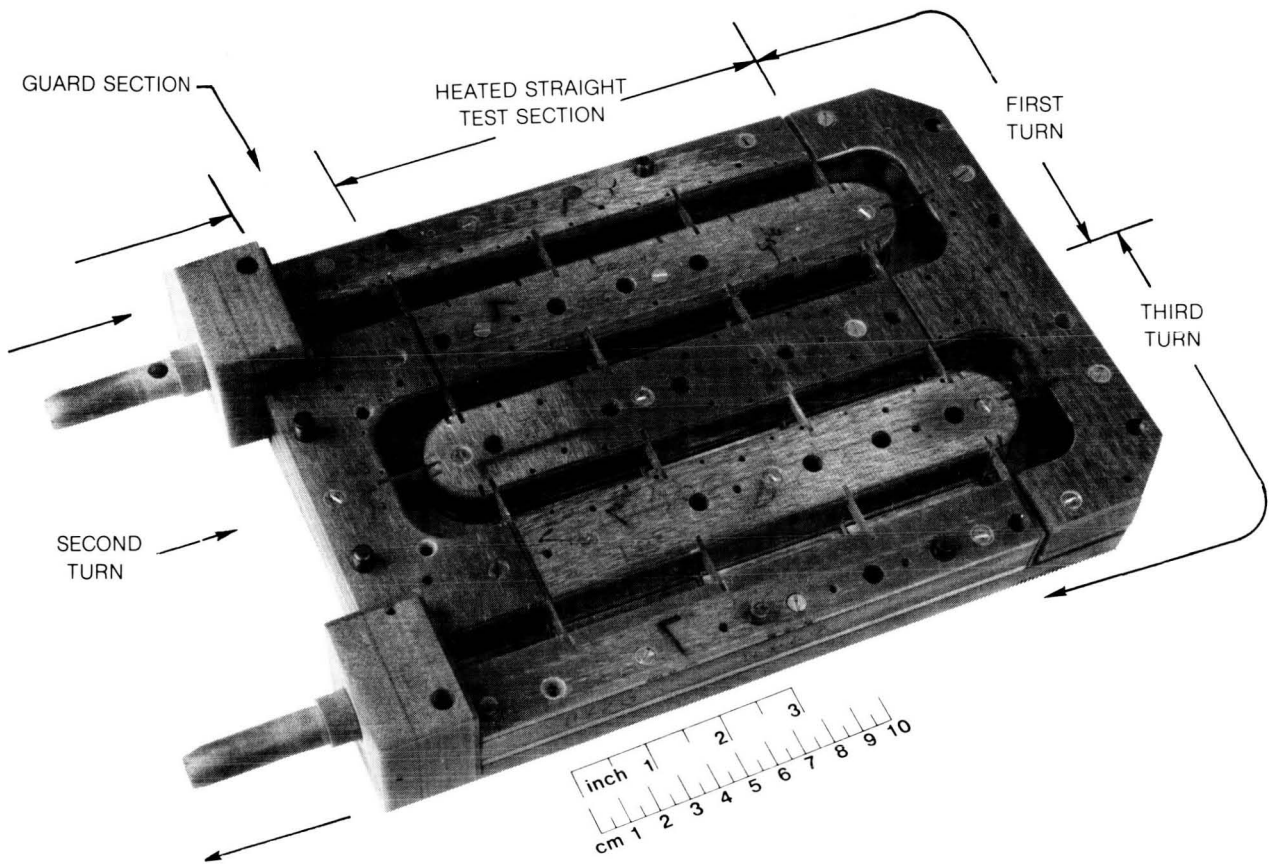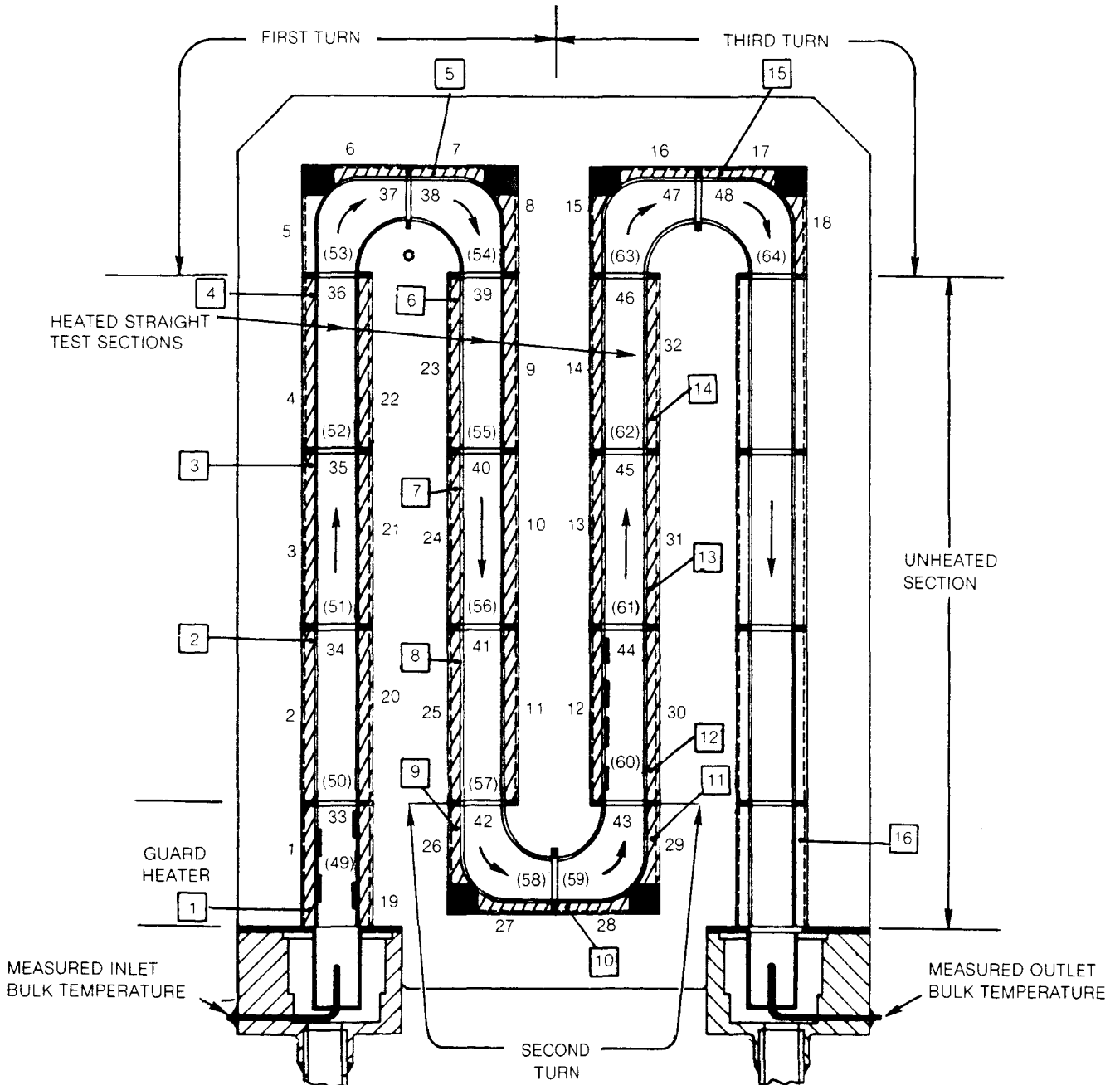
**ORIGINAL PAGE IS
OF POOR QUALITY**

Figure 1

84—7—37—2

Figure 2

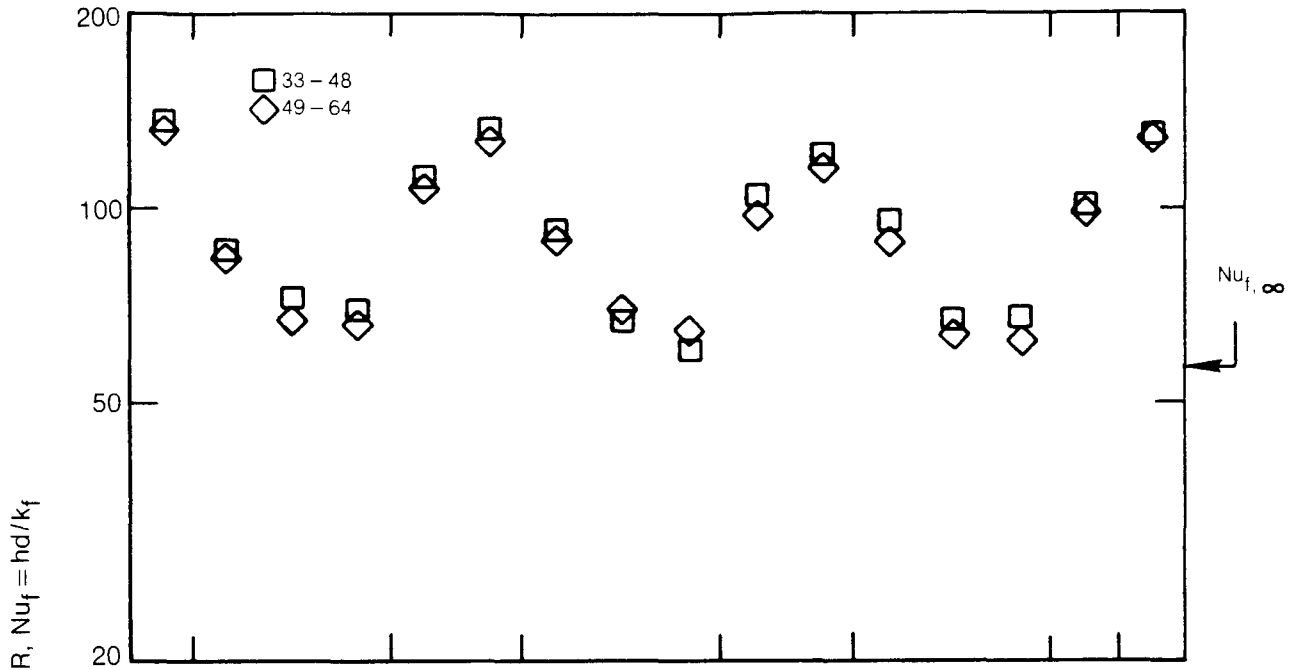# HEAT TRANSFER RESULTS

$\Omega = 0.0$ rpm
P = 146.9 psia
$\dot{m} = 0.0131$ lb/sec

$T_{wall} = 618°R$
$T_{b, inlet} = 538°R$
$\Delta T/T = 0.149$

$Re_{f, inlet} = 25260$
$R_o = 0.0$
$H/d_h = $ —

Figure 3

$Re_{f, inlet} = 25,260$

$Nu_{f, \infty} = 0.0174 \, Re_f^{0.8}$

YANG & LIAO: SQUARE DUCT
MEASURED DATA Re = 23,500

BOELTER, YOUNG & IVERSEN:
COMBINED HYDRODYNAMIC
+ THERMAL DEVELOPMENT
Re = 50,000

ALADYEV: CIRCULAR DUCT EXPERIMENT
WITH WATER, Re = 20,000

● FIRST OUTWARD STRAIGHT
SEGMENT — 4 WALL AVERAGE

■ INWARD STRAIGHT
SEGMENT — 4 WALL AVERAGE

| RANGE OF DATA

WALL SECTION NUSSELT NUMBER $\dfrac{Nu_f}{Nu_{f, \infty}}$

FULLY DEVELOPED FLOW NUSSELT NUMBER

X/D_h
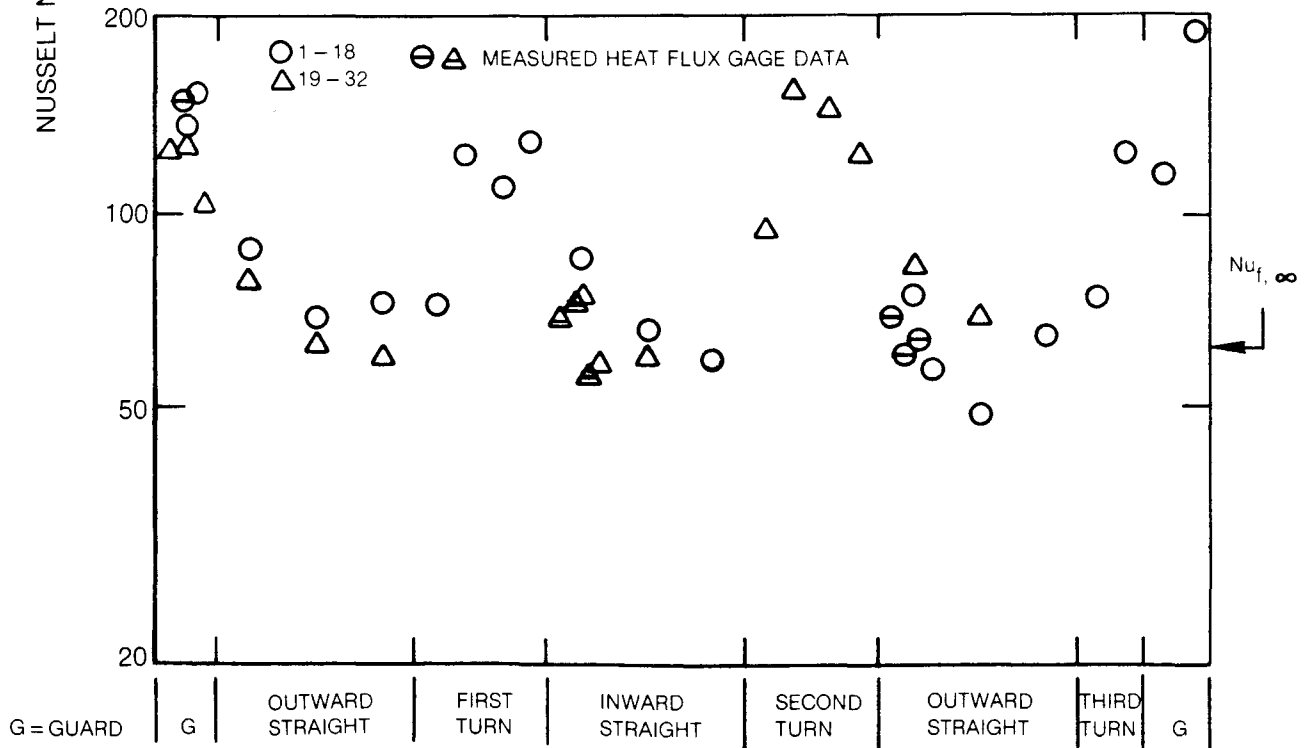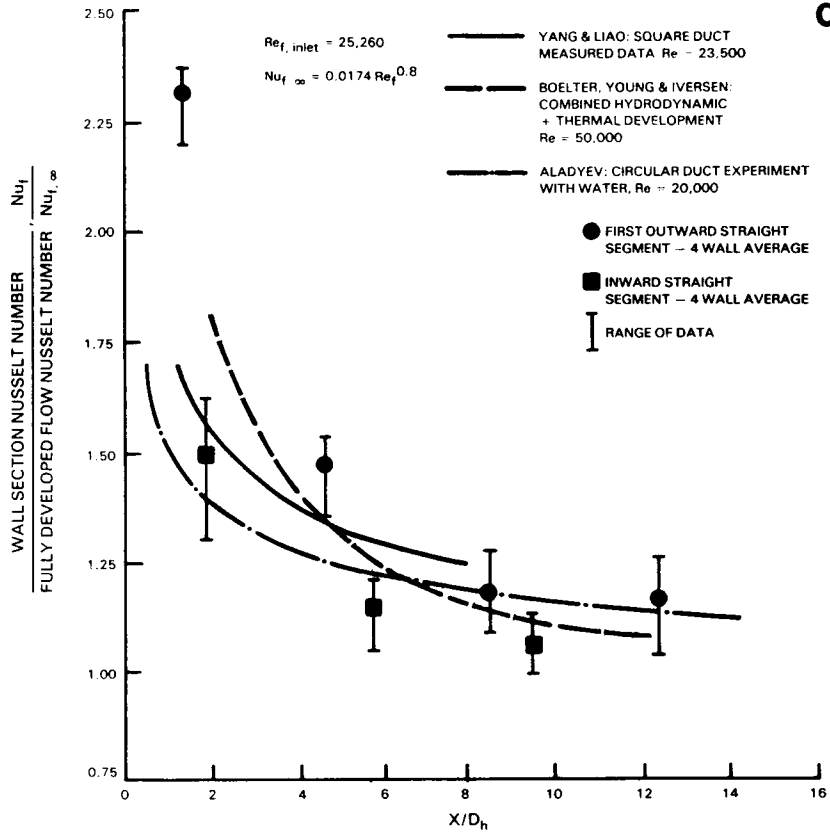
Figure 4   Entry Length Heat Transfer Comparison

PRESSURE DROP RESULTS

$\Omega = 0$ rpm
$P = 36.2$ psia
$\dot{m} = 0.0123$ lb/sec

$\Delta T = 0.0\,°F$
$Re = 25045$

$V_{in} = 39.3$ ft/sec
$Q_{in} = 4.38$ psf $= 0.843$ in H_2O

$\dfrac{\Delta P}{Q_{in}}$

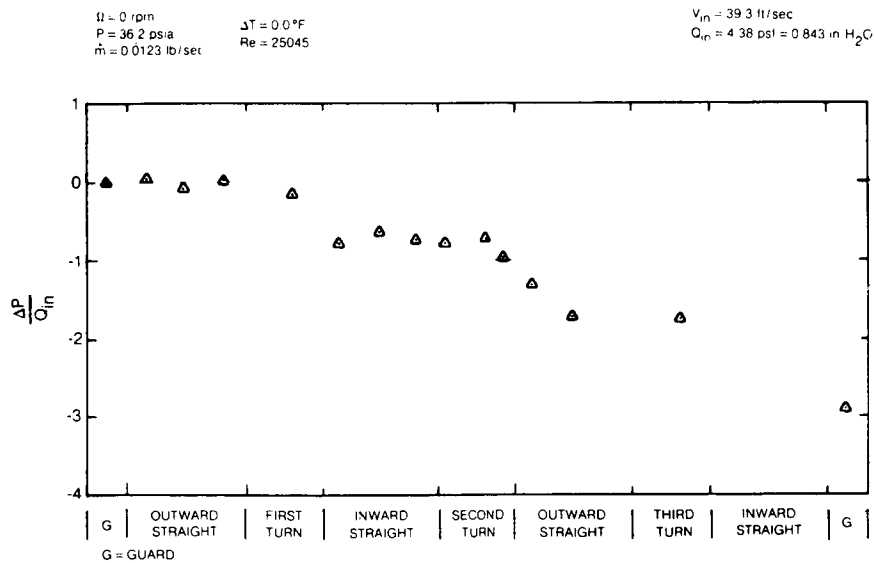| G | OUTWARD STRAIGHT | FIRST TURN | INWARD STRAIGHT | SECOND TURN | OUTWARD STRAIGHT | THIRD TURN | INWARD STRAIGHT | G |

G = GUARD

Figure 5

409

CONCLUDING REMARKS: HOST THIRD ANNUAL WORKSHOP

Daniel E. Sokolowski
National Aeronautics and Space Administration
Lewis Research Center

As reported at this workshop, the HOST Project activities are well underway and are producing results. Contractor annual and final reports are becoming available and their number will increase dramatically in the future. Workshops such as this will continue on an annual basis. The HOST Fourth Annual Workshop is tentatively scheduled for October 22-23, 1985.

The nature of the problem of durability requires not only the involvement of numerous disciplines, as discussed in the opening remarks, but also that the research be interdisciplinary. The HOST Project to date has been very successful and is due in part to unprecedented teamwork at Lewis, at the contractors, and between contractors and universities. In addition, the HOST Project is recognized for the value of focused as well as interdependent research when compared with generic, independent base R&T activities. The problem being addressed has much influence in the advocation and successful implementation of such a Project, however.

To date, $18.6 million has been invested in HOST. In FY 1985 another $9.2 million will be spent. The present plan for FY 1986-87 is for $9.2 million per year. The final year of the Project (FY 1988) has a planned budget of $6.0 million.

Finally, I want to say "Thank You" to the HOST Project Team for a job well done in conducting this workshop. In particular, I want to thank the contractor speakers; the Subproject Managers for being session chairmen; and my Assistant Manager, Bob Ensign, and our Administrative Assistant, Joanne Flowers, for helping organize and coordinate the multitude of efforts required.

1. Report No.	2. Government Accession No.	3. Recipient's Catalog No.
NASA CP-2339		

4. Title and Subtitle	5. Report Date
Turbine Engine Hot Section Technology 1984	October 1984
	6. Performing Organization Code
	533-04-1A

7. Author(s)	8. Performing Organization Report No.
	E-2267
	10. Work Unit No.

9. Performing Organization Name and Address	11. Contract or Grant No.
National Aeronautics and Space Administration Lewis Research Center Cleveland, Ohio 44135	
	13. Type of Report and Period Covered

12. Sponsoring Agency Name and Address	Conference Publication
National Aeronautics and Space Administration Washington, D.C. 20546	14. Sponsoring Agency Code

15. Supplementary Notes

16. Abstract

On October 23 and 24, 1984, the Turbine Engine Hot Section Technology (HOST) Project Office of the NASA Lewis Research Center sponsored a workshop to discuss current research pertinent to turbine engine hot section durability problems. Presentations were made concerning the hot section environment and behavior of combustion liners, turbine blades, and waves. The presentations were divided into six sessions entitled Instrumentation, Combustion, Turbine Heat Transfer, Structural Analysis, Fatigue and Fracture, and Surface Protection. The principal objective of each session was to disseminate research results to date, along with future plans. Topics discussed included modeling of thermal and fluid flow phenomena, structural analysis, fatigue and fracture, surface protective coatings, constitutive behavior, stress-strain response, and life prediction methods. Researchers from industry, academia, and government presented results of their work sponsored by the HOST Project. This publication contains extended abstracts and visual material presented during the workshop.

17. Key Words (Suggested by Author(s))

Turbine Engine Technology (HOST); Life prediction; Combustor liners; Turbine airfoils; Material behavior; Aircraft engines; Durability analysis methods

19. Security Classif. (of this report)	20. Security Classif. (of this page)	21. No. of pages	22. Price*
Unclassified	Unclassified	420	A18